NASA CR-66137

VOLUME V SUBSYSTEM AND TECHNICAL ANALYSES

BOOK 3 # TELECOMMUNICATIONS, RADAR SYSTEMS and POWER

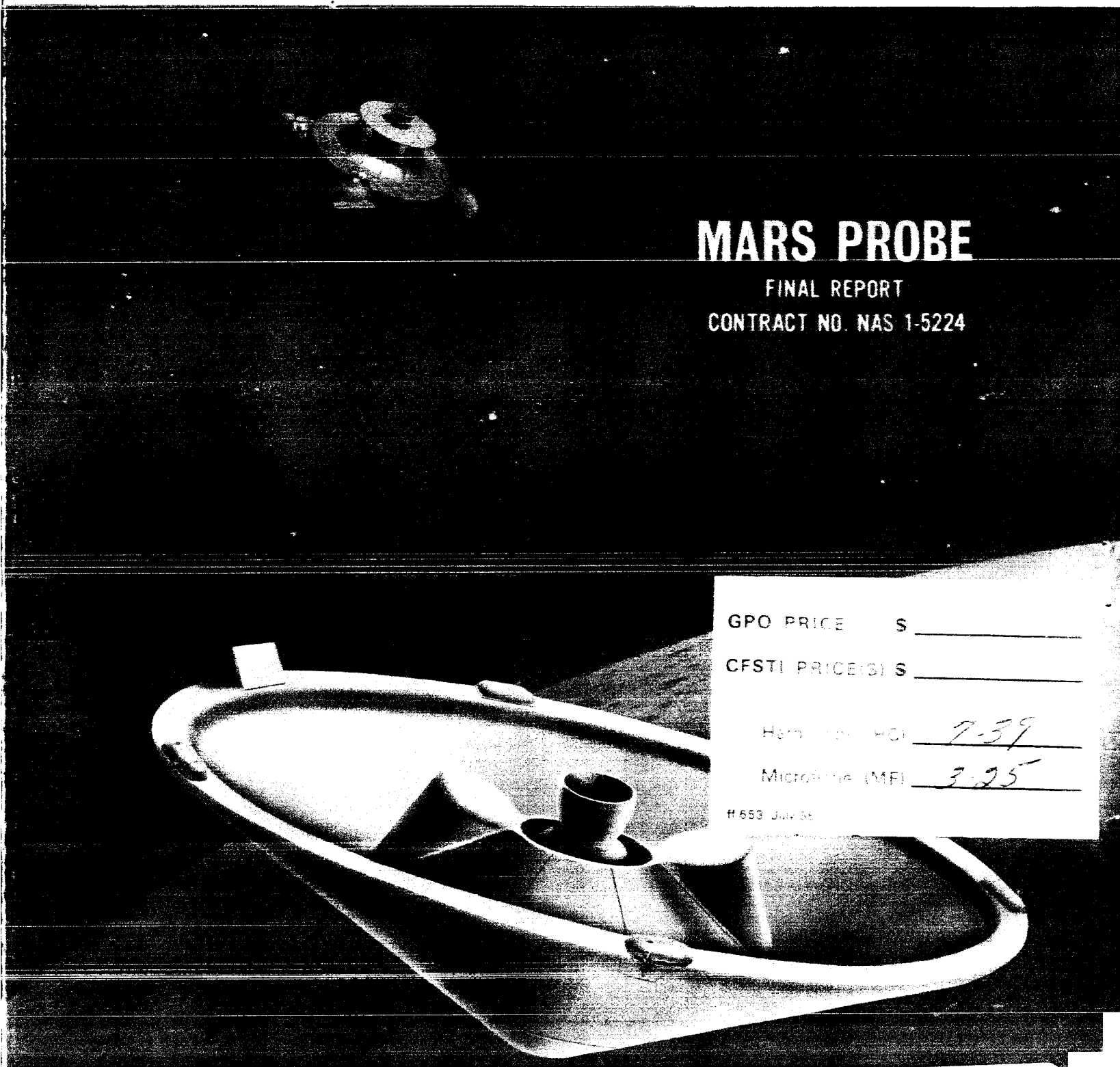

MARS PROBE

FINAL REPORT

CONTRACT NO. NAS 1-5224

GPO PRICE $ _____

CFSTI PRICE(S) $ _____

Hard copy (HC) 2.59

Microfiche (MF) .25

ff 653 July 65

N66 31825 (ACCESSION NUMBER) (THRU)

689 (PAGES) 1 (CODE)

CR-66137 (NASA CR OR TMX OR AD NUMBER) 07 (CATEGORY)

FACILITY FORM 602

AVCO CORPORATION

BOOK INDEX

VOLUME I SUMMARY

VOLUME II PROBE/LANDER, ENTRY FROM THE APPROACH TRAJECTORY

- Book 1 System Design
- Book 2 Mission and System Specifications

VOLUME III PROBE, ENTRY FROM ORBIT

- Book 1 System Design
- Book 2 Mission, System and Component Specifications
- Book 3 Development Test Programs

VOLUME IV STERILIZATION

VOLUME V SUBSYSTEM AND TECHNICAL ANALYSES

- Book 1 Trajectory Analysis
- Book 2 Aeromechanics and Thermal Control
- Book 3 Telecommunications, Radar Systems and Power
- Book 4 Instrumentation
- Book 5 Attitude Control and Propulsion
- Book 6 Mechanical Subsystems

NASA CR-66139

COMPARATIVE STUDIES OF CONCEPTUAL DESIGN AND QUALIFICATION PROCEDURES FOR A MARS PROBE/LANDER

FINAL REPORT

VOLUME V–SUBSYSTEM AND TECHNICAL ANALYSES

Book 3-TELECOMMUNICATIONS, RADAR SYSTEMS AND POWER

Prepared by

SPACE SYSTEMS DIVISION
AVCO CORPORATION
Lowell, Massachusetts

AVSSD-0006-66-RR
Contract NAS 1-5224

11 May 1966

Prepared for

NATIONAL AERONAUTICS AND SPACE ADMINISTRATION
LANGLEY RESEARCH CENTER
LANGLEY STATION
Hampton, Virginia 23365

PREFACE

The results of Mars Probe/Lander studies, conducted over a 10-month period for Langley Research Center, NASA, are presented in detail in this report. Under the original contract work statement, studies were directed toward a direct entry mission concept, consistent with the use of the Saturn IB-Centaur Launch Vehicle, wherein the landing capsule is separated from the spacecraft on the interplanetary approach trajectory, some 10 to 12 days before planet encounter. The primary objectives of this mission were atmospheric sampling by the probe/lander during entry and terrain and atmosphere physical composition measurement for a period of about 1 day after landing.

Studies for this mission were predicated on the assumption that the atmosphere of Mars could be described as being within the range specified by, NASA Mars Model Atmospheres 1, 2, 3 and a Terminal Descent Atmosphere of the document NASA TM-D2525. These models describe the surface pressure as being between 10 and 40 mb. For this surface pressure range a payload of moderate size can be landed on the planet's surface if the entry angle is restricted to be less than about 45 degrees.

Midway during the course of the study, it was discovered by Mariner IV that the pressure at the surface of the planet is in the 4 to 10 mb range, a range much lower than previously thought to be the case. The results of the study were re-examined at this point. It was found that retention of the direct entry mission mode would require much shallower entry angles to achieve the same payloads previously attained at the higher entry angles of the higher surface pressure model atmospheres. The achievement of shallow entry angles (on the order of 20 degrees), in turn, required sophisticated capsule terminal guidance, and a sizeable capsule propulsion system to apply a velocity correction close to the planet, after the final terminal navigation measurements.

Faced with these facts, NASA/LRC decided that the direct entry from the approach trajectory mission mode should be compared with the entry from orbit mode under the assumption that the Saturn 5 Launch Vehicle would be available. Entry of the flight capsule from orbit allows the shallow angle entry (together with low entry velocity) necessary to permit higher values of M/C_DA, and hence entry weight in the attenuated atmosphere.

It was also decided by LRC to eliminate the landing portion of the mission in favor of a descent payload having greater data-gathering capacity, including television and penetrometers. In both the direct entry and the entry from orbit cases, ballistic atmospheric retardation was the only retardation means considered as apecifically required by the contract work statement.

Four months had elapsed at the time the study ground rules were changed. After this point the study continued for an additional five months, during which

PRECEDING PAGE BLANK NOT FILMED.

period a new design for the substantially changed conditions was evolved. For this design, qualification test programs for selected subsystems were studied. Sterilization studies were included in the program from the start and, based on the development of a fundamental approach to the sterilization problem, these efforts were expanded in the second half of the study.

The organization of this report reflects the circumstance that two essentially different mission modes were studied -- the first being the entry from the approach trajectory mission mode and the other being the entry from orbit mission mode -- from which two designs were evolved. The report organization is as follows:

Volume I, Summary, summarizes the entire study for both mission modes.

Volume II reports on the results of the first part of the study. This volume is titled Probe/Lander, Entry from the Approach Trajectory. It is divided into two books, Book 1 and Book 2. Book 1 is titled System Design and presents a discursive summary of the entry from the approach trajectory system as it had evolved up to the point where the mission mode was changed. Book 2, titled Mission and System Specifications, presents, in formal fashion, specifications for the system. It should be understood, however, that the study for this mission mode was not carried through to completion and many of the design selections are subject to further tradeoff analysis.

Volume III is composed of three books which summarize the results of the entry from orbit studies. Books 1 and 2 are organized in the same fashion as the books of Volume II, except that Book 2 of Volume III presents component specifications as well. Book 3 is titled Development Test Programs and presents, for selected subsystems, a discussion of technology status, test requirements and plans. This Book is intended to satisfy the study and reporting requirements concerning qualification studies, but the selected title is believed to describe more accurately the study emphasis desired by LRC.

Volume IV presents Sterilization results. This information is presented separately because of its potential utilization as a more fundamental reference document.

Volume V presents, in six separate books, Subsystem and Technical Analyses. In order (from Book 1 to Book 6) they are:

Trajectory Analysis
Aeromechanics and Thermal Control
Telecommunications, Radar Systems and Power
Instrumentation
Attitude Control and Propulsion
Mechanical Subsystems

Most of the books of Volume V are divided into separate discussions of the two mission modes. Table of Contents for each book clearly shows its organization.

CONTENTS

1.0 Introduction 1

2.0 Summary, Probe/Lander Entry from the Approach Trajectory 3

2.1 Telecommunications 3

2.1.1 Study Objectives 3
2.1.2 Significant Study Results 3
2.1.3 Reference Design Summary of Characteristics 6
2.1.4 Critical Items 6

2.2 Electrical Power 8

2.2.1 Study Objective 8
2.2.2 Significant Results 9
2.2.3 Reference Design Summary of Characteristics 10
2.2.4 Critical Items 10

2.3 Radar Systems 10

2.3.1 Study Objectives 10
2.3.2 Reference Design Summary of Requirements and Characteristics 12

3.0 Summary -- Entry From Orbit 13

3.1 Telecommunications 13

3.1.1 Study Objectives and Scope 13
3.1.2 Reference Design Summary 14

3.2 Electrical Power 15

3.2.1 Study Objectives and Scope 15
3.2.2 Reference Design 16

3.3 Radar Systems 17

3.3.1 Study Objectives and Scope 17
3.3.2 Design Summary 17

CONTENTS (Cont'd)

4.0 Probe Lander, Entry from Approach Trajectory 19

4.1 General 19

4.2 Requirements and Constraints 19

4.2.1 Functional Requirements 19
4.2.2 Mission and Design Constraints 21

4.3 Design Objectives 27

4.4 Descent Relay Link RF Analysis 29

4.4.1 Communication Range Between the Flight Spacecraft and the Flight Capsule 29
4.4.2 Flight Spacecraft Receiving System Characteristics 31
4.4.3 Flight Capsule Design, Dynamics, and Antenna Constraints 32
4.4.4 Relay Frequency Selection 38
4.4.5 Flight Capsule Transmitter Power 38
4.4.6 Modulation/Detection Techniques 40

4.5 Post-Landing Relay Link RF Analysis 44

4.6 Flight Capsule Direct Link RF Analysis 46

4.6.1 Restriction of Direct Link to Post-Landing Mode 46
4.6.2 Post-Landing Direct Link Performance 50
4.6.3 Flotation Sphere Configuration 53
4.6.4 Oblate Spheroid Configuration 56
4.6.5 Comparison of Alternatives 57

4.7 Oblate Spheroid as the Reference Design 64

4.7.1 General Concept 64
4.7.2 Operational Profile 69

4.8 Flight Capsule Relay Link Radio Subsystem Description 71

4.8.1 Antenna 72

CONTENTS (Cont'd)

4.8.2 Transmitter 72
4.8.3 Flight Capsule Relay Link Radio Subsystem Summary 76

4.9 Flight Spacecraft Relay Link Radio Subsystem Description 76

4.9.1 Antenna 76
4.9.2 Receiver 78

4.10 Flight Capsule Direct Link Radio Subsystem Description 80

4.10.1 Antenna 81
4.10.2 Transmitter 83
4.10.3 Command Receiver 86
4.10.4 Summary 90

4.11 Flight Capsule Data Handling Subsystem Description 92

4.11.1 Description of Selected Approach 93
4.11.2 Major Tradeoffs 127
4.11.3 Problem Areas 145
4.11.4 Development Status 145

4.12 Flight Spacecraft Data Handling Subsystem 150

4.12.1 Description of Selected Approach 150
4.12.2 Alternate Approach 152

4.13 Flight Capsule Central Computer and Sequencer 152

4.13.1 External CC&S Description 152
4.13.2 Internal CC&S Description 155

4.14 Summary of Characteristics 157

5.0 Probe, Entry From Orbit 162

5.1 Functional Requirements 162

5.1.1 General 162
5.1.2 Constraints 162

5.2 Design Objectives 164

CONTENTS (Cont'd)

5.3 Relay Link Geometry 165

5.3.1 Flight Spacecraft Antenna Look Angles and Beamwidth .. 165
5.3.2 Flight Capsule Antenna Look Angles and Beamwidth 176
5.3.3 Communication Range 183
5.3.4 Range-Angle-Beamwidth Summary 183

5.4 Relay Link Radio Frequency Analysis 186

5.4.1 Communication Medium 187
5.4.2 Antenna Selection 228
5.4.3 Frequency Selection 238
5.4.4 Flight Capsule Transmitter Power 240
5.4.5 Modulation Selection 244
5.4.6 Relay Link Radio Frequency Performance 256
5.4.7 Failure Mode Considerations 267

5.5 Telecommunication Subsystem Description 269

5.5.1 Summary of Requirements 269
5.5.2 General Description 270
5.5.3 Flight Capsule Radio Subsystem Description 273
5.5.4 Flight Capsule Data Handling Subsystem Description ... 284
5.5.5 Flight Spacecraft Radio Subsystem Description 323
5.5.6 Flight Spacecraft Data Handling Subsystem 351
5.5.7 Summary of Characteristics 352
5.5.8 Central Computer and Sequencer 352

6.0 Electrical Power, Probe/Lander Entry from the Approach Trajectory 365

6.1 General 365

6.2 Functional Requirements 365

6.3 Power Source Description 367

6.3.1 Selected Approach 367
6.3.2 Alternative Approaches 372
6.3.3 Significant Tradeoffs 375
6.3.4 Principal Problem Areas and Development Status 380

CONTENTS (Cont'd)

6.4 Power Conditioning Equipment 380

6.4.1 Selected Approach 380
6.4.2 Alternative Approaches 383
6.4.3 Significant Tradeoffs 386
6.4.4 Principal Problem Areas and Development Status 393

6.5 Summary of System Characteristics 393

7.0 Electrical Power, Probe/Lander Entry from Orbit 395

7.1 General 395

7.2 Functional Requirements 395

7.2.1 Modes of Operation 395
7.2.2 Heat Sterilization 395
7.2.3 Charging 399
7.2.4 Power Control 399

7.3 Power Source Description 399

7.3.1 Selected Approach 399
7.3.2 Alternative Approaches 400
7.3.3 Significant Tradeoffs 401
7.3.4 Principal Problem Areas and Development Status 402

7.4 Power Conditioning Equipment 402

7.4.1 Selected Approach 402
7.4.2 Alternative Approaches 405
7.4.3 Significant Tradeoffs 407
7.4.4 Principal Problem Areas and Development Status 407

7.5 Summary of Physical Characteristics..... 407

8.0 Radar Systems 408

8.1 General 408

8.2 Functional Requirements and Constraints 409

8.2.1 Entry Trajectory and Vehicle Attitude Considerations ... 409

CONTENTS (Cont'd)

8.2.2 Altitude Measurement 412
8.2.3 Wind-Velocity Measurements 413
8.2.4 Surface Roughness 413

8.3 High Altitude R. F. Link Analysis 414

8.3.1 Range, Beamwidth, and Accuracy Requirements 414
8.3.2 Frequency Selection 414
8.3.3 Modulation Selection 420
8.3.4 Transmitter Power Selection 422

8.4 Low Altitude R. F. Link Analysis 428

8.4.1 Range, Beamwidth, and Accuracy Requirements 428
8.4.2 Frequency Selection 431
8.4.3 Modulation Selection 431
8.4.4 Transmitter Power Selection 431

8.5 Wind Velocity Measurement R. F. Link Analysis 433

8.5.1 Comparison of Radar-Type Wind Measurement Techniques 433
8.5.2 Entry from the Approach Trajectory Design 434
8.5.3 Entry from Orbit Design 434
8.5.4 Wind Velocity Error Analysis 441

8.6 Surface Roughness Measurement Analysis 446

8.6.1 Spectrum Analysis 446
8.6.2 Side-Looking Radar Technique 452

8.7 High-Altitude Radar Altimeter Subsystem Description 454

8.7.1 Description of Selected Approach 454
8.7.2 High-Altitude Altimeter Antenna System 467

8.8 Low-Altitude Radar Altimeter Subsystem Description 474

8.8.1 General 474
8.8.2 Low-Altitude Antenna System 474

8.9 Wind Measurement System Description 486

8.9.1 Entry from Approach Trajectory Design 486

CONTENTS (Concl'd)

8.9.2 Entry from Orbit Design 490
8.9.3 Comparison with Surveyor RADVS 497

8.10 Summary of Physical Characteristics 500

Appendixes A-1

A. Flight Capsule Antenna Analysis A-3

B. Flight Spacecraft B/T Synchronizer Analysis B-1

C. Battery Calculations for Reference Power Profile C-1

D. Power Control D-1

E. Derivation of a Theoretically Optimum Range Tracker E-1

F. Determination of Horizontal Motions and Attitudes with the Use of the Velocity-Attitude Sensor F-1

G. Design Considerations for the V-A Sensor G-1

H. Doppler Echo Spectrum and Altimeter Ancillary Functions H-1

ILLUSTRATIONS

Figure	1	Communication Range - 1971	24
	2	Landed Capsule Look Angle, 11 January 1972	25
	3	Communication Geometry at Entry	30
	4	Parachute Dynamics	33
	5	Relay Link Flight Capsule Look Angle Requirements	35
	6	Effect of Shape on Antenna Pattern	36
	7	Planar Spiral Antenna Pattern	37
	8	Relay Frequency Selection	39
	9	Orbit Contact Geometry	45
	10	Direct Link Separation-to-Entry Look Angles, α = 0 Degree at Entry	48
	11	Direct-Link Flight Capsule Look Angle Requirements, Zero Angle of Attack at Entry, 11 January 1972	49
	12	Efficiency Estimates for S-band Power Amplifiers	52
	13	Direct Link Data Rates	54
	14	Direct Link Look Angle Requirements	55
	15	Gain Distribution Function S-Band "V" Antenna, ψ = 90 Degrees	59
	16	Gain Distribution Function S-Band "V" Antenna, ψ = 60 Degrees	60
	17	Gain Distribution Function S-Band "V" Antenna, ψ = 30 Degrees	61
	18	Gain Distribution Function S-Band "V" Antenna, ψ = 0 Degree	62

PRECEDING PAGE BLANK NOT FILMED.

ILLUSTRATIONS (Cont'd)

Figure	19	Direct-Link Antenna Gain for Uniform and Gaussian Distributed Landed Capsule Attitudes	63
	20	Telecommunication Subsystem Block Diagram	65
	21	Relay Radio Subsystem	72
	22	Flight Capsule Relay Link Antenna	73
	23	30 Watt Flight Spacecraft FSK Transmitter	74
	24	Flight Spacecraft Receiver Configuration for Various Feed-Through Modes	79
	25	Internal Radio Subsystem	80
	26	S-Band V-Horn Antenna	82
	27	Direct-Link Radio Subsystem	84
	28	Operational Times of External DAE Science and Instruments	95
	29	Trajectory Data Summary	96
	30	External Data Automation Equipment Block Diagram	101
	31	External Telemetry Subsystem Block Diagram	110
	32	Mode 1 External Telemetry Engineering Channels	115
	33	Mode 2 External Telemetry Engineering Channels	116
	34	Mode 4 External Telemetry Engineering Channels	118
	35	Two Memory Data Storage Subsystem	124
	36	Entry-Descent Memory (EDM)	126
	37	Centralized Data Handling Equipment	129
	38	Decentralized Data Handling Equipment	130

ILLUSTRATIONS (Cont'd)

Figure	39a	One-Level Commutator	131
	39b	Two-Level Commutator	131
	40	Successive Approximation A-D Converter	134
	41	Digital Ramp A-D Converter	136
	42	Analog Ramp A-D Converter	138
	43	Voltage--Frequency A-D Converter	139
	44	Ferrite Memory Weight	147
	45	Ferrite Memory Volume	148
	46	Ferrite Memory Power Consumption	149
	47	Flight Capsule External Central Computer and Sequencer	153
	48	Flight Capsule Internal Central Computer and Sequencer	156
	49	Flight Spacecraft-Flight Capsule Communication Geometry	166
	50	Communication Geometry during Entry	167
	51	Communication Geometry for Alternate Flight Spacecraft Antenna Concepts	169
	52	Clock/Cone Angle to FS/FC Line of Sight	170
	53	Flight Spacecraft Body-Fixed Antenna Look Angle	172
	54	Flight Spacecraft Body-Fixed and PSP Antennas Look Angle Comparison	174
	55	Flight Capsule to Flight Spacecraft Look Angles, 1000 X 10,000 Kilometer Orbit	178
	56	Effect of Parachute Dynamics on Flight Capsule Look Angle	181

ILLUSTRATIONS (Cont'd)

Figure	57	Parachute Dynamics -- Flight Capsule Swing Angle, Effect of Gust Magnitude	182
	58	Communication Range Summary, 1000 X 10,000 Kilometer Orbit	184
	59	Generic Communication Link	189
	60	Geometry of Mars Relay Link	191
	61	Geometry for Determining (Ω_j / Ω)	193
	62	Maximum and Minimum Brightness (or Space) Temperature of the Sky as Seen by an Ideal Single-Polarization Antenna on Earth	197
	63	Maximum Flux Density of Various Components of Solar Radio Emission as Received on Earth	200
	64	Geometry for Determining Effects of Solar Radiation	200
	65	Frequency of Occurrence of Type II Bursts in Course of the Solar Cycle	204
	66	Starting Frequency of Fundamental Bands of Type II Bursts	205
	67	Occurrence of Type IV Bursts on Meter and Decimeter Waves as a Function of the Solar Cycle (a) 25 to 240 MHz (b) 100 to 580 MHz	209
	68	Flight Capsule Communication Through Wake Plasma	215
	69	Wake Attenuation versus Altitude	216
	70	Flight Capsule Velocity versus Apoapsis	218
	71	Atmosphere and Orbit Geometry Effects on Wake Attenuation	219
	72	Wake Attenuation versus Velocity and Altitude	220
	73	Multipath Configuration	223

ILLUSTRATIONS (Cont'd)

Figure	74	Surface Reflection Coefficient for Very Dry Ground versus Angle of Incidence	225
	75	Envelope of Received Signal	225
	76	Specular Reflection Effects	226
	77	Diffuse Reflection Effects	227
	78	Typical Turnstile Antenna Pattern	229
	79	Typical Helix Antenna Pattern	230
	80	Position of Telemetry Antenna on Flight Capsule	234
	81	Flight Capsule Antenna Pattern with Entry Shell	235
	82	Flight Capsule Antenna Pattern without Entry Shell	236
	83	Flight Capsule Antenna Pattern with and Without Tilt	237
	84	Frequency Selection Tradeoff	239
	85	Parachute-Size Descent Time Trade	241
	86	Candidate Relay-Link Communication System	245
	87	Probability Distribution of Loop Phase Error (θ_e)	251
	88	Available Performance Margin with Time Diversity	258
	89	Multipath and Off-Axis Effect	260
	90	Left Circular Pattern of Flight Capsule Antenna	261
	91	Performance Margin at Parachute Deployment without Diversity Reception	262
	92	Data Loss at 90-Degree Capsule Sway	264
	93	Flight Capsule Antenna Pattern	266
	94	Flight Capsule Telecommunication Subsystem Mechanization	268

ILLUSTRATIONS (Cont'd)

Figure	95	Flight Capsule Telecommunication Subsystem Block Diagram	272
	96	Flight Spacecraft Telecommunication Subsystem Block Diagram	274
	97	Alternative Flight Capsule Relay Antenna Design Concept	276
	98	Principal Plane Pattern of Turnstile Antenna Mounted on Mockup of Suspended Vehicle	278
	99	Nominal Thermal Response of Antenna Configuration	281
	100	Data Collection Profile	291
	101	Typical Penetrometer Outputs	297
	102	Blackout Data Recovery Concept	305
	103	Data Transmission Sequence	308
	104	Television Data Transmission Sequence	311
	105	Experiment Data Handling Subsystem Block Diagram	313
	106	Penetrometer Data Handling Equipment	314
	107	Diagnostic Data Handling Subsystem Block Diagram	317
	108	Blackout Data Storage Subsystem Block Diagram	319
	109	Television Data Storage	321
	110	Flight Spacecraft Turnstile Antenna	326
	111	Flight Spacecraft Antenna Candidates	327
	112	Flight Spacecraft Radio Subsystem	330
	113	Detailed Flight Spacecraft Radio Subsystem	332
	114	Receiver Block Diagram	334

ILLUSTRATIONS (Cont'd)

Figure	115	FSK Bit Error Probability versus Input Signal-to-Noise Ratio	337
	116	Allowable $b_0{}^r$ versus Input Signal-to-Noise Ratio	338
	117	Maximal Ratio Diversity Combiner	344
	118	Signal Detector	345
	119	Generic PCM Bit Synchronizer	347
	120	Central Computer and Sequencer Functional Block Diagram	361
	121	Power Profile	366
	122	Power Sources and Application of Constraints	368
	123	Power System Configuration Before Separation	369
	124	Typical RTG Weight versus Cold Junction Temperature	374
	125	Total System Weights for Li-Cl and RTG versus Time	376
	126	Partial Schematic -- Silver-Zinc Battery Charge Regulator	379
	127	Buck-Boost Regulator Characteristics	381
	128	Buck-Boost Regulator Schematic	382
	129	Ni-Cad Charge Regulator 1971 -- Option 1	384
	130	Ni-Cad Charge Regulator 1971 -- Option 2	384
	131	Ni-Cad Charge Regulator 1971 -- Option 3	384
	132	Pulse Width Modulated Series Transistor Regulator	387
	133	Current, Voltage, and Power Relationships for a PWM Series Transistor Regulator	388

ILLUSTRATIONS (Cont'd)

Figure 134 Partial Schematic of PWM Regulator 389

135 PWM Switching Regulator Characteristics 392

136 PWM Switching Regulator Efficiency-Load Power Relationship 392

137 Schematic Diagram of Power and Control Subsystem 396

138 Power Profile for Flight Capsule 397

139 Capacity versus Temperature for 3.5 Amp-Hour Ni-Cad Cells 403

140 Power Control Subsystem 406

141 Trajectory Data Summary 410

142 Deceleration versus Time for VM-8 Atmosphere 411

143 Altimeter Look Angle versus Altitude 415

144 Transmitter Power Requirement versus Frequency 416

145 Sky Temperature versus Frequency 418

146 Evolution of Ring Antenna 421

147 Generic Range Tracker 424

148 Discriminator Characteristic 424

149 Long Pulse ICW Radar Altimeter Waveform 426

150 Surface Illumination Geometry 427

151 Parachute Dynamics -- Capsule Swing Angle 430

152 Geometry for Range and Bandwidth Computation 437

153 V A Sensor Power Requirement 440

154 Cumulative Probability of Error in Measurement of Wind Velocity, θ = 0 Degrees 442

ILLUSTRATIONS (Cont'd)

Figure 155 Cumulative Probability of Error in Measurement of Wind Velocity, $|\theta|$ = 30 Degrees 443

156 Cumulative Probability of Error in Measurement of Wind Velocity, $|\theta|$ = 60 Degrees 444

157 Error in Wind Velocity Measurement 445

158 Wind Velocity Measurement Error versus θ 447

159 Wind Velocity Measurement Error versus ϕ 448

160 Wind Velocity Measurement Error versus Wind Direction 449

161 Maximum Wind Velocity Measurement Error versus ϕ = 180 Degrees, -100 Degrees 450

162 Maximum Wind Velocity Measurement Error versus ϕ = -5 Degrees, +100 Degrees 451

163 Echo Spectra from Various Terrains 452

164 Frequency Rate Tracker and Correlator 455

165 Principle of Psuedo-Coherent Detection 457

166 Waveforms for Long Pulse Coherent Detection 458

167 Cong-Pulse ICW Radar Altimeter Waveforms 459

168 Optimum Range Tracking Radar 460

169 Altimeter Block Diagram 462

170 Signal Level During Acquisition 465

171 Ring Antenna Concept 468

172 Balun for Triply Folded Dipole 470

173 Smith Plot of Impedance for Triply Folded Dipole 471

ILLUSTRATIONS (Cont'd)

Figure 174 High Altitude Altimeter Antenna 472

175 Pattern Measurements on Scaled Model Antenna 473

176 Pattern Measurements for Slot Antenna with Charred Dielectric 475

177 Pattern Measurements for Slot Antenna without Charred Dielectric 476

178 Polarization of Radiation Field versus Arm Length for Log Spiral Antenna 478

179 Dimensions of Log Spiral Antenna 479

180 Patterns for Principal Planes of Log Spiral Antenna..... 481

181 Cavity Depth versus Gain 482

182 Dielectric Loaded Cavity 482

183 Bandwidth Taper for 3 Dielectrics 484

184 Tapered Composite Dielectric Loading of Cavity 485

185 Auxiliary Data Processor 487

186 Block Diagram of V A Sensor 491

187 Block Diagram of Frequency Tracker 493

188 Wind Measurement Error versus θ_c 495

189 V Two-Beam Antenna for V A Sensor 497

A-1 Flight Capsule Relay Link Antenna A-5

A-2 Flight Capsule Antenna Systems A-6

A-3 Type I Balun A-7

A-4 Equivalent Circuit for Type I Balun A-7

ILLUSTRATIONS (Cont'd)

Figure	A-5	Principal Plane Pattern of 0.5λ Diameter Planar Log Spiral Antenna	A-12
	A-6	Principal Plane Pattern of 0.4λ Diameter Planar Log Spiral Antenna	A-13
	A-7	Principal Plane Pattern of 0.3λ Diameter Planar Log Spiral Antenna	A-14
	A-8	Antenna Measurements Coordinate System	A-15
	A-9	Flight Capsule Antenna Pattern,with and without Entry Shell	A-16
	A-10	Flight Capsule Antenna Pattern, with and without Tilt	A-18
	A-11	Axial Ratio versus Look Angle from Antenna Axis	A-19
	B-1	Generic Bit-Synchronizer	B-4
	B-2	Typical Phase Detector Implementation	B-5
	B-3	Linearized Sampled Data Tracking Loop	B-6
	B-4	Portion of Wideband PCM/FSK System Pertinent to Determination of $(\theta_{IN})^2$	B-11
	C-1	Flight Capsule Power Profile	C-11
	D-1	SCR Flip-Flop Circuit	D-2
	D-2	SCR Cathode Pulse Turn-Off	D-3
	D-3	Load Sensitive Pulse Turn-Off	D-3
	D-4	Morgan Circuit	D-4
	D-5	Conducted RFI Suppression with RF Ground Inaccessible	D-6
	D-6	Conducted RFI Suppression with RF Ground Accessible	D-6

Figure	D-7	Circuit for Decoupling UJT from Supply Transients	D-7
	D-8	Circuit for Eliminating Firing from SCR Gate Transients	D-8
	E-1	The Optimum Range Tracking Radar	E-2
	F-1a	VA Sensor Beam Arrangement	F-2
	F-1b	View Along Flight Capsule Spin Axis	F-2
	F-2	Coordinate System Geometry	F-5
	F-3	Body Fixed Axes x, y, z Relative to XYZ Axes	F-7
	G-1	Block Diagram of VA Sensor	G-2
	G-2	Frequency Time Relationships in FM/CW Radar	G-3
	G-3	Frequency Time Relationships in FM/CW Radar in the Presence of Doppler Shifts	G-5
	G-4	Geometry Used to Determine Range	G-7
	G-5	Geometry of Single Resolution Element on Planetary Surface	G-14
	H-1	Spread of Doppler Frequencies	H-2
	H-2	Representation of Diffuse and Specular Returns	H-3
	H-3	Trend Inversions	H-6

TABLES

Table I	Telecommunication Subsystem Salient Characteristics	7
II	Salient Characteristics of the Electrical Power Subsystem - 1971	11
III	Radar System Overall Performance and Design	12
IV	Telecommunication Subsystem Salient Characteristics	15
V	Power Subsystem Salient Characteristics	16
VI	Radar System Salient Characteristics	18
VII	Data Transmission Requirements	20
VIII	Probe/Lander General Command and Sequencing Requirements	22
IX	Significant Spacecraft Characteristics	23
X	Relay-Link Data Rates	43
XI	Comparison of Alternatives	58
XII	Telecommunication Subsystem Design Requirements	66
XIII	Flight Capsule Relay-Link Radio Subsystem Characteristics	77
XIV	Summary of Direct-Link Radio Subsystem Characteristics	91
XV	Science Instruments Handled by External DAE	94
XVI	External DAE Mode 2 Output Format	104
XVII	External Mode 3 Storage Format for Science Data	104
XVIII	External Mode 4 Output Format	106
XIX	Science Instruments Handled by Internal DAE	107
XX	Internal DAE Mode I Storage Format	108

TABLES (Cont'd)

Table	XXI	External Engineering Data Requirements	112
	XXII	Internal Telemetering Channel Assignment	119
	XXIII	Data Storage Requirements	122
	XXIV	Flight Capsule Data Handling Subsystem Summary	128
	XXV	Tradeoff Chart for Commutation Devices	133
	XXVI	Analog to Digital Conversion Tradeoff Chart	142
	XXVII	Integrated Circuit Tradeoff Chart	143
	XXVIII	Static Storage Device Summary	146
	XXIX	Flight Spacecraft Data Handling Subsystem Summary	151
	XXX	Flight Capsule Telecommunication Subsystem Operational Characteristics	157
	XXXI	Flight Capsule Telecommunication Subsystem Performance Characteristics	158
	XXXII	Flight Capsule Telecommunication Subsystem Design Characteristics	159
	XXXIII	Flight Capsule Telecommunication Subsystem Physical Characteristics	161
	XXXIV	Data Transmission Requirements	163
	XXXV	Body Fixed Antenna Position on Flight Spacecraft	171
	XXXVI	Flight Spacecraft Antenna Maximum Lock-Angle Summary	175
	XXXVII	Flight Spacecraft Antenna Minimum Beamwidth Requirements	177
	XXXVIII	Flight Capsule Antenna Look-Angle Summary -- No Wind	179

TABLES (Cont'd)

Table	XXXIX	Flight Capsule Antenna Minimum Beamwidth Requirements	180
	XL	Communication Range Summary	183
	XLI	Communication Geometry Range-Angle Summary	185
	XLII	Effective Antenna Noise Temperature Contribution Due to Planet	195
	XLIII	Characteristics of Various Solar Radio Emissions	199
	XLIV	Tabulation of K for Various Parameters	202
	XLV	Contribution to Effective Antenna Temperature Due to Solar Radiation for Various Levels of Solar Activities	203
	XLVI	Summary of Antenna Noise Temperature Produced by Various Solar Sources	210
	XLVII	Values of T_1 for Some Typical System Parameters	211
	XLVIII	Overall System Noise for Some Typical System Parameters	213
	XLIX	Expected Blackout Conditions During Entry	221
	L	Flight Spacecraft Antenna Selection	231
	LI	Assumed Relay-Link Parameters	247
	LII	Determination of Required Predetection Bandwidth	248
	LIII	Available Predetection Signal-to-Noise Ratio	250
	LIV	Performance Margin Provided by Candidate Relay-Link Modulation Techniques	254
	LV	Telecommunication Design Control Chart	257
	LVI	Telecommunication Subsystem Design Requirements	270

TABLES (Cont'd)

Table	LVII	Comparison of Flight Capsule Antenna Concepts	280
	LVIII	Flight Capsule Radio Subsystem Characteristics	283
	LIX	Experiment Data Requirements	285
	LX	Diagnostic Data Requirements	286
	LXI	Television Data Frame Format	292
	LXII	Penetrometer Design Characterisitics	294
	LXIII	Penetrometer Link Design Control Chart	295
	LXIV	Penetrometer Data Frame Format	298
	LXV	Surface Roughness Data Frame Format	298
	LXVI	Other Experiment Data Acquisition Summary	300
	LXVII	Other Experiment Data Frame Formats	301
	LXVIII	Diagnostic Data Acquisition Summary	302
	LXIX	Diagnostic Data Frame Formats	303
	LXX	Data Frame Rate Allocations	306
	LXXI	Effect of Subsystem Failure on Data Transmission	309
	LXXII	Flight Capsule Data Handling Subsystem Characteristics	324
	LXXIII	Comparison of Flight Spacecraft Antenna Concepts	329
	LXXIV	Determination of Required Mark/Space Filter Bandwidth	339
	LXXV	Flight Spacecraft Receiver Characteristics	341

TABLES (Cont'd)

Table	LXXVI	Required Number of Data Transitions to Reduce Phase Error (θ_e) to Within Some Arbitrary Percent	348
	LXXVII	Flight Spacecraft Radio Subsystem Characteristics	349
	LXXVIII	Flight Spacecraft Data Handling Subsystem Characteristics	353
	LXXIX	Telecommunication Subsystem Operational Characteristics	354
	LXXX	Telecommunication Subsystem Performance Characteristics	354
	LXXXI	Telecommunication Subsystem Design Characteristics	355
	LXXXII	Telecommunication Subsystem Weight Characteristics	359
	LXXXIII	Flight Capsule Instrumentation Power Requirements.	370
	LXXXIV	Characteristics of Ni-Cad Batteries	371
	LXXXV	Weight of Fuel Oxidizer and Tanks	377
	LXXXVI	Charge Regulator	385
	LXXXVII	Characteristics of Power Conditioning Alternates	390
	LXXXVIII	Circuit Component Breakdown for Reliability Estimate	391
	LXXXIX	Physical Characteristics of Power Subsystem	393
	XC	Salient Characteristics of the Electrical Power Subsystem - 1971	394
	XCI	List of Power Users	398
	XCII	Nickel-Cadmium Battery Characteristics	399
	XCIII	Silver-Zinc Battery Characteristics	400
	XCIV	Lithium-Chlorine Fuel-Cell Characteristics	401
	XCV	Electrical Characteristics of Load Voltage Regulator	404

TABLES (Cont'd)

Table	XCVI	Electric Subsystem Physical Characteristics	407
	XCVII	Comparison of Modulation for High Altitude Altimeter	423
	XCVIII	Transmitter Power Calculation for High Altitude Altimeter	429
	XCIX	Transmitter Power Calculation for Low Altitude Altimeter	432
	C	Signal Spectral Spreading Because of Suspended Payload Dynamics	438
	CI	VA Sensor Parameters	439
	CII	324 MHz Spiral Antenna Characteristics	477
	A-1	Parameters of the Model Spiral Antennas	A-10
	A-2	Test Matrix--Antenna Pattern Study	A-11
	A-3	Design Requirements	A-22
	B-1	Sequence of Events in Sampled Data Servo Loop	B-8
	B-2	Maximum Values of Loop Gain for Various Relative rms Errors in Sync Phase	B-13
	B-3	Number of Samples Required to Reduce the Phase Error to Within Some Specified Percent of Initial Phase Offset	B-14
	B-4	Required Number of Samples to Reduce θ_e / θ_{IN} to Within Some Acceptably Small Percent for Different Allowable rms Sync Phase Jitter	B-15
	B-5	Sequence of Events in Bit Synchronizer Tracking Loop for a Fixed Frequency Offset	B-16
	B-6	Steady State Phase Error Because of Frequency Offset for Various Combinations of Oscillator Stability and Data Transition Density	B-20

TABLES (Concl'd)

Table	C-1	Power Profile -- Preseparation to Impact	C-1
	C-2	Energy Summary	C-2
	C-3	Discharge Rates and Plateau Voltage	C-2
	C-4	Power Profile -- Post Impact	C-5
	C-5	Energy Summary	C-6
	C-6	Discharge Rate and Plateau Voltage	C-6
	C-7	Summary of Battery Characteristics -- Reference Design	C-8
	D-1	Comparison of SCR Turn-Off Circuits	D-9
	G-1	Maximum Ranges for Various Operating Attitudes for Both Stabilized and Unstabilized Payloads	G-7
	G-2	Required Modulation Characteristics for FM/CW Radar	G-9
	G-3	Quantization Error and Frequency Deviation Tradeoffs in the Lowest Altitude Range	G-11
	G-4	Signal-to-Noise Ratio Required to Achieve Various Relative rms Accuracies in Measuring Range and Range Rate	G-12
	G-5	FM/CW Radar System Parameters	G-17
	G-6	Δf and f_m for Variations in Altitude Ranges	G-17
	G-7	Power Budget for FM/CW Radar	G-18
	G-8	Transmitter Power Requirements for Various Relative rms Accuracies	G-19

GLOSSARY OF TERMS

ACS	Attitude Control System
A/D	Analog-to-digital
AGC	Automatic Gain Control
A-H	Ampere Hour
AM	Amplitude Modulation
AU	Astronomical Unit
B	Brightness
$\dot{B}$	Bit Rate
B/F	Antenna back-to-front ratio
BW	Bandwidth
b_o	i-f bandwidth
b_t	Tracking bandwidth
CC&S	Central computer and sequencer
CFO	Chute Full Open
dBm	Decibels above one milliwatt
dBW	Decibels above one watt
DDHS	Diagnostic Data Handling System
DTL	Diode Transistor Logic
EBO	Emergence from Blackout
EDHS	Engineering Data Handling System
EDM	Entry and Descent Memory
EFAT	Entry from the approach trajectory

PRECEDING PAGE BLANK NOT FILMED.

EFO	Entry from orbit
$\frac{E_R}{E_o}$	Ratio of field at a receiver due to direct and reflected signals normalized to direct signal
Es/No	Signal energy contrast
F	Noise Figure
FSK	Frequency Shift Keying
F_j	Noise figure of jth black box in generic communication link
F_T	Overall noise figure for components in generic communication link
f	True anomaly
f_B	Average clock frequency (channel bit rate)
f_d	Doppler Shift
f_o	Operating frequency
f_r	Receiver instability
f_t	Transmitter instability
G_B	Antenna Gain at back lobe
G_j	Gain of jth black box in generic communication link
G_o	Antenna gain at mainlobe
G_R	Receiving Antenna gain
G_T	Transmitting Antenna gain
IF	Intermediate frequency
IGFET	Integrated gate field effect transistor
IRIG	Inter-Range Instrumentation-Group

GLOSSARY OF TERMS (Cont'd)

k	Boltzmann's Constant
km	Kilometer(s)
LCP	Left Hand Circular Polarization
L_{MP}	Multipath Loss
Lp	Polarization loss
L_s	Space loss
L_{TC}	Transmitting circuit loss
M/C_DA	Ballistic coefficient
MFS	Multiple Frequency Shift
N. F.	Receiving system noise figure
NRZ	Non-return to zero
N_j	Additive noise introduced at jth black box in generic communication link
PAM	Pulse Amplitude Modulation
PCM	Pulse Code Modulation
PM	Phase Modulation
PN	Pseudo-random noise
PSK	Phase Shift Keying
PSP	Planetary Science Platform
PWM	Pulse Width Modulation
P_e	Probability of Error
P_T	Transmitted Power
R	Product of back-to-front antenna ratio and surface reflection coefficient

R	Range
RCP	Right Hand Circular Polarization
RCTL	Resistor-Capacitor-Transistor-Logic
RF	Radio frequency
RFI	Radio frequency interference
R_o	Surface voltage or field reflection coefficient
$R_{0\ 1,2,3}$	Distance from Mars center to spacecraft, ionosphere, atmosphere, surface.
S	Flux density at Mars
S'	Flux density at the spacecraft
S/N	Signal-to-noise ratio
$(S_j/N_j)_{in}$, $(S_j/N_j)_{out}$	Input, output signal-to-noise ratio of the jth black box in generic communication link.
$(SNR)_c$	Input carrier-to-noise ratio (CNR) measured in the same bandwidth as that in which $(SNR)_i$ is measured
$(SNR)_i$	Predetection signal-to-noise ratio in a predetection receiver IF
$(SNR)_i$	Total input signal-to-noise ratio in a predetection bandwidth b_o Hz wide
S_o	Equivalent flux density at Earth surface
T	Signal threshold value
TV	Television
T_a	Effective antenna temperature
T_{atm}	Average mars atmospheric temperature
T_B	Brightness temperature

GLOSSARY OF TERMS (Cont'd)

T_e	Effective system noise temperature
T_g	Galactic noise temperature
T_{ion}	Average Mars ionospheric temperature
T_M	Average Mars surface temperature
T_p	Planetary radiation temperature
T_{rs}	Radio star noise temperature
T_s	Thermal temperature of a body
T_s	Solar radiation temperature
T_{sky}	Apparent sky temperature
t_r	Video pulse rise time
t_s	Average time between data transitions
VCO	Voltage controlled oscillator
VM-3, -4, -7, -8	Various Mars atmospheric models
V_r	System Reference Voltage
v_c	Speed of light
W	Transmitter power
YIG	Yttrium Indium Gallium
α	Angle of Attack
β	Communication angle
γ	Flight spacecraft antenna front-to-back ratio
γ_E	Angle between the local horizontal and Flight Capsule Flight Path (entry angle)
ΔV	Velocity change

Δf_B	Frequency error in local clock
δ_R	Receiver local oscillator stability
δ_T	Transmitter stability
ϵ	Antenna efficiency
θ, θ_c	Flight Capsule sway-angle measured from true vertical
$\theta_{e(t)}$	Phase error between θ_{in} (t) and θ_o (t)
θ_{fc}	Angle between axis of flight capsule antenna and line joining flight spacecraft and flight capsule
θ_{FS}	Angle between axis of flight spacecraft antenna peak gain, and line joining flight spacecraft and flight capsule
$\theta_{in}(t)$	Input bit sync phase to phase lock loop
$\theta_o(t)$	Local clock phase in phase lock loop
λ	Wavelength
ξ_1	Fractional ionospheric absorption
ξ_2	Fractional atmospheric absorption
ρ	Mars surface reflection coefficient
ΣL_c	Sum of circuit losses
ΣL_T	Sum of adverse tolerances
σ_n^2	Variance of loop phase error
τ	Pulse width
$\tau P_s/N_o$	Signal energy contrast
ϕ	Derating factor

GLOSSARY OF TERMS (Concl'd)

ϕ	Signal phase
ψ	Parachute sway angle measured from true vertical
Ω	Solid antenna beamwidth
Ω_1	Solid angle subtended by radiation source

ACKNOWLEDGEMENT

The conduct of the study and technical preparation of this report involved the participation and close coordination of many people, all of whose contributions were important to the end results.

It is impractical to single out each individual, but the major contributors to the study, reflected in the material presented in this book, are as follows:

Responsible Manager

John J. Mahoney

Major Contributors

Name	Sections
Roy T. Bonaccorso	4, 5 & 8
Ronald L. Fante	4 & 5
Russell G. Gamache	4 & 5
James J. Hayes	4 & 5
Ira L. Jacobson	4 & 5
Monty Koslover	6 & 7
William J. Kubicki	4 & 5
James W. Modestino	4, 5 & 8
Robert W. Moody	4 & 5
John F. Natale	8
Edward D. Shane	4 & 5
Hendrick Tober	8

Approved by

Signature	Title
John J. Mahoney	Manager Advanced Electronics Department

1.0 INTRODUCTION

This book reports on the efforts conducted in the areas of telecommunication, electrical power, and radar subsystems during the LRC Probe/Lander study. Its purpose is to provide supporting material in the form of detailed analyses and tradeoff studies for the various reference design choices presented in Volumes II and III of the report. To make the book sufficiently self-contained and to avoid the situation where reading of other volumes is a pre-requisite to the understanding of this volume, certain material from other volumes is repeated.

The principal effort during the study was directed toward consideration of requirements for the 1971 mission. Although growth considerations were implicit in the work done, specific post-1971 efforts were limited to a synthesis of various types of payload to determine whether additional payloads would be compatible with the multimission entry vehicle shell.

The study considered two mission concepts. The first, designated entry from the approach trajectory (EFAT), includes a 24-hour post-landing mission in addition to a modest data-gathering mission during the ballistic entry and parachute descent phase of the Probe/Lander trajectory. The second concept, entry from orbit (EFO) (treated exclusively during the second half of the study), does not include a post-landing mission, but provides for extensive data collection during parachute descent.

In organizing the book, it was assumed that its average reader is function-oriented rather than system-oriented. As a result, this book is divided into three parts covering telecommunication, electrical power, and radar. Reference to the table of contents will, however, facilitate access to any combination of concept and functional area which has been treated.

Brief summaries of the scope and results of the EFAT and EFO studies are given in Sections 2.0 and 3.0, respectively. The work done in the area of telecommunications for the two concepts is described in detail in Sections 4.0 and 5.0. The work done in the electrical power area is presented in Sections 6.0 and 7.0.

Since the bulk of the radar studies have been related to the EFO concept, a single section (Section 8.0) is used to present all radar work.

The format followed in writing this book places emphasis on problem area identification, results, and conclusion in the body of the text, while in general, detailed analyses, including many of the lengthy arguments supporting technical conclusions have been placed in appropriate appendixes. This arrangement will increase the clarity of the discussion and facilitate overall understanding.

For the reader who has read Book 2, Volume IV of Reference 1 much of the material presented on the EFAT approach will be repetitious. The material in Sections 5.0, 7.0, and 8.0, covering the EFO case is, however, new and represents the bulk of the effort in Part II of the study.

2.0 SUMMARY, PROBE/LANDER ENTRY FROM THE APPROACH TRAJECTORY

2.1 TELECOMMUNICATIONS

2.1.1 Study Objectives

The general objectives of the effort conducted during the study were:

1. To assist in the synthesis of the scientific and engineering missions by accurate and reliable evaluation of telecommunication systems capabilities as limited by the various mission and design constraints.

2. To generate subsystem parametric data and conceptual designs, and determine their influence on the selection of the entry vehicle and on the shape, size, and general configuration characteristics of the suspended payload.

3. To define the extent and nature of the requirements imposed on the flight spacecraft by the flight capsule telecommunication systems, and to provide data necessary for resolving conflicting requirements.

4. To conduct subsystem analyses and tradeoff studies to determine the advantages and disadvantages of alternate means of mechanization capable of satisfying the estimated performance requirements.

5. To identify those areas in which significant development is required before the telecommunication system-performance requirements can be met.

6. To identify those operational, technical, or schedule problem areas which would significantly interfere with successful execution of the flight-capsule mission.

2.1.2 Significant Study Results

The following listed conclusions were drawn from the telecommunication studies of the EFAT mission:

1. It is desirable to utilize both relay- and direct-link communication systems to satisfy the minimum data requirements (collecting atmospheric data prior to landing, and planetary surface and environmental data after landing). The relay-link system should be considered as the prime means of satisfying data requirements during entry and descent; the direct-link system should be considered as the prime means of data transmission after landing.

2. Severe payload weight limitations exist for the overall entry vehicle weights considered. These limitations make it mandatory to utilize low-power-dissipation, low-weight equipment. Qualification of one or more integrated circuit techniques for this program is very desirable.

3. Basic control and sequencing of the flight-capsule subsystems should be accomplished through internal timing and sequencing devices. However, a capability for command from Earth appears attractive as a means of providing functional redundancy.

4. Study results indicate that modulation techniques not previously used on deep-space programs may be required for both the direct and relay links. Precise definition of the performance capabilities of these systems will require additional study.

5. Twenty to thirty watts is considered to be the range of reasonable nominal power requirements for either the relay or the direct-link systems. This requirement is compatible with the use of a completely solid state design for the relay link and the use of a solid state exciter in conjunction with a travelling wave tube (TWT) power amplifier in the direct link.

6. In the case of nonerectable payload designs, difficulties exist in describing performance of both a direct-link and a relay-link antenna after landing. It is expected that a statistical definition of antenna characteristics will be required to enable determination of the overall system performance.

7. Use of the flight spacecraft as a relay terminal after orbit injection does not appear attractive for a 24-hour mission. Although orbits suitable for communications contact at roughly the appropriate times can be selected, use of flight-spacecraft multiple receiving antennas, in conjunction with command control from the flight spacecraft, appears necessary to achieve the desired high level of confidence in the telecommunications system performance.

8. Assuming that no post-orbit relay communications capability is required, the nominal flight capsule requirements for the relay-link system apparently impose no prohibitive limitations on the flight spacecraft. However, three questions must be answered before the performance capability of the relay link can be firmly established. They are:

a. What is the maximum lead time and, hence, the maximum communication range between the flight spacecraft and the flight capsule at entry?

b. What are the size and pointing-accuracy limitations of the flight spacecraft antenna?

c. What is the data-rate capability between the flight spacecraft and Earth prior to orbit injection?

9. The optimum relay-link operating frequency appears to be in the region between 250 and 400 MHz. A frequency of 272 MHz has been selected as a nominal value as a result of this study.

10. Although a wideband-frequency shift keying (FSK) modulation system appears capable of satisfying relay-link data transmission requirements in 1971, development of a capability for both phase shift keying-phase modulation (PSK-PM) or FSK modulation is recommended. Uncertainties in the performance of a phase coherent system make sole reliance on a PSK-PM approach undesirable. However, the potentially higher data rate which can be achieved with the phase coherent system has some degree of growth potential.

11. The use of a repeater mode as the prime method of handling the flight-capsule data is recommended from a reliability viewpoint. Such an approach not only eliminates the necessity for bit synchronization but also eliminates the need for an automatic acquisition receiver if a coherent system is used. The flight spacecraft-to-Earth data link, however, must be capable of transmitting with a bandwidth equal to that of the relay receiver intermediate frequency (IF). Lower data-rate capabilities for the flight spacecraft will require partial or complete demodulation and detection.

12. Direct link data rates which can be achieved with non-directional antennas are very low. Emphasis must be placed on investigating techniques for minimizing data redundancy by suitable mechanization of the data automation equipment. As for the influence of non-directional antennas on the achievable data rate, the gimballed-sphere landed payload concept is far superior to the non-gimballed concept. In addition, adoption of the gimballed-sphere approach offers distinct advantages with respect to minimizing the size and complexity of the telecommunication equipment.

13. A landing at or near the sub-Earth latitude results in the optimum site for direct-link system transmission. Such a site allows communication to be established and maintained at higher elevation angles, thus reducing the influence of local Martian terrain features on the performance of the direct-link system.

2.1.3 Reference Design Summary of Characteristics

Table I presents the characteristics of the reference design selected for the EFAT mission. The relay performance indicated can be achieved with a communication range of 35, 000 km and a body fixed flight spacecraft antenna. Also of note is the fact that no post-landing relay communication capability is included. Through a relay link would be very desirable immediately after landing, size and weight restrictions on the landed capsule preclude its use.

2.1.4 Critical Items

The following items are sufficiently important to warrant early attention. In some cases, studies are required to establish the feasibility of a concept or to provide more accurate predictions of performance. In other cases, early action is required to stimulate advances in the state of the art.

2.1.4.1 Breadboard Testing of Modulation Detection Techniques

Breadboard models of several modulation systems, such as wideband FSK and non-coherent N-ary systems, should be constructed and tested immediately to obtain complete and precise system performance data.

2.1.4.2 Crystal Stability Testing

Several of the modulation techniques being considered for 1971 require oscillator crystals with high long-term and short-term phase and frequency stability. Study and measurement programs should be conducted to determine the present state-of-the-art in this area and to identify the performance capability likely to be achieved in flight capsule applications.

2.1.4.3 Antenna Performance Determination

A parametric study should be conducted to determine the performance of antennas designed for nonerectable payloads. This study should include antenna measurements for a number of candidate payload shapes and the determination of the influence of lossy ground planes on antenna performance as a function of landed attitude. Such a program could indicate the degree of confidence which can be placed on the statistical definition of antenna performance.

2.1.4.4 Flight Spacecraft Relay Support Constraints

At the earliest possible date, the constraints which the flight spacecraft will place on the relay communication link (i.e., antenna gain, operating frequency, lead time, and down link data rate) should be defined.

TABLE I

TELECOMMUNICATION SUBSYSTEM SALIENT CHARACTERISTICS

Function - Telemetry, Data Handling and Command	
Modes of Operation	Direct to Earth Relay to Flight Spacecraft
Direct Link	
Data Rate	2 bps
Transmitter Power	20 watts (minimum)
Frequency	2295 MHz 2115 MHz
Modulation	Noncoherent multiple frequency shift 32-ary
Antenna	
Type	V Horn
Relay Link	
Data Rate	64 bps
Transmitter Power	30 watts (minimum)
Frequency	267-273 MHz
Modulation	Frequency Shift Keying (FSK)
Antenna Type	Planar Logarithmic Spiral
Data Handling	
Number of Measurements	
Scientific	25
Engineering	78
Storage	
Capacity	8000 bits entry/descent 12, 000 bits landed
Type	Core

2.1.4.5 Definition of Landed Payload Type

Direct-link system performance can be considerably improved through the use of a flotation sphere payload. Such a payload configuration, however, presents many engineering problems which reduce its attractiveness. A major effort should be directed towards analysis of these problems so that decisions regarding its use can be reached as early as possible.

2.1.4.6 Scientific Instrumentation Definition

Integration problems and the severe weight limitations of the 1971 flight capsule make early definition of the scientific payload mandatory.

2.1.4.7 Reliability Test Program

Test programs should be initiated immediately to assess the impact of the heat-sterilization environment on component reliability figures. Estimates are presently being made without adequate experimental data. Delays in determining the impact of heat sterilization will be reflected in uncertainty in the amount of redundancy required in the system and the resultant inefficient use of the payload weight allowance.

2.1.4.8 Piece-Part Shock Testing and Development

An extensive program for shock testing electric parts should be initiated immediately. The weight versus shock resistance trade-off study, which should be conducted, cannot be intelligently or profitably pursued without adequate shock-test data.

2.2 ELECTRICAL POWER

2.2.1 Study Objective

The objectives of the study effort in the electrical power area were as follows:

1. To analyze power profiles in each mission phase of the various mission concepts and establish the power and total energy requirements which must be satisfied.

2. To conduct a general survey of space power-system technology to identify those power sources which are potentially applicable to the EFAT concept.

3. To assist in the overall systems analysis by providing size and weight data for parametric studies which involve the EFAT power system.

4. To select one or more power sources which are capable of meeting the system power requirements.

5. To present a sample mechanization for the selected power source and attractive alternatives.

2.2.2 Significant Results

The following is a list of important conclusions reached in the study:

1. A battery is currently the only suitable power source capable of meeting the needs of the 1971 mission. However, the severe weight penalties imposed by the use of batteries present a major technical problem. During this study, payloads based on use of nickel-cadmium batteries were developed. The performance of such batteries was only slightly degraded by sterilization. Use of nickel-cadmium batteries represents a minimum-risk approach.

2. Silver-zinc batteries (which have a higher specific energy than nickel-cadmium batteries) have not been ruled out for the 1971 and 1973 missions. However, structural and other development work, such as that performed by Douglas Aircraft is required.

3. Considerable attention must be paid to the development of more efficient energy sources, such as the lithium chlorine Fuel Cell being developed by General Motors.

4. The power-source weight problem if not solved, will very likely limit the duration of the 1973 flight capsule mission, as well as the 1971 mission.

5. Solar-powered electrical energy sources, either externally mounted or erected, are considered impractical for the 1971 and 1973 missions.

6. The use of a radioisotope thermoelectric generator (RTG) with a hard lander seems unlikely, since thermal control problems are created which have no completely satisfactory solution at this time. In addition, the ability of thermo-electric elements to withstand high impact shock is questionable.

7. The primary energy for flight capsule operation should be supplied by the flight spacecraft until flight capsule/flight spacecraft separation.

The battery charger should also be located on the flight spacecraft. All other power conditioning equipment should be in the flight capsule.

8. On the basis of the voltage requirements of the subsystems considered in the study, it presently appears that direct current (dc) power distribution rather than alternating current (ac) distribution is preferable.

2.2.3 Reference Design Summary of Characteristics

The selected reference design for a 1971 EFAT mission is based on the use of a NiCad battery. The salient characteristics of the selected power system are shown in Table II. Also included are two attractive backup designs employing a sterilizable silver zinc battery (assuming it becomes a reality) and the lithium chlorine fuel cell as primary power sources. The total power subsystem weight for the reference approach is in excess of 100 pounds. Of even greater significance is the fact that 71 pounds of battery are located in the landed capsule and hence, considerable additional weight for impact attenuation is required for battery protection. The two backup approaches are particularly attractive because of their considerably lighter weight.

2.2.4 Critical Items

The success of a 24-hour mission in 1971 is critically dependent upon the weight available for telecommunications and electrical power. Accordingly, rapid development of efficient energy sources is essential. Development of silver zinc batteries capable of providing high energy density even after subjection to a heat sterilization environment, should be pursued vigorously. In addition, the lithium-chlorine battery/fuel cell should be immediately and thoroughly investigated. The potential of this power source is sufficiently high that its use would not only alleviate weight problems in 1971 but would also allow a multi-day mission in 1973, thus avoiding the problems associated with integrating an RTG into a hard lander.

2.3 RADAR SYSTEMS

2.3.1 Study Objectives

A minimum effort was directed toward the study of radar subsystems for the EFAT concept. No requirement existed for wind measurements or the determination of surface roughness as was the case for the EFO concept. The radar system was necessary with EFAT only to provide altitude information for correlating experimental data and for initiating parachute deployment.

TABLE II

SALIENT CHARACTERISTICS OF THE ELECTRICAL POWER SUBSYSTEM - 1971

Source	Prime Nickel-Cadmium Battery	Silver-Zinc Battery	Lithium Chlorine Fuel Cell System
Delivered energy Separation to impact	184 watt hours	184 watt hours	184 watt hours
Weight-separation to impact	33 pounds	14 pounds	see post impact weight.
Delivered energy post impact	565 watt hours	565 watt hours	565 watt hours
Weight-post impact	71 pounds	28 pounds	30 pounds (supplied energy from separation to end of mission)
Output Voltage Limits Before Regulation	25 to 33 vdc	25 to 37 vdc	3.0 to 3.5 vdc*
Charge Regulator	Resistor and diode in series for unlimited trickle charge plus temperature compensated full rate charging.	Current controller with full capacity cut-off and temperature compensation.	None required, extra fuel for extra discharge.

*DC-to-DC converter required to raise voltage.

The study objectives were, therefore, limited to a cursory study to establish the radar-system design requirements and to investigate its mechanization in sufficient depth to establish feasibility.

2.3.2 Reference Design Summary of Requirements and Characteristics

The overall performance and design features for the radar system for the EFAT concept are shown in Table III.

TABLE III

RADAR SYSTEM OVERALL PERFORMANCE AND DESIGN

Maximum Altitude	250, 000 ft
Minimum Altitude	1000 ft
Accuracy	5 %
Operating Frequency	
High Altitude	18 MHz
Low Altitude	32. 1 MHz
Transmitter Power	
High Altitude	25 watts
Low Altitude	1 watt
Antenna Type	
High Altitude	Ring
Low Altitude	Spiral
System Weight	40. 5 pounds

3.0 SUMMARY - ENTRY FROM ORBIT

3.1 TELECOMMUNICATIONS

3.1.1 Study Objectives and Scope

The general objectives and scope of the telecommunications study effort regarding the entry from orbit (EFO) approach were basically the same as those of the entry from approach trajectory (EFAT) study effort described in Section 2.0. In each case, the effort was directed towards systems analyses, conceptual design synthesis, and identification of problem areas that might represent significant design, development, or schedule risks.

The study requirements for the two concepts differed in detail, however. The dissimilarities in the two study efforts reflect the fundamental differences between the basic mission concepts.

The most significant areas in which the mission concepts differed are as follows:

1. The EFO mission does not include use of a landed capsule.

2. The communication range for the EFO concept is substantially shorter than that for the EFAT concept (approximately 1700 km instead of approximately 35,000 km). In turn, this permits use of considerably higher data rates in the EFO concept, thereby increasing the feasibility of conducting more ambitious experimental missions, including television.

3. Weight is not as critical a factor in the EFO concept as it is in the EFAT concept since the former concept does not require execution of a post-landing mission with its consequent requirement for a landed capsule .

As noted above, consideration of these basic conceptual differences led to differences in the study effort.

The importance of communication between the flight capsule and the flight spacecraft made it necessary to analyze the radio frequency (RF) link more extensively in the study of the EFO concept than was the case in regard to the EFAT concept. Analysis of the EFO concept required resolution of numerous tradeoffs involving orbit dimensions, de-orbit true anomaly, parachute size, and experimental objectives before telecommunication subsystem performance requirements could

be fully defined. No such considerations were involved in the EFAT study effort. Because the weight constraints for the EFO concept were less severe, considerable redundancy was possible. This was especially advantageous because the results of a thorough analysis of the effects of local (planetary) winds on performance of the EFO flight capsule clearly indicated the desirability of providing a particular type of redundancy. Synthesis of a detailed EFO conceptual design required conduct of an antenna measurement program more extensive than that required for the EFAT conceptual design. The results of the EFO antenna measurement program permitted antenna performance to be estimated with greater accuracy than would normally be the case in a study program as broad in scope as the current Mars/Lander study. Finally, because the EFO study was concentrated on a single, relatively specific, mission concept, that concept could be explored in greater depth (as compared to the depth of the EFAT concept study).

3.1.2 Reference Design Summary

The performance requirements for the flight-capsule telecommunication subsystem were dictated primarily, in fact almost solely, by the need to accomodate television in the experimental payload. The results of earlier studies (presented in Volume V, Book 4) indicated the desirability of obtaining a minimum of nine television pictures of the Martian surface. This objective, plus the needs of the various additional instruments included in the over-all flight capsule system, made it necessary to provide the capability for transmitting a minimum of 3×10^6 bits of data during the descent phase of the mission. It was determined on the basis of both the various atmospheric models considered in the study and a conservative selection of the size of the parachute required, that a minimum of 160 seconds would be available for data transmission during the descent phase. This makes it necessary to transmit data at a rate of 18,000 bits per second if the minimum requirements for the experimental mission are to be met.

Before a telecommunication subsystem concept capable of satisfying these requirements was selected, the following design guidelines were established. These were so selected as to assure adoption of a conservative and, therefore, low-risk design approach.

1. A single-orientation, low-gain, body-fixed antenna will be used in the flight spacecraft relay link receiving subsystem.

2. Wherever feasible, low-voltage, solid-state equipment will be used to eliminate design problems associated with high-voltage arcing.

3. The flight-capsule antennas should be of a broad-beam type to avoid any necessity for completely controlling the attitude of the flight capsule during the descent phase of the mission.

4. The telecommunication subsystem must be so designed that maneuvering of the flight capsule is not required for its successful performance.

5. Sufficient subsystem redundancy must be provided to assure that no single telecommunication subsystem failure will cause loss of data.

The salient characteristics of the reference design telecommunication subsystem that satisfies the data transmission requirements, and are consistent with the guidelines above are summarized on Table IV.

TABLE IV

TELECOMMUNICATION SUBSYSTEM SALIENT CHARACTERISTICS

Flight Capsule	
Frequency	267 to 273 MHz band
Bit rate	18,000 bits/sec
Radiated power	30 watts
Modulation	FSK
Range	1700 km maximum
Antenna type	Log spiral
Weight (total)	89.6 pounds
Power consumption	183 watts
Ancillary features	Redundant systems
Delay Memory Prevents	Loss of Data in Blackout
Flight Spacecraft	
Antenna type	Body fixed turnstile
Receiver noise figure	5 db

3.2 ELECTRICAL POWER

3.2.1 Study Objectives and Scope

The short duration of the EFO mission, as compared to that of the EFAT mission, clearly indicates that a battery should be used as the source of electrical power for the flight capsule. Although the scope of the EFAT study included a comprehensive investigation of numerous alternative

electrical-power sources, the EFO study was more limited in scope. It was, essentially, centered on:

1. Selection of a battery type and size that would best satisfy the power needs of the flight capsule in a manner consistent with the various mission and design constraints and with particular regard for the sterilization requirement.

2. Selection of a power conditioning subsystem concept capable of satisfying the power, voltage, regulation, and isolation requirements of the various electrical subsystems of the flight capsule.

3.2.2 Reference Design

An hermetically sealed nickel-cadmium battery forms the nucleus of the electrical power subsystem of the flight capsule. Two such batteries, each consisting of 24 series-connected cells, together with associated dual sets of power control and regulating equipment, compose the overall electrical-power subsystem. Since each battery with its associated power-control equipment can independently supply the total power demands of the electrical subsystems of the flight capsule, the various electrical power subsystem elements are so connected that the effects of any component failure will be minimized. Table V summarizes the significant design and performance characteristics of the electrical-power subsystem.

TABLE V

POWER SUBSYSTEM SALIENT CHARACTERISTICS

Energy (per battery)	740 watt-hours
Capacity (per cell)	27 ampere-hours
Operating Voltage	28.0 volts
Regulation	± 1 percent
Trickle Charge Rate	150 ma to 250 ma
Full Charge Rate	3 amps
Total System Weight	112 pounds
Total System Volume	1 ft^3

3.3 RADAR SYSTEMS

3.3.1 Study Objectives and Scope

Successful conduct of the EFO experimental mission is strongly dependent upon the degree of accuracy with which the altitude of the flight capsule is known. For example, the vertical structure of the Martian atmosphere can be completely defined only when altitude profiles are obtained. Several critical events, such as parachute deployment and penetrometer jettisoning, are best initiated on the basis of accurate knowledge of the altitude of the capsule. Determination of the size of various surface features observed in television pictures is impossible without adequate knowledge of the altitude at which the pictures were taken. These considerations, among many others, make it highly desirable to include a radar-altitude measuring system in the flight capsule.

The approach taken during the current study was based on synthesizing a radar concept capable not only of satisfying the altitude-measurement requirements of the present flight capsule but also with potential for meeting requirements of future planetary landers.

Complete definition of the characteristics of an optimum radar system capable of satisfying the various requirements and constraints of the EFO concept would have required an effort considerably beyond the scope of this study. Instead, certain representative concepts capable of satisfying each requirement were synthesized. Subsequently a sample mechanization was generated to demonstrate the feasibility of meeting the requirements. Actually, even this relatively simple approach resulted in the expenditure of considerable effort because of the wide variety of applicable experimental and operational requirements.

3.3.2 Design Summary

The radar system selected for incorporation in the flight capsule contains three basic subsystems, as follows: a high-altitude radar altimeter, a low-altitude radar altimeter, and a 3-beam velocity-attitude sensor. Brief descriptions of the nature and function of each of these systems follow.

1. High-Altitude Radar Altimeter -- This altimeter is capable of measuring the altitude of the flight capsule during the period between the end of the radio-frequency blackout and deployment of the parachute. This represents an altitude measuring range from a maximum of 250, 000 to a minimum of 20, 000 feet.

2. Low-Altitude Radar Altimeter -- This altimeter is designed to measure the altitude of the flight capsule between the time the parachute is deployed and the time the descending capsule reaches an altitude of 1000 feet. The measurement range, therefore, is from a maximum of 30, 000 to a minimum of 1000 feet.

3. Velocity-Attitude Sensor -- This sensor is, essentially, a three-beam radar system capable of measuring both range and range rate along each of the three beams. The beams are so oriented on the flight capsule that they make an angle of 20 degrees relative to the roll axis of the capsule. This sensor will allow relatively accurate estimates to be made of the horizontal velocity of the capsule. From these estimates, planetary wind velocities can be inferred.

The two altimeters will provide data regarding the nature of the planetary surface at two widely different wavelengths, 15 meters and 1 meter, respectively.

The principal characteristics of the radar system are indicated on Table VI.

TABLE VI

RADAR SYSTEM SALIENT CHARACTERISTICS

	Velocity Altitude Sensor	Altimeter	
		High Altitude	Low Altitude
Frequency	13 GHz	18 MHz	324 MHz
Transmitter power	1 watt/beam	25 watts	1 watt
Number of beams	3	1	1
Beamwidth	5 degrees	150 degrees	100 degrees
Accuracy	5 percent	5 percent	5 percent
Modulation	FM/CW	ICW	ICW
Altitude range	10 to 30, 000 feet	20, 000 to 250, 000 feet	1000 to 30, 000 feet
Weight	9 pounds	9 pounds	
Volume	1400 in.^{3}	1000 in.^{3}	
Power consumption	15 watts	60 watts	

4.0 PROBE LANDER, ENTRY FROM THE APPROACH TRAJECTORY

4.1 GENERAL

For the entry from approach trajectory (EFAT) case considered during the study, telecommunication functions are required during the various phases of cruise, entry, terminal descent, and post landing. The requirement that the landed capsule survive a hard landing imposes severe weight and volume limitations. The necessity for using large amounts of impact attenuator places a particular permium on the size of the telecommunication equipment used since the weight of the attenuator is a function of the volume of the internal payload.

These considerations made it necessary to investigate both the relay and direct link methods of transmission from the viewpoint of the applicability of each method to each of the mission phases, and to base selection of the methods to be used not only on comparative performance but also on their compatibility with the stringent weight and volume constraints.

4.2 REQUIREMENTS AND CONSTRAINTS

4.2.1 Functional Requirements

The overall functional requirements (data preparation, communication, and control) which must be satisfied by the telecommunications system can be briefly stated as follows. The system must perform the following tasks:

1. Prepare scientific and engineering data for efficient transmission to Earth through such operations as sampling, encoding, data compression, and storage. These functions are accomplished by appropriate telemetry, data automation, and data storage equipment.

2. Establish communications contact with Earth during cruise, entry landing, and transmit experimental and system-status data to Earth. These operations are accomplished by a radio frequency (RF) telecommunication system.

3. Control the operation of all Probe/Lander subsystems. The various timing, command, routing, and trajectory-sensing functions will be performed by a central computer and sequencer (CC&S).

4.2.1.1 Data Handling and Transmission

Data transmission requirements for the EFAT mission are summarized in Table VII. In satisfying the data handling and transmission requirements, both the direct link and the relay link should be utilized to the extent that weight constraints will allow so as to minimize the probability of loss of data in the event of subsystem failures.

TABLE VII

DATA TRANSMISSION REQUIREMENTS

Mission Phase	Approximate Data Transmission Rate (bps) Required	Data Objective
Preseparation	1000	Determine integrity of Flight Capsule Subsystem
Separation	1000	Verify execution of ACS impact dispersions and ΔV events
Cruise	50 to 100	Periodic status checks
Preentry	50 to 100	Calibrate instruments in zero G
Entry*	50 to 100	Define upper atmosphere
Terminal descent	50 to 100	Define lower atmosphere
Circa impact	10	Determine survival status and local environmental conditions
Landed	10	Collect surface environmental and science data

*Approximately 7 to 14 seconds of communications blackout occurs during this phase.

4.2.1.2 Control and Sequencing

Numerous events which occur between the time the flight capsule separates from the flight spacecraft and the end of the mission (approximately 24 hours after impact) must be controlled by the central computer and sequencer. Table VIII presents a summary of these events and indicates the mission phase in which each occurs. Timing signals necessary to control the multiplexing and encoding equipment must also be provided by the central computer and sequencer. The requirement that each event critical to mission success be initiated by functionally redundant means, if possible, was one of the prime design criteria for the control sequencer.

4.2.2 Mission and Design Constraints

4.2.2.1 Communications Range to Earth

The communications range to Earth for the 1971 opportunity is presented as a function of the arrival date in Figure 1. It is assumed that the maximum range will be the range appropriate for the last day of the orbitor optimized window. Consideration has recently been given to flying constant-arrival-date trajectories. Even in such cases, however, the most probable arrival dates occur late in the window and, hence, are consistent with the last-day assumption.

4.2.2.2 Landing Site Selection and Earth View Angles

The nominal landing site is assumed to lie along the sub-Earth latitude and 30 degrees west of the sub-Earth point. The 3-sigma dispersion in landing site is taken to be 7.5 degrees in latitude and 7.5 degrees in longitude. Figure 2 indicates the relationship between the Earth elevation angle and the local (Martian) horizontal as a function of time after impact.

4.2.2.3 Flight Spacecraft

Several trajectory and equipment characteristics of the flight spacecraft must be known before a meaningful communication system analysis can be conducted. Since specific information was not available, three alternative flight spacecraft models were considered in the study. These models represent minimum, nominal, and maximum performance capabilities relative to flight capsule needs. Table IX presents the salient features of each of these models and paragraph 4.4.2 discusses these features in detail.

TABLE VIII

PROBE/LANDER GENERAL

COMMAND AND SEQUENCING REQUIREMENTS

Mission Phase	Event	Recommended Prime Initiation	Recommended Backup Initiation
Separation	Multiple ACS operations	Timer	Redundant timer
	ΔV rocket ejection	Timer	Redundant timer
Cruise	Transmitter control	Timer	Redundant timer
	Activate entry systems	Timer	Redundant timer
Entry/descent	Data storage activation	Accelerometer (longitudinal axis)	Lateral axes of accelerometer
	Data mode switching	Inertial time	VSWR monitor
	Entry vehicle jettison and parachute deployment	Accelerometer	Altimeter
	Altimeter switching	Entry shell separation loop	Entry shell redundant separation loop
	Landed capsule tethering	Altimeter	Accelerometer
	Landed capsule release	Altimeter	Accelerometer
Postlanding	Data mode switching	Timer	Command
	Transmitter control	Timer	Command

TABLE IX

SIGNIFICANT SPACECRAFT CHARACTERISTICS

	A. (Minimum Performance)	B. (Nominal Performance)	C. (Maximum Performance)
Communications Range at Entry	60,000 km	35,000 km	25,000 km
Lead Time	5 hours	3 hours	2 hours
Receiving Antenna type and gain	Body Fixed 5.5 db maximum gain	Body Fixed 10 db maximum gain	Steerable on PSP 10 db maximum gain
Receiver Noise Temperature	1450°K	1450°K	1450°K
Operating Frequency*	400 MHz	272 MHz	272 MHz
Down Link Data Rate **	<100 bit/sec	>1000 bit/sec	>1000 bit/sec
Command Capability	None	None	Yes
• Function	N/A	N/A	Landed capsule control turn-on capability
• Frequency	N/A	N/A	VHF
• Power	N/A	N/A	25w
Orbital Operation	No contact after orbit injection	No contact after orbit injection	Contact by command during period between 20-30 hours after entry
Orbit Geometry			
• Periapsis	N/A	N/A	4000 km
• Apoapsis	N/A	N/A	14,000 km
• Inclination	N/A	N/A	40 degrees
Heading	N/A	N/A	South

*The operating frequencies were selected after analysis of the over-all relay problem and should not be considered as inferred constraints.

**Data rate from the flight spacecraft to Earth.

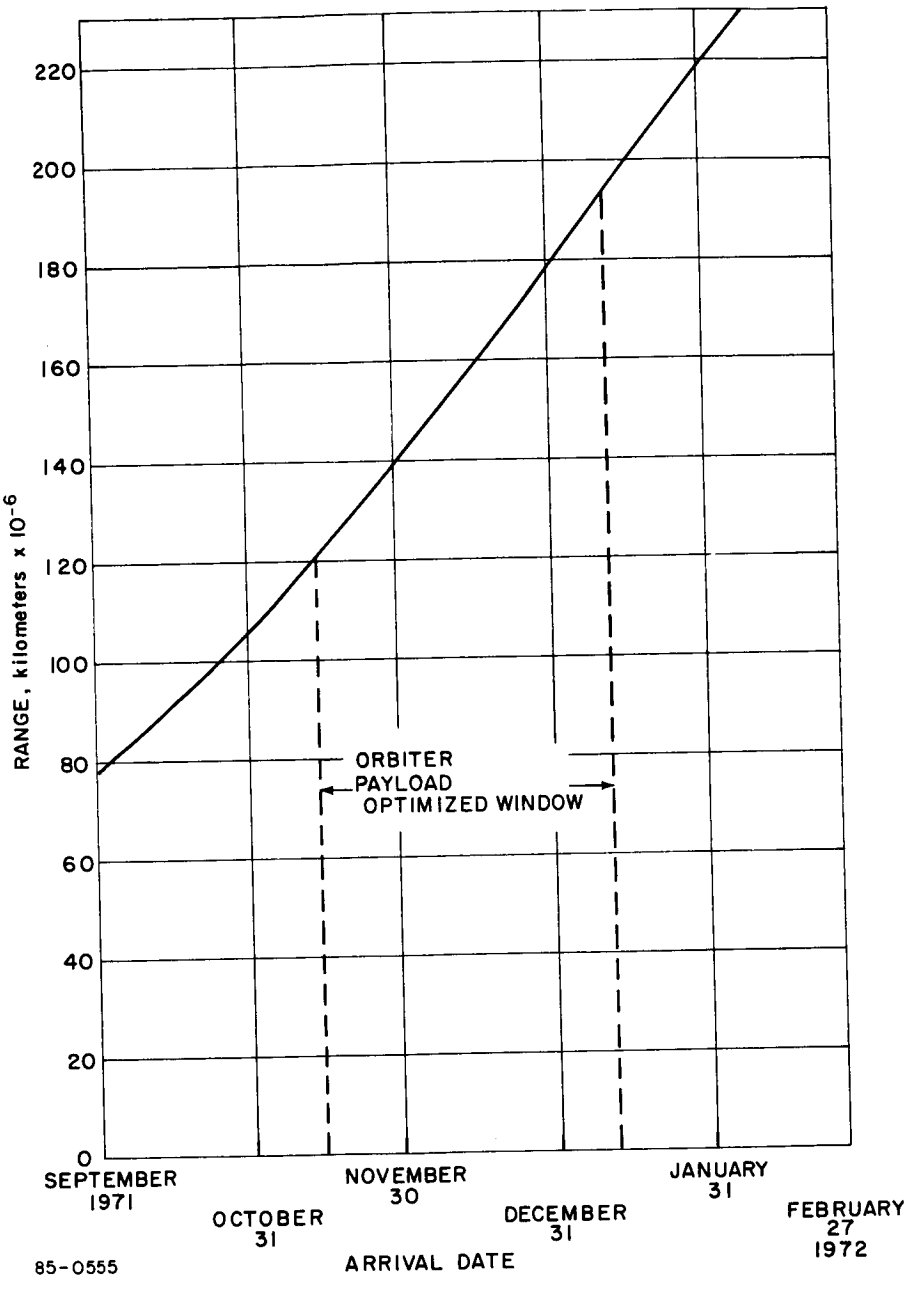

Figure 1 COMMUNICATION RANGE - 1971

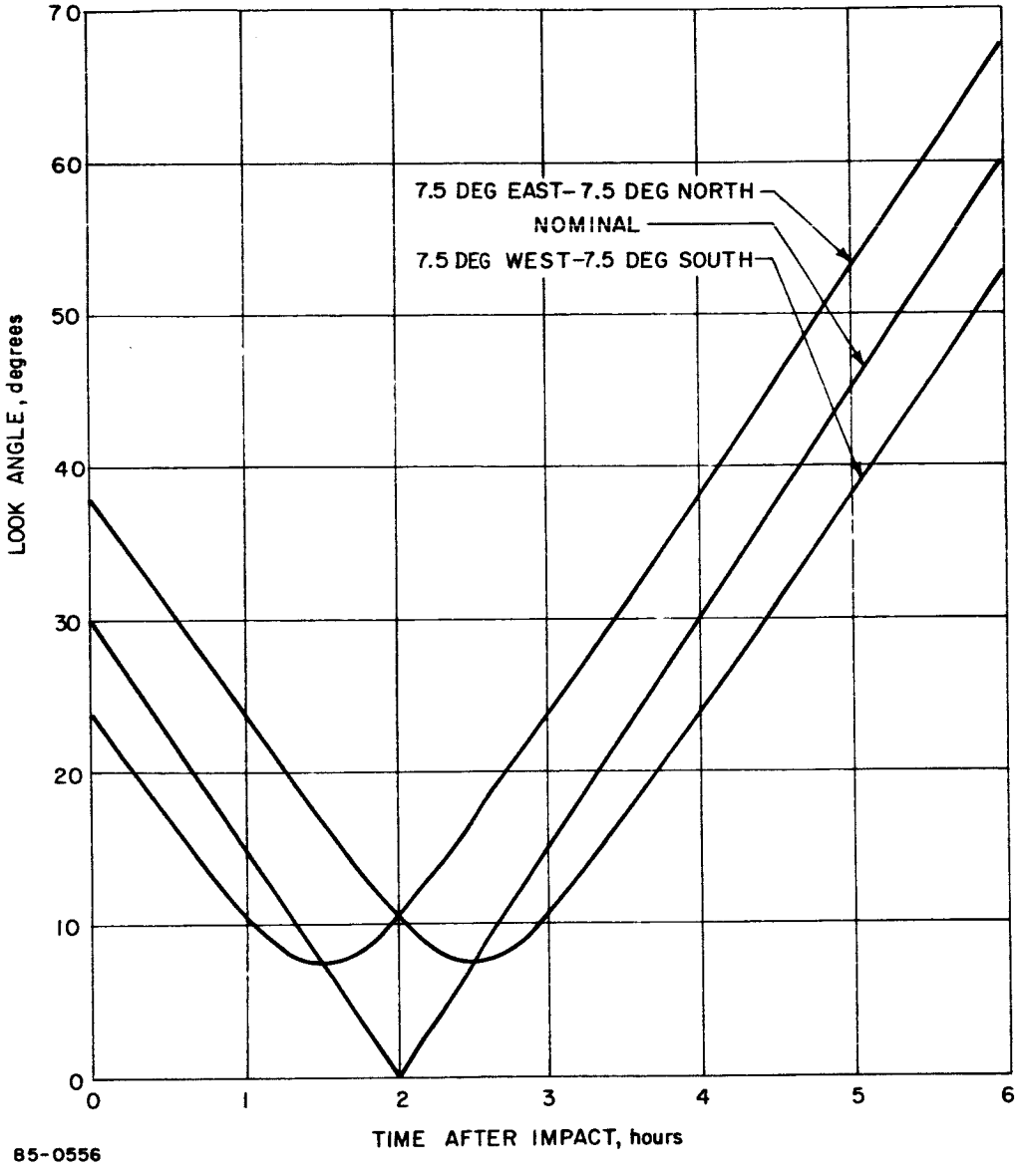

Figure 2 LANDED CAPSULE LOCK ANGLE, 11 JANUARY 1972

4.2.2.4 Flight Capsule

Two generic models of the landed capsule considered in this study were the following:

1. Flotation Sphere -- A landed capsule capable of aligning a non-steerable antenna along the local vertical. The antenna beamwidth in this case is determined by variations in the Earth look angle.

2. Oblate Spheroid -- A landed capsule which can randomly assume any orientation when landed. Large antenna pointing errors must be accepted for such a capsule configuration.

4.2.2.5 Environmental

A detailed list of the environmental criteria, including the sterilization requirements, is presented in Volume II Book 2.

4.2.2.6 Deep Space Network

The deep space network (DSN), including the deep space instrumentation facility (DSIF) and the space flight operations facility (SFOF), will be used as defined in Jet Propulsion Laboratory (JPL) document TM No. 33-83, Revision 1, The Deep Space Network - Space-Flight Operations Facility Capability and Deep Space Network Ground Communication System Development Plan.

4.2.2.7 Engineering State-of-the-Art

The technology cut-off date for the 1971 design is considered to be September 1966. That is, only those design concepts, the feasibility of which has been demonstrated and has been fully developed by that date, shall be considered in defining the 1971 mission design.

4.2.2.8 Weight

Weight, although not set quantitatively is an extremely important constraint in the 1971 design. The weight must be kept to a minimum consistent with the performance and reliability requirements.

4.2.2.9 Reliability

First-estimate reliability allocations have been made. These are presented in Volume II Book 2.

4.3 DESIGN OBJECTIVES

The criteria followed in designing the communications system were determined primarily by the following 11-point reliability design objectives:

1. The design should be conservative. That is, it should be within the scope of current technology and utilize proven concepts.

2. The design should be simple. Wherever possible, the number of steps and the amount of hardware involved in the operational sequences necessary to perform a given function should be made as small as possible. Complexity and sophistication extending beyond actual performance requirements are unwarranted.

3. The design should include provisions for minimizing the impact of failures. Redundancy should be used wherever possible consistent with weight allowances. As a minimum, alternative modes of sequence initiation, and backup modes for use in case of an event failure should be provided for all critical mission events.

4. The design should be substantiated. The basis for design selection should be fully supported by adequate documentation, including such empirical evidence as operational data or experimental results. A two-fold requirement exists in those areas of design that are based on analysis. First, all assumptions, areas of uncertainty, and undefined environmental limitations must be unambiguously identified as part of the design specification. Secondly, thorough environmental tests must be performed to substantiate the adequacy and capability of the design before type approval is granted.

5. The design should be flexible. In areas where performance is highly sensitive to interface changes or to uncertain environmental limits, adequate provisions must be made for contingencies. These may include such safety margins, derated applications, environmental protection and the like, as are adequate to accommodate changes without requiring major design revisions.

6. The design should be robust. In cases where the performance loss resulting from application of a worst-case design approach cannot be tolerated, functional redundancy is recommended. This is to be encouraged particularly when timing is a critical factor. For instance, parachute deployment could rely on an accelerometer or timer for the earliest initiation and on an aneroid barometer or radio altimeter for the latest initiation.

7. The design should be standardized. Parts, materials, and circuits should primarily be selected from those items on approved lists. Such lists should only include items developed for high reliability, compatibility with the sterilization environment, suitability for withstanding high impact forces, etc. Evidence of acceptability or, alternatively, detailed plans for tests that can produce such evidence must be available before items from non-approved sources are selected.

8. The design should be producible. The designer should give adequate consideration to the normally available quality (within the normal limts of item-to-item production variations) of the hardware selected. Wherever possible, designs should not require extensively selective screening or matching of components in fabrication. Imposition of unreasonably close tolerances (for example, relatively small limits on relatively large dimensions) must be justified in terms of necessity, fabrication requirements, and insensitivity to environmental conditions.

9. The design should be sterilizable. The design must be compatible with the terminal heat method of sterilization.

10. The design should be capable of remote automatic checkout. Sufficient engineering diagnostic sensors should be included to allow rapid and orderly determination of the ready status of the hardware and to enable equipment failures to be anticipated, detected, or diagnosed. The remote automatic checkout feature is necessary to eliminate problems induced by human intervention, to reduce delay time at launch, and to facilitate deep-space trouble shooting.

11. The design should be capable of automatic operation. It should be designed to complete the entire mission from launch through to the end of the mission without Earth-based intervention or support.

4.4 DESCENT RELAY LINK RF ANALYSIS

The following critical features formed the basis for analyzing the performance capability of the relay link:

1. Communication range between the flight spacecraft and the flight capsule
2. Flight spacecraft receiving system characteristics
3. Flight capsule design, dynamics, and constraints
4. Frequency selection
5. Flight capsule transmitter power
6. Modulation/detection techniques

4.4.1 Communication Range Between the Flight Spacecraft and the Flight Capsule

Figure 3 shows the geometric relationship between the terminal points of the relay link during the entry phase of operation. During this phase, the relay-link communication range is longer than in any other mission phase. The range is determined by the desired lead time between the flight spacecraft and the flight capsule. Selection of the lead time is based on the requirement that the relay communications mission be accomplished and that transmission of data to Earth be completed before the flight spacecraft is maneuvered into its orbit injection attitude. The exact lead time chosen is a function of the degree of conservatism with which it is selected. In the current study, three lead times, each reflecting a different degree of conservatism, were considered, as described below. As can be seen from Figure 3, the approximate communications ranges associated with the three lead times are 25,000, 35,000, and 60,000 kilometers, respectively.

1. Two Hours -- This represents the absolute minimum lead time which could be assigned on the basis of the following assumptions: 1) the entry and descent period is a maximum of 15 minutes, 2) the relay link will operate for 10 minutes after landing, 3) the flight spacecraft-to-Earth data capability is far greater than the flight capsule-to-flight spacecraft data capability and, hence, data transmission to Earth consumes no additional time, 4) the command to the flight spacecraft to assume its maneuver attitude is received immediately after the last data is sent to Earth via the relay link, 5) the flight spacecraft to Earth transit delay for the command verification signal

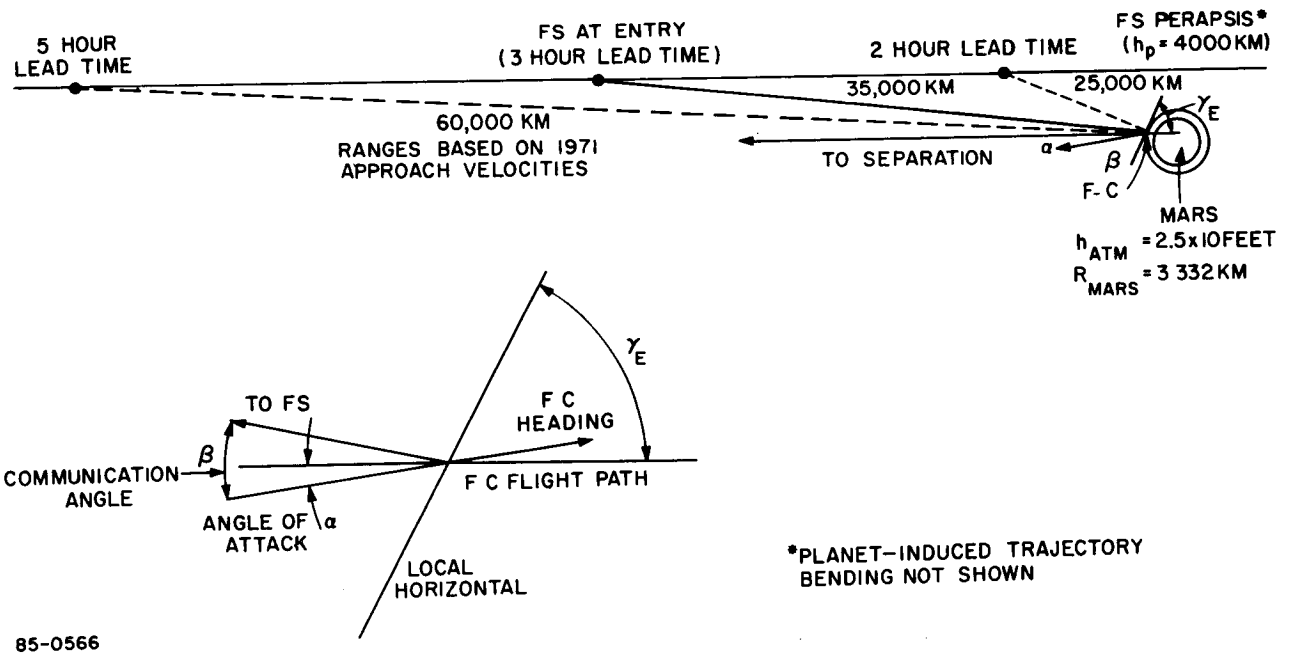

Figure 3 COMMUNICATION GEOMETRY AT ENTRY

is 11 minutes, 6) the Earth to flight-capsule transit delay for an execute command is 11 minutes, 7) 30 minutes is taken to execute the attitude change maneuver, 8) the transit delay for telemetering engineering data to Earth is 11 minutes, 9) the transit delay for an orbit injection command from Earth is 11 minutes, and 10) approximately 20 minutes is required on Earth for command decision.

2. Three Hours - This represents the nominal lead time. It includes additional time for decision making on Earth and, possibly, time for multiple attempts to attain the proper orbit injection attitude.

3. Five Hours -- This represents the maximum lead time. It includes an appropriate time allowance for multiple attempts to attain the proper orbit injection attitude, as well as considerable time to think between events.

4.4.2 Flight Spacecraft Receiving System Characteristics

As noted in paragraph 4.4.1, above, several assumptions were made regarding the flight spacecraft. The characteristics listed in Table IX reflect these assumptions. The basis on which they were selected is presented in the following paragraphs:

4.4.2.1 Antenna

1. Minimum Performance -- It was assumed that size and view-angle constraints would inhibit freedom in selecting the receiving antenna system. The highest frequency range below L-band in which an allocation can be obtained without difficulty is 400 MHz. Since system performance at and above L-band frequencies would be greatly degraded, a 400 MHz turnstile-type antenna with a maximum gain of 5.5 db was selected to meet minimum performance requirements.

2. Nominal Performance -- It was assumed that the optimum relay frequency, from a flight capsule viewpoint, could be chosen, and that the only major constraint was that the antenna be a body-fixed type. A 10-db-helix antenna was selected to meet nominal performance requirements.

3. Maximum Performance -- It was assumed that the antenna could be mounted on the planetary science platform (PSP) and pointed toward the center of the planet both during entry and after orbit injection. Such an arrangement would simplify the problem of relay-link communication after orbit injection.

4.4.2.2 Receiver Noise Temperature

No particular difficulty is expected in achieving a system noise temperature of 1450°K, but any appreciable reduction in that figure was considered impractical. Hence, a maximum noise temperature of 1450°K was assigned for all models.

4.4.3 Flight Capsule Design, Dynamics, and Antenna Constraints

Since the most critical phase of relay operation occurs during the period between the end of communications blackout and planetary impact (terminal descent), the first step in defining antenna performance requirements is examination of the flight-capsule to flight spacecraft look angles during that period. The factors which determine the look angles are: the entry angle, the angle of attack, parachute dynamics, and the range and approach asymptote. These factors are discussed in paragraphs 4.4.3.1 through 4.4.3.4.

The second step involves examination of various aspects of multi-path transmission, as discussed in paragraph 4.4.3.5.

4.4.3.1 Entry Angle

The entry angle is defined as the angle between the velocity vector of the flight capsule and the local horizontal. This angle is determined by the location of the desired impact point and the arrival date.

4.4.3.2 Angle of Attack

The angle of attack is defined as the angle between the flight path of the flight capsule and the roll axis of the flight capsule. During the later phase of entry (after blackout but before parachute deployment) this angle is relatively small due to the convergence of the flight path and roll axis as a result of aerodynamic forces.

4.4.3.3 Parachute Dynamics

The possibility of the presence of high winds near the surface of the planet makes it necessary to consider the effects of parachute dynamics. Figure 4 shows the response of the suspended capsule to a 50 ft/sec change in wind velocity. It should be noted that the net effect is a transient oscillation of the suspended capsule about a mean angle of attack.

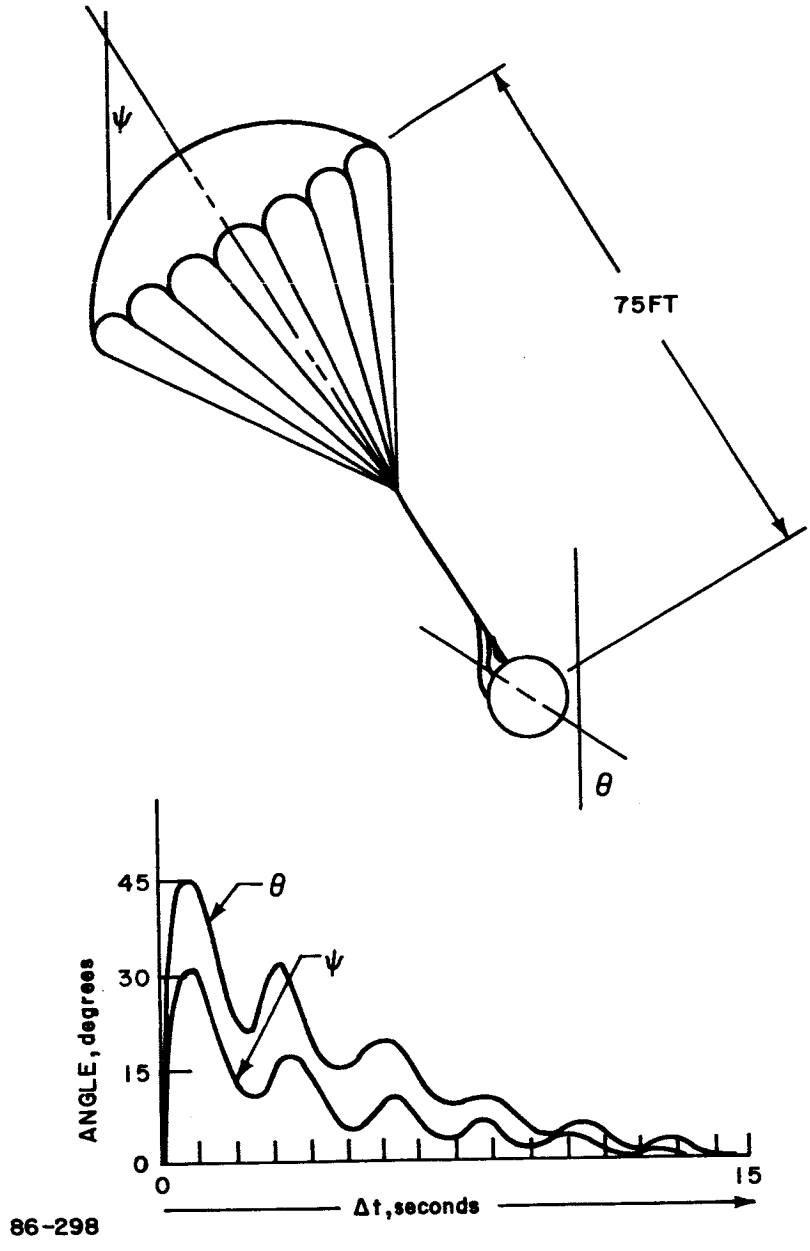

Figure 4 PARACHUTE DYNAMICS

4.4.3.4 Range and Approach Asymptote

The range between the relay-link terminals (flight capsule and flight spacecraft) during entry and descent, and the flight spacecraft trajectory, affect the value of the flight-capsule to flight-spacecraft look angles.

A composite representation of the look-angle time history for the case of a 44-degree entry angle with a 50 ft/sec wind gust during terminal descent is given in Figure 5. It is apparent that an antenna with a broad beamwidth is required for operation during this phase.

4.4.3.5 Multipath Transmission

Figure 6 shows various concepts considered in designing the suspended capsule, together with the radiation patterns characteristic of each during entry and during parachute-aided descent. It is apparent from that figure that the antenna must be designed for a number of configurations, including:

1. Flotation sphere payload without flight capsule afterbody -- Broad beamwidth antennas mounted on this shape direct considerable energy toward the planet.

2. Oblate spheroid payload without flight capsule afterbody -- Broad beamwidth antennas on this shape direct little energy toward the planet.

3. Any configuration with flight capsule afterbody -- Antennas on this type of vehicle are similar to those on the oblate spheroid in that they confine the radiation to the desired hemisphere.

The problem created when energy is directed toward the planet results from the fact that a certain fraction of this energy is reflected in the direction of the flight spacecraft. Because the suspended capsule is in motion, the flight spacecraft receives a signal, the strength of which fluctuates as a result of the time-varying cancellation and reinforcement of the direct and reflected signals. If the signal drops below the receiver threshold during a null, detection is impossible. For a complete treatment of this subject, see Appendix 4-7, in Reference 1. In summary, the desired antenna pattern is essentially hemi-omni. That is, it confines all of the energy within the desired hemisphere with approximately uniform distribution within that hemisphere. Figure 7 indicates the free space pattern of a planar spiral antenna under consideration for use on the suspended capsule during terminal descent.

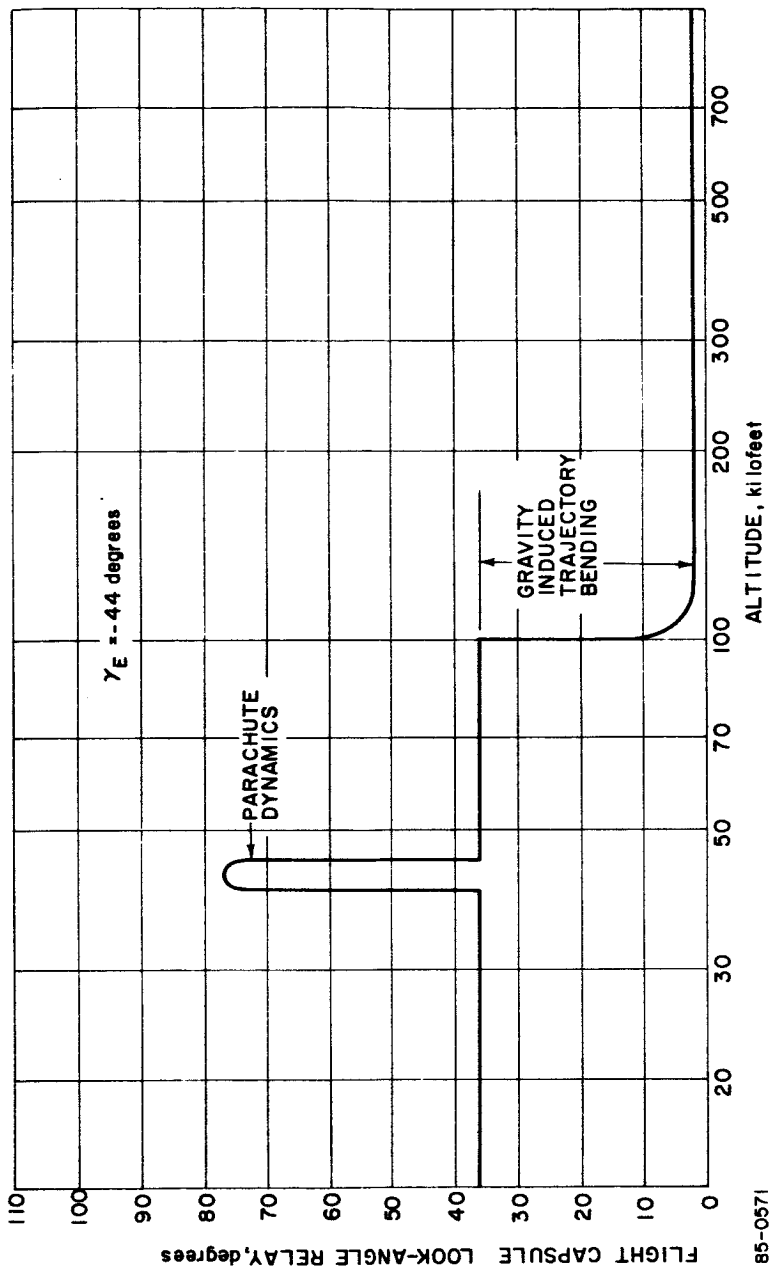

Figure 5 RELAY LINK FLIGHT CAPSULE LOOK ANGLE REQUIREMENTS

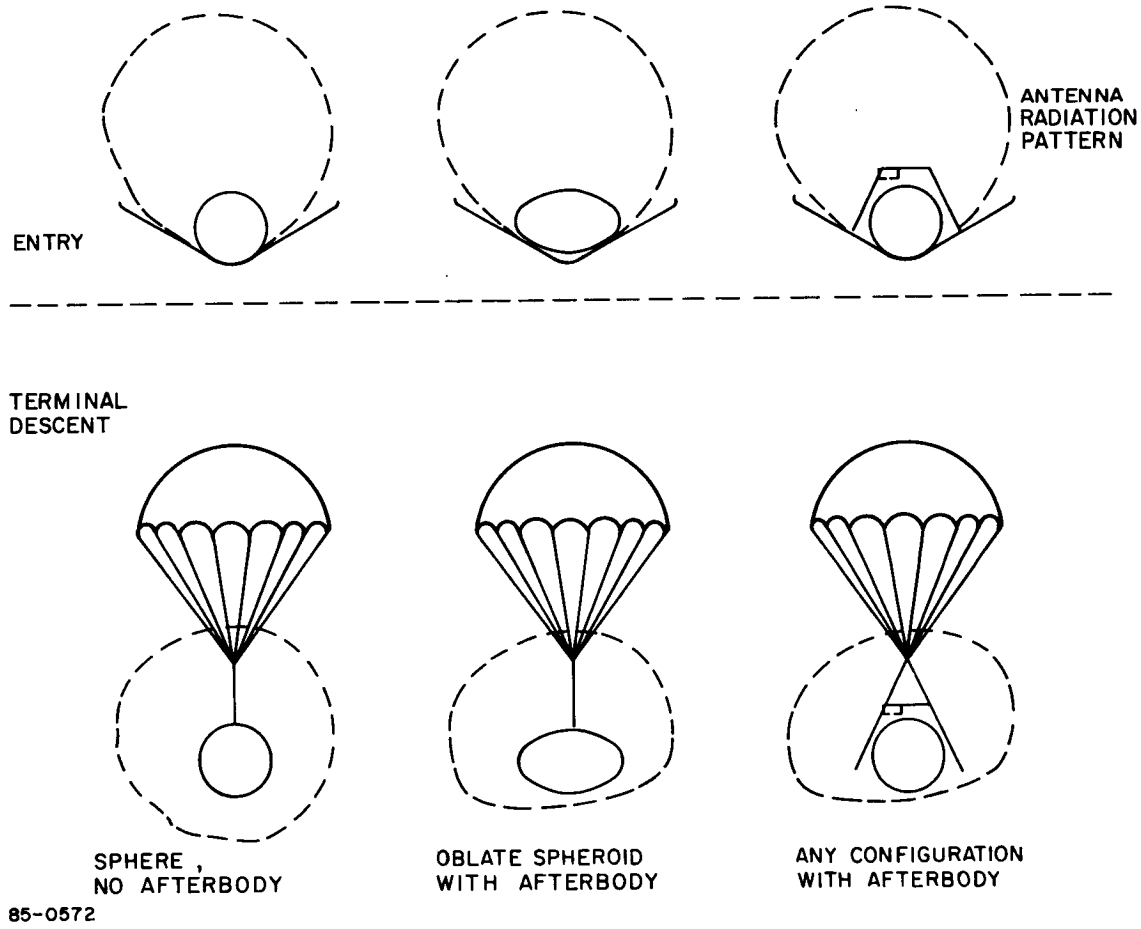

Figure 6 EFFECT OF SHAPE ON ANTENNA PATTERN

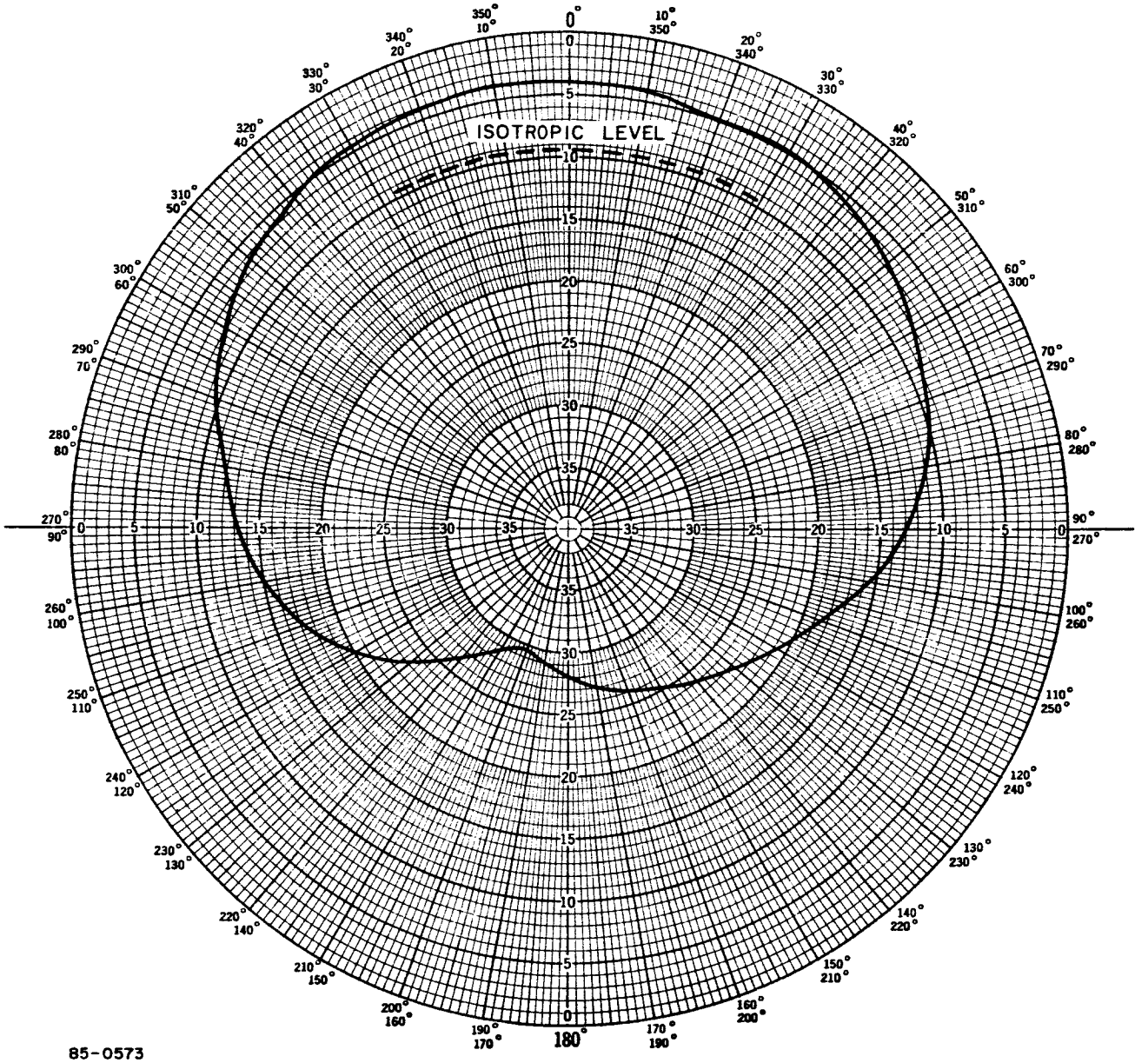

Figure 7 PLANAR SPIRAL ANTENNA PATTERN

4.4.4 Relay Frequency Selection

Figure 8 summarizes the results of a frequency selection analysis which is presented in detail in Appendix 4-6 of Reference 1. The criteria used in the selection process were the following:

1. Received signal power, assuming a fixed aperture constraint upon the flight spacecraft antenna.

2. Received signal power, assuming a fixed beam-width constraint upon the flight spacecraft antenna.

3. Transmitter power output, assuming a completely solid state design.

4. Ability to obtain a frequency allocation.

5. Weight of the transmission system and battery for a fixed data content.

All relevant factors point to selection of frequencies in the VHF region. Allocations can be obtained without difficulty at approximately 137, 272, and 400 MHz. Payload volume limitations made a frequency of 137 MHz the least attractive of the three possibilities. Of the two remaining frequency candidates, 272 MHz appears the most attractive from a weight viewpoint and was selected as the design frequency in this study.

4.4.5 Flight Capsule Transmitter Power

Selection of flight capsule transmitter power was based on the following considerations:

1. Antenna breakdown

2. State-of-the-art limitations

3. High Voltage arcing

Each of these considerations is discussed briefly in the following paragraphs

4.4.5.1 Antenna Breakdown

The problem of antenna breakdown becomes serious at low atmospheric pressures and must be considered in selecting the power level.

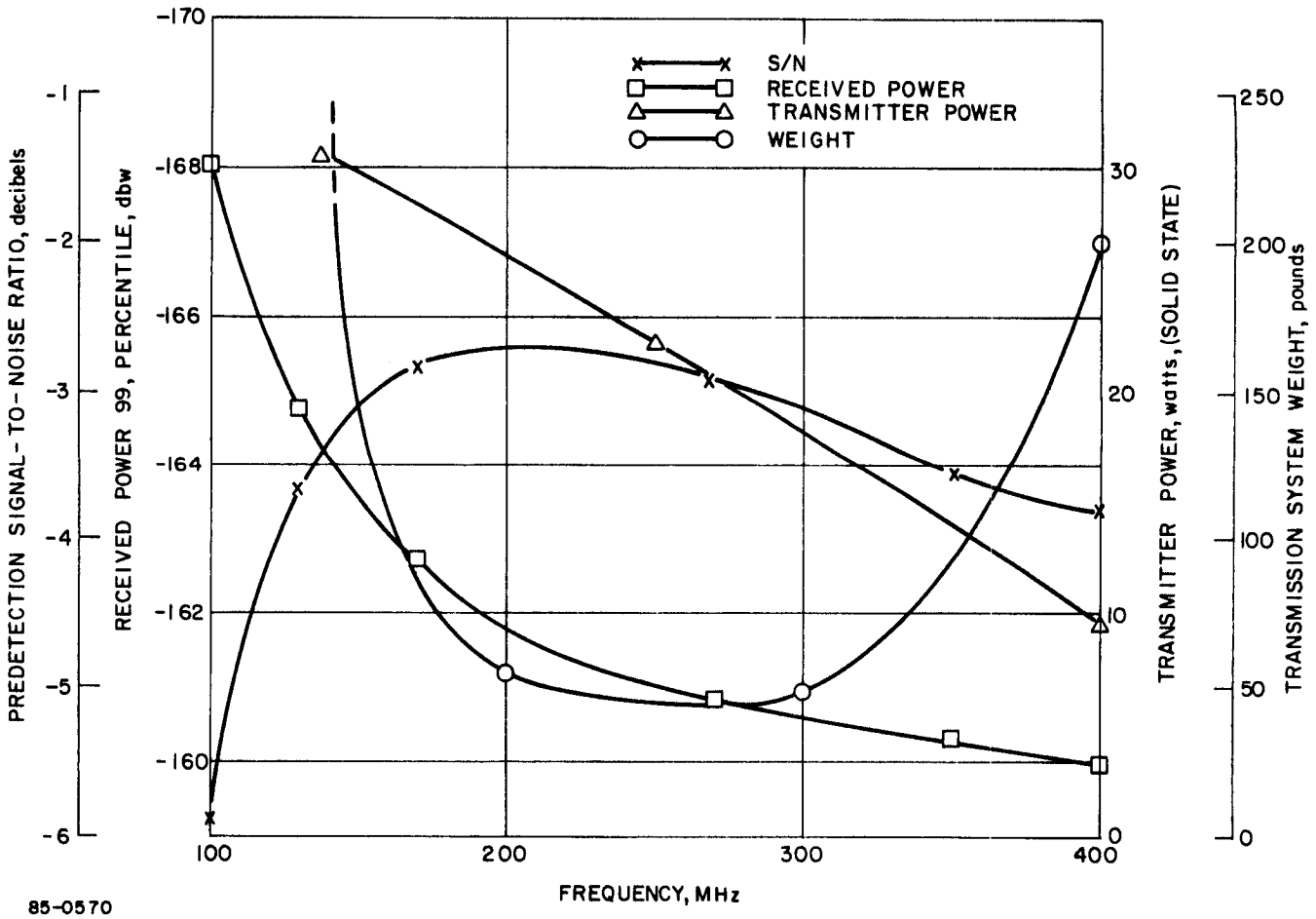

Figure 8 RELAY FREQUENCY SELECTION

Although antennas can be designed to operate in any atmosphere at any power level, experience indicates that for simple antenna configurations and, in general, for antennas with a single radiating element, care must be taken in handling power in excess of 10 watts to ensure freedom from voltage breakdown in low pressure atmospheres (see Appendix 4.4 in Reference 1). Since the flight capsule will be exposed to atmospheric pressures ranging from space vacuum up to possibly 10 millibars during entry and descent, it is considered a design risk at this time to consider transmitter power levels greater than 30 to 40 watts.

4.4.5.2 State-of-the-art Limitations

Solid state devices (transistors) are currently available with power output capabilities in the 10 to 15 watt range for carrier frequencies in the 270 to 400 MHz band of interest. It is predicted, however, that by mid 1966 this capability will have increased from 15 to 30 watts in the same frequency band. Power levels above these values can be achieved using vacuum-tube amplifiers.

4.4.5.3 High Voltage Arcing

It is desirable to avoid high voltage potentials when operating at the low atmospheric pressures expected during entry and descent because high voltage arcing is a likely hazard unless adequate precautions, such as pressurizing the high voltage components, are taken.

In summary, transmitter powers above 40 watts are unattractive because of potential antenna breakdown, and devices, such as vacuum tubes, which require high voltages, are unattractive from the viewpoint of design risk in the event of pressurization failure. As for solid state devices, while their use circumvents the high voltage problem, units with output powers above 30 watts are not currently available and are not expected to become available in the near future.

Since high voltage arcing will always consitute a design risk, 30 watts was chosen as the transmitter power level, and it is recommended that a solid state amplifier be developed to furnish that power.

4.4.6 Modulation/Detection Techniques

In choosing a suitable modulation technique for the flight capsule relay link, a number of criteria must be considered. The optimum choice must be based on a critical analysis of, and subsequent compromise among, various conflicting selection criteria. Such an analysis was conducted during the study (see Appendix 4-8, in Reference 1). A variety of communication systems were considered, including systems for both coherent and non-coherent detection applications.

The major criteria upon which selection of the relay link modulation technique was based were:

1. Relative communication efficiency

2. Compatibility with mission requirements

3. Compatibility with environment

4. Equipment complexity

5. Potential for growth.

Evaluation of the results of the analysis of these criteria are described in paragraphs 4.4.6.1 through 4.4.6.5.

4.4.6.1 Relative Communication Efficiency

From the viewpoint of overall communication efficiency, the coherent pulse-code modulation/phase shift keying, phase modulation (PCM/PSK/PM) technique appears to be the best choice for a relay data link.

4.4.6.2 Compatibility with Mission Requirements

Insofar as compatibility with mission requirements is concerned, either coherent PCM/PSK/PM or non coherent pulse-code modulation frequency-shift keying (PCM/FSK) modulation will satisfy the minimum (without television) requirements for the 1971 mission. The coherent PCM/PSK/PM system must be used as the prime relay-link communication mode in 1973 if descent television is incorporated in the mission.

4.4.6.3 Compatibility with Environment

With respect to compatibility with the environment, a noncoherent rather than a coherent modulation technique is more attractive. During entry, the radio link will be blacked out for a short period of time. As a result, a coherent system will, in all probability, lose carrier phase lock and will have to re-acquire this lock after blackout. As the amount of time available for reacquisition decreases, the communication efficiency of the coherent system will decrease correspondingly, since more and more carrier power will have to be allocated to the carrier-phase lock loop in an effort to reacquire and maintain phase lock. A similar argument applies during the terminal descent phase when exposure to high velocity wind gusts could cause the performance margin of the relay link to drop below threshold level, again resulting in the loss of carrier phase lock with coherent systems. Such a situation would not exist with a noncoherent modulation scheme such as noncoherent FSK.

4.4.6.4 Equipment Complexity

From an equipment complexity viewpoint, a noncoherent modulation technique offers some advantages relative to the coherent technique since the requirement for carrier lock is eliminated in the noncoherent scheme. The advantage is slight, however, because although additional circuits are introduced, the phase lock loop circuits required to implement coherent techniques are not particularly complex.

4.4.6.5 Potential for Growth

In the light of requirements for post-1971 missions, the coherent PCM/PSK/PM appears most attractive since it would be required for the transmission of television data.

4.4.6.6 Modulation/Detection Summary

In summary, both coherent PCM/PSK/PM and noncoherent PCM/FSK are attractive alternate modulation techniques. Coherent PCM/PSK/PM is desirable on the basis of overall communication efficiency, compatibility with mission requirements, and growth potential. Noncoherent PCM/FSK is desirable because of its compatibility with the environment and the slightly less complex equipment required for its implementation. From the viewpoint of overall mission success, the following recommendations are made:

1. A single transmitter capable of either phase modulation (PM) or frequency-shift keying (FSK) operation should be developed for the 1971 mission.

2. Payloads for the 1971 mission should be developed with FSK data-rate capabilities.

3. An experimental program designed to verify the performance of the wideband PCM/FSK system at low signal-to-noise (S/N) ratios should be initiated.

4. An experimental program designed to verify the performance of the coherent PCM/PSK/PM system with respect to acquisition and loss-of-lock characteristics in high velocity and/or deceleration regimes should be initiated.

5. Use of some form of feed-through system appears feasible. This would avoid the necessity for bit-by-bit detection on board the flight spacecraft. Considerably more work must be done in this area, however, to resolve and optimize the various required tradeoffs.

In defining the relay-link performance capability during the entry and descent phases of the mission, the noncoherent FSK modulation technique was used. Table X presents the data rates achievable with a 30 watt transmitter for the various flight spacecraft options, (see Appendix 4-9, in Reference 1 for the link calculations).

TABLE X

RELAY-LINK DATA RATES

Flight Spacecraft Model	Minimum	Nominal	Maximum
Data Rate (bps)	2	64	128

4.5 POST-LANDING RELAY LINK RF ANALYSIS

One of the Probe/Lander objectives for the 1971 mission is performance of post-landing functions for a minimum of 24 hours. An effort has been made to define a system not only capable of meeting this goal but also capable of meeting it with minimum reliance on the flight spacecraft.

The maneuver of injecting the flight spacecraft into a Martian orbit and the collection and forwarding of data from scientific experiments on the Martian surface are in themselves spectacularly difficult accomplishments. It was considered imprudent, therefore, to rely on the relay link as the sole means of accomplishing the Martian surface-data acquisition and transmittal tasks, since such an approach would require successful completion of orbit injection as a necessary condition for successful completion of the surface tasks. In view of this situation, development of a system for direct Mars-Earth communication is required as the prime post-impact communication link. As a backup, it would be desirable to have the capability for communications contact between the flight capsule and the orbiting flight spacecraft after the Martian night. This capability would provide alternative means for obtaining night-time scientific data. This would be of definite ensurance value in the event of failure of the direct link equipment at or after impact. The price paid for this capability must, however, be consistent with the expected return. After careful consideration of the many intricate operations which the flight spacecraft must execute before it can be used as an in-orbit relay link terminal, it was decided that in-orbit contact capabilities after the Martian night would be considered for incorporation in the minimum or nominal performance flight spacecraft models only if:

1. The flight spacecraft antenna system used during entry and descent could also be used for in-orbit operations without repointing (see Figure 9).

2. The mutual flight capsule/flight spacecraft visibility time is sufficiently long to be useful and sufficiently predictable to allow contact to be made without command assistance from the flight spacecraft.

Essentially, in-orbit contact capability would be considered for the minimum or nominal performance models only if little or no change had to be made in the flight-spacecraft receiving system, a system necessary to support communications prior to orbit injection.

An exhaustive analysis was conducted to select the orbit or orbits capable of satisfying constraints 1. and 2., above (see Appendix 4 -5, in Reference 1). Although several alternative orbits could provide adequate mutual visibility, the dispersion in visibility times caused by the various error sources make the required relay link transmitter operating time prohibitive* unless transmitter operation can be controlled by command from the flight spacecraft. Incorporation of this capability into the flight spacecraft was considered so difficult that command capability was eliminated from further consideration for the minimum and

*This is true principally because of the low energy-to-weight ratio attainable with nickel-cadmium batteries. Selection of a more efficient power source could, of course, lead to reconsideration and possible revision of this conclusion.

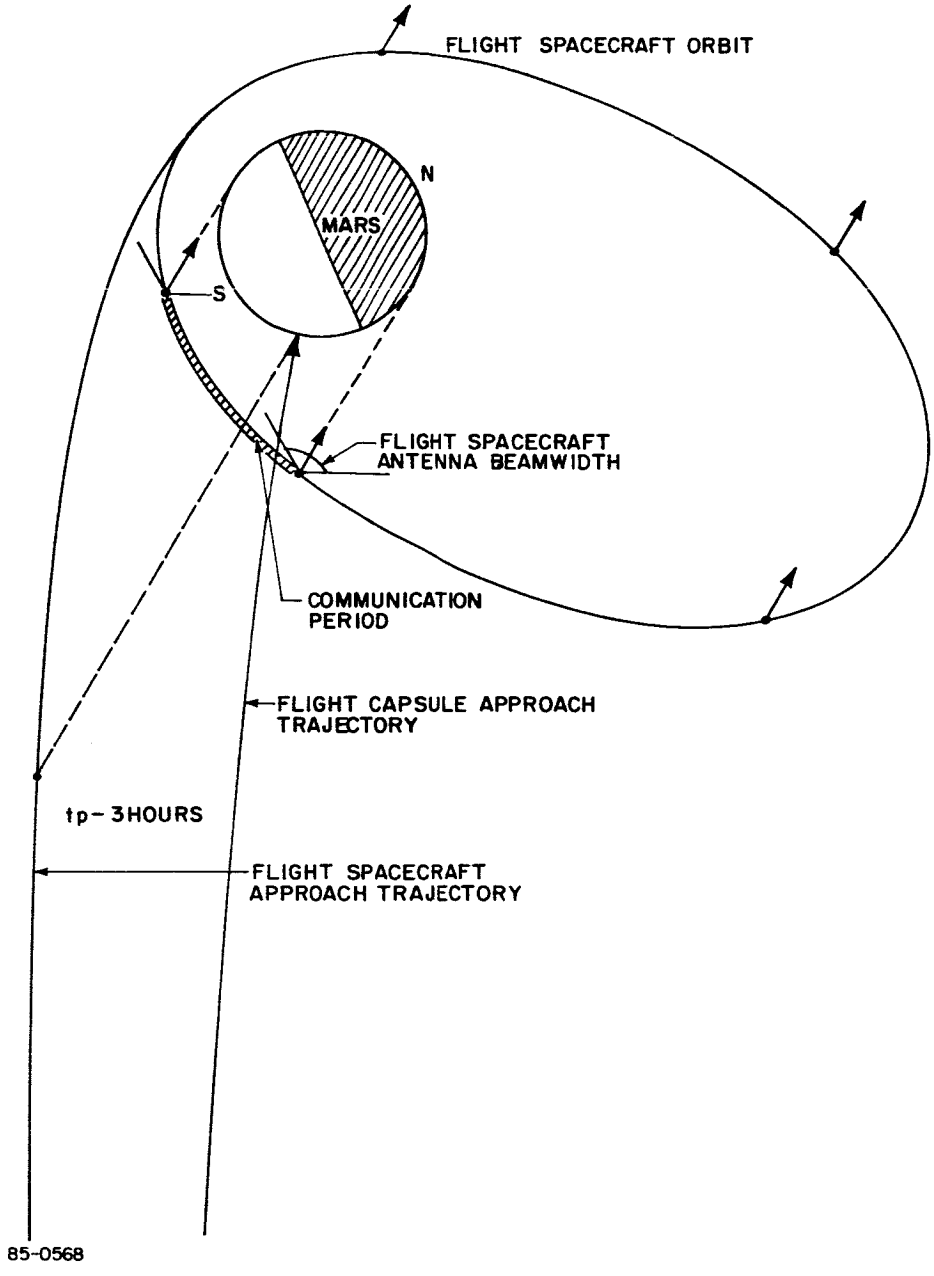

Figure 9 ORBIT CONTACT GEOMETRY

nominal performance models. However, this capability was sufficiently attractive in view of the requirements for a 30-day mission in 1973 and the potential support which could be provided by a relay link capable of operating with the flight spacecraft in orbit, that it was included in considering the maximum performance model.

As a result of the orbit geometry analysis, it was concluded that communication after the Martian night would best be accomplished by a direct link to Earth and that the in-orbit relay-link capability would be considered only for the maximum performance model.

Considerable additional weight would result from including any relay capability during post landing operations. The large antennas required for an efficient low frequency relay would significantly increase the volume of the landed capsule, and hence, the weight of the required impact attenuator.

4.6 FLIGHT CAPSULE DIRECT LINK RF ANALYSIS

4.6.1 Restriction of Direct Link to Post-Landing Mode

As noted in Paragraph 4.1.2, it may be desirable during the cruise phase and, possibly, during the early part of the entry phase, to have direct link communications capability for the following reasons: 1) to allow periodic in-transit status checks by means independent of the flight spacecraft, and 2) to provide the potential capability for collecting data during entry by using predetection recording on Earth, thereby providing a redundant means of obtaining critical entry data. This latter approach is based on the assumption that at S-band frequencies the onset of blackout occurs, if at all, at a considerably lower altitude than when very high frequencies (VHF) are used (see Appendix 4-4, in Reference 1).

Data-rate capabilities during the pre-impact phases of the mission differ from those achievable after landing only because of the differences in antenna capabilities. The following alternatives were considered in estimating antenna performance requirements in the cruise and entry phases:

1. Alignment of the flight-capsule spin axis with the velocity vector at the time of flight spacecraft/flight capsule separation and acceptance of the resultant antenna axis-to-Earth pointing loss.

2. Alignment of the flight capsule spin axis at the time of separation of the flight capsule from the flight spacecraft on such an axis as to obtain a near-zero angle of attack at entry and acceptance of the resultant antenna pointing loss.

3. Alignment of the flight capsule spin axis with the Earth vector to avoid the antenna pointing loss.

Figure 10 illustrates the look angles to Earth during the cruise mode as a function of arrival date for the first two alternatives. Relatively large pointing losses would result in these cases if any attempt were made to incorporate a narrow-beam antenna.

If, however, it is possible to align the spin axis of the vehicle along the Earth vector (the third alternative), communication with Earth during the cruise mode can readily be achieved. Such alignment (Earth-oriented during cruise) would not be free from problems since it would result in large angles of attack at entry with accompanying nutation of the antenna beam at high altitudes. Estimates of the look-angle envelope as a function of altitude are presented in Figure 11. As can be seen from Figure 11 the motion resulting from the large angle of attack at entry produces peak look angles to Earth as large as those produced by alignment of the vehicle spin axis for a zero angle of attack at entry. Analysis of the preceding alternatives led to the following conclusions:

1. Communication with Earth during cruise-mode operation can be accomplished by aligning the spin axis of the vehicle along the Earth vector. However, this results in large angles of attack at entry and, possibly, in both a weight penalty and a reduction in the flight capsule's drag coefficient.

2. No attempt will be made to use a directional antenna during the entry phase, a time when look angles will be large regardless of cruise attitude.

3. The best compromise, if cruise and entry phase communications are, in fact, required, appears to be based on adjustment of the vehicle spin axis to satisfy aerodynamic needs, use of a low-gain antenna, and acceptance of the penalty of a reduced data rate. For example, if an antenna with a 3-db beamwidth of 100 degrees were used and a 5-db degradation due to phase and amplitude modulation induced by vehicle spin is assumed, data rates of from 2 to 4 bits/sec (using a noncoherent 32-ary system) could be obtained with a transmitter power level of 20 watts.

The preceding discussion was based upon the following two assumptions:

1. The value of the direct link as a backup means of communications during cruise mode operation would justify the added complexity introduced by its inclusion in the design. This is an especially important consideration, since certain flight capsule concepts would require two

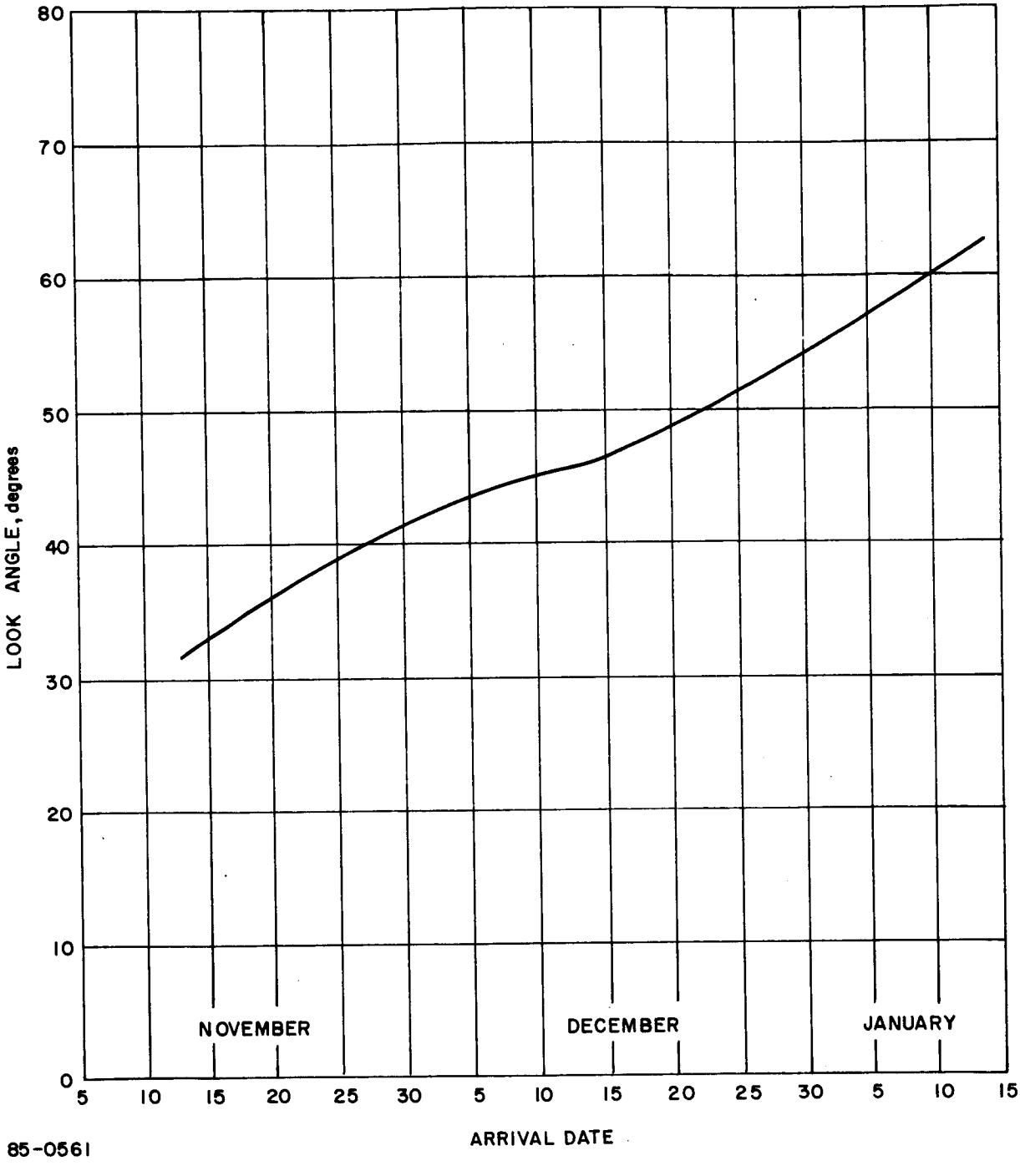

Figure 10 DIRECT LINK SEPARATION-TO-ENTRY LOOK ANGLES, $\alpha = 0$ DEGREE AT ENTRY

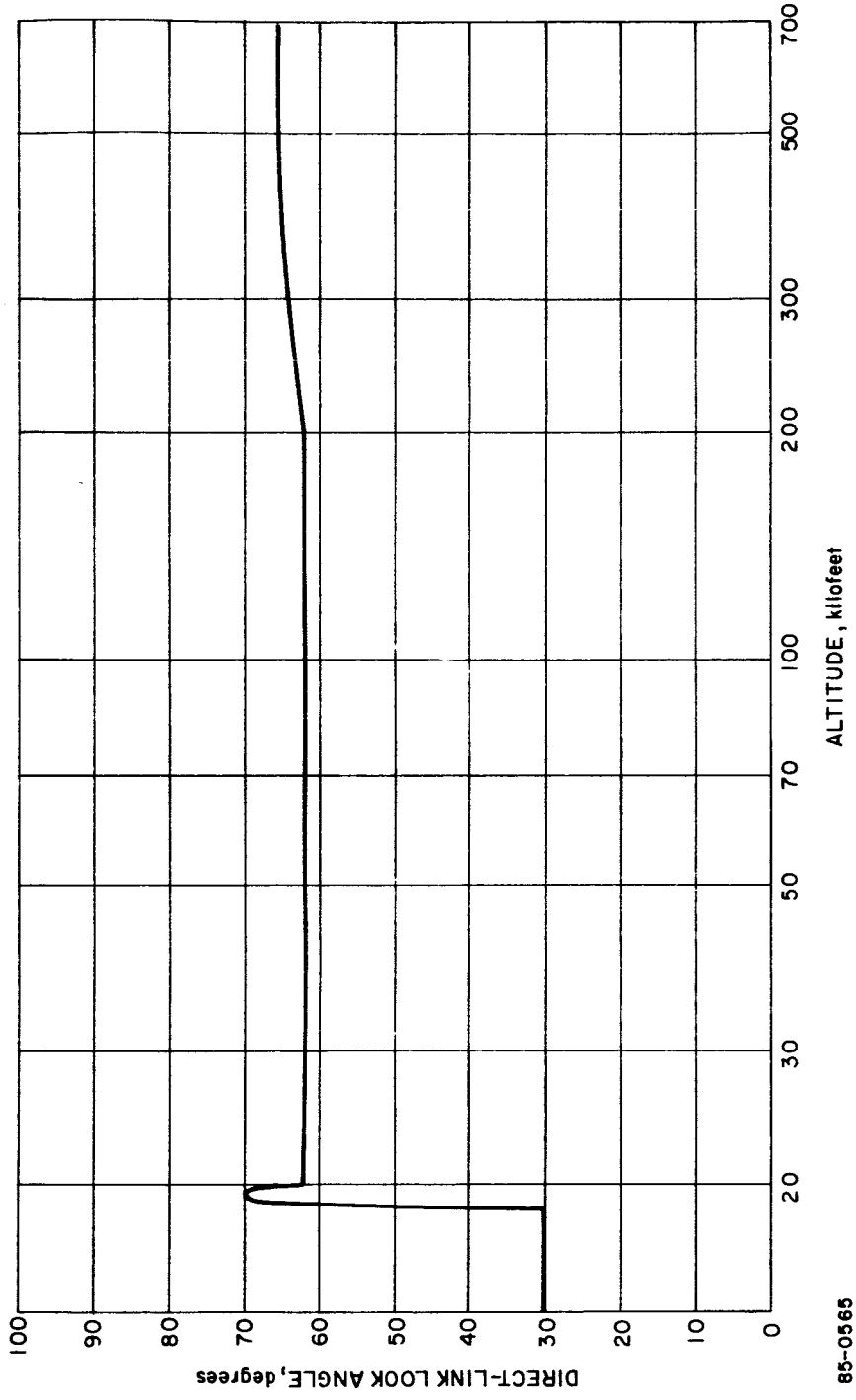

Figure 11 DIRECT-LINK FLIGHT CAPSULE LOOK ANGLE REQUIREMENTS, ZERO ANGLE OF ATTACK AT ENTRY, 11 JANUARY 1972

separate direct link telecommunications systems, one for pre-impact, the other for post-impact operation.

2. Attenuation through the near wake is negligible down to an altitude sufficiently low that meaningful entry data can be collected before blackout begins.

The validity of either one of these assumptions cannot be established without further study. For the present, therefore, the capability for direct-to-Earth communications during the cruise and entry phases of the mission will be considered only as a potentially attractive option, rather than as a primary mode of operation.

4.6.2 Post-Landing Direct Link Performance

It presently appears that the 1971 flight capsule will be relatively simple in concept and will be incapable of utilizing a high-gain antenna. As a result, its direct link communications capabilities will be limited. Furthermore, there is considerable uncertainty regarding terrain characteristics in the vicinity of the impact point. Both of these considerations dictated adoption of a conservative approach in selecting data rates. In analyzing the performance capability of the direct link, the following critical features formed the basis for the evaluations.

1. Communication range to Earth
2. Receiving terminal characteristics
3. Flight capsule transmitter power
4. Modulation/detection techniques
5. Antenna performance

These considerations are discussed in paragraphs 4.6.2.1 through 4.6.2.5, respectively.

4.6.2.1 Communication Range to Earth

The communications range to Earth is a constraint discussed earlier in Paragraph 4.2.2.

4.6.2.2 Receiving Terminal Characteristics

The deep space network (DSN), including the deep space instrumentation facility (DSIF) and the space flight operations facility (SFOF), will be utilized as discussed in Paragraph 4.2.2.

4.6.2.3 Flight Capsule Transmitter Power

The following practical considerations determine the transmitter power used:

1. Potential antenna breakdown problems

2. State-of-the-art limitations on power generating devices.

Potential antenna breakdown problems were discussed previously; (see paragraph 4.4). It was concluded that due to present uncertainties in estimates of the Martian atmospheric composition, it is not wise at this time to consider transmitter power levels greater than 40 watts.

For direct-link communications, a carrier frequency at S-band is dictated to be compatible with the DSN receiving terminal characteristics. Solid state devices for power generation at S-band frequencies are currently limited to power output capabilities in the 1 to 2 watt range, and the prospects for substantial increases (to powers in the 20- to 30-watt range) in the near future are not promising. Although it is desirable to avoid high potentials and to remain within solid-state capabilities (as was done in selecting the entry and descent relay-link transmitter power), the same option is not available for selection of the direct-link transmitter power if the approach taken is to operate near the antenna breakdown limit of 40 watts. It will be later shown that avoidance of high voltages by limiting the direct link transmitter power to the solid state power range of 1 or 2 watts would result in unacceptable direct-link performance. For this reason, the direct link will require the acceptance of the high-voltage design risk which may be avoided in the relay-link design. Figure 12 presents the achievable efficiency as a function of power for several tubes at S-band frequencies. Two significant conclusions can be drawn from this data:

1. Efficiency improves somewhat with increasing power. Hence, the energy required per bit transmitted decreases with increasing power.

2. Existing hardware for space use is available in the less than 20-watt region using the more efficient tube types.

In summary, 20 watts was chosen as the direct-link transmitter power level since unacceptable link performance results if the solid-state limitation of 1 to 2 watts was accepted to avoid potential high-voltage breakdown.

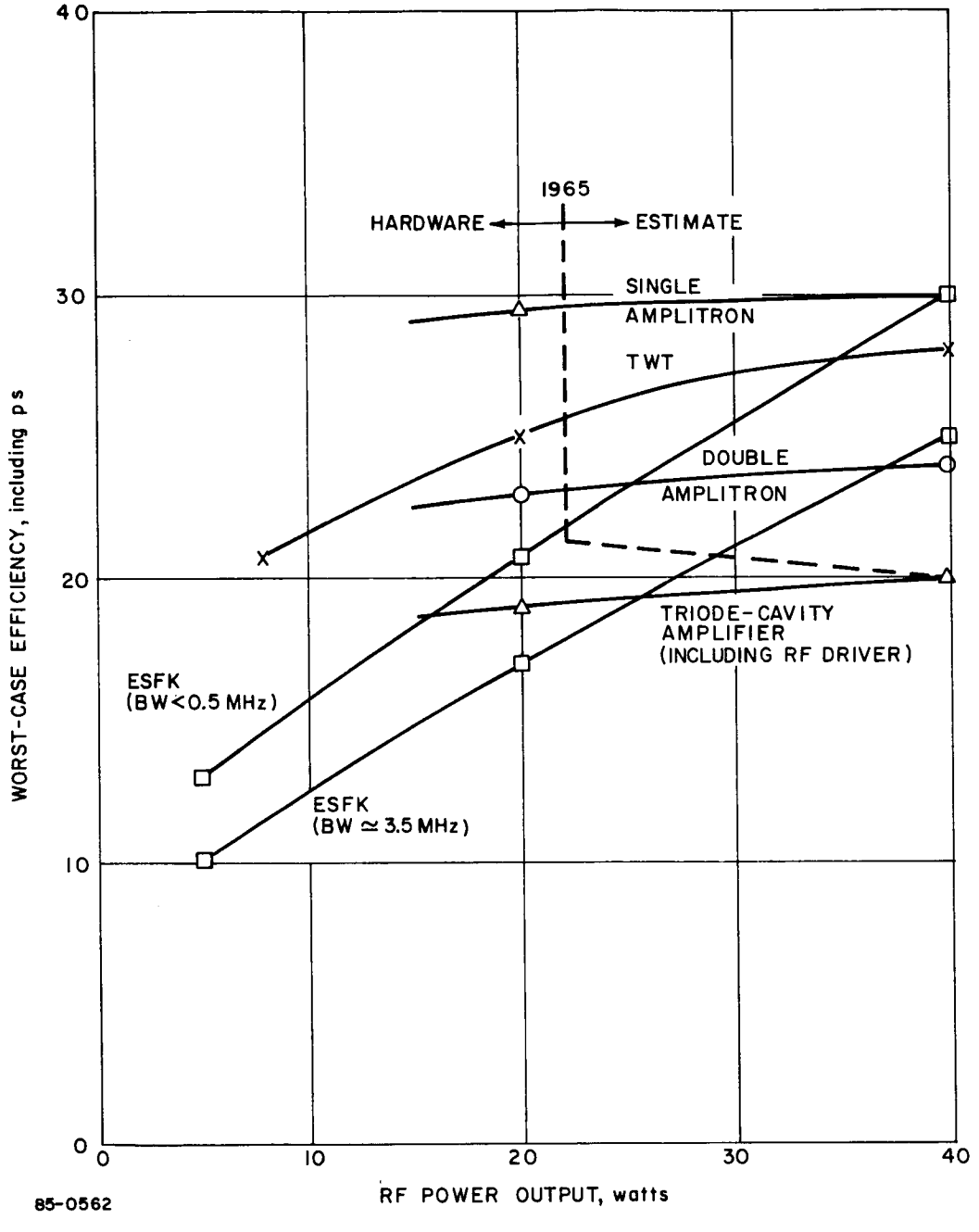

Figure 12 EFFICIENCY ESTIMATES FOR S-BAND POWER AMPLIFIERS

4.6.2.4 Modulation/Detection Techniques

Because previous deep-space programs have used a coherent PCM/PSK/PM approach, it is natural to consider use of the same approach for the flight-capsule direct link. However, for antenna gain-transmitter power products of 8.5 dbw or less, the efficiency of coherent PCM/PSK/PM is reduced to zero as a result of the carrier power requirements (see Figure 13). To a great extent, this reduction results from the fact that oscillator instability thwarts attempts to reduce the receiver noise bandwidth. The PCM/PSK/PM data presented in Figure 13 is based on carrier-loop bandwidths of 12 and 5 cycles. If smaller bandwidths were used, some relief is obtained. However, the restrictions resulting from the use of smaller bandwidths are intolerable (see Appendix 4-3, in Reference 1). Comparative studies of binary coherent systems and N-ary noncoherent systems indicate that if the power-gain product is less than 10 db, there is little choice but to use the more efficient N-ary system. Figure 3 shows the efficiency of a 32-ary MFS system assuming optimum detection. If, however, the power-gain product is between 10 and 15 db, either the N-ary or the phase modulation system could be used, although there is less risk associated with use of the N-ary system. At power-gain levels above 15 db, the phase modulation system would probably be chosen because of its proved performance in other deep-space programs.

4.6.2.5 Antenna Performance

Since the transmitter power for the direct link was established as 20 watts (13 dbw), as noted previously, antenna performance must be examined before a decision can be reached as to which modulation technique is recommended. Knowledge of antenna performance will determine the power-gain product required for this decision.

Two types of landed payloads were considered during the study. They were: 1) a flotation-sphere configuration in which the major direction of radiation from the antenna can be in a predetermined direction relative to the local vertical, thus making the antenna design quite straight-forward and its performance predictable and 2) an oblate spheroid configuration in which the major direction of radiation from the antenna is a random variable dependent upon the attitude assumed by the landed capsule. These two configurations are discussed in detail in paragraphs 4.6.3 and 4.6.4.

4.6.3 Flotation Sphere Configuration

For this payload configuration, the antenna beamwidth, and hence, gain

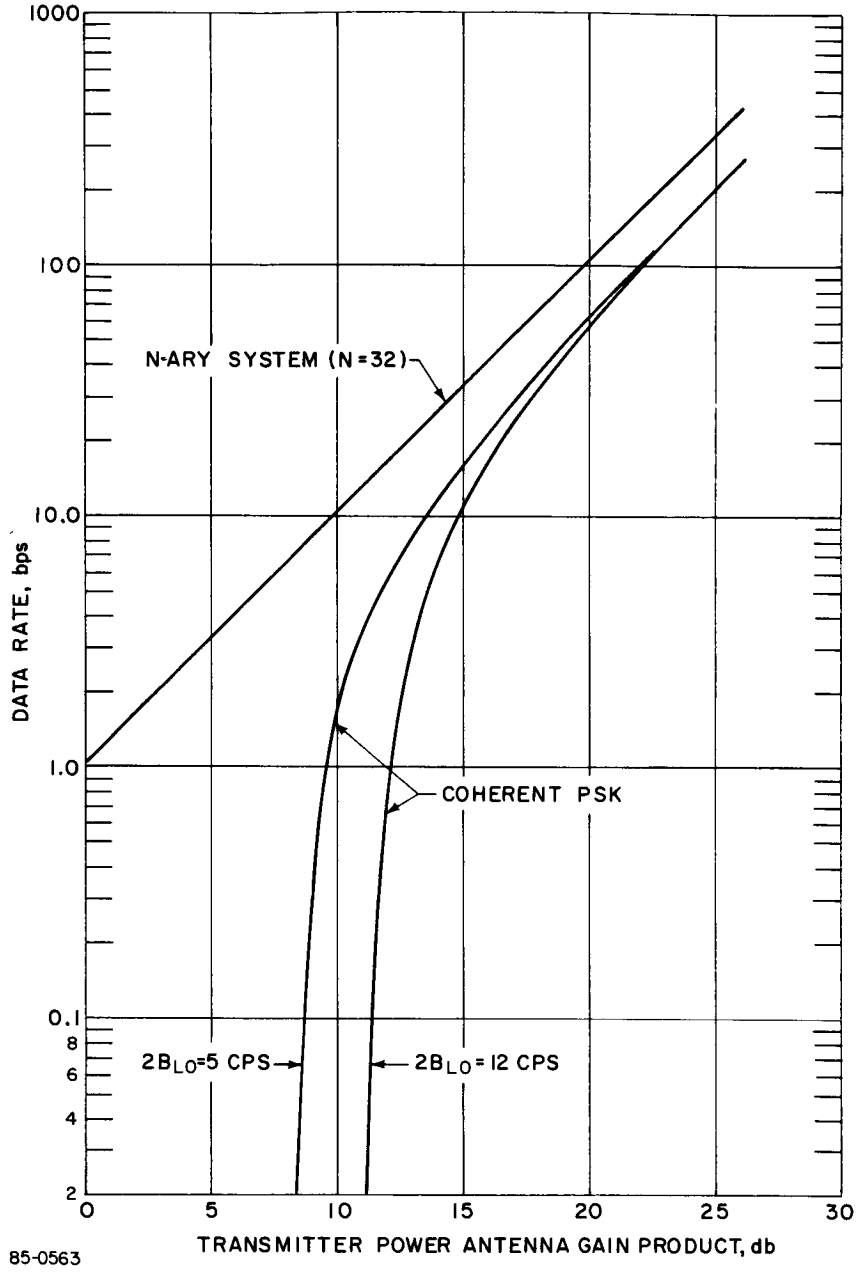

Figure 13 DIRECT LINK DATA RATES

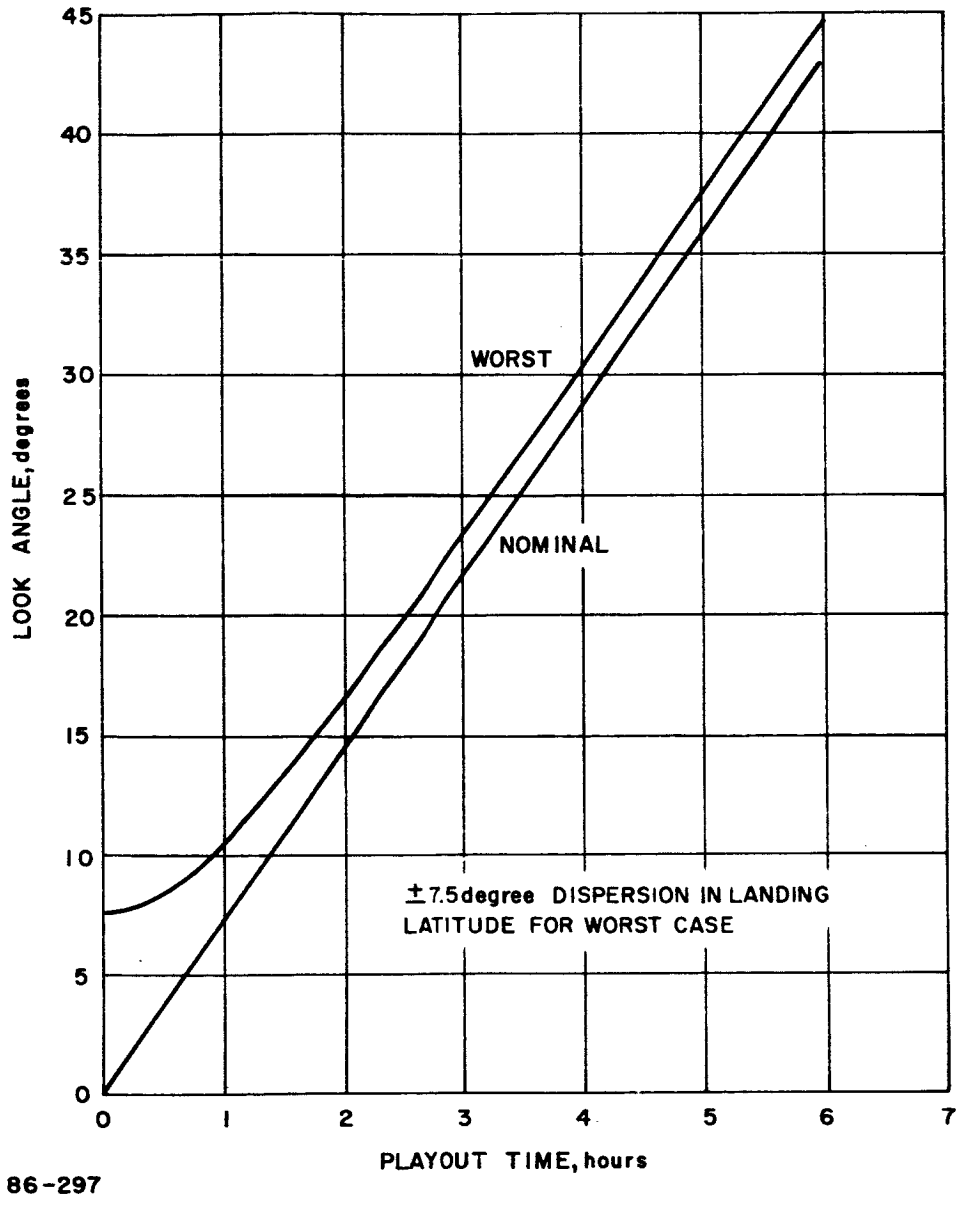

Figure 14 DIRECT LINK LOOK ANGLE REQUIREMENTS

is determined principally by Earth-to-Mars geometric considerations, including:

1. Landing-site latitude relative to the sub-Earth point.

2. The desired transmission time to Earth.

3. Errors in knowledge of the arrival time.

For a treatment of direct-link communication-system look angles, see Appendix 4-1 in Reference 1. Figure 4 shows the required look angles, as a function of transmission time, for a landing site at the sub-Earth latitude on the last day of the orbiter window. For an antenna-axis alignment error of +5 degrees relative to the vertical and a 3-hour transmission time, the required beamwidth is 55 degrees. This corresponds to gains of from 5.0 to 10.0 db at the 27.5 degree points, depending upon the type of antenna used and whether or not beam-shaping techniques are employed. In defining the communication capabilities described in this section, a conservative gain value of 5.5 db was used.

This gain results in a power-gain product of 18.5 dbw and dictates selection of coherent PCM/PSK/PM as the recommended modulation technique.

4.6.4 Oblate Spheroid Configuration

A brief analysis was sufficient to show that major problems were associated with use of mechanically steerable antennas on the flight capsule for the 1971 mission hard landing. The problems were so formidable that use of such antennas should be avoided unless their absence imposes unacceptable limitations on the mission. Elimination of mechanically steerable antennas from further consideration left the following types of antennas as candidates for mission use with the oblate spheroid payload configuration.

4.6.4.1 Electronically Steerable Arrays

Although a thorough analysis of the feasibility of using this type of antennas was not completed, preliminary results indicate that severe equipment complexity would result from use of electronically steerable antenna arrays on a non-gimballed payload. Steering information would have to be provided either by on-board equipment or by suitable command from Earth. On-board steering control capable of crude pointing of the antenna could be obtained by using a system based on a combination of time data and knowledge of the local vertical. The gains which could be realized by application of this technique would be on the order of 10 to 13 db if a large number of radiating elements were used.

4.6.4.2 Multiple Individually Selectable Antennas

This concept is based on use of a number of moderately high gain antennas, such as horns, and selection of the antenna or antennas which point toward Earth at a given time. Again, as noted in regard to the electrically steerable antennas, command or on-board vertical sensing and timing capabilities would be required. Integration problems and competition between the direct-link antennas and the relay-link antenna for space and viewing angles (if the latter link were used after landing) make selection of this approach unattractive.

4.6.4.3 Fixed Low Gain Antenna

For the oblate spheriod configuration, the use of a fixed low-gain antenna involves the minimum technical risk but entails a significant reduction in performance capability. Despite its limitations, this type of antenna is receiving the greatest consideration for use on landed capsules based on a non-gimballed design. In such applications any orientation must be assumed possible, with a particular probability of occurrence assigned to each orientation. Therefore, antenna-performance (gain) data based on pattern measurements made on particular antenna types, must be presented in a probabilistic manner. See Appendix 4-2, in Reference 1 for a complete treatment of this aspect.

Figures 15 through 18, extracted from the referenced appendix, present the cumulative distributions of antenna gain for different orientations of the payload after landing. These distributions are confined to a cone of radiation of 60-degrees, half-angle centered about the local vertical. This limitation minimizes the effects of multipath which is prevalent in directions which make small angles with the surface. Figure 19 presents the antenna gain distributions, based on both the assumption that the landing attitude is a random variable with a uniform distribution (a very pessimistic assumption), and the assumption that the distribution is Gaussian with a mean angle of 0 degree relative to the horizontal and a standard deviation of 30 degrees.

If above-threshold performance during more than 99 percent of time is assumed to constitute an acceptable operational condition, then a worst-case antenna gain of -7 db can be assigned for a uniform distribution, and of -5.9 db for a Gaussian distribution. This gain (7 db) results in a worst-case power-gain product of +6 dbw and leads to selection of N-ary modulation as the recommended technique.

4.6.5 Comparison of Alternatives

Table XI, compiled by combining the results discussed in the previous paragraphs, provides a matrix of alternatives from which a clear picture

TABLE XI

COMPARISON OF ALTERNATIVES

Payload	Binary Coherent PSK-PM Modulation		N-ary (32 Level)		Remarks
	Transmitter Power 20 watts	Transmitter Power 40 watts	Transmitter Power 20 watts	Transmitter Power 40 watts	
Flotation Sphere	8 bps*	16 bps*	32 bps*	64 bps*	Superior from communications viewpoint
Oblate Spheroid uniform distribution	0	0	2	4	Landed slope distribution, pessimistic, very conservative
Oblate Spheroid gaussian distribution	0	0	4	8	Landed slope distribution probably realistic

*A margin of 3.5 db has been applied to the system to permit operation in the linear portion of the curve.

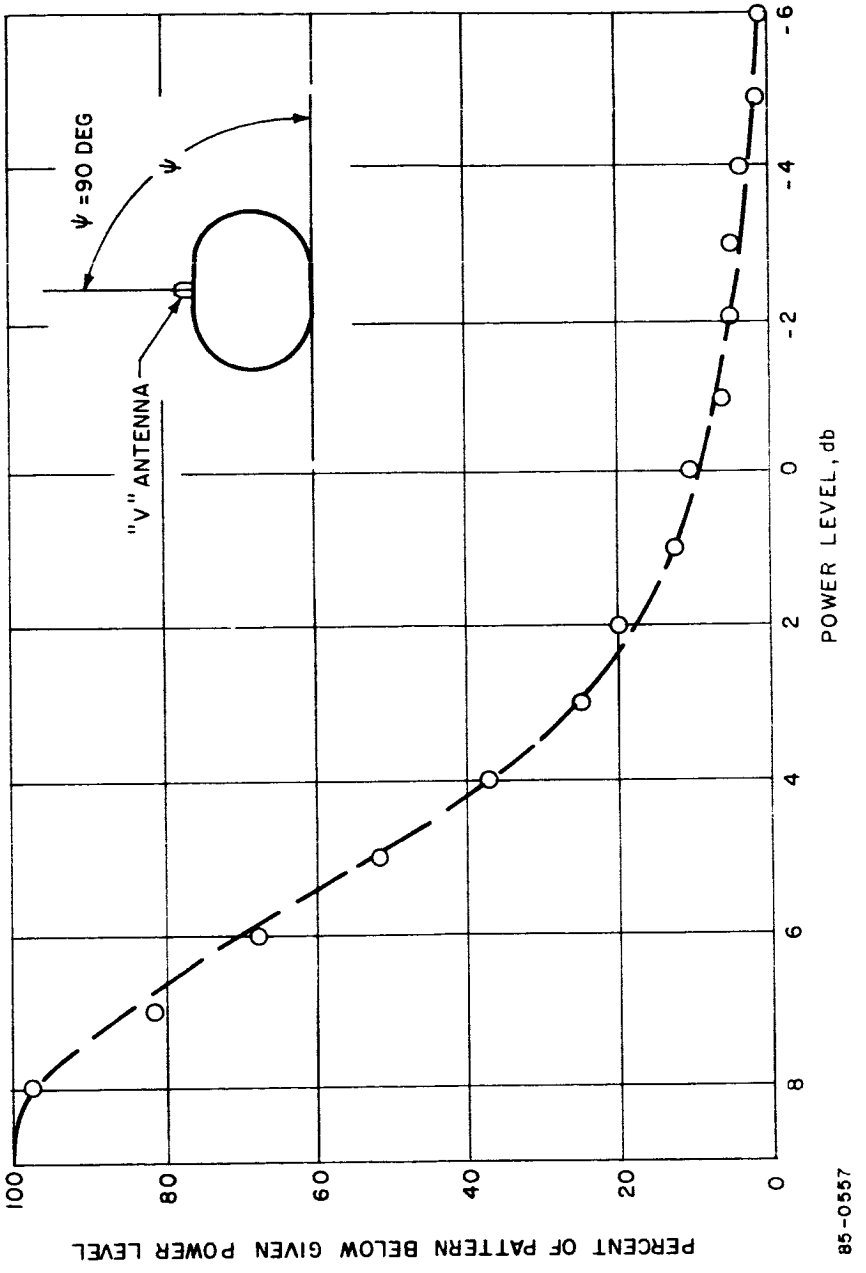

Figure 15 GAIN DISTRIBUTION FUNCTION S-BAND "V" ANTENNA, ψ = 90 DEGREES

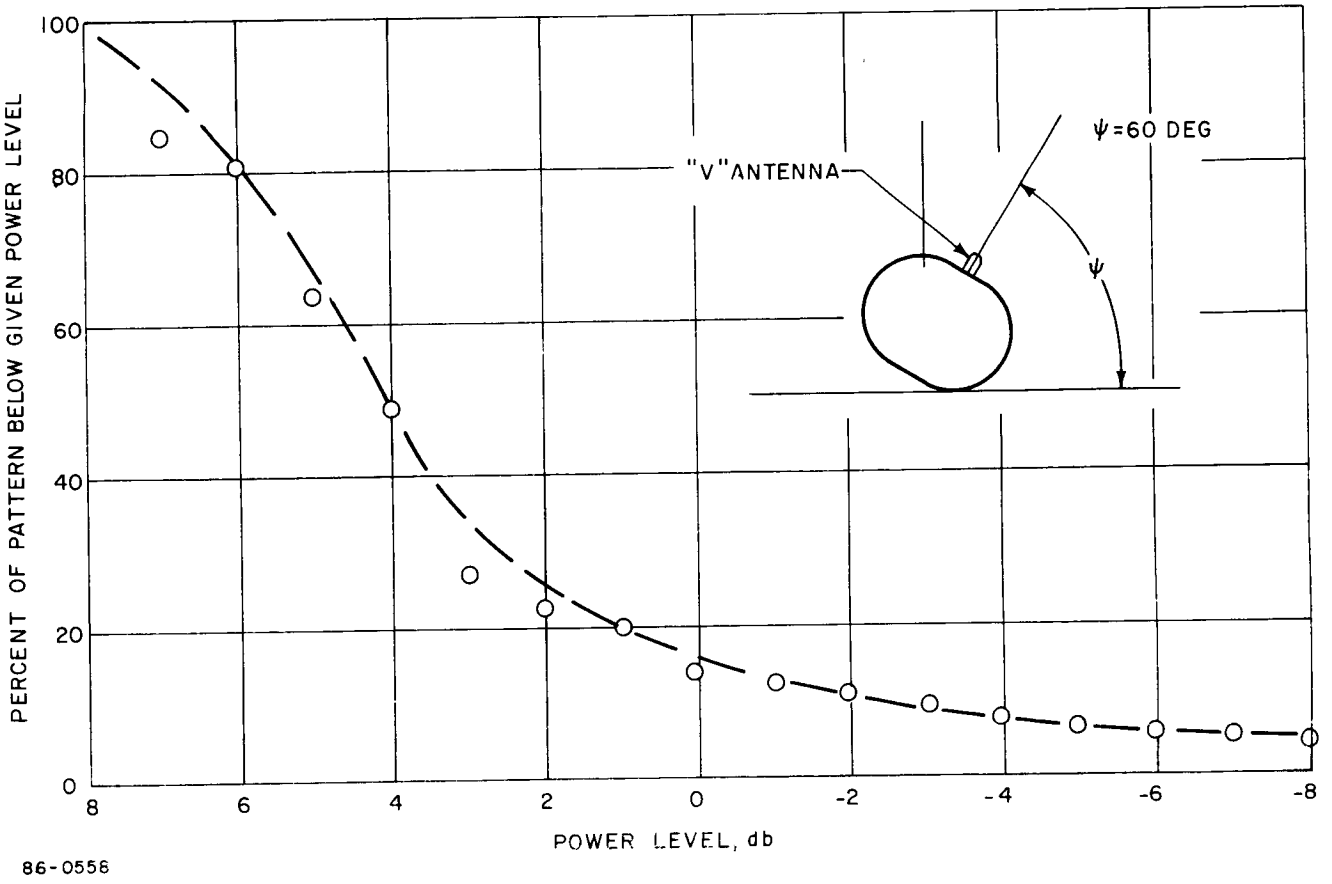

Figure 16 GAIN DISTRIBUTION FUNCTION S-BAND "V" ANTENNA, ψ = 60 DEGREES

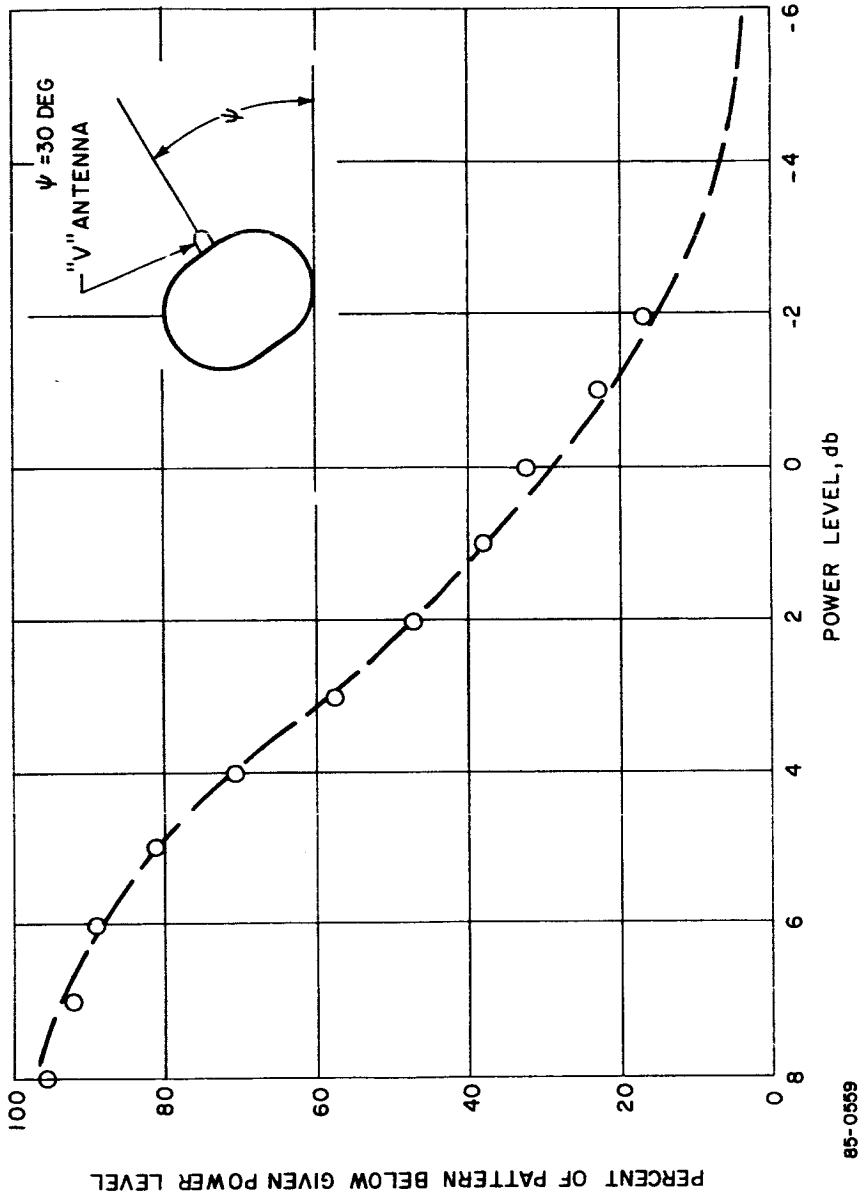

Figure 17 GAIN DISTRIBUTION FUNCTION S-BAND "V" ANTENNA, ψ = 30 DEGREES

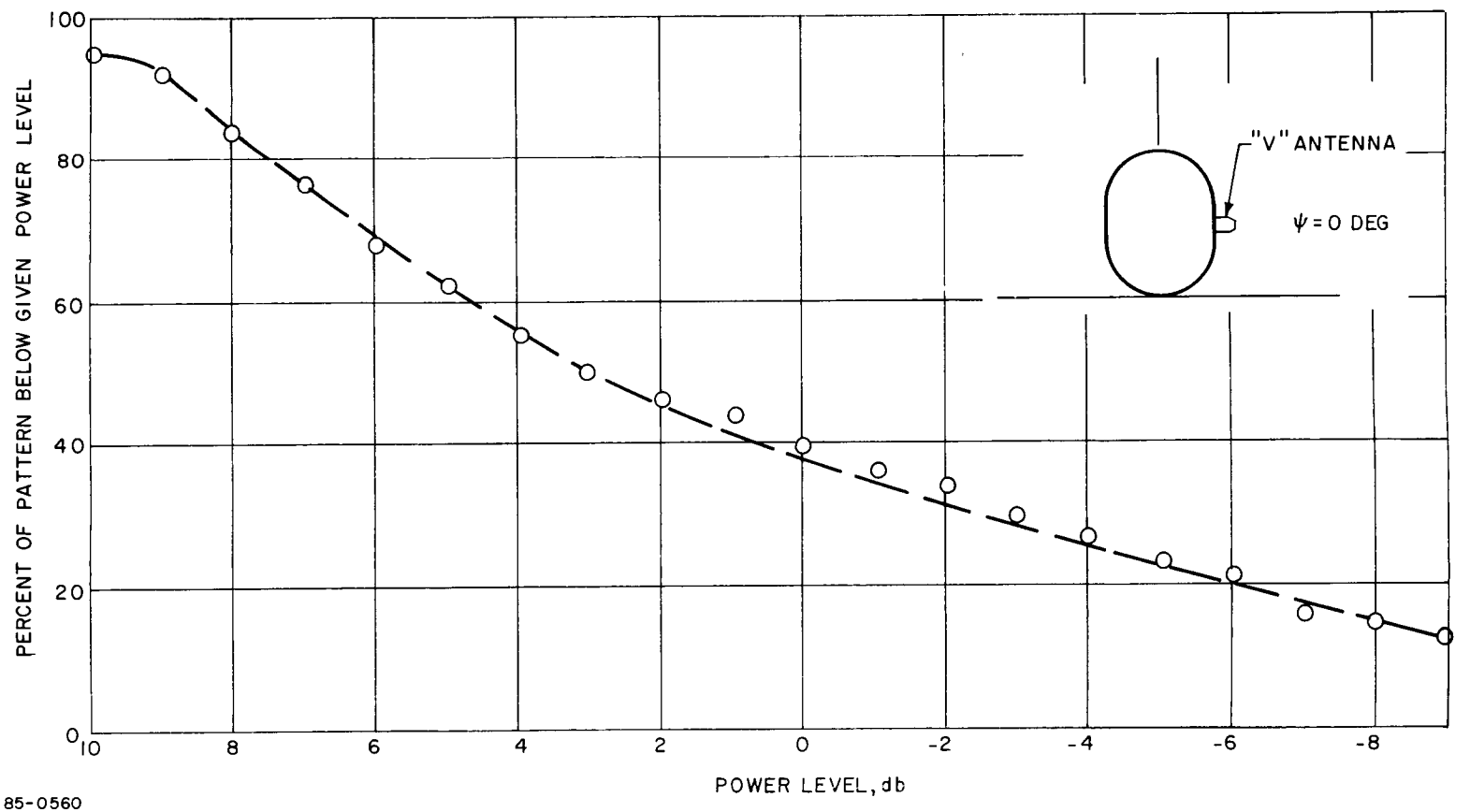

Figure 18 GAIN DISTRIBUTION FUNCTION S-BAND "V" ANTENNA, $\psi = 0$ DEGREE

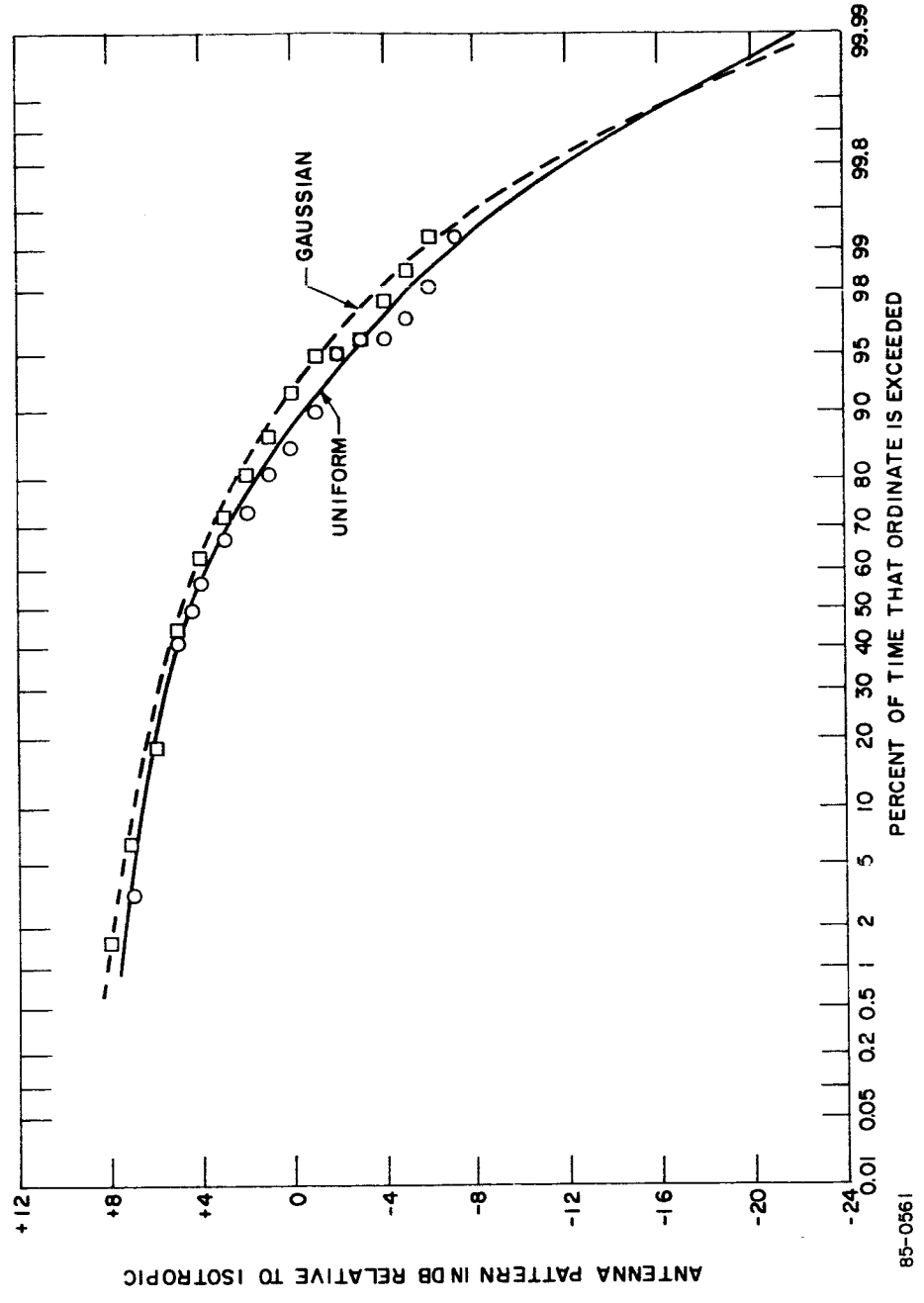

Figure 19 DIRECT-LINK ANTENNA GAIN FOR UNIFORM AND GAUSSIAN DISTRIBUTED LANDED CAPSULE ATTITUDES

of the interaction of the various factors which influence performance capability of the direct link in the post-landing phase can be obtained.

4.7 OBLATE SPHEROID AS THE REFERENCE DESIGN

4.7.1 General Concept

The telecommunication subsystem selected for detailed mechanization is one which satisfies the design requirements presented in Table XII and is compatible with the oblate spheroid configuration. The flight-capsule telecommunication functions are divided between two functionally independent subsystems; one, the external subsystem, is associated with those descent phases of the mission that occur between separation and tethering of the payload, and the other, the internal subsystem, is associated with the post-landing phase of the mission. The two-system approach was selected for the following reasons:

1. With the exception of the three-axis accelerometer, all scientific instruments used during the entry and parachute-aided descent phases of the mission are located outside the landed capsule. Monitoring of these instruments by a data-handling subsystem inside the landed capsule would create a complex interface problem.

2. Proper operation of the attitude control system requires many event initiation signals which are supplied by the central computer and sequencer (CC&S). This inter-relationship too, would create a complex interface problem if only an internal CC&S were used.

Figure 20 shows the flight capsule portion of the telecommunication subsystems in block diagram form. In outline form, the telecommunication subsystem consists of the following:

External System

Radio subsystem

VHF antenna

Voltage standing wave ratio monitor

RF switches

Redundant VHF transmitters (2)

Data-handling subsystem

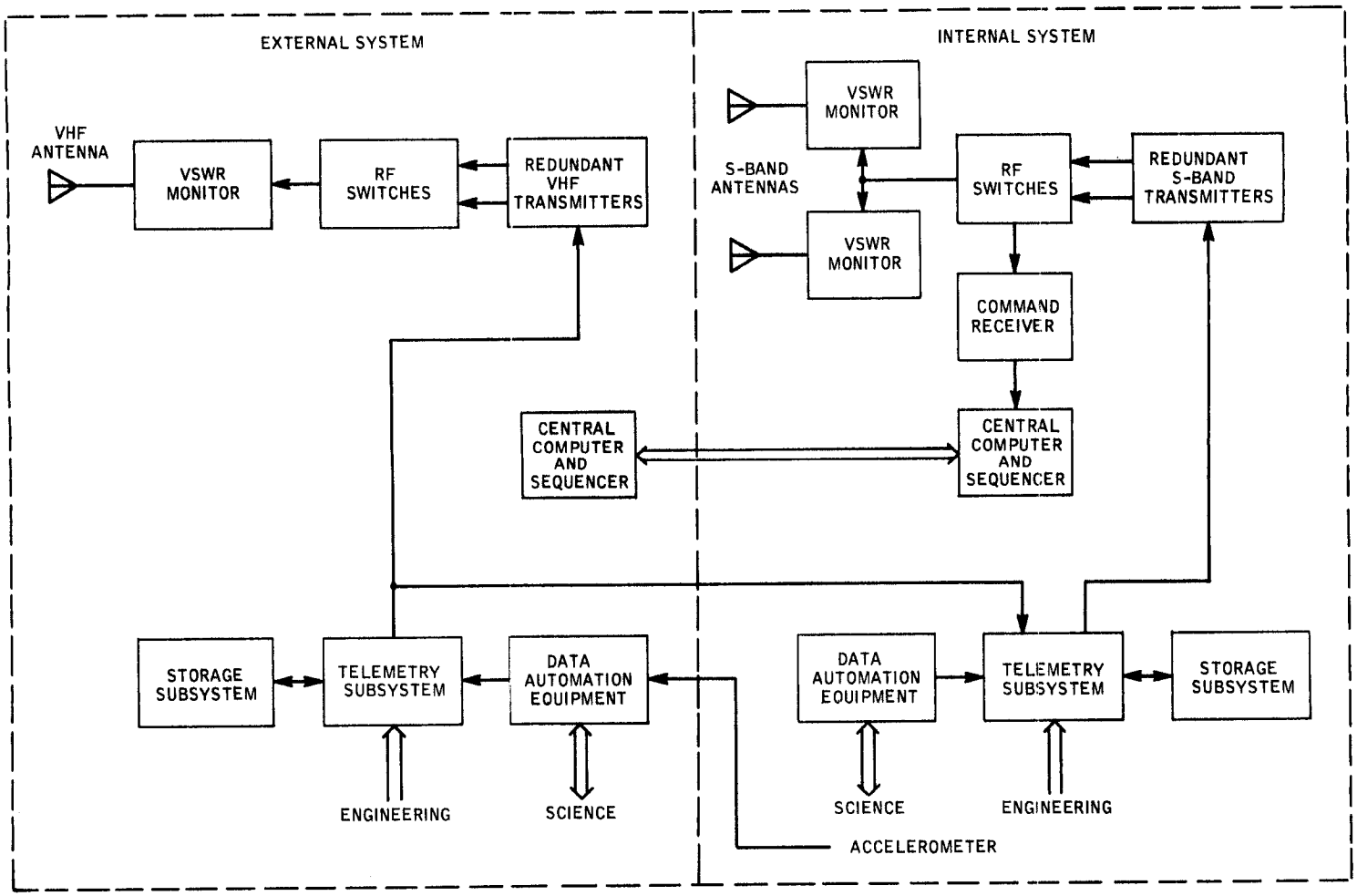

86-1264

Figure 20 TELECOMMUNICATION SUBSYSTEM BLOCK DIAGRAM

TABLE XII

TELECOMMUNICATION SUBSYSTEM DESIGN REQUIREMENTS

RELAY DATA LINK	
1. Operational phase	Prelanding
2. Frequency	272 MHz
3. Modulation	FSK
4. Transmitter power	30 watts
5. FC antenna type	Log Spiral
6. FS antenna type	Helix (body-fixed)
7. FS receiver noise figure	5 db
8. Data rate	64 bps
9. Range	35,000 km (max.)
DIRECT DATA LINK	
1. Operational phase	Postlanding
2. Frequency	2300 MHz
3. Modulation	MFS or LCM
4. Transmitter power	20 watts
5. FC antenna type	V Horn
6. Data rate	2 bps
7. Range	2×10^8 km (max.)

TABLE XII (Concl'd)

DIRECT COMMAND LINK	
1. Operational phase	Postlanding
2. Frequency	2113 MHz
3. Modulation	Coherent PSK-PM
4. Noise figure	6 db
5. FC antenna type	V-horn
6. Data rate	1 bps
7. Range	2×10^8 km
8. Transmitting equipment	DSIF

Data-automation equipment

Telemetry subsystem

Storage

Central computer and sequencer subsystem

Internal System

Radio subsystem

S-band antennas

RF Switches

Redundant S-band transmitters (2)

S-band command receiver

Data handling subsystem

Data-automation equipment

Telemetry subsystem

Storage

Central computer and sequencer subsystem

Both relay-link and direct-link telemetry channels are provided for functional redundancy. During the prelanding phases, only relay link transmission is employed, but to minimize the possibility of data loss, critical science and engineering data collected during entry and terminal descent is stored for subsequent transmission directly to Earth after landing. In the subsystem described here, direct-link communications are not attempted during the prelanding phases for the following reasons:

1. The mission requirements can be fully met using the relay link alone.

2. Relay-link performance during these phases is vastly superior to direct-link performance. Direct-link communications capability is provided, however, in the maximum performance telecommunications subsystem since blackout may not occur at S-band frequencies at as high an altitude as it does at VHF during entry.

During the post-landing phase, only direct link transmission is employed. This channel operates shortly after landing and again after completion of one Martian diurnal cycle. No relay-link backup support is provided since the disadvantages of relay-link performance in the post-orbit injection phase of the mission appear to outweigh possible advantages. See Appendix 4-5 in Reference I for a complete treatment of in-orbit communications. Command capability is provided via direct link and only for the landed phase of the mission.

Although command capability prior to landing would be desirable, it is not provided in the nominal performance configuration because continuous operation of the command receiver for the 12 days between separation and impact would impose an intolerable battery-weight penalty.

The data handling subsystem is divided into two data handling sections and one storage section. The data-handling sections include the data-automation equipment and the telemetry subsystem. The data-automation equipment handles all scientific instrumentation: the telemetry subsystem handles all engineering data. The reasons for this division of functions are:

1. A failure in either subsystem will not compromise operation of the other.

2. The acquisition requirements for the scientific instrumentation data and for engineering data are dissimilar.

3. The science instrumentation package is more susceptible to change than are the engineering requirements, therefore, use of two subsystems presents a less complex interface problem.

4.7.2 Operational Profile

The telecommunications subsystem shown in Figure 20 operates in a variety of data acquisition and transmission modes. These are discussed in the following paragraphs.

4.7.2.1 External Telecommunication Subsystem

The external subsystem operates in the following five modes:

1. External Mode 1 - Preseparation/Separation Checkout -- The flight capsule is functionally checked out and the subsystem is used 1) during automatic checkout prior to launch, 2) periodically during the in-transit phase prior to separation, and 3) during the separation phase. Data are available at the flight spacecraft prior to separation either via hard line from both the internal and the external telemetry subsystems, or via a radio link from any transmitter through parasitic antennas on the sterilization canister. The data rate in this operating mode is 1024 bps.

2. External Mode 2 - Post-separation Checkout -- The status of the flight capsule is checked periodically via the relay link during the cruise phase between separation and entry. Five minutes before entry (t_e - 5 minutes) a final flight-capsule status check starts. During this check, operation of all entry and descent science instruments, with the exception of the radiometer, is also monitored. The external system then continues to operate in external mode 2 and transmits data at 64 bps via the relay link until impact unless external mode 4 operation is initiated.

3. External Mode 3 - Entry Data Storage -- During this mode, initiated at entry when 0.1 g is sensed, critical entry data (e.g., data from the radiometer) is stored. Storage begins at this time because communications blackout occurs shortly after 0.1 g is sensed. This mode is concurrent with external mode 2.

4. External Mode 4 - Entry/Descent Data Transmission -- During operation in this mode, initiated 11 seconds after 10 g is sensed (10 g + 11 seconds), the format of external mode 2 is changed. The data stored during external mode 3 operation is substituted for much of the engineering and other science data which is no longer required. Data is transmitted via the relay link at a rate of 64 bps. The system is so designed that transmission of all data stored during communication blackout (external mode 3) will be transmitted before impact even if the parachute should fail to open. During operation in this mode, the first 15 frames of data played out via the relay link are also stored in the internal data storage section of the subsystem for subsequent post-landing transmission to Earth via the direct link. This provides a functionally redundant path for transmission of the critical entry/descent data in the event of relay link failure.

5. External Mode 5 - Standby -- During this mode, all subsystems requiring battery power, except for the CC&S master-timer sequencer used to initiate external mode 2 operation, are turned off.

4.7.2.2 Internal Telecommunication Subsystem

The internal system operates in the following two modes:

1. Internal Mode 1 - Impact Data Storage -- During operation in this mode, which is initiated when the flight capsule is tethered, the impact science, post-impact engineering, and post-impact science data is stored.

2. Internal Mode 2 - Direct Link Transmission -- During this mode, first initiated 1 hour after 0.1 g is sensed, the 15 frames of data stored during external mode 4 is transmitted to Earth at a rate of 2 bps. This mode is initiated again 24 hours later. At this time, the data collected after completion of the first direct-link transmission is transmitted to Earth at a rate of 2 bps.

4.8 FLIGHT CAPSULE RELAY LINK RADIO SUBSYSTEM DESCRIPTION

Two functionally independent radio subsystems in the telecommunication subsystem provide data-transmission capability for all phases of the flight capsule mission. One subsystem, referred to as the external radio subsystem, is located on the outside of the landed capsule and forms part of the external telecommunication system. It is used for relay-link transmission of data collected during the prelanding phases of the mission. The other radio subsystem, referred to as the internal radio subsystem, is located inside the landed capsule and forms part of the internal telecommunication system. It is used for direct-link transmission to Earth of data collected during the post-landing phases of the mission.

Figure 21 shows the relay-link radio subsystem in block diagram from. Two block-redundant relay-link transmitters are shown in this figure. Block redundancy is used for the following reasons:

1. The relay link is the prime data link from the time of separation until impact. During this period, the external system is used alone and no functionally-redundant direct link is available as a backup means of communication.

2. Although functional redundancy is provided by the direct link after landing, it can only handle the critical entry and descent data.

3. Use of two identical units in parallel provides increased assurance against loss of function as the result of component or piecepart failure.

Block redundancy is, of course, not as attractive as functional redundancy in providing assurance against loss of function in the case of causal type failure (i.e., a design failure or failure due to overstress from some unforeseen contigency), because both units would probably experience the same type of failure. However, such problems are avoided by operating only one transmitter at a time and by using appropriate failure-detection techniques and a switching network connected in series with the two redundant transmitters.

The penalty imposed by this type of block redundancy consists of: 1) decreased reliability, since the failure detection and switching circuits are entered as serial elements in the system, 2) increased weight and volume (approximately double), and 3) a slight increase in power consumption as a result of switching element operation.

A three-port circulator is used to protect the transmitters during entry when high values of VSWR will be experienced during relay-link radio blackout and radiated power is reflected back into the radio subsystem. The solid state transmitter is not capable of dissipating the additional reflected power, therefore, a circulator is used to transfer the reflected power to an appropriate dummy load.

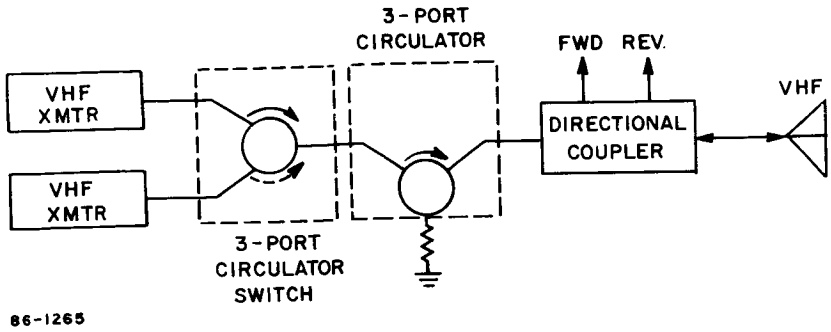

Figure 21 RELAY RADIO SUBSYSTEM

4.8.1 Antenna

Two candidate antenna configurations were considered for relay-link application; 1) a pair of crossed slots fed in phase quadrature to produce circular polarization, and 2) a planar logarithmic spiral antenna which is inherently circularly polarized. The pattern coverage provided by the two alternative configurations is very similar (see Appendix 4-2, Reference 1). Accordingly, the choice between them was based on the consideration that the logarithmic spiral is a more broad-band type of antenna. As such, its operating characteristics will be less affected by the severe environments experienced by the flight capsule during entry than would the relatively narrow-band crossed-slot antenna.

Figure 22 is a cross-sectional view of the proposed logarithmic spiral antenna. The antenna consists essentially of three major subassemblies, a copper clad laminated circuit board on which the spiral antenna element is etched, a quarter-wavelength resonant cavity in back of the spiral element, and a balun feed network.

4.8.2 Transmitter

Completely solid-state VHF transmitters were selected for the relay-link radio subsystem. The reasons for selecting an all solid-state approach were discussed in Paragraph 4.4.5.

Figure 23 shows, in block diagram form, the following major items of the relay transmitter: 1) two highly-stable fifth-overtone crystal-controlled oscillators operating in the 90 MHz region, 2) a frequency-shift-keyed (FSK) modulator in which selection of the mark and space carrier is controlled by the input modulation signal, 3) a transistorized frequency tripler (3 x frequency multiplier), and 4) a 30-watt, solid-state, power amplifier output stage.

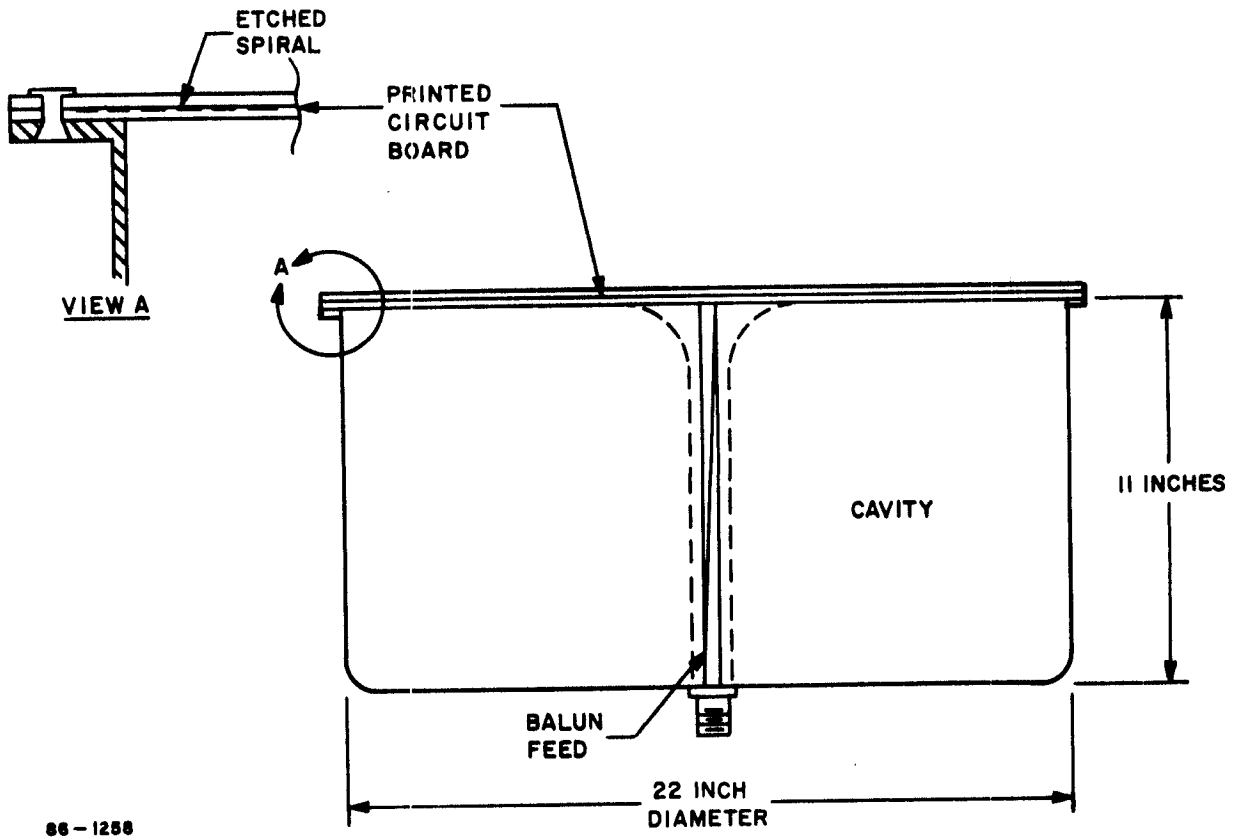

Figure 22 FLIGHT CAPSULE RELAY LINK ANTENNA

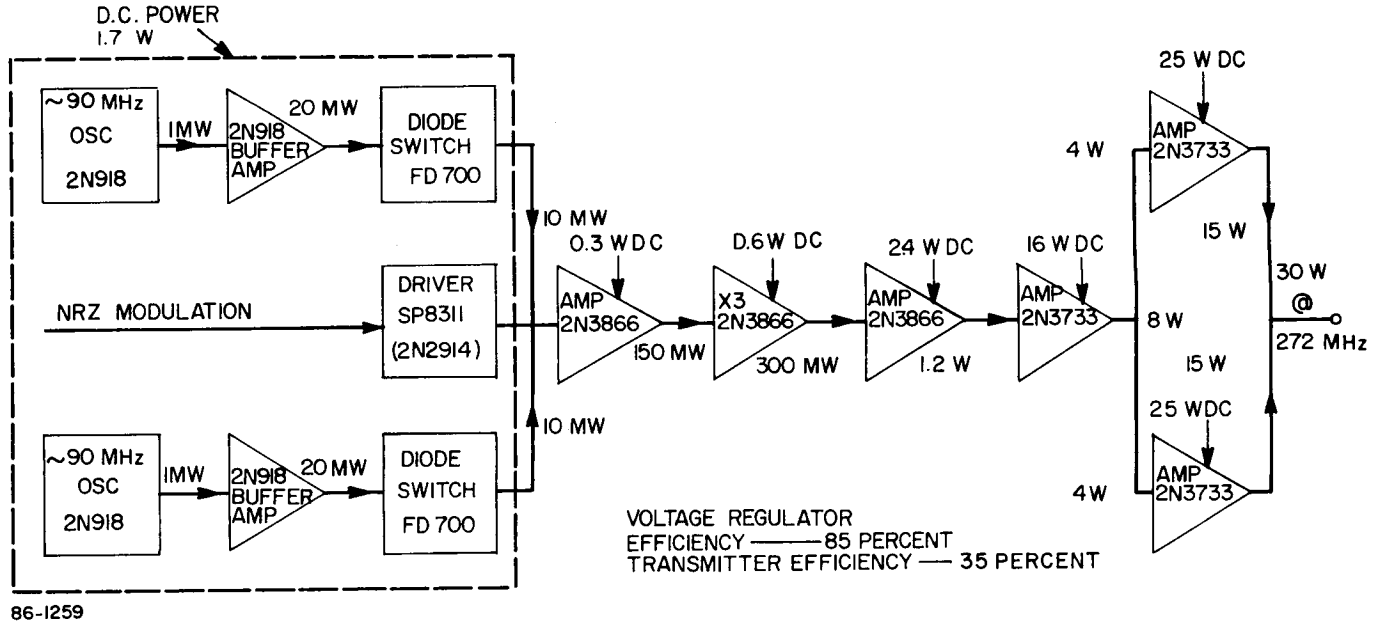

Figure 23 30 WATT FLIGHT SPACECRAFT FSK TRANSMITTER

The two crystal-controlled oscillators, each operating in the 90 MHz region, provide two discrete frequencies. Common base, crystal-controlled Colpitts-type oscillator circuits will be used. Stability requirements as stringent as ± 0.001 percent can be met if the following steps are taken in designing the oscillator.

1. The oscillator tank circuit and feedback network are designed to overcome the effects of changes in transistor input and output admittances which would otherwise tend to cause oscillator frequency pulling.

2. The oscillators are operated at a low power level. As a result, frequency drifting caused by self-heating of the crystal will be negligible.

3. Thermal stability is a prime factor in biasing the oscillator transistors.

4. Only high-quality crystals, the thermal sensitivity of which is accurately and stringently specified, are used.

The oscillators will meet the ± 0.001 percent frequency stability requirement within four seconds or less after initial turn-on. Since loading factors affect the frequency stability of an oscillator, a separate buffer amplifier will follow each oscillator to provide isolation. Essentially, the buffer amplifiers will be common emitter Class A amplifiers in which a certain amount of gain is sacrificed to obtain the desired isolation. A diode switch controlled by a switch driver will follow each oscillator-buffer combination. When the input modulation signal is in the range from +1 volt to +2 volts, the switch driver will close the switch following the higher frequency oscillator (the mark channel) and will open the switch following the lower frequency oscillator. When the input modulation signal is at ground potential, the switch driver will close the switch following the lower frequency oscillator (the space channel) and will open the switch following the higher-frequency channel. It will be possible to switch at rates ranging from 10 Hz to over 1000 Hz with this switching scheme. The input impedance of the switch driver will be 100,000 ohms. The diode switches will each consist of one FD700 diode. The insertion loss of either switch when closed, will not exceed 3 db. Isolation between the ON channel and the OFF channel will be at least 16 db. A single common-emitter Class A amplifier will be used immediately after the diode switches. It will amplify the RF power to a level high enough for efficient operation of a frequency tripler. The frequency tripler and the next two amplifier stages will consist of common emitter Class AB stages. The driver stage and the parallel output stages will be modified common emitter Class C stages. Parallel transistors will be used in the output stage to provide the required output power.

The use of separate base drive circuits and separate emitter resistors for the output transistors will assure stability and an equal distribution of the load.

Output power for the maximum load VSWR will vary less than 0.2 db over the entrie operating temperature range.

4.8.3 Flight Capsule Relay Link Radio Subsystem Summary

Table XIII summarizes the salient characteristics of the flight-capsule relay-link radio subsystem. This subsystem is used only during the pre-landing phases of the flight capsule mission.

The antenna, a planar logarithmic spiral, is inherently circularly polarized and provides a 6 db on-axis gain. Broad-beam coverage is required during descent when exposure to wind gusts can cause considerable swaying of the flight capsule. The off-axis gain, corresponding to the maximum look angle to the flight spacecraft during swaying of the flight capsule, is -4 db.

Two transmitters are used to obtain block redundancy. The 30-watt output power is obtained by parallel operation of two 15-watt transistorized amplifiers. Modulation is frequency-shift-keying (FSK) at a rate of 64 bps.

The stringent frequency stability requirement (± 0.001 percent) can be met by using fifth overtone crystal oscillators, by imposing strict oscillator specifications, and by appropriate selection of parts after their exposure to a sterilization heat cycle.

4.9 FLIGHT SPECECRAFT RELAY LINK RADIO SUBSYSTEM DESCRIPTION

4.9.1 Antenna

As noted in Table IX, it was assumed that a body-fixed antenna having 10 db peak gain would be used for the nominal performance flight spacecraft.

A helix, radiating in the axial, or end fire mode is a suitable candidate to satisfy these requirements. Such an antenna, designed for operation at 270 MHz, would be 30 inches long and 16 inches in diameter and mounted over a 35-inch diameter ground plane. This antenna has a nearly circularly polarized beam, a gain of 10 db above an isotropic radiator on axis and a half-power beamwidth of approximately 60 degrees. The axial, or end-fire mode, is most simply generated by connecting the inner conductor of the input coaxial feed line to the helix and terminating the outer conductor of the coaxial line in the ground plane. The ground plane may be a continuous sheet or may consist of a pattern of interconnected radial and concentric conductors.

TABLE XIII

FLIGHT CAPSULE RELAY-LINK RADIO SUBSYSTEM CHARACTERISTICS

ANTENNA	
Quantity	1
Type	Planar log spiral
Frequency	272 MHz
Gain	
On-Axis	6 db
Off-Axis	-4 db at ± 90 degrees
Polarization	Circular
TRANSMITTER	
Quantity	2
Frequency	272 MHz
Frequency stability	± 0.001 percent
Output power	30 watts
Modulation	FSK
Data rate	64 bps

4.9.2 Receiver

A number of options are available concerning the flight-spacecraft relay-link receiving equipment concept. They include bit-by-bit detection on-board the flight spacecraft or feed-through schemes in which the data demodulation function is performed on Earth rather than onboard the flight spacecraft. With a feed-through scheme, the flight spacecraft complexity can be reduced since components such as the bit synchronizer, data demodulators and decision circuitry can be located on Earth.

4.9.2.1 Bit-by-Bit Detection

Bit-by-bit detection on-board the flight spacecraft is discussed in detail in Paragraph 5.5.4. Although the discussion presented there is directed toward a very high data rate (18,000 bps) relative to the 64 bps of concern here, the concept would apply equally well to lower data rates (see also Appendix 4-8, in Reference 1).

4.9.2.2 Feed-Through

There are a number of feed-through options available to the flight spacecraft. However, each of these options assumes certain flight spacecraft to Earth data-link capabilities. It is obvious that the feed-through system data rate cannot exceed the data rate of the slowest link; e.g., if the flight-capsule to flight-spacecraft link is capable of supporting a higher data rate than the flight spacecraft-Earth link, then the data rate will be determined by the latter. Thus, use of a feed-through scheme appears attractive only in those situations in which the flight spacecraft to Earth link can support a high data rate. In situations in which this is not true, bit-by-bit detection on board the flight spacecraft is preferable. The availability of a high bit-rate flight spacecraft to Earth link is assumed in the following discussion. Two of the feed-through options (sample and store, and wide-band repeater) available to the flight spacecraft are illustrated in Figure 24.

In the sample and store mode, the FSK signal is demodulated, filtered by a low-pass filter, sampled, quantized, digitized, and stored (in digital form) for subsequent playback over the flight-spacecraft to Earth link. At the expense of a considerable increase in flight-spacecraft to Earth traffic, this option allows detection to be performed at Earth by use of an appropriate bit synchronizer. The low-pass filter following the subtractor has a cut-off frequency (f_{co}) several times higher than the relay link bit rate (B). For instance, if $f_{co} = 2B$, sampling must then be done at a rate of at least $2f_{co} = 4B$ samples per second. Thus, four samples will be taken during the relay link bit duration of τ seconds. If the samples are further quantized into 64 levels, 24 flight spacecraft to Earth bits will then be needed to

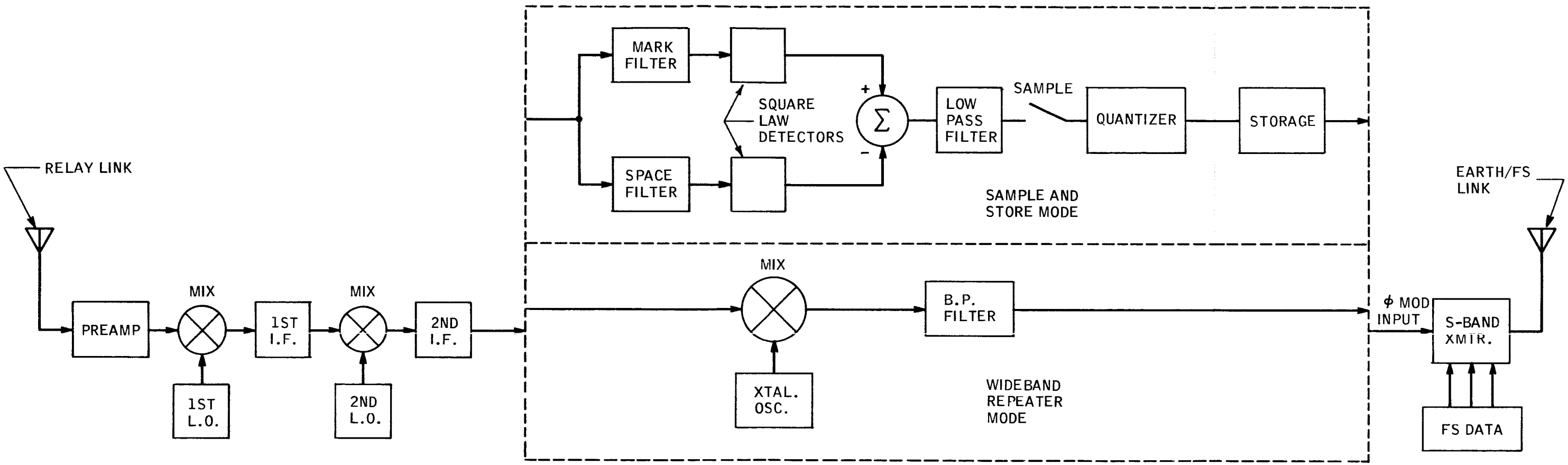

Figure 24 FLIGHT SPACECRAFT RECEIVER CONFIGURATION FOR VARIOUS FEED-THROUGH MODES

79-1

represent each relay link bit. This operation is very wasteful of flight spacecraft to Earth bits. Such a condition can be tolerated only if this link can support a high data rate.

The other feed-through option involves a wideband repeater mode. In this mode, suitable equipment in the flight spacecraft is used to perform broadband repeater functions to transmit to Earth the predetection intermediate frequency (IF) output of the flight spacecraft VHF receiver. This can be accomplished by using the IF output as a subcarrier on the flight spacecraft to Earth-link transmitter. For a more detailed treatment of this subject, see Appendix 4-8, in Reference 1.

4.10 FLIGHT CAPSULE DIRECT-LINK RADIO SUBSYSTEM DESCRIPTION

The direct-link radio subsystem is used to transmit post-landing data directly to Earth. It forms part of the internal telecommunication subsystem and is located inside the landed capsule. This radio subsystem is used also to receive commands, coming directly from Earth. Figure 25 shows the direct-link radio subsystem in block-diagram form. Two S-band antennas are shown in this figure. Two antennas are considered necessary because the landed orientation of the oblate spheroid configuration is probabilistic. Present plans, therefore, are to excite only that antenna which is aligned more closely to the local vertical. This assures maximum antenna radiation away from the planet surface. If the landed capsule should come to rest on edge, it is planned to excite both antennas simultaneously, thereby obtaining maximum coverage.

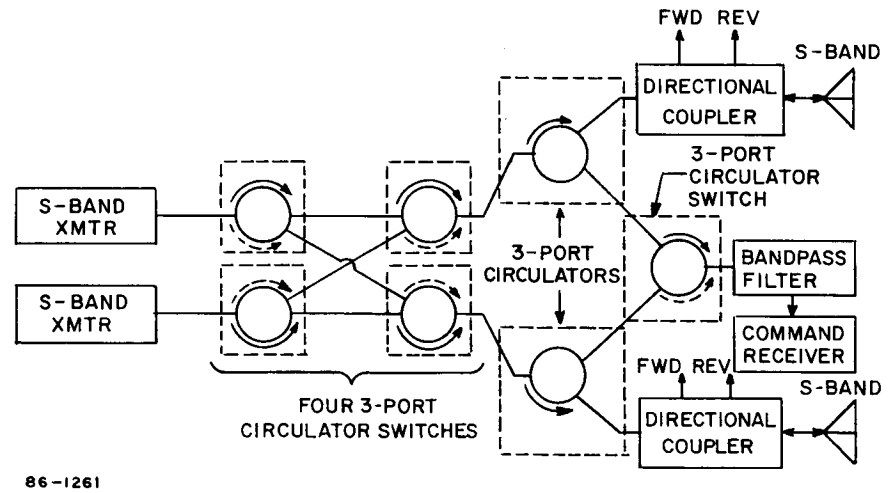

Figure 25 INTERNAL RADIO SUBSYSTEM

This antenna concept requires use of two independent transmitters to provide the same effective radiated power from each antenna. *

Except for the contingency of landing on edge, the transmitters are block redundant and are intended for alternative use; both, of course, are used in the event the capsule lands on edge. These transmitters were made block redundant for the following reasons:

1. The direct link is the primary data link during the landed phase, the period when the internal telecommunication system is used.

2. Use of two identical units in parallel provides protection against loss of function as the result of component or piece-part failure. The discussion presented in paragraph 4.8, relative to the block redundancy reliability of the relay transmitter, is equally applicable to the direct-link concept presented here.

4.10.1 Antenna

The reference design concept is based on use of an oblate spheroid configuration. Multiple antennas are, therefore, required for the direct link to provide nearly omnidirectional capability regardless of the orientation of the landed capsule. Figure 26 shows the reference-design direct-link antennas. Two identical V-type horn antennas, mounted on opposite sides of the spherical portion of the landed capsule will be used. These antennas will provide the required omnidirectional coverage. Each is excited at a slightly different S-band frequency. The bandwidth is wide enough to allow transmission of data at a frequency of approximately 2300 MHz and reception (of command signals) at a frequency of approximately 2110 MHz.

Operation and performance of the antenna depend upon the orientation of the landed package. An antenna selection system in the telecommunication subsystem is used to control excitation of the two antennas. This system is designed to sense gravity and to select the antenna which is facing away from the surface of the planet. If the tilt angle exceeds a pre-set maximum, both antennas are excited at slightly different frequencies. The frequency difference will assure null cancellation and thereby provide a resultant composite pattern which satisfies the minimum gain requirement.

The V-type antennas consist essentially of tapered sections of waveguide with circular posts placed at the center of each aperture. Each antenna is excited by a probe inserted into the E-field of the waveguide. The probe is an extension of the center conductor of the input coaxial transmission line. The probe is tapered to optimize transfer of power from the input coaxial transmission line to the waveguide radiator. A semi-rigid coaxial cable is used for the antenna feed line.

* A reduction in effective radiated power of one-half would result if a single fixed-power transmitter excited both antennas.

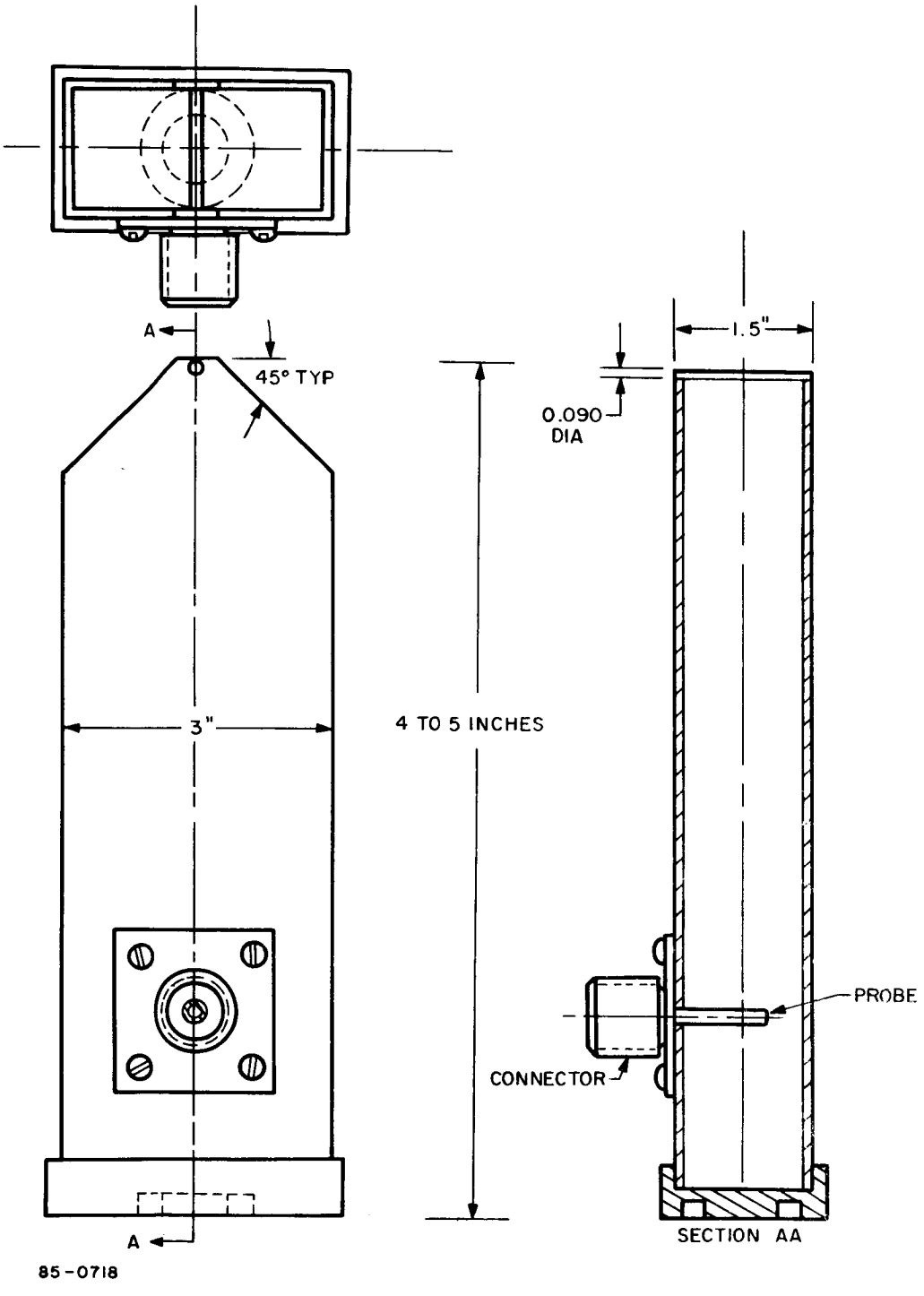

Figure 26 S-BAND V-HORN ANTENNA

Conventional S-band waveguide with a 3.0 x 1.5 -inch cross section is used for the antenna. The H-plane of the waveguide is tapered at an angle of 45 degrees to broaden the 10 db beamwidth and optimize the coverage in the hemisphere in front of the antenna. The antenna will be supported by a tubular stand-off. An alternative possibility for supporting the V-type antenna is based on filling the VHF cavity with a foam-type dielectric material. However, this approach imposes an overall weight penalty.

While it is most desirable, from the viewpoint of optimizing radiation coverage to have the radiating aperture protrude from the landed package, such an installation makes the hollow-tube waveguide structure very vulnerable to landing shock despite the fact that it is surrounded by impact attenuator. To minimize impact shock damage, therefore, the radiator will be filled with a dielectric material, the density of which is close to that of the crush-up material. This will help to disperse the impact loads from the circular post at the center of the aperture. Without this dielectric support, the impact shock could collapse the antenna aperture.

Use of dielectric material in the waveguide will also serve to reduce the effective width of the waveguide by an amount equivalent to the square root of the dielectric constant. Eccofoam FPH or an acceptable equivalent would be suitable for use as the dielectric.

Ridge loading of the waveguide will also reduce the effective width of the waveguide. Care must be taken, however, in designing the ridge section to avoid introducing excessive phase errors at the aperture of the antenna, with resultant asymmetries in the overall radiation pattern.

The antenna can be backfilled with nitrogen and sealed against moisture leaks to enhance its power-handling characteristics.

4.10.2 Transmitter

Two block-redundant 20-watt S-band transmitters were selected for the direct data link. The desirability of using the N-ary modulation technique for the direct data link has been discussed in paragraph 4.4.6. Several means of implementing such a technique in the direct link transmitter are discussed there.

A block diagram indicating the conceptual design of the direct link transmitter is shown in Figure 27. Only one of the transmitters is shown in detail. The other is fully block redundant.

On command from the CC&S to initiate operation of the telecommunication subsystem in internal mode 3, binary coded data is read out of the surface memory in the internal data-storage subsystem. This data passes through the internal telemetry subsystem, and then enters the binary-to-N-ary

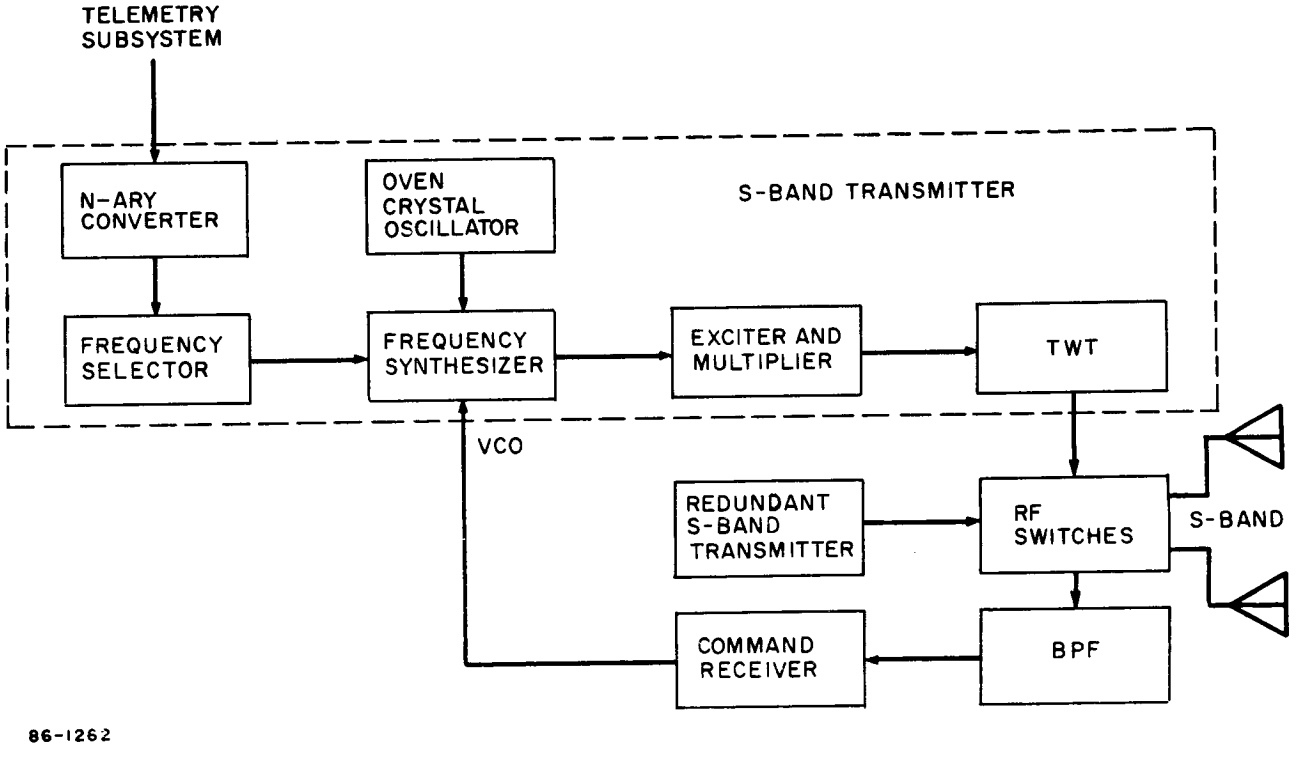

Figure 27 DIRECT-LINK RADIO SUBSYSTEM

converter (in this case, N = 32) in the transmitter. The converter accepts the data and selects one of 32 output frequencies as appropriate to represent the data. The 32 frequencies, all in the VHF band (or lower than VHF), are generated by the frequency synthesizer. A single crystal-controlled oscillator provides the basic frequency from which the others are synthesized. The difference between adjacent synthesized frequencies is constant. The frequency selector, which receives its input from the binary-to-32-ary converter, controls the output radio frequency (ourput RF).
The frequency-synthesizer output signal is multiplied to the desired S-band frequency and its power amplified to 20 milliwatts (mw) in the exciter. The 20-watt output power required for telemetry transmission to the deep space instrumentation facility (DSIF) is provided by a traveling wave tube (TWT) amplifier which has 30 db gain. A suitable bandpass filter is used to eliminate harmonic or spurious frequencies generated by the TWT. The TWT amplifier output signal is coupled to the S-band antennas through RF circulator switches. The switches are also used to couple command signals received at the S-band antennas into the command receiver.

4.10.2.1 Frequency Synthesizer

Various aspects of microwave frequency, non-digital frequency synthesizer design were studied. It was not considered desirable to design a completely solid-state synthesizer for direct operation at S-band frequencies. Instead, the approach adopted was based on designing a frequency synthesizer to operate in a suitable lower radio frequency (RF) band (in this case, in the 40 to 50 MHz range in the VHF band), and to obtain the desired microwave frequency output with a suitable frequency multiplier. Development of such a unit (frequency synthesizer plus frequency multiplier) for use in the landed capsule seems feasible. The binary-to-32-ary converter and the frequency selector could each be incorporated in the transmitter as submodules. In the direct-link radio subsystem described here, the output frequencies are basically derived from two reference sources. One is an oven-stabilized, crystal-controlled oscillator, the other is a voltage-controlled oscillator (VCO) in the command receiver. In the absence of an incoming signal, the crystal-controlled oscillator serves as the frequency source. When the command-carrier signal is detected, however, the frequency source is switched. Instead of the crystal-controlled oscillator, the VCO becomes the frequency source, as indicated in Figure 27.

The spectral purity of the oscillator output signals is very important. The degree of purity is determined by the level of undesired harmonics, the intermodulation-product outputs, and the amount of incidental frequency and audio modulation (FM and AM). The non-digital frequency synthesizer considered in this study employs mixers, dividers, and multipliers to generate the required frequencies. If achievement of

the necessary level of spectral purity appears to be a serious system or development problem, it may be desirable to use an alternative digital synthesizer design. Reduced size and a high level of spectral purity are the primary advantages of a digital technique. The principle disadvantage, however, is the higher power drain of the digital synthesizer especially when S-band frequencies separated by less than 20 kMz are involved. The frequency spacing of the 32 carriers is, therefore, an important system parameter since it affects the selection of frequency synthesizer technique.

4.10.2.2 Power Amplifier

From an efficiency viewpoint, the TWT and the Amplitron are the first and second choices, respectively, for amplifier applications at 20 watts (see Appendix 4-14, in Reference 1). Approximately the same degree of complexity is involved in the power supply for each device. The TWT requires several different high-voltage inputs; the Amplitron requires additional control circuitry to cope with possible loss of the input signal. The demonstrated reliability and availability of the TWT appear to give this device a unique advantage in S-band amplifier applications. Therefore, the TWT was selected for use in the reference-design amplifier.

4.10.3 Command Receiver

Direct-link command reception capability, as an alternative to automatic CC&S-controlled operations, is provided for the post-landing phase of the flight-capsule mission. Commands are used as a secondary means of regulating operation of the flight capsule. Means for command control of the flight capsule prior to separation are also provided. It is assumed, however, that such commands will be received by the flight spacecraft and passed on to the flight capsule via hard-line. It would also be desirable to have command capability during the prelanding phases after separation. This capability is not included, however, because the need to operate the command receiver, detector, and decoder continuously for the 12 days between separation and impact would impose an unacceptable battery weight penalty.

4.10.3.1 Assumptions and Constraints

The following assumptions and constraints formed the basis on which design of the command receiver configuration evolved:

1. Only a direct-link (S-band) command channel will exist.

2. Operation of the command channel will not require the presence of the direct data link, but if such a link were available it

would be employed to improve the level of confidence in correct reception of commands from Earth.

3. The flight-capsule energy constraints are of prime importance.

4. The error rate for the data channel is significantly higher than that for the command channel.

5. The number of commands transmitted to the flight capsule during any communications interval is small (less than 10).

The first occasion for command contact is soon after impact. Similar occasions are presented each subsequent time the landed capsule-to-Earth geometry is favorable, a condition which exists once during each Martian day.

4.10.3.2 Command Reception Considerations

To attain a high level of confidence in correct reception of commands from Earth, three factors require detailed attention. The design concept must provide not only minimum probability, but also 1) of loss of commands as a result of occurrence of an unlock condition, 2) of loss of command word synchronization, 3) that an erroneous command would be recognized, but also maximum probability of recognition of correct commands.

1. Loss of Lock -- The probability of loss of lock, with resulting loss of mission commands, can be minimized by the adoption of either of the following two approaches or some combination of these approaches:

a. Minimum Loop Stress -- Stress in the phase-lock acquisition loop can be reduced by making several independent Earth-transmitter S-band uncertainty scans after the initial scan is completed. Each of these uncertainty scans should be in a different region of VCO uncertainty range. In such a multiple-scan approach the same group of commands would be transmitted after each lock attempt.

b. Compensated Loop Stress -- Circuits necessary for measuring the VCO stress and for automatically introducing such bias compensation in the VCO feed-back loop as may be required to remove the measured stress can be incorporated. Such an approach might result in need for only one S-band carrier scan. Since automatic measuring and biasing is complex and unproven at present, the multiple scan approach is more advisable.

2. Loss of Synchronization -- Loss of command-word synchronization can be minimized either by the use of a long pseudo-random

noise (PN) sequence capable of being used for bit and word synchronization, or by use of a flywheel synchronization approach in conjunction with fixed-length commands and a simple synchronization pattern search.

3. Command Recognition -- The availability, data rate, error rate, and coding structure of the S-band direct link influence command recognition and decoding capabilities, as follows:

a. Continuous Data Link Availability -- If the S-band data link were continuously available during the time the command link is being established as well as during transmission of commands, the command link could be locked up and operated with a high degree of confidence in the correct flow of information because the telemetry data available could be used to confirm command data. By detecting bit errors and word-timing errors via the telemetry link, the command decoder would have to perform complex functions designed to improve error detection or word-timing lockup ability. In addition, since a data link would be continuously available, there would be no need to store and examine received commands to determine their validity or to determine whether or not there was possible need for transmitting information to Earth.

b. Periodic Data Link Availability -- If the S-band data link were available only for a short period, it would not be available to assist in command-channel lock up. A short transmission by the data channel could, however, be used to confirm command-channel lock up and to telemeter the fact that command words had been accepted. This, of course, is predicated on the assumption that the commands had been transmitted, received, and stored in the command subsystem prior to the S-band data-link transmission.

The latter situation would exist in the concept presently under consideration, since the direct data link is operated only twice, once for approximately 2 hours starting shortly after impact, and again for approximately one hour on the Martian day after the day of impact.

4.10.3.3 Selected Approach

One method for providing command reception capability for the landed capsule is based on adapting the space-proven Mariner command subsystem to the present application. A description of the main features of such a subsystem follows.

The basic differences between the Mariner command receiver and that required for the flight capsule are: 1) inclusion of a low-noise preamplifier, 2) a carrier loop-noise bandwidth of 5 Hz instead of 20 Hz, and 3) the requirement for handling only discrete commands.

The command receiver consists primarily of a continuously operating, narrow-band, double-superheterodyne, automatic phase-tracking receiver and a command detector and decoder.

The required isolation between the command channel and TWT amplifier is provided by the RF circulators and a suitable band-pass filter installed between the RF circulators and the command receiver.

The receiver will operate on a nominal frequency of 2113 MHz. Its basic functions will be coherent translation of the frequency and phase of the receiver RF signal, and transmission of a composite command signal to the command detector and decoder.

The unmodulated phase frequency of the transmitted RF carrier will be controlled in accordance with either of the following two non-coherent modes:

1) When no signal is present at the receiver, the phase and frequency of the unmodulated carrier will be controlled by the oven-stabilized crystal-controlled oscillator.

2) When the receiver is locked to the signal transmitted from Earth, the command detector receives both the demodulated command signal and a pseudo-random noise (PN) synchronization signal. The command signal contains the command word information: the synchronization signal provides the phase reference data required for coherent phase demodulation of the command signal subcarrier.

The command detector processes the synchronization signal, acquires phase coherence (locks up) with the command signal, and establishes both bit synchronization and a phase reference signal. By multiplying the command-word information subcarrier by the phase reference signal and subsequently applying the resultant signal to a matched filter and detector, the bits that compose the command word are recovered. In turn, the command decoder receives the command word bits, interprets the command word transmitted from Earth, and supplies the appropriate output to the flight spacecraft subsystem or subsystems utilizing the command word. The command detector also generates a detector lock alarm signal whenever the detector is out of lock with the command signal. The detector lock alarm signal is used to inhibit command decoder.

The command detector and command decoder also provide the flight capsule telemetry subsystem with signals that are subsequently converted into telemetry information concerning functional operation of the command subsystem. Some discrete commands (momentary switch closure) that could be used to provide functional backup support for landed phase events are:

a. Jettison impact attenuators

b. Start internal mode 1

c. Deploy instruments

d. Start internal mode 2

e. Switch to backup S-band transmitter.

4.10.4 Summary

Table XIV summarizes the salient characteristics of the flight-capsule direct-link radio subsystem. This subsystem, used only during the post-landing phase, has both transmit and receive capabilities.

Two antennas, one on either side of the oblate spheroid configuration, provide essentially omnidirectional radiation. In the nominal mode of operation, only the antenna more closely aligned to the local vertical would be excited.

Two transmitters are used to provide block redundancy. The 20-watt output power is provided by a TWT amplifier. Multipath frequency shift modulation is used; this is a non-coherent modulation technique in which each one of 32 discrete frequencies is paired with an associated one of the 32 (2^5) combinations obtained from the 5-bit contents of the data words. A single command receiver based on the Mariner concept is used to provide functional redundancy for the CC&S.

TABLE XIV

SUMMARY OF DIRECT LINK RADIO SUBSYSTEM CHARACTERISTICS

ANTENNA	
Quantity	2
Type	V Horn
Frequency	S-band (2110-2300 MHz
Beamwidth	Omnidirectional
Gain	
a) On-Axis	5 db
b) Off-Axis	-7 db minimum*
TRANSMITTER	
Quantity	2
Frequency	2300 MHz
Output power	20 watts
Modulation	Multiple frequency shift MFS (32 ary)
COMMAND RECEIVER	
Quantity	1
Frequency	2113 MHz
Noise figure	6 db
Modulation	Coherent PSK/PM

*Since landed capsule orientation is probabilistic, the off-axis gain stated, will be exceeded with 99 percent probability. See Appendix IV. 4-2 of reference 1 for complete analysis.

4.11 FLIGHT CAPSULE DATA HANDLING SUBSYSTEM DESCRIPTION

Two independent data-handling subsystems are used in the flight capsule telecommunications subsystem. They provide means for collecting data from the science and engineering instrumentation, for converting this data into a form compatible with transmission via relay or direct links in real time, and, when necessary, for storing it for subsequent non real-time transmission over these same links. One subsystem, located external to the flight capsule, handles data collected during the separation-to-impact phases of the mission. The other subsystem, located inside the landed capsule, handles data collected after landing. Each subsystem contains the following listed items:

Data Automation Equipment (DAE)

Telemetry Subsystem (T/MS)

Data Storage Subsystem (DSS)

The DAE handles all data provided by scientific instruments. The T/MS handles all engineering and event data. Data from both the DAE and telemetry subsystems are stored in the data-storage subsystem. Both the DAE and T/MS data are routed through the telemetry subsystem. The reasons for this approach are:

1. A failure in either the DAE or the telemetry subsystem will not compromise operation of the other.

2. The science instrumentation package is more susceptible to change than are the engineering requirements as the program develops. The effect of such changes on the various interfaces is minimized by using two subsystems.

3. Interfaces with other subsystems are simplified if there is a central data routing point. For example, only one data source can modulate the transmitters; hence, a single routing point should be available to control data flow.

Several tradeoff studies were performed in regard to the DAE and T/MS. The results of these studies provided the basis from which the mechanization of both the DAE and telemetry subsystems evolved. The various tradeoff studies are presented in detail in paragraph 4.11.2. In some instances, the conclusions applied only to the DAE and not to the telemetry subsystem. Such differences are noted separately in the discussion of the telemetry subsystem (paragraph 4.11.1.2).

4.11.1 Description of Selected Approach

4.11.1.1 Data Automation Equipment

The final configuration of the DAE is based on the conclusions reached in the tradeoff studies as applied to the actual DAE data handling requirements. The DAE consists of two independent subsystems. One subsystem, the external DAE, is located outside of the landed capsule and is used for handling scientific data collected during the entry through impact phases of the mission. The other subsystem, the internal DAE, is located inside the landed payload and is used for handling scientific data collected after landing. Descriptions of the external and internal DAE subsystems follow.

1. External DAE Requirements -- The external DAE handles scientific data collected from the instruments listed in Table XV. The operational times during which data are collected are shown in Figure 28. The solid lines in that figure represent the mission phases during which the given instrument is operational. A series of alternate short and long dashed lines indicate the mission phases during which data from certain of the instruments must be stored. This data must be stored because the instruments which generate the data are operated at times when real-time radio communication via the relay link is blacked out. The start of the various phases of the mission is indicated, in abbreviated form, in Figure 28, e.g., 0.1 G, emergence from blackout (EBO), chute full open (CFO). The mission phases to which these abbreviations refer are shown in Figure 29, which illustrates the sequence of events, and the time and altitudes at which these events occur. The time given for each event represent extremes over the range of possible trajectories, i.e., the shortest entry/descent times are based on: 1) the Model 3 (lowest density) atmosphere, 2) a 90-degree entry angle, and 3) the highest entry velocity. The longest entry/descent times are based on: 1) the Model 2 (highest density) atmosphere, 2) a shallow entry angle, and 3) the lowest entry velocity. The basic objective in designing the external DAE was to provide the maximum amount of data during all phases from entry through impact regardless of the atmosphere encountered, the entry angle, the entry velocity, or the occurrence of failures. Short dashed lines are used in Figure 28 to represent the mission phases during which the outputs of various instruments will actually be monitored by the external DAE. It can be seen that the actual operating intervals always exceed the required intervals. The reasons for this overlap are discussed on an event-by-event basis in paragraphs a. through c., which follow.

TABLE XV

SCIENCE INSTRUMENTS HANDLED BY EXTERNAL DAE

Instrument	Outputs	Location	Sampling Rate		Accuracy	
			Required	Actual	Required (bit)	Actual (bit)
Altimeter	1	Support Structure	1/sec	1 sec	7	7
Pressure transducer	2	Support Structure	1/2 sec	1/2 sec	7	7
Temperature transducer	2	Support Structure	1/2 sec	1/2 sec	7	7
Gas chromatograph	8	Support Structure	5 samples	1/8 sec	7	7
Mass spectrometer	6	Support Structure	5 samples	1/8 sec	7	7
Acoustic device	3	Support Structure	5 samples	1/8 sec	7	7
Beta scatter	1	Support Structure	1/5 sec	1/4 sec	7	7
Accelerometer	3	Inside Flight Capsule	1/sec	1/sec	10	10
Radiometer	6	Heat shield	1/sec	1/sec	7	7
	32					

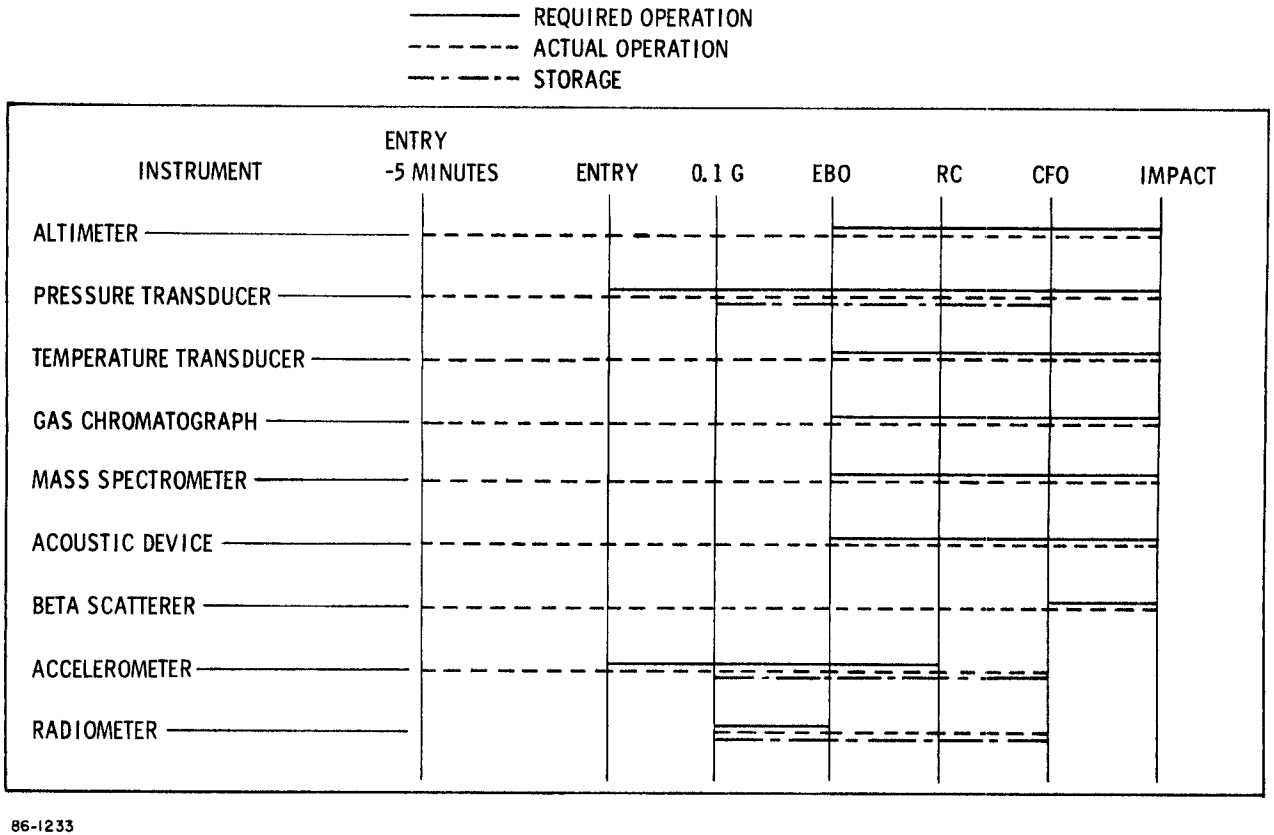

Figure 28 OPERATIONAL TIMES OF EXTERNAL DAE SCIENCE AND INSTRUMENTS

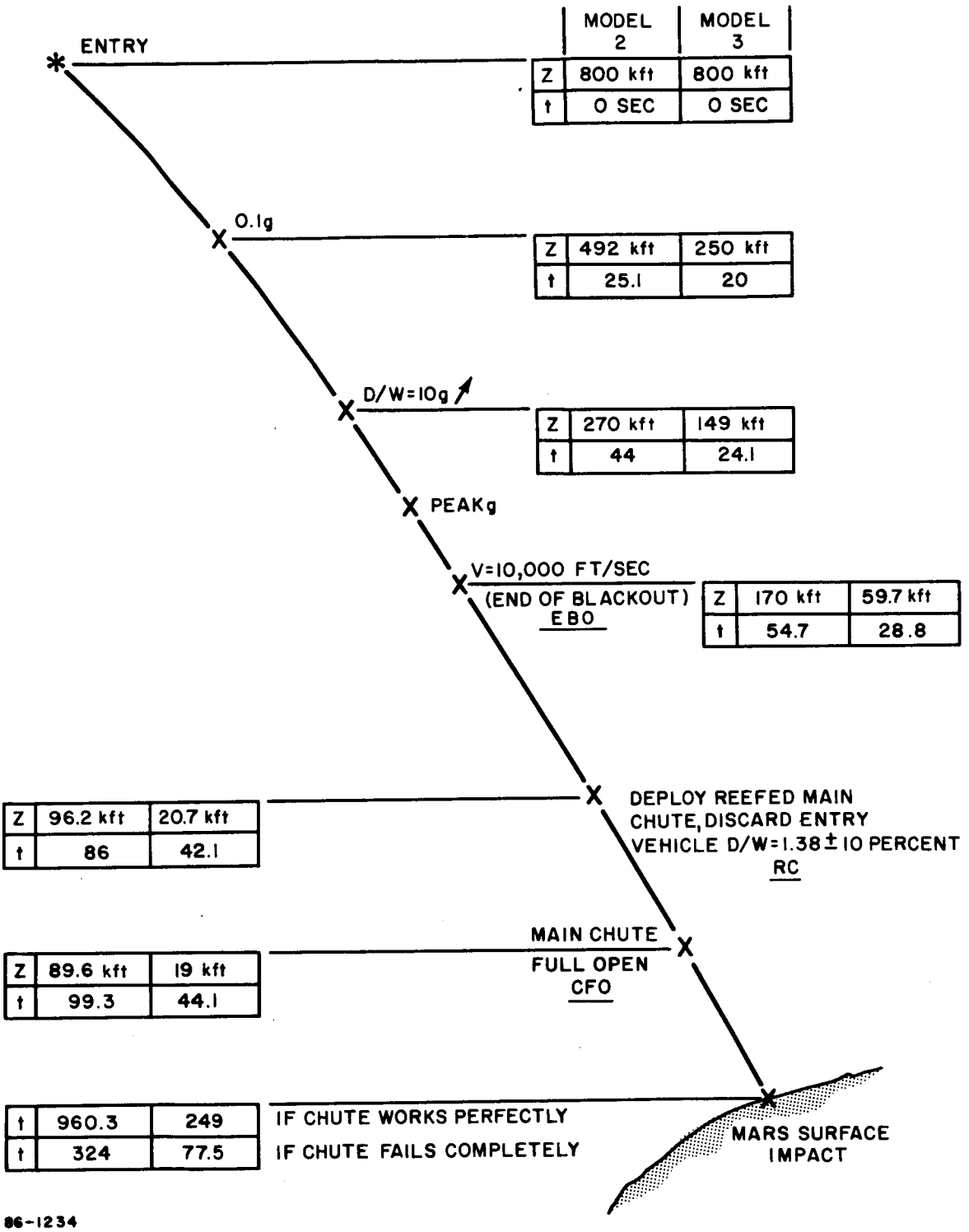

Figure 29 TRAJECTORY DATA SUMMARY

a. Entry -- Some scientific instruments must start to operate at entry. In the current flight-capsule concept there is no direct method of determining when entry (defined as reaching an altitude of 800,000 feet during descent) actually begins. The altimeter on the flight capsule can only operate at much lower altitudes. However, the time from separation to flight-capsule entry into the Martian atmosphere is known to within 3 minutes. The cruise sequence in the CC&S, therefore, could be used to start the external DAE and science instruments 3 minutes before entry (t_e - 3 minutes). However, the time finally selected is 5 minutes before entry (t_e - 5 minutes), as shown in Figure 28. This early initiation allows time for a 2-minute final engineering status check shortly before entry. Although it would be desirable to use the 0.1-g accelerometers as a backup means for initiating external DAE and instrument operation and the engineering status check, the accelerometers themselves are among the items turned on at t_e - 5 minutes by the CC&S. As a result, no functionally redundant backup means of initiation exists. The block-redundant timer in the CC&S is, essentially, the backup means for initiating this event. It should be noted from Figure 28 that monitoring of all science instruments, with the exception of the radiometer, begins at t_e-5 minutes. The design philosophy is based on real-time transmission by the relay link of the data collected from these instruments during the period from initiation until impact. This eliminates loss of data even if no other event subsequent to initiation at t_e - 5 minutes successfully occurs. This approach is believed to be the simplest one that could be taken consistent with the need for providing the maximum amount of data and for minimizing the impact of possible subsequent system failures. The radiometer is not included among the instruments turned on at this time because its useful operational life occurs when radio communications will be blacked-out. If no event other than initiation of the t_e - 5 minute sequence occurs as programmed, any radiometer data played out before or after blackout would be useless.

b. Blackout -- Certain instrument data must be stored because it is collected during communications blackout (for a detailed analysis of the communication blackout, see Appendix IV.4-4, in Reference 1). Blackout starts shortly after deceleration reaches 0.1 g. It is both practical and convenient, therefore, to start data storage when the 0.1 g deceleration level is sensed. It is not practical to begin storing data at t_e - 5 minutes, since, as is explained below, the resultant increase in stored data is not consistent with the provisions made for alternative modes of operation, the initiation of which is contingent upon occurrence of various possible failures. Determination of the 0.1-g event is sensed directly by the 3-axis accelerometer inside the landed package. Sensing of a deceleration of 0.1 g on any one of the 3 axes initiates the storage start signal. A functionally redundant means of providing backup support exists as follows.

The forward and reverse power monitored via the directional coupler in the external radio subsystem (see Figure 21) will be used to determine the VSWR. When the VSWR increases, thereby indicating the start of blackout, an appropriate signal will be given to initiate data storage. Data will continue to be stored either until the chute full-open (CFO) event occurs or until 75 seconds has elapsed following sensing of 0.1 g deceleration (0.1 g + 75 seconds). This 75-second period is longer than the time between 0.1 g and CFO, as shown in Figure 29, for either the Model 2 or Model 3 atmosphere. The two events described above (t_e - 5 minutes and 0.1 g) start acquisition of data from all entry-descent science instruments. Initiation of only the t_e - 5 minute sequence will result in a partial mission success since only that data acquired and stored during blackout would be lost if both the 0.1 g signal and its backup signal (provided by the VSWR monitor), fail to initiate data storage. The stored data must be played out via the relay link before impact. Playout of the data is initiated as the communication blackout ends. This event, end of blackout (EBO), is sensed directly by the VSWR monitor used previously to provide backup support for the 0.1 g event. Again, a functionally redundant means of backing up the primary (VSWR monitor) means of sensing EBO is provided. The backup means will be a signal provided 11 seconds after a 10 g level is sensed as acceleration increases (10 g + 11 seconds). The discussion in c., which follows describes the events that occur after EBO. The discussion is based on a worst-case assumption, that is, that the initiation signal will be provided by the backup means (10 g + 11 seconds). If initiation occurs in response to the primary means (VSWR monitor), results even better than those described, will be achieved.

c. Emergence from Blackout (EBO) -- There are two reasons for selecting 10 g + 11 seconds as the time to initiate playout of the stored data. First, the 10 g + 11 seconds time period is as long as or longer than the longest time between the start and end of blackout (10 g to EBO) shown in Figure 29 for either the model 2 or model 3 atmosphere. At EBO, relay-link communication will be re-established and data stored during the period between the 0.1 g and EBO events can then be transmitted in addition to the real-time data being played out following EBO. Second, the period between 10 g + 11 seconds and the time of impact is long enough to allow all data stored during blackout to be transmitted via the relay link even if the parachute should fail to open. This consideration explains why data storage is not initiated at t_e - 5 minutes. If storage started much before 0.1 g, there would not then be enough time for all of the data acquired between t_e - 5 minutes and EBO to be played out before impact. Specifically, it would result in loss of the last data stored -- the vital data acquired during blackout.

From 10 g + 11 seconds on, data from instruments initiated at t_e - 5 minutes (except that from the accelerometers) will be played out in real-time. This real-time data will be interspersed with the non-real time data stored after the 0.1 g-sequence was initiated. This procedure will continue unchanged until impact. Even if the parachute does not open, the time from 10 g + 11 seconds to impact is consistent with the time required for playout of slightly more data than that acquired during blackout. However, there would be a partial loss of required data because real-time transmission of acceleration data would then stop at 10 g + 11 seconds instead of at the time the reefed chute (RC) is deployed, as indicated on Figure 28. These are the only data that would be lost if the parachute should fail to open. If it does open, the time between 10 g + 11 seconds and impact is consistent with the time required for complete transmission via the relay link of all real-time and non-real-time data collected during entry and descent. These data would also include the accelerometer data stored until CFO and played out subsequent to CFO.

The first 15 frames of real-time and non-real-time data being played out via the relay link after EBO are concurrently stored in the landed capsule's internal data storage subsystem and in the external data-storage subsystem. This is done for the following reasons. First, if the parachute is successfully deployed and opened but the relay link fails, the only functionally redundant transmission link is the direct link inside the landed capsule intended for use after landing. Accordingly, to minimize loss of data in the event of relay link failure, the entry-descent data handled by the external DAE must also be stored in the internal data-storage subsystem. Second, only that amount of entry-descent data consistent with the direct link transmission capabilities should be stored in the internal data storage subsystem. The design philosophy adopted was based on storing in the internal data storage subsystem all blackout data (that is, external mode 3 operation) plus a representative sample of both post-blackout data and those taken during descent by parachute. The data-storage format was so chosen that this philosophy can be realized by storing only the first 15 frames of external mode 4 data in the internal data storage subsystem memory.

2. External DAE Functional Description -- As indicated in Table XV, all instruments operational during the entry and descent phases of the mission, with the exception of an accelerometer, are located outside the landed capsule, either on the structure or on the heat shield. Accordingly, data from these instruments, except the accelerometer, is handled by the external data automation equipment. This approach minimizes interface problems between the external and internal data automation equipment.

The decentralized data-handling concept shown in Figure 30 was selected for the external DAE. For a discussion of centralized and decentralized concepts, see paragraph 4.11.2. The output signal of the individual analog-to-digital (A/D) converters, located in each scientific instrument, is an analog voltage. The chief advantage of this concept is the fact that digital, rather than analog data is transferred over the relatively long wires used to connect instruments to the centrally located multiplexer of the DAE. This approach effectively minimizes the problem of electrical noise pickup normally present when analog data is transmitted over long lines.

The recommended A/D converter for each instrument is a voltage-to-frequency converter (voltage controlled oscillator, VCO). In addition to the A/D converters that supply digital data to the centrally located multiplexer in the DAE, the Beta scatterer experiment supplies digital data directly in the form of a pulse train. These data are handled by direct count in a 14-stage binary counter. Use of commutators located inside the landed capsule and adjacent to those scientific instruments which have many analog outputs (as indicated on Figure 30) is recommended, although such an approach represent a departure from the practice followed on Mariner. The gas chromatograph with eight outputs is typical of the multi-output instruments used. Several distinct advantages are gained by this arrangement (serially connected instrument-commutator-converter). For example, by commutating the analog data before its voltage-to-frequency conversion, only a single converter is needed for each multi-output instrument instead of separate converters, one for each data line. Furthermore, only a a single line rather than multiple lines is then needed to convey data from the instrument location to the DAE. This considerably simplifies the overall wiring design of the system.

The weight penalty imposed by addition of a commutator to the instrument assembly was offset by the weight saved by using one instead of several converters at each instrument location.

Design of a commutator for use at the instrument location presents no problem. Since no instrument has more than eight data output channels, the commutator logic matrix can be very simple and straightforward.

A brief description of overall DAE operation follows. The programmer supplies appropriate timing signals to the various commutators and voltage-to-frequency converters in response to mode-control signals and clock signals from the CC&S. Analog voltage data, sampled by a commutator, is linearly converted to appropriate frequency data by a voltage-to-frequency converter.

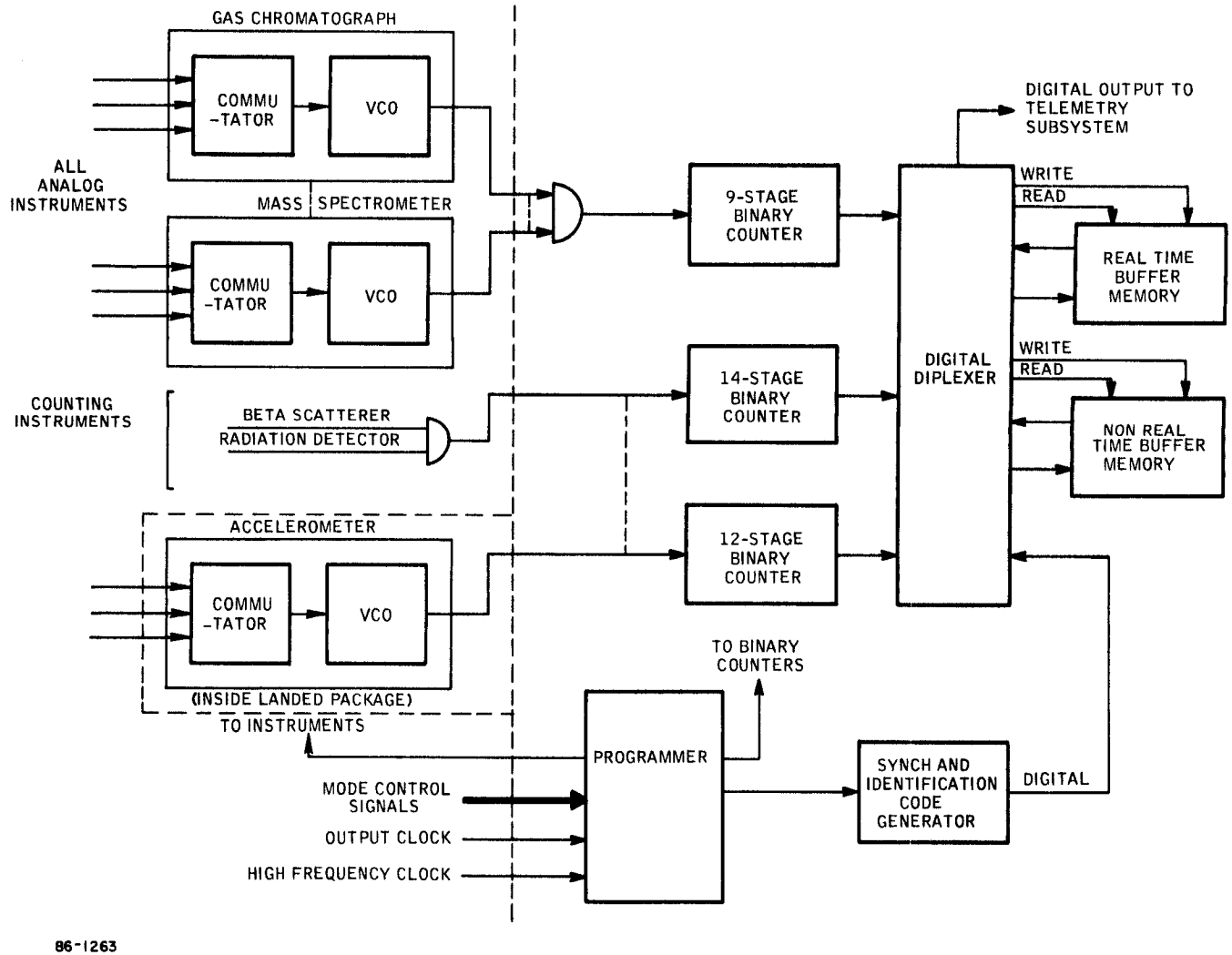

Figure 30 EXTERNAL DATA AUTOMATION EQUIPMENT BLOCK DIAGRAM

The converter center frequency is 320 kHz and varies from 256 kHz to 384 kHz (320 kHz ± 20 percent) over the full 0 to 5 volt range of the analog input signal.

The frequency data, itself an analog of the input analog voltage, is routed to the digital multiplexer. This unit is housed, together with the programmer, a binary counter, a synchronization and identification code generator, a real-time buffer register, and a non-real-time buffer register, in a single, centrally-located package. The digital multiplexer, in response to timing signals from the programmer, connects the various frequency converters to the appropriate binary counter in a programmed sequence. Except for accelerometer data which requires 10-bit accuracy, all other analog data requires 7-bit accuracy. The following is a description of the operation of a typical A/D converter for 7-bit accuracy data.

During the time a given converter is connected to the counter, its output frequency is sampled as follows. The actual sampling period begins when the binary counter receives a 1-msec gating pulse. The leading edge of the pulse is used to reset the counter to zero. The counter then begins to count the number of cycles of the converter output signal. The counter is so designed that for the 1-msec sampling period only the number of cycles exceeding 256 is considered significant in terms of instrument output data (other than zero output). A count of 256 or less is considered to represent a zero count (because it corresponds to a converter output signal of 256 kHz, that is, a zero-voltage output signal from the instrument).

At the end of the 1-msec sampling period, the converter is disconnected from the counter and the binary contents of the counter are shifted out (in response to appropriate shift pulses from the programmer) through the digital multiplexer and into either the real-time buffer register or the non-real-time buffer register. The real-time buffer register is used for temporary storage of data acquired during sampling of the scientific instrument output data. The non-real-time register is used for data to be entered in the storage subsystem.

The data from each of the scientific instruments must be sampled almost simultaneously, particularly since a high degree of data correlation is required. If, for example, the data from several instruments must be sampled at a rate of one sample per second, then the sampling period for each instrument must be considerably less than one second. The data from that instrument is then sampled again at successive one-second intervals. In the system described here, all instrument data outputs listed in Table XV are sampled in a maximum of 58 msec. This sampling cycle time is based on allowing a

1-msec sample counting period for each instrument output requiring 7-bit accuracy and an additional 1-msec period for reading the contents of the binary counter into the digital multiplexer. The binary counter for 7-bit accuracy data is a 9-stage counter, but only 7 stages of its contents are actually read into the digital multiplexer. Nine stages are needed because in 1-msec a count of 256 is obtained if the oscillator frequency is 256 kHz (zero volts).

If at the end of the 1-msec gate the ninth stage of the binary counter has been incremented, the contents of the first 7 stages are transferred to the digital multiplexer. If for some reason the ninth stage has not been incremented, the contents of the first 7 stages are not transferred to the digital multiplexer, the counter is cleared, and the sample is read as zero.

A slight modification in the DAE operation described above is required for accelerometer data. The required accuracy of accelerometer data is 10-bits, rather than the 7-bit accuracy required for all other analog instruments. The accelerometer data is handled in the manner described above, except that the sampling interval is extended from 1 ms to 8 ms and a twelve-stage counter is used instead of a nine-stage one. In this case a count of less than 2048 is considered to represent a zero and a count of 3072 is considered to represent the full-scale output. The difference between these counts is 1024, the number of levels required for 10-bit accuracy. Accelerometer data is obtained concurrently with the 7-bit data, therefore, 24 msec are allocated for reading data into the 12-stage counter (8 msec for each of 3 outputs) and approximately 1 msec is allocated for reading each count into the digital multiplexer. Total cycle time, therefore, for accelerometer data is approximately 27 msec.

Three DAE mode-control signals, corresponding to the three mission modes are provided as follows: postseparation checkout (external mode 2), entry data storage (external mode 3), and entry/descent data transmission (external mode 4). A different output data format is provided for each of these three modes. External modes 2 and 3 are concurrent modes. External mode 1 is an engineering mode and is not, therefore, pertinent to this discussion. The format for each of the 3 DAE external modes is as follows:

a. External Mode 2 - Post-Separation Checkout -- The format for external mode 2 output is shown on Table XVI. It is, essentially, a 560-bit frame, or sequence, composed of 534 data bits (42 7-bit data words and 24 10-bit data words) preceded by a 21-bit synchronization code word and a 5-bit mode identification code word. The 21-bit synchronization code word contains a 7-bit Barker code word, the complement of that word, and the same Barker code word repeated, as follows:

TABLE XVI

EXTERNAL DAE MODE 2 OUTPUT FORMAT

Function	Channels	Bits
Synchronization	3	21
Mode identification	1	7
Spare	1	7
Altimeter	6	42
Pressure	8	56
Temperature	8	56
Time from 0.1 g	1	7
Gas chromatograph	8	56
Mass spectrometer	6	42
Acoustic	3	21
Beta scatterer	2	14
Accelerometer	24	168
Spare	9	63
Total	70	562

TABLE XVII

EXTERNAL MODE 3 STORAGE FORMAT FOR SCIENCE DATA

Function	Channels	Bits
Pressure	2	14
Acceleration	3	21
Radiometer	6	42
Total	11	77

1 110 010 0 001 101 1 110 010

Two difference mode- identifying code words will be used, one for external mode 2, the other for external mode 4. The 534-bit data content of the external mode 2 output will be stored in a 534-bit real-time register. The synchronization and mode identification code words are added in the digital multiplexer.

b. External Mode 3 - Entry Data Storage -- The format for external mode 3 is shown on Table XVII. It consists of a 77-bit frame composed of 11 7-bit data words. These words will be stored in the 77-bit non-real-time register and will be read into the external data storage subsystem via the telemetry subsystem.

c. External Mode 4 - Entry/Descent Data Transmission -- The format for external mode 4, shown on Table XVIII, is similar to that for external mode 2. The principle differences are:

(1) The external mode 4 identification code is used.

(2) The 240 accelerometer channel bits are not used.

(3) Stored external mode 3 scientific and engineering data is used.

Real-time science and engineering data is interspersed with stored external mode 3 data under control of the CC&S.

3. Internal DAE Requirements -- The internal DAE handles data from the scientific instruments listed in Table XIX.

This table also indicates the number of outputs associated with each instrument, the required sampling rate, the actual sampling rate, the required accuracy, and the actual accuracy. Science instrument data is sampled at regular intervals starting at impact.

4. Internal DAE Functional Description -- Since the basic internal DAE concepts are similar to those of the external DAE, they do not require a separate discussion. The internal DAE, however, operates in only one mode, internal mode 1. The format of internal mode 1 is shown in Table XX. The format consists of a four-frame set of data. The data for each 4-frame set is collected at 6-hour intervals, starting with collection of one complete set of 4 frames of data at impact. In all, 20 frames of data (5 sets of 4 frames) will be acquired during the required 24-hour duration of the post-impact mission.

TABLE XVIII

EXTERNAL MODE 4 OUTPUT FORMAT

Function	Channels	Binary Bits
Synchronization	3	21
Mode identification	1	7
Time from 0.1 g	1	7
Altimeter	6	42
Pressure	8	56
Temperature	8	56
Gas chromatograph	8	56
Mass spectrometer	6	42
Acoustic	3	21
Beta scatterer	2	14
Engineering data	8	56
*Frame count	2	14
*Engineering data	2	14
*Pressure	4	28
*Accelerometer	6	42
*Radiometer	12	84
Totals	80	560

*External Mode 3 data

TABLE XIX

SCIENCE INSTRUMENTS HANDLED BY INTERNAL DAE

Instrument	Outputs	Sampling Rate		Accuracy	
		Required	Actual	Required (bits)	Actual (bits)
Alpha scatterer	200	5 samples	5 samples	5	5
Cosmic radiation	1	1/hour	1/hour	7	7
Gas chromatograph	8	5 samples	5 samples	7	7
Force anemometer	6	4/day	5 samples	7	7
Microphone	2	4/day	5 samples	7	7
Surface radiation	1	1/hour	1/hour	7	7
Pressure transducer	2	2/hour	2/hour	7	7
Temperature transducer	2	1/hour	1/hour	7	7
Acoustic device	3	1/hour	1/hour	7	7
Water detector	1	1/hour	1/hour	7	7
Atmospheric temperature	2	2/hour	2/hour	7	7

TABLE XX

INTERNAL DAE MODE 1 STORAGE FORMAT

Function		Channels	Bits
Frame 1	α scatterer	75	525
Frame 2	α scatterer	70	490
	Spare	5	35
	Total	75	525
Frame 3	Pressure	24	168
	Atmospheric temperature	24	168
	Cosmic radiation	6	42
	Surface radiation	6	42
	Surface temperature	12	84
	Microphone space	2	21
	Spare	1	—
	Total	75	525
Frame 4	Acoustic	18	126
	Water detector	6	42
	Gas chromatograph	8	56
	Hot coil anemometer	6	42
	Force anemometer	6	42
	Spare	31	217
	Total	75	525

Two non-real-time buffer registers (core-type) will be used for data smoothing. Data smoothing is required because the data will be collected at different sampling rates during each 6-hour period. Data to be used in frames 3 and 4 of each set of 4 frames will be stored in the buffer registers as required during each 6-hour period. At the end of each 6-hour period, the contents of these registers are stored in the internal memory. Alpha scatterer data will be read directly into the internal storage memory at the end of each 6-hour period. Shifting of frame 3 and 4 data out of buffer registers will be controlled by the internal CC&S. The programmer will provide appropriate synchronization and identification code words once each frame. All data acquired by the internal DAE will be stored in the internal-storage subsystem. Readout of all internal DAE data will be controlled by the internal CC&S.

4.11.1.2 Telemetry Subsystem

The telemetry subsystem consists of those equipments required to: gather and condition flight capsule engineering data, gather and condition science instrument engineering data, and transmit the assembled T/M data to either the data storage subsystem (DSS) or radio frequency (RF) links in accordance with appropriate signals from the central computer and sequencer (CC&S).

Two telemetry subsystems are employed. One, which is external to the landed capsule, operates during all external modes. The other, located inside the landed capsule, operates during all internal system modes.

The philosophy followed in designing the telemetry subsystem was based on the following three objectives: 1) transmission of telemetry data must interfere as little as possible with transmission of science instrument data during the operational phases of the flight capsule mission, 2) failure within the telemetry subsystem must not adversely affect transmission of science instrument data during the operational phases of the flight-capsule mission, and 3) failure within the science instrument data handling and conditioning system must not prevent real-time transmission of telemetry data.

A modified form of the decentralized subsystem concept used for both the external and internal DAE subsystems is the basis for the external telemetry subsystem concept. A block diagram of the external telemetry subsystem is shown in Figure 31. The T/M and DAE subsystem concepts differ to some extent, 1) a separate commutator and voltage-to-frequency converter is used for each T/M external mode of operation, instead of for each instrument or sensor, 2) a steady train of engineering data samples will be acquired in the T/M subsystem. This is in

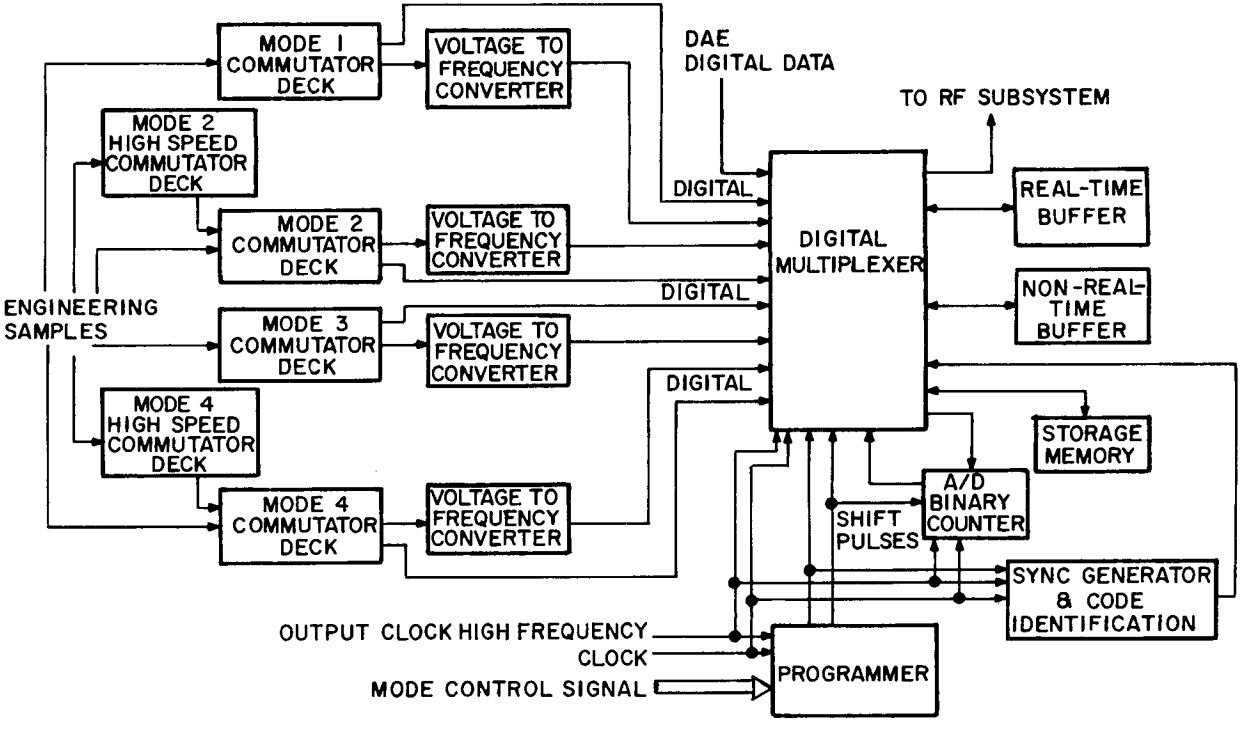

86-1236

Figure 31 EXTERNAL TELEMETRY SUBSYSTEM BLOCK DIAGRAM

contrast to the essentially simultaneous instrument sampling approach used in the DAE concepts, 3) the T/M subsystem accuracy requirement is five bits instead of seven bits and, finally, 4) the digital multiplexer in the T/M subsystem acts as a central routing point for all data.

The DAE concept of having separate commutators and converters in each instrument was not followed in mechanizing the telemetry subsystem because much of the engineering data is event data, that is, it is binary data which only indicates whether an event did or did not occur. This data does not require the noise immunity provided for the analog data handled by the DAE subsystem. Both the single and multi-level commutation schemes described in the DAE tradeoff studies are used in the T/M subsystem. Since the high degree of correlation required for the scientific instrument data is not required in the case of the various engineering samples, both the cross-strapping advantages gained by use of single level commutators and the multiple sampling speed advantages provided by use of a multi-level commutator can be fully realized.

1. External Telemetry Subsystem Requirements -- The external telemetry subsystem handles the engineering and event data listed in Table XXI. A 5-bit accuracy is required for all engineering analog data. The presence or absence of a single binary bit is used to indicate whether or not the event with which it is associated occurred. The external telemetry subsystem also acts as the central routing point for all data collected, stored, and transmitted by the relay link during the preseparation through impact phases of the mission.

2. External Telemetry Subsystem Functional Description -- A mode-by-mode description of external telemetry subsystem operation follows:

a. External Mode 1 -- Preseparation/Separation Checkout -- During external T/MS operation in this mode all engineering data will be gathered, conditioned, and transmitted from the flight capsule. At various times during the mission, a complete checkout of the landed package and of the science data system will be performed. At a minimum, this checkout will be made once before launch, once during cruise while the flight capsule is still mated to the flight spacecraft, and once more immediately before separation of the flight capsule from the flight spacecraft. These checkouts 1) determine whether or not the science instruments are in operating condition, and 2) determine the status of all flight capsule subsystems. A full dynamic checkout cannot be performed without including many items of auxiliary equipment. Such items would serve no useful purpose during actual acquisition of scientific data. Instead, output signals from the science instrument will be simulated by injecting appropriate signals into the

TABLE XXI

EXTERNAL ENGINEERING DATA REQUIREMENTS

Measurement	Sampling Rate	Analog/ Binary	Mode
Sterilization canister pressure	1/min	A	1
Sterilization canister separation	1/min	B	1
Continuity loop sterilization separation	1/min	B	1
Separation switch, sterilization canister	1/min	B	1
Separation switch, flight capsule	1/min	B	1
Continuity loop, umbilical	1/min	B	1
Gyro output	1/min	A	1
ACS error signal	1/min	A	1
ACS system gas pressure	1/min	A	1
Safe and initiate, ACS, and velocity	1/min	B	1
ACS solenoid Current	1/min	B	1
Δ V continuity loop	1/min	B	1
Spin rocket continuity loop	1/min	B	1
Δ V rocket ignition	1/min	B	1
Spin rocket ignition	1/min	B	1
Velocity	1/min	A	1
External battery voltage	1/min	A	1, 2, 4
Internal battery number 1 voltage	1/min	A	1
Propulsion support package separation switch	1/min	B	1
Relay transmitter number 1 current	1/min	B	1, 2, 4

TABLE XXI (Concl'd)

Measurement	Sampling Rate	Analog/ Binary	Mode
Relay transmitter number 2 current	1/min	B	1, 2, 4
Safe and initiate, parachute heat shield, external payload	1/min	B	2, 4
Continuity; chute, heat shield, external payload	1/min	B	2, 4
Despin rocket ignition	1/min	B	1, 2, 4
Parachute deployment squib current	1/sec	B	2, 4
Parachute deployment separation switch	1/sec	B	2, 4
External battery temperature	1/min	A	1, 2, 4
Heat sink temperature	1/min	A	1
Flight Capsule internal temperature	1/min	A	1
External science current	1/min	A	1, 2, 4
ACS system current	1/min	A	1
VHF antenna forward power (external)	1/min	A	1, 2, 4
Parachute disreef squib current	1/sec	B	4
Parachute disreef continuity loop	1/min	B	4
Heat shield deployment squib current	1/sec	B	4
VHF antenna reverse power (external)	1/min	A	1, 2, 3, 4
Central computer and sequencer clock rate	1/min	B	1, 2, 4
Power conditioning voltages	1/min	A	1, 2, 4
Reference voltages	1/min	A	1, 2, 4
Storage	1/min	B	2, 4
Flight Capsule time	1/min	A	1, 2
Fuze monitoring on all power users	1/min	B	1, 2, 4
Redundancy indicators	1/min	B	1, 2, 4

signal conditioner circuits (or at any other suitable signal injection points). This will enable the data-handling subsystems to be checked statistically. The engineering data accumulated during such a checkout will, of course, be valid data and will serve as an additional check on the status of the data-handling systems. The format for external mode 1 will be a 560-bit frame consisting of 105 5-bit words preceded by 30 synchronization and identification code bits and one 5-bit spare channel. This frame length is identical to the DAE external mode 2 frame shown in Table XVI. Each external mode 1 frame is composed of three repeated sequences of the 35 5-bit words, as shown in Figure 32, preceded by 7 additional 5-bit words. Six of the seven additional words represent synchronization and mode identification words: the seventh is a spare channel (35 x 3 x 5 bits plus 7 x 5 bits = 560 bits). The external mode 1 data is routed to the VHF relay link transmitter for real-time transmission to the flight spacecraft at a rate of 1024 bits/sec. It is also available to the flight spacecraft via hard line from the flight capsule prior to separation.

b. External Mode 2 - Post-Separation Checkout -- The external mode-2 output-frame construction is identical to that of the mode 1 frame, i.e., it consists of three repeated sequences of 35 channels of commutated 5-bit analog and digital data words preceded by 6 channels of 5-bit synchronization and mode identification words and a 5-bit spare channel. The data on the 35 commutated channels are different, however, from the external mode-1 data. The external mode-2 data list is shown in Figure 33. Other differences between external modes 1 and 2 are as follows: 1) During external mode-2 operation, alternate frames of science and engineering data are transmitted by the relay link to the flight spacecraft. This explains why the external mode 1 and mode 2 frames were each made 560 bits long. They had to be compatible in length to permit transmission of alternate frames. The synchronization code used for the telemetry subsystem is identical, however, to the one used by the external DAE. 2) The data rate for external mode-2 operation is only 64 bits/sec (instead of 1024 bits/sec) since this mode is used near entry, a time when the distance between the flight spacecraft and the flight capsule is much greater than the distance over which external mode-1 communication occurs.

c. External Mode 3 - Entry Data Storage -- In external mode 3, the forward power and reverse power of the VHF relay link will be sampled alternately at a rate of one sample of each per second. The power data will be stored as it is acquired. These data are taken in addition to the 11 channels of science data that are also being stored. The two sets of data (VHF power and science) will be interspersed under control of the external T/M subsystem.

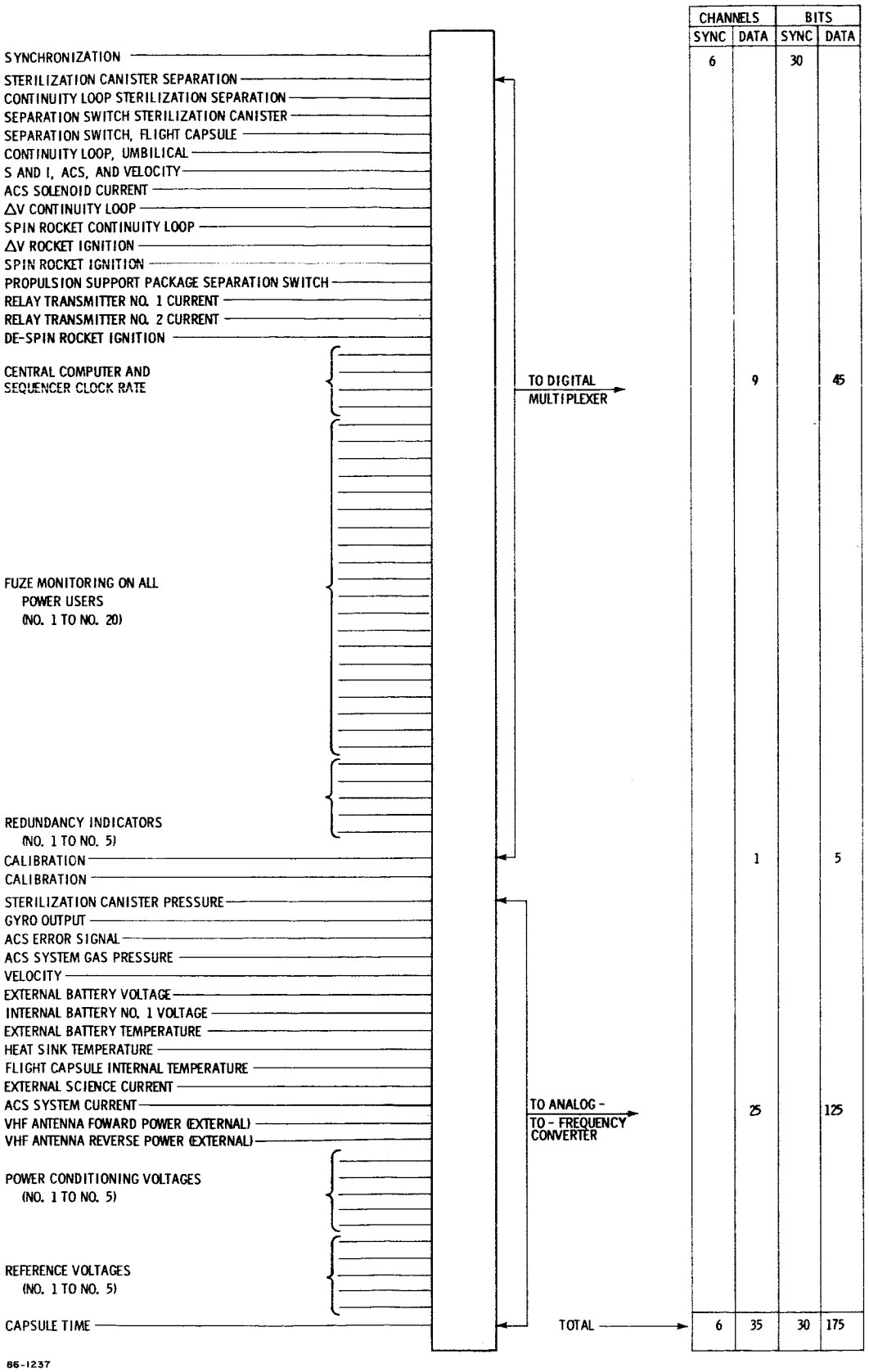

Figure 32 MODE 1 EXTERNAL TELEMETRY ENGINEERING CHANNELS

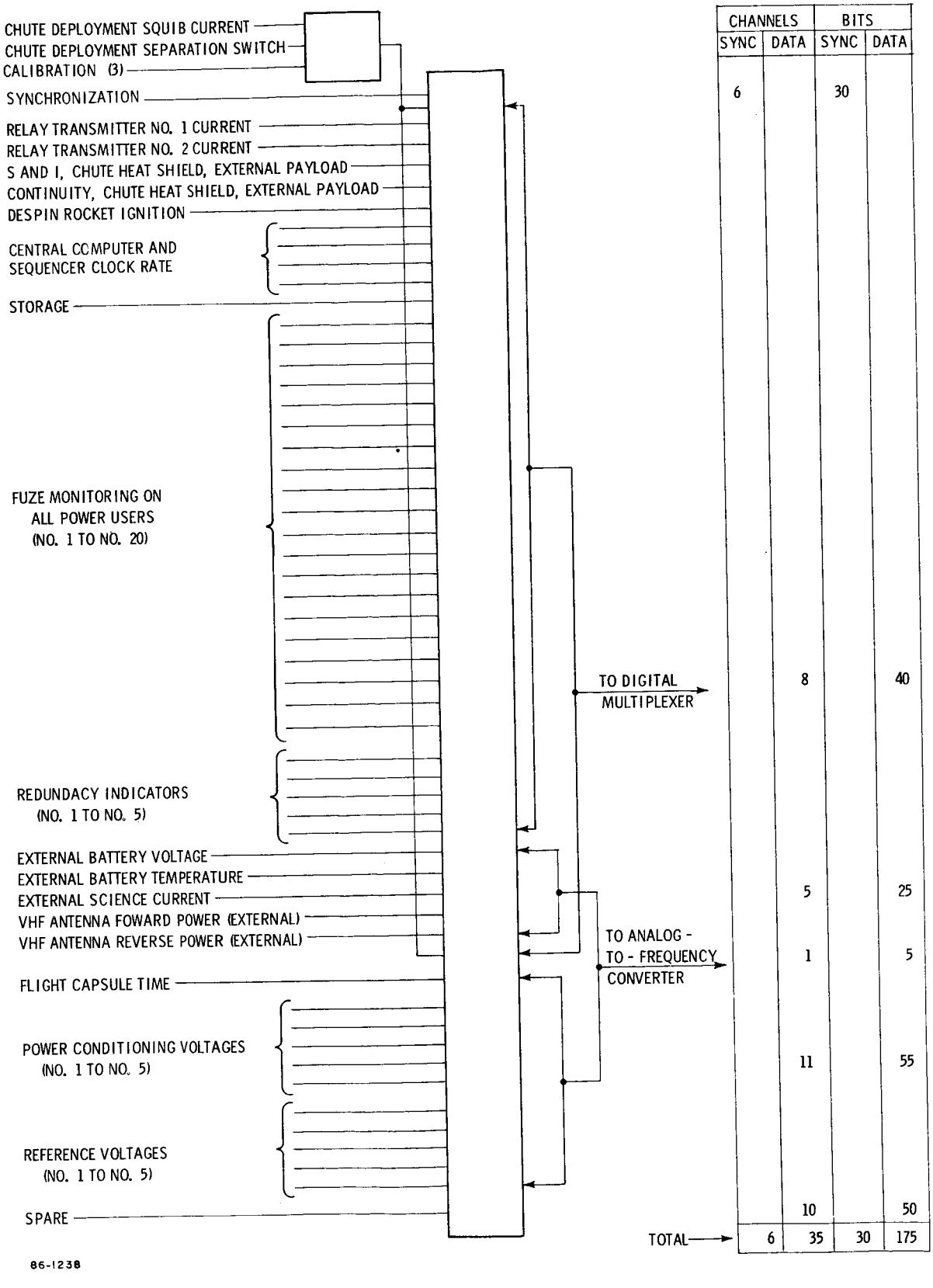

	CHANNELS		BITS	
	SYNC	DATA	SYNC	DATA
	6		30	
TO DIGITAL MULTIPLEXER		8		40
EXTERNAL BATTERY VOLTAGE EXTERNAL BATTERY TEMPERATURE EXTERNAL SCIENCE CURRENT VHF ANTENNA FOWARD POWER (EXTERNAL) VHF ANTENNA REVERSE POWER (EXTERNAL)		5		25
TO ANALOG - TO - FREQUENCY CONVERTER		1		5
FLIGHT CAPSULE TIME POWER CONDITIONING VOLTAGES (NO. 1 TO NO. 5)		11		55
REFERENCE VOLTAGES (NO. 1 TO NO. 5) SPARE		10		50
TOTAL	6	35	30	175

Figure 33 MODE 2 EXTERNAL TELEMETRY ENGINEERING CHANNELS

d. External Mode 4 - Entry/Descent Data Earlier Transmission -- The output frame format for external T/M mode 4 is the same as that for DAE external mode 4. The format is shown in Table XVIII. Frame construction is controlled by the CC&S. Each 560-bit frame consists of 80 7-bit channels. These include 42 channels of real-time science data, 8 channels of real-time engineering data, 26 channels of data stored in external mode 3, and 4 channels of synchronization and frame identification data. The 4 synchronization and frame identification channels precede the data channels. The 8 channels of real-time engineering data are used to subcommutate the data on the 35 five-bit channels shown in Figure 34. As this figure indicates, the commutator is divided into 4 parts and, there are 4 corresponding 49-bit groups. The complete frame will be stored in the real time buffer register shown in Figure 31. During transmission, data from this frame will be interspersed, 49 bits at a time, with the remaining real-time and non-real-time data listed in Table XVIII. As a result, it will take 4 complete external mode 4 frames to play out the one frame of engineering data shown in Figure 34.

3. Internal Telemetry Subsystem Requirements -- The basic concept of the internal telemetry subsystem is identical to that of the external telemetry subsystem described in paragraph 2,above. The only significant operational difference is in the engineering and event data which are handled. The internal T/M data are listed in Table XXII.

4. Internal Telemetry Subsystem Functional Description -- A description of the modes of internal T/M subsystem operation follows:

a. Internal Mode 1 - Landed Data Storage -- In internal mode 1, the 560-bit frame format consists of 106-five-bit words preceded by 30 bits of synchronization and identification code words. The format is the same as that for external T/M modes 1 and 2. One frame of the engineering data shown in Table XXII will be acquired and stored at impact for subsequent transmission via the direct link during operation of the internal T/M subsystem in internal mode 2. This frame is in addition to the 4 frames of science data shown in Table XX. Although a total of 21 frames of data are stored during internal mode 1 operation, only 16 frames are required for use during the remaining portion of the landed phase because the first 5 frames are cleared shortly after impact. For a complete treatment of data acquisition during this mode, see paragraph 4.11.1.1.

b. Internal Mode 2 -- Direct Link Transmission -- During operation in this mode, the 15-frames of data stored during the entry-descent phase of the mission, plus the 5 initial frames of data acquired

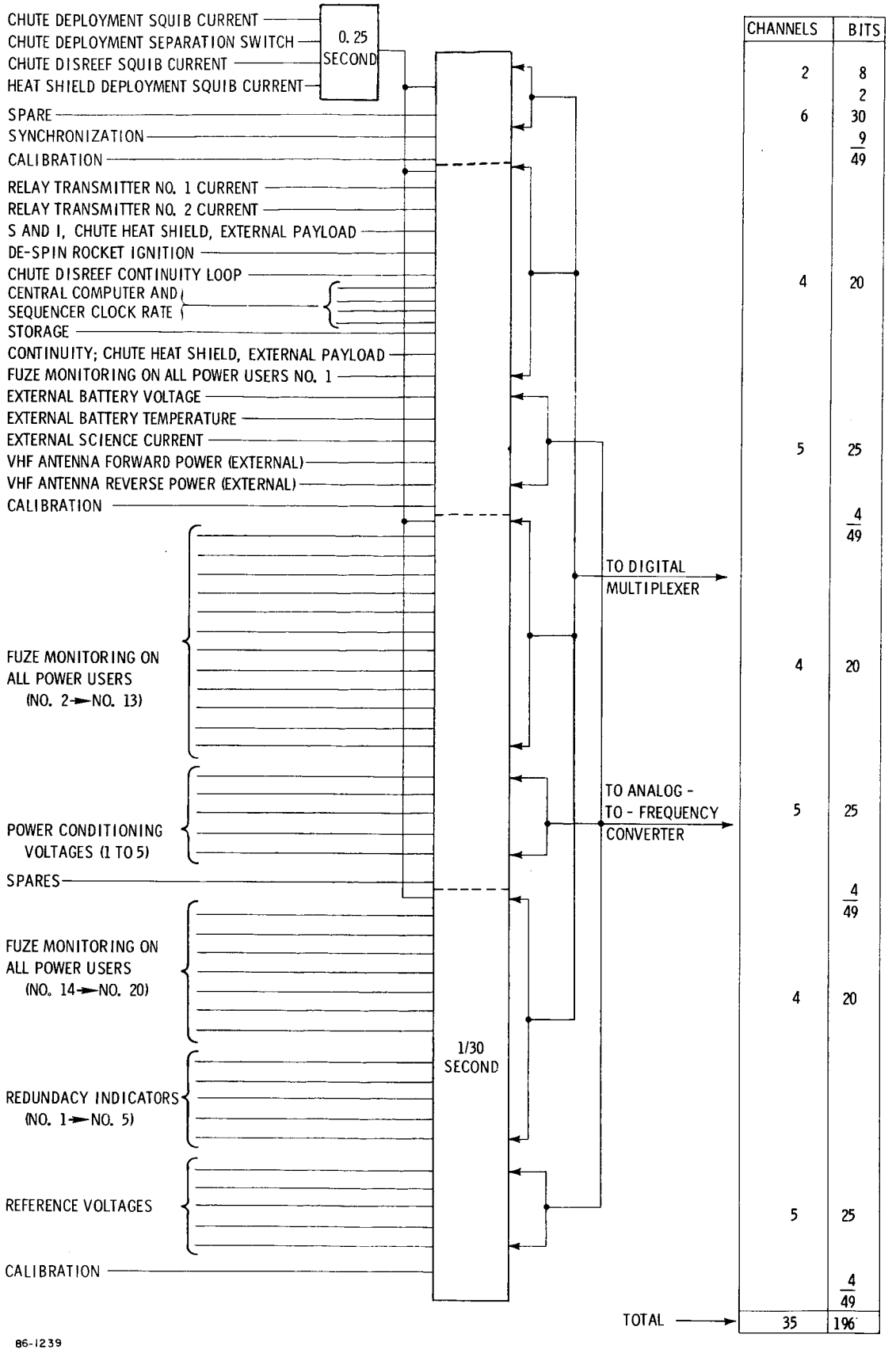

Figure 34 MODE 4 EXTERNAL TELEMETRY ENGINEERING CHANNELS

TABLE XXII

INTERNAL TELEMETERING CHANNEL ASSIGNMENT

Measurement	Sampling Rate	Analog/ Binary	Mode
Pressure transducer	2/hour	A	1
Temperature transducer	1/hour	A	1
Acoustic transducer	1/hour	A	1
Internal battery number 1 voltage	1/min	A	1
Internal battery number 2 voltage	1/min	A	1
Propulsion support package separation switch	1/min	B	1
Command receiver number 1 current	1/min	B	1
Direct exciter number 1 current	1/min	B	1
Direct exciter number 2 current	1/min	B	1
Direct amplifier number 1 current	1/min	B	1
Direct amplifier number 2 current	1/min	B	1
Internal battery number 1 temperature	1/min	A	1
Internal battery number 2 temperature	1/min	A	1
Heat sink temperature	1/min	A	1
Capsule internal temperature	1/min	A	1
R. F. amplifier number 1 temperature	1/min	A	1
R. F. amplifier number 2 temperature	1/min	A	1
Internal science current	1/min	A	1
S-Band antenna number 1 forward power	1/min	A	3
S-Band antenna number 2 forward power	1/min	A	3

TABLE XXII (Concl'd)

Measurement	Sampling Rate	Analog/ Binary	Mode
Command receiver number 1 receiver signal strength	1/min	A	1
Command verification	1/min	B	1
Command verification, quantitative, as required	1/min	B	1
Tether cutter squib current	1/sec	B	1
Safe and initiate; impact attenuator science deployment	1/min	B	1
Impact attenuator deployment squib current	1/min	B	1
Science experiments deployment command	1/min	B	1
Cosmic radiation detector deployed	1/min	B	1
Surface radiation detector deployed	1/min	B	1
Alpha scatter detector deployed	1/min	B	1
Surface temperature sensor deployed	1/min	B	1
Dust particle detector	1/min	B	1
S-Band antenna number 1 reverse power	1/min	A	3
S-Band antenna number 2 reverse power	1/min	A	3
Central computer and sequencer clock rate	1/min	B	1
Power conditioning voltage	1/min	A	1
Reference voltages	1/min	A	1
Storage	1/min	B	1
Capsule time	1/min	B	1
Fuze monitoring in all power users	1/min	B	1
Redundancy indicators	1/min	B	1

in internal mode 1 will be read out of internal storage and routed through the internal telemetry subsystem to the direct link transmitter at a rate of 2 bits/sec. The internal memory will then be cleared and subsequently used for data storage as noted in the description of internal mode 1 operation. Approximately 24 hours after landing, the 16 additional frames will be transmitted to Earth via the direct link at a rate of 2 bits/sec. It should be noted that the internal memory size is determined by the requirement to store 20 frames of data (15 entry-descent data frames plus the first 5 internal mode 1 frames).

4.11.1.3 Data-Storage Subsystem

It is evident from the discussions presented in paragraph 4.11.1 and 4.11.2 that there must be both an external (entry and descent) and an internal (surface) memory. The external memory will be used entirely for storage of entry data. These data will be played out to the flight spacecraft during descent. The internal memory is organized in 2 sections, one for recording the first 15 consecutive frames of external T/M mode 4 data, the other for recording surface data. Both the external and internal memories are described in detail in paragraph 2., below.

1. Data Storage Subsystem Requirements -- The data storage subsystem (DSS) provides storage capability for both the telemetry subsystem and the data-automation equipment. The DSS is capable of storing inputs from both of these sources. All data, however, is routed through the telemetry subsystem. The DSS will also provide the buffering required to accommodate a variety of different input and output data rates. During certain phases of the projected mission, it will be necessary to perform both storage and buffering functions simultaneously.

The maximum data storage requirements described in paragraphs 4.11.1 and 4.11.2 are summarized in Table XXIII.

a. Input and Output Bit Rates -- The average input data-rate ranges from approximately 10 bits/sec at the surface to a maximum of 100 bits/sec during entry. The output data rate ranges from 2 bits/sec if a direct S-band link to Earth is used, to 64 bits/sec if the flight spacecraft relay link is used.

b. Format -- For compatibility with the data automation equipment and with the radio subsystem, the data storage subsystem must 1) accept serial input data, and 2) produce regenerated serial data in the same sequence as the data was presented as input to the memory. Thus, the storage is serial, first in, first out.

TABLE XXIII

DATA STORAGE REQUIREMENTS

1) Entry and Descent Memory	
Science data bits	5775 (77 bits x 75 frames)
Identification bits	525 (7 bits x 75 frames)
Telemetry bits	525 (7 bits x 75 frames)
Unused storage locations (spares)	400 (5 percent)
TOTAL	7225
2) Surface Memory	
a) Entry and Descent Input	
15 frames of external Mode 4 data	7875 (525 bits x 15 frames)
Identification bits	105 (7 bits x 15 frames)
Unused Storage locations (Spares)	400 (5 percent)
Subtotal 8380	
b) Surface Input at Impact	
Science	2100 (525 bits x 4 frames)
Engineering	525 (525 bits x 1 frame)
Identification	35 (7 bits x 5 frames)
Unused storage locations (spares)	100 (3 percent)
Subtotal	2760
TOTAL (a + b)	11, 140 (with 500 spares)
c) Additional Surface Input after Impact	
Science and Engineering	8400 (525 x 16)
Spares	2740*
TOTAL	11,140

*Difference between total (a+b) shown in b) and required science and engineering shown in c) is explained by the fact that the surface memory is cleared shortly after impact.

The data storage subsystem must be capable of simultaneously recording and reading-out data at different input and output rates. This requirement necessitates use of buffered inputs and outputs to the memory system.

c. Storage Philosophy -- From the viewpoint of DSS operation, the mission includes three prime phases: entry, descent, and surface. In addition, consideration must be given to two forms of partial mission failure; ;either failure of the parachute to open, or failure of the relay link to function properly. A comprehensive storage philosophy, broad enough to cover all three of the prime phases and both failure possibilities, has been adopted. This philosophy is implemented as follows: some of the data recorded during entry will be played out in the descent phase even if the parachute does not open. If it does open, all of this data will be played out before impact. In either case, this stored entry data will also be read out and interspersed with real-time descent data for storage in the internal (surface) memory. About 1 hour after impact, critical entry and descent data stored during those phases will be played out to Earth. During this transmission, the entry and descent data will be interspersed with the initially collected surface-science data. Approximately 24 hours after landing, a second set of science data will be transmitted to the deep space instrumentation facility (DSIF).

2. Data Storage Subsystem Functional Description -- The basic elements of the DSS include an entry-descent memory, a surface memory, memory control circuits, and input and output interface circuits. A two-memory system using ferrite core storage elements, as shown in Figure 35 has been selected for the 1971 mission. The inputs for the data storage subsystem consist of data-automation equipment signals and telemetry signals (all data is routed through the telemetry subsystem), input clock and output clock signals, and mode control signals from the CC&S. DAE or TM data appear at the DSS input in synchronism with the input clock whenever data storage is required (as determined by appropriate mode-control signals). The outputs from the two-memory DSS are fed to the T/M subsystem for routing to the radio subsystem. A description of the two basic memories follows:

The external memory is also referred to as the entry and descent memory, or entry/descent memory (EDM). Entry and descent data are fed into it for the 75 seconds that follow the start of the external DSS mode 1 operation, or until the main parachute opens. From the start of external DSS mode 4 operation (11 seconds after acceleration increases to the 10-g level) data readout of this memory is interspersed with real-time science and engineering measurement data for real-time playout to the flight spacecraft. This process continues until impact.

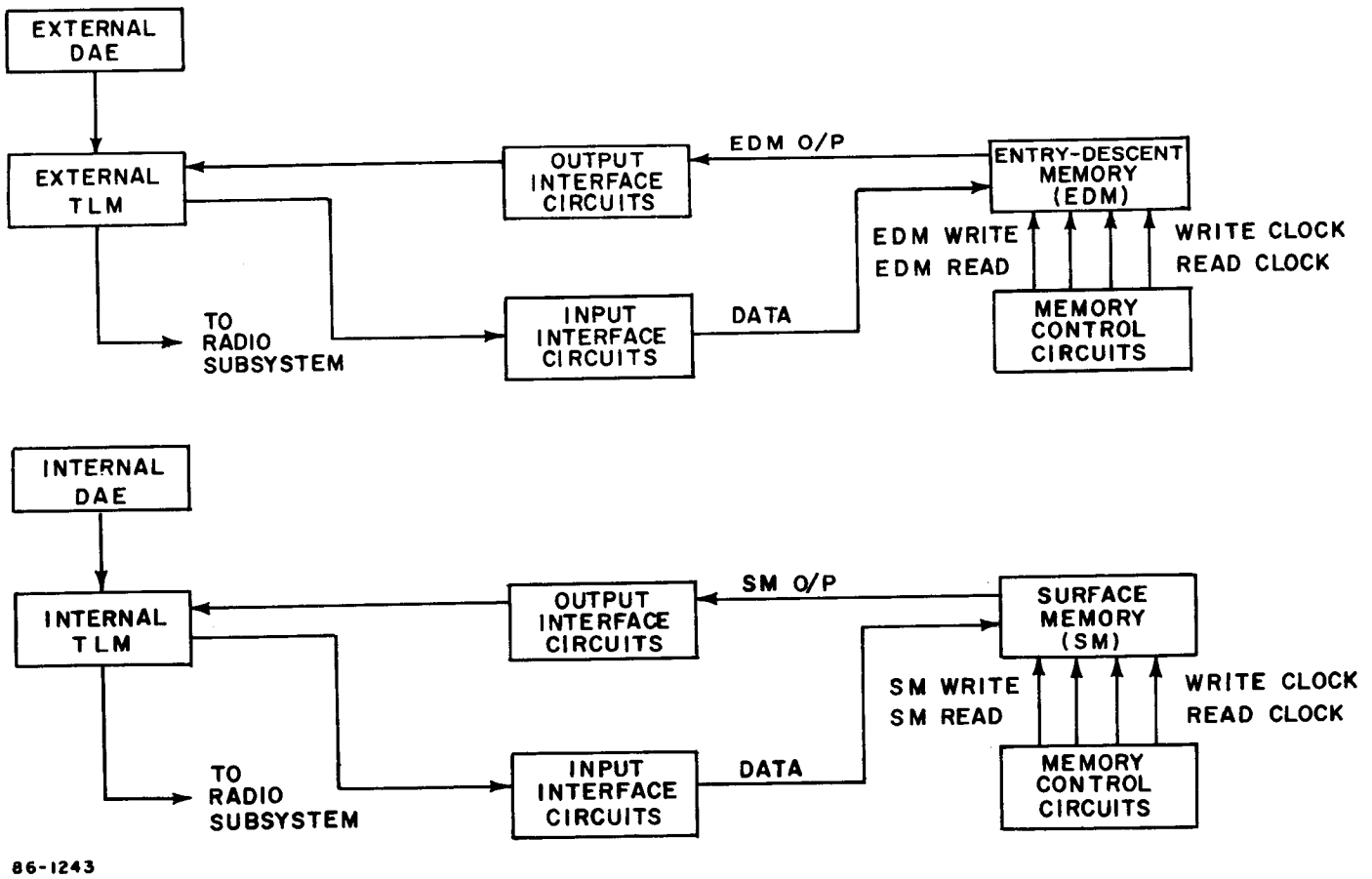

Figure 35 TWO MEMORY DATA STORAGE SUBSYSTEM

The internal memory is also referred to as the surface memory (SM). The SM stores the first 15 consecutive frames of external DSS mode 4 data plus all impact, post-impact science, and post-impact engineering data. The impact data consists of one frame of engineering data and four frames of science data. During internal mode 2 the data is read out of the memory.

In response to mode control signals from the CC&S, and synchronous with the input and output clocks, the memory control circuits generate write clock, read clock, entry/descent memory write and read commands, and surface memory write and read commands, as appropriate to govern the various modes of DSS operation.

The entry-descent memory, shown in Figure 36, accepts data when an entry-descent memory write command is presented. The serial data is transferred from a shift register into the memory in response to this command. Upon receipt of an entry-descent memory read command, the entry-descent memory generates an output data bit synchronously with the read clock. Immediately thereafter the data bit is regenerated and again stored in the memory at the same location as that from which the data bit was originally read out. This is done to allow for repeated read-out of the same data when there is adequate time to do this. Adequate time will not be available for redundant read-out if the parachute fails to open.

Surface memory operation is identical to entry/descent memory operation.

The DSS is capable of operating in two alternative external modes and three alternative internal modes. Brief descriptions of DSS operation in each of these modes follow:

a. External Mode 3 -- Writing into the entry/descent memory begins.

b. External Mode 4 -- Operation in this mode begins 11 seconds after the increasing acceleration of the flight capsule reaches 10 g (10g + 11 seconds). Writing into the surface memory begins, writing into the entry/descent memory continues, and reading from the entry/descent memory begins.

c. Internal Mode 1 -- During operation in this mode, data is written into the surface memory. Writing begins at impact and at successive 6-hour intervals during the 24-hour period following landing.

d. Internal Modes 2 and 3 -- Data are read out of the surface memory for transmission to Earth via the direct link.

4.11.1.4 Flight Capsule Data Handling Subsystem Summary; The flight capsule data handling subsystem, consisting of the data automation equipment, telemetry subsystem, and data storage subsystem, controls the collection of all flight-capsule data. The external data

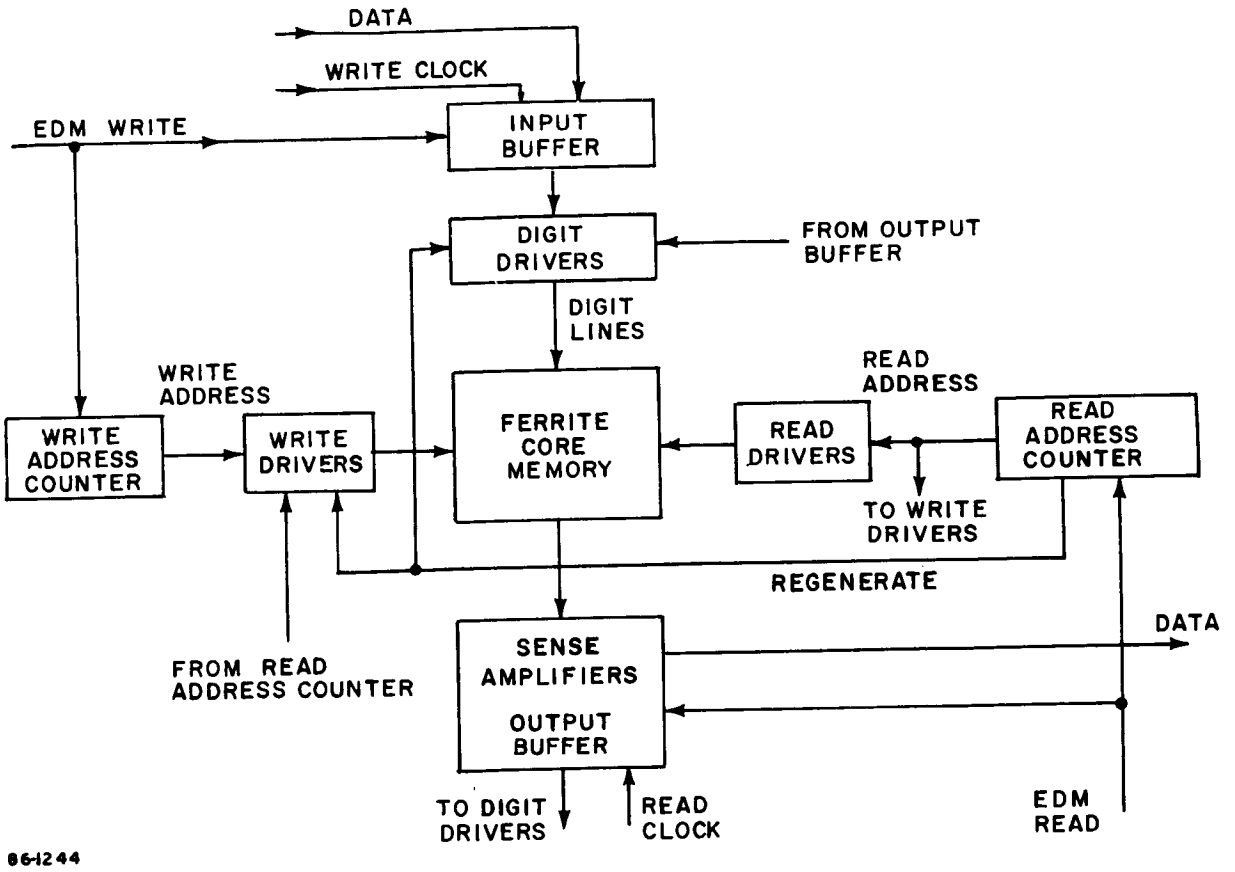

Figure 36 ENTRY-DESCENT MEMORY (EDM)

handling subsystem operates prior to impact in any one of four modes. The internal data handling subsystem is used after landing and operates in a single mode. A summary of the characteristics of both the internal and external data-handling subsystems is presented in Table XXIV.

4.11.2 Major Tradeoffs

A number of tradeoff studies were performed. The results of these studies served as the basis from which the mechanization of both the DAE and T/M subsystems evolved. In certain instances, the conclusions of these studies discussed below are applicable only to the DAE and not to the telemetry subsystem. Such differences are noted separately in the discussion of the telemetry subsystem.

4.11.2.1 Centralized versus Decentralized Data-Handling Equipment

Two generic types of data-handling equipment were considered in this study. One of them, which can be called the centralized type, uses a single centralized commutator to handle data from all instruments. The commutator, in turn, supplies data to a single centralized analog-to-digital-converter. The second type, which can be called the decentralized type, uses separate commutators and A/D converters in close proximity to each of several groups of instruments. Figure 37 shows a simplified block diagram of centralized DHE: Figure 38 shows a simplified block diagram of decentralized DHE. The advantages of the centralized approach are simplicity, and reduction in the amount of required hardware through the use of a single analog-to-digital converter. The principal disadvantage of this approach is the necessity for bringing many analog signals to a central location. This usually involves long analog data lines with the attendant noise problems. The decentralized approach, on the other hand, uses more equipment since each group of instruments requires a separate A/D converter. However, data errors resulting from noise are substantially reduced since digital rather than analog data are transferred over the long data lines. Digital data are, of course, far less sensitive to noise.

4.11.2.2 Multi-Level versus One-Level Commutation

In a commutation system in which different input sources must be sampled at a variety of sampling rates, either a single-level commutator system or a multi-level, multi-commutator system may be used. These systems are illustrated in Figures 39A and 39B, respectively. The principle advantage of the single-level commutator is that loss of any one channel due to random failure or overloads will not affect any other channel. Only the data on the channel which failed will be lost. A further advantage is flexibility, that is, the ability to change sampling rates by merely rewinding the inputs to the commutator. The major disadvantage of the single-level commutator approach is the greater number of components required as compared to the number required for a multi-level system, and attendant increases in size, weight, and power requirements. It should be noted, however, that control of

TABLE XXIV

FLIGHT CAPSULE DATA HANDLING SUBSYSTEM SUMMARY

Data Automation Equipment	
External	
Measurements	32 (real time), 11 (nonreal time)
Accuracy	7 bits
Channels	80
Internal	
Number of measurements	228
Accuracy	7 bits (5 bits for α scatterer)
Channels	75
Telemetry Subsystem	
External	
Number of measurements	70
Accuracy	5 bits
Channels	41 (includes 6 for sync)
Internal	
Number of measurements	70
Accuracy	5 bits
Channels	41 (includes 6 for sync)
Data Storage Subsystem	
External	
Capacity	7225 bits
Type	Ferrite core
Internal	
Capacity	11, 140 bits
Type	Ferrite core

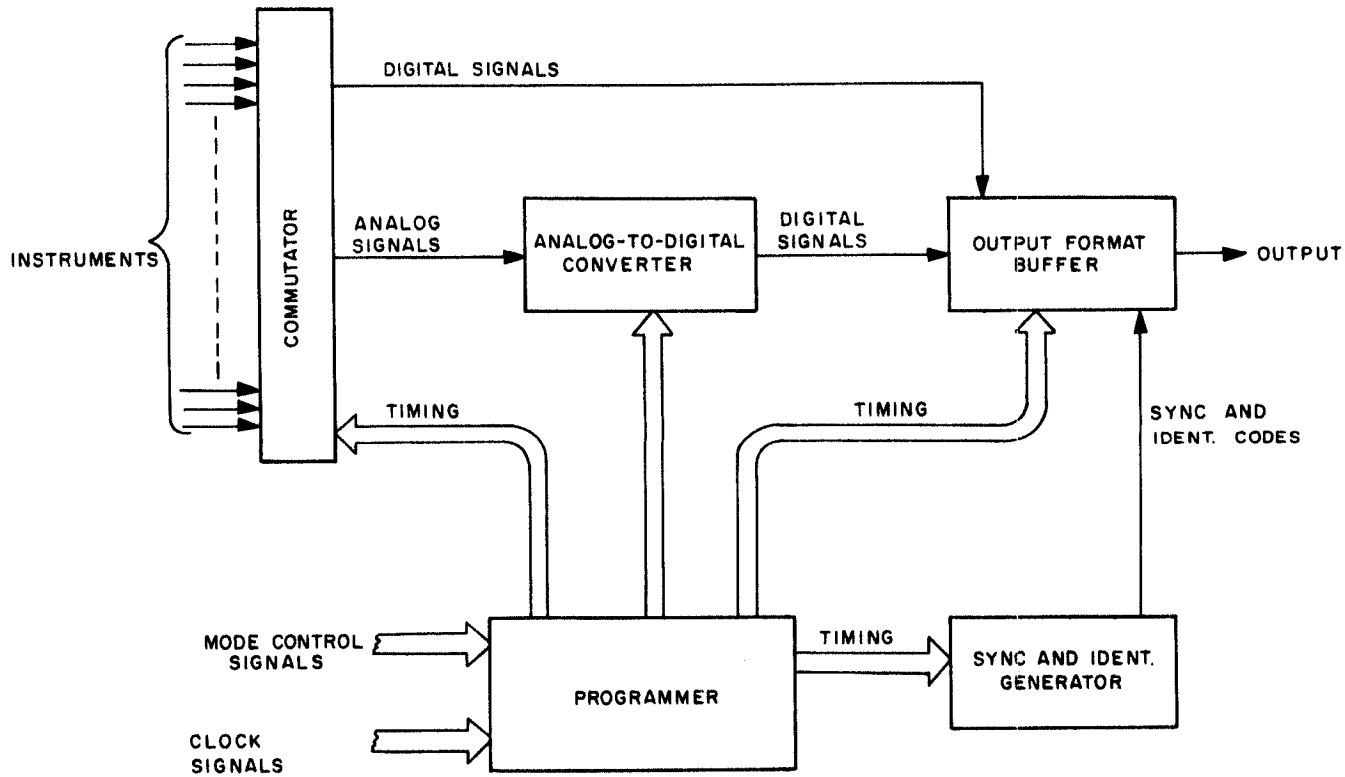

Figure 37 CENTRALIZED DATA HANDLING EQUIPMENT

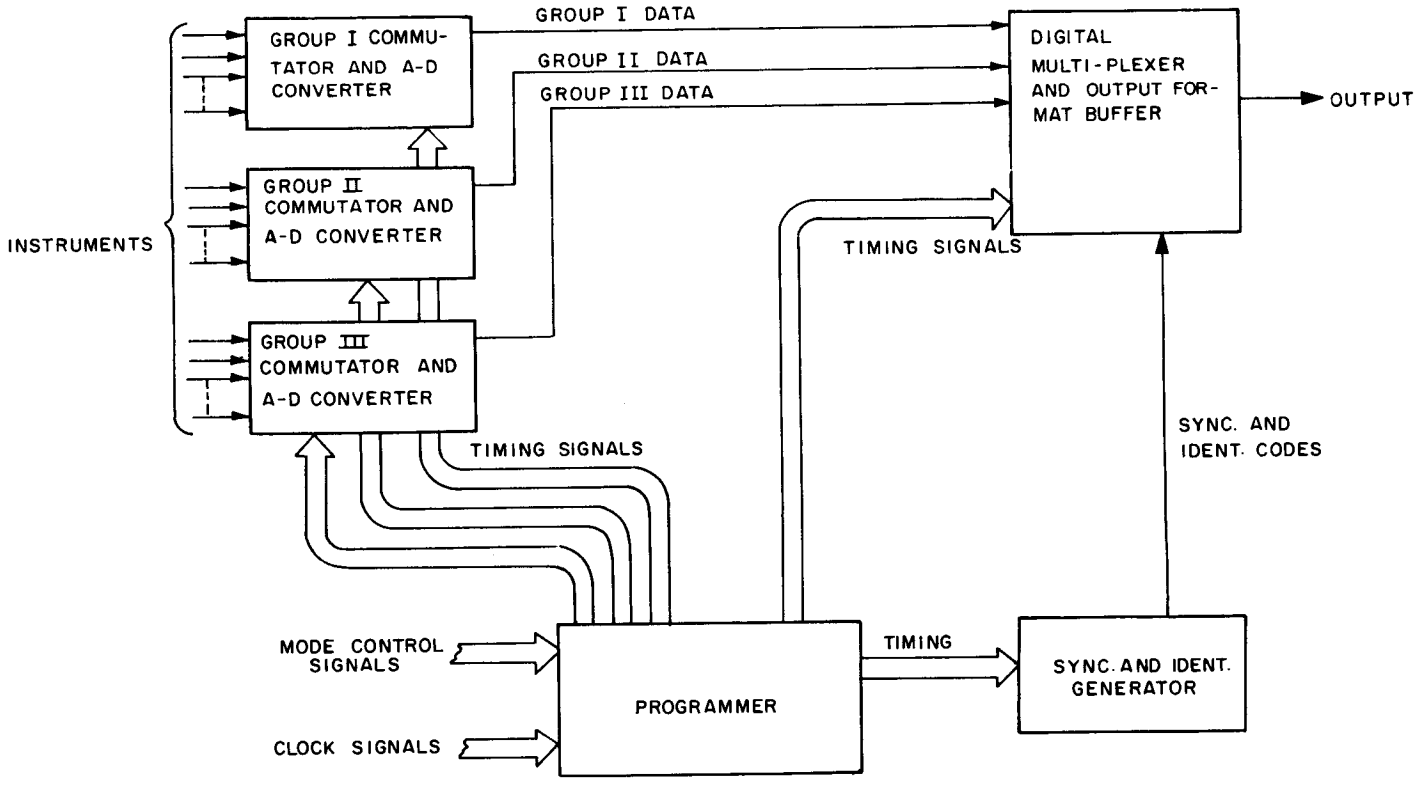

85-1789

Figure 38 DECENTRALIZED DATA HANDLING EQUIPMENT

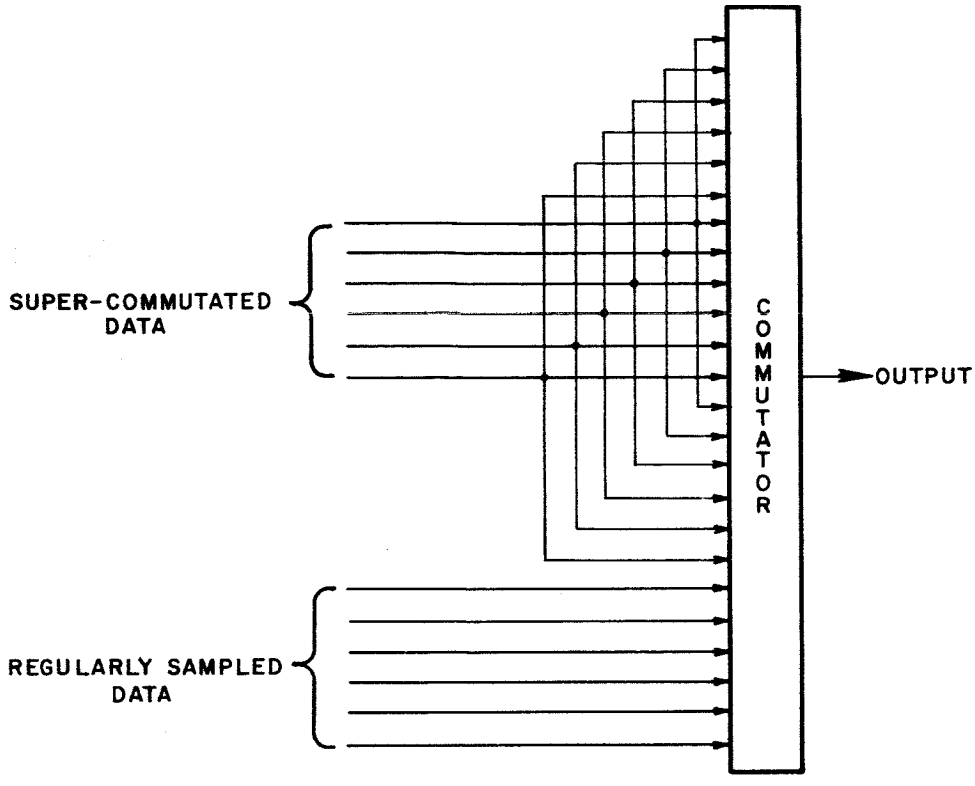

Figure 39a ONE-LEVEL COMMUTATOR

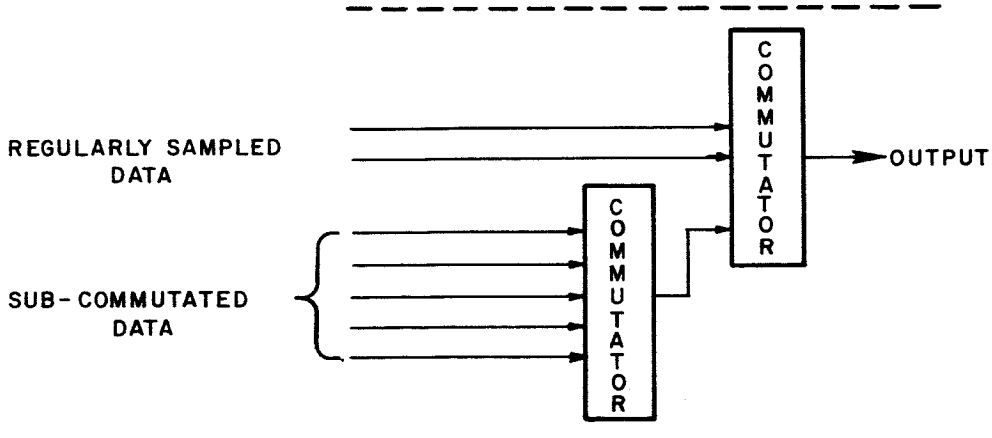

Figure 39b TWO-LEVEL COMMUTATOR

the one-level device is extremely simple, so that some compensatory savings in the size, weight, and power requirements can be realized in the control circuits.

4.11.2.3 Commutation Devices

It is assumed in this analysis that all signals will be high-level signals, that is, their full scale or peak values will range from 1 to 5 volts. Many solid-state commutation devices capable of handling signals in this range are currently available. Table XXV lists several of these devices and presents their salient electrical and physical characteristics. The numbers enclosed in parentheses on that table represent a relative ranking of the devices. The lower the number, the better the device is with respect to the given characteristic.

It was concluded on the basis of the information summarized on Table XXV that the metal-oxide semiconductor (MOS) field-effect transistor has best available combination of desirable properties.

4.11.2.4 Analog to Digital Converters

Four methods for analog to digital (A/D) conversion of high-level (1 to 5 volts) signals are commonly in use: these are referred to as the successive-approximation, digital ramp and counter, analog ramp and counter, and voltage-to-frequency counter methods. These methods are described and the relative advantages and disadvantages of each are identified in paragraphs 1. through 4., below. The conclusions regarding selection of the optimum analog to digital converter for the DAE are summarized in paragraph 5. below.

1. Successive Approximation -- The successive approximation technique, shown in block diagram form in Figure 40 is used to convert an analog voltage into a binary number N, such that the voltage, $(V) = (N)(V_r)$, where V_r is a system reference voltage. If V is always less than V_r, N will always be less than unity, and can be expressed as a sequence of binary digits, a_1, a_2, a_3, ... a_n, where n is (1) the number of bits in the conversion and (2) equal to or greater than the binary logarithm of the number of quantization levels. To obtain binary digit a_k, the analog voltage is first compared with one-half the reference voltage ($V_r/2$). The first bit, a_1, is then set to ONE if the analog voltage is greater than one-half the reference voltage, or to ZERO it it is less than one-half the reference voltage. In the second step, the analog voltage is compared with one-fourth the reference voltage ($V_r/4$) if the first bit was set to ZERO, or with three-fourths the reference voltage ($3V_r/4$) if the first bit was set to ONE. If the second comparison is positive, that, if $V = V_r/4$ or $V = 3V_r/4$, the second bit, a_2, is set to ONE, or, if the second

TABLE XXV

TRADEOFF CHART FOR COMMUTATION DEVICES

Device	Fault Isolation (a)	Offset Voltage mV	Z Off >100 K	I_L (device off)	Cross-Talk Error	Type Of Drive	Weight-Size (b)	Speed	Remarks
Gated comparator	Good (1)	1-5 (2)	Yes (1)	High (3)	None (1)	DC (1)	1 (3)	High (1)	Used at input to analog to digital converter
Diode switch	Poor (2)	10-100 (3)	No (2)	High (3)	Medium (3)	DC (1)	0.5 (2)	Medium (2)	Input-output short is most probable failure
Transistor switch	Poor (2)	1-5 (2)	Yes (1)	Low (2)	Small (2)	AC (2)	2 (4)	Medium (2)	Input-output short is most probable failure
MOS field-effect transistor switch	Good (1)	None (1)	Yes (1)	Very Low (1)	Small (2)	DC (1)	0.1 (1)	Medium (2)	Enhancement mode only
Thin-film field effect transistor switch	Poor (2)	None (1)	No (2)	High (3)	Small (2)	DC (1)	0.1 (1)	Medium (2)	Enhancement mode not available

(a) Good fault isolation implies the principal device failure mode will not affect other channels.

(b) Expressed as the number of integrated circuits per channel.

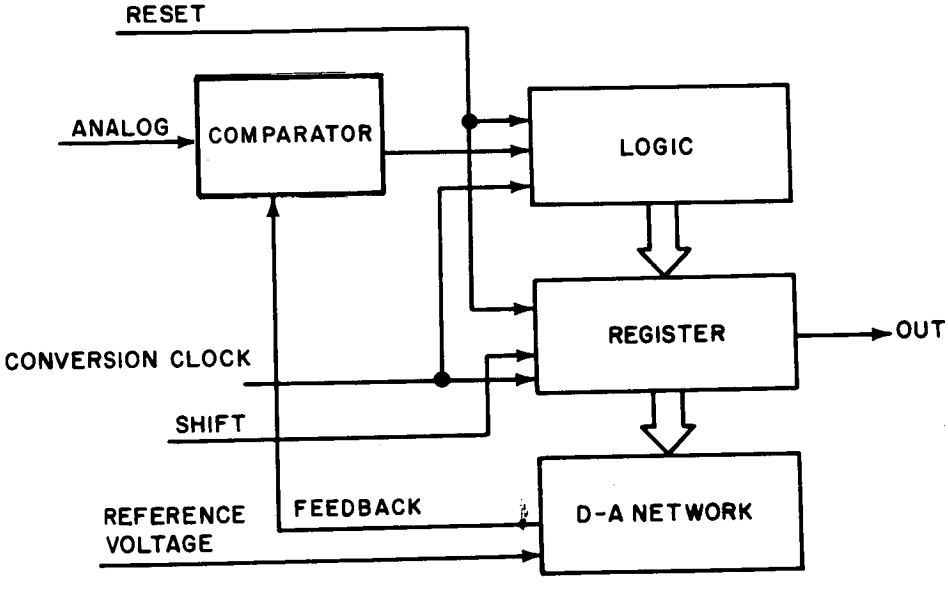

Figure 40 SUCCESSIVE APPROXIMATION A-D CONVERTER

comparison is negative, it is set to ZERO. This process continues until n bits have been determined.

As indicated in Figure 40, this method requires an analog comparator, an n-bit register, a digital-to-analog conversion network, and a logic control unit. The n-bit register is used to store the results of the successive comparisons between the input analog voltage and the output voltage of the digital-to-analog network. The comparisons are made in the comparator. The digital-to-analog network converts the digital number stored in the register into a precise voltage level directly proportional to the partially converted result in the register. The logic unit controls storage of the partial bits in the register. Storage is sequential, beginning with the most significant bit and ending with the least significant bit.

The output of this type of converter is obtained by operating the register in a shift-register mode with the shifting under control of a shift clock. The conversion takes place synchronously with an input conversion clock.

The advantages of this conversion technique are:

a. High Speed -- The number of conversion steps is less than or equal to the binary logarithm of the number of quantization levels.

b. High Accuracy -- The accuracy is determined only by the accuracy of the comparator and of the digital-to-analog network, both of which can be designed to provide very high levels of accuracy. Accuracies within 0.1 percent under a wide range of environmental conditions can be achieved without difficulty.

c. Controlled Digitizing Time -- Since the number of conversion steps is fixed by the number of quantization levels, the time for a complete conversion at a fixed conversion clock rate is also fixed.

The primary disadvantage of this technique is the fact that the system is complex -- both in its logic and in the hardware needed to implement the logic.

2. Digital Ramp and Counter -- The digital ramp and counter technique for analog to digital conversion operates by entering successive clock pulses in a counter (usually a binary counter) until the number (N) in the counter satisfies the equation $V = N V_r$ where V is the analog voltage and V_r is a system reference voltage. The converter is shown in block diagram form in Figure 41. Each time the counter is incremented during the count, the number in the counter is converted

to an analog voltage by a digital to analog converter. This voltage is then compared to the analog input voltage in a comparator. When the comparator senses that the input and feedback voltages are equal, the counter is stopped. The number stored in the counter is then shifted out. The shift out is synchronous under control of a shift clock. The advantages of this conversion technique are:

a. High Accuracy -- The accuracy is determined only by the accuracy of the comparator and the digital-to-analog network, both of which can be designed to provide a high level of accuracy. Accuracies within 0.1 percent under a wide range of environomental conditions can be met without difficulty.

b. Relative Simplicity -- This technique does not require a complex logic unit, and the circuits used to implement the techniques are simple.

The disadvantages of this technique are:

a. Slow Speed -- The maximum number of counts which must be recorded and, therefore, the maximum number of steps required, is equal to the number of quantization levels. The digital-to-analog converter must change state at each one of these steps.

b. Unknown Digitizing Time -- The time required to complete a conversion is directly proportional to the analog voltage. As a result, it is unpredictable except in the case of the upper voltage limit.

c. Sampling Point Error -- Unless a forward-backward type counter and two-level comparator are used, the exact time at which the input equalled the final number is not known if the input should change during a conversion. If forward-backward counting capability is incorporated, it must be able to count at high-speed or the converter may not be fast enough to track a rapidly-varying input.

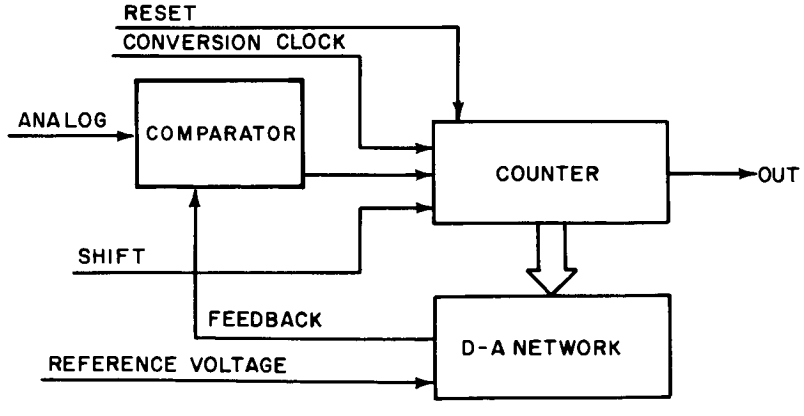

Figure 41 DIGITAL RAMP A-D CONVERTER

3. Analog Ramp and Counter -- The analog ramp and counter technique for analog to digital conversion is similar to the digital ramp and counter technique. The principle difference is that the feedback voltage is furnished directly by an analog ramp voltage generator instead of a digital generator. For a block diagram of such a converter, see Figure 42. A gate in the ramp generator opens at the start of the ramp and closes when the feedback voltage is equal to the analog voltage input. This gate is also used to control a counter. The counter registers, or counts clock pulses during the period that the gate is open. The number in the counter when the gate closes represents the converted, that is, the digital, value of the analog voltage input. The contents of the counter are then shifted out at a synchronous rate under control of a shift clock.

The advantages of this conversion technique are:

a. Great Simplicity -- The analog ramp generator circuit is relatively simple for low and medium accuracy applications.

b. Remote Comparison -- The comparator and ramp generator, since they are relatively simple circuits, can be located near the analog data source. The signal transmitted to the counter, is, therefore, a digital signal and as such it is less subject to noise than the original analog signal. A set of comparators and ramp generators, one for each transducer, can be digitally multiplexed into a single counter. In effect, this forms a combined commutator-converter.

c. High Speed -- The speed of operation is limited only by that of the ramp generator. Extremely high speed comparators and counters are readily available.

The disadvantages of this technique are:

a. Relatively Low Accuracy -- It is difficult to design an analog ramp generator capable of conversion with better than 95 percent accuracy over a wide range of environmental conditions. The basic difficulty results from the fact that the analog ramp voltage must be linear, not with respect to time, but with respect to the conversion clock signal.

b. Sampling-Point Error -- The sampling point is not known in the case of varying inputs.

c. Unknown Digitizing Time -- The time required to complete a conversion is proportional to the analog input. As a result, it cannot be predicted except in the case of the upper voltage limit.

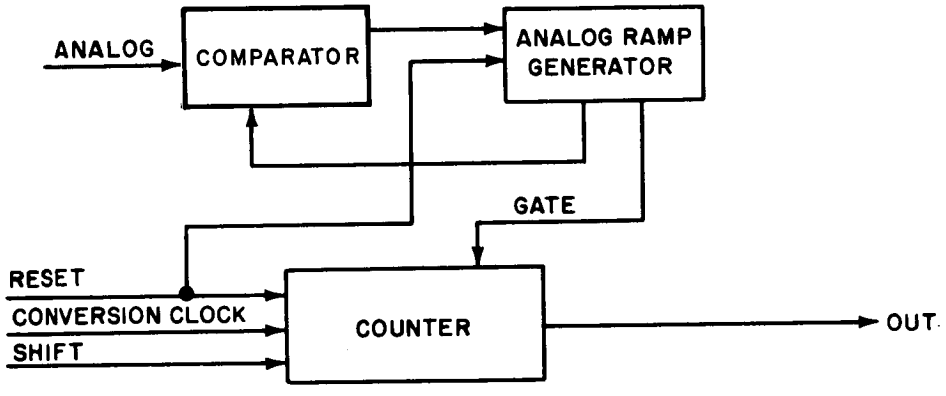

Figure 42 ANALOG RAMP A–D CONVERTER

4. Voltage-to-Frequency Converter and Counter -- The voltage-to-frequency converter and counter technique shown in block diagram form in Figure 43 is based on the concept of first converting the input analog voltage to a proportional frequency, and then counting cycles of the resultant signal. The cycles are counted for a fixed time by a suitable counter. A time-base generator establishes a fixed duration counting period on the basis of signals from the conversion clock. The output signal is obtained from the counter by shifting bits out in accord with synchronization signals provided by a shift clock.

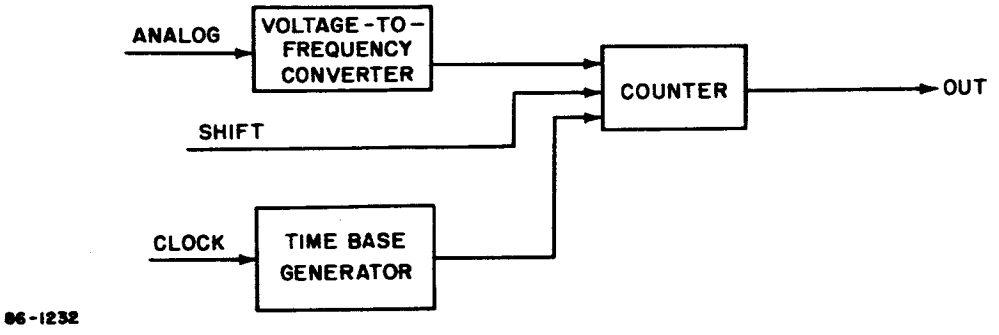

Figure 43 VOLTAGE--FREQUENCY A-D CONVERTER

The advantages of this conversion technique are:

a. High Accuracy at Slow Speeds -- If sampling rates are moderate (that is, from 10 to 100 samples per second), accuracies within 0.1 percent can be obtained for input frequencies below 1.0 MHz. Voltage-to-frequency converters and counters are readily available.

b. Simplicity -- Simple circuits based on well-known techniques can be used.

c. Average-Reading -- The digitized result is the average level of the input signal for the conversion time used.

d. Fixed Conversion Time -- A fixed duration conversion period is an inherent feature of operation of this type of device.

e. Remote Operation -- The voltage-to-frequency converter, since it is small and simple, can be located near the data source. The signal transmitted to the counter, is therefore, essentially digital. As

such, it is less subject to noise than an analog signal. A voltage-to-frequency converter can be provided at each sensor, and the data can be commutated by switching the converters on and off.

The principle disadvantage of this technique is the fact that high resolution requires a reduced operating speed. There is a practical upper limit to the frequencies which can be handled and to the conversion times which can be achieved.

5. Summary -- The principle characteristics of the four types of analog to digital converters discussed in paragraphs 1. through 4., above, are summarized in Table XXVI. This table also indicates the relative ranking of each of the four types with respect to speed, accuracy, complexity, noise sensitivity, fixed digitizing time, and remote sensing capability. The relative rank of each technique is indicated by numbers in parentheses. The lower the number, the better the device is in regard to that characteristic.

It is evident from this table that the voltage-to-frequency converter technique is the most attractive for this mission. Accordingly, this technique has been selected for use in the flight-capsule data-handling equipment.

4.11.2.5 Parts Selection for Logic Circuits

Selection of an optimum logic device for system implementation is a basic consideration in system design and operation. The devices evaluated included conventional transistor devices, integrated monolithic bipolar devices, integrated monolithic field effect devices and multi-chip integrated devices.

Selection of the specific types of devices to implement the logic circuits was based on the conclusions summarized on Table XXVII. This table briefly describes the various devices and indicates their relative rating in respect to reliability, size, power consumption, radiation resistance, noise immunity and logic versatility. The numbers in the table indicate the relative ranking of the devices. The overall rank of each device (the lower the number, the better the device) is as follows:

Conventional Modules	17
Resistor-Capacitor-Transistor Logic (RCTL) Devices (Texas Instruments 51-series)	17
Low Power Diode Transistor Logic (DTL) Devices (Fairchild Semiconductor 1100-series)	12

Integrated Monolithic Field Effect Transistor (IGFET) Devices	12
Multi-Chip Integrated Circuits	16

From the data presented, it was concluded that the low power DTL (Fairchild 1100-series) device is the optimum logic module for implementing the logic circuits. If the present rate of development continues, however, integrated gate-field effect transistor (IGFET) circuits may be an equal or better choice than the DTL devices by the time the engineering state-of-the-art cut-off date (September 1966) is reached.

4.11.2.6 Data-Storage Subsystem

1. Memory Organization -- Two alternative approaches to memory organization were considered, as follows:

a. Bit-by-bit Serial Memories -- Systems which are internally organized on a one-bit-at-a-time basis are variously known as bit-by-bit, bit-serial, or bit-organized systems.

b. Word-organization Memories -- Any memory device which records or plays back more than one bit at a time can be classified as a word-organized (WO) memory, whether or not the storage words correspond to actual data words.

The bit-by-bit serial memory approach was selected for the data storage system on the basis of its minimum need for peripheral circuits. Its relatively slow speed, as compared to that of a word-organized memory, was not considered a disadvantage in view of the low data rates required in the flight-capsule mission.

2. Moving Media Recording versus Static Storage Devices -- Two alternative general categories of approaches to memory implementation were evaluated. These are discussed in paragraphs a. and b. below.

a. Moving Media -- The following types of storage devices using moving continuous media were considered of interest in this study:

Magnetic tape recorders

Magnetic wire recorders

Dielectric tape recorders

Magnetic drum recorders

TABLE XXVI

ANALOG TO DIGITAL CONVERSION TRADE-OFF CHART

Type	Speed	Accuracy	Complexity	Noise Sensitivity (a)	Digitizing Time	Remote Sensing
Successive-approximation	High (1)	High (1)	Complex (3)	High (2)	Yes (1)	No (2)
Digital ramp-counter	Low (3)	High (1)	Simple (2)	High (2)	No (2)	No (2)
Analog ramp-counter	High (1)	Low (3)	Very Simple (1)	High (2)	No (2)	Yes (1)
Voltage-to-frequency and counter	Moderate (b) (2)	Moderate (b) (2)	Very Simple (1)	Low (1)	Yes (1)	Yes (1)

(a) Reading may be affected by a fast noise pulse; non-integrating.

(b) Speed-accuracy product is constant.

TABLE XXVII

INTEGRATED CIRCUIT TRADEOFF CHART

	Reliability	Size	Power	Radiation Resistance	Noise Immunity	Logic Versatility
Conventional Modules	4 Fair	5 Poor	1 Excellent	2 (A) Good	3 Fair	2 Good
Resistor-Capacitor - Transistor Logic (RCTL) Devices (T_I 51 Series)	2 Good	2 Good	3 Fair	3 Good	4 Fair	3 Poor
Low Power Diode Transistor Logic (DTL) Devices (Fairchild 1100-Series)	1 Excellent	3 Good	2 Good	3 (A) Good	2 Good	1 Excellent
Integrated Monolithic Field Effect Transistor (IGFET) Devices	3 Good	1 Excellent	2 Good	1 (A) Good	1 Excellent	4 Poor
Multi-Chip Integrated Circuits	5 Fair	4 Fair	1 Excellent	No Data 2	2 Good	2 Good

A - Typical of family type.

1) The advantages of moving medial recording for flight capsule applications include:

Large data capabilities (up to 10^8 bits)

High bit packing density (bits/in.^{2}) in large capacity units.

Choice of destructive or nondestructive readout of command.

Successful operation at high impact shock levels (500 g for short duration).

Satisfactory results of tests at levels as high as 1000 g are predicted.

No power consumption when not operating.

2) The disadvantages of moving media recording for flight capsule applications include:

Start and stop time (and associated data gaps)

Difficulty in achieving interspersed read-write operation.

High-power consumption per bit during slow operation.

Sterilizable tape not available at present, although prospects appear good for their future availability

Magnetic tape devices have many advantages in comparison with other moving continuous recording media evaluated. For their contemplated application in the flight capsule, however, particularly for the 1971 mission, magnetic tape recorders have serious disadvantages (e.g., inefficiency in start and stop mode operation, current lack of sterilizable tape, inability to meet 1000-g impact shock requirement). They were, therefore, dropped from further consideration for the 1971 mission. Magnetic tape devices would be a logical choice to supplement static storage systems on post-1971 missions during which their high storage capacity could be used advantageously.

b. Static Storage Devices -- The following types of static storage devices were evaluated in this study.

Monolithic Ferrite

Ferrite cores

Ferrite films

Metallic films

Etched metallic toroids

Ferrite beads, rods, tubes

Coated, plated, or wrapped wires

Table XXVIII summarizes the characteristics of these static storage devices. Of the various ferrite devices, ferrite cores possess a distinct advantage relative to other ferrite devices in that they are already space-proven. Core memories are competitive with monolithic ferrite storage devices at present, as shown by the data presented in Figures 44, 45, and 46. The requirement for conservative design based on current technology suggests that core memories be used, although projections for monolithic ferrites indicate many advantages associated with the use of this component.

4.11.3 Problem Areas

The 10-bit accuracy requirement for the accelerometer measurements made during entry is a potential problem area. Obtaining this accuracy with equipment unattended for approximately 1 year will be extremely difficult. With the voltage-to-frequency conversion technique suggested for encoding the analog data, the oscillator frequency shift caused by aging can be handled by calibration techniques. The difficulty, however, lies in obtaining a reference voltage source capable of providing a known calibration signal for such an extended period of time.

4.11.4 Development Status

4.11.4.1 Parts List -- The flight-capsule mission profile and environmental constraints require that the parts and materials used in the design of the flight equipment exhibit good long-term stability, be unaffected by sterilization procedures and possess as low an inherent magnetic moment as possible. To assure selection of only those parts and materials which can meet these requirements, standard parts and material lists must be established.

4.11.4.2 Storage Subsystem -- Although core memories were selected for the purpose of the mechanization analysis, the advantage of higher packing densities offered by other memory types, such as monolithic ferrites, warrant development of such alternative memories for the 1971 or 1973 mission.

TABLE XXVIII

STATIC STORAGE DEVICE SUMMARY

Type	Packing Density	Drive Power	Reliability	Weight	Cost	Other
Monolithic Ferrite	High	Low	High	Low	Low	Word-organized system
Ferrite cores	Lower	Low	High	High	Low	Space proven
Ferrite film	Low	High	High	Low	Low	
Metallic film	High	Low	Poor	Low	High	Low output signals
Etched metallic toroids	Good	Low	Poor	Low	High	
Ferrite beads	Good	Low	Low	Medium	High	
Plated wires	Low	Low	Low	High	High	Inherent NDRO

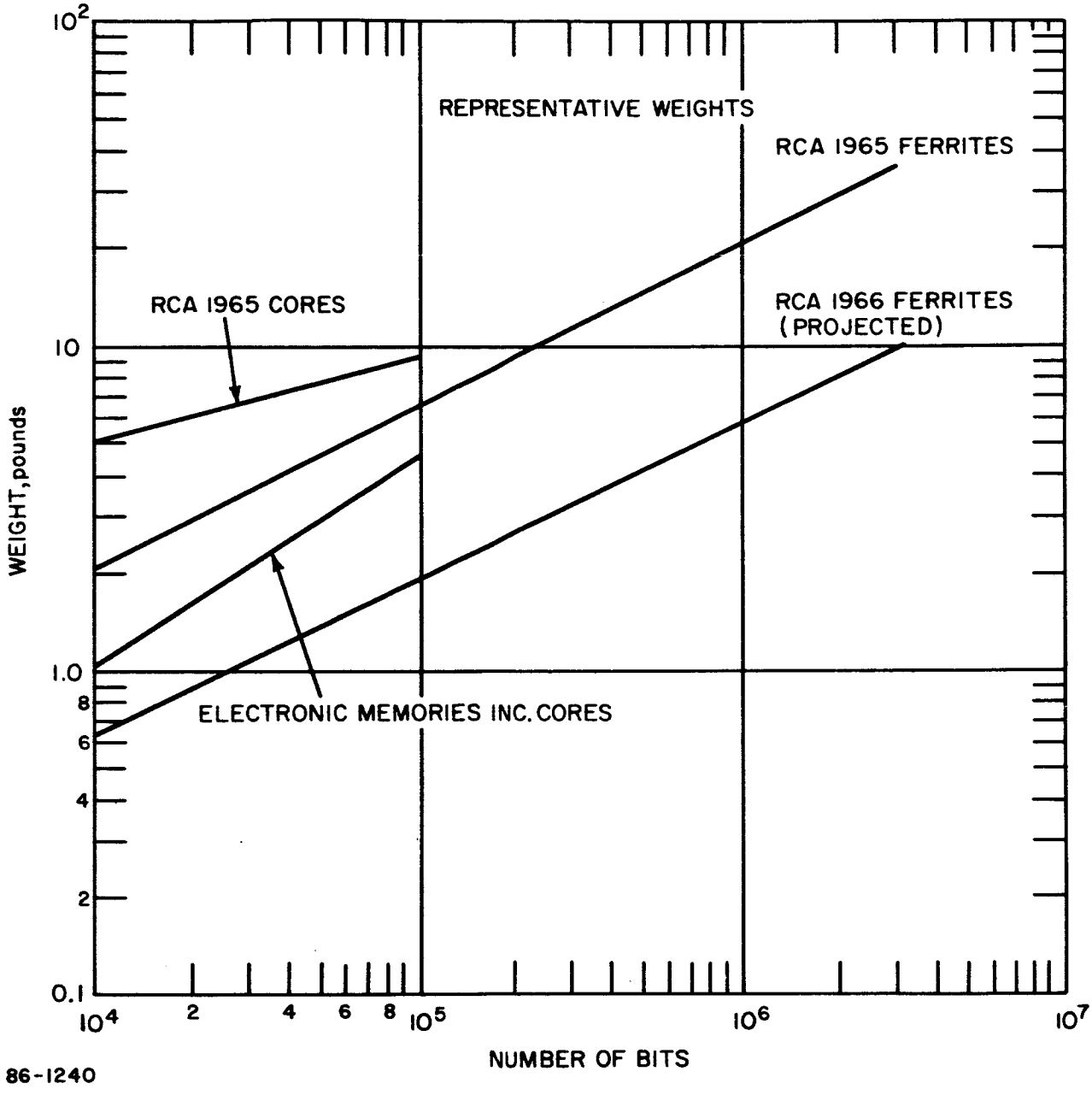

Figure 44 FERRITE MEMORY WEIGHT

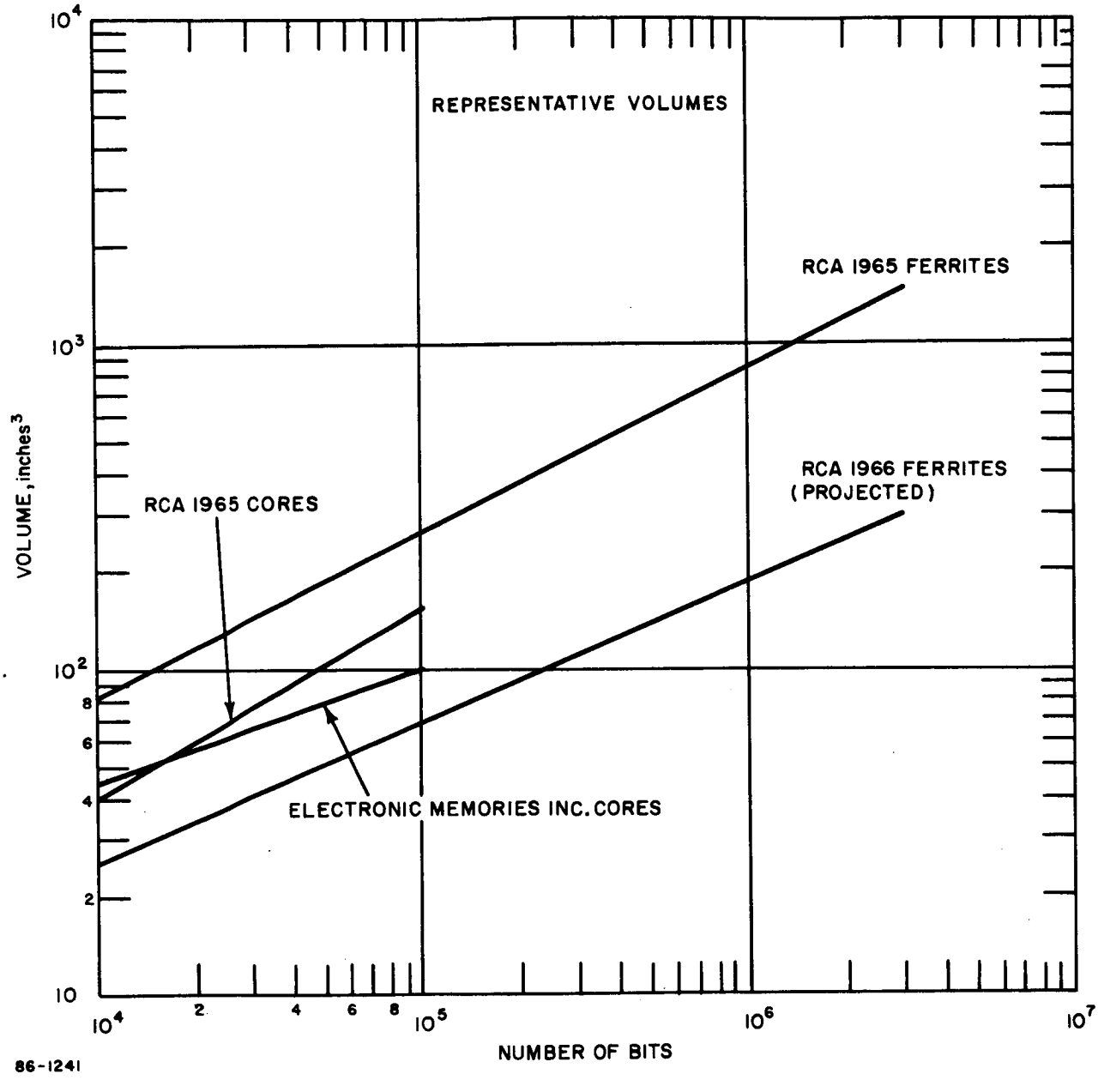

Figure 45 FERRITE MEMORY VOLUME

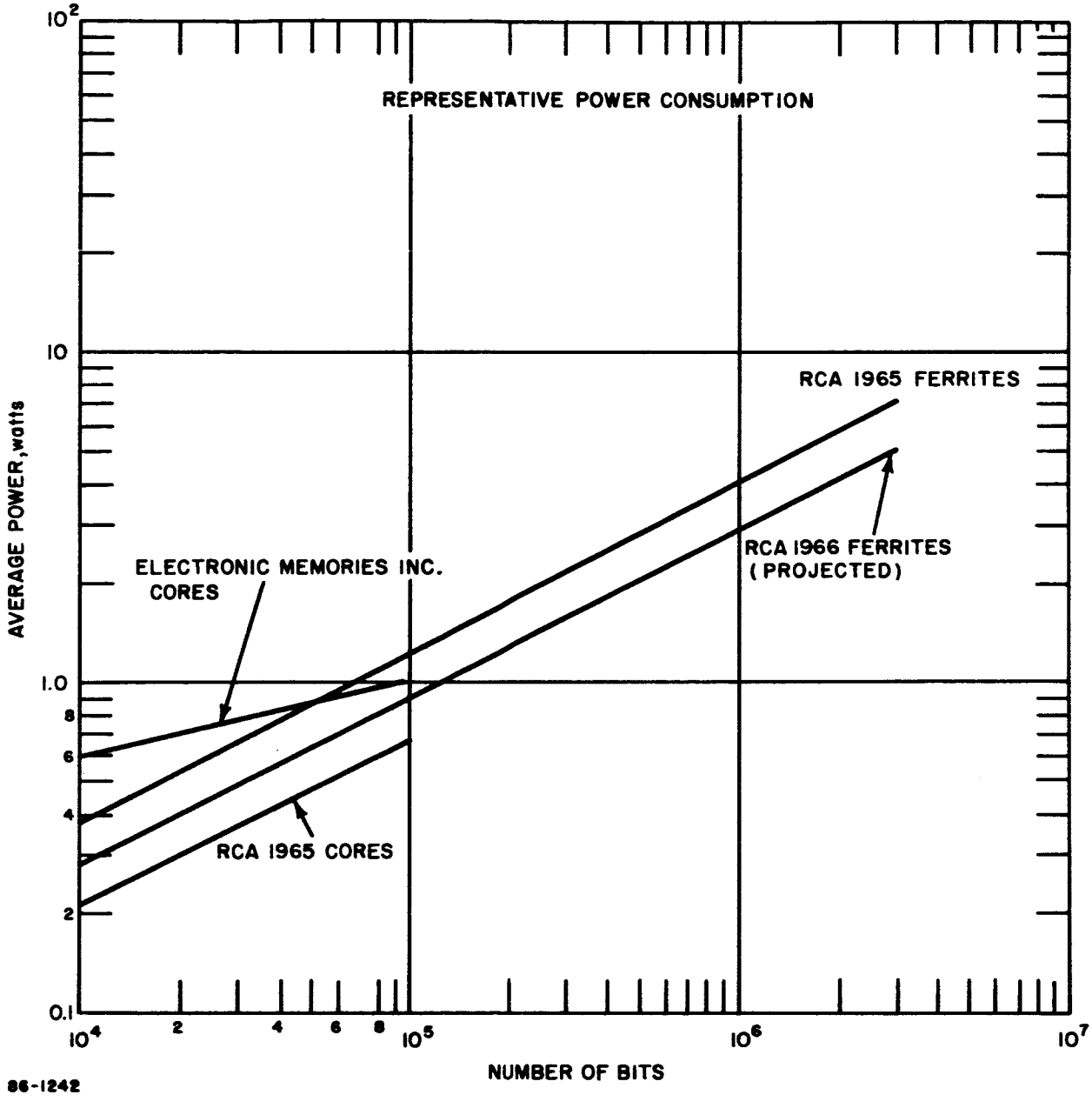

Figure 46 FERRITE MEMORY POWER CONSUMPTION

4.12 FLIGHT SPACECRAFT DATA HANDLING SUBSYSTEM

4.12.1 Description of Selected Approach

The flight-spacecraft data handling subsystem consists of the equipment required to collect and store the data received from the flight capsule. Two alternative methods have been proposed for handling flight-capsule data on the flight spacecraft.

1. One method is based on demodulating and detecting all the digital data on the flight spacecraft and storing the data for subsequent retransmission to Earth.

2. The other approach is based on operating the flight-spacecraft data-handling equipment in a feed-through mode. With this technique the data-detection function is transferred from the flight spacecraft to the Earth receiving station. This scheme somewhat reduces the flight-spacecraft receiving -system complexity in that only a minimum amount of data-handling equipment is required.

A discussion of the feed-through approach follows. The first approach (demodulate and detect) is described in paragraph 4.12.2. A number of feed-through options are available for the flight spacecraft. Each, however, assumes presence of a discrete combination of data-handling capabilities. Paragraph 4.9 contains a description of all the feed-through options.

The only feed-through scheme which requires data-handling capability is one where the frequency-shift keying signal is demodulated, low-pass filtered, sampled, quantized, and digitally stored for subsequent playback over the flight spacecraft to Earth link. This scheme can be used only if the flight spacecraft to Earth link can handle the additional data rate this approach requires. Each relay link bit must be represented by at least 28 spacecraft-Earth bits. The sampling and quantization of the demodulated signal on the flight spacecraft will be handled by the same process used for any other instrument output. The output will be sampled at 4 times the relay link data rate. The samples will be first converted into a 7-bit digital word in analog to digital converter. The digital word will then be stored in the tape recorder for subsequent playout. The total 10^6-bit storage capability is consistent with storing relay-link data at a rate of 64 bps for a period, the duration of which corresponds to the time between entry and impact (800 seconds).

The flight-spacecraft data-handling subsystem will sample and quantize the output waveform from the flight spacecraft receiver. The sampling rate required to quantize the output waveform is at least four times the relay-link data rate in order to meet the low pass filter cutoff frequency requirements and to satisfy the requirement that sufficient samples are taken to permit accurate reconstruction of the analog waveform. Each sample will be quantized into 128 levels (7-bit word) and stored for subsequent playout. The storage capacity of the tape recorder will be consistent with that required to store all the flight capsule data covering the period from entry to impact. The design requirements are summarized in Table XXIX.

TABLE XXIX

FLIGHT CAPSULE DATA HANDLING
SUBSYSTEM SUMMARY

Data handling scheme	Feed-through
Received Flight Capsule data rate	64 bps
Flight Spacecraft sampling rate	64 x 4 sps (minimum)
Quantization levels	128
Data storage	
Type	Tape recorder
Capacity	10^6 bits
Operational	Entry-Impact

In other feed-through schemes in which the data demodulation function is transferred from the flight spacecraft to the Earth receiving station, no data-handling equipment is required aboard the spacecraft because the IF output of the flight spacecrafts VHF receiver is simply re-transmitted to Earth.

4.12.2 Alternate Approach

An alternate approach to the problem of handling the flight-capsule data received aboard the flight spacecraft requires detection and storage of all of the digital data on the flight spacecraft. Although this scheme increases the equipment complexity considerably, it permits a substantial reduction in the flight-spacecraft to Earth data rate relative to that required by the feed-through scheme. A complete description of the data-handling equipment required to implement this approach is provided in paragraph 5.5.5.

4.13 FLIGHT CAPSULE CENTRAL COMPUTER AND SEQUENCER

The flight capsule central computer and sequencer (CC&S) subsystem performs timing, sequencing, and associated computational functions for the flight capsule. A master time base is provided for use in all computations and sequences. The initiation of all events in the appropriate sequence is provided by properly timed outputs to other subsystems. Computations are performed to solve equations involving time, acceleration, and altitude. Four basic sequences require control. These may be identified by the mission phases with which they are associated. They are the separation, cruise, entry-descent, and landed sequences. These sequences are primarily initiated in one of two ways: by a time-determined signal (for example a signal from the cruise sequence) or by occurrence of an identifiable but nontimed event (for example, indication by the radar altimeter that a certain altitude has been reached). The cruise sequence is intitiated by command through the flight spacecraft CC&S. The separation and entry-descent sequences are initiated by the cruise sequence. The landed sequence is initiated by an accelerometer at impact.

Two separate CC&S subsystems comprise the overall central computer and sequencer. The first subsystem, used from preseparation to impact, is located outside the landed capsule, and is, accordingly, called the external CC&S. The other subsystem, located within the landed capsule and referred to as the internal CC&S, operates from the time of impact through the end of the mission.

4.13.1 External CC&S Description

The external CC&S provides timing and sequencing services for the flight capsule subsystems from before separation of the flight capsule from the flight spacecraft until impact. This CC&S initiates flight capsule events in the three different sequences described in paragraphs 4.13.1.1 through 4.13.1.3.

Figure 47 shows the external CC&S in functional block-diagram form. This figure shows both the primary and the backup sources of initiation signals, together with the major events initiated for each phase of the mission controlled by the external CC&S.

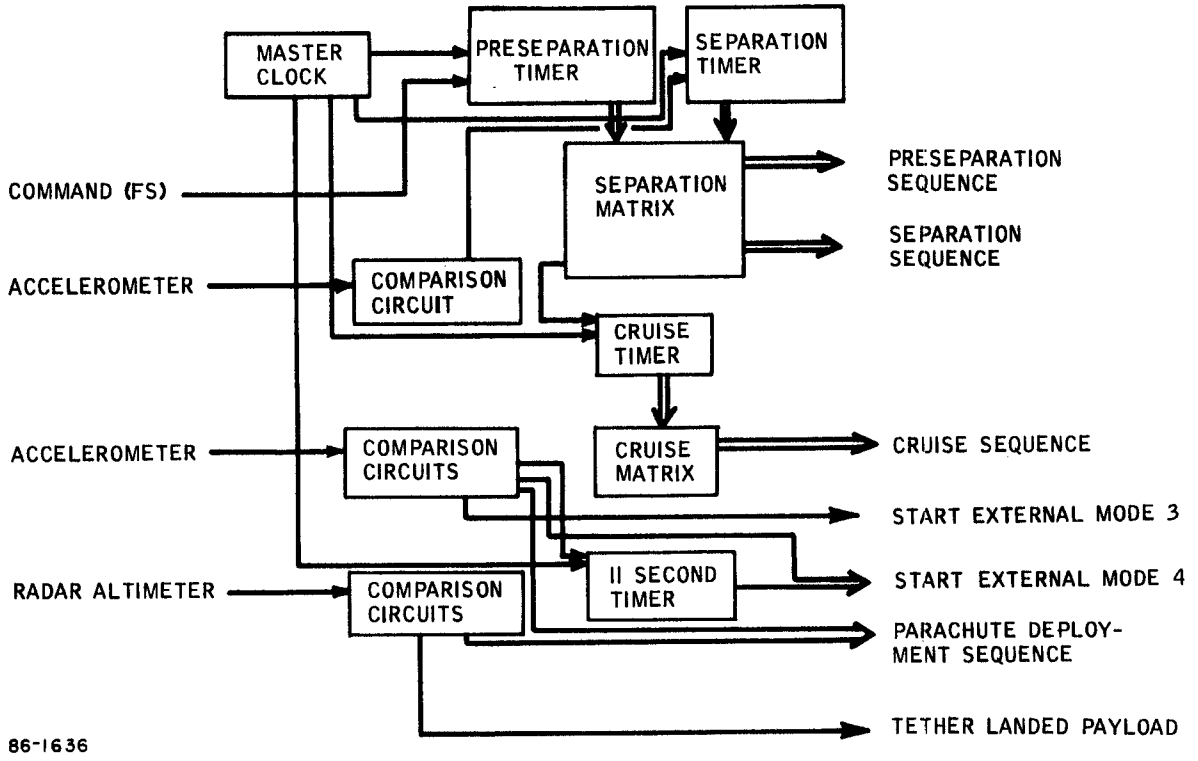

Figure 47 FLIGHT CAPSULE EXTERNAL CENTRAL COMPUTER AND SEQUENCER

4.13.1.1 Separation Sequence

The separation sequence controls all flight-capsule events from 240 minutes before separation to 15 minutes after separation. During this time, the external CC&S initiates preseparation checkout (external mode 1), and separation operations.

The discrete events initiated are as follows:

Apply test voltage to ACS and gyros

Turn flight capsule systems on

Turn all flight capsule systems off (except ACS and gyros)

Transmit flight capsule direct link via FS

Turn off flight capsule direct link via FS

Actuate external mode 1 (preseparation checkout)

Start post-separation timers 1 and 2

Initiate flight capsule ΔV maneuver

Terminate ΔV propulsion

Initiate flight capsule attitude control maneuver

Jettison propulsion structure.

4.13.1.2 Cruise Sequence

The cruise sequence controls all flight-capsule events during the cruise phase, that is, from 15 minutes after separation until 5 minutes before entry. During this phase, external mode 2 operation (post-separation checkout) is initiated once each day. Except for those times during which it is operating in external mode 2, the CC&S operates the flight capsule in external mode 5, a standby mode.

4.13.1.3 Entry-Descent Sequence

The entry-descent sequence controls all flight capsule events from 5 minutes before entry to impact. During this time, the following-listed major events are initiated:

Start external mode 2 (pre-entry checkout)

Start external mode 3 (entry data storage)

Start external mode 4 (entry-descent data transmission)

Arm entry and landed pyrotechnics

Deploy reefed parachute

Disreef parachute

Deploy science probes

Tether landed capsule

4.13.2 Internal CC&S Description

The internal CC&S provides timing and sequencing services for the landed capsule subsystems from impact through the end of the mission. It initiates landed capsule events in a single sequence, called the landed sequence. This sequence starts when the landed capsule is tethered and ends with the end of the mission. During this period, the following-listed events are initiated by the internal CC&S.

Energize internal mode 1 (impact data storage)

Jettison parachute and external payload

Terminate direct link transmission

Jettison impact attenuator

Deploy cosmic radiation detector and atmospheric temperature probe

Deploy surface radiation detector

Deploy alpha scatterer and surface temperature detectors

Deploy anemometer and microphone

Energize internal mode 2 (direct-link transmission)

Terminate direct link transmission

Figure 48 shows the internal CC&S subsystem in functional block diagram form. This figure shows both the primary and the backup sources of initiation signals as well as the major events initiated by the internal CC&S. The internal CC&S contains a master timer and a post-impact sequencer matrix.

Although it is desirable to be able to initiate all sequences by functionally redundant signals, functionally redundant initiation is not possible during certain times (such as during portions of the post-landing science mission). In such cases, backup means of initiation are provided wherever possible through direct link command from Earth. This capability exists, of course, only during that portion of the Martian day when Mars and Earth are mutually

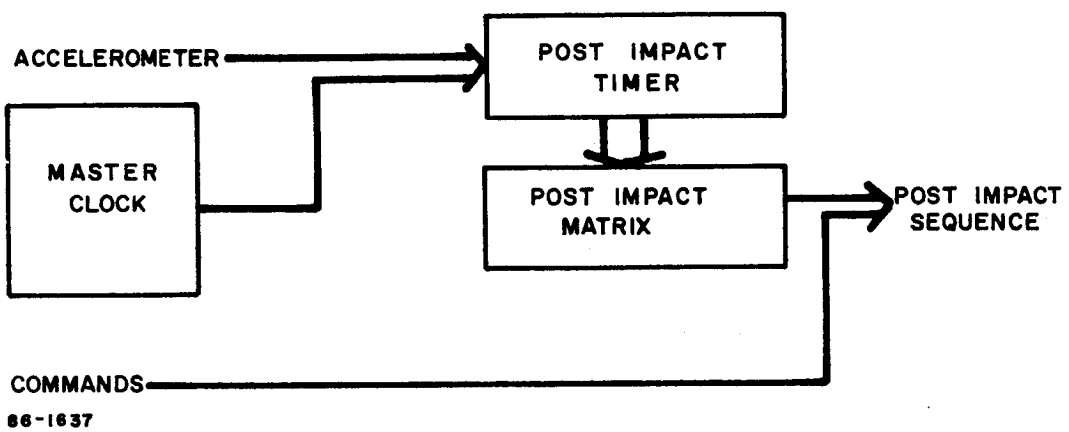

Figure 48 FLIGHT CAPSULE INTERNAL CENTRAL COMPUTER AND SEQUENCER

visible. Further redundancy is obtained by using block-redundant master timers in both the external and internal CC&S subsystems.

4.14 SUMMARY OF CHARACTERISTICS

The telecommunication subsystem consists of two functionally independent systems: one, called the external system, is used during the separation to lander tethering phase of the mission; the other, called the internal system, is used during the landed phase of the mission. As the names imply, the external system is physically outside of the landed payload and the internal system is located within it. The operational, performance, design, and mechanical characteristics of the overall telecommunications subsystem are summarized in Tablex XXX through XXXIII, respectively. For a complete discussion of parts and materials selection, packaging, and magnetic cleanliness aspects of the subsystem, see Appendixes IV.4-12, IV.4-13 and IV.4-11, respectively, in Reference 1.

TABLE XXX

FLIGHT CAPSULE TELECOMMUNICATION SUBSYSTEM
OPERATIONAL CHARACTERISTICS

Mission Control	Internal Programming with Command Backup
Data transmission	Relay and direct links
PERIODS OF COMMUNICATION	
Relay data	
Separation	15 minutes
Cruise	2 minutes per day
Entry-descent	Continuous
Direct Data	
Landed at impact	2 hours starting 1 hour after landing
Landed 24 hours after impact	1 hour
Direct Command	
Landed	Backup to CC&S when in view of earth

TABLE XXXI

FLIGHT CAPSULE TELECOMMUNICATION SUBSYSTEM PERFORMANCE CHARACTERISTICS

Data Transmission	
Direct data rate	2 bps
Total transmitted bits (impact to end of mission)	Approximately 25, 000
Relay data rate	64 bps
Total transmitted bits	Approximately 130, 000 (Model 3 atmosphere)
	Approximately 180, 000 (Model 2 atmosphere)
Command Reception	
Direct link	1 bps
Relay link	None

TABLE XXXII

FLIGHT CAPSULE TELECOMMUNICATION SUBSYSTEM DESIGN CHARACTERISTICS

Direct Data Link	
Frequency	2300 MHz
Transmitter power	20 watts CW
Modulation system	Noncoherent N-ary MFS
Antenna gain	-7 db (3σ minimum)
Direct Command Link	
Frequency	2113 MHz
Receiver noise figure	7 db
Modulation scheme	Coherent PSK/PM
Antenna gain	-7 db (3σ minimum)
Relay Data Link	
Frequency	272 MHz
Transmitter power	20 watts CW
Modulation system	Noncoherent FSK
Antenna gain	-7 db (3σ minimum)
Data Handling Channels	
Science	Approximately 300
Engineering	Approximately 100

TABLE XXXII (Concl'd)

Storage Capacity	
Pre-landing	Approximately 8000 bps
Post-landing	Approximately 12, 000 bits
Power Requirements (watts)	
External System	
FSK transmitters	55. 0
Data automation equipment	2. 0
Telemetry	2. 0
Entry descent memory	0. 6
Central computer and sequencer	4. 0
Internal System	
Direct link transmitters	90. 0
Command receiver	2. 0
Data automation equipment	3. 5
Telemetry	2. 0
Surface memory	0. 6
Central computer and sequencer	2. 0

TABLE XXXIII

FLIGHT CAPSULE TELECOMMUNICATION SUBSYSTEM PHYSICAL CHARACTERISTICS

Item	Quantity	Weight (pounds)	Volume (in^3)
External Equipment			
FSK transmitters	2	3	70
Data automation equipment	1	3	80
Telemetry	1	2	80
Central computer and sequencer	1	6.2	185
Entry descent memory	1	1	50
Miscellaneous RF	1	2.0	80
VHF relay-link antenna	1	2.5	4800
Internal Equipment			
Direct-link transmitters	2	12.0	300
Command receiver	1	5	115
Data automation equipment	1	5.5	180
Telemetry	1	3	80
Surface memory	1	1	50
Central computer and sequencer	1	3.4	100
Miscellaneous RF	1	7.0	446
S-band direct-link antenna	2	2.5	45
Total		59.1	6,661

5.0 PROBE, ENTRY FROM ORBIT

5.1 FUNCTIONAL REQUIREMENTS

5.1.1 General

The telecommunication subsystem must satisfy the following basic functional requirements.

1. It must provide the data handling and storage required by the flight-capsule engineering and diagnostic instrumentation.

2. It must transmit to Earth, via a relay link through the flight spacecraft, the engineering and diagnostic data collected during the cruise, entry, and descent phases of the flight capsule mission.

The data transmission objectives are summarized on a phase-by-phase basis in Table XXXIV.

5.1.2 Constraints

5.1.2.1 Environment difficulty is associated with controlling the attitude of the suspended capsule during the parachute descent phase of the mission. This attitude uncertainty makes the use of directional antennas impractical and thereby imposes severe limitations on the effective radiated power (ERP) which can be obtained. Reflections from the planet surface further limit radio link performance through multi-path signal fading.

Attenuation of radio frequency energy by the plasma created by aerodynamic heating during entry limits the time during which the communications medium is suitable for data transmission. This condition makes it necessary to store critical entry data for later transmission.

5.1.2.2 Performance

The relay-link performance margin, defined as the ratio of nominal received signal level to the nominal threshold signal level, must be equal to or greater than the linear sum of the adverse tolerances (expressed in db) associated with all relay-link parameters.

5.1.2.3 Flight Spacecraft

The severe data-rate limitations associated with a direct-to-Earth radio link make it necessary to use the flight spacecraft as a relay terminal to transfer data collected by the flight capsule to Earth.

TABLE XXXIV

DATA TRANSMISSION REQUIREMENTS

Mission Phase	Approximate Data Rate Required (bps)	Data Objectives
Preseparation	1000	Determine operating integrity of flight capsule subsystems
Separation	1000	Verify execution of ACS manuevers and ΔV events
Cruise	50 to 100	Periodic status checks Calibrate instruments in zero G
Entry*	1000	Define upper atmosphere
Descent	18,000	Define lower atmosphere Define surface characteristics

*Approximately 87 seconds of radio blackout occurs during this phase

Reasonable relay-link performance requires that the communications range between the flight capsule and the flight spacecraft be minimized during the entry and descent phases of the flight-capsule mission. The orbital position of the flight spacecraft must, therefore, be directly overhead and either at or near periapsis at the time of flight-capsule impact. It is also desirable to minimize the flight spacecraft complexity introduced by the requirements of relay-link operation by using only body fixed (non-tracking) antennas on the flight spacecraft. To use such antennas without, however, severely degrading relay-link performance, the position and orientation of the flight-spacecraft relay-link antenna must be so selected that the total look-angle variation of the antenna over the complete range of flight spacecraft orbits considered will be minimized during the entry and descent phases of the flight capsule mission. These requirements are discussed in further detail in paragraph 5.3.

5.2 DESIGN OBJECTIVES

The following guidelines established by Avco reflect a conservative approach in synthesizing the design of a telecommunication subsystem for Mars Probe/Lander applications.

1. Use a single-orientation, low-gain, body-fixed antenna on the flight spacecraft for a wide range of orbits.

2. Allow selection of a low-risk flight capsule parachute.

3. Where feasible, use low voltage, solid state equipment to eliminate design problems associated with high-voltage arcing.

4. Avoid the necessity for a flight-spacecraft maneuver as a prerequisite for obtaining the desired flight-spacecraft flight-capsule separation attitude.

5. Design the telecommunication subsystem such that there will be no need to use a flight capsule attitude control system (ACS) to restrict the flight capsule look angle, allowing an increase in flight-capsule antenna gain.

6. Employ such subsystem redundancy that failure of any single telecommunication subsystem component (black-box) will not result in loss of data.

These guidelines are, of course, in addition to the design guidelines listed in paragraph 4.4.

5.3 RELAY LINK GEOMETRY

From a telecommunication viewpoint, the geometrical factors which primarily influence both the relay link performance and the flight-spacecraft orbit-position constraints are:

1. Flight-spacecraft relay-link antenna look angles
2. Flight-capsule antenna look angles
3. Communication range between the flight capsule and the flight spacecraft.

Figure 49 shows the relative flight spacecraft-flight capsule geometry for a typical (1000 x 10,000 km) orbit. The time markers shown in that figure indicate the relative flight capsule and flight spacecraft positions at various times between separation and flight-capsule impact. Three flight-spacecraft positions are shown during the entry/descent portion of the flight-capsule mission. The center position shows the axis of the flight spacecraft relay-link antenna so aligned that the antenna points directly at the flight capsule at some time during capsule entry and descent. As discussed in the next section, the two extremes of flight-spacecraft position during flight-capsule entry and descent represent the uncertainty regarding the time from separation to flight capsule impact. These uncertainties are a function of atmospheric and entry angle contingencies. The extremes of the range of uncertainties are selected to be symmetric about the landing site to minimize both the communications range and the flight spacecraft relay link antenna look-angle relative to the flight capsule.

5.3.1 Flight Spacecraft Antenna Look-Angles and Beamwidth

The flight capsule to flight spacecraft look angle, which determines the flight spacecraft relay-link antenna beamwidth requirement and, ultimately, its gain, is defined as the angle between the axis of the main lobe of the flight spacecraft relay link antenna and the line of sight to the flight capsule.

The problem during flight-capsule entry and descent is one of ensuring that the flight spacecraft will be overhead no matter which atmosphere the flight capsule may encounter. In Figure 50, the position of the flight spacecraft during flight-capsule parachute descent is shown for each atmosphere. The central angle represents the total range of the angle traversed by the flight capsule from entry to parachute deployment.

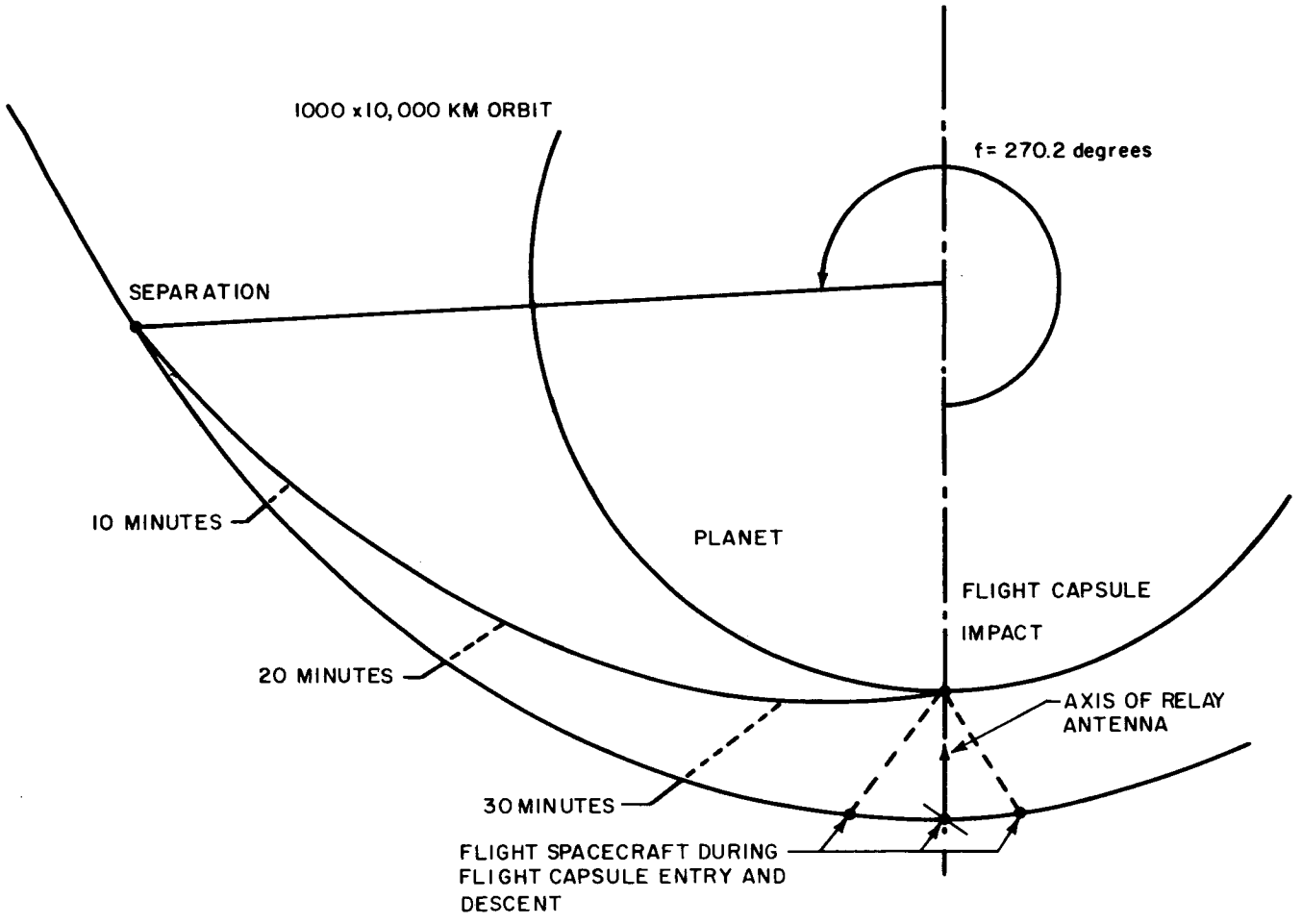

Figure 49 FLIGHT SPACECRAFT-FLIGHT CAPSULE COMMUNICATION GEOMETRY

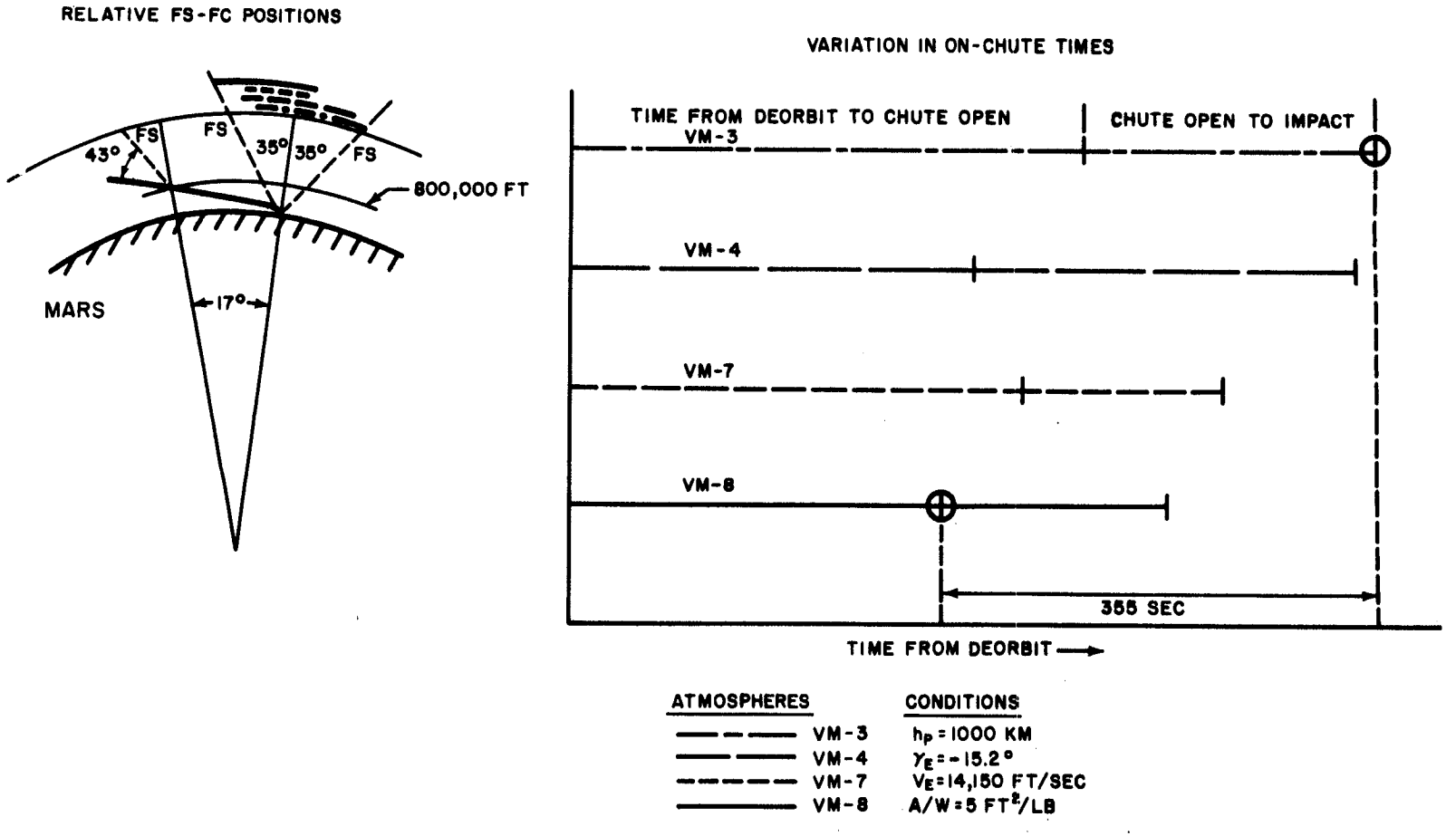

760146P

Figure 50 COMMUNICATION GEOMETRY DURING ENTRY

In attempting to align the flight spacecraft overhead during parachute-aided descent of the suspended capsule, anticipated dispersions in the positions of both the flight spacecraft and the descending capsule must be considered. The flight capsule position is affected primarily by dispersion in the entry velocity and the entry angle, and by the atmosphere encountered. The flight spacecraft position is affected primarily by the dispersion in the time from de-orbit to flight-capsule entry, and secondarily by dispersion in flight spacecraft orbital parameters. The time from parachute deployment in the VM-8 atmosphere to impact in the VM-3 atmosphere is 355 seconds, as shown on Figure 50.

As these considerations indicate, the flight spacecraft relay-link antenna look angles depend on the antenna concept selected. Figure 51 illustrates the difference in flight-spacecraft look-angle variation during flight-capsule entry and descent for two alternative flight-spacecraft antenna concepts.

In the first concept, it is assumed that the antenna is body-fixed on the flight spacecraft and that the mounting orientation is such that the axis of the antenna points along the line of sight to a particular point along the flight path of the descending parachute-suspended capsule. The point selected is one which occurs midway during the 6-minute descent time interval allowed for atmosphere and entry-angle dispersions. Negative and positive look-angles are defined as angles appearing clockwise and counterclockwise, respectively, as shown in Figure 51.

In the second concept, it is assumed that the antenna is mounted on, or slaved to, the planetary science platform (PSP) which tracks the center of the planet. Midway during the 6-minute descent time interval allowed to accommodate the various dispersions, the antenna will be aligned in a position similar to that selected for the body-fixed antenna.

5.3.1.1 Body-Fixed Antenna

For a body-fixed flight-spacecraft antenna, either a single orientation of the body antenna on the flight spacecraft can be selected for all orbits considered, or the antenna can be oriented before launch to accommodate a specific orbit.

1. Orientation on Flight Spacecraft -- Figure 52 shows the variation in clock/cone angle of the flight spacecraft to the flight capsule line of sight during the period from separation to impact for a typical orbit. The antenna position angles selected to obtain maximum flight spacecraft antenna gain during capsule descent are those occurring

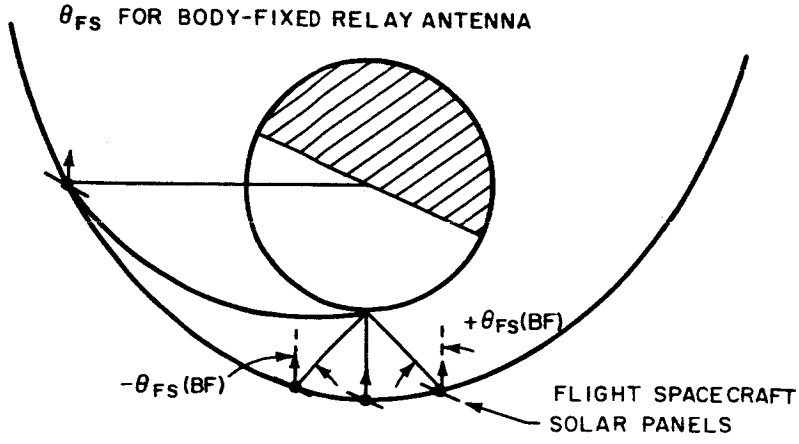

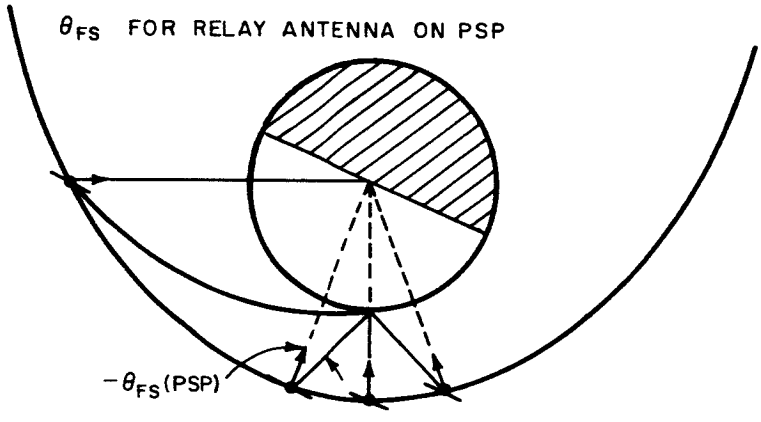

ANGLE	DEFINITION
θ_{FS} (BF)	ANGLE BETWEEN FLIGHT SPACECRAFT ANTENNA AXIS AND LINE OF SIGHT TO FLIGHT CAPSULE
θ_{FS} (PSP)	ANGLE BETWEEN LOCAL VERTICAL AND LINE OF SIGHT TO FLIGHT CAPSULE

86-2771

Figure 51 COMMUNICATION GEOMETRY FOR ALTERNATE FLIGHT SPACECRAFT ANTENNA CONCEPTS

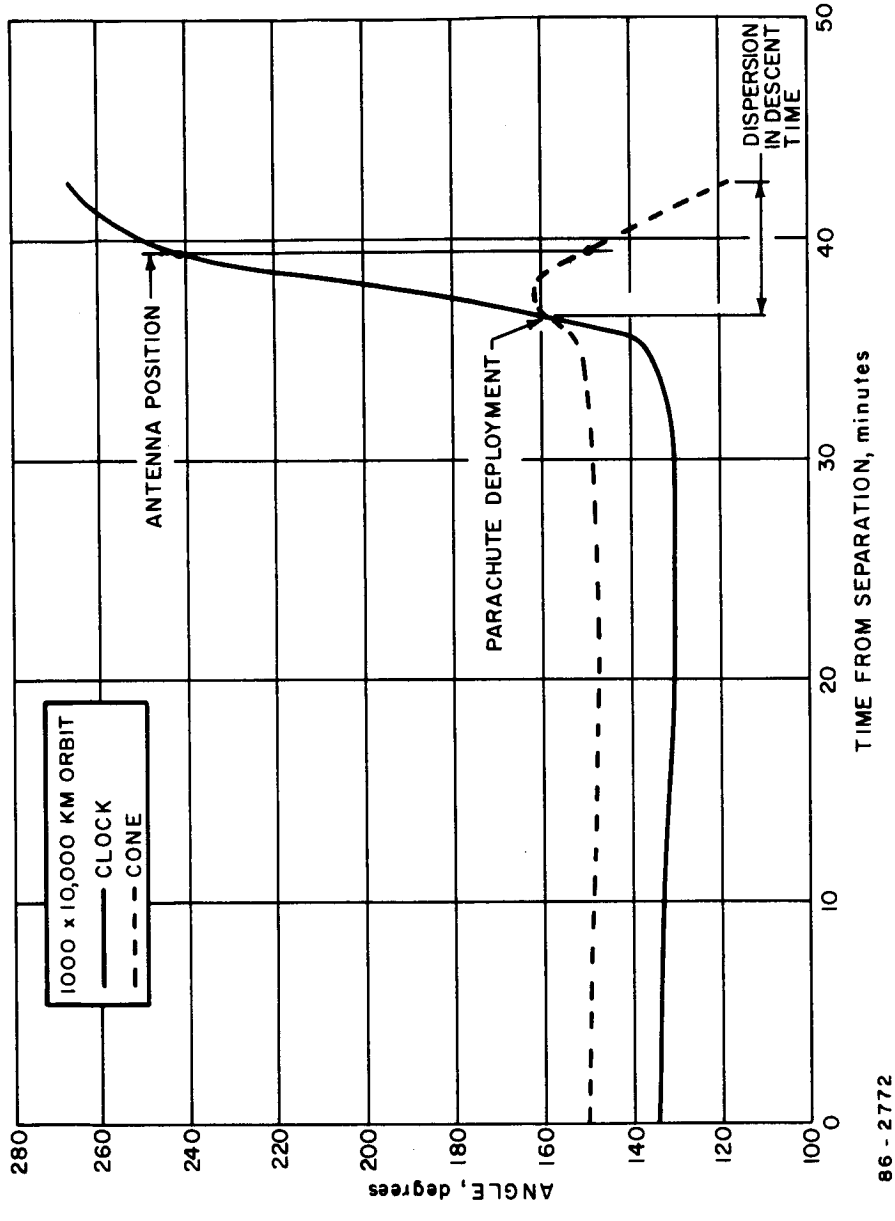

Figure 52 CLOCK/CONE ANGLE TO FLIGHT SPACECRAFT/FLIGHT CAPSULE LINE OF SIGHT

midway during the dispersion in descent time. Table XXXV shows the corresponding position angles in the case of a body-fixed antenna suitably positioned prior to launch to accommodate a specific orbit. Also shown are position angles for a body-fixed antenna so oriented that the alignment is the same for all orbits considered.

TABLE XXXV

BODY FIXED ANTENNA POSITION ON FLIGHT SPACECRAFT

1. Body-fixed: Repositioned Periapsis (kilometers)	Apoapsis (kilometers)		
	4000	10,000	20,000
700	199°/160°	230°/155°	237°/152°
1000	226°/156°	241°/150°	245°/147°
1500	252°/140°	252°/140°	252°/141°

Key: Clock/cone

2. Body-fixed: Single Position

Clock: 234 degrees

Cone: 153 degrees

2. Look-Angles -- The total variation in flight spacecraft look-angles from separation to impact determines the flight spacecraft antenna beamwidth requirements. Figure 53 shows the total flight spacecraft to flight capsule look-angle for a body-fixed antenna orientation (cone angle: ~241 degrees, clock angle: ~150 degrees) selected for a 1000 x 10,000 kilometer orbit. The look-angle will be zero degree approximately midway during the period encompassing the dispersion in descent time after parachute deployment.

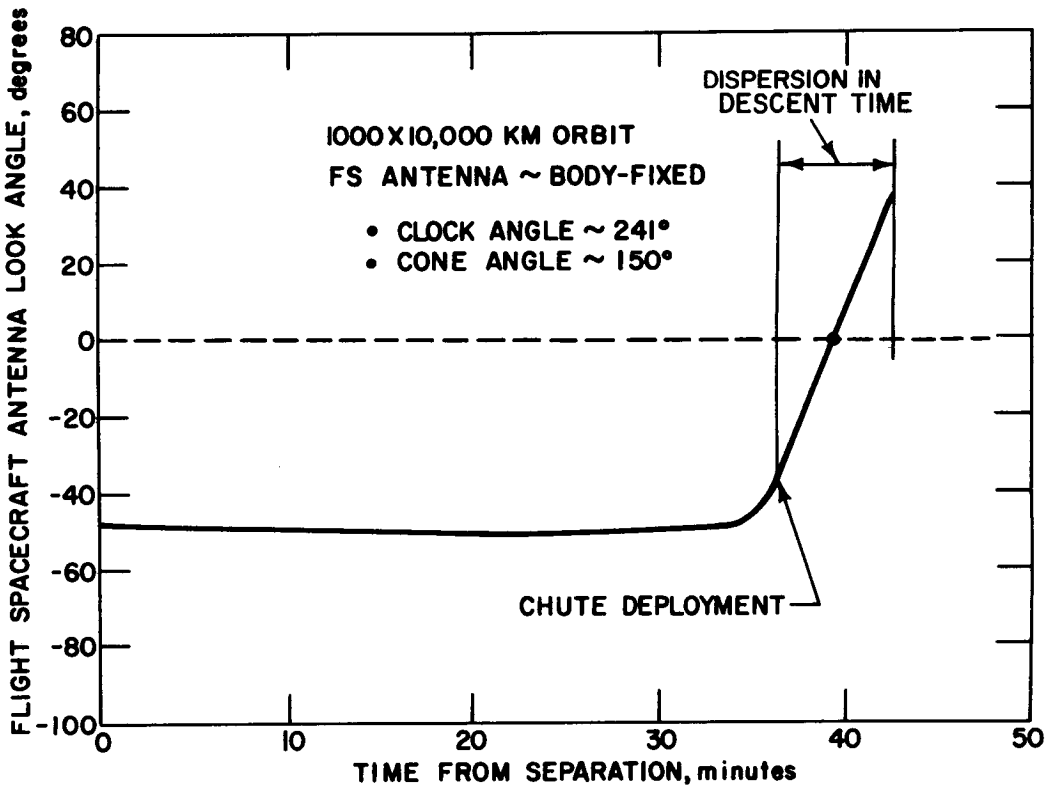

760160P

Figure 53 FLIGHT SPACECRAFT BODY-FIXED ANTENNA LOOK ANGLE

The largest positive look-angle occurs at the latest impact point in the descent time dispersion. The largest negative angle occurs during the cruise phase after separation. A summary of maximum look-angles for body-fixed antennas and for all orbits considered is given in paragraph 5. 3. 1. 3.

5. 3. 1. 2 Planetary Science Platform Antenna

For an antenna mounted on, or slaved to, the planetary science platform (PSP), the look-angle variation during the flight-capsule entry/descent is always less than that of a body-fixed antenna, as shown on Figure 51. This situation is desirable since it allows increased antenna gain for relatively smaller total beamwidths. Figure 54 compares the total flight spacecraft to flight capsule look-angle variation of an antenna on the PSP with the total variation for the previously considered body-fixed antenna. For the orbit under consideration (1000 x 10, 000 kilometer) the total look-angle variation for the PSP antenna is less than that for the body-fixed antenna during all portions of the flight-capsule mission. This is not the case for all orbits considered, however, as the following discussion indicates.

5. 3. 1. 3 Summary

Table XXXVI summarizes the maximum look-angle excursions of the antenna concepts considered in paragraphs 5. 3. 1. 1 and 5. 3. 1. 2. Look-angle data is given in this table for two cases of body-fixed antennas, one in which the antenna is positioned before launch as appropriate for a specific orbit, and the other in which a single position is used for all orbits under consideration.

In the case of the antenna positioned before launch, the maximum negative and positive look-angles occur for the same orbit (700 x 20, 000 km) and are -70 and +50 degrees, respectively (a range of 120 degrees). In the single position case, the maximum negative look-angle (-74 degrees) occurs for the 700 x 4000 km orbit, and the maximum positive look-angle (+52 degrees) occurs for the 700 x 20, 000 km orbit. Therefore, the maximum total look-angle variation (126 degrees), for the first case (position before launch) is only 6 degrees less than the maximum variation for the single position case (120 versus 126 degrees).

Similarly, the maximum negative and positive entry/descent look-angles for the PSP antenna occur with the 700 x 20, 000 km orbit and are ± 40 degrees. For a total trajectory PSP antenna, the maximum

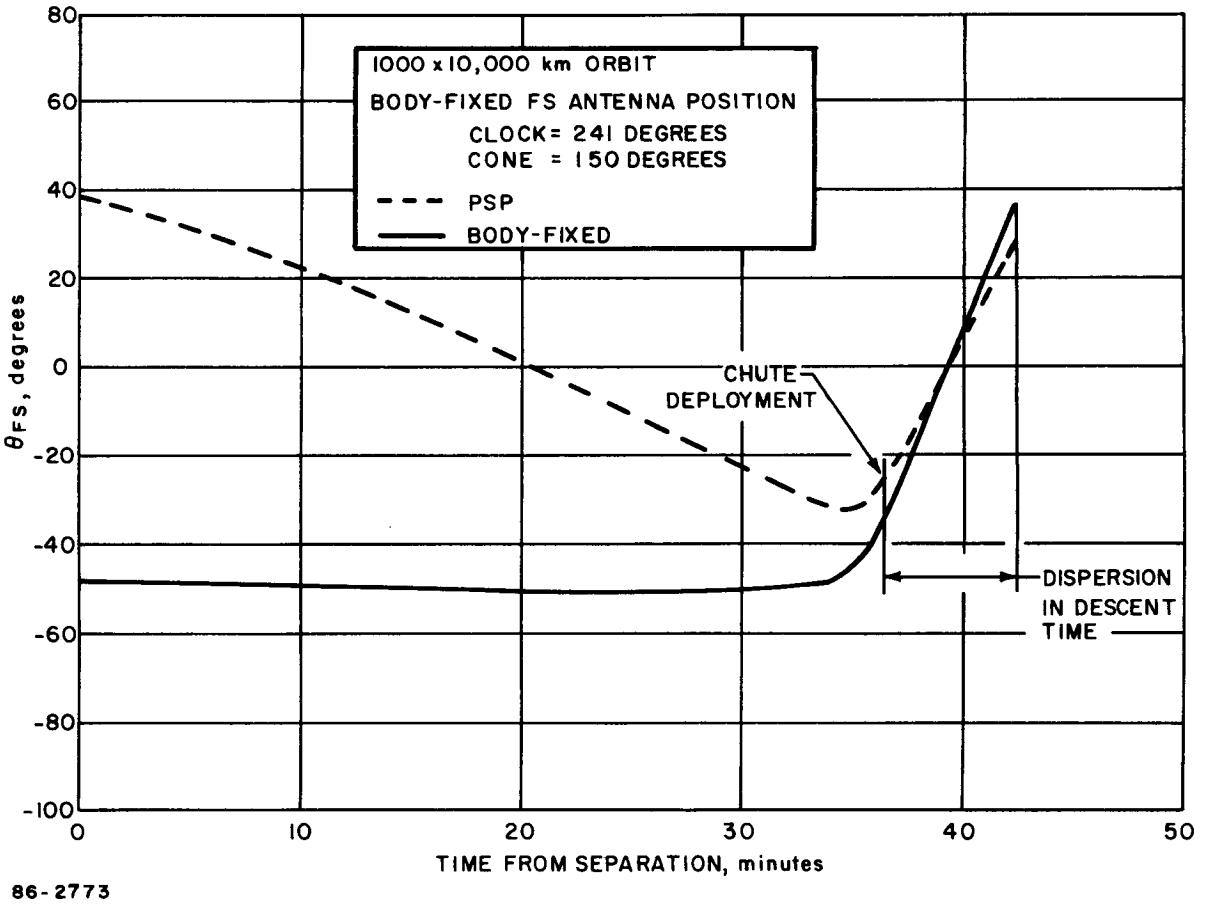

Figure 54 FLIGHT SPACECRAFT BODY-FIXED AND PSP ANTENNAS LOOK ANGLE COMPARISON

TABLE XXXVI

FLIGHT SPACECRAFT ANTENNA MAXIMUM LOOK-ANGLE SUMMARY

Periapsis (kilometers)	Apoapsis (kilometers)		
	4000	10,000	20,000
	Body-Fixed Antenna, Repositioned		
700	-58°/42°	-66°/48°	-70°/50°
1000	-47°/32°	-52°/36°	-55°/38°
1500	-30°/21°	-33°/24°	-36°/24°
	Body-Fixed Antenna, Single Position		
700	-74°/26°	-69°/45°	-69°/52°
1000	-51°/28°	-48°/40°	-48°/45°
1500	-14°/37°	-18°/39°	-21°/39°
	PSP Antenna, Entry/Descent Only		
700	-33°/33°	-38°/38°	-40°/40°
1000	-25°/25°	-27°/27°	-28°/28°
1500	-15°/15°	-16°/16°	-17°/17°
	PSP Antenna, Total Trajectory		
700	-37°/33°	-41°/38°	-44°/40°
1000	-30°/38°	-33°/36°	-35°/35°
1500	-19°/91°	-21°/81°	-23°/74°

negative look-angle (-44 degrees) occurs with the 700 x 20,000 km orbit while the maximum positive look-angle (+ 91 degrees) for that antenna occurs with the 1500 x 4000 km orbit. Therefore, the total look-angle variation for the entry/descent PSP antenna is 55 degrees less than the total variation for a PSP antenna used for all trajectories (80 versus 135 degrees).

The antenna beamwidth must be at least as wide as the total look-angle variation. Table XXXVII summarizes the minimum beamwidth requirements for both antenna concepts (body-fixed and PSP-mounted) and for all orbits considered. The body-fixed antenna beamwidths are 5 degrees wider than the total look-angle variation. The additional beamwidth was provided to accommodate the sun angle change that occurs during the 10 days the flight spacecraft is in orbit. The beamwidth of a PSP antenna to be used for the total trajectory and for all orbits considered is approximately 5 degrees wider than the beamwidth required by a single-position body-fixed antenna.

5.3.2 Flight Capsule Antenna Look-Angles and Beamwidth

The flight capsule to flight spacecraft look-angle is defined as the angle between the flight capsule longitudinal axis and the line of sight between the flight capsule and the flight spacecraft. The reason for selecting the flight capsule longitudinal axis as the antenna reference axis is discussed in the following paragraph.

5.3.2.1 Antenna Orientation

During the flight capsule parachute-assisted descent, the flight spacecraft is positioned directly over the flight capsule at the midpoint in the dispersion in flight capsule descent times. At this time the longitudinal axis of the flight capsule is aligned along the local Martian vertical (assuming no wind). A zero degree look-angle is obtained at this time, therefore, if the flight capsule longitudinal axis is selected as the antenna reference axis.

5.3.2.2 Nominal Look-Angles, No wind Condition

The total look-angle variation for the period from separation to impact, determines the flight capsule antenna beamwidth requirements.

Figure 55 shows flight capsule look-angle variations for the 1000 x 10,000 km orbits used previously to illustrate the flight spacecraft look-angle variations.

TABLE XXXVII

FLIGHT SPACECRAFT ANTENNA MINIMUM BEAMWIDTH REQUIREMENTS

Periapsis (kilometers)	Apoapsis (kilometers)		
	4000	10,000	20,000
	Body-Fixed Antenna, Repositioned		
700	105°	119°	125°
1000	84°	93°	98°
1500	56°	62°	65°
	Body-Fixed Antenna, Single Position		
	130° (all orbits)		
	PSP Antenna, Entry/Descent Only		
700	66°	76°	80°
1000	50°	54°	56°
1500	30°	32°	34°
	PSP Antenna, Total Trajectory		
	135° (all orbits)		

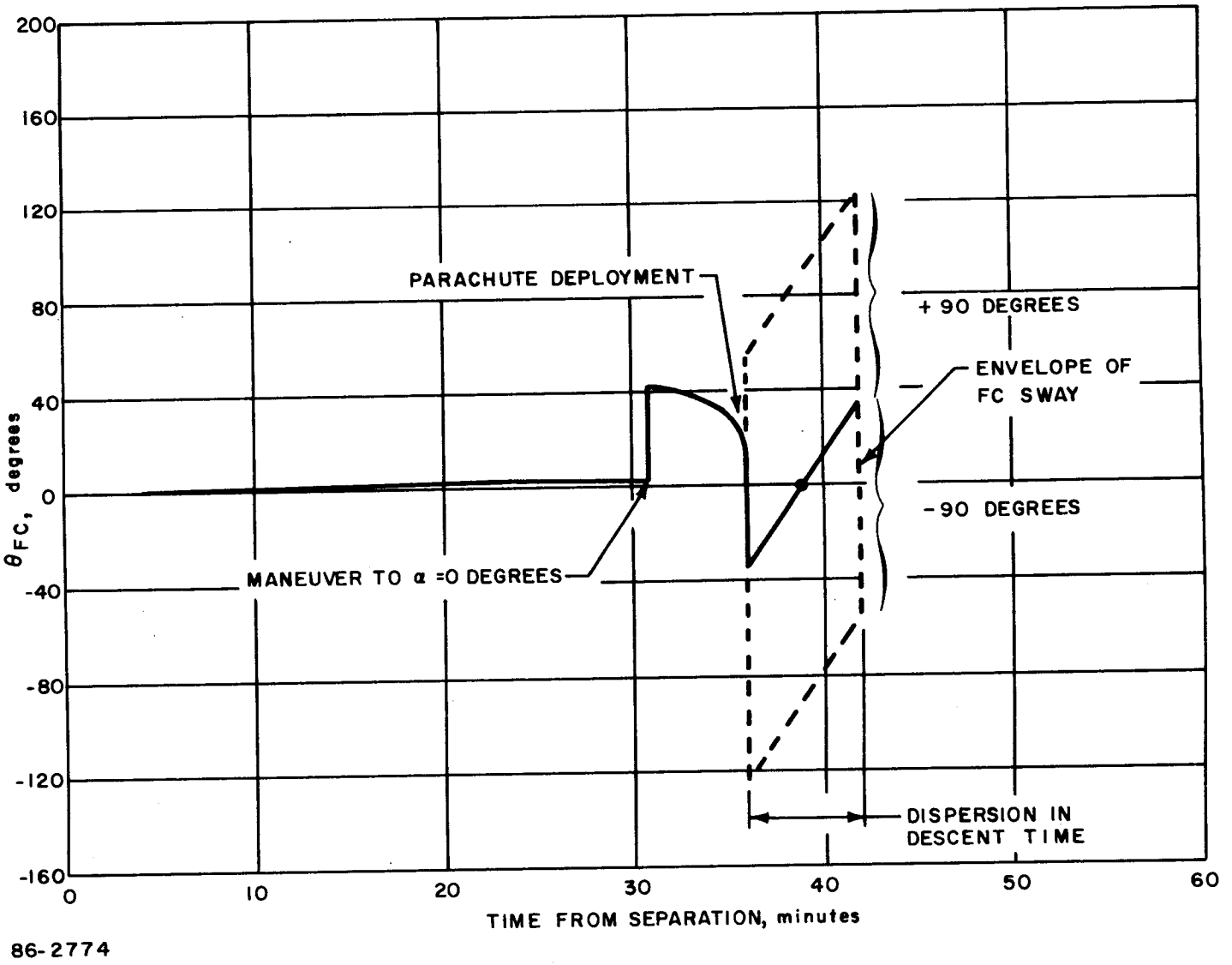

Figure 55 FLIGHT CAPSULE TO FLIGHT SPACECRAFT LOOK ANGLES, 1000 × 10,000 KILOMETER ORBIT

At the midpoint in the dispersion in descent times after parachute deployment, the look-angle is zero degrees. The look-angle can assume large values at two points in the trajectory. The first occurs when the flight capsule maneuvers to a zero angle of attack attitude prior to entry. The second large value is reached during descent if the parachute-suspended flight capsule is exposed to large magnitude wind gusts. Such gusts would cause considerable swaying of the flight capsule, with resultant large look-angles.

The discussion here is limited to the nominal variations in the antenna look-angle. The effects of wind gusts are considered in detail in paragraph 5. 3. 2. 3.

It can be seen from Figure 55 that the largest positive look-angle occurs when the flight capsule maneuvers to a zero angle of attack attitude and that the largest negative look-angle occurs at the time of parachute deployment. Table XXXVIII summarizes the nominal look-angle conditions for all of the orbits considered. The largest nominal look angle variations occur with the 700 x 20, 000 km orbit (-45 to +50 degrees). The antenna look-angle variations are increased substantially, however, when the effects of possible wind gusts are included, as discussed in the next paragraph.

TABLE XXXVIII

FLIGHT CAPSULE ANTENNA LOOK-ANGLE SUMMARY--NO WIND

Periapsis (kilometers)	Apoapsis (kilometers)		
	4000	10,000	20,000
700	-41°/42°	-44°/48°	-45°/50°
1000	-33°/46°	-35°/43°	-37°/41°
1500	-22°/61°	-23°/60°	-25°/58°

5.3.2.3 Effects of Wind Gusts During Descent

During descent, the parachute-suspended flight capsule will be exposed to any large magnitude wind gusts that may occur. The effect of wind gusts on the flight-capsule antenna look-angle is illustrated in Figure 56. As that figure indicates, the flight capsule antenna look-angle (θ_{FC}) is shown for two conditions of the flight capsule swing angle (θ_C).

In the first condition (θ_C = 0 degree), θ_{FC} is the nominal look-angle occuring during descent. In the second condition ($\theta_C > 0$ degree), the nominal θ_{FC} is increased. The capsule swing angle θ_C can, of course either increase or decrease θ_{FC}, according to the direction of the wind. Since the time (or times) at which wind gusts can occur during descent are probabilistic, and since the direction of such wind gusts is also probabilistic, the maximum flight capsule look-angle must be increased by the worst-case magnitude of the antenna swing angle (θ_C). Figure 57 shows the flight capsule swing angle (θ_C) as a function of time for three different wind-gust magnitudes. In the case of the largest magnitude gust (200 ft/sec) θ_C reaches a peak value of 90 degrees. For this reason, the envelope of flight capsule sway was shown on Figure 55 as ± 90 degrees.

Table XXXIX summarizes flight-capsule antenna-beamwidth requirements for all orbits considered, including the effects of wind gusts of 200 ft/sec. The broadest beamwidth required is 270 degrees. This maximum is needed to provide coverage for the 700 x 20,000 km orbit.

TABLE XXXIX

FLIGHT CAPSULE ANTENNA MINIMUM BEAMWIDTH REQUIREMENTS

Periapsis (kilometers)	Apoapsis (kilometers)		
	4000	10,000	20,000
700	262°	268°	270°
1000	246°	250°	254°
1500	224°	226°	230°

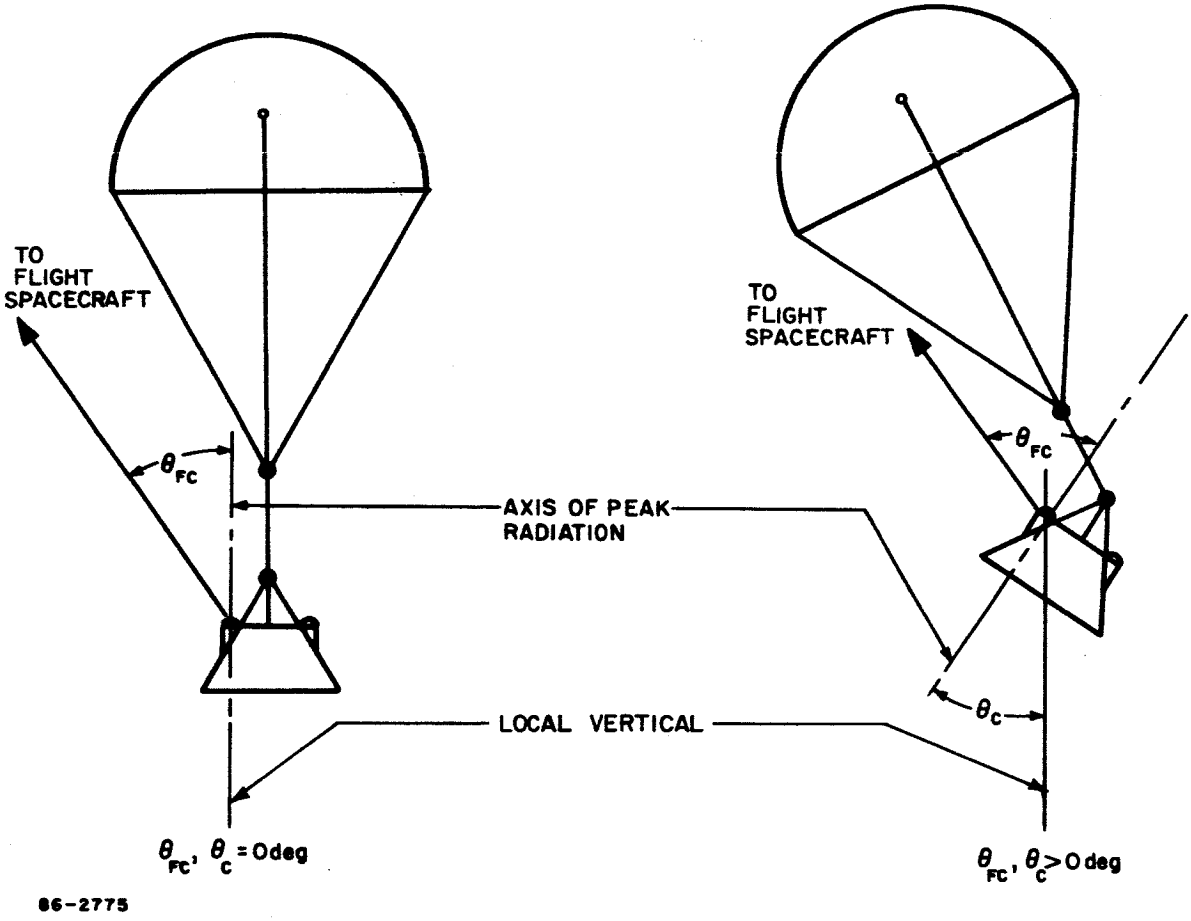

Figure 56 EFFECT OF PARACHUTE DYNAMICS ON FLIGHT CAPSULE LOOK ANGLE

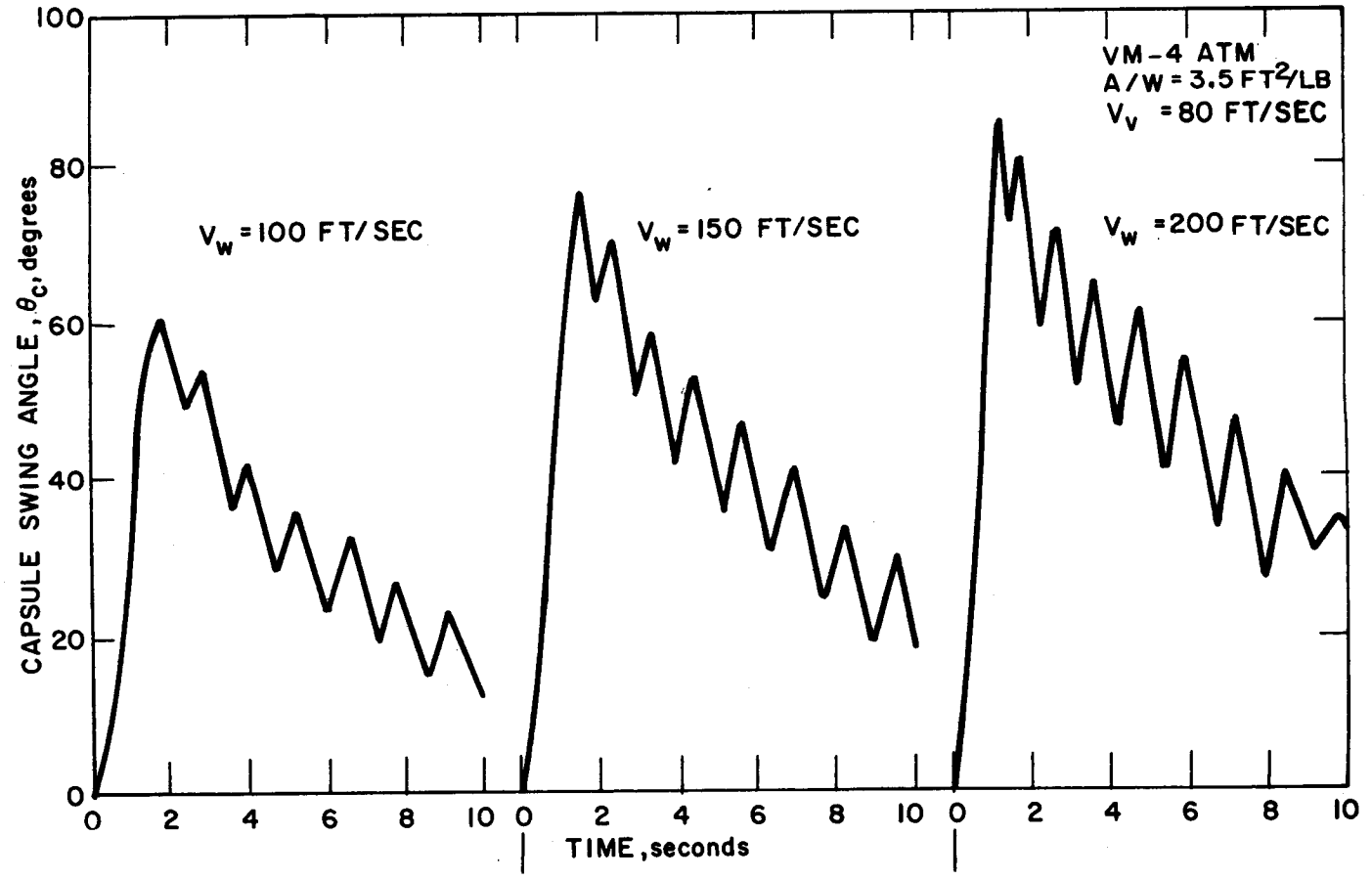

25-1181

Figure 57 PARACHUTE DYNAMICS--FLIGHT CAPSULE SWING ANGLE, EFFECT OF GUST MAGNITUDE

5.3.3 Communication Range

The communication range is defined as the line of sight distance between the flight spacecraft and the flight capsule. Figure 58 illustrates the variations in the communication range over the period from separation to impact for a 1000 x 10,000 km orbit. The minimum range during entry/descent is reached at the midpoint in the descent-time dispersion. Although the maximum range occurs during the period from entry to parachute deployment, it is shown in paragraph 5.4.6 that the relay link performance margin is at a minimum during parachute-assisted descent due to wind gust effects. Table XL summarizes the maximum communication ranges for all orbits considered. The longest range over which relay-link communication must be maintained is 1700 km. This occurs for the 1500 x 20,000 km orbit.

TABLE XL

COMMUNICATION RANGE SUMMARY

Range (kilometers)			
Periapsis (kilometers)	Apoapsis (kilometers)		
	4000	10,000	20,000
700	1200	1240	1300
1000	1300	1340	1400
1500	1620	1640	1700

5.3.4 Range-Angle-Beamwidth Summary

Table XLI summarizes the communication range, flight spacecraft body-fixed antenna position angles, and the flight spacecraft and flight capsule antenna beamwidth requirements as a function of the three periapsis altitudes considered. With the exception of the total trajectory PSP antenna beamwidth requirements, both the flight capsule and flight spacecraft antenna beamwidth requirements decrease as periapsis increases. The potential improvement in relay link performance provided by increased antenna gain (as a result of decreased beamwidth) is offset, however, by the increase in range which accompanies an increase in the periapsis altitude.

The maximum flight capsule antenna beamwidth required under no-wind conditions is 100 degrees. Consideration of wind gusts to 200 ft/sec

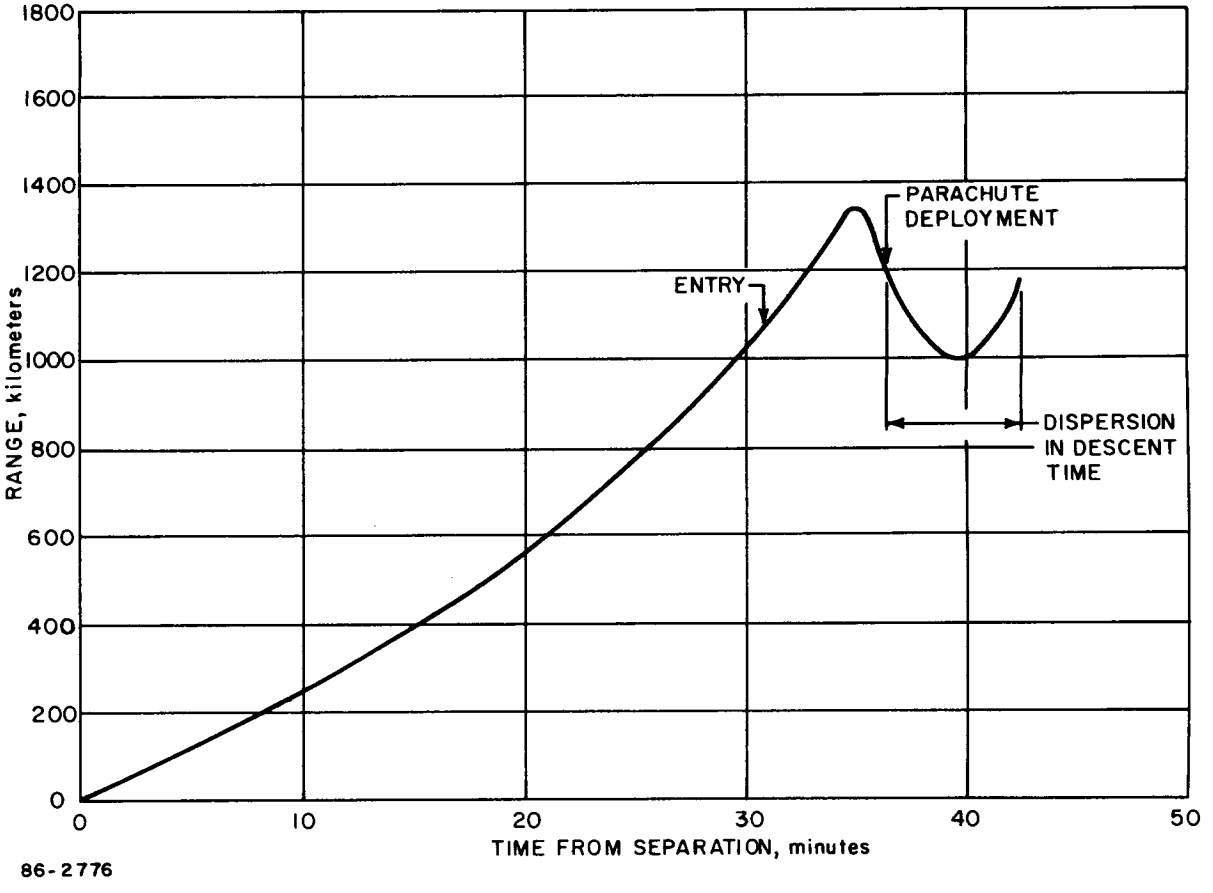

Figure 58 COMMUNICATION RANGE SUMMARY, 1000 x 10,000 KILOMETER ORBIT

TABLE XLI

COMMUNICATION GEOMETRY RANGE-ANGLE SUMMARY

Periapsis Altitude	700 km	1000 km	1500 km	ALL
Range	1300 km	1400 km	1700 km	1700 km
FS Antenna Position				
Clock	199° - 237°	226° - 245°	252°	234°
Cone	160° - 152°	156° - 147°	140°	153°
FC Antenna Beamwidth				
Without wind	95°	78°	83°	97°
With 200 ft/sec wind	270°	254°	230°	270°
FS Antenna Beamwidth				
Body-Fixed (repositioned)	125°	100°	65°	125°
Body-Fixed (single position)	125°	100°	65°	130°
PSP				
(entry/descent)	85°	60°	40°	85°
(total trajectory)	90°	80°	120°	135°

increase this value to a maximum of 270 degrees. In effect, the flight capsule antenna must provide nearly omnidirectional coverage. Little improvement can be obtained by limiting orbits to a 1500 km minimum periapsis since the minimum required beamwidth will still remain very large -- 230 degrees for that periapsis altitude.

A beamwidth of 130 degrees is required for a single-position body-fixed flight spacecraft antenna. This is 5 degrees wider than that required by a body-fixed flight spacecraft antenna designed to be appropriately positioned before launch for the particular orbit to be used. The 130 degree beamwidth requirement indicates that the body-fixed antenna must provide nearly hemi-omni coverage.

A PSP antenna used for the total trajectory would require a beamwidth slightly larger than that required by a body-fixed antenna, although a substantial decrease in required PSP antenna beamwidth could be realized if only the entry/descent portion of the mission were considered. On the basis of this analysis it is reasonable to conclude that a single-position body-fixed antenna is the best candidate for flight spacecraft relay link antenna applications from the viewpoint of minimum total beamwidth and maximum simplicity.

5.4 RELAY LINK RADIO FREQUENCY ANALYSIS

The following critical factors formed the basis for evaluating the radio frequency (RF) performance capabilities of the relay link.

1. Relay link
2. Communication medium
3. Antenna concept
4. Operating frequency

5. Transmitter power

6. Modulation-detection technique

The effects of relay link geometry with its constraints on range and on the beamwidths of flight capsule and flight spacecraft antennas were discussed in Paragraph 5.3. The remaining critical factors in the relay link RF analysis are discussed in detail in paragraphs 5.4.1 through 5.4.5. Paragraphs 5.4.6 and 5.4.7, respectively, present an analysis of the relay link RF performance and failure mode considerations.

5.4.1 Communication Medium

The performance of the flight spacecraft-flight capsule RF relay link is affected to a significant degree by the medium in which the link must operate. As will be discussed in detail in subsequent paragraphs, the effective noise temperature of the flight spacecraft relay link RF receiver is degraded by the thermal radiation emanating from a number of sources and intercepted by the flight spacecraft relay link antenna. Radio frequency attenuation, or blackout, occurs as the result of plasma formation that accompanies flight capsule entry. In addition, multi-path reflections from the planet surface cause signal fading.

5.4.1.1 Flight Spacecraft Receiver Noise Model

1. Introduction -- The following paragraphs accurately define a suitable noise model for the flight spacecraft relay link data receiver. Such a model is necessary if relay communication link nominal parameters and tolerances are to be determined with sufficient accuracy to allow development of a reasonable and logical philosophy regarding system operational margins. In this discussion, it is assumed that the flight spacecraft is in the vicinity of Mars and communicating via a relay link with the flight capsule which has entered the Martian atmosphere. All sources of noise which tend to increase the

effective noise temperature of the spacecraft receiver will be considered. In particular, the contribution from each noise source will be analyzed in detail and its effect on the overall system noise temperature will be determined.

2. Generic Communication Link -- Definition of a suitable flight spacecraft receiver noise model can be reduced essentially to the problem of assessing the performance of the generic communication link illustrated in Figure 59. The quantities $G_j \mid j = 1, 2, \cdots \}$ shown in Figure 59 represent the respective exchangeable gains (or attenuation) of the various black boxes making up the overall communication link. Likewise the quantities $N_j \mid j = 1, 2, \cdots \}$ represent the additive noise introduced at the respective black boxes. In addition, for each component in the communication link illustrated in Figure 59, there exists a quantity, F_j, called the noise figure. F_j is defined as follows.

$$F_j = \frac{(S_j/N_j)_{in}}{(S_j/N_j)_{out}} \tag{1}$$

where S_j/N_j is the signal to noise ratio (SNR) existing at the appropriate terminal (output or input) of the j^{th} component in the communication link. The overall noise figure for n components in cascade is given as[2]

$$F_T = F_1 + \frac{F_2 - 1}{G_1} + \frac{F_3 - 1}{G_1 G_2} + \cdots \frac{F_n - 1}{\prod_{j=1}^{n-1} G_j} \tag{2}$$

In this analysis, however, it is important to obtain results that are useful in the preparation of a telecommunications design control chart. Equation (2) is awkward in this regard. The effective system noise temperature may be defined more conveniently for this purpose as follows:

$$T_e = T_1 + \frac{T_2}{G_1} + \cdots \frac{T_n}{\prod_{j=1}^{n-1} G_j} \tag{3}$$

The major noise contributions for the generic system under consideration will be due to units 1 through 4 as shown on Figure 59. Equation (3) can then be written as:

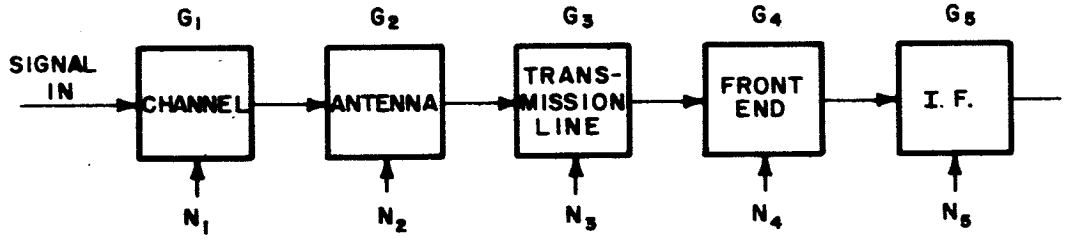

Figure 59 GENERIC COMMUNICATION LINK

$$T_e = T_1 + \frac{T_2}{G_1} + \frac{T_3}{G_1 G_2} + \frac{T_4}{G_1 G_2 G_3} \qquad (4)$$

The problem reduces to determining the quantities $T_j \{ j = 1, 2, 3, 4 \}$ and assessing their effect on overall system performance.

3. Evaluation of Noise Contributions

a. Channel -- In analyzing the noise contributed by the channel portion of the overall communication link, a simplified model in which a linear addition of signal plus noise is assumed will be considered. This assumption is reasonable for a direct line-of-sight link, such as the relay link that does not utilize a scatter mechanism as the primary propagation mode.

The geometry of the relay link is illustrated in Figure 60. The spacecraft antenna intercepts thermal radiation from a number of sources. The effect of this radiation is an increase in the effective noise temperature of the system. It is customary[3] to equate the total received noise power to that which would have been received by an equivalent black body, at temperature T_a, which completely surrounds the antenna. Since an antenna terminated in its radiation resistance is in thermodynamic equilibrium with the equivalent black body, the temperature (T_a) is that temperature to which the radiation resistance of the antenna must be raised in order to produce the same effect as the black body. Thus, in order to account for all sources of noise, it is only necessary to compute the effective antenna temperature T_a.

The equivalent black-body temperature of a body depends upon its ability to absorb energy. It can be shown[4] that the equivalent antenna temperature produced by a body at thermal temperature T_s with fractional absorption of electromagnetic energy ξ, is given by the following.

$$T_a = \xi T_s \qquad (5)$$

This expression is correct only when the solid angle subtended by the source of radiation is greater than the antenna beamwidth in steradians. When the solid angle, Ω_1, subtended by the source is less than the antenna beamwidth, Ω, in steradians, the expression

$$T_a = \xi T_s \left(\frac{\Omega_1}{\Omega} \right) \qquad (6)$$

must be used.

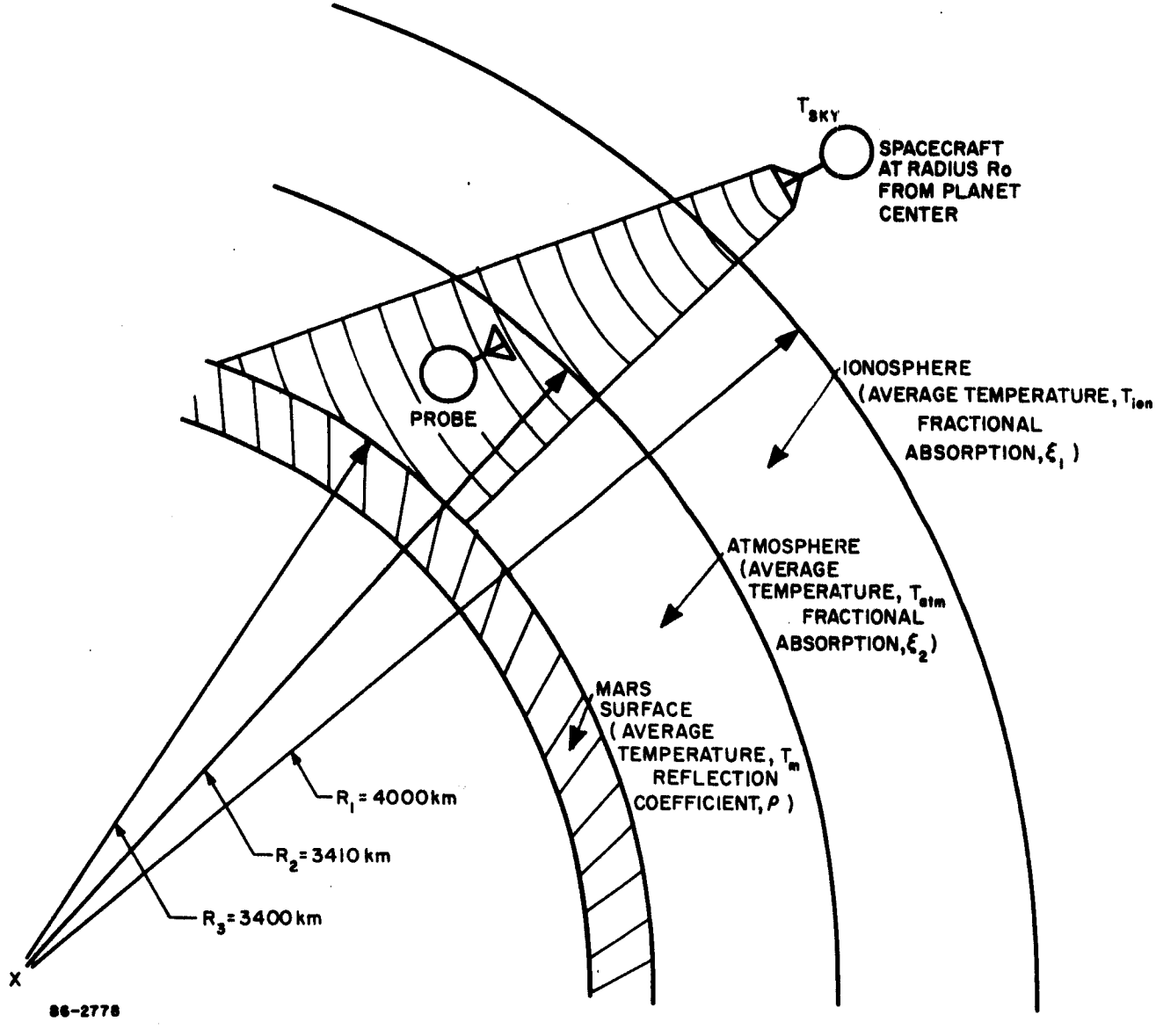

Figure 60 GEOMETRY OF MARS RELAY LINK

Thus, referring again to Figure 60, it can be seen that the effective antenna temperature at the flight spacecraft is given as

$$T_1 = T_{sky} + \left(\frac{\Omega_1}{\Omega}\right) \xi_1 \, T_{ion} + \left(\frac{\Omega_2}{\Omega}\right)\left(1 - \xi_1\right) \xi_2 \, T_{atm} \tag{7}$$

$$+ \left(\frac{\Omega_3}{\Omega}\right)\left(1 - \xi_1\right)\left(1 - \xi_2\right) \xi_3 \, T_M$$

The geometrical considerations on which the determination of (Ω_1/Ω) is based are shown on Figure 61.

From that figure, it is evident that

$$\frac{\Omega_j}{\Omega} = \frac{\int_0^{\theta_j/2} \sin\theta \, d\theta \int_0^{2\pi} d\phi}{\Omega} \tag{8}$$

$$= \frac{2\pi\left[1 - \cos\frac{\theta_j}{2}\right]}{\Omega}$$

where:

$$\frac{\theta_j}{2} = \tan^{-1}\frac{R_j}{R_0}$$

It would, of course, now be possible to construct a table giving values of (Ω_1/Ω) for typical values of R_o, and various antenna half-power beamwidths, θ. However, the effort involved in performing the computations necessary to compile such a table is not warranted at the present time as will be obvious after a consideration of the relative magnitudes of the quantities in Equation (7). If, for example, a worst case is assumed, that is $(\Omega_j/\Omega) = 1 \{ j = 1, 2, 3 \}$, then Equation (7) becomes

$$T_1 \cong T_{sky} + \xi_1 T_{ion} + \xi_2(1 - \xi_1) T_{atm} \tag{9}$$

$$+ (1 - \xi_1)(1 - \xi_2) \xi_3 \, T_M$$

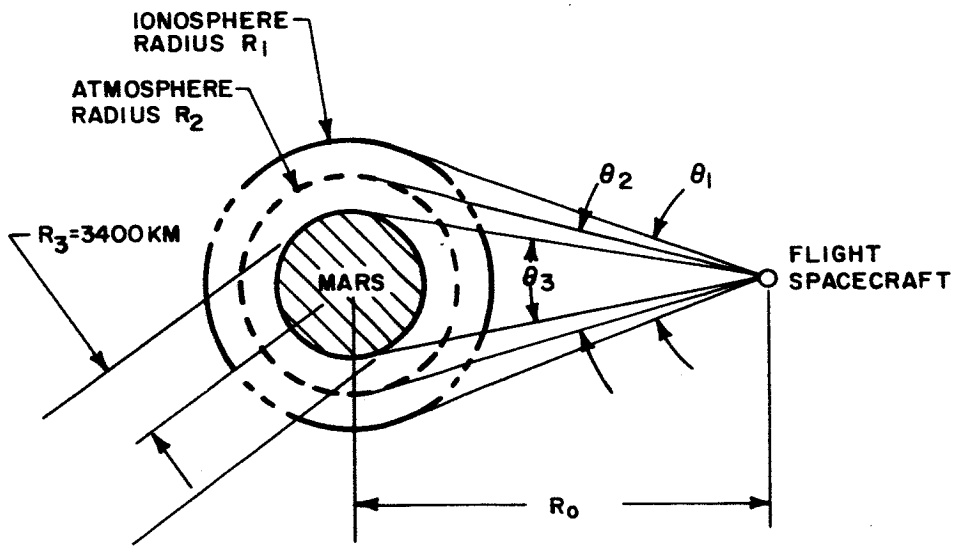

Figure 61 GEOMETRY FOR DETERMINING (Ω_j/Ω)

Consider, then, each of the terms in the above expression (Equation 9). The electron temperature of the ionosphere T_{ion}, will be taken as the predicted worst-case (VM-3 atmosphere model) value of 200° K. The fractional absorption, ξ_1, is shown in paragraph 5.4.1.2 to be approximately 0.04. Thus, the contribution of the antenna effective noise temperature due to the ionosphere becomes

$$\xi_1 T_{ion} = (0.04)(200°K) = 8°K \tag{10}$$

This value is essentially negligible.

As for the contribution due to the atmosphere, T_{atm} can be taken as 275°K (worst case VM-3 atmospheric model). The quantity ξ_2 depends upon the atmospheric constituents. However, the worst case condition can be determined by evaluating ξ_2 for the much denser atmosphere of Earth. The atmospheric attenuation in dB/km vs. wavelength is plotted in Kerr[5]. That data indicates that at $\lambda \approx 1$ meter, the attenuation is approximately 0.005 db/km. Assuming a standard atmosphere 10 km high, the attenuation is approximately 0.05 dB. Thus $\xi_2 = 0.011$, and the contribution due to the atmosphere is approximately

$$\xi_2(1 - \xi_1) T_{atm} \approx (0.011)(0.96)(275°K) = 2.6°K \tag{11}$$

This value, too, is essentially negligible.

Now considering the planet itself, assuming that $T_M = 296°$ K (Reference 2, page 163) (a worst-case condition) then

$$(1 - \xi_1)(1 - \xi_2)\xi_3 T_M = (0.96)(0.989)\xi_3 (296°K) \tag{12}$$

The relationship between the quantity ξ_3 and the reflection coefficient, ρ, of the Martian surface is given by the following expression,

$$\xi_3 = (1 - \rho) \tag{13}$$

The appropriate value for ρ can be obtained from two published[6,7] results of radar observations of the planet Mars. The results given in both papers are in substantial agreement. It is also obvious from these results that the reflection coefficient varies considerably over the surface of the planet. On the basis of a worst-case condition (taken from both papers) of $\rho = 0.03$, then $\xi_3 = 0.97$, and Equation (12) becomes

$$(1-\xi_1)(1-\xi_2)\,\xi_3\,T_M \approx 272°K \qquad (14)$$

Although this number is significant, it must be remembered that it has to be weighted by the factor Ω_3/Ω given by Equation (8). Table XLII gives representative values for the antenna noise temperature (T_{am}) contribution due to the planet when this factor is taken into consideration.

TABLE XLII

EFFECTIVE ANTENNA NOISE TEMPERATURE CONTRIBUTION DUE TO PLANET

Periapsis Altitude (kilometers)	θ (beamwidth) (degrees)	T_{am} (°K)
700	60	272
	80	272
1000	60	272
	80	243
1500	60	272
	80	207

As an example, the table shows that if the flight spacecraft is at a periapsis of 1,500 km, and the antenna beamwidth is 80 degrees, the effective antenna noise temperature due to the planet is approximately 207°K. It remains now only to consider the contributions due to extraplanetary noise. These are represented by the quantity T_{sky} in Equation (9). This noise temperature component includes noise from a number of different sources. The major sources are:

a) Galactic Noise (T_g)

b) Radio Stars (T_{rs})

c) Solar Radiation (T_s)

d) Planetary Radiation (T_p)

These are discussed in the following paragraphs.

The radio noise, from the galaxy (galactic noise, T_g) is attributed to radiation from the galaxy itself. This is considered to be the most widely distributed of the various extra-planetary sources of radiation. Such radiation appears to be present to some degree in all directions. It is most intense, however, when looking toward the center of the galaxy, and it is at a minimum when observed along the pole about which the galaxy revolves. A plot of the maximum and minimum galactic-noise brightness temperature[8] versus frequency is illustrated in Figure 62. The brightness temperature is defined as the temperature in degrees Kelvin, of an ideal black-body radiator that has the same "monochromatic brightness" (Reference 2, page 14) as the given area of the sky. The term "brightness" is defined for the purposes of this analysis as the received flux density in watts/m^2/Hz that would be received by an antenna which has a beamwidth of one steradian. The brightness (B) and brightness temperature (T_B) are related through the Rayleigh-Jeans approximation to Planck's law. The relationship is:

$$B = \frac{2kT_B}{\lambda^2} \quad \frac{\text{watts}}{m^2/\text{Hz}/\text{steradian}} \tag{15}$$

Since the galaxy constitutes an extended source, it will be assumed as a worst case that the solid angle subtended is larger than the antenna beamwidth. The contribution to the antenna temperature due to galactic noise (T_g) is then equal to T_B. This is true, however, only if the main lobe of the antenna is pointed at the galaxy. In reality, the galaxy may be viewed through a side or backlobe; in such cases the galactic brightness temperature should be weighted by the front-to-back ratio of the antenna. It is also possible for the planet to be in a direct path between the center of the galaxy and the spacecraft and along the main-lobe axis. In this case, the galactic brightness temperature should be weighted by the effect of the shadowing afforded by the planet.

To avoid unnecessarily complicating the analysis, a worst-case condition and a best-case condition will again be assumed. In the worst case, it will be assumed that the center of the galaxy is viewed through the main lobe. In such a case, $T_g = T_B$. In the best case it will be assumed that the center of the galaxy is viewed through the backlobe and, hence, $T_g = T_B/\gamma$, where γ is the flight spacecraft receiving antenna front-to-back ratio. From Figure 62 it can be seen that at approximately 300 MHz (1-meter wavelength)

$$T_B = 400°K \tag{16}$$

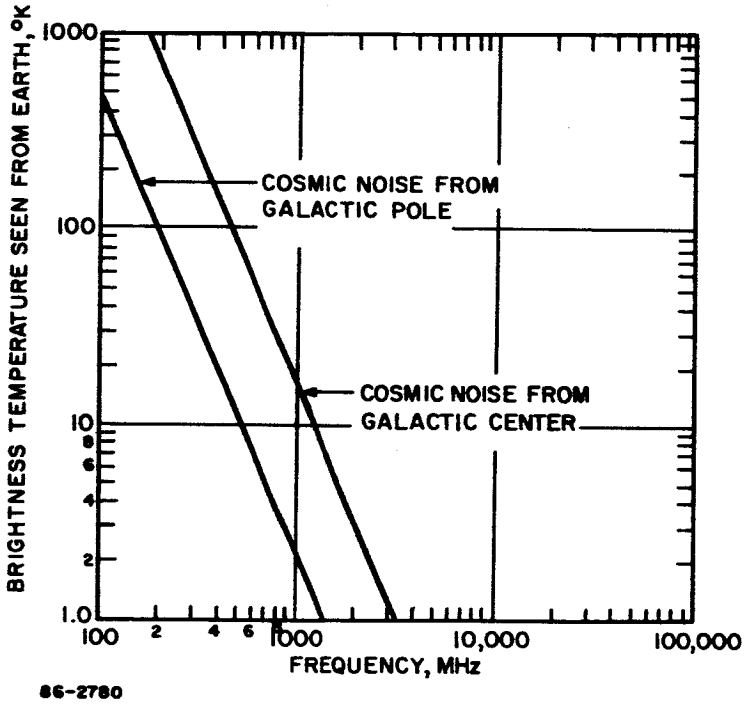

Figure 62 MAXIMUM AND MINIMUM BRIGHTNESS (OR SPACE) TEMPERATURE OF THE SKY AS SEEN BY AN IDEAL SINGLE-POLARIZATION ANTENNA ON EARTH

In the discussion that follows it will be assumed that γ = 10 dB, and that accordingly the quantity T_g can range from 40°K to 400°K.

Smith[9] points out by an example that the noise contribution due to radio stars (T_{rs}) is negligible relative to the galactic background noise unless extremely high-gain, narrow-beam antennas are used. Since this is not the case for the Mars relay link, the effects of radio stars on the generic model communication link can be neglected.

The sun, on the other hand, is a strong emitter of electromagnetic radiation (T_s). The intensity of such radiation from the sun varies with time in an extremely complex and unpredictable way. The radio frequency emission from the sun has three distinct components:[10] that originating from the quiet sun, that from bright regions, and that from such transient disturbances as solar flares. Table XLIII (taken from Reference 3) indicates the different types of solar radio emissions and their characteristics. Figure 63 illustrates the solar flux density and equivalent brightness temperature as a function of wavelength that would be produced on the surface of the Earth. To use these values, the distance between Mars and the sun must be scaled (by the inverse square law). Since Mars is at a mean distance of 1.52 astronomical units (AU) from the sun, the scale factor is $(1/1.52)^2$ = 0.432. Thus, the solar flux density and brightness temperature shown in Figure 63 for Earth must be multiplied by 0.432 to make them applicable to Mars. In the vicinity of Mars the solar noise arrives at the spacecraft antenna terminals via two paths - direct radiation, and reradiation from the planet itself. Accurate knowledge of the pertinent geometry is necessary to determine the exact proportion of each. To avoid computational difficulties due to the many possible geometries, it will be assumed that the geometry will be as illustrated in Figure 64. As shown there, the sun is considered to be directly behind the flight spacecraft and on the Mars-flight spacecraft axis.

The effective antenna noise temperature caused by radiation received via the direct path through the backlobe is, then,

$$T_{S_1} = \frac{\lambda^2 S G_B}{4 \pi k} \qquad (17)$$

where:

S = Flux density at Mars

G_B = Antenna gain at backlobe

k = Boltzman's constant

TABLE XLIII

CHARACTERISTICS OF VARIOUS SOLAR RADIO-EMISSIONS

Type	Duration	Diameter	Apparent Temperature (°K)	Spectrum	Polarization	Origin	Remarks
Quiet sun	11-year cycle	$\geq$ 32 ft increasing with wavelength	$< 10^6$	m, dm, cm	Unpolarized	Thermal	
Slowly varying component	Days to months	Same as for spots and faculae	$<2 \times 10^6$	m, dm, cm	Unpolarized	Thermal	Complex behavior on cm wavelengths with circular polarization
Type I bursts or Noise Storms	Hours to days	Small (minutes of arc)	$\sim 10^9$	m	Circularly polarized	Cerenkov	Simultaneous continuum and short bursts
Type II bursts	Minutes complex		$< 10^{11}$	m, dm; 50 MHz bandwidth slow drift	Usually unpolarized	Plasma oscillations	Due to shock waves; follows start of flare
Type III bursts	Seconds; often in groups	up to 10 ft increasing with wavelength	$> 10^{11}$	m, dm; 5 MHz bandwidth fast drift	Usually unpolarized	Plasma oscillations; Synchrotron; Cerenkov	Caused by fast-escaping particles; flare-associated
Type IV bursts	Minutes to hours	up to 10 ft increasing with wavelength	$\sim 10^{11}$	m, dm, cm	Often circularly polarized	Synchrotron	Often 10 to 20 minutes after flare; upward motion; cosmic ray association
Type V bursts	Minutes	Large	$\sim 10^{11}$	m; wide bandwidth	Sometimes elliptically polarized	Synchrotron	Following type III

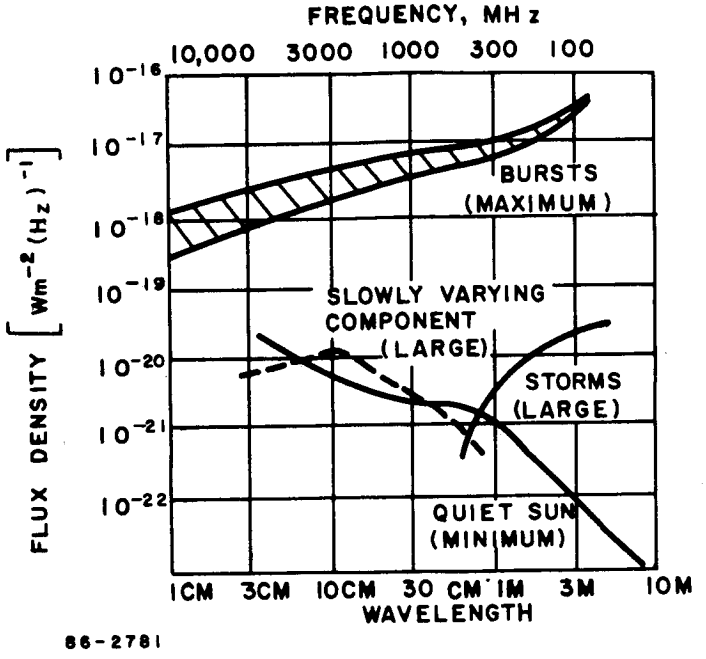

Figure 63 MAXIMUM FLUX DENSITY OF VARIOUS COMPONENTS OF SOLAR RADIO EMISSION AS RECEIVED ON EARTH

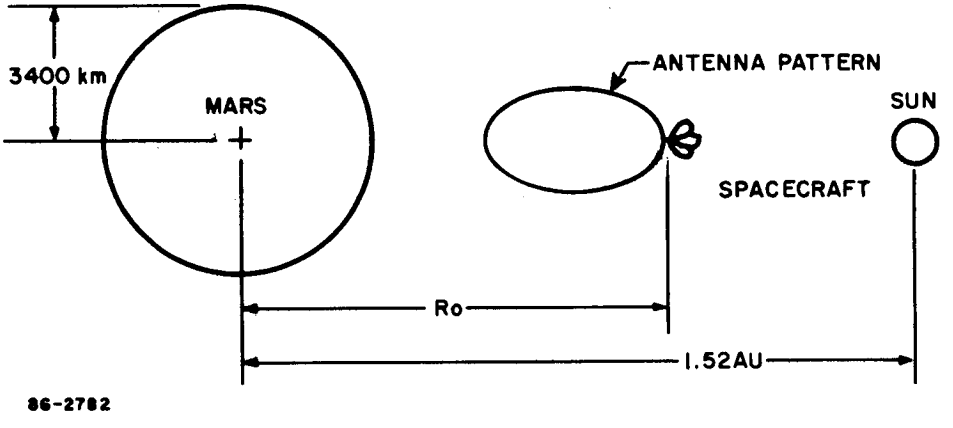

Figure 64 GEOMETRY FOR DETERMINING EFFECTS OF SOLAR RADIATION

The noise power received due to reradiation from the planet into the antenna main lobe can now be considered. The power intercepted by the planet is equal to the product of the flux density, S , and the projection of the planet, πR_3^2 , where R_3 is the radius of Mars (3400 km). Insofar as reradiation is concerned, the planet acts like a sphere which has the property that it scatters radiation uniformly in all directions. Thus, the flux density at the spacecraft at a radius R_o is

$$S' = \frac{\rho \pi R_3^2 S}{4 \pi R_o^2} \tag{18}$$

where: ρ = is the reflection coefficient of the planet surface.

Appropriate values for ρ can be obtained from the two previously referenced articles. Taking a worst case of $\rho = 0.15$, as given in both papers, then

$$S' = \left(\frac{0.15}{4}\right)\left(\frac{R_3}{R_o}\right)^2 S \tag{19}$$

The antenna temperature due to reflection from the planet then becomes

$$T_{s_2} = \frac{\lambda^2 (0.15)}{4}\left(\frac{R_3}{R_o}\right)^2 \frac{S G_0}{4 \pi k} \tag{20}$$

where: G_0 = antenna gain in main lobe.

The total contribution to the antenna temperature is, therefore,

$$T_s = T_{s_1} + T_{s_2} = \frac{\lambda^2 S}{4 \pi k}\left[G_B + \left(\frac{0.15}{4}\right)\left(\frac{R_3}{R_0}\right)^2 G_0\right] \tag{21}$$

Letting

$$S = (0.432) S_o \tag{22}$$

where S_o = equivalent flux density at Earth surface and

$$G_B = \frac{G_0}{\gamma} \tag{23}$$

where γ = antenna front-to-back ratio.

Equation (21) then becomes

$$T_s = \frac{\lambda^2 (0.432)}{4 \pi k} G_0 S_0 \left[\frac{1}{\gamma} + \left(\frac{0.15}{4} \right) \left(\frac{R_3}{R_o} \right)^2 \right] \quad (24)$$

or

$$T_s = K S_o \quad (25)$$

The quantity K is given in Table XLIV for various combinations of G_0, γ, and periapsis altitudes at a wavelength of one meter.

TABLE XLIV

TABULATION OF K FOR VARIOUS PARAMETERS

Periapsis Altitude (kilometers)	G_o (decibels)	γ (decibels)	K
700	6	10	1.25×10^{21}
		20	3.56×10^{20}
	10	10	3.13×10^{21}
		20	8.9×10^{20}
1000	6	10	1.21×10^{21}
		20	3.21×10^{20}
	10	10	3.03×10^{21}
		20	8.01×10^{20}
1500	6	10	1.17×10^{21}
		20	2.78×10^{20}
	10	10	2.94×10^{21}
		20	6.95×10^{20}

Some typical system parameters can be taken from that table and the effects of solar radiation for different levels of activity can then be calculated. As an example, for a periapsis of 700 km, G_o = 6 db, and γ = 10 db, the contribution to effective antenna temperature for different levels of solar activity are as illustrated in Table XLV. The values of flux density used to compute the quantities in Table XLV were taken from Figure 63. The value of flux density corresponding to solar flares, as taken from this figure, is about an order-of-magnitude higher than that reported elsewhere (see Reference 3, Figure 7-6, page 126 or Reference 9, page 596). Nevertheless, even if the more conservative value is taken, it is evident that the effects of solar flares will present a serious problem in regard to relay link communications.

TABLE XLV

CONTRIBUTION TO EFFECTIVE ANTENNA TEMPERATURE DUE TO SOLAR RADIATION FOR VARIOUS LEVELS OF SOLAR ACTIVITY

Solar State	T_S Total (°K)
Quiet	1.25
Storm	2.5
Flare*	12,500 / 1250

*Larger temperature corresponds to data from Reference 3, page 14. The lower temperature corresponds to data reported in Reference 3 and elsewhere.

The frequency of occurrence of solar flares of such a magnitude as to interrupt communications must also be considered.

Solar radio bursts have been observed on all wavelengths from millimeter and centimeter wavelengths down to meter and dekameter wavelengths. In this analysis, only bursts at meter wavelengths need be considered since the proposed Mars relay communication link is intended to operate in the vicinity of 300 MHz (approximately 1-meter wavelength). The different types of flares and their pertinent characteristics are tabulated in Table XLIII.

Type I flares, or solar storms, produce an effective antenna temperature of only 1.25°K, and hence, as indicated on Table XLV, their effects can be neglected.

Type II bursts are relatively rare events, occurring only about once every 50 hours even during periods of maximum sunspot activity. A plot (see Reference 10, page 336) of the frequency of occurrence of Type II bursts for the years 1949-1961 is illustrated in Figure 65.

This figure indicates a marked increase in occurrence of Type II bursts concurrent with increased sunspot activity. It is also observed that the maximum sunspot activity occurred in 1957-1958. Since the period of maximum sunspot activity is 11.2 years, the next period of maximum sunspot activity should occur in approximately the period 1968-1969. It should also be noted that considerable sunspot activity can be expected to exist until approximately 1971. The level of solar activity should be somewhat lower after 1971, if the data portrayed in Figure 65 is typical of the Type II burst phenomenon. Since Mars Probe/Lander missions are contemplated for the 1971 and 1973 opportunities, it is obvious that these missions will follow so closely after the decrease in activity of the solar cycle that they will probably experience some solar radio emissions. This observation only serves to emphasize the fact that the presumably obscure factor of solar radio emission must be carefully considered in overall mission design.

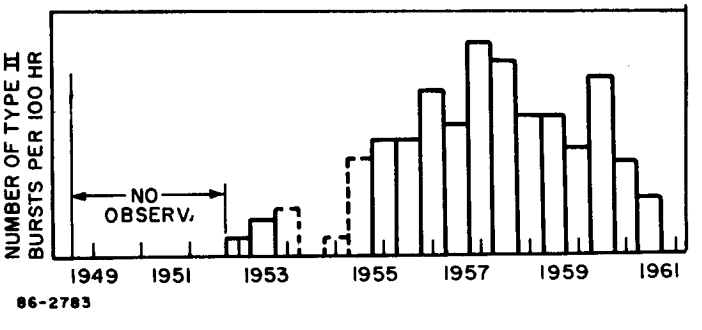

Figure 65 FREQUENCY OF OCCURANCE OF TYPE II BURSTS IN COURSE OF THE SOLAR CYCLE

Kundu (see Reference 10, page 281) emphasizes that on a shorter time scale than that shown in Figure 65 the bursts do not appear to be randomly distributed in time, but tend to occur in groups over a period of several days. Nevertheless, in order to determine the effects of such solar bursts on overall mission success, a uniform distribution of approximately one burst per 50 hours during the time of maximum sunspot activity will be assumed. The total duration of a Type II burst is, typically, on the order of 5 to 10 minutes. Such a period, while relatively short is potentially capable of blacking out a complete Mars entry mission whose total communication time is on the order of from several hundred seconds to approximately 6 minutes. However, certain characteristics of Type II bursts can be considered favorable, as the following discussion indicates.

The onset of a typical Type II burst is sudden and marked by almost simultaneous appearance of a fundamental frequency and a second harmonic of that frequency. The second harmonic can equal or exceed the intensity of the fundamental. The fundamental frequency most commonly starts in the range between[11] 75 and 100 MHz, but has been observed to start as high as 240 MHz. Figure 66 gives some idea of the relative occurrence of various starting frequencies. This figure is taken directly from Reference 10, page 340.

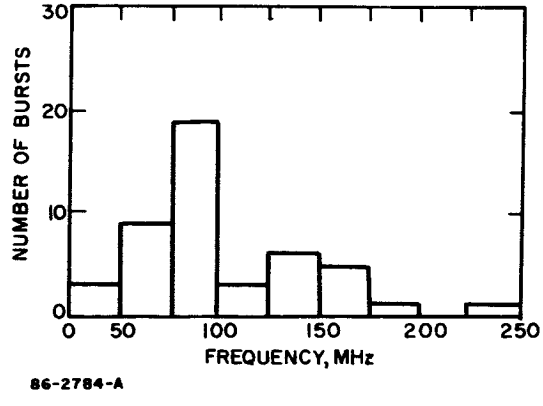

Figure 66 SORTING FREQUENCY OF FUNDAMENTAL BANDS OF TYPE II BURSTS

If any noise from a Type II burst is to affect relay link communication operating at approximately 300 MHz, the starting frequency must be at least 150 MHz. The approximate probability with which the starting frequency is 150 MHz or greater can be determined numerically from Table LI. This value is approximately one-seventh. Thus, the relative frequency of occurrence of Type II bursts that have starting frequencies of at least 150 MHz is one every 350 hours.

In addition to the relative frequency of their occurrence, the effects of the very rapid drift that is characteristic of Type II bursts must also be considered. The mean drift rate is about[10] 1 MHz in the frequency region of interest. The emission which is confined to a band approximately 50 MHz wide, drifts from the starting frequency toward lower frequencies. Thus, the maximum duration of the blackout at any one frequency can be 50 seconds. It is difficult, however, to interpolate the probability distribution of blackout time with any real accuracy in view of the meager statistics available on the occurrence of Type II bursts. Nevertheless, the relative frequency of occurence of a Type II burst capable of disrupting communications to any extent can be determined to be less than one in 350 hours. Assuming that the maximum duration of a Type II burst is approximately 10 minutes, the probability of occurrence of a Type II burst in any given 10-minute time interval suitable for a planetary entry mission is less than

$$P = \frac{10}{(60)\ (350)} \approx 0.0005 \qquad (26)$$

This is, of course, an extremely low value. Thus, it appears that the adverse effects of occurrence of Type II bursts can be eliminated from further consideration.

The Type III, or fast drift, burst, is the most commonly occurring feature of the solar spectrum. A Type III burst is characterized by a narrow emission band that drifts rapidly from high to low frequencies. The rate of drift is in excess of 20 MHz at the frequency range of interest. Although these bursts occur sporadically, they occur

much more frequently than Type II bursts. The typical rate of occurrence is about (Reference 10, page 275) three bursts per hour during periods of maximum sunspot activity. The rate is considerably less during periods of minimum sunspot activity. They have a much shorter duration (typically measured in seconds) than the Type II bursts. However, Type III bursts have a strong tendency to occur in groups of from 2 to 10 or more individual bursts that often are unresolved. Thus, it appears that the Type III bursts can have a very pronounced influence on system performance. However, as was the case for Type II bursts, Type III bursts have certain characteristics that tend to nullify such seemingly disastrous effects.

The characteristics of the Type III burst that are of greatest importance are their typically short time durations and fast drift rates. Both of these characteristics appear to be related, however, since fast drift rates imply a short time spent in any one portion of the spectrum. Kundu (Reference 10, page 281) states that for the 1-meter wavelengths, the time duration at any one frequency tends to decrease with increasing frequency. Single-frequency, high-time resolution studies indicate that the durations of individual bursts are short, that is, on the order of about 0.25 seconds at 200 MHz and 0.18 seconds at 400 MHz. For a maximum duration of the single burst of about 0.25 seconds, and assuming a sequence of 10 bursts, it can be seen that the occurrence of a Type III burst could potentially disrupt as much as 2.5 seconds of communications time. Such a situation is not too critical for the longer communications time characteristic of lander missions. However, in the case of failure-mode operation resulting from failure of the parachute to open, the mission time may be extremely short. Occurrence of a Type III burst could then jeopardize the complete mission. Again, however, there is a saving possibility. It has been reported[12] that the flux density due to Type III bursts is generally less than 10^{-20} watts/m^2/Hz. In such a case, the antenna noise temperature contribution due to Type III bursts will be approximately 12.5°K for the same parameters as were used in calculating the entries in Table XLV. It is obvious, then, that meaningful prediction of the antenna noise temperature requires knowledge of the statistical distribution of flux density. Although Reference 12 states that the flux density due to Type III bursts is usually less than 10^{-20} watts/m^2/Hz, the possibility exists (although with small probability) that the received flux density can exceed this value by several orders-of-magnitude. The probability of a burst exceeding the stated normal maximum level would certainly be a significant mission parameter. If this number is significantly less than the overall probability of mission success, the contribution due to a Type III noise burst can, of course, be neglected. Unfortunately, this probability cannot be computed from the meager statistics available regarding Type III bursts. This is one area in which additional effort should be expended.

A Type IV burst appears as a continuum of long duration, characterized by a persistent, nearly featureless emission over a broad range of frequencies. This type of burst, when it occurs, occurs after intense solar flares, and usually follows a Type II burst. It may last for a period of from 10 minutes to several hours. The flux density produced by Type IV burst radiation is quite severe. It ranges from (Reference 10, page 396) approximately 5×10^{-22} watts/m^2/Hz to about 10^{-18} watts/m^2/Hz. Occurrence of a Type IV burst is, however, a relatively rare event. They occur less than 30 times per year during periods of maximum sunspot activity and less often during periods of lesser sunspot activity. Figure 67 gives some indication of the relative frequency of occurrence of Type IV bursts.

The effects of radiation from Type IV bursts can be dismissed from further consideration because of their relatively low frequency of occurrence.

Type V bursts follow Type III bursts and are characterized by a broadband continuum radiation lasting for 1 to 3 minutes after the Type III burst. The flux density produced by the Type V burst is very intense. However, the bursts radiate most strongly on frequencies below 150 MHz, and often the high-frequency boundary is relatively well defined by a sharp cutoff. Thus, the Type V burst should not affect a data relay link operating at 300 MHz.

Having considered the important solar radio emissions, it is now possible to construct a table summarizing the effects of each. This has been done in Table XLVI. This table was compiled on the basis of the same system parameters as those used in deriving Table XLV.

Intensive nonthermal radiation (T_p) coming from the planet Jupiter has been observed. Although there is no reason to believe that Jupiter is the only planet exhibiting a nonthermal emission, no such emissions have yet been detected in the solar system except those from Jupiter and from the Sun. The emissions from Jupiter, however, are characteristically at 18 MHz. They will not, therefore, interfere with relay communications at 300 MHz. Thus, contributions because of planetary radiation can be neglected.

From the preceeding discussion of channel noise contributions, it can be concluded that the sky temperature will be essentially that due to galactic noise alone. Although solar noise has been shown to present potential hazards to relay link communications, the probability of occurrence of solar emissions of sufficient intensity to totally disrupt communications is, as noted above, extremely small. Thus, from Equation (9), the effective antenna temperature can be determined as follows.

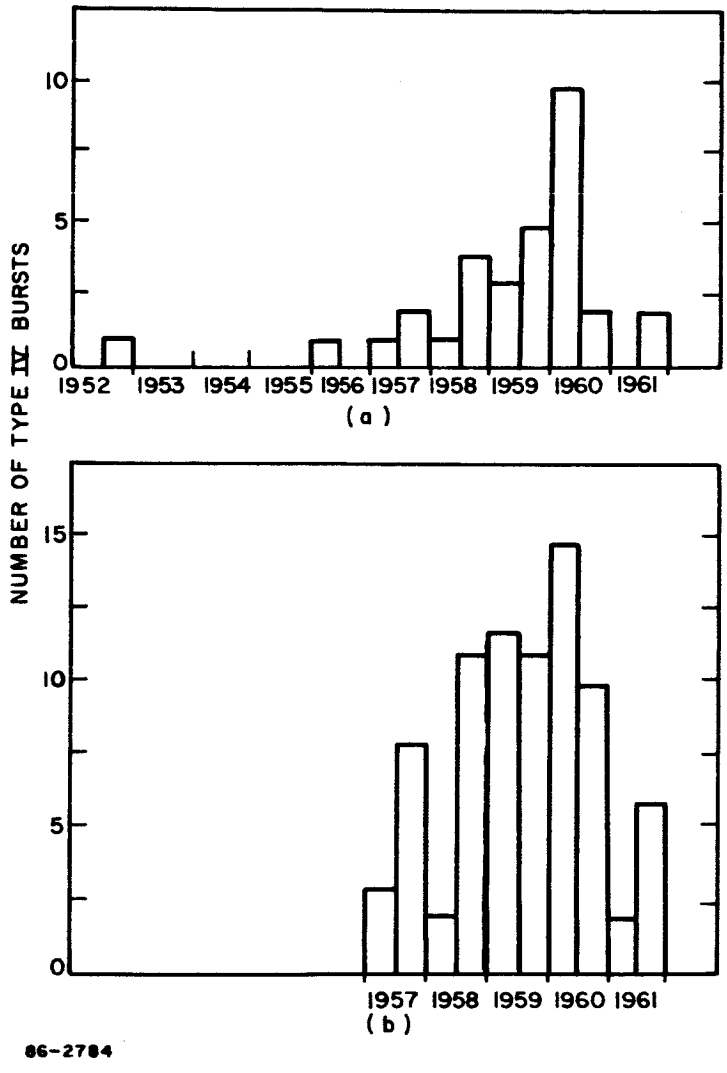

Figure 67 OCCURENCE OF TYPE IV BURSTS ON METER AND DECIMETER WAVES AS A FUNCTION OF THE SOLAR CYCLE (a) 25 TO 240 MHz, (b) 100 TO 580 MHz

TABLE XLVI

SUMMARY OF ANTENNA NOISE TEMPERATURE PRODUCED BY VARIOUS SOLAR SOURCES

Source	T_S (max) (°K)	Remarks
Quiet component	1.25	Negligible
Type I burst or storm	2.5	Negligible
Type II burst	12,500 / 1250	Probability of occurrence is approximately 0.0005
Type III burst	12.5	Occurs quite frequently. More accurate statistics required on the flux density distribution. At 125°K, the contribution is negligible, however, even if Ta were much larger, the type III burst is of extremely short duration and would interfere with communications for no more than a few seconds.
Type IV burst	12,500 / 1250	Probability of occurrence is even less than for type II burst
Type V burst	12,500 / 1250	Emission spectrum is limited to approximately 150 MHz and hence will not interfere with relay data link operating at 300 MHz.

$$T_1 \approx T_g + (1-\xi_1)(1-\xi_2)\,\xi_3\,T_m \tag{27}$$

Appropriate values for the second quantity in Equation (27) are found from Table XLII. From these values, it is possible to construct a table indicating total effective antenna temperature, T_1, as a function of several typical system parameters. This has been done in Table XLVII.

TABLE XLVII

VALUES OF T_1 FOR SOME TYPICAL SYSTEM PARAMETERS

Periapsis (kilometers)	θ (beamwidth) (degrees)	$T_{1\,worst}$ (°K)	$T_{1\,best}$ (°K)
700	60	672	312
	80	672	312
1000	60	672	312
	80	643	283
1500	60	672	312
	80	607	247

It should be noted, however, that T_1 could increase to as high as 13,000°K due to solar emissions whose occurrence is, however, unlikely as Table XLVI indicates.

b. Antenna -- The noise contributions due to sidelobes have been covered previously. Only the antenna efficiency noise contributions now remains to be considered. The antenna noise temperature (T_2) contribution due to antenna efficiency, ϵ, is

$$T_2 = T_0(1-\epsilon) \tag{28}$$

where $T_0 = 290°K$

For an efficient radiating structure, this contribution will be negligible.

c. Transmission Line -- The transmission line noise contribution (T_3) for a transmission line of fractional loss L is given by the following expression

$$T_3 = L\ T_0 \tag{29}$$

Again, if the loss in the transmission line is kept small, this contribution is negligible.

d. Receiver Front End -- The excess noise contribution due to the Receiver front end (T_4) is given in terms of the receiver noise figure F, as

$$T_4 = (F - 1)\ T_0 \tag{30}$$

4. Resultant System Noise Temperature -- In 3. above, the excess noise contributions from each of the components 1 through 4 in the generic communication link illustrated in Figure 59 were evaluated. The total system noise temperature can now be determined from Equation (4) as

$$T_e = T_1 + T_2 + \frac{T_3}{\epsilon} + \frac{T_4}{\epsilon(L - 1)} \tag{31}$$

or, substituting equivalent values, as

$$T_e \approx T_1 + (1 - \epsilon)\ T_0 + \frac{L\ T_0}{\epsilon} + \frac{(F - 1)\ T_0}{\epsilon(L-1)} \tag{32}$$

The overall system noise figure can then be obtained from T_e as follows.

$$F_s = 1 + \frac{T_e}{T_0} \tag{33}$$

It is possible at this point to tabulate T_e and F_s for different values of the system parameters. Rather than do this for all possible combinations of variables, however, it will be done only for the typical case where: ϵ = 80 percent and L = 3.0 db. The overall effective noise temperature, T_e, and resultant noise figure F_s for such a case, is tabulated in Table XLVIII. This tabulation has been performed for both a worst case and a best case. These represent, respectively, the maximum and minimum values of galactic noise temperature, T_g.

TABLE XLVIII

OVERALL SYSTEM NOISE FOR SOME TYPICAL SYSTEM PARAMETERS

Periapsis Altitude (kilometers)	θ (Beamwidth) (degrees)	F (decibels)	Te (Best) (°K)	Te (Worst) (°K)	Fs (Best) (decibels)	Fs (Worst) (decibels)
700	60	3	814	1174	5.80	7.04
		6	1630	1990	8.20	8.96
		10	4050	4410	11.73	12.09
	80	3	814	1174	5.80	7.04
		6	1630	1990	8.20	8.96
		10	4050	4410	11.73	12.09
1000	60	3	814	1174	5.80	7.04
		6	1630	1990	8.20	8.96
		10	4050	4410	11.73	12.09
	80	3	785	1145	5.69	6.94
		6	1601	1961	8.14	8.91
		10	4021	4381	11.74	12.07
1500	60	3	815	1174	5.80	7.04
		6	1630	1990	8.20	8.96
		10	4050	4410	11.73	12.09
	80	3	749	1109	5.54	6.83
		6	1565	1925	8.06	8.83
		10	3985	4345	11.58	12.04

As an example, for a periapsis altitude of 700 km and a half-power antenna beamwidth of 60 degrees, the overall system noise figure will be between 8.20 and 8.96 db (for the two cases considered) for a receiver whose front-end noise figure is 6.0 db.

5. Conclusions and Recommendations -- It is apparent from the preceding discussion that the flight spacecraft receiving subsystem will be affected by an irreducible noise contribution which tends to degrade subsystem performance. Adequate design margins must be allowed for this factor. Table XLVIII summarizes the resultant increase in noise figure for several typical system parameters. From this table, adequate margin allowances for operating system parameters can be predicted for the ranges of interest.

As discussed previously, although the contemplated 1971-1973 missions will closely follow a solar activity cycle, the probability of a complete failure of the relay data link due to solar bursts is quite small. The effects of the more frequently occurring Type III bursts, however, should be studied more thoroughly. In particular, statistics regarding the distribution of received flux density should be obtained.

5.4.1.2 Radio Blackout Due to Plasma Attenuation

During entry, the transmitted signal from the flight capsule may be severely attenuated, or blacked out, by a plasma surrounding the entry vehicle. The following factors affecting radio frequency blackout are discussed below:

1. Entry velocity and atmospheric properties

2. Antenna location

3. Heat shield material

In this analysis of plasma-induced radio blackout, four Martian atmospheric models (VM-3, VM-4, VM-7, and VM-8) and entry velocities from 12,500 to 15,200 ft/sec were considered. All calculations were based on an assumed signal propagation path angle of 30 degrees relative to the vehicle wake axis, as shown in Figure 68. For calculation purposes, it was assumed that temperature, atmospheric density, electron concentration, and collision frequency in the stagnation region were in a state of thermochemical equilibrium. The results of these calculations were then used as a basis for defining electron concentration and collision frequency profiles in the wake region. In defining these profiles a frozen flow state was assumed.

Plasma attenuation is determined in accordance with the following five-step approach: 1) divide the inhomogeneous plasma into N homogeneous layers, 2) calculate the complex dielectric constant in each layer, 3) solve Maxwell's equations exactly for a plane wave in each layer, 4) apply the boundary conditions that E-tangential and H-tangential are everywhere continuous, and 5) evaluate the transmission, reflection, and dissipation coefficients.

The degree of plasma-induced attenuation will vary widely depending upon the orbit chosen and the atmospheric model used. If blackout occurs, the duration of transmission loss may similarly vary according to the orbit and atmospheric model under consideration.

1. Entry Velocity and Atmosphere -- The entry velocity is determined by the orbital parameters and is one of the prime factors determining the degree of plasma attenuation. Small variations in the entry angle and the ballistic coefficient (M/C_DA) may also determine the degree of plasma attenuation, although to a lesser extent than does entry velocity. Entry velocities may vary between 12,500 and 15,200 ft/sec, depending upon the apoapsis and periapsis of the orbit considered. Figure 69 shows a plot of wake attenuation versus altitude, both for the two extremes of entry velocity and for the two atmospheric models that

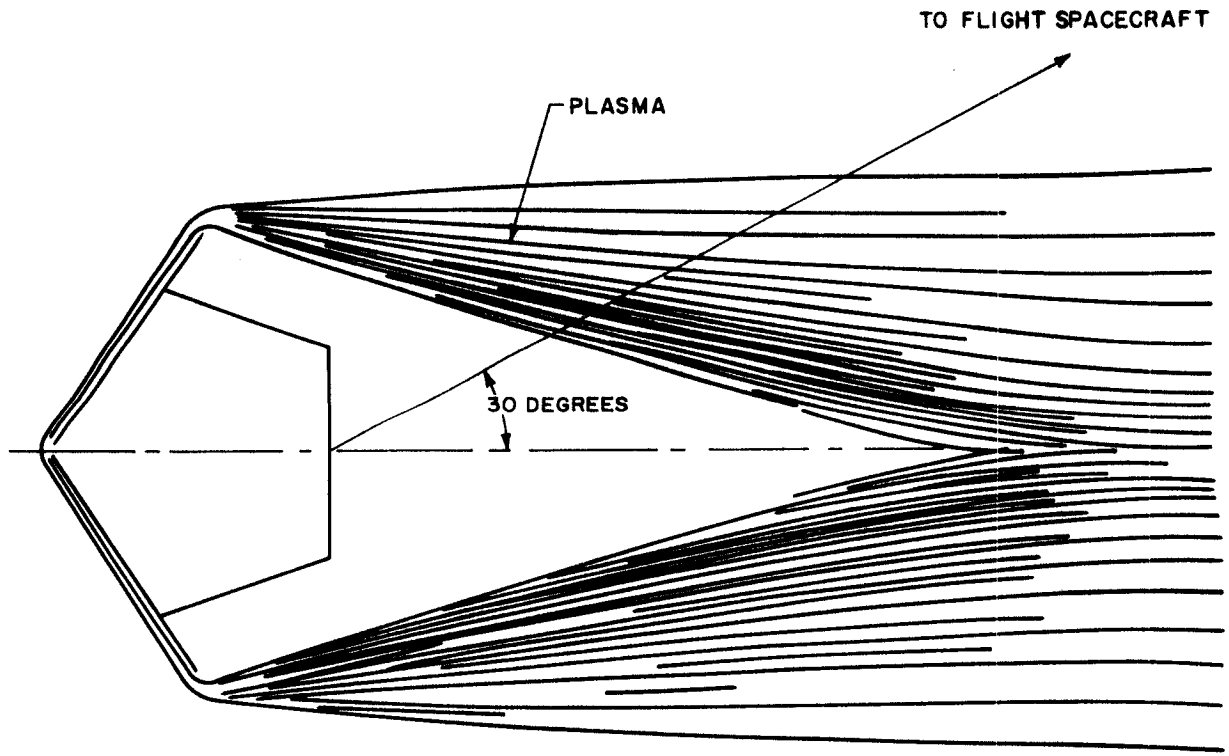

Figure 68 FLIGHT CAPSULE COMMUNICATION THROUGH WAKE PLASMA

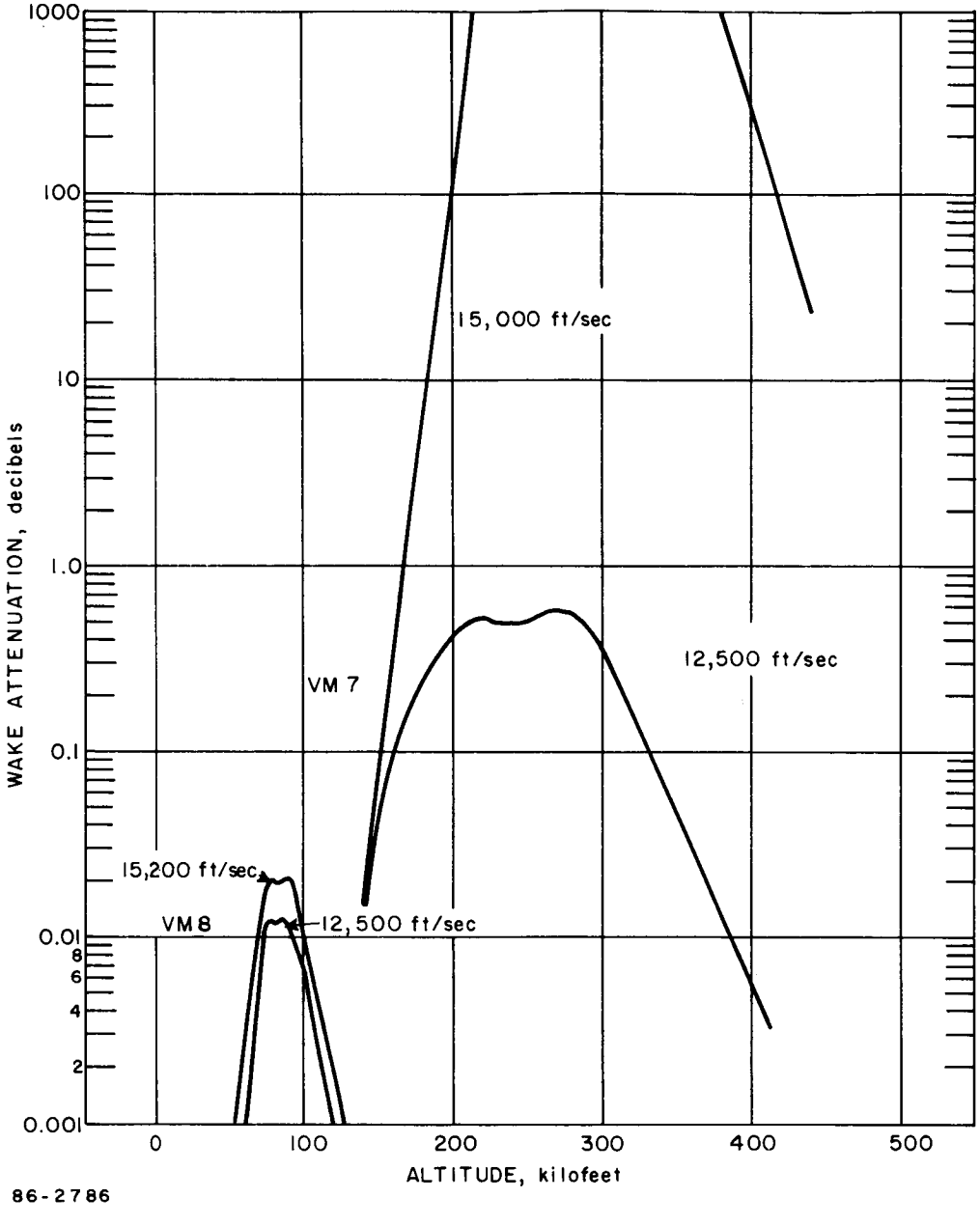

Figure 69 WAKE ATTENUATION VERSUS ALTITUDE

resulted in the most and the least-wake attenuation (the VM-7 and VM-8 models, respectively).

As Figure 69 shows, the wake attenuation for the VM-8 atmosphere will be negligible (less than 0.03 db). If the VM-7 atmosphere is encountered, however, wake attenuation will increase to very high values for entry velocities much above 12,500 ft/sec. Figure 70 is a plot of flight capsule entry velocity (entry velocity is defined here as the velocity at 0.1 g) as a function of apoapsis for the two extremes (700 and 1500 km) of periapsis. It can be seen from this figure that entry velocities will be significantly above 12,500 ft/sec for all except low-eccentricity orbits. For all orbits considered in the present discussion, therefore, blackout conditions are possible if the VM-7 atmosphere is encountered.

Figure 71 shows the peak magnitude of wake attenuation as a function of periapsis for the extremes of both apoapsis and atmosphere. This figure is based on the combined effects of entry velocity and atmosphere. It can be seen that no blackout will occur if the VM-8 atmosphere is encountered and that the extent of wake attenuation can change by several orders-of-magnitude as a function of orbit geometry if the VM-7 atmosphere is encountered.

Figure 72 shows a plot of entry velocity versus altitude for a 700- x 20,000-km orbit in which the VM-3 atmosphere is encountered. Wake attenuation in that atmosphere is quite similar to that obtained in the VM-7 atmosphere. This figure also indicates various constant values of wake attenuation in db's. As Figure 72 indicates, emergence from blackout is rapid for an altitude increment of less than 25,000 feet.

2. Antenna Location -- Plasma losses are also a function of antenna location since attenuation is dependent not only upon the total number of electrons along the transmission path but also upon electron concentration. Electron concentrations are higher toward the front of the vehicle. Accordingly, shorter blackout times may result in the case of an antenna located on the afterbody.

3. Heat Shield Material -- The presence in the heat shield material of contaminants that have low-ionization potentials will significantly increase attenuation during the high velocity (on the order of 15,000 ft/sec), high temperature, phase of entry. Concentrations of sodium or potassium of greater than 100 ppm will certainly cause blackout in the VM-7 atmosphere for high velocities. In this regard, it should be noted that the Purple Blend heat shield material contains 10^4 ppm sodium. For velocities below 12,000 feet per second, however, charring of the heat shield takes place but there is very little ablation of the contaminant-containing portions of the heat shield material.

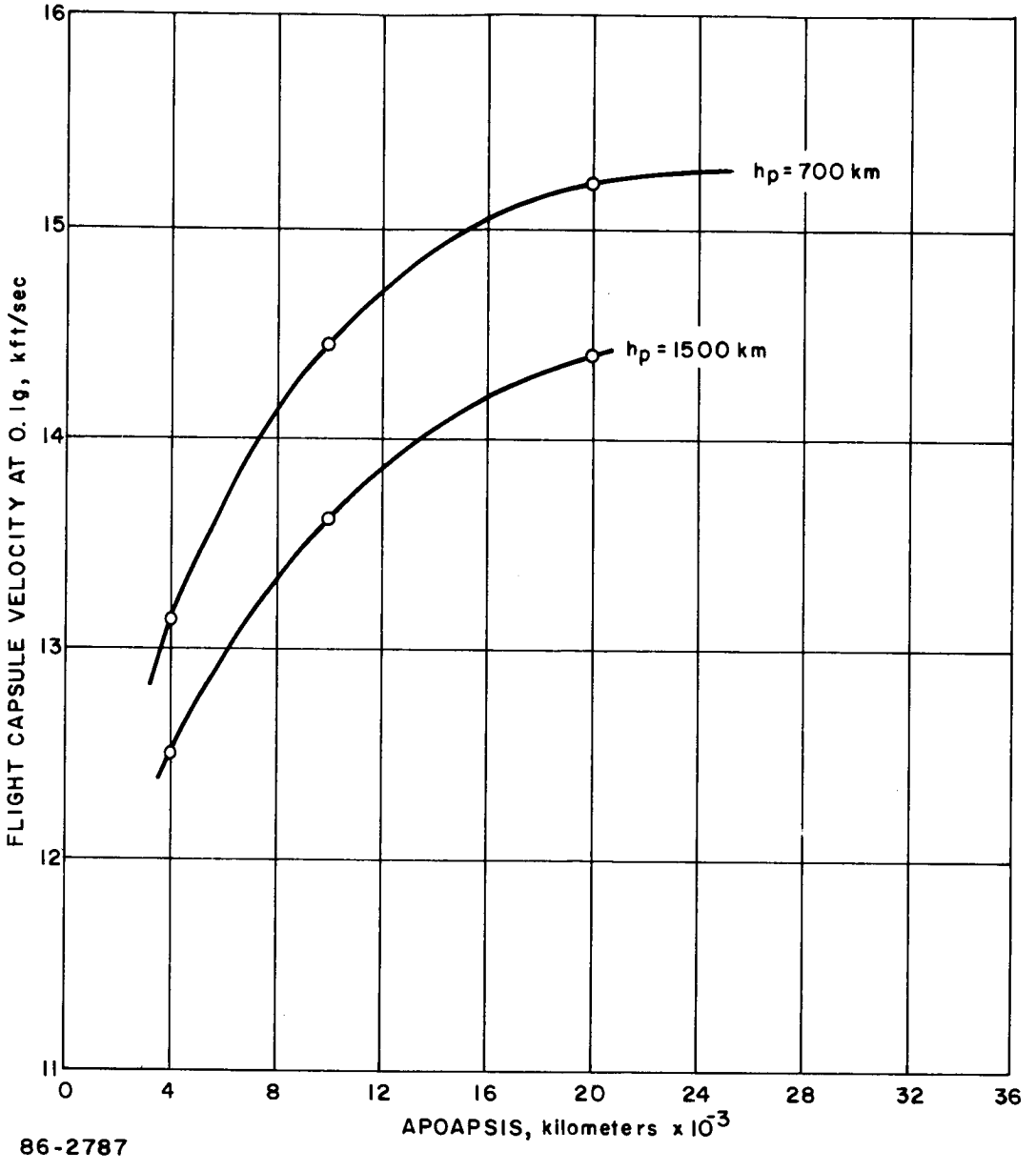

Figure 70 FLIGHT CAPSULE VELOCITY VERSUS APOAPSIS

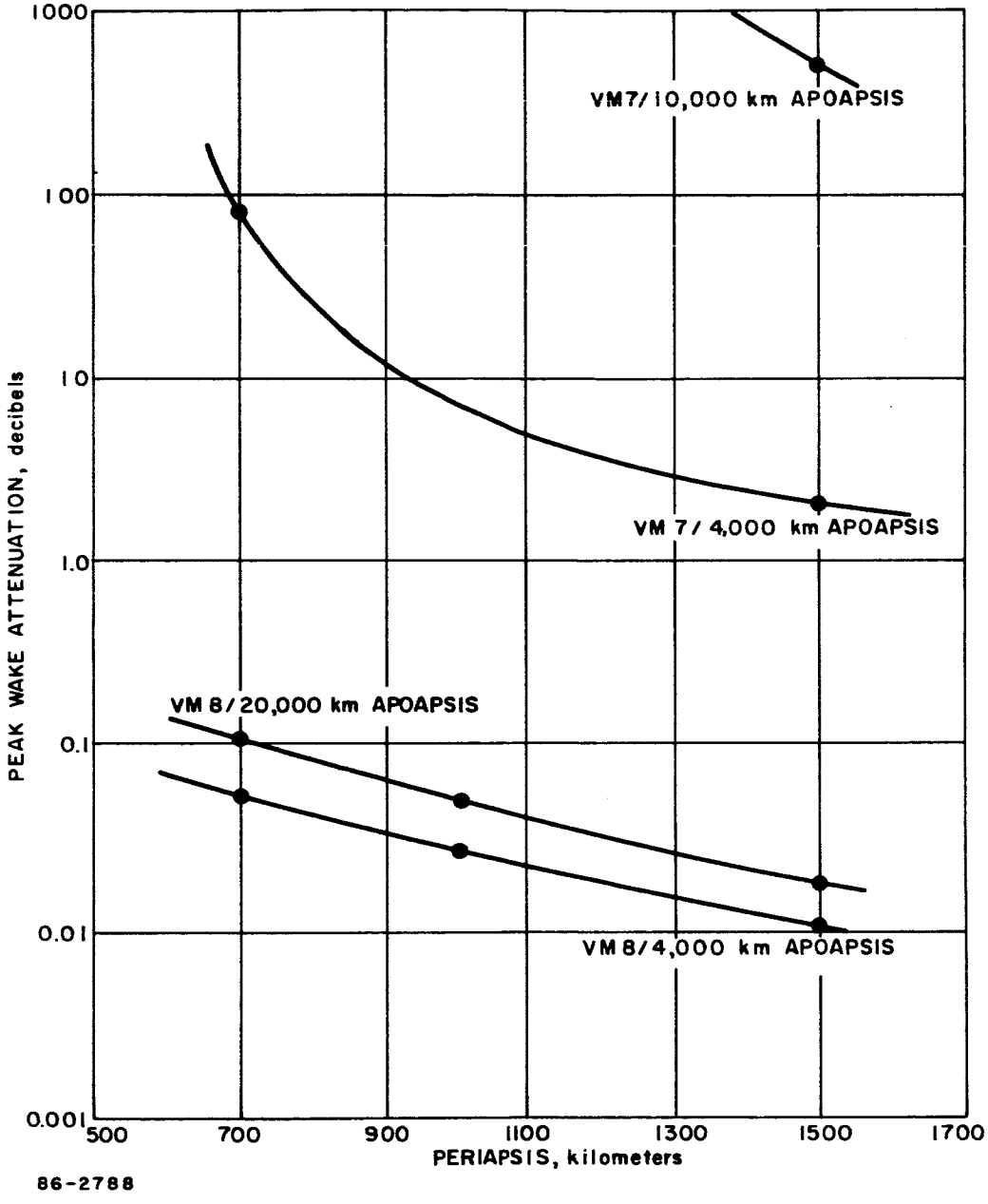

Figure 71 ATMOSPHERE AND ORBIT GEOMETRY EFFECTS ON WAKE ATTENUATION

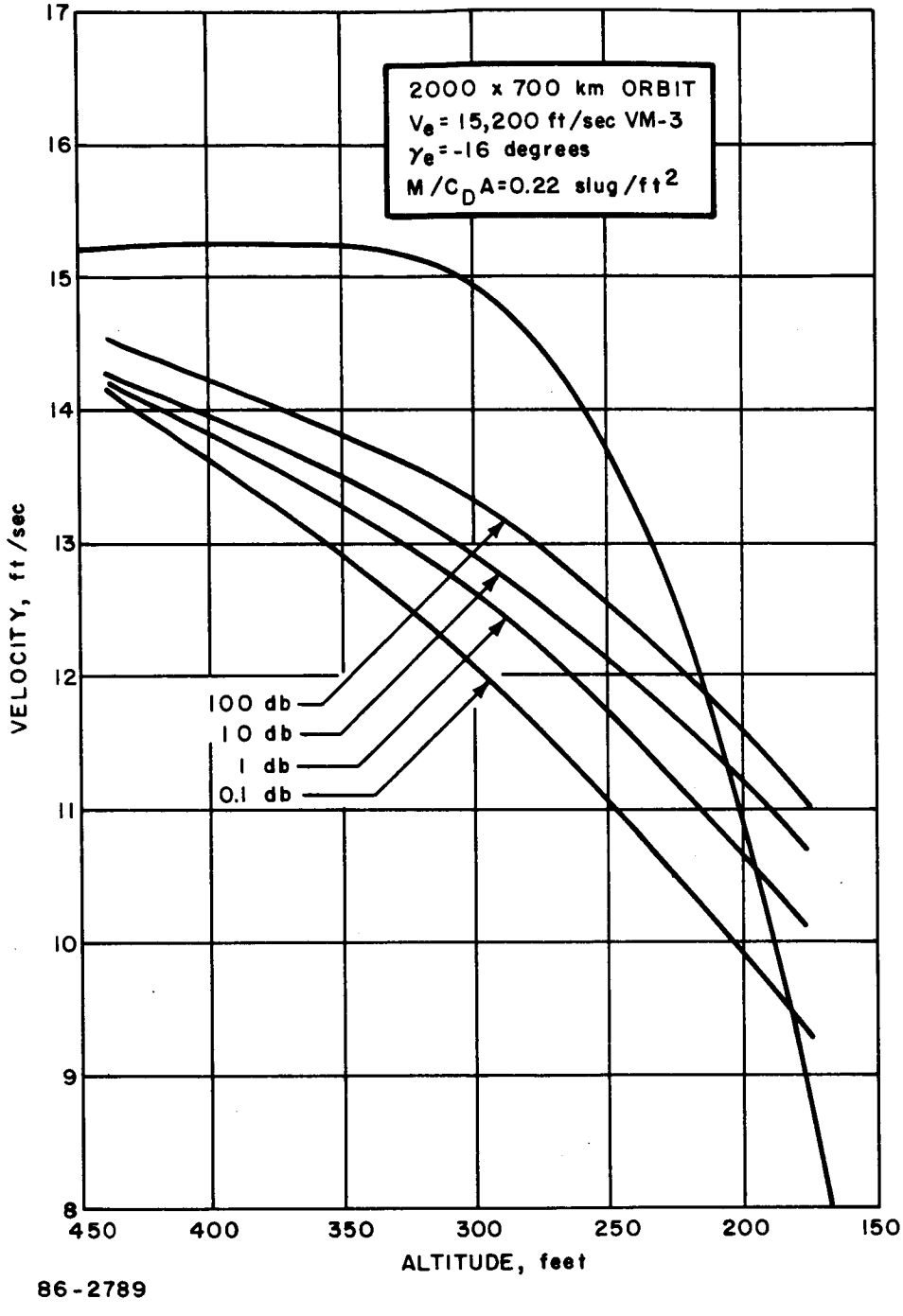

Figure 72 WAKE ATTENUATION VERSUS VELOCITY AND ALTITUDE

Contaminants in the heat shield material may increase attenuation during blackout or even cause blackout times significantly longer than would be the case when blackout occurs in clean air.

4. Summary -- Table XLIX shows expected blackout conditions for the nine orbits and four atmospheric models considered. The maximum and minimum plasma attenuation for a given entry velocity can be expected to occur in the VM-7 and VM-8 atmospheres, respectively.

TABLE XLIX

EXPECTED BLACKOUT CONDITIONS DURING ENTRY

Orbit (kilometers)	Atmospheric Model			
	VM-3	VM-4	VM-7	VM-8
700 x 4000	blackout	uncertain	blackout	no blackout
700 x 10, 000	blackout	blackout	blackout	no blackout
700 x 20, 000	blackout	blackout	blackout	no blackout
1000 x 4000	uncertain	no blackout	blackout	no blackout
1000 x 10, 000	blackout	blackout	blackout	no blackout
1000 x 20, 000	no blackout	blackout	blackout	no blackout
1500 x 4000	blackout	no blackout	uncertain	no blackout
1500 x 10, 000	blackout	uncertain	blackout	no blackout
1500 x 20, 000	blackout	blackout	blackout	no blackout

Blackout may not occur at all in either the VM-4 or VM-8 atmospheres if low apoapsis orbits are selected and if heat shields free of contaminants are used. In the VM-3 or VM-7 atmospheres, however, there may be blackout periods even under these same conditions (low apoapsis orbits, contaminant-free heat shields).

A conservative viewpoint is that blackout may be said to begin at 0.1 g and end when the flight capsule's velocity decreases to 10,000 ft/sec. On the basis of this definition and available trajectory information, it can be determined that blackout (when it does exist) lasts for a minimum of 34 seconds and a maximum of 87 seconds.

5.4.1.3 Multipath Considerations

Figure 73 is a pictorial representation of the signal received at the spacecraft from the flight capsule during its descent phase*. As shown, the total signal at the receiver will consist of both a direct signal from the flight capsule and an indirect signal resulting from scattering and reflection of the direct signal by the Martian surface. In general, the indirect, or scattered, signal will consist of two components: one is a coherent specular component, the other is a randomly diffuse component. If the reflecting surface is perfectly smooth, the diffuse component is zero; if, however, the reflecting surface is very rough, the specular component is negligible.

An analysis of the computation of the mean square reflected power from the surface relative to the incident power is presented in Section IV, Appendix IV 4-7 of Reference 1. With the aid of this analysis, expressions for the probability of error in detection can be and, in fact, have been derived for both the wideband PCM/FSK and the PCM/PSK/PM systems (see Sections V and VI of the above mentioned appendix). For a surface sufficiently smooth that the reflected signal is primarily specular, the normalized envelope of the signal received at the flight spacecraft will be,

$$\frac{E_R}{E_o} = \sqrt{1 + R^2 + 2R \cos \phi} \qquad (34)$$

where $R = (B/F)\,|R_o|$, the product of the surface voltage (or field) reflection coefficient and the antenna back-to-front voltage (or field) ratio and E_R/E_o is the ratio of the resultant field at the receiver due to the direct and reflected signals normalized relative to the direct signal. The back-to-front ratio for specular reflection is defined as the ratio between the field strength in the direction of the reflected path and the field strength in the direction of the direct path.** For the conditions shown on Figure 73, the back-to-front ratio would be the ratio of the field strength at b on the antenna pattern to the field

*Prior to the descent phase (i.e., during entry) the payload is inside the entry vehicle and the effects of multipath propagation should be reduced due to the shielding provided by the entry vehicle structure.

**Since circularly polarized antennas are used, the right and left circular patterns are used to determine the field strength of the direct signal and the reflected signal, respectively.

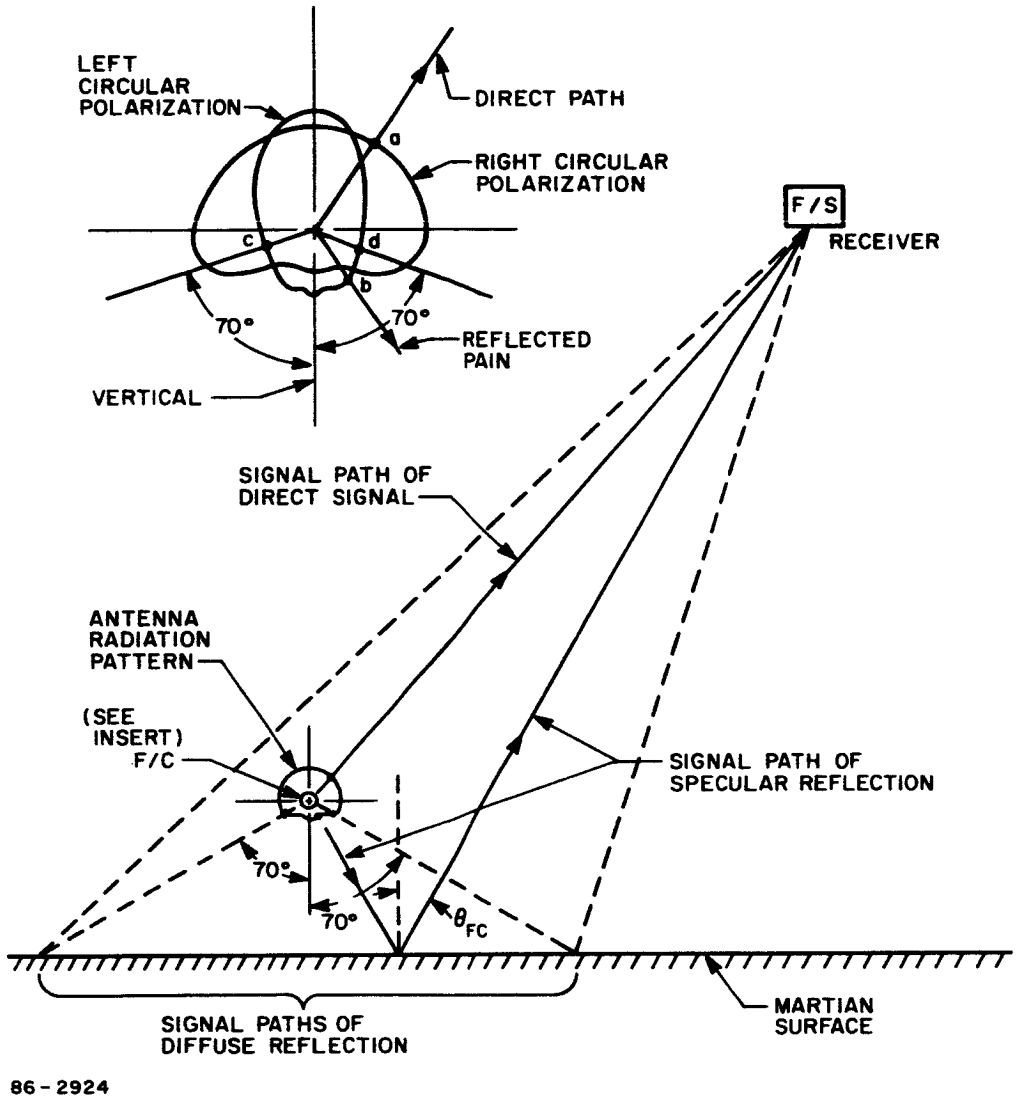

Figure 73 MULTIPATH CONFIGURATION

strength at a. Figure 74 is a plot of the voltage reflection coefficient, $|R_o|$, versus the angle of incidence, θ_{FC}, for very dry ground, which is the composition assumed for the Martian crust.

The received signal envelope, as calculated from Equation 34, is shown on Figure 75. If the capsule is descending with a constant velocity, ϕ will be directly proportional to time. Therefore, the percentage of time that a signal threshold value, T, will be exceeded can be equated to the percentage of 2π radians that T is exceeded. Thus,

$$\begin{matrix}\text{percent of time that} \\ \text{T is exceeded}\end{matrix} = \frac{2\pi - (\phi_2 - \phi_1)}{2\pi} \times 100 \tag{35}$$

where ϕ_1 and ϕ_2 are found from the solution of

$$T = \sqrt{1 + R^2 + 2R \cos \phi_{1,2}} \tag{36}$$

In the absence of the multipath reflected signal, E_R/E_0 will be unity 100 percent of the time. Additional transmitter power is required to raise the received signal level to the unperturbed level of $E_R/E_0 = 1$ for 100 percent of the time when a multipath reflected signal is present. That is, if an additional transmitter power of W watts were employed, the level of the entire curve of E_R/E_0 would be raised an amount equal to $\sqrt{(W_o + W)/W_o}$, where W_o is the original transmitter power. Thus, W can be so chosen that if $W_o + W$ watts are transmitted, system performance would be the same as if no multipath reflected signal were present. Figure 76 shows the additional power, W, (in db relative to W_o) required to negate the multipath effect for various percentages of time. For example, to assure that there would be no system performance degradation (due to multipath effects) for 90 percent of the time under the condition that $R = (B/F)|R_o| = -8$ db, 4 db of additional power, W, would be necessary.

In the case of a rough surface, the reflected signal is no longer coherent. Rather, it is composed of contributions from random scatterers. Accordingly, a probabilistic approach is required in analyzing multipath effects. The percentage of time that the received resultant signal exceeds a certain threshold, T, can be calculated on the basis of the analysis given in Section IV of Appendix IV. 4-7 in Reference 1. Results of such calculations indicate that the magnitude of the resultant signal is approximately the same for either a fairly rough surface or a very rough surface. Figure 77 shows the results of such a computation. As noted previously, R represents the product of the back-to-front antenna ratio and the surface reflection coefficient. In this case (rough surface), however, the back-to-front ratio is defined as the ratio between the average field strength over ±70 degrees of the antenna pattern

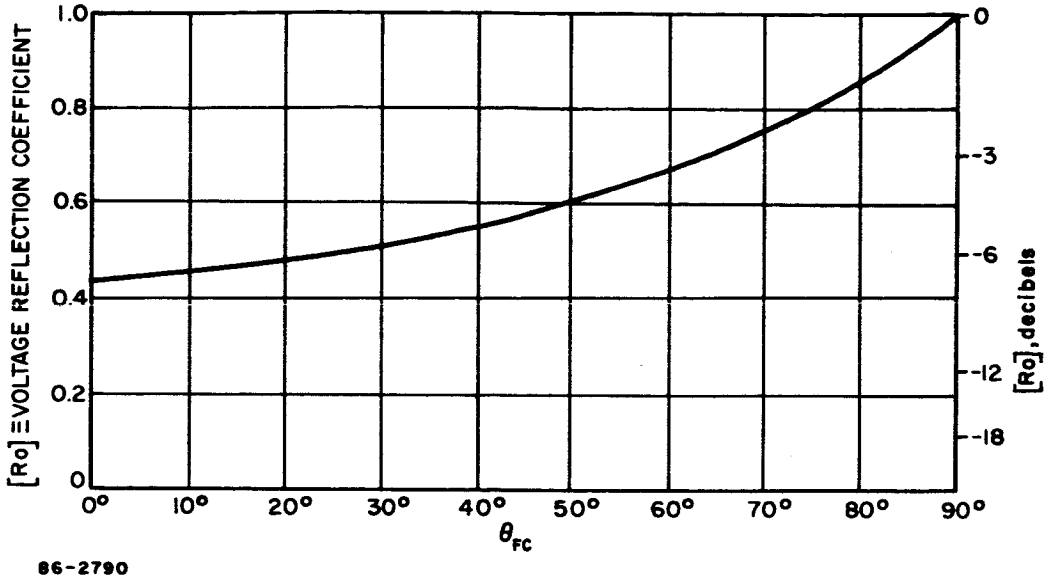

Figure 74 SURFACE REFLECTION COEFFICIENT FOR VERY DRY GROUND VERSUS ANGLE OF INCIDENCE

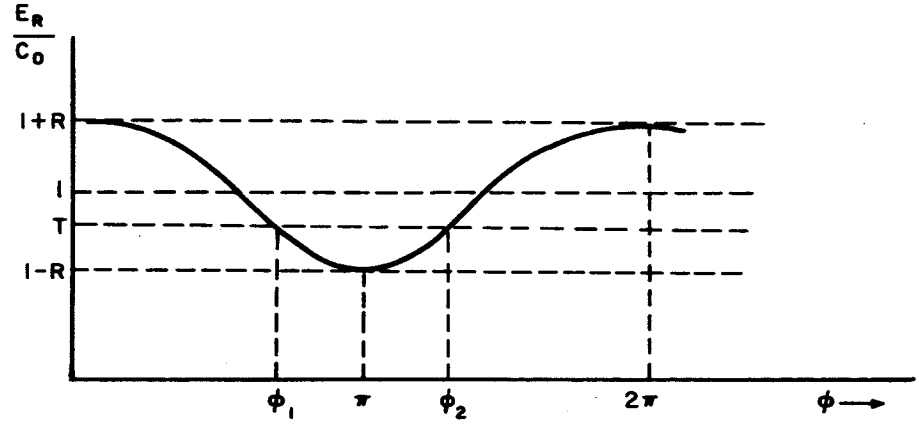

Figure 75 ENVELOPE OF RECEIVED SIGNAL

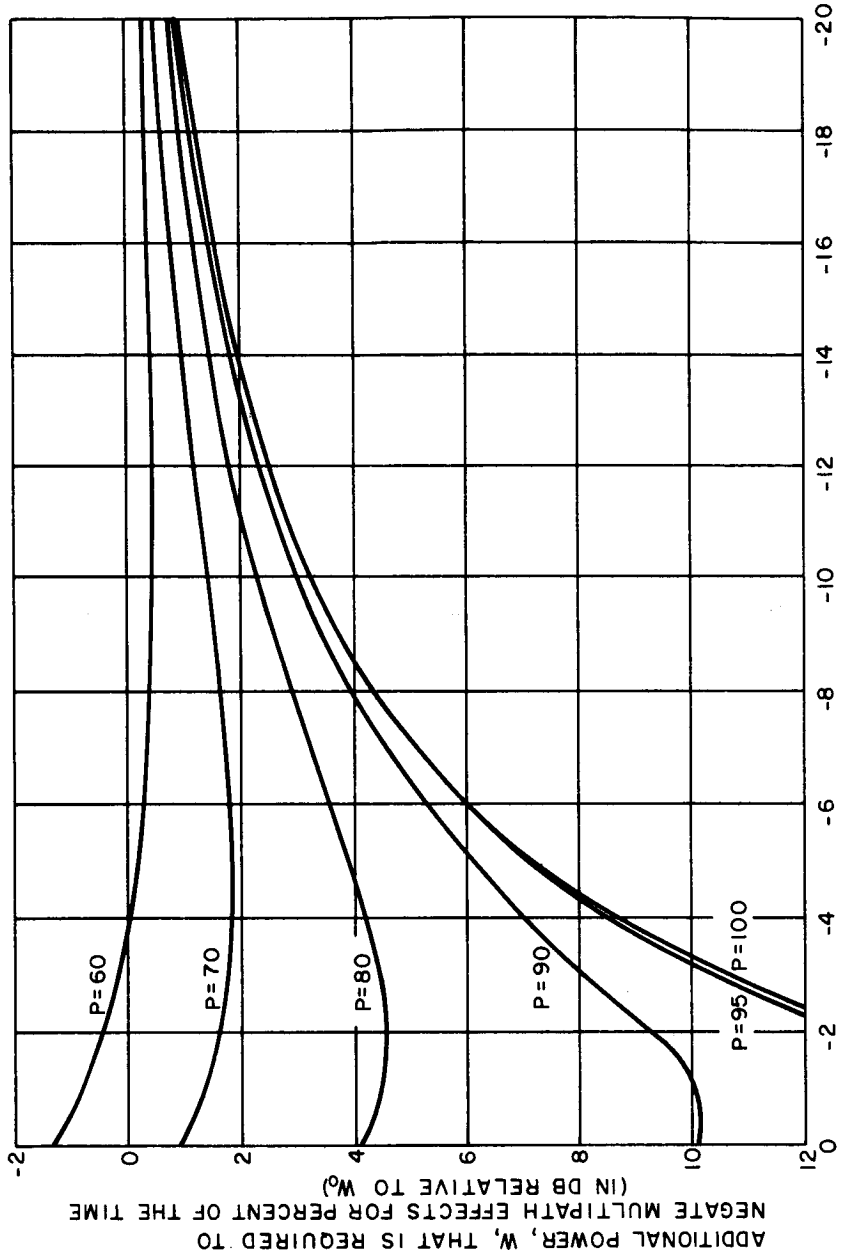

Figure 76 SPECULAR REFLECTION EFFECTS

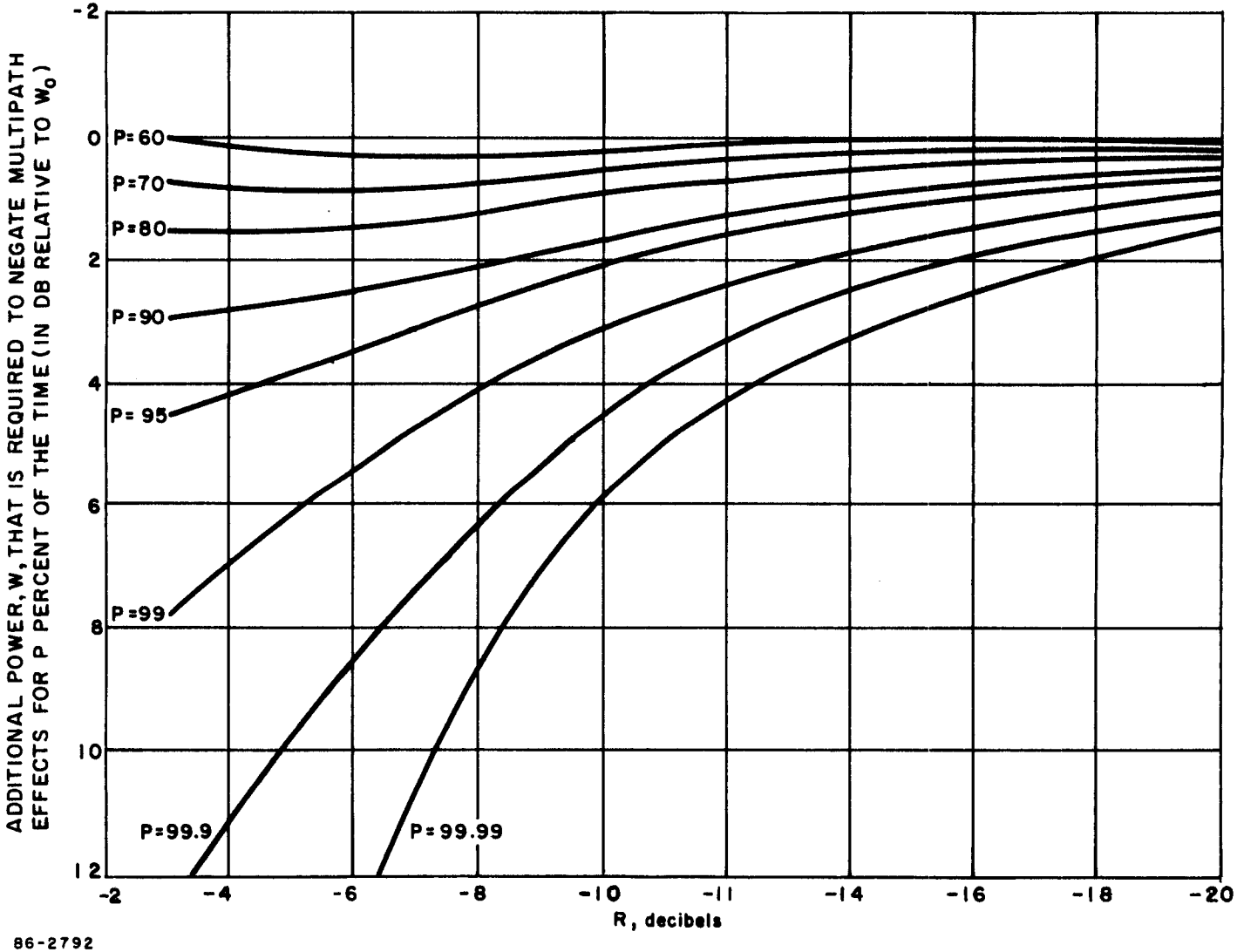

Figure 77 DIFFUSE REFLECTION EFFECTS

in the direction of descent and the field strength of the direct path transmission. This relationship is indicated pictorially in Figure 73. It can be seen from that figure that the strength of the back-scattered signal, essentially, is the average field strength from a point c to point d on the antenna pattern.

The considerations discussed above have direct application in determining multipath losses for a PCM/FSK system. However, the presence of tracking loops in PCM/PSK/PM systems involves other considerations. An analysis applicable to such a system (PCM/PSK/PM) is presented in Section VI of Appendix IV. 4-7 of Reference 1. The results of that analysis are tabulated in Section II of that same appendix.

5.4.2 Antenna Selection

The minimum beamwidths required by the flight spacecraft and flight capsule antennas are shown in Table XLI. Antenna concepts based on satisfying these beamwidth requirements are presented in paragraphs 5.4.2.1 and 5.4.2.2.

5.4.2.1 Flight Spacecraft Antenna Selection

In Table XLI, the beamwidth requirements for both body-fixed and planetary science platform (PSP) controlled flight spacecraft antennas are presented. This table is expanded further in Table L. The latter table includes data regarding selection of body-fixed antennas not only for all orbits under consideration but also, as a gross function, for two specific ranges of orbit periapsis altitudes. In Table L the recommendations regarding the type of antenna, either turnstile or helix type, are based upon the beamwidth required. For beamwidths above 100 degrees, a wide beamwidth antenna such as a turnstile is a reasonable choice. Figure 78 shows a typical radiation pattern for this type of antenna. Gains greater than 0 db (isotropic level) can be obtained for total beamwidths up to 160 degrees. A more directive antenna, such as a helix type, can be considered for beamwidths less than 100 degrees. Figure 79 shows a typical radiation pattern for this type of antenna. Gains greater than 0 db can be obtained for total beamwidths up to 100 degrees (60 degrees less than the turnstile). However, the on-axis gain of the helix-type antenna is 10 db (3 db better than that of the turnstile type antenna). Although alternative antenna concepts offer similar performance (see Appendix 4-1 of Reference 1), the turnstile and helix-type antennas described here are considered reasonable choices.

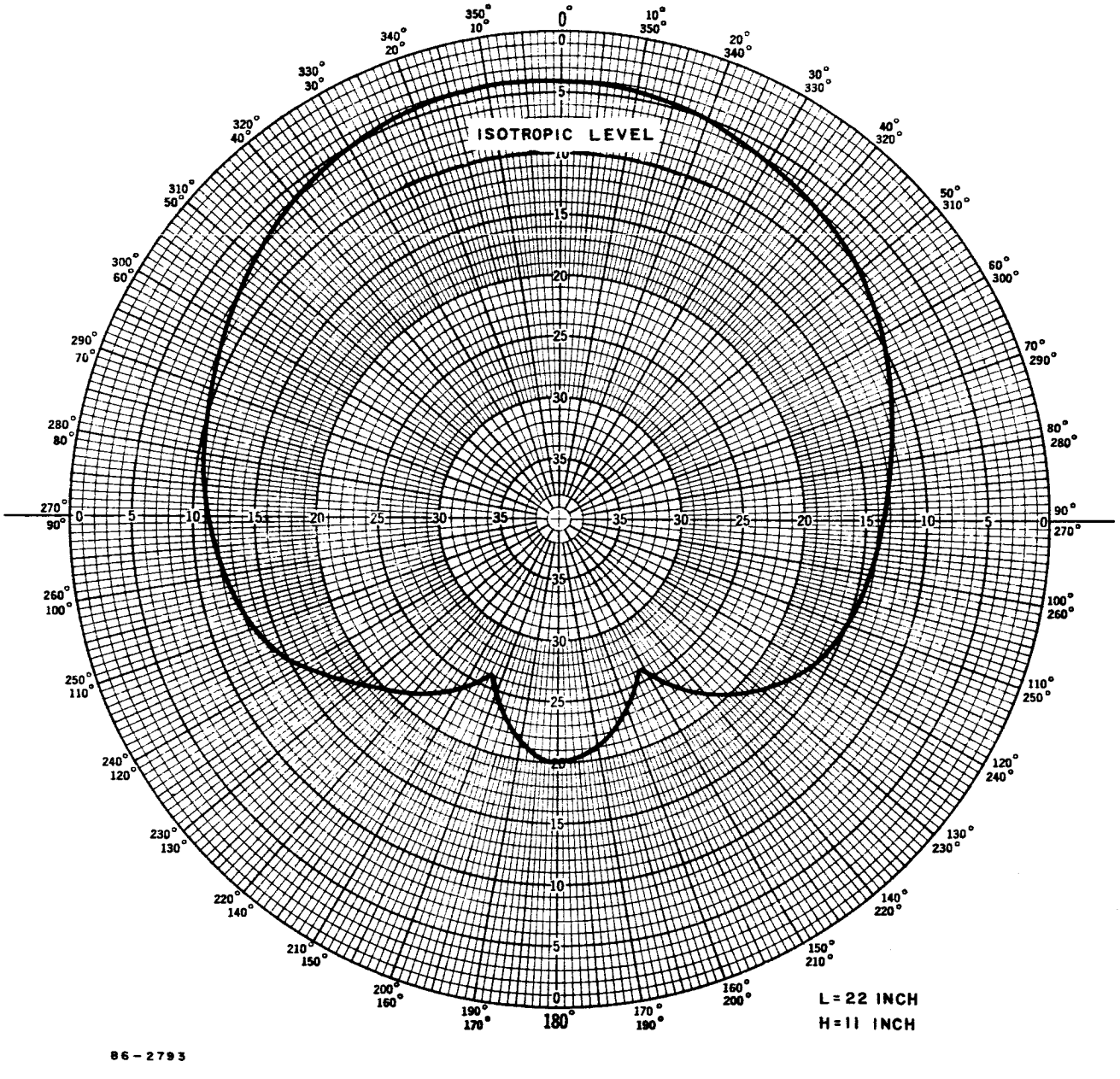

Figure 78 TYPICAL TURNSTILE ANTENNA PATTERN

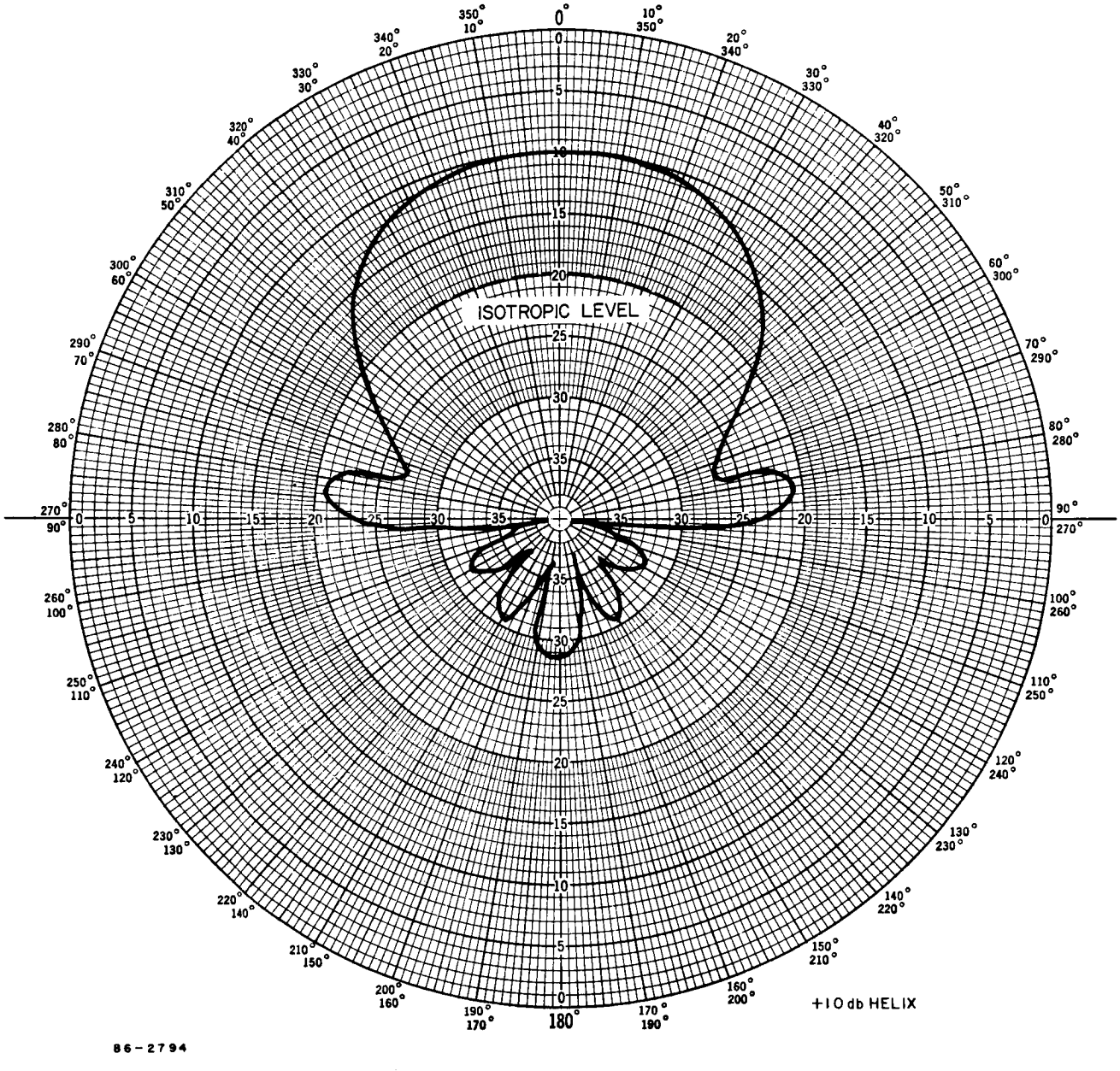

Figure 79 TYPICAL HELIX ANTENNA PATTERN

TABLE L

FLIGHT SPACECRAFT ANTENNA SELECTION

Concept	Orbit Range (kilometers)	Adjustable Antenna Position	Beamwidth (degrees)	Antenna Type	Margin (decibels)
Body-Fixed	All	No	130	Turnstile	Reference
	All	Yes	125	Turnstile	+1
	700 - 1000 Periapsis	Yes	125	Turnstile	+1
	1000 - 1500 Periapsis	Yes	100	Turnstile	+2
PSP	Total Trajectory	Yes	135	Helix	-6
	Entry/Descent	Yes	85	Helix	+3

Three different approaches in regard to the use of a body-fixed antenna were considered as follows.

The first approach was based on use of a single, body-fixed, turnstile-type antenna designed to accommodate the entire range of orbits under consideration. A beamwidth of 130 degrees is required in this approach. The relay link performance margin defined on the basis of this concept was subsequently used as a reference to which the performance margin of the other two antenna concepts (body-fixed antenna adjusted prior to launch and PSP antenna) were compared. A discussion of relay link antenna performance is presented in paragraph 5.4.6.

The second approach was based on use of an antenna adjusted prior to launch to provide the optimum pointing direction for the particular orbit

selected for the mission. In this case, the beamwidth requirement for the flight spacecraft antenna could be reduced to 125 degrees. This results in an improvement of 1 db in the performance margin, an improvement attributed to an increase in antenna gain resulting from use of a narrower beamwidth.

In the third approach, flight spacecraft antenna requirements were examined as a gross function of orbit range selected. For orbits with periapsis altitudes between 1000 and 1500 km, a beamwidth of 100 degrees is required: for orbits with periapsis altitudes between 700 and 1000 km, a beamwidth of 125 degrees is required, as noted previously. No additional improvement in the performance margin is obtained for orbits in the periapsis range from 700 to 1000 km since the beamwidth requirements discussed above were determined on the basis of an orbit with a periapsis altitude of 700 km. A 2-db improvement relative to the reference performance margin can be obtained if the orbit range is restricted to periapsis altitudes in the 1000 to 1500-km range.

Two approaches regarding use of a helix-type antenna controlled by the PSP were considered. In one approach the antenna would be used throughout the trajectory. There would then be a 6-db degradation in the performance margin. This degradation could be reduced to approximately 1 db of a turnstile antenna instead of a helix antenna were selected. However, the primary reason for using the PSP is to maximize the gain during entry/descent.

The second approach, therefore, involves the use of a PSP-controlled helix-type flight capsule antenna during these portions of the mission. In this case there would be a performance margin improvement of approximately 4 db relative to the reference performance margin.

Although the alternative approaches to the use of a body-fixed antenna offer potential antenna gain improvements due to the slightly narrower beamwidth required (once a nominal orbit is selected), they are more sensitive to dispersions in the achieved flight spacecraft orbit. Such a sensitivity is, of course, a potentially undesirable operational penalty.

Despite the fact that a PSP-controlled helix type antenna offers the greatest improvement in relay link performance during entry/descent, the overall performance of the relay link with such an antenna is somewhat poorer than that obtained with a body-fixed antenna. Therefore, the first body-fixed antenna concept discussed above (single position for all ranges of orbits) has been selected as the reference design.

5.4.2.2 Flight Capsule Antenna Selection

The flight capsule antenna beamwidth requirements were summarized in Table XLI paragraph 5.3.4 indicated that the selected flight capsule antenna would have to provide nearly omnidirectional coverage. However, as noted in paragraph 5.1.4.3, severe multipath signal fading can occur if the antenna back-to-front (B/F) ratio approaches unity. These conflicting requirements complicate the problem of flight capsule antenna selection. Many alternative approaches were considered during this study (see Appendix 4-2 of Reference 1). The selected concept is based on use of a planar logarithmic spiral antenna. Figure 80 shows the location of the relay link (telemetry) antennas on the flight capsule. Two antennas are used for redundancy (see paragraph 5.4.7).

Antenna performance is affected by the presence or absence of the entry shell, as shown in Figures 81 and 82, respectively. Prior to jettisoning of the entry shell, the antenna pattern is essentially hemi-omni. After jettisoning of the entry shell, slightly greater coverage is obtained. The antenna patterns shown in Figures 81 and 82 are patterns actually measured during tests on a scaled mockup of the flight capsule.

As can be seen from Figure 82, the minimum gain is -17 db for a 270-degree beam (the maximum required). As shown in Figure 80, the antennas are tilted toward the longitudinal axis of the flight capsule. This is done to make the antenna pattern coverage more symmetrical about the flight capsule's longitudinal axis, as shown in Figure 83. This figure shows a plot of antenna gain at a constant look angle of 135 degrees, the largest look angle (including the effects of capsule sway due to 200 ft/sec wind gusts), and with the flight capsule rotated about the longitudinal axis. It can be seen from this figure that if the antennas are not tilted, relatively deep nulls occur in the antenna pattern (due, in part, to shadowing effects by the flight capsule). These nulls can be minimized, however, by directing more energy into the shadow regions. This can be accomplished by slightly inclining the antenna axes toward the flight capsule's longitudinal axis. Although antenna performance similar to that described here can be obtained with the alternative approaches discussed in Appendix 4-2, of Reference 1, the planar logarithmic spiral type antenna was selected as the reference design for the flight capsule since it is inherently a wide bandwidth device. It is not, therefore, subject to detuning problems likely to occur with other concepts.

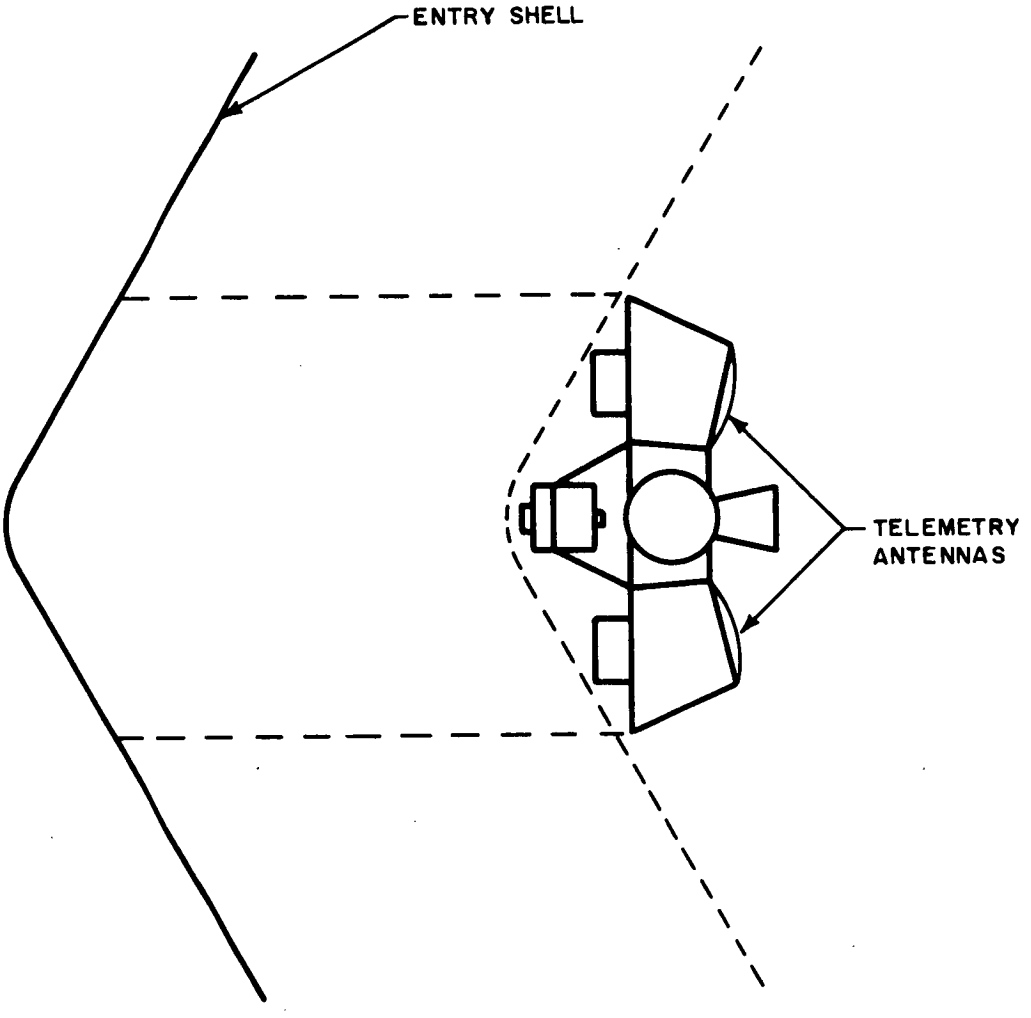

Figure 80 POSITION OF TELEMETRY ANTENNAS ON FLIGHT CAPSULE

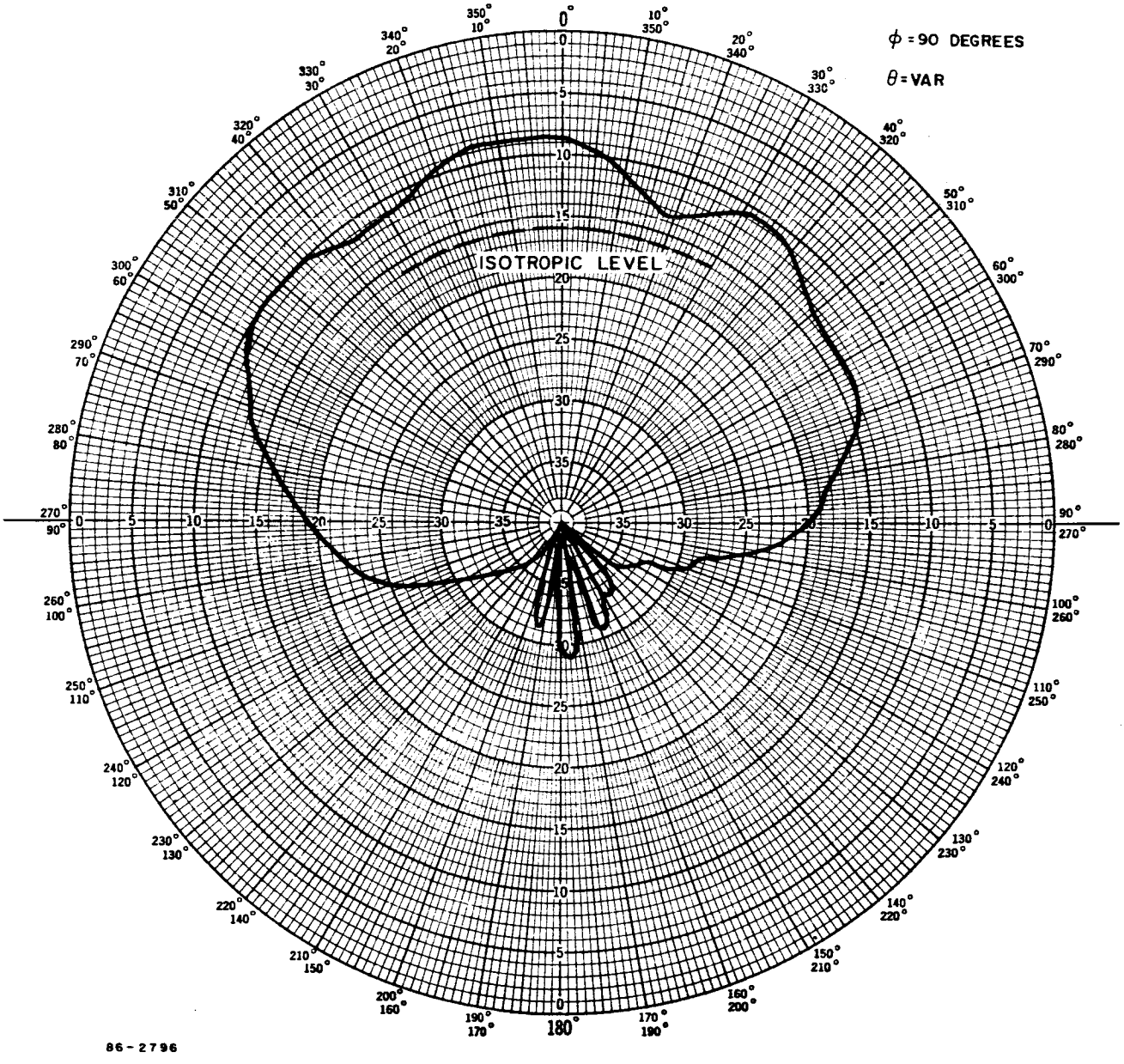

Figure 81 FLIGHT CAPSULE ANTENNA PATTERN WITH ENTRY SHELL

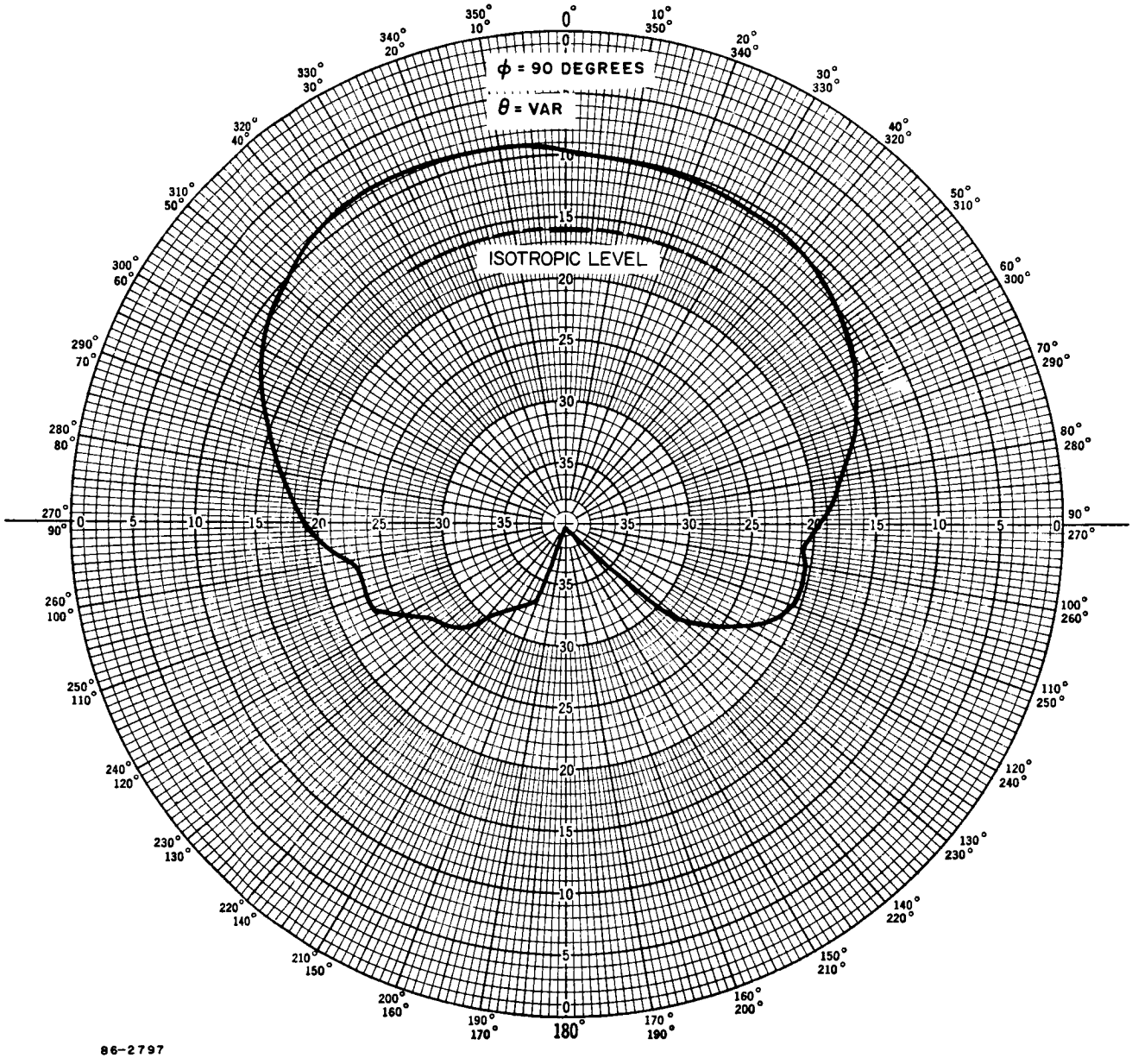

Figure 82 FLIGHT CAPSULE ANTENNA PATTERN WITHOUT ENTRY SHELL

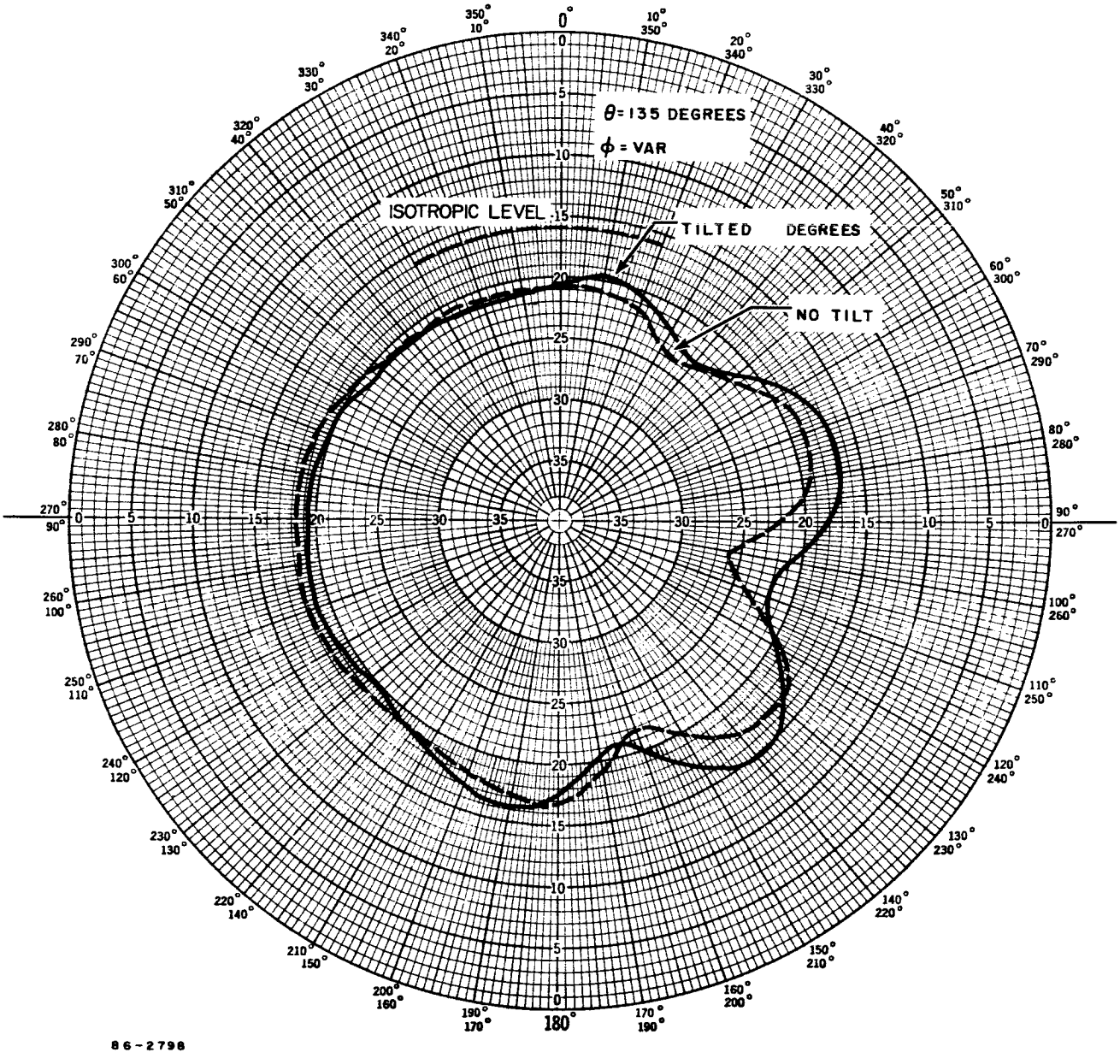

Figure 83 FLIGHT CAPSULE ANTENNA PATTERN WITH AND WITHOUT TILT

5.4.3 Frequency Selection

In paragraph 5.3 it was shown that both the receiving (flight spacecraft) and transmitting (flight capsule) terminals of the relay link required broad beamwidth antennas. The performance (gain) of such broad beamwidth antennas will be essentially constant over a wide range of exciting frequencies. For these conditions, the received signal power at the flight spacecraft is inversely proportional to the square of the carrier frequency; hence, if no additional factors were to influence the decision, the selected relay frequency should be as low as possible. However, there are many additional factors which do influence the frequency selection process (see Appendix of Reference 1). The most significant are the following:

1) Cosmic Noise,

2) Receiver Noise Figure,

3) Transmitter Efficiency,

4) Antenna Size, and

5) FCC Frequency Allocations

Figure 84 summarizes the results of the frequency selection analysis. First, the relative transmitter power required to overcome the propagation loss (the inverse square of frequency) is shown normalized to the power required by a 100 MHz transmitter and without regard for galactic noise. Second, the additional transmitter power required to overcome the additional noise power introduced in the flight spacecraft receiver due to degraded amplifier noise figures at higher frequencies is shown normalized to a 100 MHz receiver. Third, the additional input power required to operate higher frequency transmitters due to decreasing solid state device efficiency is shown normalized to the input power required by a 100 MHz transmitter.

Finally, the total input power required as a function of frequency, which is the sum of the factors described above is shown. It can be seen that all relevant factors indicate that a broad optimum exists in the VHF band. Allocations in this band can be obtained at 137 MHz, 272 MHz and 400 MHz. Of these, 137 MHz appears least attractive due to the relatively large flight capsule and flight spacecraft antennas that would be required. The selected design point is 272 MHz, which appear most attractive both from an efficiency viewpoint and availability of hardware in the existing (215 MHz to 260 MHz) VHF band used on the test ranges. If vacuum tube rather than solid state devices were used, the effect of efficiency would not be as pronounced; however, the conclusions reached would not be altered.

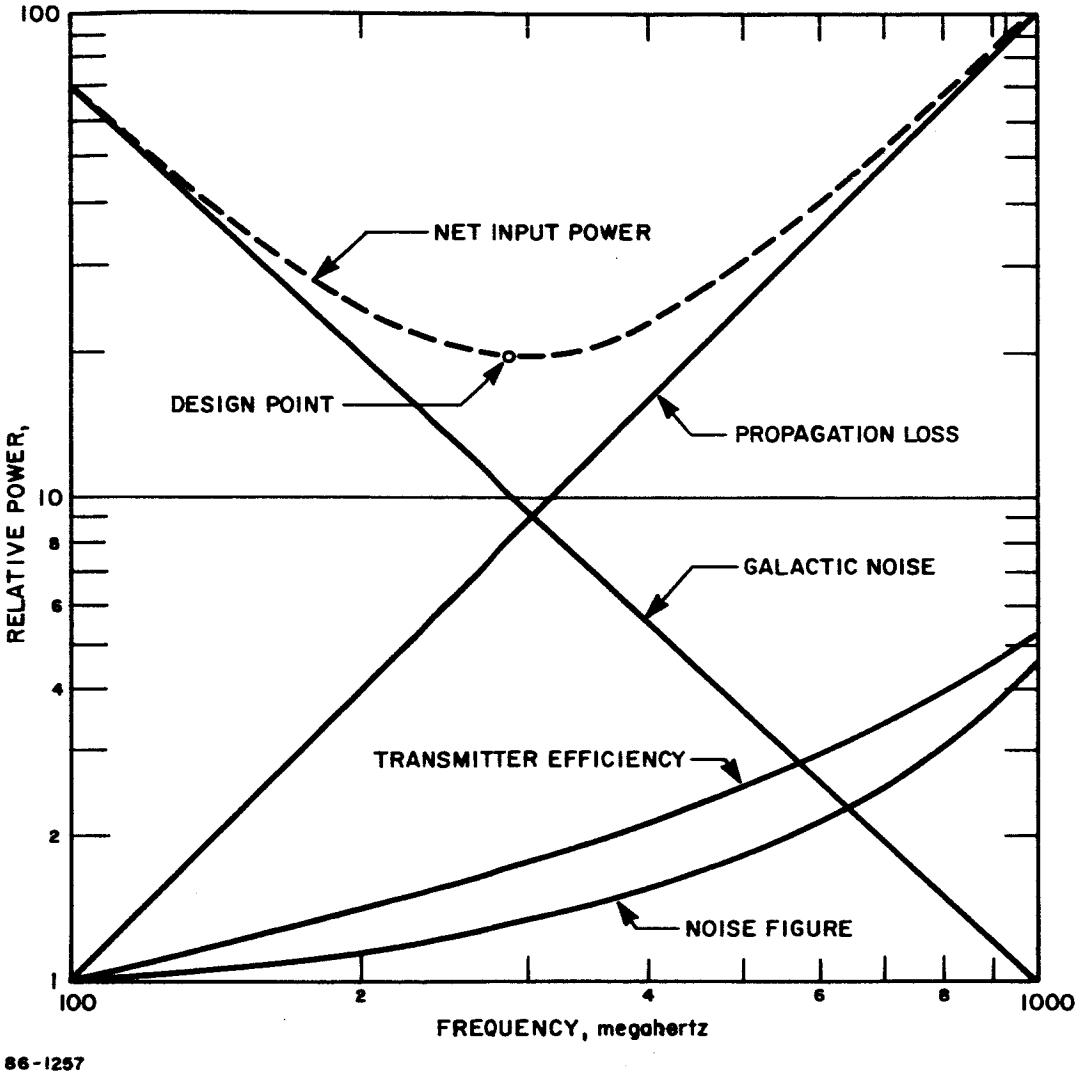

Figure 84 FREQUENCY SELECTION TRADEOFF

5.4.4 Flight Capsule Transmitter Power

The total number of bits collected and the time available for transmission directly determine the data rate required during descent and, correspondingly the transmitter power. A minimum-data descent mission, consisting primarily of nine TV pictures, would require collection of approximately 2.5×10^6 bits. The transmission time during descent is related to the parachute diameter, as shown in Figure 85. The data rate required to transmit the bit content of a minimum data mission is shown for various values of descent time and associated parachute diameters. For a parachute 81 feet in diameter, which is about the size of the existing Apollo parachute, the required data rate is approximately 15,000 bps. Efforts to reduce the required data rate even further by using larger diameter parachutes are considered to entail an unnecessary design risk at this time.

A limiting value on data rate reduction is reached at descent times of 400 seconds and longer (although this is not shown in Figure 85) due to low flight capsule-flight spacecraft elevation angles which make multipath signal fading a severe problem.

Although a data rate of 15,000 bps is required for the transmission of data acquired on a minimum-data descent mission, an 18,000 bps rate was selected as the design data rate to allow design of a telecommunications subsystem which does not require changes in the data mode after flight spacecraft-flight capsule separation.

At this data rate (18,000 bps), approximately 240 watts of RF power would be required to maintain a simple relay link above threshold during the large flight capsule swing angles which may be experienced during descent (see paragraph 11.8). Transmitter power this high is considered impractical from the viewpoint of such factors as: potential antenna breakdown, thermal control, state-of-the-art power device limitations, and high voltage arcing.

Although various forms of diversity techniques tend to reduce this RF power level requirement, as noted in paragraph 11.8, the four factors listed above formed the basis for transmitter power selection. These factors are discussed briefly below.

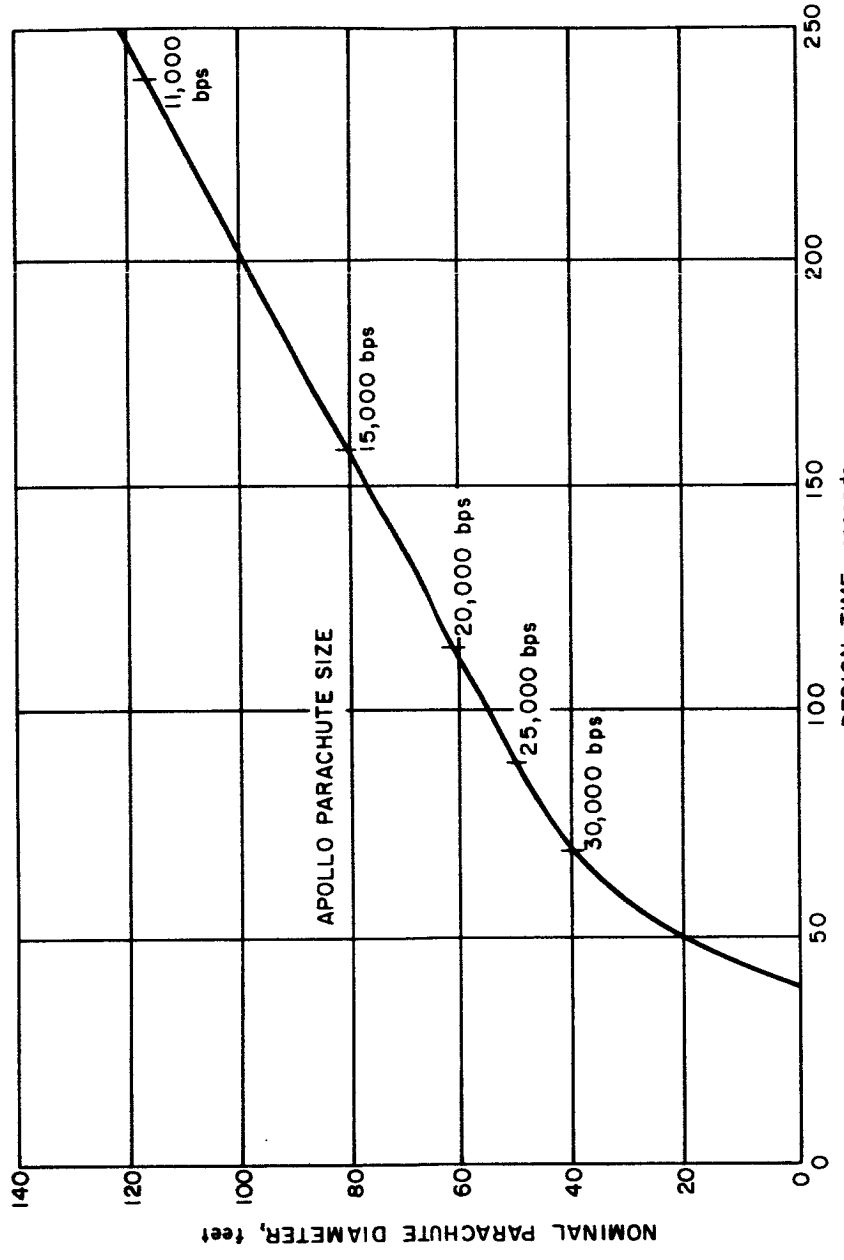

FIGURE 85 PARACHUTE-SIZE DESCENT TIME TRADE

5.4.4.1 Antenna Breakdown

The problem of antenna breakdown becomes serious at low atmospheric pressures and must be considered in selecting the transmitter power level. Although antennas can be designed to operate in any atmosphere at any power level, experience indicates that for simple antenna configurations and, in general, for antennas with a single radiating element, care must be taken in handling power levels above 10 watts to ensure freedom from voltage breakdown in low pressure atmospheres. Since the flight capsule will be exposed to atmospheric pressures ranging from space vacuum up to possible 10 millibars during entry and descent, it would be a design risk at this time to consider transmitter power levels greater than 30 to 40 watts.

5.4.4.2 Thermal Control

As presently conceived, the flight capsule transmitter will be operating continuously for 5 hours (4 hours before separation of the flight capsule from the flight spacecraft and up to one additional hour between separation and impact). On the basis of transmitter efficiencies currently attainable with state-of-the art devices, it is doubtful that simple heat-sink configurations can provide adequate cooling at levels much above 50 watts while the transmitter is operated for the required time. Above the 50-watt level active thermal control would probably be required. This is especially true if thermal insulation is required to maintain the transmitter above some minimum temperature when it is not operating. Such is the case with the flight capsule transmitter. Prior to flight capsule separation from the flight spacecraft the transmitter requires insulation to maintain its nonoperating temperature above the specified -55°C lower temperature limit. During transmitter operation the insulation reduces the maximum heat-sink efficiency.

An alternative approach and one that would allow higher transmitter power to be used is based on operating the transmitter intermittently during the preseparation phase. This mode of operation, however, has two particularly undesirable features. One, it would make continuous monitoring of transmitter performance from Earth impossible.

during the critical preseparation checkout period, and two, mission success would become dependent upon correct response to an additional discrete command from the flight spacecraft to turn the transmitter on shortly before separation.

5.4.4.3 State-of-the-Art Limitations on Device Power Handling Capabilities

Solid-state devices (transistors) currently available have power output capabilities in the 10- to 15-watt range for carrier frequencies in the 270-400 MH_z band of interest. It is predicted, however, that by mid-1966 this capability will increase to 15 to 30 watts for the same frequency band. Power levels above these values can, of course, be achieved with currently available vacuum tube amplifiers.

5.4.4.4 Avoidance of High Voltages

It is desirable to avoid high-voltage potentials when operating at the low-atmospheric pressures expected during entry and descent. High-voltage arcing is possible under such conditions unless adequate precautions, such as pressurizing the high-voltage components, are taken.

In summary, transmitter powers above 40 watts are unattractive because of potential antenna breakdown. Powers above 50 watts are unattractive because of thermal control problems. Devices requiring high voltages (vacuum tubes) are unattractive from the viewpoint of design risk because of the possibility of pressurization failure. Finally, solid-state devices with output powers above 30 watts are not currently available and are not expected to be available in the near future although their use would circumvent the high voltage problem.

Since high-voltage arcing will always constitute a design risk and passive thermal control is desirable, 30 watts was chosen as the transmitter power level; and it is recommended that a solid-state amplifier be developed to provide the required power.

5.4.5 Modulation Selection

5.4.5.1 Introduction

A number of selection criteria must be considered in choosing a suitable relay link. Clearly, no one system will, nor should it be expected to, outperform other possible systems in all categories. The choice of an optimum communication system involves first a critical and balanced analysis of the various conflicting selection criteria and, second, agreement on the compromises, or tradeoffs, necessary to define an optimum system.

In the following paragraphs some of the more important of these selection criteria are examined for a number of communication systems considered as candidates for a relay data link between the flight capsule and an orbiting flight spacecraft. Both coherent and non-coherent techniques are among the candidate relay link modulation techniques discussed. The discussion of non-coherent systems covers both tracking and non-tracking systems. A diagram illustrating the classification of relay link communication systems of interest is shown in Figure 86.

The major selection criteria to be considered relative to relay link modulation techniques include: relative communication efficiency, compatability with mission requirements, compatability with environment, and equipment complexity.

5.4.5.2 Relative Communication Efficiency

One of the most important of these basic selection criteria is relative communication efficiency. Communication efficiency is usually measured in terms of the rate at which data can be communicated with a specified reliability for a given expenditure of signal power. The relative communication efficiency is typically determined from curves of the bit-error probability obtainable over the data link versus the input signal-to-noise ratio (SNR) for each of the candidate systems.

A complete analysis of each of these candidate relay link modulation techniques was provided in the Part 1 report (Reference 1). That report included curves illustrating the bit-error probability performance of each of the candidate relay link modulation techniques as a function of the intermediate frequency (IF) SNR. These curves are referred to often in the following discussion of the relative communication efficiency of the various modulation systems considered.

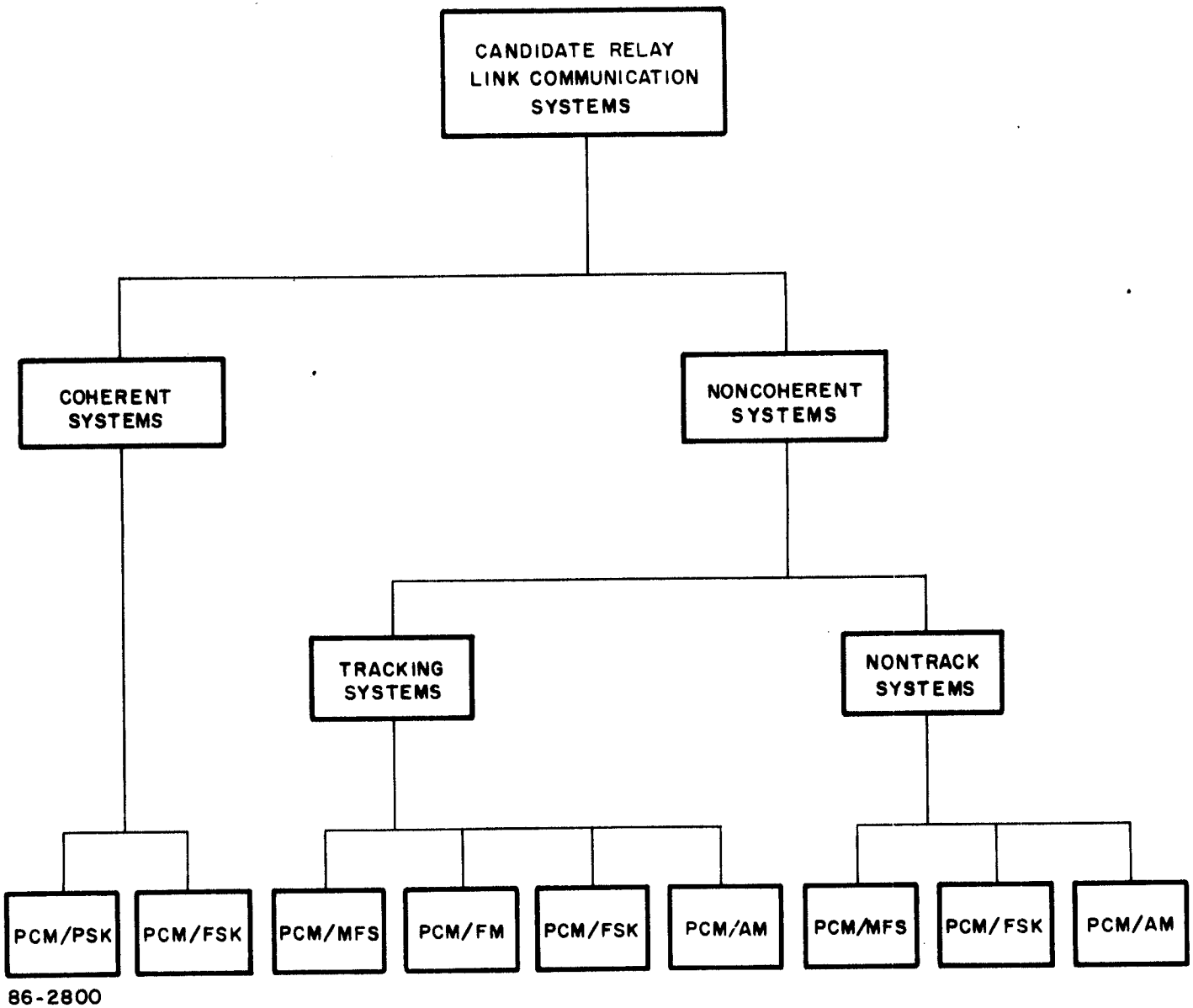

Figure 86 CANDIDATE RELAY-LINK COMMUNICATION SYSTEM

The relative communication efficiency of each of the candidate systems was assessed on the basis of a nominal design case. The assumed nominal relay link parameters, given in Table LI are representative of the values used in evaluating relay link performance, as described in paragraph 5.4.6. A number of alternative routes can be taken in arriving at some suitable measure of relative communication efficiency. Although selection of a basis for comparing system performance is somewhat subjective, there should be sufficient justification for selecting the method actually used. Since the relay data link must provide a specified bit rate to satisfy the overall engineering and science mission, it was decided to compare performance of the candidate systems in relation to this rate. In this approach, performance of each of the candidate systems is compared as a fixed bit rate of 18, 000 bps. The performance margin provided by each of the systems under these conditions is considered indicative of relative communication efficiency. An analysis of each of the systems at a bit rate of 18, 000 bps and for the assumed relay link parameters given in Table LI follows. Terms used in the various equations that follow are as used on Table LI unless otherwise defined.

The input SNR is calculated from the relationship written in logarithmic notation

$$(SNR)_i = (P_R/N_o) - b_o \tag{37}$$

where:

$(SNR)_i$ = Predetection signal-to-noise ratio appearing in receiver intermediate frequency (IF)

P_R = Receiver power

N_o = Noise spectral density

b_o = The predetection bandwidth, in db above 1 Hz

The predetection bandwidth is determined by the operating bit rate, oscillator stabilities, and anticipated doppler shift. The predetection bandwidth, b_o , is found from the expression:

$$b_o = 3\dot{B} + f_T + f_R + f_d \tag{38}$$

where:

$\dot{B}$ = Bit rate (18, 000 bps)

f_T = Transmitter stability (± 0. 005 percent)

TABLE LI

ASSUMED RELAY-LINK PARAMETERS

Symbol	Parameter	Value	Tolerance (decibels)
f_o	Operating Frequency	272 MHz	
P_T	Transmitted Power (30 watts nominal)	44.8 dbm	±0.5
G_T	Transmitter Antenna Gain	+5.8 db	±1.0
G_R	Receiver Antenna Gain	+5.5 db	±1.0
N.F.	Receiving System Noise Figure	+9.0 db	±0.5
R	Range	1000/17000 km	
δ_T	Transmitter Stability	±0.005%	
δ_R	Receiver L.O. Stability	±0.0001%	
L_{TC}	Transmitting Circuit Loss	-0.5 db	±0.5
L_{MP}	Multipath Loss	-2.0 db	
L_P	Polarization Loss	-0.7 db	
ΣL_T	Sum of Adverse Tolerances		3.5 db

Note: Entries in this table are taken from the Relay Link Telecommunications Design Chart presented in section 5.4.6

f_R = Receiver instability (± 0.001 percent)

f_d = Doppler shift

It is assumed in this discussion that relay link communication will be blacked out during entry until the flight capsule velocity reaches 10,000 ft/sec. Under these conditions, the maximum Doppler shift corresponding to a velocity of 10,000 ft/sec is given by:

$$f_d = f_o \left(\frac{10^4 \text{ ft/sec}}{v_c} \right) \tag{39}$$

where:

f_o = Operating frequency

v_c = Speed of light

At an operating frequency of 272 MHz, the maximum doppler shift is 2.76 kHz. From Table LII, it is seen that the transmitter stability is ± 0.005 percent and that the receiver stability is ± 0.0001 percent. Table LII illustrates determination of the required predetection bandwidth for an assumed operating frequency of 272 MHz. As Table LII indicated, the required predetection bandwidth will be approximately 85 kHz for a bit rate of 18,000 bps.

TABLE LII

DETERMINATION OF
REQUIRED PREDETECTION BANDWIDTH

Quantity	Value (Hz)
$3\dot{B}$	54,000
f_T (± 0.005%)	27,200
f_R (± 0.0001%)	544
f_d (v = 10,000 ft/sec)	2,760
b_o =	84,504

The ratio of available receiver power (P_r) to predetection noise spectral density (N_o) is determined from:

$$P_R/N_o = P_T + G_T + G_R - N_o - L_s - \sum L_c - \sum L_t - L_M \quad (40)$$

where:

ΣL_c = sum of circuit losses

L_s = space loss

L_M = system margin

The space loss, L_s, is given as

$$L_s = 32.45 + 20 \log_{10} f_{MHz} + 20 \log_{10} R_{km} \quad (41)$$

where:

f_{MHz} = frequency in megahertz

R_{km} = range in kilometers

For $R_{km} = 1000$,

$$L_s = 141.15 \text{ db} \quad (42)$$

And for $R_{km} = 1700$,

$$L_s = 145.87 \text{ db} \quad (43)$$

The sum of the circuit losses, on the basis of the values given in Table LI, is

$$\sum L_c = L_c + L_{mp} + L_p \quad (44)$$

$$= 3.2 \text{ db}$$

The transmitter power is assumed to be +44.8 dbm, as noted in Table LI. The noise spectral density, N_o, corresponding to a 9-db noise figure (NF) is -165 dbm/Hz. From Equation (40) therefore, for $R_{km} = 1000$.

$$P_R/N_o = (73.25 - L_m)\ \text{db/Hz} \tag{45}$$

and for R = 17, 000 km

$$P_R/N_o = (68.53 - L_m)\ \text{db/Hz} \tag{46}$$

Table LIII indicates the predetection SNR available for b_o = 85 kHz. The entries on that table were calculated on the basis of Equation (37).

TABLE LIII

AVAILABLE PREDETECTION SNR

Range (kilometers)	$(SNR)_i$
1000	23.95 db-L_m
1700	19.23 db-L_m

The various curves presented in Reference 1 can now be used to obtain the SNR required to achieve a specified bit error probability. This quantity is equated to the available SNR given by Table LIII and the resulting expression is then solved for the system margin, L_M.

As an additional constraint on the coherent and noncoherent tracking systems, the maximum acquisition time is assumed to be 10 seconds. For coherent systems, this implies that the APC (Automatic Phase Control) tracking bandwidth is in excess of 340 Hz, as determined by the methods defined in Reference 1.

1. Coherent Systems -- For coherent systems, the required signal energy contrast

$(\tau P_s/N_o)$ is given as

$$(\tau P_s)/N_o = b_o \tau [(SNR)_i - (SNR)_c] \tag{47}$$

where

$(SNR)_i$ = Resultant signal-to-noise ratio appearing in receiver IF

$(SNR)_c$ = Carrier-to-noise ratio in receiver IF

If the operating noise-bandwidth of the carrier tracking loop is given as $2B_L$ Hz $(SNR)_{2BL}$, then the IF carrier-to-noise ratio can be related to the signal-to-noise ratio in the loop by the expression

$$(SNR)_c = (2B_L / b_o)(SNR)_{2B_L} \tag{48}$$

Springett[13] has shown that for the loop SNR of interest the approximate relationship between the SNR and the variance of the phase noise in the output is

$$(SNR)_{2B_L} = 1/(2\sigma_n)^2 \tag{49}$$

where

σ_n^2 = variance of loop phase error

The allowable phase noise in the output must be so chosen that the probability of losing lock is very small. In particular, the SNR in the loop noise-bandwidth must never be allowed to reach a value such that there is high probability of skipping cycles. It can be shown that the loop will skip cycles whenever the phase error, θ_e, exceeds 90 degrees. Thus, there should be only a small probability that the phase error in the loop will exceed 90 degrees.

The probability distribution of loop phase error is illustrated in Figure 87.

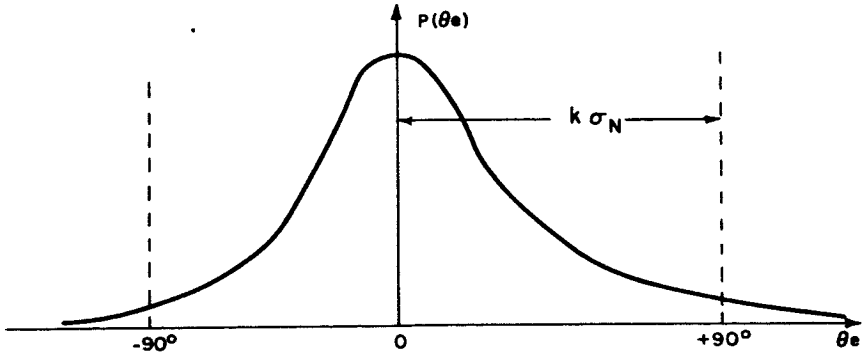

Figure 87 PROBABILITY DISTRIBUTION OF LOOP PHASE ERROR (θ_e)

If the probability of remaining in lock is 6σ then the 1σ, or rms, value of the phase jitter in the loop must be 15 degrees. From Equation (42)

$$(SNR)_{2B_L} \approx 8 \tag{50}$$

Thus, the SNR in the loop must be greater than 9 db in order to ensure that the probability of losing lock is small. Equation (48) then becomes

$$(SNR)_c \geq 8(2B_L/b_o) \tag{51}$$

From equation (47), then, the signal energy (E_s)-to-noise spectral density (N_o) available for data modulation is given by

$$\frac{E_s}{N_o} = \frac{rP_s}{N_o} \leq b_o r\,[(SNR)_i - 8(2B_L/b_o)] \tag{52}$$

where the value of $(SNR)_i$ is given on Table LIII, b_o = 85 kHz, and $2B_L$ = 340 Hz.

To achieve a bit error rate of 1×10^{-3}, the quantity rP_s/N_o must be 6.8 db for a coherent PCM/PSK system and 9.8 db for a noncoherent PCM/PSK system. It is now possible to solve for the performance margin, L_M. The results of performance margin calculations, L_M, are tabulated in a later section.

2. Noncoherent Systems

a. Tracking Systems -- A number of tracking-type noncoherent systems have been considered for possible application as a relay link for data transmission between the flight capsule and flight spacecraft. The specific systems considered are indicated in Figure 86. All of these systems possess a common characteristic in that they acquire and track a transmitted carrier signal to reduce the a priori frequency uncertainty, thereby allowing proper operation of the data demodulators. As a result, the power required for carrier acquisition and tracking reduces the total power available for data demodulation. For each of the noncoherent tracking schemes considered, there exists an expression for the probability of bit error, P_e, in terms of the ratio of signal energy to noise spectral density, rP_s/N_o, appearing at the input to the noncoherent demodulator. The relationship between rP_s/N_o and P_e is discussed in detail in Reference 1. In the system under consideration,

$$rP_s/N_o = b_o r[(SNR)_i - (SNR)_c] \tag{53}$$

where:

$(SNR)_i$ = total input SNR in a predetection bandwidth b_o Hz wide

$(SNR)_c$ = input carrier-to-noise ratio (CNR) measured in the same bandwidth as that in which $(SNR)_i$ is measured.

The input carrier-to-noise ratio is given by

$$(SNR)_c = (CNR)_{b_t} / b_o \tau \tag{54}$$

where $(CNR)_{b_t}$ is the carrier-to-noise ratio measured in a tracking bandwidth, b_t Hz wide. In general, the carrier-to-noise ratio in the tracking bandwidth, b_t, will have to be at least 10 db to avoid below-threshold performance. Thus, an upper bound on the available signal energy contrast, $\tau P_s/N_o$, is

$$\tau P_s/N_o \leq b_o \tau \left[(SNR)_i - \frac{10}{b_o \tau}\right] \tag{55}$$

It should be noted that if any data transfer is to take place, then

$$(SNR)_i > 10/b_o \tau \tag{56}$$

By substituting equation (55) in the appropriate expression for P_e for each of the systems considered, a limit can be placed on the bit-error probability corresponding to a given input SNR and value of b_o. This is, in fact, the performance margin provided by the modulation techniques of interest. The performance margin calculated for each of the tracking-type noncoherent systems considered is presented in Table LIV.

b. Nontracking Systems -- In the nontracking, noncoherent systems there is no requirement for carrier power allocated to tracking. Accordingly, the total received signal power is available for data demodulation. The expressions for bit-error probability with these systems depend quite generally on the input SNR. Each of the wide-band nontracking, noncoherent modulation techniques considered has been thoroughly analyzed in Reference 1. Expressions and curves of P_e versus input SNR are presented in that reference. These results were used in determining the respective performance margins for the various wide-band non-tracking non-coherent systems.

3. Summary -- Table LIV indicates the performance margin of each of the relay link modulation techniques under consideration. These margins are based on the nominal parameters given in Table LI for a relay link with a bit rate of 18, 000 bps and a bit-error probability rate, P_e, of 1×10^{-3}. Table LIV illustrates the relative communication efficiency of each of the relay link modulation techniques evaluated. A number of conclusions concerning relative communication efficiency can be drawn from this table.

The coherent PCM/PSK/PM system provides the maximum performance margin, and, hence, offers the best relative communication efficiency. If the choice of relay link modulation were to be made solely on the basis of relative communication efficiency, the coherent PCM/PSK/PM system would be chosen.

This is not the case, however. Other important selection criteria must be considered. Only after adequate consideration has been given to each of these criteria can a definite choice be made among the relay link modulation techniques under consideration.

It should also be noted from Table LIV that for the nominal design case considered, nontracking, noncoherent systems perform better than tracking-type noncoherent systems. This operation is due, of course, to the fact that the latter require relatively large amounts of carrier power to allow above-threshold operation.

TABLE LIV

PERFORMANCE MARGIN PROVIDED BY CANDIDATE RELAY LINK MODULATION TECHNIQUES FOR $\dot{B}$ = 18,000 BPS AND $P_e = 1 \times 10^{-3}$

System \ Range	1000 km	1700 km
I. COHERENT	db	db
A. PCM/PSK/PM	23.7	19.1
B. PCM/FSK/PM	20.6	16.0
II. NONCOHERENT		
A. Tracking		
a. PCM/MFS	19.9	14.8
b. PCM/FM	17.7	13.0
c. PCM/FSK	17.1	12.4
d. PCM/AM	17.4	12.7
B. Non Tracking		
a. PCM/MFS	22.6	17.9
b. PCM/FSK	18.6	13.9
c. PCM/AM	20.1	15.4

Additional criteria governing modulation technique selection are discussed in paragraph 5.4.5.3

5.4.5.3 Other Selection Criteria

The relay link modulation techniques under consideration were evaluated with respect to the remaining major selection criteria. A summary of the results of the evaluation follows.

1. Either coherent PCM/PSK/PM or noncoherent PCM/FSK modulation will satisfy mission requirements.

2. From the viewpoint of compatability with the environment a noncoherent rather than a coherent modulation technique is more attractive since the radio link may experience blackout for a short period of time during entry. As a result of blackout, a coherent system will very likely lose carrier phase lock and will have to perform the added task of reacquiring this lock after blackout. As the amount of time allocated for reacquisition is decreased, the communication efficiency of the coherent system will degrade correspondingly because a greater amount of carrier power will have to be allocated to the carrier phase lock-loop. A similar argument applies in the descent phase during which the flight capsule exposure to large wind gusts could cause conditions under which the relay link performance margin would drop below the threshold level, again causing the coherent link to lose carrier phase lock. This situation does not exist in the case of a noncoherent modulation scheme such as noncoherent FSK.

3. A noncoherent modulation technique is favored over a coherent one from an equipment complexity viewpoint since there is no carrier-lock requirement with its associated circuits in the noncoherent scheme.

5.4.5.4 Conclusions

On the basis of a thorough consideration of applicable modulation selection criteria and a detailed evaluation of various modulation techniques with respect to these criteria, it was concluded that a noncoherent wide-band PCM/FSK system should be developed as the relay link. This choice will significantly increase overall mission reliability because the PCM/FSK technique is considerably simpler than the more efficient but more complex coherent PCM/PSK/PM technique, and because it is more compatible with the environments typical of a planetary entry mission.

5.4.6 Relay Link Radio Frequency Performance

The relay link RF performance margin is defined as the ratio of received signal level to the threshold signal level. This relationship is indicated in Table LV where the performance margin is computed for a single point (parachute deployment) in the 1,000 x 10,000 kilometer orbit and for the body-fixed single-position flight spacecraft antenna discussed in paragraph 5.4.2. Each parameter affecting relay link performance is entered in the table in terms of the nominal value with an appropriate sign and an assigned tolerance. The listed tolerance represents the degree of uncertainty in regard to the nominal value. All significant parameters affecting relay link performance and their nominal values have been discussed in preceding paragraphs. By definition, relay link performance is considered acceptable if the nominal margin exceeds the sum (in db) of the adverse (negative) tolerances.

As can be seen from Table LV, the nominal relay link performance margin just after parachute deployment is 20 db and the sum of the adverse tolerances in only -4.5 db.

Figure 88 is a plot of the nominal performance margin for the period from separation to impact for the 1,000 x 10,000-km orbit and based upon use of a flight spacecraft antenna positioned before launch to accommodate the flight capsule mission from the 1000 x 10,000-km orbit. The data from which this curve was plotted was obtained by incorporating data from the design control chart shown in Table LV in a computer program which, among other functions, calculates the three trajectory parameters significant from telecommunications viewpoint, i.e., range, flight capsule look angle, and flight spacecraft look angle. All other parameters, including tables of flight capsule and flight spacecraft antenna gain as a function of look angle, serve as input to the computer program, as Figure 88 shows, the performance margin is well above the threshold level (maximum adverse tolerance) over the entire trajectory except during two periods.

The first period occurs during entry when the radio link signal is attenuated, or blacked out, by the flight capsule wake plasma. The magnitude of attenuation is a function of the flight capsule's entry velocity and the atmosphere encountered, as discussed earlier in paragraph 5.4.1.2. For the case shown, it is assumed that the VM-3 atmosphere is encountered. If the VM-8 atmosphere is encountered, the degradation in margin due to plasma attenuation would be negligible. Provision is made in the design for continuous transmission during entry. However, since blackout may occur, provision is also made for storing entry data and for transmitting it after a delay of 100 seconds.

The second period occurs during parachute descent when exposure to wind gusts (see paragraph 5.3.2.3) could cause the suspended capsule to sway

TABLE LV

TELECOMMUNICATION DESIGN CONTROL CHART

Orbit: 1000 x 10,000 km	FC Antenna: Planar Log Spiral
FC Position: Chute Deployment	FS Antenna: Turnstile
Frequency: 272 MHz	FS Antenna Position:
Modulation: FSK	Clock: 234 degrees
Transmitter Power: 20 watts	Cone: 153 degrees

Parameter	Nominal Value (decibels)	Tolerance (decibels)
1. Transmitter power (dbw)	+14.8	±0.5
2. Transmitting circuit loss	-0.5	±0.5
3. Transmitting antenna gain (at θ_{FC} = -35 degrees)	+5.5	±1.0
4. Space loss (R_{LS} = 1190 km)	-142.7	--
5. Multipath loss	-1.0	maximum
6. Ionospheric loss	negligible	
7. Receiver antenna gain (at θ_{FS} = -31 degrees)	+6.0	±1.0
8. Polarization loss	-0.5	--
9. Receiving circuit loss	included in 14	
10. Net circuit loss	-133.2	±2.5
11. Net received power (dbw)	-118.4	±3.0
12. Boltzmann's constant	-228.6	--
13. Reference temperature (290°K)	24.6	--
14. Noise figure	+9.0	±0.5
15. System noise spectral density	-195.0	±0.5
16. Data rate (18,000 bps)	+42.6	--
17. Required E/N_o (square law detection)	+14.0	+0.5 -0.0
18. Required threshold power (dbw)	-138.4	+1.5 -1.0
19. Performance margin	+20	+4.0 -4.5

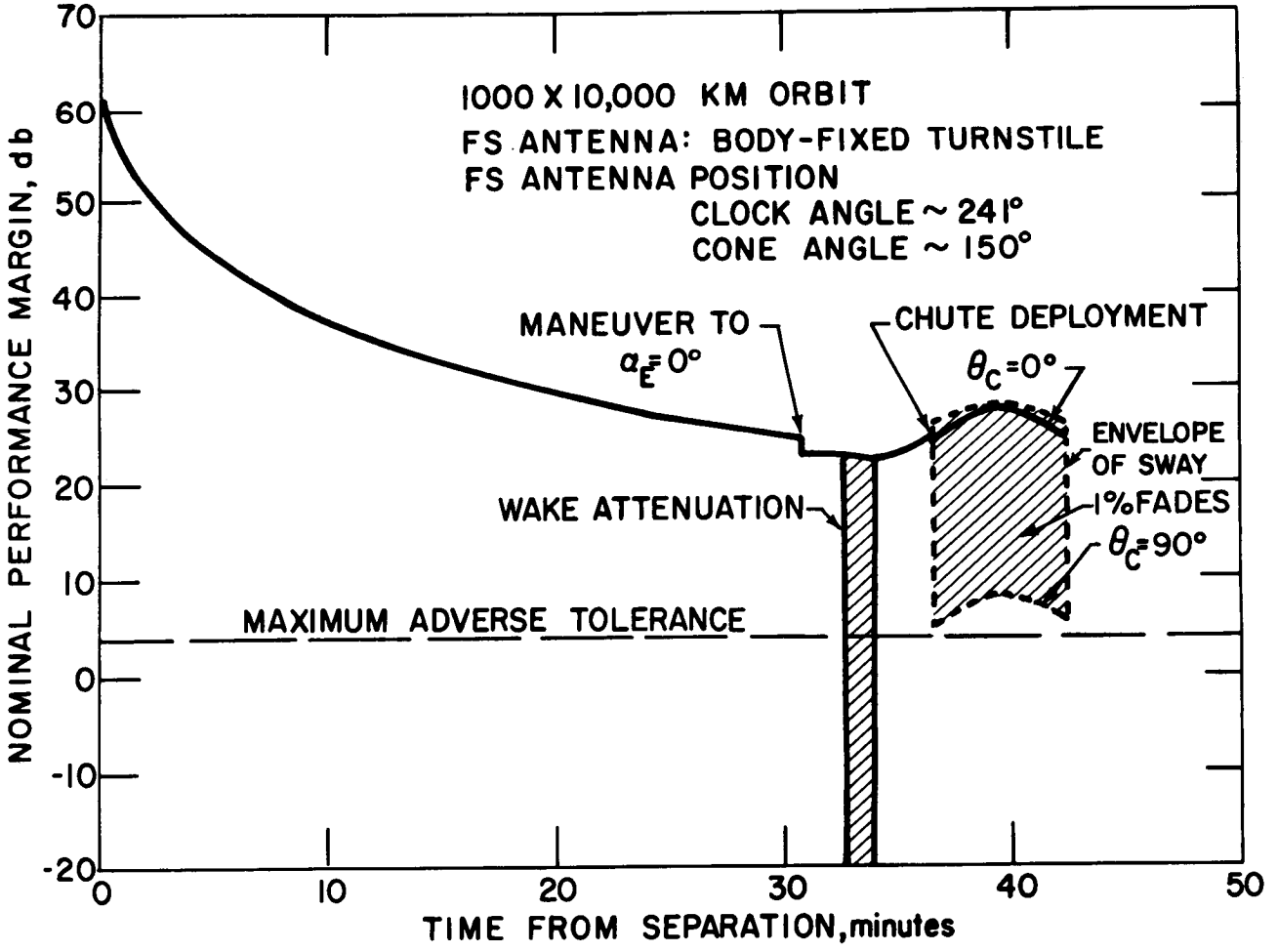

Figure 88 AVAILABLE PERFORMANCE MARGIN WITH TIME DIVERSITY

as much as 90 degrees relative to the local vertical. As the sway angle increases, the probability of data loss increases due to both a reduction in flight capsule antenna gain and an associated increase in the probability of signal fading as a result of multipath reflections from the planet surface. As noted in paragraph 5.4.1.3, the extent of multipath signal fading is a function of the flight capsule antenna back-to-front ratio. It was stated there that two antenna gains are involved. One is the "front" antenna gain, the gain obtained for a direct ray to the flight spacecraft: the other is the the "back" antenna gain, the gain obtained by the reverse polarization sense and at the appropriate angle to cause reflected signal interference. Figure 89 illustrates the direct and reflected rays. Since a polarization reversal occurs with the reflected rays, the "back" gain is the gain obtained with the opposite polarization sense. Figure 82 can be used to determine the "front" gain obtained as a function of look angle for a right circularly polarized antenna. At 35 degrees, the look angle resulting just after parachute deployment for a 1000- x 10,000-km orbit, the "front" gain is 5.5 db. The "back"gain is obtained from Figure 90 which is a plot of the left circular component obtained at a look angle of 145 degrees ($180^{o} - \theta_{FC}$). It can be seen from this figure that the highest "back" gain is -7 db. The back-to-front ratio, therefore, is -12.5 db. The effective front-to-back (F/B) ratio must also include the surface reflection coefficient (R_o). This coefficient is a function of the grazing angle. For the condition described here, the grazing angle is 55 degrees. This corresponds to an R_o of 6 db as discussed in paragraph 5.4.1.3. The effective F/B ratio is, therefore, greater than -18 db and the resulting multipath degradation is approximately 1 db (see Figure 76). Different values of θ_{FC}, caused by either a change in the flight capsule - flight spacecraft geometry or a change in the swing angle, θ_{FC}, or both, result in different values of F/B ratios and multipath losses.

Figure 91 shows the relay link performance margin as a function of capsule swing angle (θ_c) for a condition in which no form of diversity reception is used. Diversity is defined here as a general technique in which two or more copies of a signal are suitably processed by an appropriate selection or combination scheme to obtain a consistently higher degree of message-recovery performance than could be achieved if any one of the individual copies were used alone. As indicated in Figure 91, relay link performance will drop below the threshold level (maximum adverse tolerance line) for values of θ_{FC} greater than 70 degrees. At 90 degrees, the design point, relay link performance is 9 db below threshold. To regain this lost margin by simply increasing the flight capsule's transmitter power would result in a requirement for a 240-watt transmitter. This is unacceptable from the viewpoints of thermal control, antenna breakdown, and state-of-the-art capabilities, as discussed in paragraph 5.4.4.

Various forms of diversity reception were explored in an effort to find more acceptable means for improving the link margin at very large swing

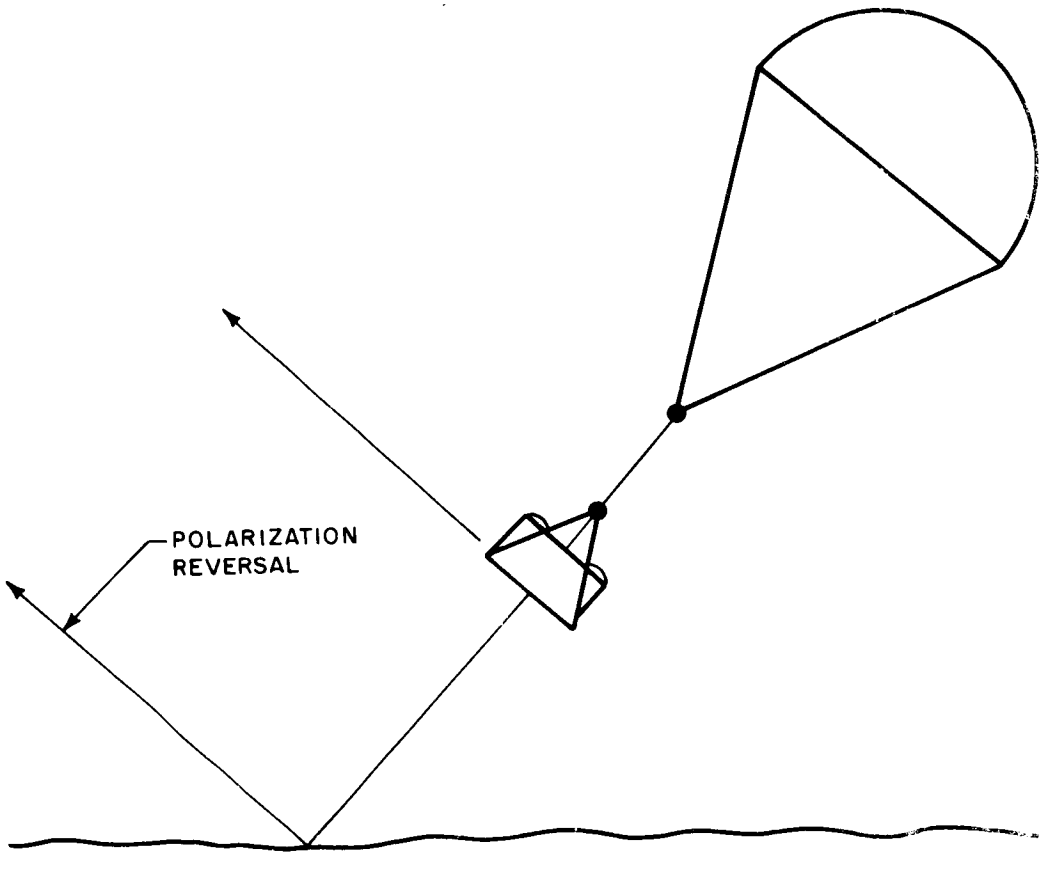

Figure 89 MULTIPATH AND OFF-AXIS EFFECT

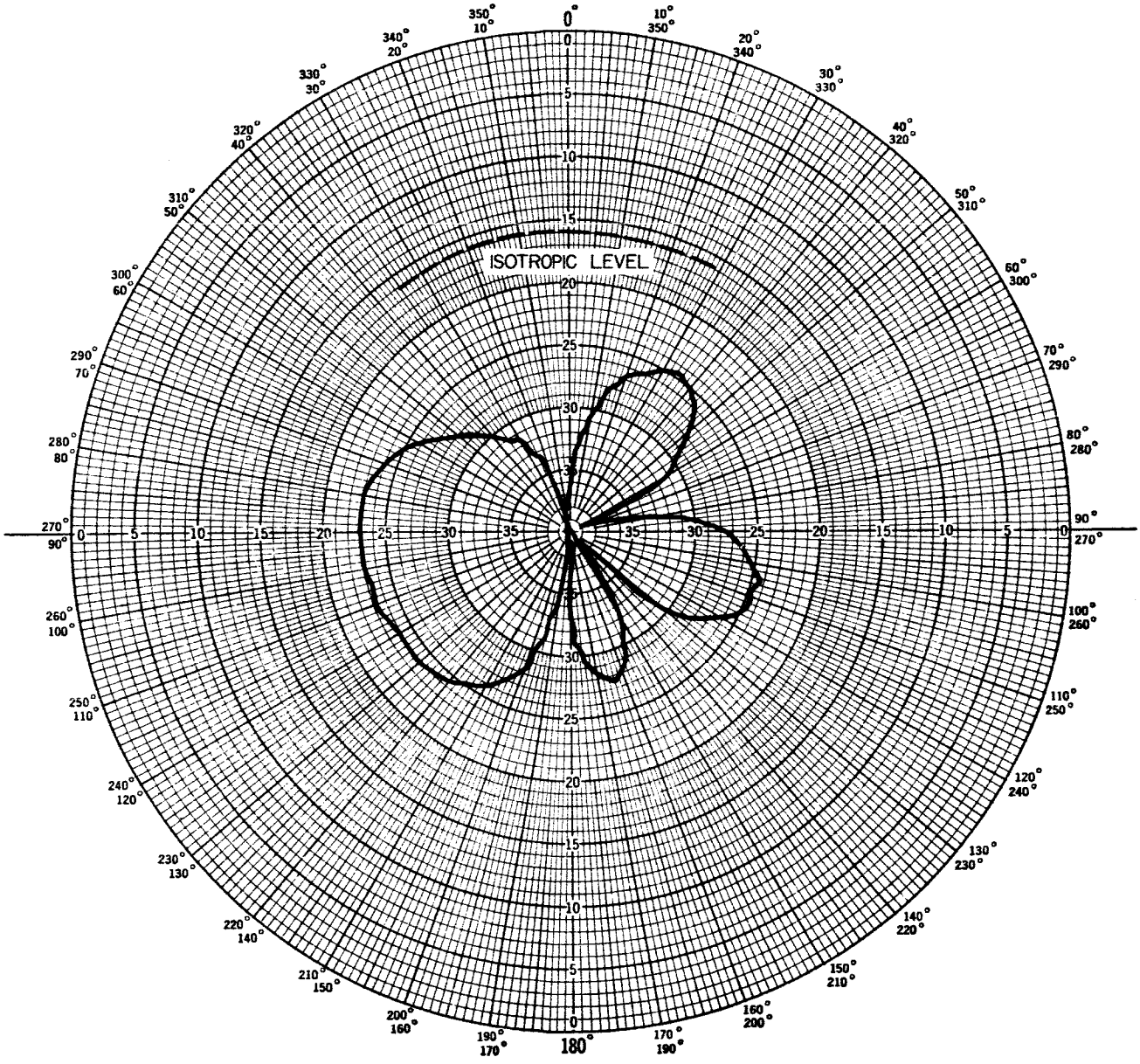

Figure 90 LEFT CIRCULAR PATTERN OF FLIGHT CAPSULE ANTENNA

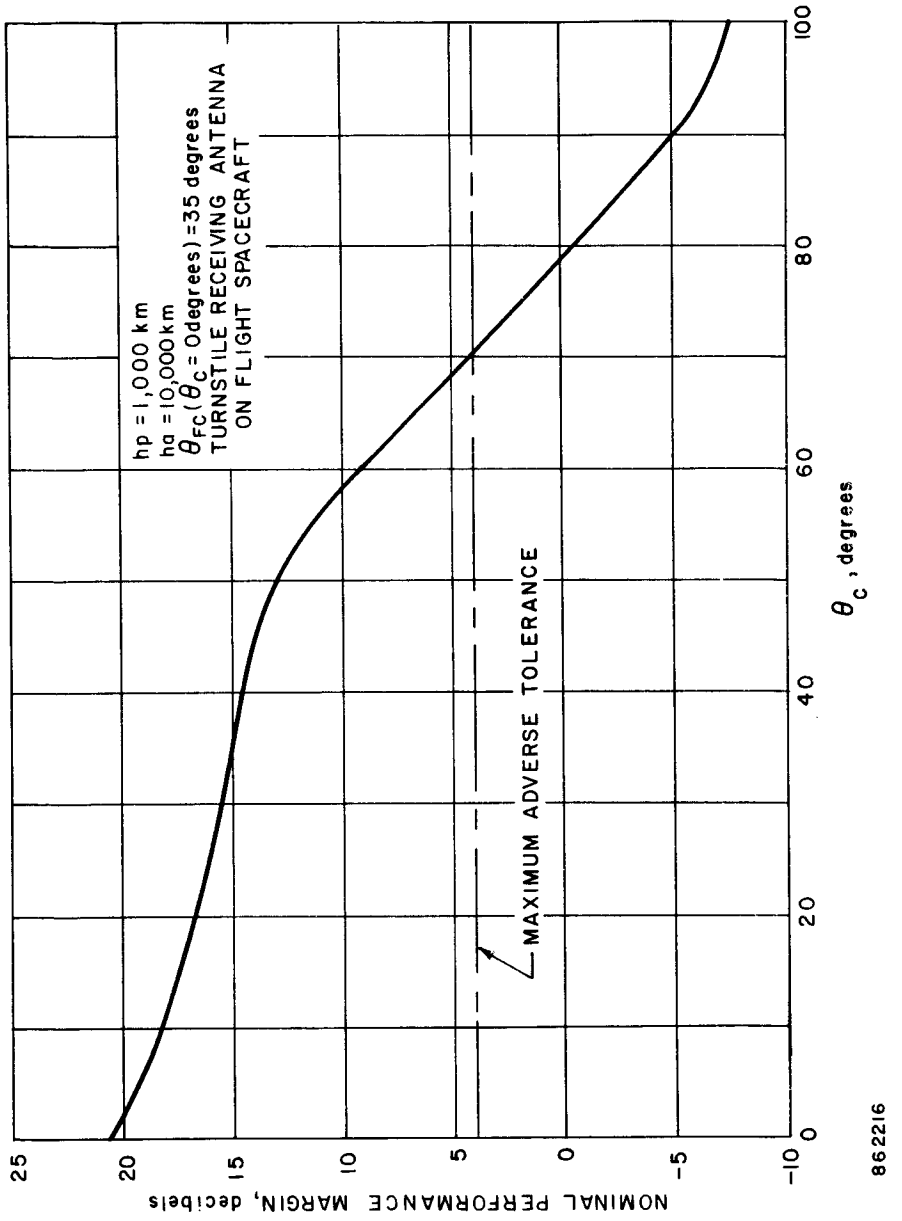

Figure 91 PERFORMANCE MARGIN AT PARACHUTE DEPLOYMENT WITHOUT DIVERSITY RECEPTION

angles. The probability of data loss at a capsule swing angle of 90 degrees is shown as a function of periapsis altitude for several such reception modes in Figure 92. Without diversity reception, there is a 20-percent probability that data will be lost each time the flight capsule swings 90 degrees from the local vertical. If time diversity is employed, the same data transmitted at one point in time is transmitted again, but delayed by a fixed-time interval. If the wind gusts are not correlated in time and if time diversity is employed, the probability of data loss is the square of the probability of data loss without time diversity.

On the assumption that a 1-percent probability of data loss is an acceptable performance criteria, it can be seen from Figure 92 that when time, polarization (left circular and right circular), or frequency (two discrete carrier frequencies) diversity is used alone, performance is unacceptable. Performance is improved, however, by combining time diversity with either polarization or frequency diversity. By combining time and frequency diversity the 1-percent criterion is satisfied for all orbits considered. By combining time and polarization diversity the criterion is met only for orbits that have a minimum periapsis of 1500 kilometers.

If no additional factors were considered, the combined time and frequency diversity technique should be selected. The improvement obtained, however, should outweigh any accompanying disadvantage. In this case, the disadvantage would be either a reduction in the data rate by a factor of 2 (to avoid exceeding the 30-watt transmitter power level), or an increase in the power level by a factor of 2 (to allow the data rate to be doubled -- to 36,000 bits per second). These alternative penalties are inherent in use of a combined time and frequency diversity technique, as indicated in the follwing discussion.

One condition necessary for frequency diversity reception is simultaneous transmission of identical data over each of two (or more) discrete frequency links. Inclusion of time diversity in addition to frequency diversity would, of course, require transmission of the same data twice, the second time at a fixed-time interval following initial transmission. This would, therefore, result in doubling the total number of bits transmitted. Neither alternative is attractive. A reduction in data rate would compromise mission performance: an increase in the power level would constitute a design risk from the viewpoint of the high-voltage arcing problem associated with use of the vacuum tube amplifiers that would be required to achieve power levels above 30 watts. However, if overall mission requirements dictate selection of the frequency and time diversity combination, the latter alternative (an increase in the power level) is recommended.

In the case of combined time and polarization diversity, the highest probability of data loss is 4 percent for a periapsis altitude of 700 km, as shown

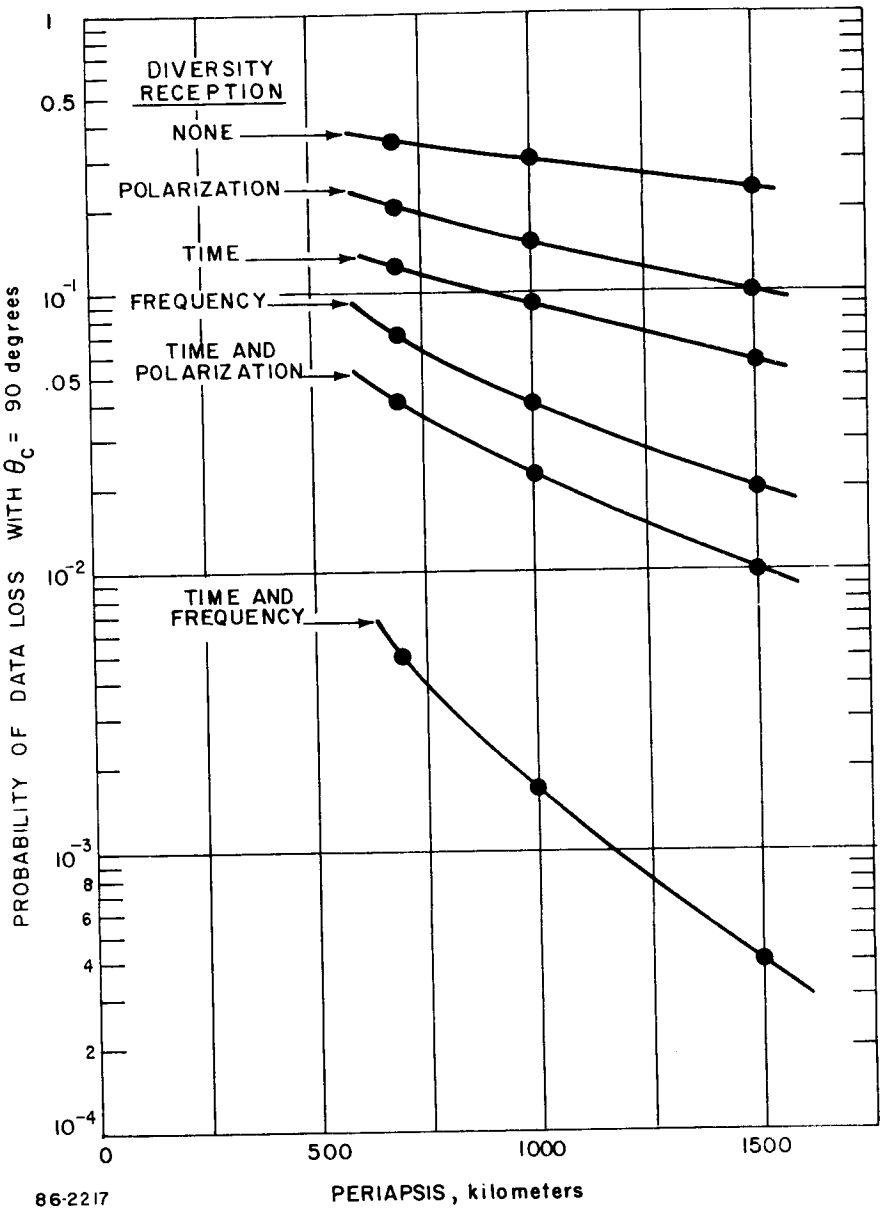

Figure 92 DATA LOSS AT CAPSULE SWAY ANGLE OF 90 DEGREES

in Figure 92. Although this technique does not meet the 1-percent criterion it is attractive in that it does not require any change in the design data rate. Since two independent radio links are already included in the telecommunication subsystem design to provide the required redundancy (see paragraph 5.4.7), each discrete radio link will require polarization diversity reception at the flight spacecraft. It is important to note that the objective of using polarization diversity in this case is not the transmission of one sense of polarization, for example, right hand, via antenna 1 and the opposite polarization sense via antenna 2. Rather, both antennas would transmit the same polarization sense, but both left-hand and right-hand polarization would be sensed by the flight spacecraft antenna subsystem.

Figure 93 illustrates the improvement in link performance that is obtained by using polarization diversity reception at the flight spacecraft. This figure shows the left-hand and right-hand circular polarization antenna patterns obtained at a look angle of 110 degrees and with the flight capsule rotated about its longitudinal axis. As this figure indicates, deep nulls would occur in the pattern if either polarization sense alone were detected at the flight spacecraft. The relay link performance margin would be well below threshold in the deep nulls.

As Figure 93 also shows, detection of both polarization senses at the flight spacecraft results in a substantial improvement relative to reception of either polarization sense, since the nulls that occur when one polarization sense is received are filled by reception of the opposite sense.

It is important to consider the fact that the relative performance of the left-handed and right-handed polarization senses of the flight spacecraft antenna are approximately equal only for very large look angles (above 100 degrees). For look angles up to approximately 90 degrees, the right-hand sense exhibits much better performance than that obtained with the left-hand sense. Therefore, inclusion of the polarization diversity reception capability at the flight spacecraft terminal with its attendant complexity (see paragraph 5.5.4.2) will improve relay link performance only during those times when the flight capsule sway is such that the total look angle exceeds 100 degrees. For look angles less than 100 degrees, relay link performance is the same regardless of whether or not polarization diversity is used.

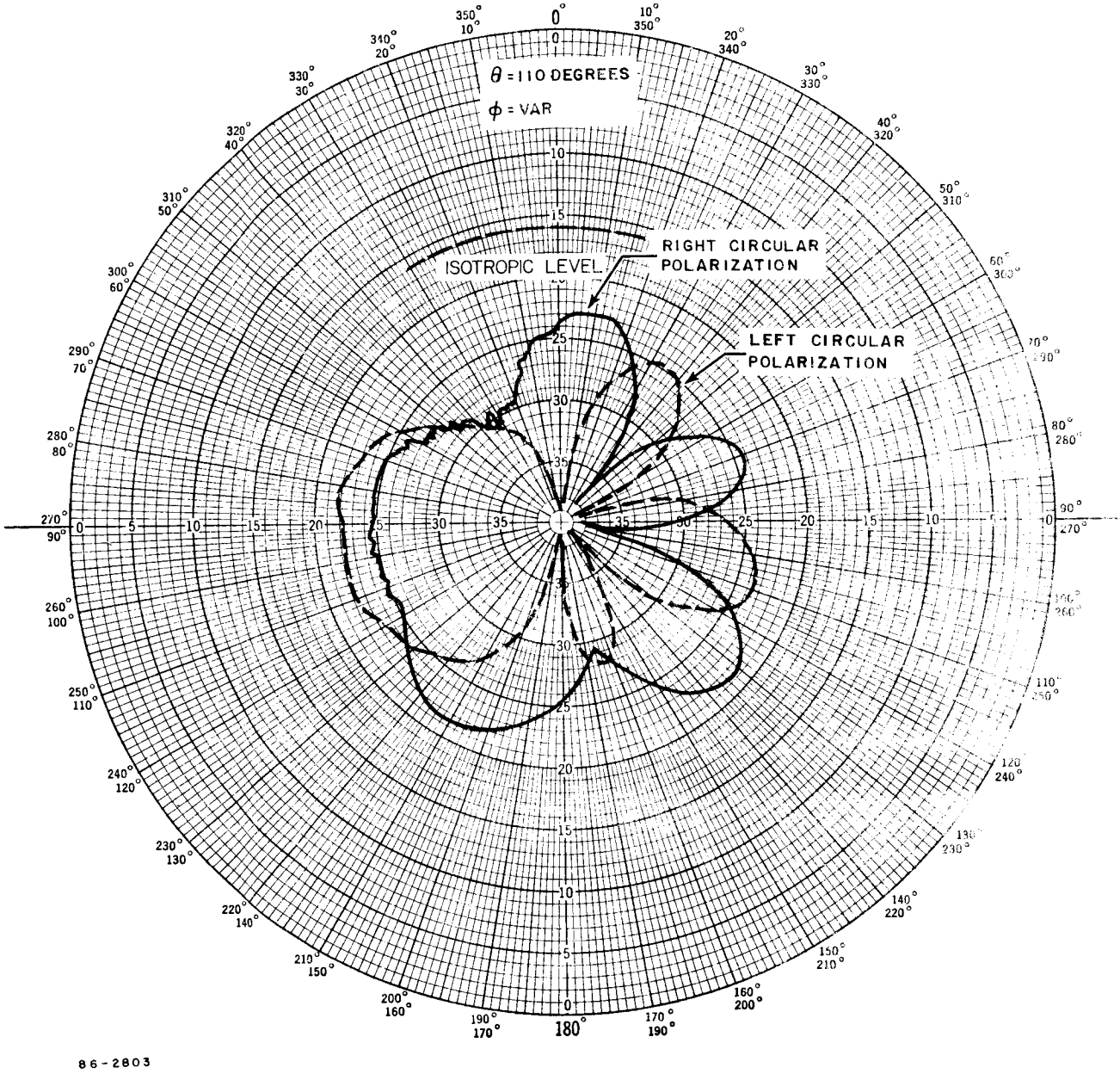

Figure 93 FLIGHT CAPSULE ANTENNA PATTERN

When combined polarization and time diversity is used, identical data need not be transmitted simultaneously as is required when a frequency diversity is combined with time diversity. Time diversity can be added by simply delaying the data transmitted on the alternative RF relay link.

In selecting the form of diversity reception to be employed, it is important to remember that both the 1-percent acceptance criterion and the uncorrelated wind gust model that was assumed are subjective constraints. It is clear, however, that time diversity in combination with either polarization or frequency diversity requires look angles greater than 100 degrees for acceptable performance. Of the two alternatives (time or frequency diversity) to be combined with polarization diversity it can be argued that by proper selection of the time diversity interval, for example, a few seconds, the capsule sway angle will be reduced to 70 degrees or less (see Figure 57). The relay link performance margin would then be above threshold without need for either polarization or frequency diversity as long as another wind gust did not occur before the flight capsule oscillation transient has decreased to a low angle value. Despite this consideration, the desire to maintain an overall conservative approach dictates selection of combined time and polarization diversity as the diversity technique to be synthesized in the conceptual design because such a technique has the least impact on other system parameters.

5.4.7 Failure Mode Considerations

The proposed telecommunication concept features totally redundant subsystems. This approach allows the use of time diversity techniques to ensure data retrieval even under the most adverse fading conditions experienced during the mission. As shown in the simplified block diagram of the telecommunication subsystem (Figure 94), all engineering and diagnostic data is fed to the corresponding data handing equipment in each subsystem. Rather than modulate radio subsystem I solely by data-handling subsystem I, and radio subsystem 2 solely by data-handling subsystem 2, it is more advantageous from the reliability standpoint to sequence the data alternately to the RF subsystems from each data-handling subsystem. This scheme will result in a recovery of all the data despite any single subsystem failure and recovery of one-half of the data in the event of any two non-redundant subsystem failures. If a one-to-one relationship rather than the alternating scheme were employed, all data would be lost if certain non-redundant failures, such as a failure in radio subsystem I and a failure in data-handling subsystem 2, occurred.

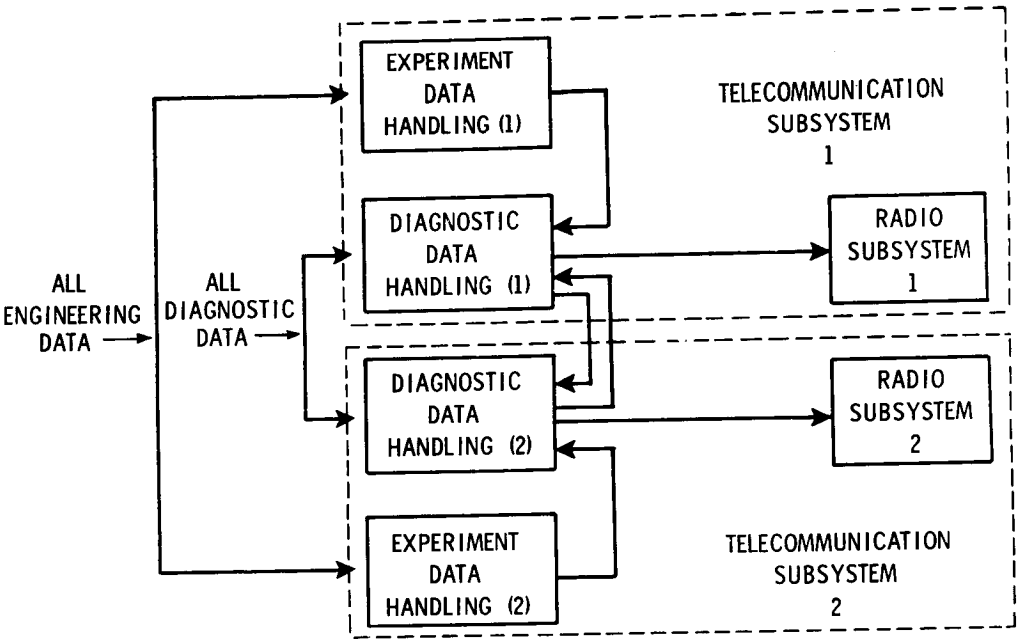

PROPOSED MECHANIZATION PROVIDES FOR:

- Total Data Retrieval For Any Single Failure
- Partial To Total Data Retrieval For Multiple Failures
- Time Diversity
- Delayed Transmission of Blackout Data

"60231P

Figure 94 FLIGHT CAPSULE TELECOMMUNICATION SUBSYSTEM MECHANIZATION

5.5 TELECOMMUNICATION SUBSYSTEM DESCRIPTION

The overall telecommunication subsystem consists of the equipment located in the flight capsule for collecting, storing, and transmitting data and the equipment located in the flight spacecraft for receiving and storing the transmitted flight-capsule data for subsequent retransmission to Earth via the flight-spacecraft telemetry link. In outline form, the overall telecommunication subsystem includes:

1. Flight-Capsule Radio Subsystem
    a. Antenna
    b. Transmitter
    c. Three-Port Circulator
    d. Directional Coupler
2. Flight Capsule Data Handling Subsystem
    a. Experiment Data-Handling Equipment
    b. Diagnostic Data-Handling Equipment
    c. Data-Storage Subsystem
3. Flight Spacecraft Radio Subsystem
    a. Antenna
    b. Receiver
4. Flight-Spacecraft Data-Handling Subsystem

5.5.1 Summary of Requirements

The telecommunication subsystem selected for detailed mechanization satisfies the design requirements presented in Table LVI. The requirements listed in this table summarize the conclusions reached on the basis of the studies described in paragraph 5.4.

TABLE LVI

TELECOMMUNICATION SUBSYSTEM DESIGN REQUIREMENTS

1. Frequency	272 MHz
2. Data rate	18,000 bps
3. Transmitter power	30 watts
4. Modulation	Frequency shift keying (FSK)
5. Flight capsule antenna	
Type	Planar logarithmic spiral
Gain	Above -17 db in 270 degrees beamwidth
6. Flight spacecraft antenna	
Type	Turnstile (body-fixed)
Gain	Above 2 db in 130 degrees beamwidth
Position	Clock: 234 degrees - Cone: 153 degrees
7. Flight spacecraft receiver noise figure	9 db (system)
8. Diversity reception	Polarization and time

5.5.2 General Description

One possible concept in the flight-capsule portion of the telecommunication subsystem is a totally redundant approach, such as that shown in block-diagram form in Figure 95. This figure shows the functional interfaces between the major flight-capsule items. One separate portion of each redundant data handling subsystem is used to handle only experiment data. Another separate portion is used to handle only diagnostic data. The reasons for this division are:

1. A failure in either portion will not compromise operation of the other portion.

2. The data-acquisition requirements are dissimilar.

3. The experiment instrumentation requirements are more susceptible to change than the diagnostic requirements; therefore, a less complex interface results from the use of two separate data-handling apparatus.

The diagnostic data-handling portion of the overall data-handling subsystem is also used as the central data routing point. This is done to obtain a single source of data modulating the transmitter.

The data-storage portion of each redundant data-handling subsystem consists, primarily, of a delay memory used to store data collected during radio blackout which may occur during entry and, also, a television data-storage section which is used to store three picture sets of television data. It can be seen from Figure 95 that the source of the data used to modulate each redundant transmitter is its corresponding diagnostic data-handling subsystem. This same data is also shown routed to the alternative diagnostic data-handling subsystem. This approach reduces the probability of total data loss for certain combinations of failures in the redundant subsystems and is discussed in more detail in paragraph 5.5.4.2.

As shown in Table XXXIV, the highest data rate during the flight capsule mission is required during descent, when television data is collected. During all other phases of the mission, the required data rate is at least an order of magnitude less than that required to handle television data. To obtain the highest data efficiency (ratio of useful information transmitted to total data transmitted) one or more in-flight changes would be required in the operating mode of the flight-capsule portion of the telecommunication subsystem. A corresponding change would then have to be made in the operating mode of the flight spacecraft portion of the telecommunication subsystem to enable an efficient data detection and storage scheme to be maintained in the flight-spacecraft receiver.

This approach -- in-flight change in operating modes -- is, however, inconsistent with the overall objective of maximizing the probability of mission success by minimizing the number of discrete events that must be successfully accomplished. Therefore, it was decided to design the flight-capsule telecommunication subsystem to operate in only one data-transmission made, a mode capable of handling the highest required data rate. This decision, of course, has a resultant impact on design of the flight spacecraft telecommunication subsystem.

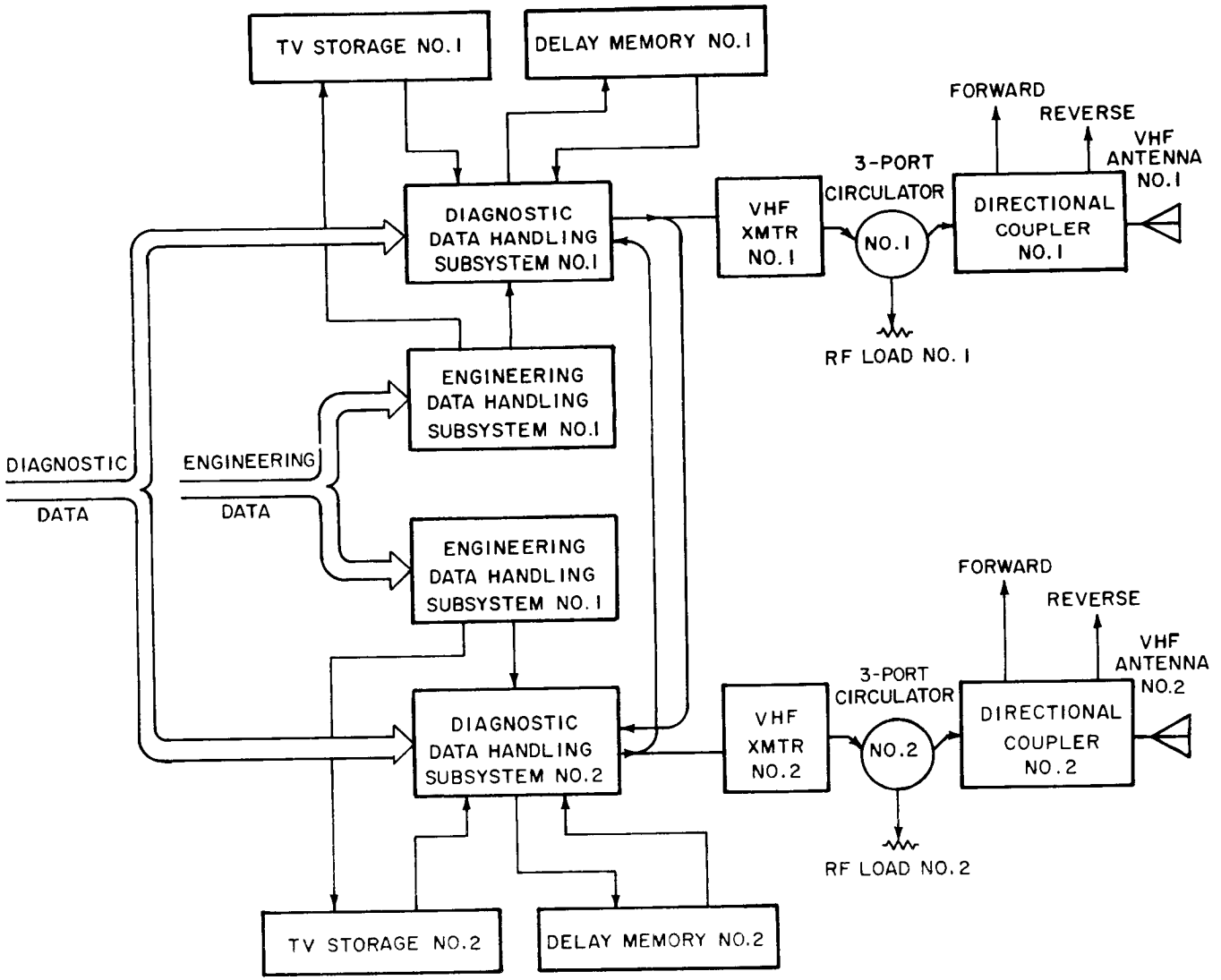

Figure 95 FLIGHT CAPSULE TELECOMMUNICATION SUBSYSTEM BLOCK DIAGRAM

Figure 96 is a block diagram of one concept of the flight-spacecraft portion of the telecommunication subsystem. The concept shown there is based on using polarization diversity reception, signal detection on board the flight spacecraft, and continuation of the total redundancy approach adopted for the flight capsule telecommunication equipment. It would be desirable to employ a single data mode for the flight spacecraft equipment for the same reason that a single operating mode was selected for the flight capsule. However, if a single mode were used, not only would the total data storage capacity required by the flight spacecraft for relay data exceed 100 million bits, but also only a small fraction of these bits would represent useful data since the duration of the critical entry/descent portion of the flight capsule mission is much shorter than the total mission duration from separation to impact. For this reason, the flight spacecraft equipment was designed to operate in two data-storage modes. During operation in the first mode, which starts prior to separation and continues until shortly before entry, the detected relay-link data from the flight capsule are stored at periodic intervals. During operation in the second mode, which starts shortly before entry and continues through flight-capsule impact, the detected relay-link data is stored continuously. These concepts are discussed in detail in the following descriptions of each of the major subsystems.

5.5.3 Flight Capsule Radio Subsystem Description

Two redundant flight-capsule radio-frequency (RF) subsystems are used in the telecommunication subsystem. Both are designed to operate continuously for approximately 5 hours: 4 hours before separation and up to 1 hour from separation to impact.

5.5.3.1 Antenna

1. Description of Selected Approach -- As stated in paragraph 5.4.2.2, a planar logarithmic spiral was selected as the conceptual design antenna for use in the case of entry from orbit. This same type of antenna was also selected for the entry from approach trajectory case, as discussed in paragraph 4.8.1. The dimensions of the antenna described in the latter paragraph were characteristic of that type of antenna; i.e., a one-half wavelength (0.5λ) diameter radiating surface backed by a quarter-wavelength (0.25λ) cavity. Of the two dimensions, the cavity depth is the more critical from the viewpoint of its effect on antenna gain. As shown in Figure 80, the flight-capsule telemetry antennas have a significant impact on the afterbody shape. In an effort to find a way to minimize this impact, three planar logarithmic spiral antennas, each having a different diameter, were constructed. Their performances were then compared to determine whether or not the antenna size could be significantly reduced.

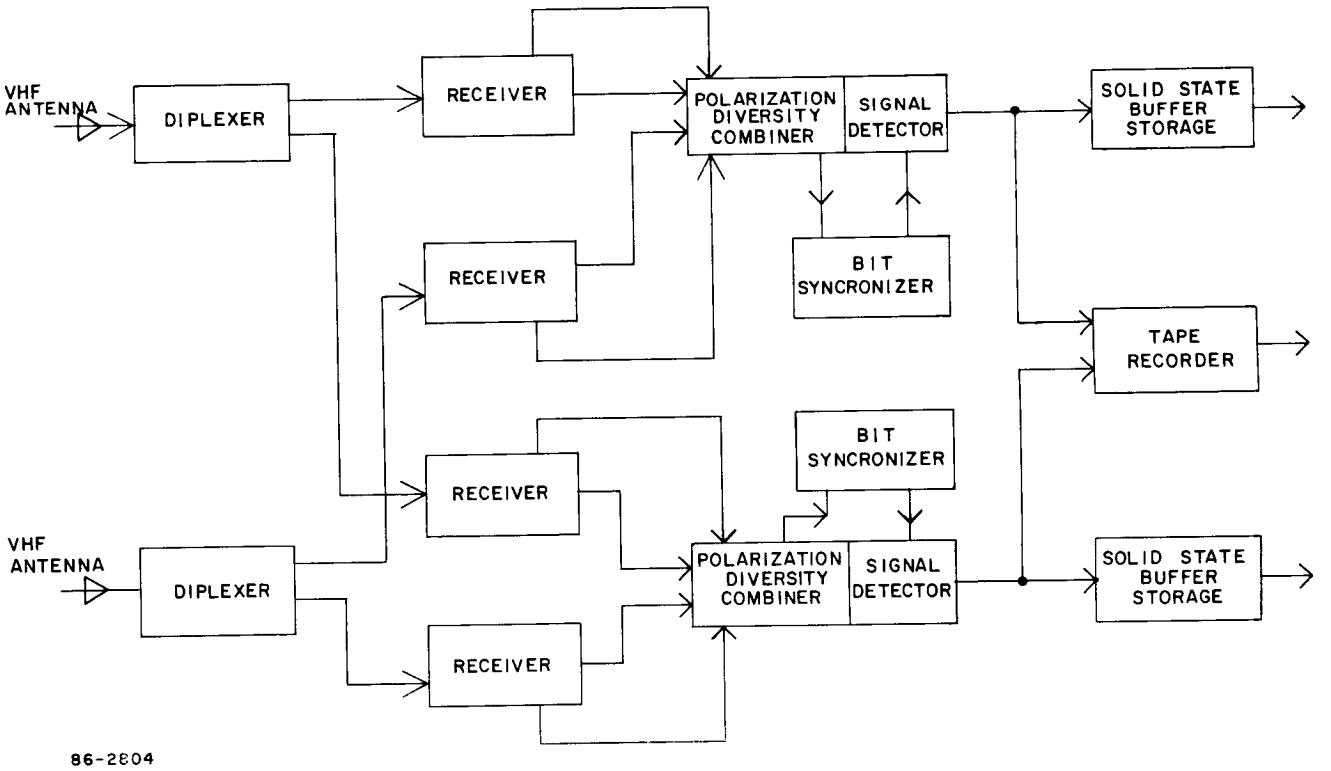

Figure 96 FLIGHT SPACECRAFT TELECOMMUNICATION SUBSYSTEM BLOCK DIAGRAM

The diameters selected were 0.5, 0.4, and 0.33 λ. Comparison of measured free-space patterns showed little difference between the performance of the 0.5λ and 0.4λ diameter antennas. Their calculated directivities were also in close agreement. The performance of the 0.33λ diameter antenna was significantly (3 db) worse than that of the other two. Since the performance obtained with the 0.4λ diameter antenna was essentially the same as that obtained with the larger 0.5λ diameter antenna, and since the smaller antenna represents a significant decrease in size (18 inches in diameter versus 22 inches), the smaller antenna was selected for the conceptual design.

The measured antenna patterns obtained during tests with this antenna mounted on a scaled mockup of the flight capsule were shown in Figures 81, 82 and 83. Appendix A presents additional performance and design information for this antenna.

2. Alternative Approaches -- In paragraph 5.4.2.2 it was shown that it was necessary to tilt the planar logarithmic spiral antennas approximately 15 degrees towards the longitudinal axis to obtain symmetrical antenna performance about the flight-capsule longitudinal axis. When the antennas were not tilted, relatively deep nulls occurred in the antenna pattern due to shadowing effects by the non-dielectric flight capsule. It would be logical to assume that this problem might be eliminated by using an antenna mounted on the axis of flight capsule symmetry; i.e., its longitudinal axis. The problem, of course, with this location is the presence of the ΔV rocket on the longitudinal axis. Unless a method could be found which either used the rocket nozzle as part of the antenna or mounted an antenna around the nozzle, the antenna would have to be placed elsewhere. Therefore, the planar logarithmic spirals, whose use is not compatible with either of these alternatives, were mounted closely adjacent to the longitudinal axis. Use of the rocket nozzle as part of the antenna was not investigated in depth since selection of such an approach could force design compromises either in the antenna or the rocket nozzle, or in both.

Figure 97 is a sketch of an approach in which two turnstile antennas are mounted symmetrically about the rocket nozzle. Two antennas are used to maintain the total redundancy approach.

The antenna concept shown in this figure is a departure from a simple turnstile in that the antenna is not centrally fed, the antenna arms are bent at the extremities, and the center portion of the antenna is wrapped around the rocket nozzle. Feeding the antenna at the extremities would allow the proper phasing networks (cable lengths) to be located inside the flight capsule. Bending of the antenna arms at the extremities results in better antenna performance at look-angles

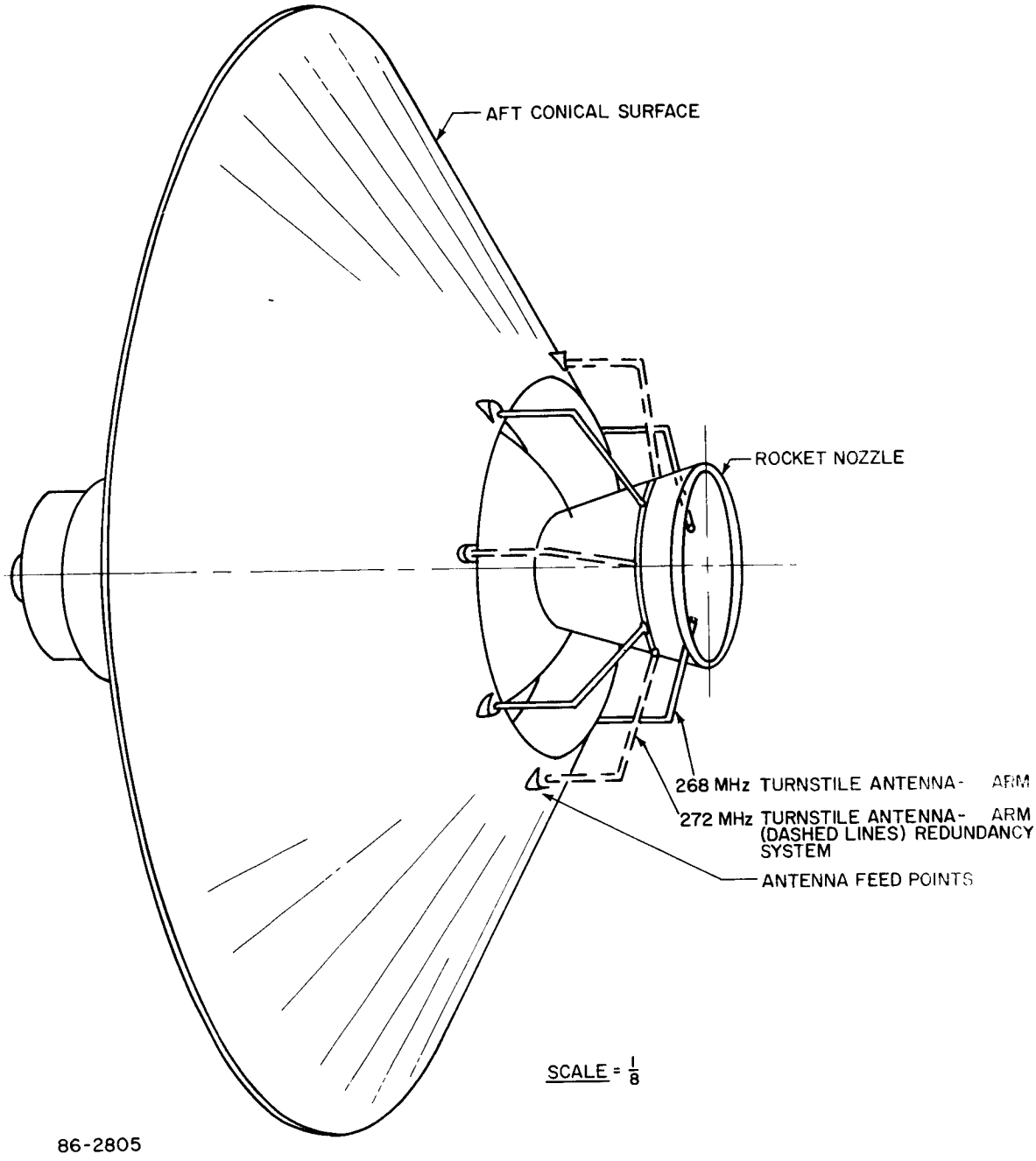

Figure 97 FLIGHT CAPSULE RELAY ANTENNA DESIGN CONCEPT

greater than 90 degrees. Wrapping a portion of the antenna around the rocket nozzle does not seriously degrade the antenna performance. Figure 98 is the measured antenna pattern obtained for an antenna based on the concept and mounted on a scaled mockup of the flight capsule. Comparison between this figure and Figure 82 (a similar antenna pattern obtained with the planar logarithmic spiral concept) shows that the turnstile approach is superior at look angles greater than 110 degrees and approximately equal in performance at other look-angles. Although it appears possible to obtain adequate antenna performance with this concept, the turnstile antenna approach was not selected as the conceptual design because such an antenna not only is exposed to extreme temperatures at the rocket-nozzle interface but also is more susceptible to detuning problems than is the planar logarithmic spiral antenna. The turnstile approach represents an attractive alternative, however, and is worthy of additional study.

Several other approaches to the problem of obtaining uniform antenna performance around the flight-capsule axis of symmetry were considered briefly. These included the following concepts:

a. Array of slots on the circumference of the afterbody

b. Annular slot plus an array of slots on the circumference of the afterbody.

c. Annular slot plus use of the rocket nozzle energized as a monopole.

d. Conical helix mounted around the rocket nozzle.

The concepts based on using slot arrays (concepts 1 and 2 above) would require six (6) to eight (8) slots, each one-half wavelength (22 inches) long and one-quarter wavelength (11 inches) deep. These concepts were considered unattractive from a physical design viewpoint in that the array would be large and bulky, especially if the total redundancy approach were applied. The slot-array design would also be unattractive from an electrical design viewpoint due to the complexity of the feed network.

The concept of using an annular slot plus the rocket nozzle energized as a monopole (concept 3 above) has merit, provided the rocket nozzle is at least one-quarter wavelength in height. This concept was not studied in depth because its selection could necessitate design compromises in either the antenna or the rocket nozzle or both.

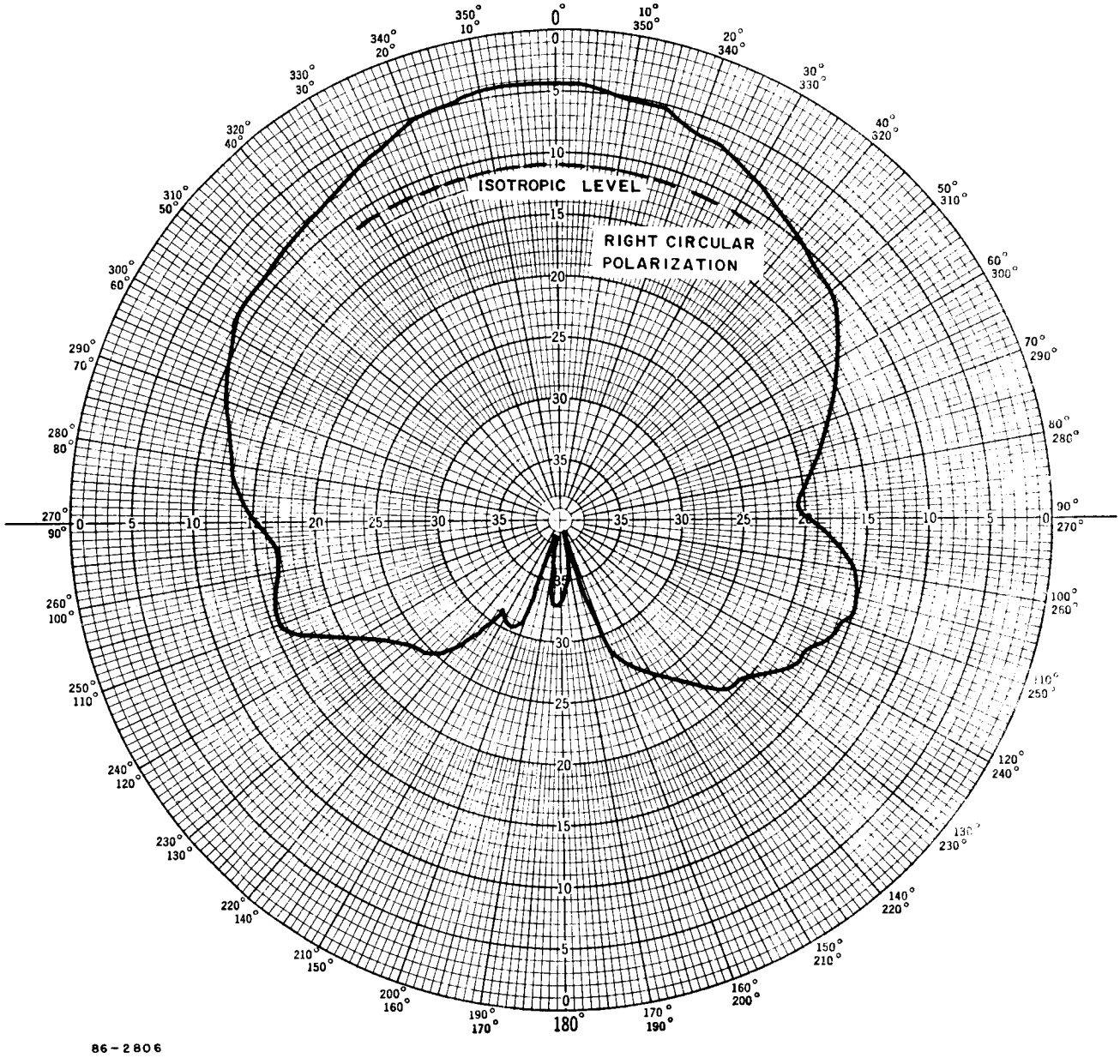

Flight 98 PRINCIPAL PLANE PATTERN OF TURNSTILE ANTENNA MOUNTED ON MOCKUP OF SUSPENDED VEHICLE

The concept of using a conical helix mounted around the rocket nozzle (concept 4 above), particularly, an antenna with the apex of the cone truncated at the exhaust port of the nozzle, is a possible approach. However, it has many drawbacks, including antenna dependence on both the height and diameter of the nozzle, inability to achieve redundant design, feeding problems, and antenna exposure to high nozzle temperatures.

Table LVII summarizes the advantages and disadvantages of each of the antenna concepts considered.

3. Principle Problems -- The principle anticipated problems in regard to antenna design are those associated with the environments to which the antenna will be exposed. The most severe of these environments from a design viewpoint is exposure to the heat produced when the ΔV rocket is fired, or, possibly, heating during entry.

The problem with the planar logarithmic spiral-antenna concept is that of protecting the antenna from the high temperatures produced by the rocket plume.

As for concepts in which the antenna is part of, or in proximity to, the nozzle, there is the additional problem of high nozzle temperatures.

Figure 99 is a plot of the expected surface temperature of the planar logarithmic spiral antenna as a function of the thickness of a Teflon radome, or heat shield, used to protect the antenna from the effects of the ΔV rocket plume. It can be seen that the shield must be approximately one-half inch thick to keep the antenna surface temperature below 200°F.

5.5.3.2 Transmitter

Completely solid state very high frequency (VHF) transmitters were selected for use in the relay link radio subsystem. These transmitters could employ the same design concepts selected for the transmitters described for use in the case of entry from the approach trajectory (see paragraph 4.8.2). The only significant differences are the higher data rate used to modulate the transmitter in the present case (18,000 bps versus 64 bps used in the case of entry from approach trajectory), and the fact that at the higher data rate the frequency stability requirement can be relaxed to a value consistent with state-of-the-art equipment ($\pm$ 0.005 percent) without significantly affecting link performance.

TABLE LVII

COMPARISON OF FLIGHT CAPSULE ANTENNA CONCEPTS

Antenna concept	Advantages	Disadvantages
Planar Logarithmic	Simple mechanical and electrical design Wide bandwidth	Not located of FC longitudinal axis*, hence, pattern not symmetrical. Affects afterbody shape
Turnstile	On FC longitudinal axis*. Simple mechanical design	Subjected to high heat pulse when ΔV rocket fired. Difficult feed network design.
Annular slot plus rocket nozzle energized as monopole	On FC longitudinal axis*.	Dependent upon rocket nozzle height. Subjected to high heat pulse when ΔV rocket fired.
Slot arrays	Around FC longitudinal axis*.	Large, bulky design Difficult feed network design Deep nulls possible in pattern.

*The flight capsule longitudinal axis is the axis of symmetry.

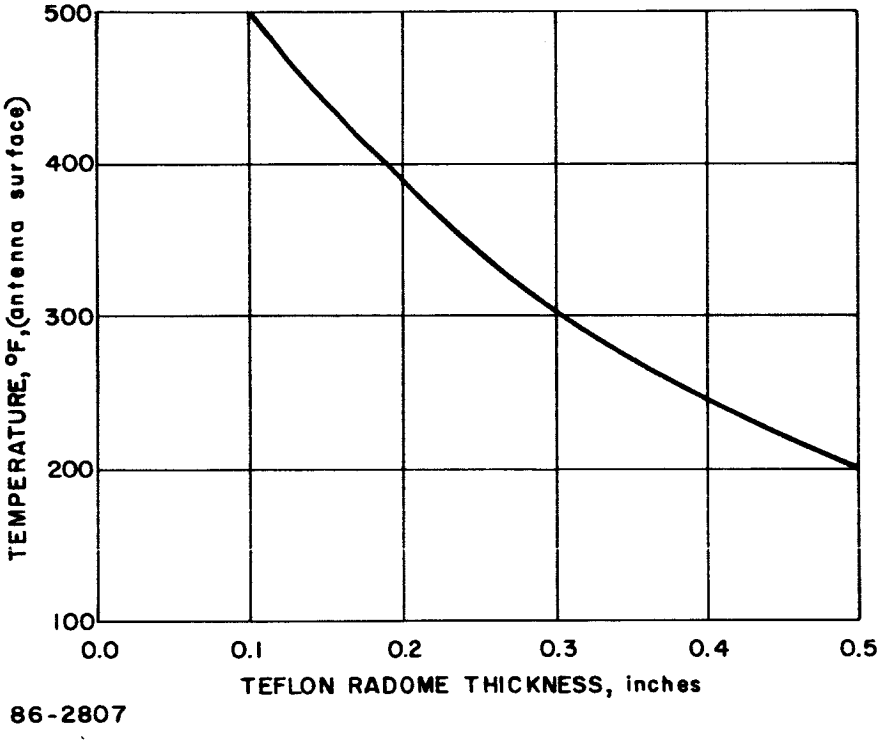

Figure 99 NOMINAL THERMAL RESPONSE OF ANTENNA CONFIGURATION

5. 5. 3. 3 Circulator and Directional Coupler

The three-port circulator is used to protect the transmitter during entry. During that period, the voltage-standing wave-ratio (VSWR) will reach high values when the radio link is blacked out and the radiated power is consequently reflected back into the radio subsystem. The solid-state transmitter is not capable of dissipating the additional reflected power; a circulator is used to transfer the reflected power to an appropriate load.

The directional coupler is dual-directional; that is, it is used to monitor both the forward and the reverse (reflected) transmitter power. Its use provides a means for determining when radio blackout starts and terminates during entry.

5. 5. 3. 4 Flight Capsule Radio Subsystem Summary

Table LVIII summarizes the salient characteristics of the flight capsule radio subsystem. The two planar logarithmic spiral antennas are inherently circularly polarized and provide an on-axis gain of approximately 6 db. Since active redundancy is employed, two discrete frequencies are required. If the antennas were excited with identical frequencies and at the same time, deep interface nulls could occur in the resultant antenna pattern.

Broad beam coverage is required during descent when exposure to wind gusts can cause considerable swinging of the flight capsule. The off-axis gain, corresponding to the maximum flight capsule look angle to the flight spacecraft during flight capsule swing, is -17 db.

Two transmitters, each operating at a different frequency, are used to obtain active block redundancy. The output power of each transmitter is 30 watts. This power level is obtained through parallel operation of two 15-watt transistorized amplifiers.

TABLE LVIII

FLIGHT CAPSULE RADIO SUBSYSTEM CHARACTERISTICS

Antenna	
Quantity	2
Type	Planar logarithmic spiral
Frequencey	272 MHz and 268 MHz
Gain	
On-Axis	6 db
Off-Axis	above -17 db in 270° beamwidth
Polarization	Circular
Transmitter	
Quantity	2
Frequency	272 MHz and 268 MHz
Frequency stability	± 0.005 percent
Output power	30 watts
Modulation	Frequency shift keying (FSK)
Data rate	18,000 bps

5.5.4 Flight Capsule Data Handling Subsystem Description

5.5.4.1 Requirements

To meet overall mission requirements, the flight-capsule data-handling subsystem must perform the following functions.

1. Provide data handling and storage services for both the experiment and diagnostic instrumentation.

2. Time multiplex (commutate) experiment and diagnostic signals.

3. Condition certain flight capsule experiment and diagnostic signals as necessary to match their characteristics to those of the respective encoding circuits.

4. Control and synchronize the experiment instruments so that the instrument internal sequence is known.

5. Provide the necessary sampling rates, including both essentially simultaneous and variously sequential sampling, to ensure collection of meaningful experiment data.

6. Perform the necessary conversions and encoding of the several forms of experiment data and place them in a suitable format.

7. Buffer experiment data, which occur at different and sporadic rates, and make them available to the time multiplexer at various but constant desired rates.

8. Use binary-coded data from the multiplexed experiment and diagnostic data to frequency-shift-key (FSK) modulate the radio frequency carrier of the flight capsule to flight spacecraft telemetry subsystem.

9. Provide a time-delayed (stored) binary replica of certain experiment and diagnostic data for inclusion in the time multiplexed data sequence.

The specific experiment and diagnostic data requirements are listed in Tables LIX and LX, respectively. The experiment data requirements are grouped into four categories according to the flight-capsule mission phase during which data are collected from the instruments within the groups.

TABLE LIX

EXPERIMENT DATA REQUIREMENTS

Measurement	Sampling Rate	Accuracy	Type of Output	No. of Outputs
1. Television	6.7 kHz(1)	5 bits	digital	3
2. Penetrometer	40 kHz	0.1 ms	analog	4
3. Surface Roughness	150 sps	7 bits	digital	1
4. Other Experiments(2)				
Accelerometers	1 sps	0.1 percent	analog	6
Temperature	1 sps	1 percent	analog	2
Pressure	1 sps	1 percent	analog	2
Water Detector	1 sps	1 percent	analog	1
Velocity-Attitude	1 sps	1 percent	analog	10
Beta Scatter	1 sps	14 bits	count	1
Radar Altimeter Range	1 sps	7 bits	digital	1
Range Rate	1 sps	7 bits	digital	1
Gas Chromatograph	0.2 sps	1 percent	analog	8
Acoustic	0.2 sps	1 percent	analog	3
Mass Spectrometer	0.2 sps	1 percent	analog	160
Radiation Detector	0.2 sps	14 bits	count	4

(1) Each set of three pictures recorded on the image tubes in the TV subsystem will be erased simultaneously in six seconds.

(2) All instruments in this category must be sampled simultaneously to provide time correlation of the samples.

TABLE LX

DIAGNOSTIC DATA REQUIREMENTS

	Measurement	Sample Rate (sps)	Accuracy	Type of Output*
1	Mass spectrometer temperature	0.2	5 percent	A
2	Mass spectrometer pressure	↓	↓	↓
3	Mass spectrometer current			
4	Gas chromatograph temperature			
5	Gas chromatograph pressure			
6	TV package temperature internal			
7	TV heater control voltage			
8	TV package pressure			
9	Sterilization canister pressure			
10	Roll θ inhibit monitor			
11	Pitch θ inhibit monitor			
12	Yaw θ inhibit monitor			
13	Propulsion engine temperature			
14	Transmitter 1 temperature			
15	Transmitter 1 current			
16	Transmitter 2 temperature			
17	Transmitter 2 current			
18	Battery No. 1 temperature			
19	Battery No. 2 temperature			
20-22	Sterile canister temperature 1 - 3			
23-38	Heat shield temperature 1 - 16			
39	After body internal pressure			
40-47	Afterbody temperature 1 - 8			
48	Parachute pack pressure			
49	Vibration X, Y, and Z Outer ring at 0 degrees			
50	Vibration X, Y, and Z forward truss member 0 degree			
51	Vibration X, Y, and Z forward truss member 0 degree			
52	Vibration X, Y, and Z forward truss member 90 degrees			
53	Vibration X, Y, and Z main support structure			
54-69	Structure temperature 1 - 16			
70-77	Heat shield ablation 1 - 8			
78-85	Pressure 1 - 8			
86-89	Penetrometer 1 - 4 temperature			
90-91	TV package temperature (external) 1 - 2			
92-103	Component box temperature 1 - 12			
104-106	ACS Nozzle Temperature 1 - 3	↓	↓	↓

*A Analog, D- Digital

TABLE LX (Cont'd)

Measurement		Rate (sps)	Accuracy	Type of Output*
107	Propulsion ignition signal (prime)	0.2	±0.1 sec	D
108	Propulsion ignition signal (back-up)			
109	Propulsion igniter continuity loop			
110	ACS system current		2 percent	A
111	ACS System voltage			
112-113	ACS tank 1 and 2 pressure			
114	Penetrometer 1 battery charge current		1 percent	
115	Penetrometer 2 battery charge current			
116	Penetrometer 3 battery charge current			
117	Penetrometer 4 battery charge current			
118	Altimeter current			
119	Altimeter voltage			
120	Doppler current			
121	Doppler voltage			
122	Camera A beam current			
123	Camera A target voltage			
124	Camera A AGC voltage			
125	Camera A clamp (black) level			
126	Camera A high voltage			
127	Camera B beam current			
128	Camera B target voltage			
129	Camera B AGC voltage			
130	Camera B clamp (black) level			
131	Camera B high voltage			
132	Camera C beam current			
133	Camera C target voltage			
134	Camera C AGC voltage			
135	Camera C clamp (black) level			
136	Camera C high voltage			
137-140	Photocell 1 current-photocell 4 current			
141-143	ACS inverter voltage phase 1-3			
144	ACS roll gyro output			
145	ACS pitch gyro output			
146	ACS yaw gyro output			
147	ACS roll error signal			
148	ACS pitch error signal			
149	ACS yaw error signal			
150-152	Gyro package temperature 1 - 3			
153	Roll angle limit cycle verification			
154	Pitch angle limit cycle verification			
155-156	+Roll nozzle 1 and 2 operation			

TABLE LX (Cont'd)

	Measurement	Sample Rate (sps)	Accuracy	Type of Output*
157-160	+Pitch nozzle 1 and 2 operation	0.2	1 percent	A
161-162	-Pitch nozzle 1 and 2 operation			
163-164	+Yaw nozzle 1 and 2 operation			
165-166	-Yaw nozzle 1 and 2 operation			
167-168	ACS manifold pressure 1 and 2			
169	Parachute load cell output			
170	Transmitter 1 forward power			
171	Transmitter 2 reverse power		5 percent	
172	Transmitter 2 forward power		1 percent	
173	Transmitter 2 reverse power			
174	Battery 1 charge current			
175	Battery 1 voltage			
176	Battery 2 charge current			
177	Battery 2 voltage			
178	External voltage 1 monitor			
197	External current 1 monitor			
180	External voltage 2 monitor			
181	External current 2 monitor			
182	Propulsion ignition signal (prime)		±0.1 sec	D
183	Roll reference angle		0.1 percent	A
184	Pitch reference angle			
185-188	Gimbal angle 1 - 4			
189	Penetrometer 1 start signal and backup		±2 sec	D
190	Penetrometer 1 deployment signal and backup			
191	Penetrometer 1 separation			
192	Penetrometer 2 start signal and backup			
193	Penetrometer 2 deployment signal and backup			
194	Penetrometer 2 separation			
195	Penetrometer 3 start signal and backup			
196	Penetrometer 3 deployment signal and backup			
197	Penetrometer 3 separation			
198	Penetrometer 4 start signal			
199	Penetrometer 4 deployment signal			
200	Penetrometer 4 separation			
201	Camera A erase lamp status		±1 sec	
202	Camera B erase lamp status			
203	Camera C erase lamp status			
204	Gimbal release confirmation			

TABLE LX (Concl'd)

	Measurement	Sample Rate (sps)	Accuracy	Type of Output*
205	Depressure sterile canister signal (prime)	0.2	±1 sec	D
206	Depressure sterile canister signal (backup)			
207	Depressurization valve operation			
208	Sterile canister separation signal (prime)			
209	Sterile canister separation signal (backup)			
210	Sterile canister FLSC detonator, continuity			
211-214	Sterile canister separation			
215	FS/FC mechanical separation signal (prime)			
216	FS/FC mechanical separation signal (backup)			
217	FS/FC separation			
218	FS/FC electrical separation signal (prime)			
219	FS/FC electrical separation signal (backup)			
220	Umbilical separation			
221-222	ACS gas supply valve 1 and 2 monitor			
223	Nose cap eject signal (prime)			
224	Nose cap			
225	Nose cap separation			
226	Pressure port open signal (prime)			
227	Pressure port open signal (backup)			
228	Entry shell electrical disconnect signal (prime)			
229	Entry shell electrical disconnect signal (backup)			
230	Entry shell separation signal (prime)			
231	Entry shell separation signal (backup)			
232	Entry shell continuity monitor			
233	Entry shell separation			
234	Change altimeter frequency command (prime)			
235	Change altimeter frequency command (backup)			
236	Change data mode command (prime)			
237	Change data-mode command (backup)			
238	Camera A shutter confirmation		± 5 sec	
239	Camera B shutter confirmation			
240	Camera C shutter confirmation			
241	Enable time gate pulse			
242	Camera A take picture command			
243	Camera B take picture command			
244	Camera C take picture command			
245	Parachute deployment signal (prime)		±0.5 sec	
246	Parachute deployment signal (backup)			
247	Parachute mortar continuity loop			
248	Parachute deployment monitor			

Figure 100 shows the required data collection profile from separation to impact for all engineering and diagnostic data.

5.5.4.2 Selection of Data Frame Format

In pulse code modulation (PCM) systems a data frame is defined as an integral number of digital words which includes a single synchronizing signal. Since a single serial-binary wavetrain must be used to modulate the transmitter, and since this wavetrain must include both experiment and diagnostic data, it would be desirable to select the data frame length or lengths for both of these sets of data such that they could be interspersed easily. The simplest method would be to make all data frames of equal length, regardless of their data content and to use the same frame synchronization bit pattern with each frame. The frame synchronization pattern is not the frame identification pattern. The latter, of course, must be different for each frame allocated to a given set of instruments.

Since television data are by far the largest single user of data capacity, data frame characteristics compatible with this data were selected. The approach taken in this study was to base the frame length on that of a single line of television data and make all other frames of experiment and diagnostic data equal to this frame in length and synchronization pattern. This is one of the many approaches which could have been used. The frame length and synchronization pattern were also selected to be compatible with the requirements of the inter-range instrumentation group (IRIG) telemetry standards (Reference 14).

1. Television Frame Format -- Each television picture consists of 200 lines of data. Each line contains 200 elements and each element is converted to a 5-bit digital word (whose content indicates any one of 32 different shades of grey). A television data frame based on one line of data must, therefore, include the 1000 bits of data in the line (200 elements x 5 bits), a frame synchronization pattern, a frame identification word, and other data as required. Table LXI shows the television frame format selected for this study. Although only 1000 data bits are contained in one line, the selected frame length is 1064 bits. The additional bit positions are used for frame synchronization and various identification and performance data. The synchronization pattern suggested in the IRIG telemetry standards is an n-bit pattern selected under the dual criteria that 1) the probability of displacement of the pattern by ±1 bit is minimized, and 2) the probability of pattern displacement by 2 to (n-1) bits is less than a prescribed maximum. The following 31-bit synchronization pattern satisfies these criteria:

0101011010100101101001101010111

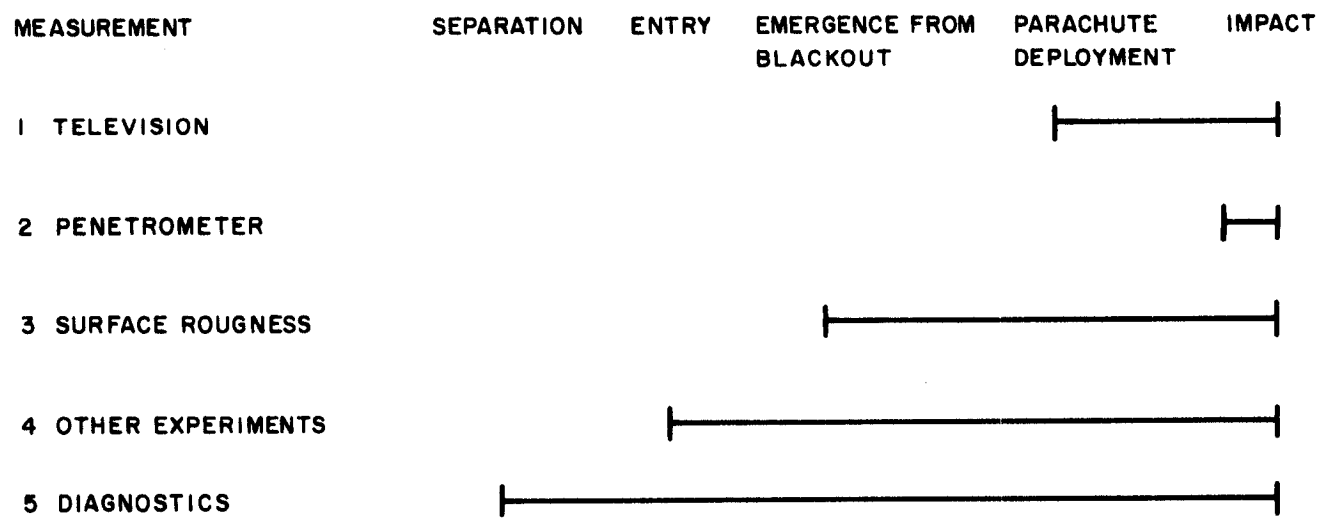

Figure 100 DATA COLLECTION PROFILE

TABLE LXI

TELEVISION DATA FRAME FORMAT

TV data (one line)	1000 bits
Synchronization pattern	31
Frame identification	4
Picture identification	4
Line identification	8
Camera identification	2
TV performance data	7
Spares	7
Total	1064 bits
Total (one picture)	212, 800 bits

Use of this pattern was assumed when 31 bits were allocated for frame synchronization.

The remaining additional bit positions were allocated as follows. Four bits were allowed for frame identification, e.g., to identify a frame as a television frame or other type of frame. This allows up to 16 different types of frames to be identified (which is more than adequate). Four bits were allocated to identify the picture sets being transmitted. This is sufficient because it is expected that no more than 16 picture sets will be transmitted. Eight bits were allocated for line identification. This is the minimum necessary to identify each of the 200 lines per picture. Three cameras are used to take nested pictures, therefore, two bits had to be allocated to identify the camera. Up to 14 bits were allocated for television performance data to make the total frame length 1064 bits.

Although not evident from the above discussion, the frame length must also be exactly divisible by seven. This is necessary for compatibility with the diagnostic data-word length (7 bit). This also

simplifies the timing required in constructing the diagnostic and other experiment frames. The 1064-bit frame selected satisfies this requirement, also. Table LXI shows that the total number of transmitted bits per television picture is approximately 6 percent greater (212,800 bits versus 200,000 bits) than the total number of actual data bits.

As noted earlier in Table LIX, the television data are acquired by three television cameras whose image tubes are erased simultaneously 6 seconds after the images are exposed. Since the number of bits per picture is 212,800, the rate that television data are acquired from the three cameras is 106,400 bits per second. Since this rate exceeds the rate capability for data transmission (18,000 bps) television data must be stored and the generation of new television data must be inhibited until transmission of the stored data is completed.

2. Penetrometer Data Frame -- Penetrometer data is obtained from the four separate penetrometers deployed shortly before flight capsule impact. The shortest time between impact of the last penetrometer to be deployed and flight capsule impact is 7 seconds. All penetrometer data must be acquired, conditioned, and transmitted from the flight capsule to the flight spacecraft within this time period, if the flight capsule serves as a relay terminal between the penetrometers and the flight spacecraft. The approach taken in this study was based on adapting the Apollo program penetrometer system to the Mars mission. The Apollo system is currently being studied by Ford, Philco, Aeronutronic, under Contract NASI-4923 for Langley Research Center. The design characteristics of that system are shown in Table LXII. It can be seen from this table that analog data is transmitted from each penetrometer at a rate of 40 kHz.

Table LXIII shows the penetrometer-link performance margin, assuming that the flight capsule is used as a relay terminal. It can be seen from this table that although the maximum range between any penetrometer and the flight capsule is only 3000 feet the worst case performance margin (nominal margin minus the magnitude of the sum of adverse tolerances) is 1.6 db. Under worst-case conditions, therefore, the penetrometer link will be operating near its threshold level. If the flight spacecraft were to be used as the receiving terminal for penetrometer data, the range would be several orders of magnitude longer and the performance margin would then be negative (below threshold) under all conditions. Hence, if the Philco system is to be adapted for Mars mission use, the flight capsule, not the flight spacecraft, must be used as a relay terminal. This is the approach taken here.

TABLE LXII

PENETROMETER DESIGN CHARACTERISTICS

Frequency band	400 - 450 MHz
Modulation	PAM/FM
Modulation frequency	40 kHz
Modulation deviation	± 150 kHz
Radiated power (each penetrometer)	0.5 watt
Frequency stability	± 0.005 percent
Frequency shift on impact	± 50 kHz
Transmitting antenna	
Type	Crossed loops
Polarization	All axial ratios both senses
Receiver	
IF bandwidth	700 kHz
Noise figure	15 db

Several alternative approaches exist for handling the penetrometer data demodulated by the flight capsule penetrometer receivers: 1) all data received from each penetrometer from deployment to impact could be converted to digital form, interlaced with other data and transmitted to the flight spacecraft; 2) since penetrometer data collected prior to penetrometer impact is meaningless, only the data received following a predetermined time interval after penetrometer deployment could be converted to digital form, etc; 3) the time of penetrometer impact could be determined from the data received at the flight capsule and only the actual impact data could be converted to digital form, etc.

The first and second approaches, although very simple, result in the acquisition and storage of large quantities of data which must be then transmitted to the flight spacecraft within 7 seconds.

TABLE LXIII

PENETROMETER LINK DESIGN CONTROL CHART

Parameter	Nominal (db)	Tolerance (db)
1. Transmitter	-3*	±1
2. Transmitting circuit losses	-1	± 0. 5
3. Net transmitting antenna gain	0	+0 -4
4. Space loss (at 3000 foot maximum)	-84. 40	--
5. Peak receiving antenna gain	+5. 5	± 0. 5
6. Receiving antenna pointing loss	-4. 5	± 5
7. Receiving antenna shadowing loss	-1. 5	± 1. 5
8. Polarization loss	-5. 0	+4. 5 -5. 0
9. Receiving circuit loss	-3. 0	± 1. 5
10. Net received power	-96. 9*	+14. 5 -19. 0
11. FM bandwidth (b_o)	58. 5	--
12. Boltzmann's constant	-228. 6	--
13. Reference temperature	24. 6	--
14. Noise figure	15	± 1
15. Signal to noise ratio	12	--
16. Threshold received power	-118. 5*	± 1
17. Margin	21. 6	+15. 5 -20

*dbw

Even if the time of impact were known to within 1 second, 200,000 bits of data would be stored for a single penetrometer (assuming conversion accuracy of only 5-bits). In the 7 seconds remaining between penetrometer impact and flight capsule impact the data rate that must be allocated to a single penetrometer would be approximately 30,000 bps. This, of course, exceeds the total transmitted data rate capability.

The third approach in which the time of penetrometer impact is determined from the received data, is the approach considered here. The time of penetrometer impact is determined by digitizing the demodulated analog samples and initiating data storage when the digitized sample exceeds a selected threshold value. Figure 101 shows the two extremes expected of the range of typical penetrometer outputs. As this figure indicates, the longest expected duration of a single penetrometer impact pulse is approximately 60 milli-seconds and the shortest is less than 5 milliseconds. The magnitude of the expected deceleration (g) pulse varies by two orders of magnitude. Rather than store the magnitude of all samples occuring above the threshold value, it is possible to select a discrete number of g levels and measure the time between g level crossings and further reduce the data requirements.

Initial study of the scientific requirements for penetrometer data (see volume V, Book 4) has established the following data specifications:

1) 15 g-levels should be used, 2) the time accuracy between successive g-level crossings should be 0.1 millisecond, 3) the maximum time between successive g-level would be 6 milliseconds, and 4) capability should be included for storing two discrete g-pulses with each penetrometer. The first of the two pulses should cover the full 15 g-levels, the second should cover only 10 g-levels. From these initial data requirements it can be seen that a maximum of 50 samples will be acquired from each penetrometer (15 g-levels in increasing order and 15 in decreasing order for the first pulse; 10 in increasing order and 10 in decreasing order for the second pulse). Six data bits must be allocated for time measurement between samples since up to 60 timing pulses are required to provide a resolution of 0.1 millisecond. Four additional bits are allocated to identify each of the 15 g levels.

Based on these considerations, 500 bits of data are acquired from each penetrometer at 50 samples, 10 bits per sample. A total of 2000 data bits is collected from the 4 penetrometers. Therefore, two 1064-bit data frames must be allocated to penetrometer data. The penetrometer frame format is shown in Table LXIV. This frame is identical to the TV frame with respect to length and synchronization pattern.

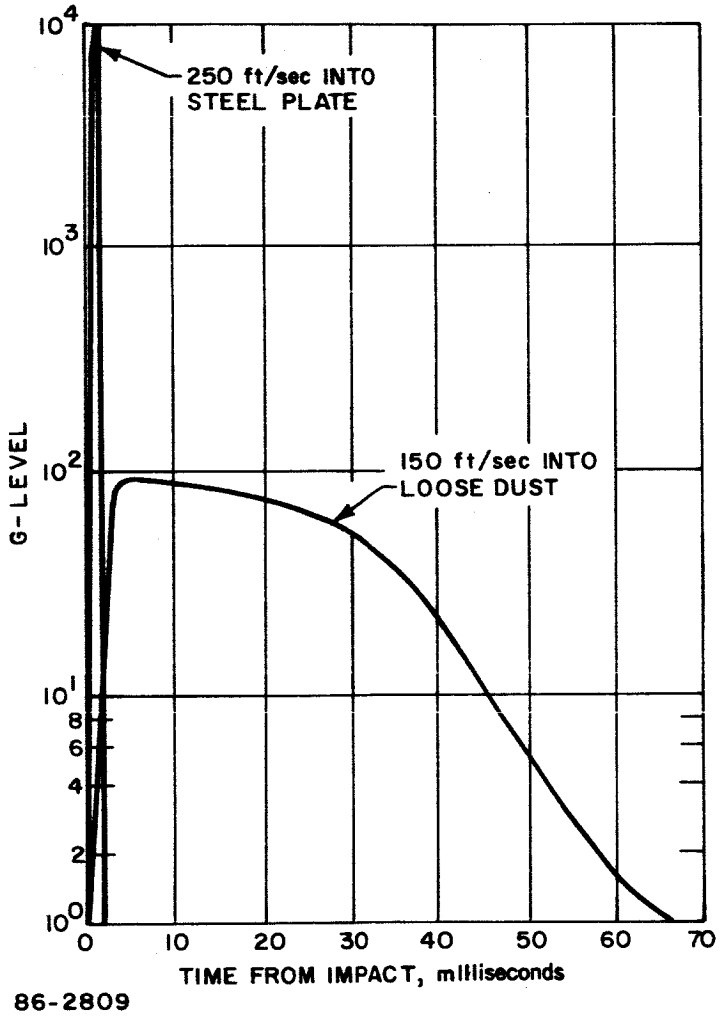

Figure 101 TYPICAL PENETROMETER OUTPUTS

TABLE LXIV

PENETROMETER DATA FRAME FORMAT

Penetrometer 1 Data		500 bits
Penetrometer 2 Data		500
Synchronization pattern		31
Frame identification		4
Spares		29
	total	1064

Note: An additional frame is required for penetrometers 3 and 4

3. Surface Roughness Data Frame - The radar altimeter processes the radar return data to obtain a measure of surface roughness (see Section 8.0). These data are quantized and stored independently. It is not stored by the data handling subsystem. The data handling subsystem is, however, required to read the surface roughness data (7-bit words) out of storage at a rate of 150 words per second. The surface roughness data frame format is shown in Table LXV.

TABLE LXV

SURFACE ROUGHNESS DATA FRAME FORMAT

Surface roughness data		1029 bits
Synchronization pattern		31
Frame identification		4
	total	1064

Since 1029 data bits in a single frame represent only 147 seven-bit words, the transmitted frame rate must be slightly higher than one per second to satisfy the 150 samples per second requirement.

4. Other Experiment Data Frame - Table LIX showed four categories of experiment measurements. The first three categories each consisted of one type of measurement. The fourth category groups together those instruments whose respective outputs require a high degree of time correlation at the time of each sampling. It can be seen from Table LIX that the data supplied by such instruments includes data in analog, digital, and count form. The analog data are converted to either 10-bit or 7-bit digital words, the number of bits depending on the accuracy required. The sampling rates required are either one sample per second or one sample every five seconds. Table LXVI shows the total number of data bits accumulated in one sample period at each of the two sampling rates, assuming all data are accumulated essentially simultaneously. It can be seen from this table that use of a complete 1064-bit data frame each second for the data collected each second would be extremely wasteful of data capacity. It is also evident that a single 1064-bit data frame cannot contain all the data collected once every 5 seconds. The approach taken in this study, therefore, was to allocate three separate data frames for the data collected at the two sampling rates. One frame consists of five samples of the data collected once per second: the two other frames include the data collected once every 5 seconds. Table LXVII shows the data frame formats of the three data frames.

5. Diagnostic Data Frame Format - Table LX listed the specific diagnostic data handling requirements. It can be seen from the table that diagnostic measurements must be sampled once every 5 seconds. Unlike the other experiment measurements, the diagnostic data samples need not be taken simultaneously. On Table LXVIII, the specific data measurements listed on Table LX are grouped in four categories according to the accuracy required. All measurements in Group A are converted into 7-bit digital words. Measurements 107 to 109 in this group correspond to event that data requires timing accuracy of +0.1 second.

Rather than sample these measurements at a high rate, the approach adopted in this study was based on starting a counter immediately after a sample is taken and then reading the contents of the counter at the next sample period. If the measured event did not occur between samples, the counter contents would then indicate the maximum count. If, however, the event did occur, the counter would stop at the time of event occurrence and the contents of the counter would then be read into the data handling subsystem.

TABLE LXVI

OTHER EXPERIMENT DATA ACQUISITION SUMMARY

Experiment	Type of Output	Number of Outputs	Digital Accuracy	Sampling Rate	Bits per Sample (bits)
Accelerometer	Analog	6	10-bit	1/second	60
Temperature	Analog	2	7-bit	1/second	14
Pressure	Analog	2	7-bit	1/second	14
Water detector	Analog	1	7-bit	1/second	7
Velocity attitude	Analog	10	7-bit	1/second	70
Beta scatter	Count	1	14-bit	1/second	14
Radar altimeter					
Range	Digital	1	7-bit	1/second	7
Range rate	Digital	1	7-bit	1/second	7
				total	193
Gas chromatograph	Analog	8	7-bit	1/5 second	56
Acoustic densitometer	Analog	3	7-bit	1/5 second	21
Mass spectrometer	Analog	160	7-bit	1/5 second	1120
Radiation detector	Count	4	7-bit	1/5 second	28
				total	1225

TABLE LXVII

OTHER EXPERIMENT DATA FRAME FORMATS

Data (1/sec)		895 bits*
Synchronization pattern		31
Frame identification		4
Spares		134
	total	1064
Mass spectrometer data		560 bits**
Gas chromatograph data		56
Synchronization pattern		31
Frame identification		4
Spares		413
	total	1064
Mass spectrometer data		560 bits**
Acoustic densitometer		21
Radiation detector		28
Synchronization pattern		31
Frame identification		4
Spares		420
	total	1064

*The number of bits collected in 5 samples.
**One-half the total number per sample.

TABLE LXVIII

DIAGNOSTIC DATA ACQUISITION SUMMARY

Group	Measurements	Type of Output	Number of Outputs	Required Accuracy	Digital Accuracy	Sampling Rates (sps)	Bits Per Sample Interval* (bits)
A	1 ____ 106	Analog	106	5 percent	7-bit	0.2	742
	107 ____ 109	Digital	3	±0.1 sec	7-bit	0.2	21
	110 ____ 113	Analog	4	2 percent	7-bit	0.2	28
	114 ____ 181	Analog	68	1 percent	7-bit	0.2	476
B	182 ____ 188	Analog	7	0.1 percent	10-bit	0.2	98**
C	189 ____ 200	Digital	12	±2 sec	1-bit	1	120
	201 ____ 245	Digital	45	±1 sec	1-bit	1	225
D	246 ____ 256	Digital	11	±0.5 sec	1-bit	2.0	110
							1820

*A sample interval is assumed to be 5 seconds.
**It is assumed that each 10-bit sample occupies two 7-bit data channels.

All measurements in group B are converted into 10-bit digital words. Since there are many more 7-bit diagnostic data words than 10-bit words, the data frame length selected is an integral number of 7-bit words. To simplify timing requirements, each 10-bit word occupies two 7-bit data channels in the diagnostic data frame.

Groups C and D consists of binary event data, hence a single 7-bit data channel can be used for 7 separate events. As can be seen from Table LXVIII, the total number of bits collected in one 5-second sampling interval exceeds the number that can be included in a single 1064-bit data frame. Accordingly, two separate data frames are allocated for the diagnostic data. Table LXIX shows the formats of these two frames.

TABLE LXIX

DIAGNOSTIC DATA FRAME FORMATS

Data		910 bits
Synchronization pattern		31
Frame identification		4
Spares		119
	total	1064
Data		910 bits
Synchronization pattern		31
Frame identification		4
Spares		119
	total	1064

5.5.4.3 Data Transmission Sequence

In the preceding discussion of data-frame format selection, it was shown that eight discrete frames of data are used; six for experimental data (2 for penetrometer data, one for surface roughness, 3 for other experimental data), and two for diagnostic data. Of the six experiment data frames, the three other experiment data frames must be transmitted

once every 5 seconds, the surface roughness data frame must be transmitted at a rate slightly greater than once per second, the two penetrometer data frames must be transmitted once every 7 seconds, and the television frame rate should be as high as possible to obtain as many pictures as possible. The television frame rate can be determined after allowance for both the diagnostic data frame rate and the frame rate that must be allocated for transmission of data stored during radio blackout. It can be seen from Tables LXVIII and LXIX that the diagnostic data frame rate must be two frames every 5 seconds.

As the data collection profile shown in Figure 100 indicates, only diagnostic and other experiment data require collection during entry (when radio blackout will probably occur). The approach taken in this study to prevent loss of these data was based on transmitting the data collected during entry regardless of the fact that the radio link may be blacked out, simultaneously storing the appropriate diagnostic and experiment data frames in a first-in first-out buffer memory to create a time delay, and subsequently retransmitting the delayed data. This approach is feasible as long as the time delay is greater than the expected duration of blackout and less than the time between the end of blackout and flight-capsule impact. Radio blackout will probably begin about the time the first sensible deceleration level is reached and end when the flight capsule velocity is reduced to approximately 11,000 ft/sec.

The maximum time from the start to the end of blackout, for all trajectories of interest is 87 seconds, as shown in Figure 102. This time would always be ample for retransmitting the critical entry data if the parachute operates correctly. If the parachute is not deployed, the minimum time between blackout emergence and flight capsule impact will be 113 seconds for all trajectories considered.

By selecting a mean time between these extremes; that is, 100 seconds as the delay time, additional allowance will be provided to cover the possibility of blackout periods slightly longer than expected and additional time will be available for retransmission in the event the impact point is higher than the mean surface level. This is the approach selected in this study. It results in a frame rate of one data frame per second for blackout data.*

Table LXX summarizes the required and allocated data frame rates for each of the different types of data frames. In each case, the allocated frame rate is equal to or greater than the required frame rate. The allocated frame rates were so chosen that except for the

* Two diagnostic and three other engineering frames are collected every five seconds.

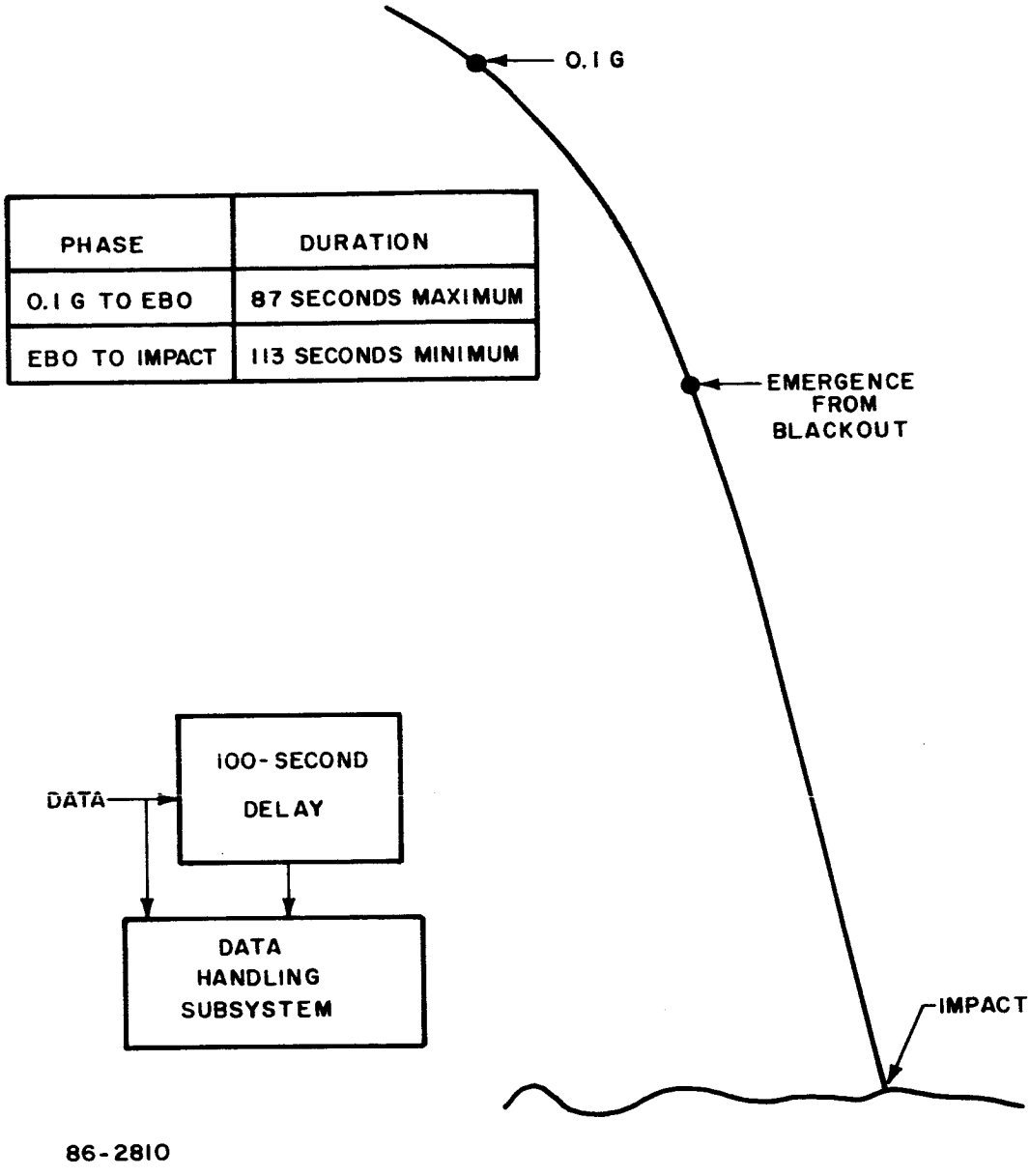

Figure 102 BLACKOUT DATA RECOVERY CONCEPT

TABLE LXX

DATA FRAME RATE ALLOCATIONS

Data Frame	Frame Rate Required	Frame Rate Allocated	Date Rate (bps)
Penetrometer	2 per 7 seconds	2 per 5 sec	426
Surface Roughness	slightly above 1 per sec	6 per 5 sec	1276
Other Experiment	3 per 5 sec	3 per 5 sec	638
Diagnostic	2 per 5 sec	2 per 5 sec	426
Blackout Data	1 per sec	5 per 5 sec	1064
Television	As high as possible	68 per 5 sec	14,470
		Total	18,300

television data, the data sequence could be repeated every 5 seconds. The television frame-rate allocation was based on consideration of the data rate capability constraints and the data rates required to satisfy all other experiment and diagnostic data requirements. The transmitted data rate required to meet the frame rate allocations is 18,300 bps. This is very close to the 18,000 bps data rate used as the basis for evaluating relay link performance as discussed in paragraph 5.4.

Figure 103 shows the data transmission sequence, that is, the sequence in which the previously described frames are transmitted to the flight spacecraft. It can be seem from this figure that 68 frames (lines) of television data are interspersed with 18 frames of engineering, diagnostic, and blackout data in a 5 second period, as shown in Table LXX. Within each 5-second period, 34 frames of television data are interspersed with 9 frames of engineering and diagnostic data at 2.5 second intervals. This is done to obtain time diversity in the transmitted sequence. The time diversity is obtained without equipment penalties by taking advantage of the fact that the flight capsule contains two actively redundant telecommunication subsystems. It can be seen from Figure 103, that the data from data handling subsystem 1 is transmitted to the flight spacecraft via radio subsystem 1 during the first 2.5-second time interval and these same data are then retransmitted to the flight spacecraft, this time from data handling subystem 2 via radio subsystem 2 during the second 2.5-second time interval. It can also be seen from this figure that although the data sequence in each of the redundant data handling subsystems is repeated every 5 seconds, the sequences are not identical and are alternated between the two redundant radio subsystems.

Although the data transmitted in any given 5-second sequence is the same from each redundant subsystem the order in which the data is transmitted is not identical. This is done to obtain time diversity. The data from each redundant data handling subsystem are transmitted alternately via each of the redundant radio subsystems every 5 seconds. This approach reduces the probability of total data loss as a result of a combination of subsystem failures. Table LXXI is a simple truth table showing the effects of subsystem failure on data transmission. Under the data transmission columns, the non-alternated data frames heading referes to a condition in which data frames from data handling subsystem 1 modulate only radio subsystem 1 and, similarly frames from data handling subsystem 2 modulate only radio subsystem 2. The alternated data frames heading referes to the approach taken in this study in which the sequences of data from the redundant data handling subsystems are alternated between the redundant radio subsystems. It can be seen from this table that if the non-alternated approach is taken, failures in both corresponding data handling and radio subsystems will result in a total loss of data. If the alternating approach is taken,

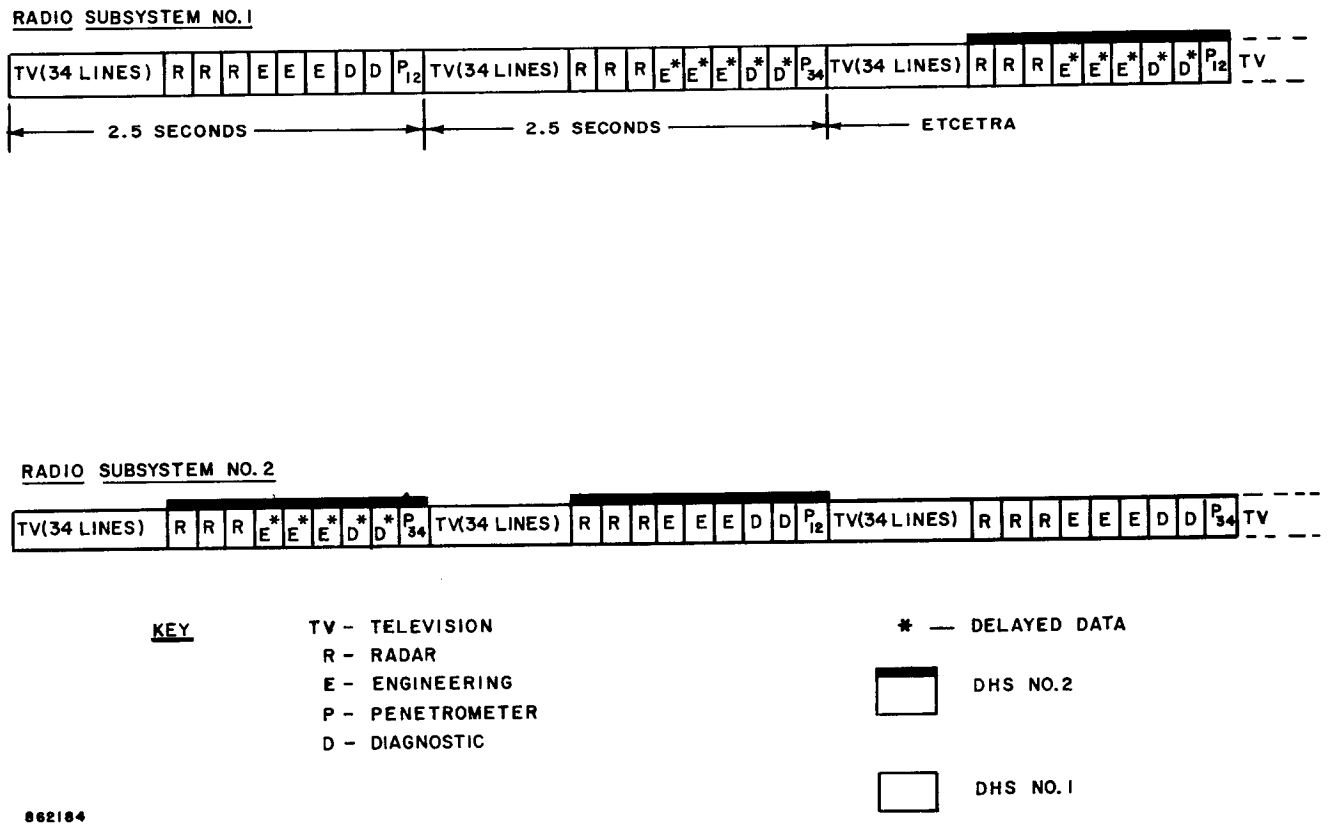

Figure 103 DATA TRANSMISSION SEQUENCE

TABLE LXXI

EFFECT OF SUBSYSTEM FAILURE ON DATA TRANSMISSION

Operating State				Data Transmission	
Data Handling Subsystem 1	Data Handling Subsystem 2	Radio Subsystem 1	Radio Subsystem 2	Nonalternated Data Frame	Alternated Data Frames
0	1	0	1	0	1
0	1	1	0	1	1
1	0	0	1	1	1
1	0	1	0	0	1
1	1	1	1	1	1
1	1	0	0	0	0
0	0	0	0	0	0

1 - Subsystem operating, data transmission
0 - Subsystem failed, no data transmission

only a partial loss of data would occur for the same failure mode. The data lost would be every other 5-second sequence of data, that is, one-half of the total data transmitted. With either approach it can be seen from Table LXXI, at least two non-redundant subsystem failures must occur regardless of the approach before all data is lost.

The sequence in which television data is transmitted was purposely not discussed in the preceding paragraphs. Since the television data sequence is not repeated every 5 seconds, 600 frames of television data, representing three 200-line television pictures, must be transmitted before a new sequence of pictures may be started. Furthermore, it is desirable to select a television data transmission sequence such that data are played out in the following order: C-camera data, followed by B-camera data, followed by A-camera data. This scheme is based on the fact that the shortest expected descent time allows transmission of approximately 10 pictures at the television data transmission rate. Since there are three pictures in each set, the tenth picture will be the first picture in the fourth set. Because the C-camera is the highest resolution camera, a picture from this camera is the logical candidate to be transmitted as the tenth picture. In general, the last picture before impact shall be from the highest resolution camera (C-camera).

Figure 104 shows a television transmission sequence which satisfies this requirement and also provides the alternated data sequence required for failure allowance and time diversity transmission. The alternated data sequence does not begin until the first 2.5 second time interval is completed. At this time only data from redundant C-camera memories is being transmitted, and the process continues until the C-camera data is completely transmitted. This data will be followed by B-camera and then A-camera data. The 2.5 second time diversity mentioned earlier is obtained by transmitting the first 34 frames of C-camera data from one of the redundant data handling subsystems during the first 2.5 second interval, but delaying playout of the same data from the alternate data handling subsystem until the second 5-second time interval. Rather than transmitting no television data during the otherwise dead time occurring every other frame in the first 2.5 second interval, the first 34 frames of B-camera data will also be transmitted. These 34 frames of B-camera data will still benefit from time diversity, but their transmission will be delayed by approximately 14 seconds rather than the 2.5 seconds used for all other frames.

5.5.4.4 Conceptual Design

Two actively redundant data handling subsystems were selected for use in the flight capsule portion of the telecommunication subsystem. They provide the means for collecting and storing the experiment and diagnostic data and for converting such data into a form suitable for transmission

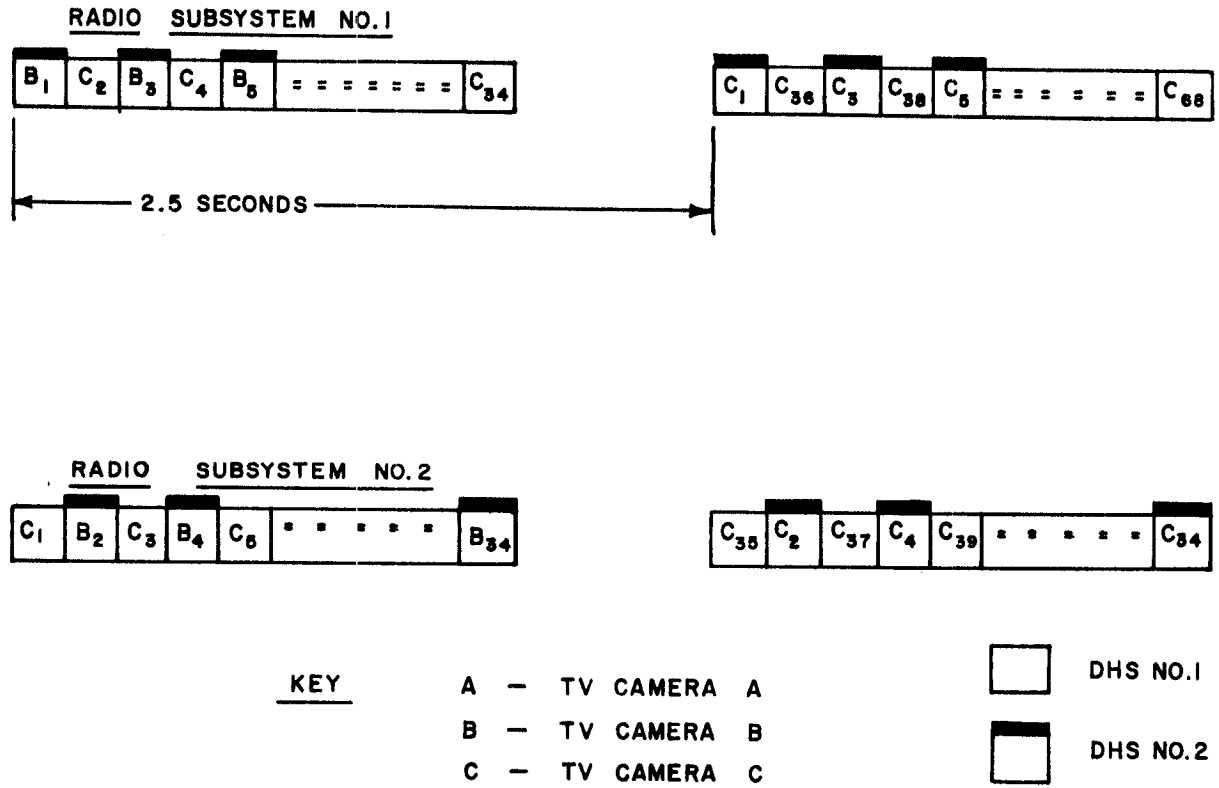

862185

Figure 104 TELEVISION DATA TRANSMISSION SEQUENCE

to the flight spacecraft. The approach taken in this study was based on use of a flight-capsule data handling subsystem which contained the following items:

1. Experiment data handling subsystem

2. Diagnostic data handling subsystem

3. Data storage subsystem

Separate portions of the data-handling subsystem were allocated to handle the experiment and diagnostic instruments for the following reasons:

1. A failure in either the experiment or diagnostic portion would not compromise the operation of the other portion.

2. The data acquisition requirements are dissimilar.

3. The experiment instrumentation requirements are more susceptible to change than the diagnostic requirements, therefore, a less complex interface results from the use of two separate portions.

It was assumed that the experiment data-handling subsystem would handle only that data provided by the experiment instruments and that the diagnostic data-handling subsystem would handle only diagnostic and event data. It was further assumed that the diagnostic data-handling subsystem would serve as the central routing point for all data modulating the RF transmitter.

1. Experiment Data Handling Subsystem -- Figure 105 shows the experiment data-handling subsystem concept in block diagram form. This concept is similar to that of the external data-automation equipment described in paragraph 4.11. The major tradeoffs leading to selection of the design concepts shown in Figure 105; that is, decentralized approach, voltage controlled oscillator (VCO) analog-to-digital (A/D) converters, are the same as those discussed in paragraph 4.11.2. A brief description of possible methods of handling the three forms of experiment data is given in the following paragraphs.

a. Penetrometer Data -- Figure 106 shows a block diagram of one concept for converting the pulse amplitude modulated (PAM) data from one of the four penetrometer receivers into digital form. The PAM data is monitored by 15 threshold detectors. Each threshold represents one of the selected g levels. When the first (lowest g level) threshold is exceeded, the logic circuitry transfers a 4-bit word

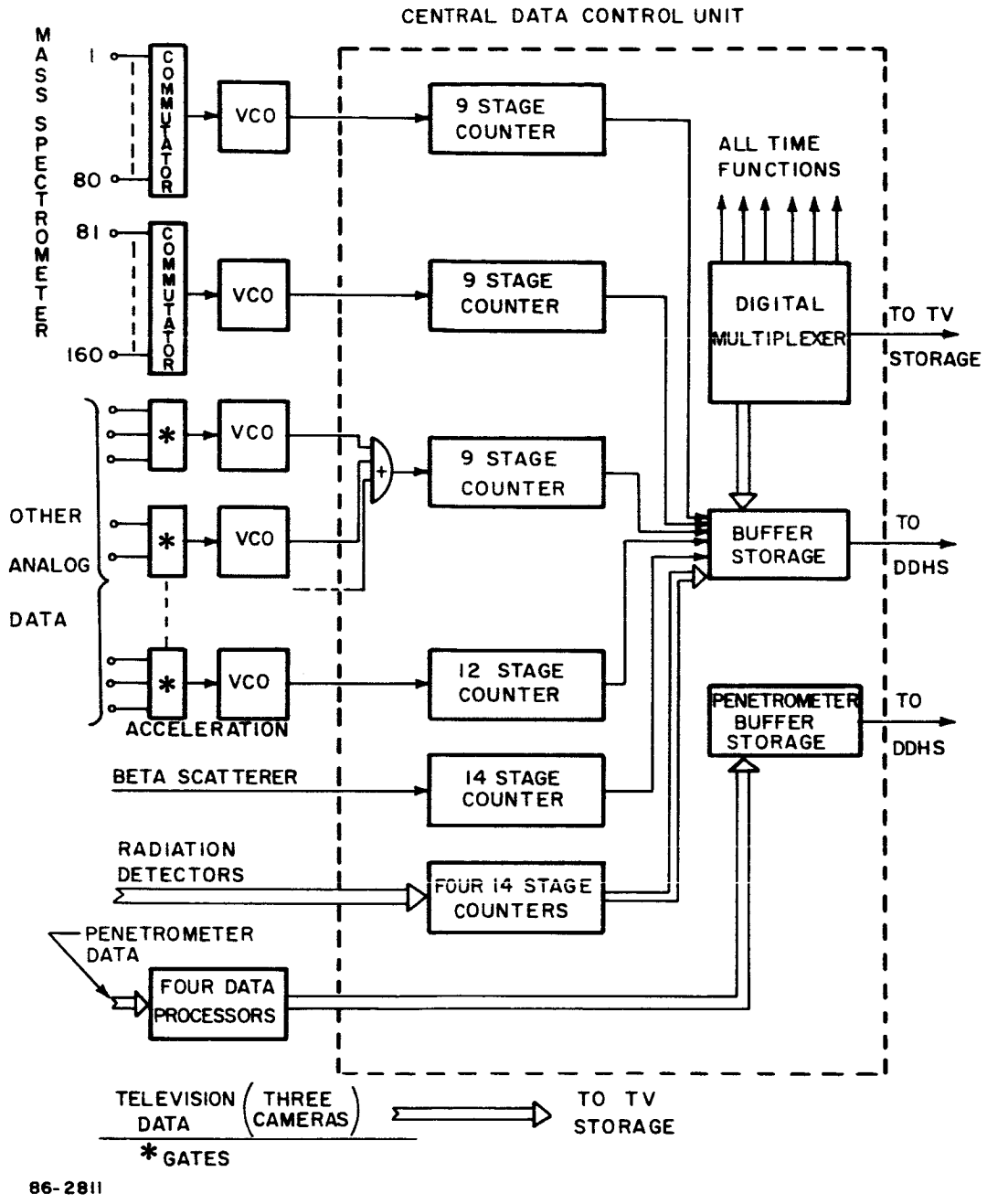

Figure 105 EXPERIMENT DATA HANDLING SUBSYSTEM BLOCK DIAGRAM

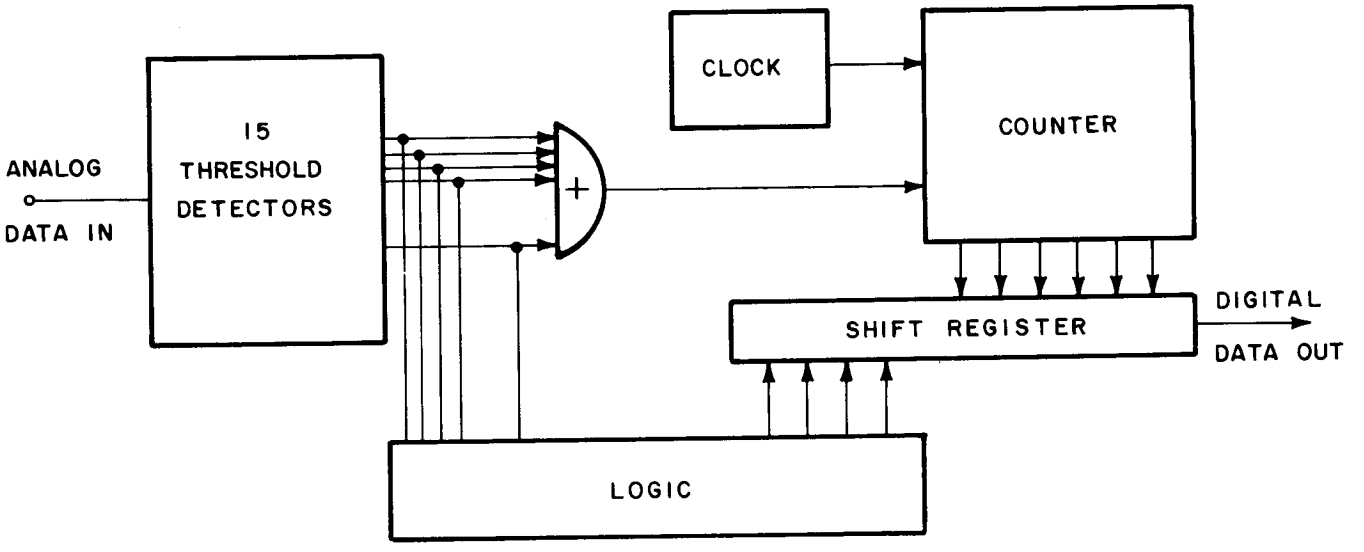

86-2812

Figure 106 PENETROMETER DATA HANDLING EQUIPMENT

representing this g level to the shift register, the contents of the counter are transferred to the shift register, the counter is reset to zero, and the shift register is read out then cleared. When each succeeding threshold is reached, the operation described above is repeated. The digital data read out of the shift register is transfered to a buffer memory for storage until the data is transmitted at the appropriate time in the transmission sequence.

b. Analog Data -- Analog data, sampled periodically by a commutator or gate, is linearly converted to a frequency by voltage-to-frequency converter (a VCO). The converter output signal (320 kHz ± 20 percent) is entered in a counter in the central data control unit.

During the time a given converter is connected to the counter, the converter output frequency is sampled, as follows. The actual sampling period begins when the binary counter receives a 1-millisecond gating pulse. The leading edge of the pulse is used to reset the counter to zero. The counter then begins to count the number of cycles of the converter output signal. The counter is so designed that for the 1-millisecond sampling period only that number of cycles exceeding 256 is considered significant in terms of instrument output data (other than zero output). A count of 256 or less is considered to represent a zero count because it corresponds to a converter output of 256 kHz or less, that is, to a zero voltage output signal from the instrument. At the end of the 1-millisecond sampling period, the converter is disconnected from the counter and if the contents of the counter is 256 or more, the binary contents of the counter are shifted out through the digital multiplexer to the buffer register. The buffer register is used for temporary storage of sampled data prior to its transmission at the appropriate time in the data-transmission sequence. The data from some of the instruments must be sampled almost simultaneously to provide a high degree of data correlation. If the data from several instruments must be sampled at a rate of, for example, one sample per second, then the sampling period for each instrument must be considerably less than one second. The data from that instrument is then sampled again at successive one second intervals. In the system described here, all instruments requiring 7-bit accuracy, as listed in Group 4 of Table LIX, and that are sampled once per second are sampled in a maximum of 38 milliseconds. This sampling cycle time is based on allowing one-millisecond counting time for each sample and an additional millisecond for reading the contents of the binary counters into the digital multiplexer. The instruments in group 4 that are sampled once every 5 seconds are sampled in a maximum of 160 milliseconds based on the same reasoning. Although the binary counter used for 7-bit accuracy data is a 9-stage counter, only the contents

of the first 7 stages (least significant stages) are actually read into the digital multiplexer. Nine stages are needed because a count less than 256 is read as zero volts. At the end of the one-millisecond gate, and if the ninth stage of the binary counter has been incremented, the contents of the first 7 stages are transferred to the digital multiplexer. If the ninth stage has not been incremented, the counter contents represent a frequency less than 256 kHz, hence the contents of the first 7 stages are not transferred to the digital multiplexer and the sample is read as zero.

The previous is applicable with only a slight modification to the counter required for accelerometer data. The required accuracy of accelerometer data is 10-bits, rather than the 7 bits required by all other analog instruments. This 10-bit data is handled in a manner similar to that described above. However, the sampling interval is extended from 1 to 8 ms and a twelve-stage counter instead of the nine-stage one discussed earlier is used. In this case, a zero count less than 2048 is read as a zero count and the full scale count is 3072. The difference between these counts is 1024 (10 binary bits). The accelerometer data is obtained concurrently with the 7-bit data, therefore, 48 milliseconds are allocated to reading data into the 12-stage counter (8 milliseconds for each of three outputs) and approximately one millisecond for reading each count into the digital multiplexer. Total cycle time then is approximately 54 milliseconds.

c. Count Data -- Data from the radiation detectors and beta scatterer is in pulse form. The number of pulses from these instruments are counted (in 14-stage binary counters) each sampling interval.

2. Diagnostic Data Handling Subsystem -- Figure 107 shows the diagnostic data handling subsystem concept in block diagram form. Sampling, encoding, and buffering of the diagnostic and experiment data are handled in essentially the same way. However, the diagnostic data-handling subsystem also performs the additional function of time multiplexing all data into an appropriate data transmission sequence for use in modulating the transmitter.

The commutation scheme is based on use of a 40 analog-channel main multiplexer, the equivalent of 18 additional main multiplexer channels for digital data, and ten 20-channel subcommutators feeding the main multiplexer. The main multiplexer sampling rate is one frame per second: the subcommutator frame sampling rate is one frame every 5 seconds. All analog data in groups A and B as listed in Table LXVIII subcommutated onto the 40 analog-channels of the main multiplexer. Ten main multiplexer channels (the equivalent of 70 binary events) are allocated to handle group C data as listed in that table. The remaining 8 main multiplexer channels are allocated to handle data listed

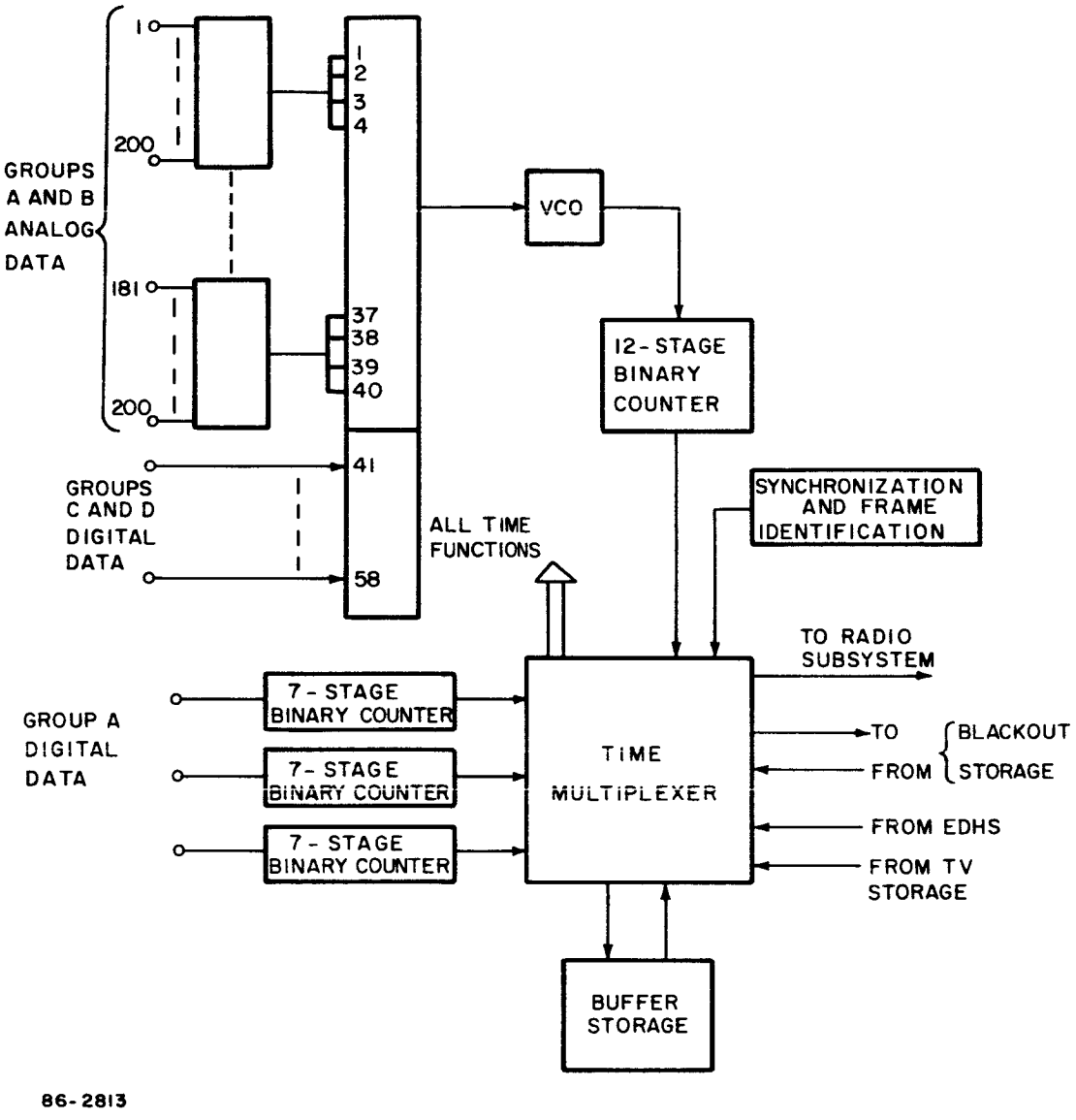

Figure 107 DIAGNOSTIC DATA HANDLING SUBSYSTEM BLOCK DIAGRAM

under group D on that table. The digital data in group A of table LXVIII monitored separately in three 7-stage binary counters whose contents are sampled once every 5 seconds. In 5 seconds, therefore, 290 channels of analog and digital data are collected from the main multiplexer. In addition, 3 channels of group A digital data on a spare 7-bit channel are collected. This totals 294 channels of 7-bit data, all of which are stored in a buffer memory. At the appropriate time in the transmission sequence, the data is played out of storage together with 31 bits added synchronization and 4 bits added for frame identification. These are added every 147 data-channels (one-half of the total collected in 5 seconds) are played out. The result is two 1064-bit frames of diagnostic data.

3. Data Storage Subsystem -- The data storage subsystem is designed to meet two primary functional requirements. One, it must store certain experiment and diagnostic data, which is collected during radio link blackout, and make this data available for transmission 100 seconds after blackout in the same sequence as it was acquired. Two, it must store television data, which is acquired at a relatively high data rate, and make these data available subsequently for transmission at the rate required.

a. Radio Blackout Data Storage -- In the discussion of the data transmission sequence presented in paragraph 5.5.4.2, it was shown that during radio link blackout 3 frames of other experiment data and 2 frames of diagnostic data are collected and transmitted every 5 seconds. This represents an average frame rate of one frame per second. Hence, in 100 seconds 100 frames of data, that is, 106,400 bits of data must be stored for transmission after blackout is ended. A blackout data storage subsystem concept is shown in block diagram form in Figure 108. As this figure shows, the memory address is controlled by either a read counter or a write counter. Since the read and write operations need not be performed concurrently as can be seen from the data transmission sequence shown in Figure 103, there is a 2.5 second interval between read/write cycles. During the read cycle, the data stored at memory addresses corresponding to 5 frames of engineering and diagnostic data will be destructively read out of the memory. During the write cycle, 5 frames of new engineering and diagnostic data will be read into the memory locations emptied 2.5 seconds earlier. During the next read cycle the next 5 frames of engineering and diagnostic data in the stored sequence will be read out of the memory and replaced with 5 new frames of data

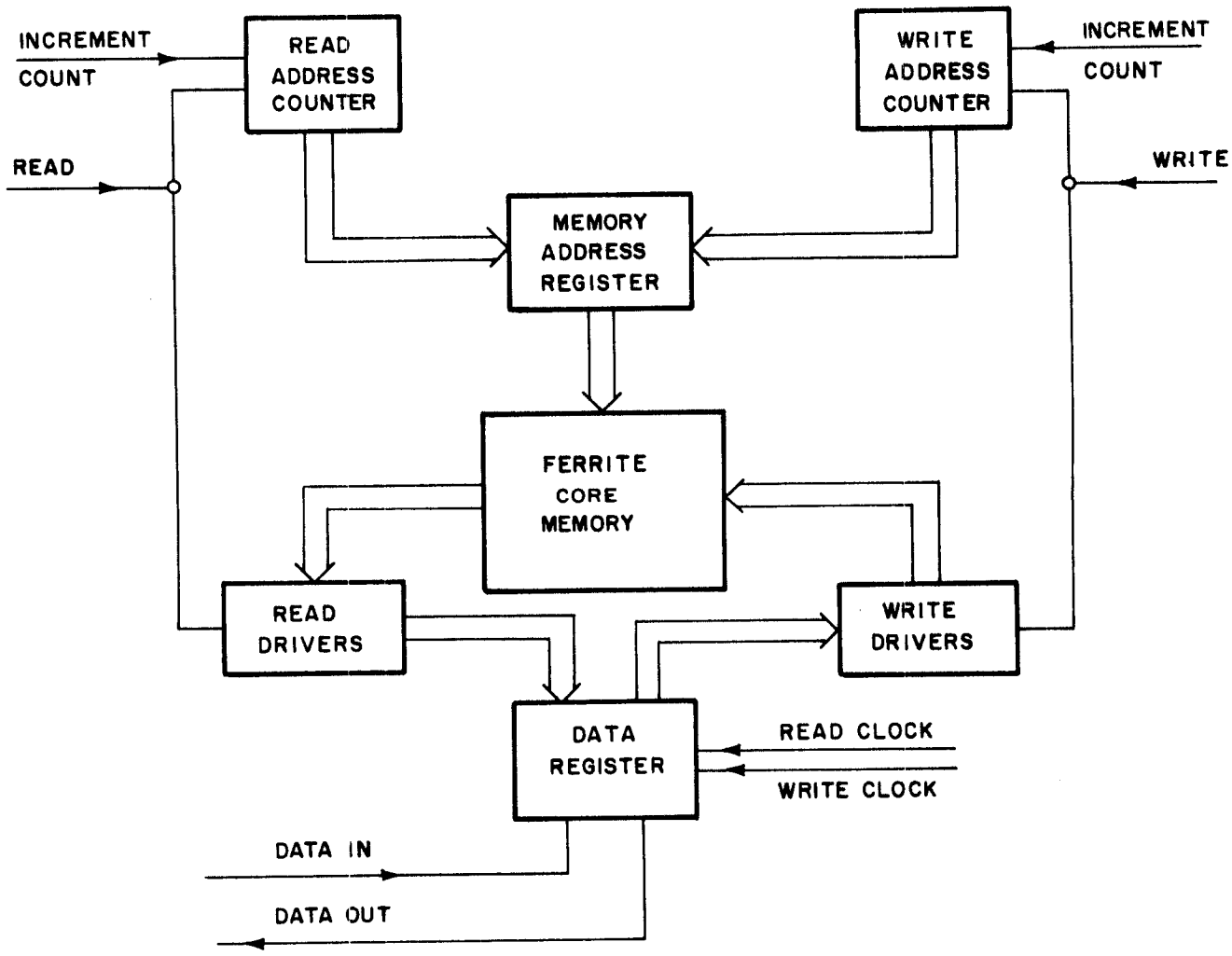

Figure 108 BLACKOUT DATA STORAGE SUBSYSTEM BLOCK DIAGRAM

during the following write cycle. This procedure continues until the contents of all memory locations have been read and then replaced with new data. The same procedure is continued in an uninterrupted manner from the start of the flight capsule mission until impact. Use of this technique assumes that the data collected during blackout is transmitted after blackout but prior to flight capsule impact even if the parachute is not deployed. Furthermore, no data mode change is required to sense the start or end of radio blackout.

b. Television Data Storage -- During parachute assisted descent, at least three-picture sets (each having three pictures) of television data are acquired. The images on the tubes are erased simultaneously after the 6-second interval immediately following picture exposure. Three alternative schemes for sequencing the storage and transmission of television data are shown in Figure 109. Each scheme provides a 10-second picture taking period during which a set of three pictures is taken as soon as the television platform is vertically oriented (i. e., whenever the suspended capsule swing angle is less than 45 degrees). Immediately following taking of the pictures, the pictures are transferred to storage during a 6-second interval.

As shown in Figure 104, 68 lines of television data are read out of storage every 5 seconds. Transmission of a set of three 200-line pictures will, therefore require approximately 44 seconds.

Scheme 1 is a completely serial sequence in which transmission of television data is delayed until the data is completely read into storage. This could result in a loss of up to 16 seconds per picture set (the equivalent of more than one picture per set). In scheme 2, transmission of television data delayed only during the read-in of the first set of three pictures. Subsequent sets are read into storage while the previously stored data are being read out. This can be accomplished by adding storage capacity for one additional picture for the A-camera. As pointed out in paragraph 5. 5. 4. 2 the camera data is played out in the following sequence: C-camera, B-camera, and then A-camera. In two-thirds of the time required to transmit a complete set of three picutres, therefore, storage for pictures C and B will be empty and capable of receiving new data. By including storage capacity for one additional A-camera picutre, a new set of pictures can be taken during the interval that the A-camera picture

SCHEME 1 ONE MEMORY PER CAMERA

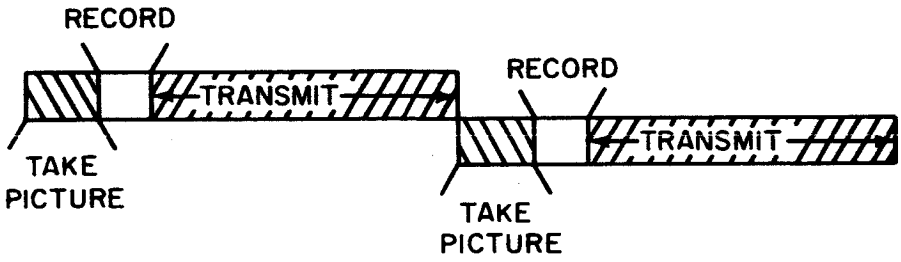

SCHEME 2 ADDITIONAL STORAGE FOR ONE PICTURE

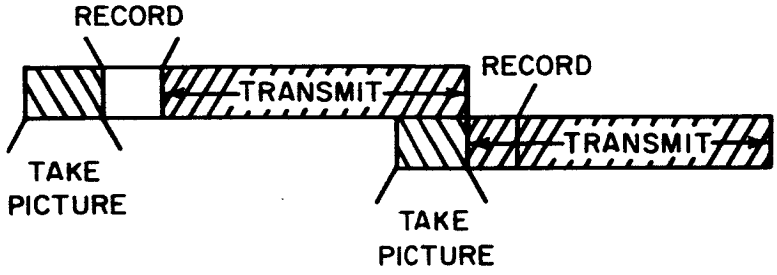

SCHEME 3 SIMULTANEOUS READ IN-READ OUT

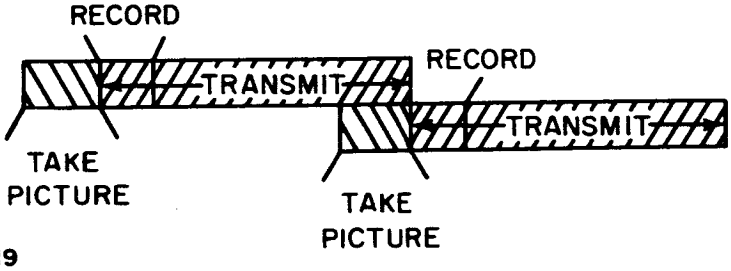

862219

Figure 109 TELEVISION DATA STORAGE

is being played out of storage. The new picture from A-camera will then be stored in the additional storage. The time required to empty storage of the A-camera picture is approximately 15 seconds. Although this is not quite long enough to satisfy the requirements for a 10-second picture taking interval and a subsequent 6-second recording interval, it is close enough to be acceptable. This scheme (2) results in obtaining one additional picture (this picture could be the high resolution picture from the C-camera which would make the scheme even more desirable. However, use of this scheme could result in the loss of approximately one-half of a picture in the sequence C, B, A due to the first 6-second period during which data is being read into storage but no data is being read out.

In scheme 3, a simultaneous read in-read out memory is provided to eliminate the first 6-second delay during which the pictures are transferred from the vidicon image tube to storage. Although somewhat complicated in mechanization, this scheme is feasible and would result in the possibility of obtaining half of an additional B picture. However, since the capability exists in scheme 2 to obtain an additional C picture, the desirability of obtaining one half of an additional B picture is offset by the fact that the resolution of B picture will be the same as that of the previously obtained C picture. Therefore, the scheme 2 has been selected because it does not introduce the complexity of simultaneous read in and read out. The block diagram of each television storage subsystem is essentially the same as that shown for blackout data storage in Figure 108.

c. Selection of Storage Media -- A detailed discussion of the tradeoffs between various storage media under consideration was presented in paragraph 4. 11. 7. 6. Table XXVIII in that section showed that both monolithic ferrites and ferrite cores are each good candidates for storage applications. The approach taken in regard to the radio blackout and television storage application presented here was to assume that ferrite cores would be used for the radio blackout storage and monolithic ferrites for the television storage. The selection was based on the fact that the space-proven ferrite cores are competitive in physical and power consumption characteristics for applications in the order of 100, 000 bits and that a substantial improvement in physical characteristics is obtained if monolithic ferrites are selected for applications on the order of one million bits.

5.5.4.5 Summary

Table LXXII summarizes the salient characteristics of the flight-capsule data-handling subsystem. Two actively redundant subsystems are used. The basic data-transmission sequence period, that is, the period in which all data except television data is sampled and transmitted, is 5 seconds. Time diversity is employed in the transmitted data. This is achieved by delaying the transmission of data from one of the redundant subsystems by 2.5 seconds. During each 5-second data transmission sequence period 86 frames of data are transmitted.

Of these frames, 68 are television data frames, 13 are frames associated with all other experiment and diagnositic data, and 5 frames contain other experiment and diagnostic data that has been stored for 100 seconds and retransmitted. All frames are of equal length (1064 bits) and all use the same synchronization code (a 31-bit pseudo-random noise, PN, code word).

Two types of data storage are used; a ferrite core memory that provides a 100-second delay for data collected during blackout and a monolithic ferrite memory that provides storage capability for 4 television pictures. The capability of storing 4 rather than 3 pictures allows new picture data to be stored concurrently with transmission of previously stored data.

5.5.5 Flight Spacecraft Radio Subsystem Description

The selected flight-spacecraft radio-subsystem conceptual design employs polarization diversity reception, and signal-detection onboard the flight spacecraft. It also continues the total redundancy approach adopted for the flight capsule telecommunication equipment. A block diagram of the flight-spacecraft portion of the telecommunication subsystem was shown earlier in Figure 96. In that figure, all items except the data storage equipment comprise the flight spacecraft radio subsystem.

5.5.5.1 Antenna

1. Description of Selected Approach -- The antenna concept selected for the flight spacecraft is a dual turnstile system. One system is phased to receive right circular polarization: the other is phased to receive left circular polarization. The signal received from the flight capsule will be predominantly right circularly polarized as long as the flight-capsule antenna look angle to the flight spacecraft is less than 100 degrees. During parachute-assisted descent the flight capsule look angle may be greater than 100 degrees if the suspended capsule is exposed to large magnitude wind gusts. At such

TABLE LXXII

FLIGHT CAPSULE DATA HANDLING SUBSYSTEM CHARACTERISTICS

Quantity	2
Data sequence period	5 seconds
Time diversity	2.5 seconds
Data frames per period	
Television	68
Penetrometer	2
Surface roughness	6
Other experiment	3
Diagnostic	2
Blackout data	5
Frame format	
Length	1064 bits
Synchronization	31-bit psuedo-random noise (PN code word)
Frame identification	4 bits
Data accuracy	7-bit, 10-bit, count, as required
Channel capacity (equivalent 7-bit)	
Experiment analog	186
Experiment digital	8
Diagnostic analog	200
Diagnostic digital	18
Data storage	
Delay (blackout)	
Type	Serial, destructive read-out, ferrite core
Read-in rate	Approximately 18, 000 bps
Read-out rate	Approximately 18, 000 bps
Capacity	Approximately 100, 000 bits
Television	
Type	Word, destructive read-out, Monolithic Ferrite
Read-in rate	Approximately 35, 000 bps
Read-out rate	Approximately 18, 000 bps
Capacity	Approximately 850, 000 bits

times the left circularly polarized signal may predominate. A sketch of the proposed antenna system is shown in Figure 110. The system includes two bent turnstile antennas mounted above a radial electrical counterpoise. The dipoles are fed through a quarter wave balum; two dipole pairs are phased to receive right circularly polarized signals and the other two dipole pairs are phased to receive left circularly polarized signals. The interaction between the two antennas is expected to be minimal.

A single turnstile antenna positioned over a finite ground plane and referenced to a circularly polarized transmitting source, will have an on-peak gain of approximately 6 db. The turnstile arms in the proposed system are bent to form an umbrella-like structure to improve the off-axis axial ratio. The radius of arm curvature, as well as the size and type of ground plane influences the axial ratio and the antenna pattern. Greater arm curvature produces lower axial ratios at large look angles at the expense of greater beamwidth and lower average gain in the forward hemisphere.

Figure 78 showed a typical antenna pattern obtained with this type antenna. The antenna bandwidth will be approximately 6 percent and will be symmetrical about the center frequency.

2. Alternative Approaches -- Several other antenna designs are possible candidates for the flight-spacecraft antenna-system applications. These included a helix, a corner reflector, and a planar spiral antenna. Figure 111 shows each of these antennas, including the selected turnstile, and indicates the characteristic dimensions of each.

Two antennas must be used on the flight spacecraft to satisfy the polarization diversity reception requirement. Use of either the planar spiral or corner reflector concepts would require twice the volume needed by a single such antenna. However, the helix and the turnstile antennas are well suited to the development of a right circularly and left circularly polarized antenna system which will not exceed the volume occupied by a single antenna of such types (helix, turnstile). For example, two helices may be counter-wound with respect to each other with minimum interaction between them, or two turnstile antennas may be mounted within the volume normally occupied by a single antenna, as shown in Figure 110. A 10 db on-axis gain helix designed to operate at a frequency of 270 MH_Z would be 30 inches long and would require a ground plane approximately one-wavelength in diameter. The turnstile would extend approximately one quarter wavelength above a ground plane of similar size.

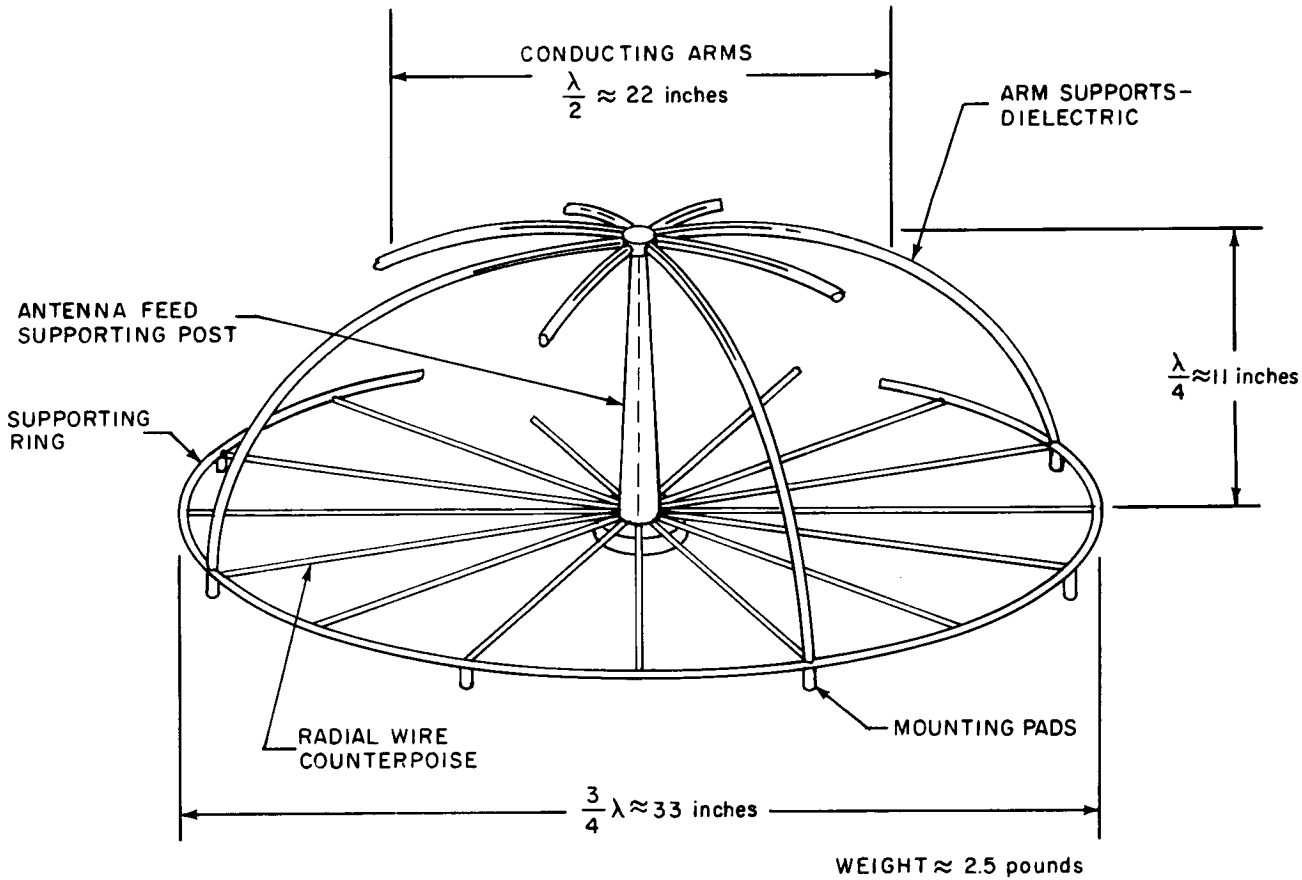

Figure 110 FLIGHT SPACECRAFT TURNSTILE ANTENNA DESIGN CONCEPT

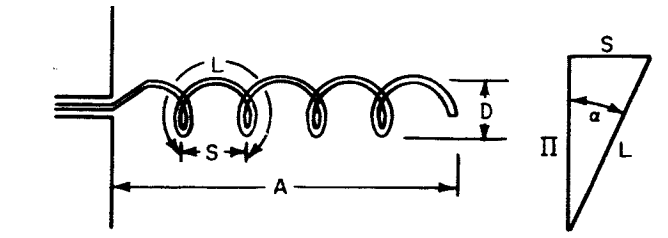

HELIX
D=16 inches
A=30 inches
α=12.5 degrees

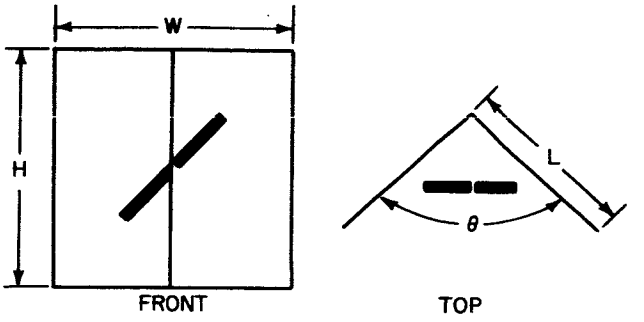

CORNER REFLECTOR
L = H = 50 inches
θ =100 degrees

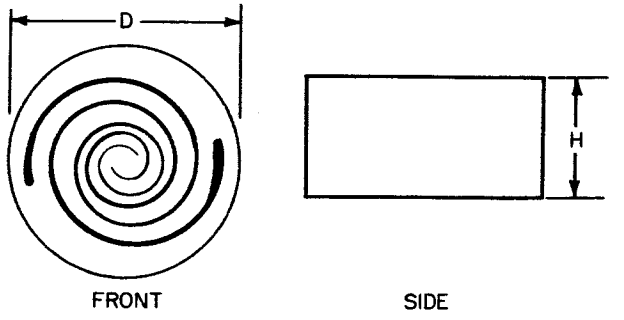

PLANAR SPIRAL
D = 20 inches
H = 12 inches

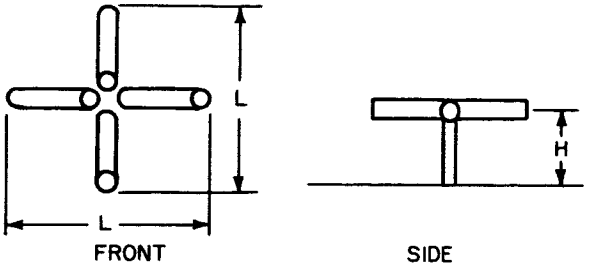

TURNSTILE
L =22 inches
H = 11 inches

86-2815

Figure 111 FLIGHT SPACECRAFT ANTENNA CANDIDATES

Another approach considered was based on use of the turnstile antenna as two (2) orthogonal linear dipoles. The dipole outputs could then be summed at the output of two receivers (one for each dipole). This approach, however, introduces twice the noise power at the summing network. Its effective output, therefore, is 3 db below that of the selected approach. Table LXXIII summarizes the advantages and disadvantages of each concept considered.

5.5.5.2 Receiving Subsystem

The proposed noncoherent PCM/FSK relay data link will operate in the VHF band and will utilize polarization and time diversity reception techniques to provide added protection against the effects of anticipated signal fading. Although the proposed diversity schemes have been described elsewhere in this report, it is convenient to consider the implementation of these schemes in any discussion of mechanization of the flight spacecraft receiver. Likewise since proper operation of the PCM/FSK relay data link requires accurate bit timing, it is logical to include a discussion of the bit synchronizer in any consideration of flight-spacecraft receiver implementation. The following paragraphs, therefore, will consider not only the mechanization of the flight spacecraft receiver but also the implementation of the diversity combiner and the bit synchronizer. The proposed relay data link will achieve time diversity by redundant transmissions at two distinct frequencies. A diplexer will be required to enable the same antenna structure to accommodate both frequencies. This diplexer is also described in the following discussion of the flight-spacecraft receiving subsystem.

The relationship between the various components of the flight spacecraft radio subsystem is illustrated in Figure 112.

The antenna subsystem output contains both a right-hand circularly polarized component and a left-hand circularly polarized component.

These components are applied to a pair of diplexers, one diplexer for each direction of polarization. The diplexers each produce two output signals. One, at frequency f_1, corresponds to the real-time signal transmitted by the flight capsule: the other, at frequency f_2, corresponds to the time-delayed redundant signal transmitted by the flight capsule. The four diplexer outputs are subsequently applied to the receiver subsystem.

Functionally, the receiver subsystem accepts (via the flight spacecraft's antenna subsystem and diplexers), transmitted signals from

TABLE LXXIII

COMPARISON OF FLIGHT SPACECRAFT ANTENNA CONCEPTS

Antenna Concept	Advantages	Disadvantages
Turnstile (selected approach)	Two antennas* can occupy the volume normally allocated to one. Simple mechanical and electrical design	
Helix	Same as turnstile High on-axis gain	Gain at large look-angles poorer than turnstile. Poor off-axis axial ratio
Orthogonal dipoles	Same as turnstile	Three db loss in performance relative to selected approach.
Planar spiral	Simple mechanical and electrical design Wide bandwidth	Requires twice the volume of single antenna for polarization diversity reception
Corner reflector	Same as turnstile	Same as planar spiral

*For polarization diversity

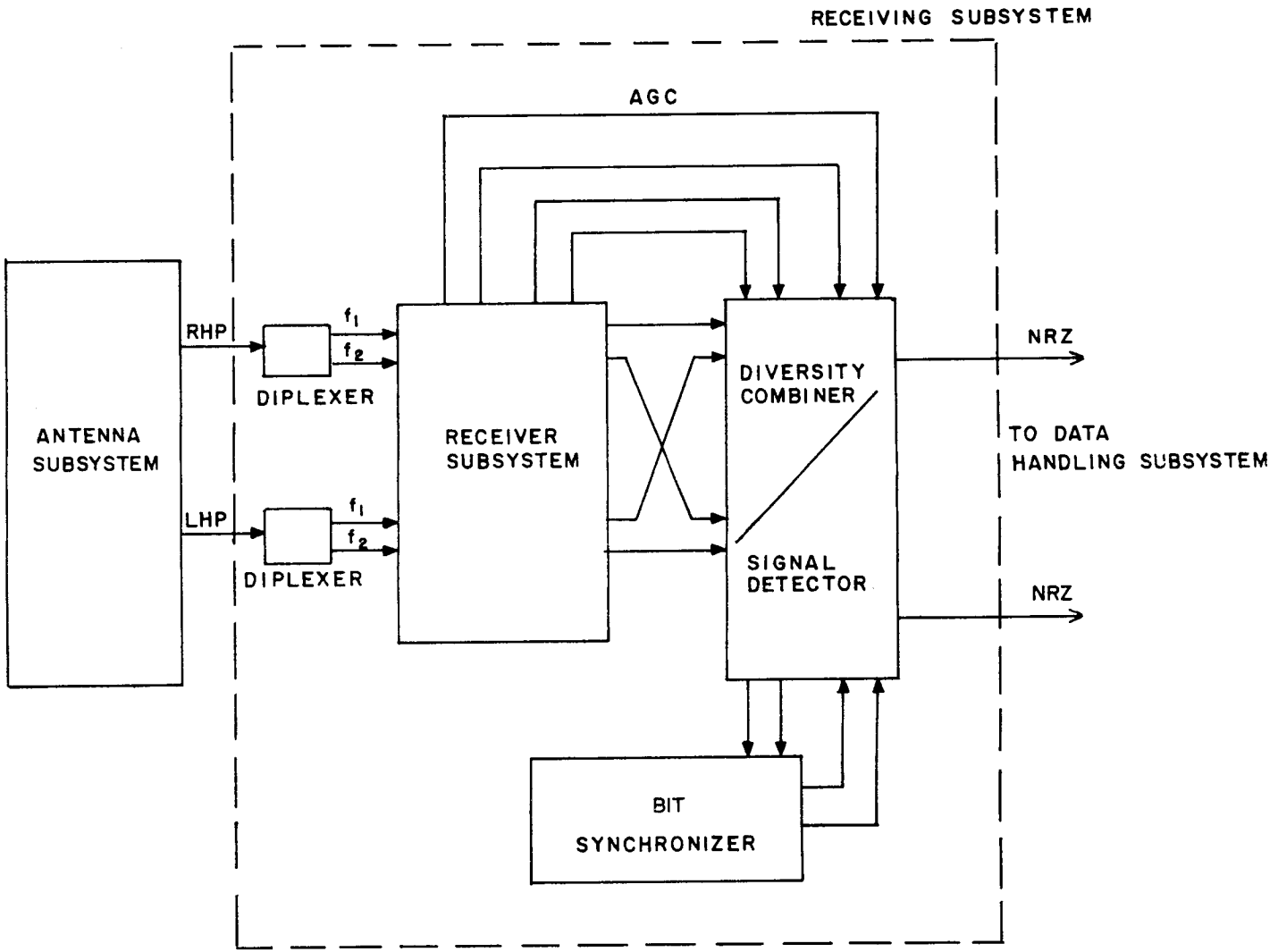

86-2816

Figure 112 FLIGHT SPACECRAFT RADIO SUBSYSTEM

the flight capsule, and provides suitably amplified envelope-detected output signals to the diversity combiner/signal detector. The receiver subsystem contains four similar FSK receivers. Each receiver accepts a single diplexer output and produces a non-return to zero (NRZ) output signal. These output signals represent the difference of the square-law envelope-detected outputs of the mark and space channels.

The appropriate diversity channel outputs from the receiver subsystem are combined and individual bit detection is performed in the diversity combiner/signal detector section of the flight spacecraft's radio subsystem. Polarization diversity reception is achieved by combining signals of the same frequency but of opposite directions of polarization. Since two separate sets of signal pairs must be combined, two separate combiners are required. The appropriate combining weights are derived from the automatic gain control (AGC) outputs of the respective diversity channels.

All bit decisions will be made in the diversity combiner signal detector. The bit timing is provided by the bit synchronizer which accepts the combined noisy NRZ outputs of the diversity combiner and provides appropriate synchronization signals to the integrate and dump bit detectors. The output of the Diversity Combiner/signal detector subsequently consists of a pair of essential noise-free binary sequences. These represent, respectively, the data transmitted from the flight capsule at frequency f_1 and f_2. These outputs are fed directly into the buffer storage section of the flight-spacecraft data-handling subsystem. The stored data are then re-timed and the output of the data-handling subsystem is applied to the flight spacecraft transmitter for transmission to Earth. More detailed description of the components of the flight spacecraft receiver subsystem as illustrated in Figure 112 are presented below.

1. Selected Approach -- A detailed block diagram of the proposed flight-spacecraft radio subsystem is shown in Figure 113. This diagram is a more detailed version of the generalized diagram shown in Figure 112. The proposed implementation of each of the components shown in Figure 113 is discussed in detail in the following paragraphs.

a. Diplexer -- A frequency selective diplexer is needed to separate the real-time and the time-delayed components of the transmitted signal. One is transmitted at 268 MHz and the other at 272 MHz. The diplexer must provide from 20 to 30 db isolation between output ports and do this with only a small insertion loss. Ordinarily, RF power levels in receiving equipment are such that they do not

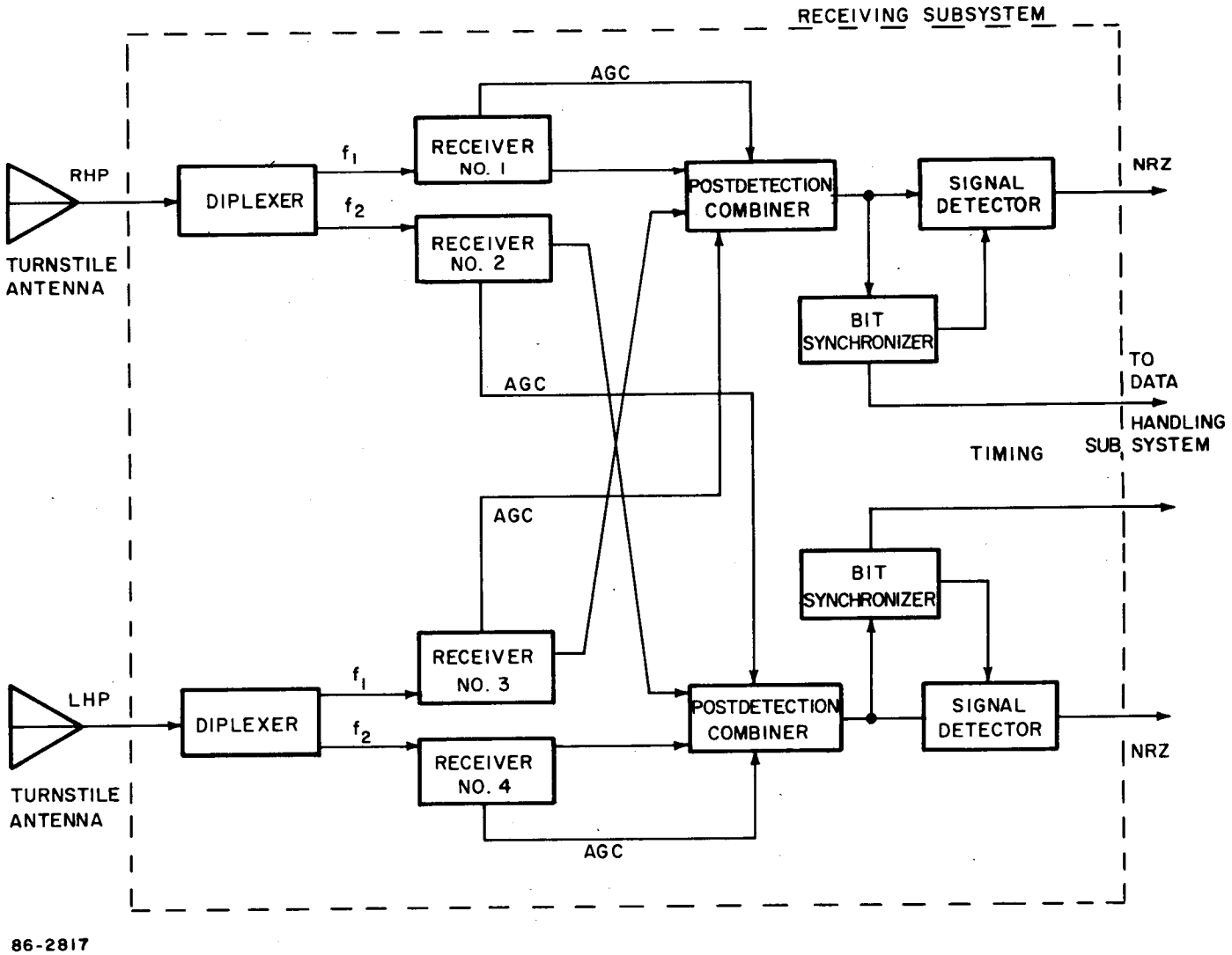

Figure 113 DETAILED FLIGHT SPACECRAFT RADIO SUBSYSTEM

present any breakdown problems. However, as will be discussed presently, the flight spacecraft receiving subsystem must operate in high RF power level environments during certain phases of the mission. This factor must be considered in designing the diplexer.

Several vendors provide diplexers capable of meeting the various design requirements. One such device is the Model MT230 diplexer with the above characteristics manufactured by Rantec Corporation. This component has been used previously at Avco/MSD in a missile application and is suitable for the present application. Pertinent characteristics of the Model MT230 diplexer are:

Insertion loss	1.5 db maximum
Isolation	20 db minimum
VSWR	1.5 db maximum
Dimensions	8 x 2 x 2 inches
Weight	28 oz.

b. Receiver -- A block diagram of a single diversity channel receiver is illustrated in Figure 114. The input RF section contains a circulator, limiter, and low-noise preamplifier. The limiter is necessary to protect the receiving subsystem and, in particular, the sensitive pre-amplifier from excessive power levels during:

1) The periodic in-transit status checks during the cruise phase.

2) The period when the transmitter is energized prior to flight capsule orbit injection.

3) The time immediately after separation and before entry during which status checks must be performed and the space loss in not sufficient to reduce the received power to a safe level.

The limiter will utilize silicon diodes in a simple shunt configuration. These devices are readily available from a number of different vendor sources. Typically, they will limit at approximately +10 to +15 dbm and will have a small-signal insertion loss of less than 0.3 db. The possible use of yttrium-indium-galluim (YIG) diode limiters has also been considered for this application, however, these devices do not appear particularly attractive at VHF.

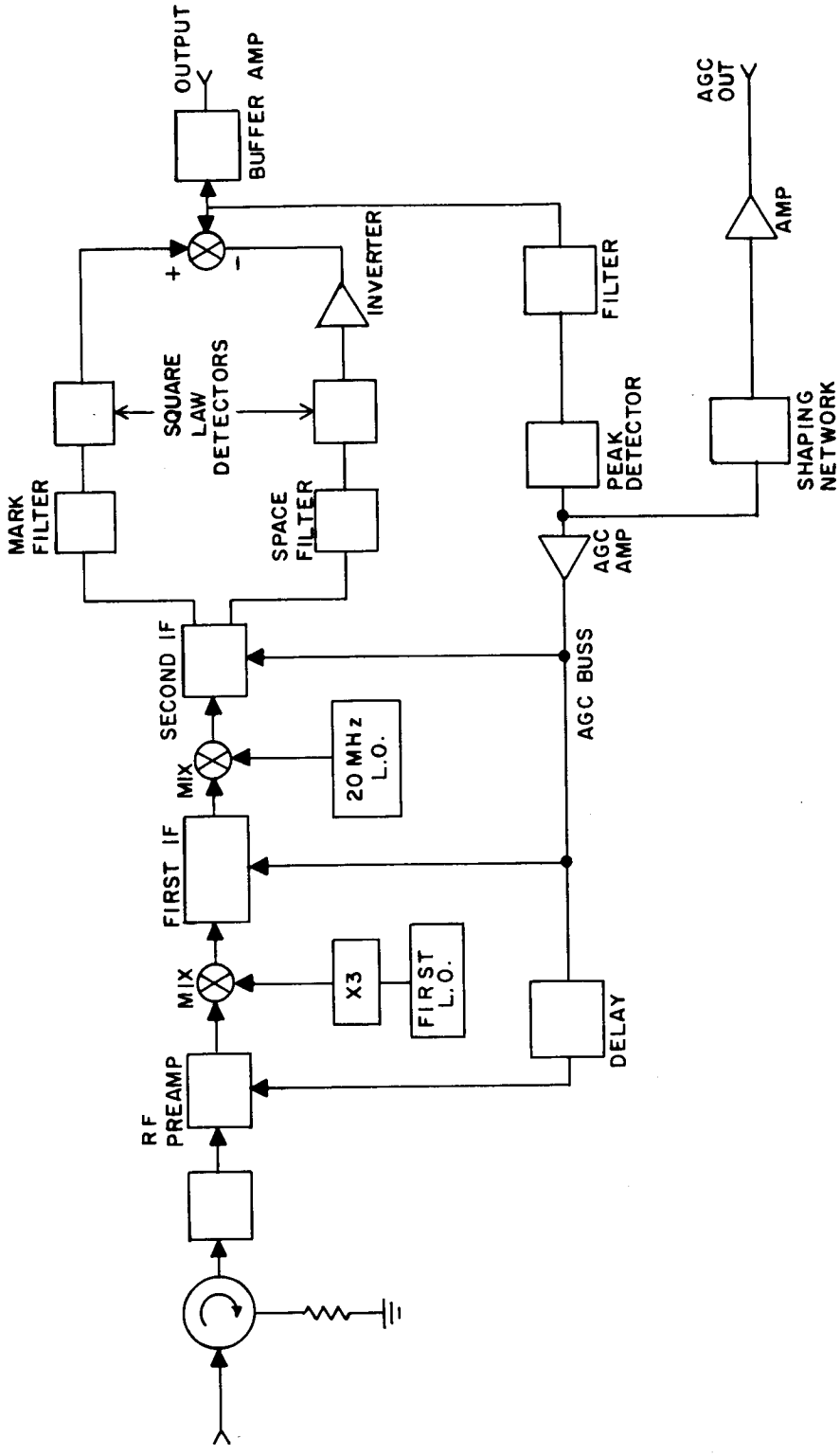

Figure 114 RECEIVER BLOCK DIAGRAM

The diode limiter will not interfere with reception when the received signal level is below the limiting level. When the input signal level is above the limiting level, however, the excess power is reflected back to the input. These reflections will generally result in extreme variations in the diplexer characteristics unless the diplexer output can be adequately isolated from the limiter input. This can be accomplished with the addition of a loaded circulator as shown in Figure 114. The circulator will provide an isolation of 20 db minimum with a maximum insertion loss of only 0.5 db, maximum. A suitable unit for this application is the model CYA-100-fc circulator manufactured by Western Microwave Laboratories, Inc. This unit measures approximately 6-inch diameter x 1-3/8 inches high and weighs approximately 10 ounces.

The limiter is followed by an RF preamplifier. The principle requirements for the preamplifier are that it presents a low input noise figure and that it provide adequate RF gain to assure that the noise figure of the succeeding mixer intermediate frequency (IF) combination is sufficiently isolated.

In selecting and designing the RF preamplifier, careful consideration must be given to the dynamic range problem. As noted previously, the flight-spacecraft receiving subsystem will be subject to wide ranges of input power levels. It may be argued that for over-all system success, the receiving subsystem need only operate reliably at the input signal levels to be experienced when the flight capsule has entered the Martian atmosphere. However, there must be some provision for system checkout to determine the operational status of the flight capsule before actual injection. Any such system checkout should logically be carried out at actual design ratings. This approach, of course, implies a very high received signal level. It would be advantageous, therefore, to design the receiver to accept these high signal levels. Such a receiver would then be able to operate reliably over extremely wide ranges of input power levels. The limiter preceeding the RF pre-amplifier helps to limit the maximum applied RF power, unfortunately, there is a practical limit to the lowest limiting level that can be obtained with state-of-the-art devices. Thus, the RF preamplifier's operating range should correspond to the range between the receiver threshold and the lowest limiting level obtainable with the limiter used. The receiver threshold level is defined here as the input signal level that causes the resultant bit-error rate to exceed 1×10^{3}. On the basis of previous findings it is a simple matter to convert the receiver threshold level into an absolute signal level at the receiver input terminals.

Figure 115 illustrates the relationship between the IF signal-to-noise ratio (SNR) and the bit-error probability in the noncoherent PCM/FSK system. The parameter B_o on that figure and in the following discussion represents the ratio of predetection bandwidth to bit rate.

A plot of the allowable b_o versus predetection SNR necessary to achieve a given bit error probability of 1×10^{-3} ($P_e = 1 \times 10^{-3}$) is illustrated in Figure 116.

From these curves it is possible to determine the receiver threshold level in terms of an absolute signal level at the receiver input terminals. However, this requires complete specification of the receiver. Although the discussion of the complete specification is postponed until later, the following example will illustrate determination of the absolute level. If the value of $b_o r$ is 10, the threshold value of the IF SNR, from Figure 116, is approximately 4 db. If the bit rate is 18,000 bps, then b_o is 180 kc; and for a noise figure of 6 db, the noise power in the predetection bandwidth is -115.5 dbm.* For a threshold predetection SNR of 4 db, then, the threshold signal power at the receiver input terminals is -111.5 dbm. The limiting level will be approximately +10 dbm. This figure indicates that the input operating range of the preamplifier will be on the order of 121 db - clearly a sizeable task for any device. The dynamic range requirements are relaxed somewhat if AGC is provided in the RF preamplifier. Incorporation of AGC in the RF preamplifier, however, usually upsets the noise figure and selectivity characteristics of the preamplifier. It would be highly undesirable to allow this to happen during the critical atmospheric entry phase, although such changes may possibly be tolerated during the checkout and status monitoring phases. It appears advantageous, therefore, to provide some form of delayed AGC to the front end. This approach enables the power levels presented to the first mixer to be limited to a tolerable level and the receiver spurious noise problems to be thereby minimized.

Because of the dynamic range problems and AGC requirements, a low-noise solid-state (transistor) RF preamplifier configuration appears as the best choice. Several manufacturers offer suitable silicon transistor amplifiers with AGC capabilities and noise figures on the order of 3 db. When the effects of diplexer, circulator, and limiter losses are taken into account, however, a 3-db noise figure at the RF preamplifier produces an overall noise figure of approximately 6 db in any one diversity channel when the noise is measured at the respective diplexer input port.

* A reference temperature of 290°K is assumed in this calculation.

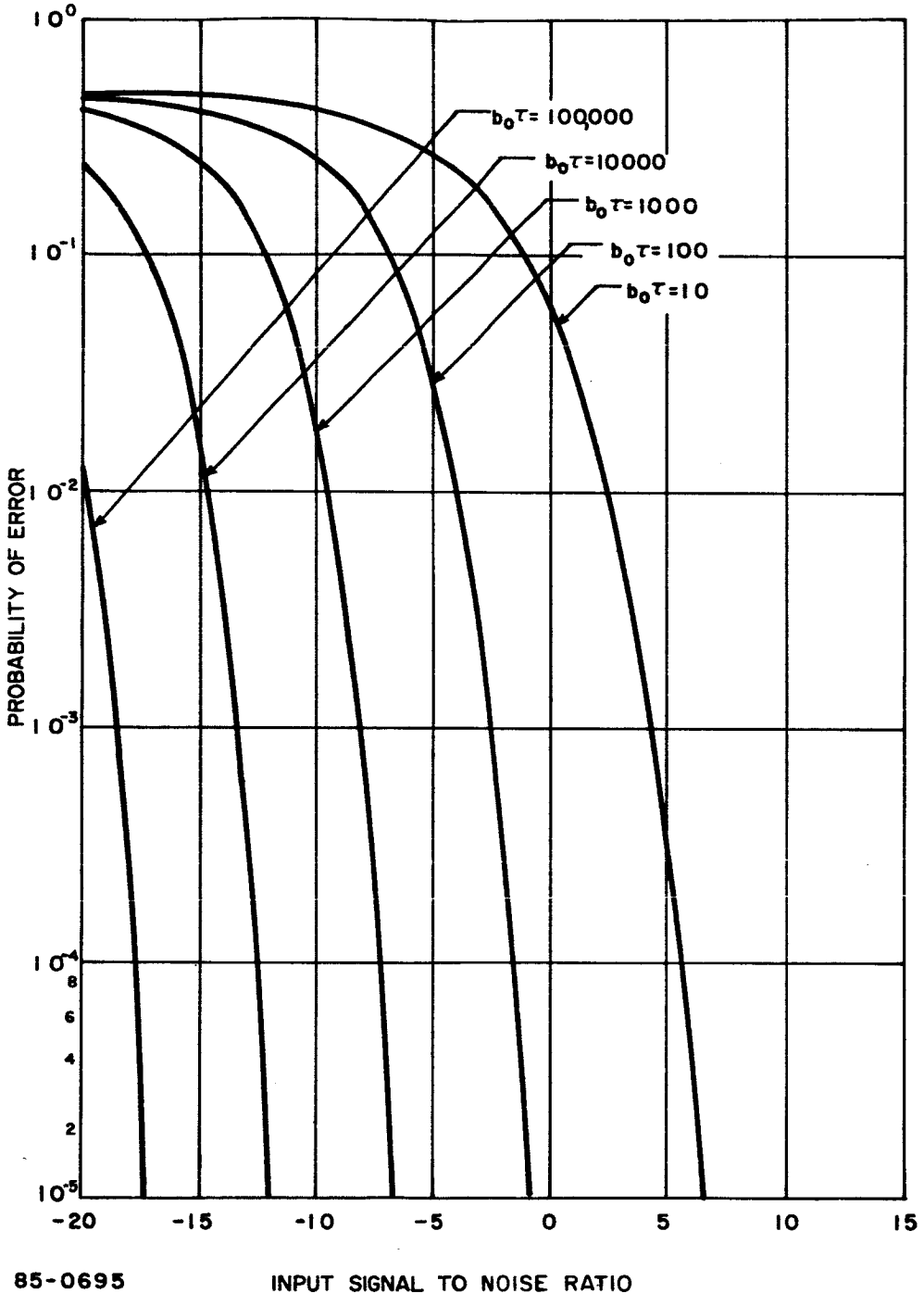

Figure 115 FSK BIT ERROR PROBABILITY VERSUS INPUT SIGNAL-TO-NOISE RATIO

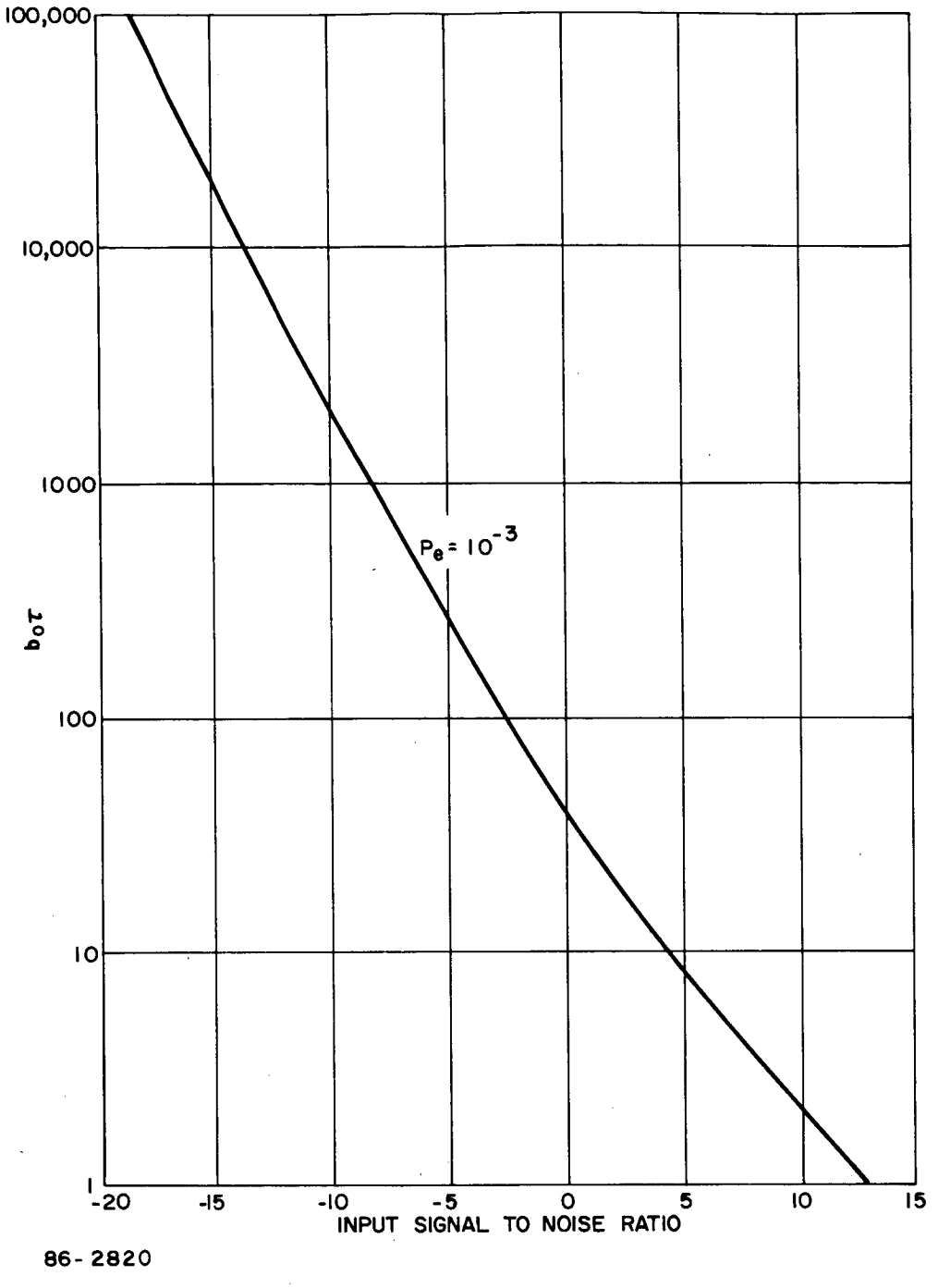

Figure 116 ALLOWABLE $b_o\tau$ VERSUS INPUT SIGNAL-TO-NOISE RATIO

The block diagram of the proposed flight spacecraft receiver illustrated in Figure 114 shows a double-conversion receiver. This type of receiver was selected on the basis of gain distribution, image rejection, and filter fabrication considerations. The mark and space filters are required to pass the modulated signal without distortion in the presence of relatively large uncertainties due to doppler shifts and equipment frequency instabilities. The 3-db bandwidth, b_o, of the mark and space filters is determined from the experssion

$$b_o = 3B + f_t + f_r + f_d$$

where:

B = bit rate (18,000 bps)

f_t = Transmitter frequency instability (± .005 percent)

f_r = Receiver instability (± .0001 percent)

f_d = Doppler shift

Table LXXIV illustrates the calculation of the required bandwidths for a system with an assumed carrier frequency of 272 MHz.

TABLE LXXIV

DETERMINATION OF REQUIRED MARK/SPACE FILTER BANDWIDTH

Quantity	Value (Hz)
$3\dot{B}$	54,000
f_T (± 0.005%)	27,200
f_R (± 0.0001%)	544
f_d (ν = 10,000 ft/sec)	2,760
b_o	84,504

The table indicates that for a bit rate of 18,000 bps, the required mark and space filter bandwidths will be approximately 85 kHz. Use of an IF frequency of 10 MHz makes it convenient to use crystal filters for the mark and space channel filters. A conservative choice of a 4:1 form factor for the filters simplifies the temperature compensation problem and avoids serious distortion of phase characteristics near the edge of the filter pass-band. The minimum required IF bandwidth centered at 10 MHz is then determined from the mark and space filter separation. If, for example, the 60-db point of the mark filter must coincide with the 3-db point of the space filter and vice versa, the mark and space filter separation will be found to be approximately 200 kHz. The required second IF bandwidth will then be approximately 500 kHz. This is a typical telemetry receiver bandwidth at 10 MHz. The first IF will be 30 MHz and will have a bandwidth of approximately 1 MHz. Choice of a frequency of 30 MHz for the first IF eases the RF preamplifier image rejection problem somewhat. Furthermore, since there will be two parallel relay data links operating with a separation of only approximately 4 MHz, the first IF will provide additional rejection for the unwanted signal.

The first local oscillator (LO) frequency will be derived from the tripled (3x) output of a fifth-overtone crystal controlled oscillator operating in the 80 to 90 MHz range. This approach represents a compromise between stability and system complexity considerations.

The second LO will be a 20 MHz fundamental-mode crystal-controlled oscillator.

The outputs of the mark and space channel filters are square-law envelope-detected and subtracted. This difference signal is filtered and peak detected to provide the AGC signal. The peak detector output is subsequently heavily filtered in accord with the required AGC time constant, and then amplified to provide the AGC control signals. The AGC signal, which is taken from a buffer circuit at the receiver output, is used to control the diversity combiner. It is, therefore, so shaped that it will be linear with respect to the input signal level in dbm. Suitable delay is also provided for the AGC signal to the RF section (front end) of the receiver. The AGC bandwidth will be adjusted as necessary to correspond to the highest anticipated signal fading rate. The suitably buffered square-law envelope detected and differenced outputs of the mark and space channels appear at the receiver output terminals. Table LXXV summarizes the characteristics of the flight spacecraft's single-diversity-channel receiver.

TABLE LXXV

FLIGHT SPACECRAFT RECEIVER CHARACTERISTICS

Frequency	268/272 MHz
Type	Double conversion superheterodyne
Noise figure	9 db
Image rejection	60 db minimum
IF rejection	80 db minimum
Threshold signal level at antenna terminal	-138.4 dbw
Receiver limiting level	+10 dbm
Dynamic range	123 db
Local oscillator stability	± 0.0001 percent
1st IF	
Center frequency	30 MHz
Bandwidth	1 MHz
2nd IF	
Center frequency	10 MHz
Bandwidth	500 kHz
Mark/Space	200 kHz
Frequency separation	
Mark/Space filter bandwidths	85 kHz
Detector type	Square law envelope detector
AGC response	Adjustable
AGC output	Linear with respect to input signal level in dbm
Weight	3.5 pounds
Power	4 watts

c. Diversity Combiner/Signal Detector -- The Diversity Combiner/Signal Detector is designed to provide appropriate combinations of the individual diversity channels, and to perform bit-by-bit detection of the combined signal. The combining action is controlled by the AGC voltage that appears at the output of the individual diversity channels. Bit-detection timing is provided by the bit synchronizer described in d., below.

The proposed diversity scheme utilizes maximal-ratio or ratio-squared combining. A maximal-ratio combiner, by definition, delivers the maximum signal-to-noise (S/N) power ratio value obtainable from any locally derived linear combination of the available signals. Using the nomenclature suggested by Brennan[15] for the optimum sum of the output of the diversity channels.

$$f(t) = \sum_{j=1}^{N} a_j f_j(t) \qquad (1)$$

where $f_j(t)$ is the total signal out of the j^{th} diversity channel and can be represented by

$$f_j(t) = s_j(t) + n_j(t) \qquad (2)$$

where

$s_j(t)$ = the signal component in the jth diversity channel

$n_j(t)$ = the noise component superimposed on $s_j(t)$

a_j = the weighing constant by which the magnitude of $f_j(t)$ is adjusted to yield the optimum improvement in the sum

Optimum output SNR occurs when

$$a_j = \frac{s_{j\,(rms)}}{\langle n_j^2 \rangle} \qquad (3)$$

where

$S_{j\,(rms)}$ = the local rms value of $s_j(t)$

$\langle n_j^2 \rangle$ = the mean square noise of the jth diversity channel

If p_j represents the SNR of the j^{th} diversity channel, the improvement factor of the output SNR is

$$\gamma = \frac{P}{P_s} = \sum_{j=1}^{N} \left(\frac{P_j}{P_s}\right) \tag{4}$$

where p_s is the SNR of the best channel. As an example, if two diversity channels are used, and each provides the approximately same SNR, p_s , then the improvement in output SNR is 3 db.

In actually implementing the maximal-ratio combining scheme, means must be provided for continuous adjustment of the quantity a_j as given by Equation (3).

It has become common in current telemetry practice to provide an output AGC voltage which is almost linear with respect to the input signal strength in dbm. Such an AGC output will be provided in the flight spacecraft receiving subsystem. This output will provide useful engineering and diagnostic data regarding the received signal strength. It will also be used to control the combining ratios. If it is assumed that the noise on each channel is equal, the difference between the output AGC voltages is a measure of the relative signal strengths of the channels. The difference, therefore, can be used to provide the optimum combining weights. Any inter-channel variations in the AGC characteristics can be effectively eliminated by proper initial alignment of the combiner. The proposed diversity combiner is shown in block diagram form in Figure 117. The differences in AGC voltages are determined in the difference amplifier whose output is applied to a weighting network. The weighting network makes the appropriate adjustments in the multiplying factors a_1 and a_2 . The outputs of the appropriately weighted channels are added and the sum is applied to a video amplifier that has a variable gain. The variable gain function is provided to enable the combined video output to be maintained at a level fairly constant. The gain control signal is derived from the addition of the AGC voltages from the individual diversity channels. Any variations in the AGC characteristics of the two channels can be compensated for by appropriate initial alignment of the gain-and zero-adjust potentiometers.

The signal detector will be packaged with the diversity combiner. This device will take the form of a conventional integrate-and-dump type network. A typical circuit for a device of this type that has been used frequently in laboratory experiments at Avco is illustrated in Figure 118.

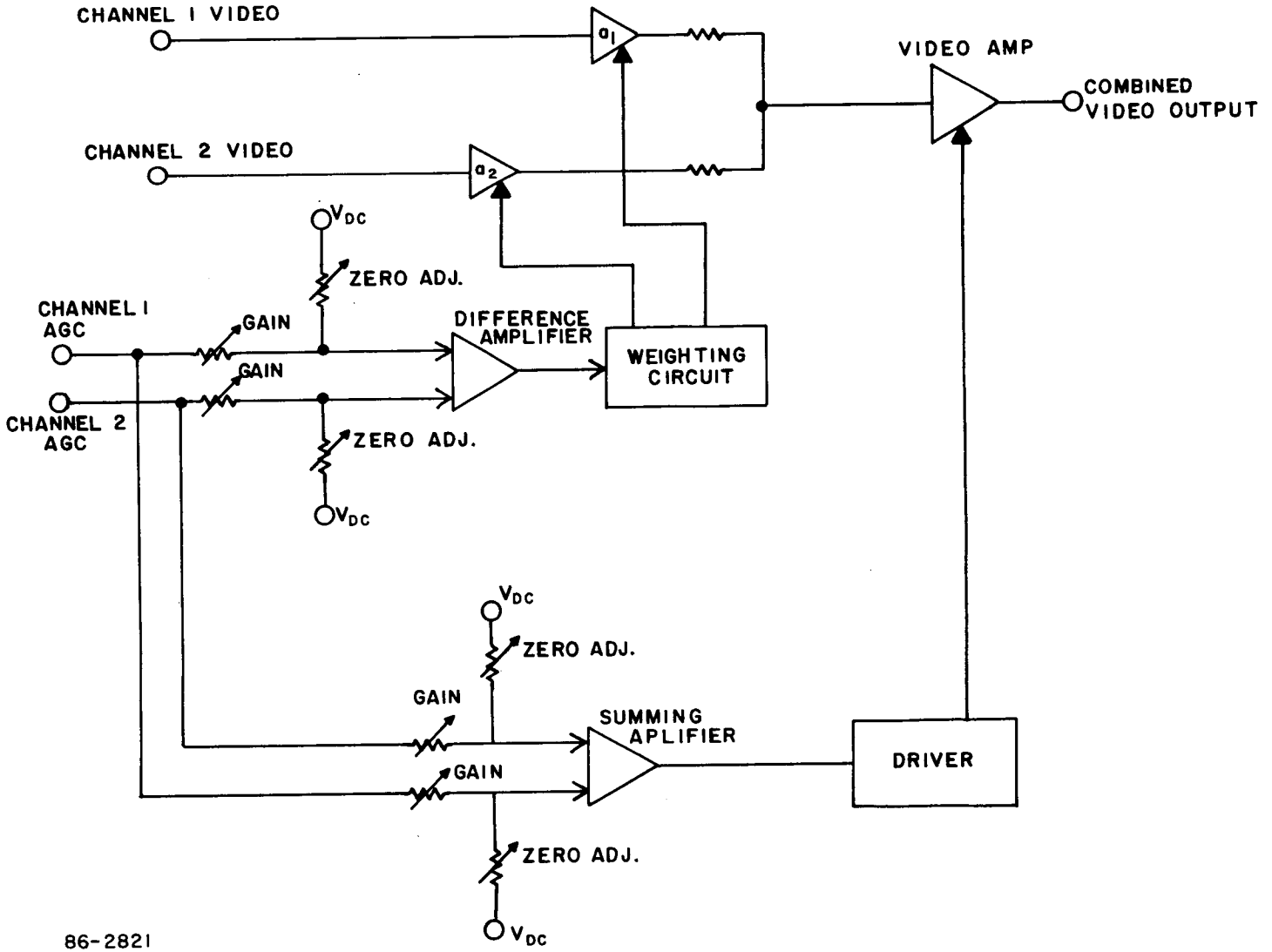

Figure 117 MAXIMAL RATIO DIVERSITY COMBINER

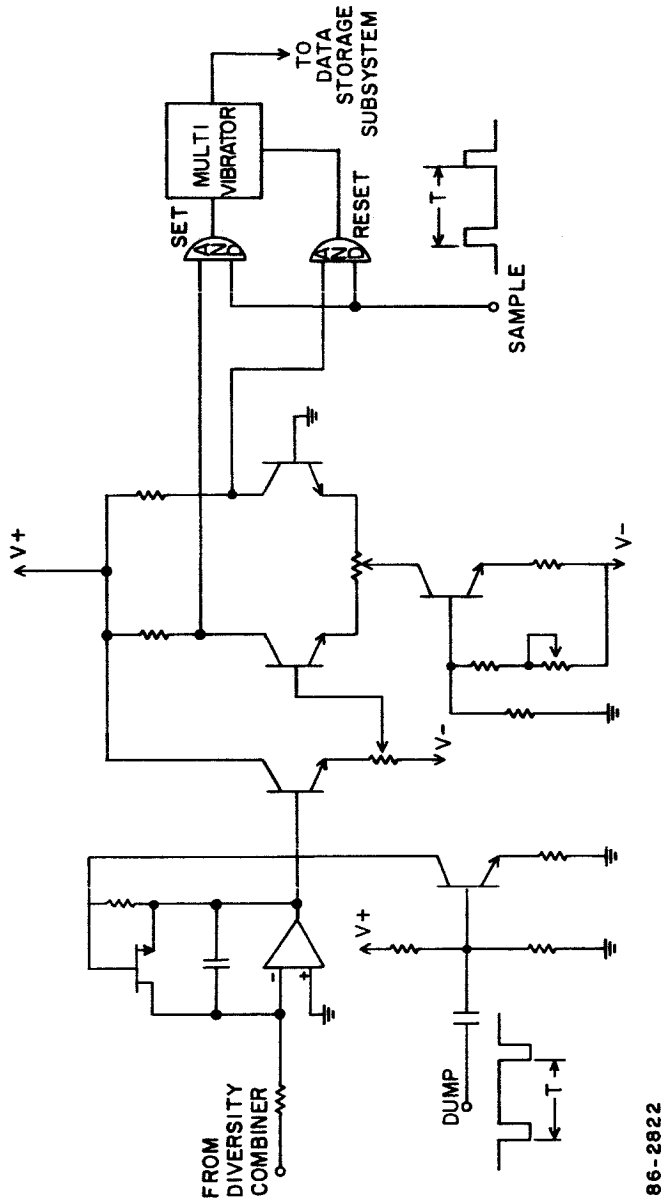

Figure 118 SIGNAL DETECTOR

d. Bit Synchronizer -- A detailed analysis of the wide-band noncoherent PCM/FSK system appeared in Reference 1. It was shown there that for optimum performance, an integrate-and-dump type bit detector should be utilized. This recommendation is predicated on the assumption that correct bit timing is provided by equipment on the flight spacecraft. A bit synchronizer, therefore, is included in the flight spacecraft's required receiving subsystem to provide such timing.

The output of the flight spacecraft receiver subsystem will be in the form of a serial NRZ sequence. This output is applied to a bit synchronizer which synchronizes a local clock to the received data sequence. The synchronizer provides sample and dump pulses to the signal detector, and also provides the reconstituted clock signal as an additional output. The reconstituted clock output signal will be recorded on two separate tracks of the tape recorder used for data storage during the entry phase. One track will be available for possible tape speed compensation use in the recorder; the other track will provide means for synchronizing the flight spacecraft data-handling system. In addition, various diagnostic-type output signals, such as sync-lock indicator and RMS sync jitter, will be provided. The proposed bit synchronizer will use an analog phase lock-loop to acquire and track the received data clock.

Many alternative configurations are possible for the bit synchronizer. An exhaustive analytical and experimental investigation would be required to determine the optimum configuration compatible with the overall flight spacecraft radio subsystem design. Rather than attempt such a study, at this time it is more instructive to describe a generic bit-synchronizer configuration whose performance characteristics can be readily determined. Most pulse code modulation (PCM) bit synchronizers are merely variations on a single basic configuration and their performances are roughly comparable. A block diagram of a generic bit synchronizer is shown in Figure 119. The noisy video output of the diversity combiner is filtered and passed through a nonlinear device to produce a spectral component at the appropriate bit rate. This bit-rate component is subsequently applied to the tracking loop.

The VCO output, in effect, then reprsents the reconstituted data clock signal, or local clock signal. This signal is then suitably shaped to enable it to be used for sample and dump functions in the bit detector. Performance of a generic bit synchronizer that uses a simple first-order tracking loop has been analyzed in detail as reported in Appendix B of this book. As discussed in the appendix, there was one essential tradeoff; acquisition time versus rms sync phase jitter. Table LXXVI which has been extracted from Appendix B illustrates the nature of this tradeoff. From the table the number of data transitions required to reduce the phase tracking error (θ_e) to within some arbitrary percent

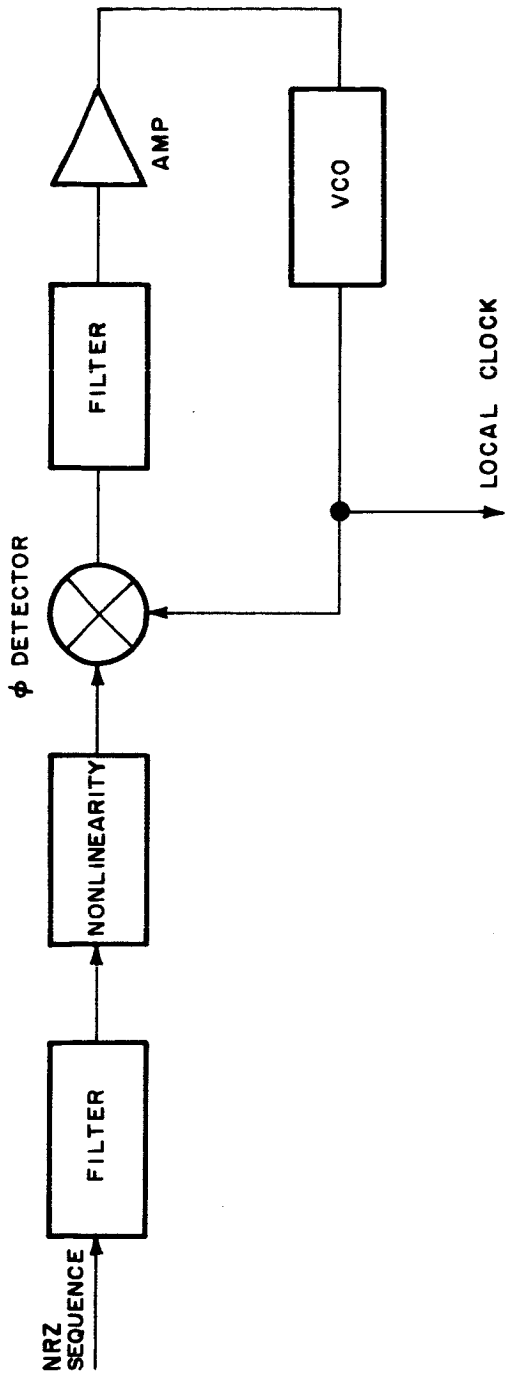

Figure 119 GENERIC PCM BIT SYNCHRONIZER

of its initial value (θ_{in}) can be determined for different values of sync phase jitter. As an example, if a 5-percent rms sync-phase jitter is tolerable, only 20-data transitions will be required to reduce the initial phase offset to within 1 percent of its initial value. If the data transition density is at least one in every ten data bits, acquisition will take approximately 0.01 seconds.

TABLE LXXVI

REQUIRED NUMBER OF DATA TRANSITIONS TO REDUCE PHASE ERROR θ_e TO WITHIN SOME ARBITRARY PERCENT OF INITIAL PHASE OFFSET

θ_o rms (percent)	θ_e /θ_{IN} (percent)	Number of Transitions
1	1	560
	5	370
	10	280
5	1	20
	5	13
	10	10
10	1	3
	5	2
	10	2

As Appendix B also shows, a steady-state phase error will result due to frequency offset. However, for the example given above the steady-state phase error will be approximately 1.7 degrees for an easily obtainable stability of 1×10^{-4}. Its effect on system performance will be therefore negligible.

2. Principal Problem Areas and Development Status -- The complete design of the flight spacecraft radio subsystem is based on a low-risk, high-reliability philosophy. The techniques and hardware used to implement the design have, for the most part, been thoroughly tried and tested in numerous space and ground-based applications. The principal problem area is the bit synchronizer. Although, as shown in Appendix B, this device can be readily implemented to provide performance adequate for the present application, an exhaustive analytical and experimental investigation with the following objectives remains to be conducted:

a. To determine the optimum bit synchronizer configuration consistent with overall receiving subsystem requirements.

b. To assess bit-error performance sensitivity to bit sync errors.

c. To determine experimentally the acquisition and tracking capabilities of promising bit synchronizer configurations.

d. To investigate the feasibility and desirability of using coding schemes that will increase the bit-transition density, thereby enhancing performance of the bit synchronizer.

5. 5. 5. 3 Summary

Table LXXVII summarizes the salient characteristics of the flight spacecraft radio subsystem. Two turnstile antennas are used; one antenna is phased to receive only right circularly polarized signals, the other is phased to receive only left circularly polarized signals. Both antennas receive both of the flight capsule carrier frequencies.

The two redundant polarization diversity receivers each contain two double-conversion superheterodyne receivers, a maximal ratio diversity combiner, and a bit synchronizer. The receiver noise figure, referenced to the antenna terminal, is 9 db. This figure includes a sky temperature effect and is based on use of a pre-amplifier with an assumed noise figure of 3 db. The threshold sensitivity is -138. 4 dbw for a bit-error rate of 1 error per thousand bits ($P_e = 10^{-3}$).

TABLE LXXVII

FLIGHT SPACECRAFT RADIO SUBSYSTEM CHARACTERISTICS

Antenna	
Quantity	2
Type	Turnstile
Frequency	268/272 MHz
Gain	
On-Axis	6 db
Off-Axis	-1 db in 130° beam
Polarization	Left/Right circular
Efficiency	60 percent
Receiver	
Quantity	2
Type	Polarization diversity
Frequency	268/272 MHz
Frequency stability	±0.0001 percent
Modulation	Frequency shift keying (FSK)
Noise figure	
Preamplifier	3 db
Referred to antenna	9 db
Pre-detection bandwidth	85 kHz
Matched filter bandwidth	18 kHz
Threshold sensitivity	-138.4 dbw

5.5.6 Flight Spacecraft Data Handling Subsystem

The flight spacecraft data handling subsystem consists primarily of a data storage medium used to store data transmitted from the flight capsule after its separation from the flight spacecraft. The duration of the flight capsule mission from separation through impact is approximately 1 hour. Since the flight capsule portion of the telecommunication subsystem operates in a single data transmission mode at a data rate of 18,000 bits per second (bps), approximately 55 million bits, are transmitted via each of the two redundant relay links. This results in a total of 110 million bits for both links. Of these bits, only a relatively small number represent useful data since the maximum duration of the critical descent portion of the flight capsule mission, considering dispersions in descent time, angle of entry, etc. is only 355 seconds. In an attempt to reduce the total storage requirement, the flight spacecraft equipment is designed to operate in two data-storage modes.

Figure 96 shows the flight spacecraft portion of the telecommunication subsystem in block diagram form. Two different data storage media are shown in that figure; one a solid-state type, the other a tape recorder. The solid-state storage is designed to be used during the first storage mode. Operation in that mode starts prior to separation and continues until shortly before entry. In this mode, 10 seconds (180,000 bits) of data from each of the redundant receivers would be stored every 5 minutes. During the 5 minutes between each of the 10-second storage periods, the flight spacecraft equipment reads the stored data out of the buffer memories at a rate of 600 bps each. This timing arrangement is not a critical requirement, since the flight capsule data transmitted prior to entry is highly redundant diagnostic data. If the 600 bps rate is too high, or too low, the 5-minute sampling rate could be altered to be compatible with the flight spacecraft data rate allocated to the Mars probe experiment. A 10-second sampling interval was selected to allow two complete sequences of flight capsule data to be stored (the sequence of flight capsule data is repeated every 5 seconds). Ten seconds is also adequate to allow the 2.5-second time-delayed data to be stored.

In the second mode of operation, which begins shortly before flight capsule entry and ends after flight capsule impact, the tape recorder is used to store data continuously. In this discussion use of a two-track data recorder (one track for each redundant relay link) is assumed, although two separate recorders would be required if the total redundancy approach were applied. Use of a single recorder was assumed in this approach since it is possible to use the flight spacecraft tape recorder associated with the flight spacecraft mission as a backup recorder in the event of failure of the relay link tape recorder. Although the descent portion of the flight capsule mission is a maximum of 355 seconds including dispersions, the maximum time from entry (800,000 feet) for impact, for

all orbits considered, is 800 seconds. A 1000-second storage time has been assumed here in determining the tape recorder capacity. At a data rate of 18,000 bps the recorder must provide storage for 18 million bits for each of the two redundant relay links, that is, for a total of 36 million bits.

Since the tape recorder must be turned on shortly before the flight capsule enters the Martian atmosphere, and since the time from separation to entry is a function of orbit geometry, a quantitative command may have to be transmitted from Earth to update the tape recorder turn-on time.

Table LXXVIII summarizes the flight spacecraft data-handling subsystem characteristics.

5.5.7 Summary of Characteristics

The telecommunication subsystem consists of two actively redundant subsystems in both the flight capsule and the flight spacecraft. Both time and polarization diversity are used in transmitting and receiving the flight capsule data. The operational, performance, design, and physical characteristics of the overall telecommunications subsystem are summarized in Tables LXXIX, LXXX, LXXXI, and LXXXII, respectively.

5.5.8 Central Computer and Sequencer

5.5.8.1 Objectives and Requirements

The central computer and sequencer (CC&S) subsystem performs all timing, sequencing, and related computational functions for the flight capsule. In its timing function, the CC&S provides a time base for use in all computations and sequences. In performing its sequencing functions, the CC&S initiates all events in appropriate order by providing properly timed outputs to other subsystems. Computations are performed to solve equations involving time, acceleration,and altitude.

Seven sequences of events require control by the CC&S. These are the checkout sequence, electrical stimulation sequence, separation sequence, master sequence, entry sequence, parachute and penetrometer deployment sequence, and TV picture sequence.

TABLE LXXVIII

FLIGHT SPACECRAFT DATA HANDLING SUBSYSTEM CHARACTERISTICS

Operating modes	2
Types of storage	Solid state, tape recorder
Solid state storage	
Quantity	2 (redundant)
Type	Ferrite core
Mission phase	Separation to entry
Operation	Continuous (read-in 10 seconds, read-out 5 minutes)
Read-in rate	18, 000 bps
Read-out rate	600 bps
Capacity	180, 000 bits
Tape recorder	
Quantity	1
Type	Reel/Reel, dual track
Mission phase	Entry to impact
Operation	Continuous (read-in)
Read-in rate	18, 000 bps
Read-out rate	As required by FS
Capacity	36 million bits

TABLE LXXIX

TELECOMMUNICATION SUBSYSTEM OPERATIONAL CHARACTERISTICS

Communication link	Relay to Earth via orbiting flight spacecraft.
Modes of operation	Single data collection and transmission mode in flight capsule. Two data storage modes in flight spacecraft.
Periods of communication	Continuous except during radio blackout at entry.*
Redundancy	Total, actively.

*Data collected during radio blackout lasting up to 87 seconds is delay stored in a continuously operating 100-second buffer memory and retransmitted prior to impact.

TABLE LXXX

TELECOMMUNICATION SUBSYSTEM PERFORMANCE CHARACTERISTICS

Data rate	18,000 bps
Bit error rate	1 per 1000
Total transmitted data	Approximately 55 million bits via each of two redundant subsystems.
Relay link margin	
Nominal	20 db minimum
During blackout	Below threshold*
During 200 ft/sec wind gusts	Probability of data loss less than 1 percent.**

*See comment at bottom of preceding table.

**Diversity reception techniques on board flight spacecraft reduce effects of multipath signal fading at large capsule swing angles (+90 degrees) to an assumed acceptable level (1 percent).

TABLE LXXXI

TELECOMMUNICATION SUBSYSTEM DESIGN CHARACTERISTICS

Redundancy	Two, totally active-redundant telecommunication subsystems are used.
RADIO SUBSYSTEM	
Frequency	268 MHz and 272 MHz
Modulation scheme	Noncoherent frequency shift keying (FSK)
Data rate	18,000 bps
Transmitters	
Type	All solid state
Output power	30 watts CW
Frequency stability	± 0.005 percent
Flight Capsule Antennas	
Type	Planar logarithmic spirals
Gain	Above -17 db in 270-degree beamwidth
Polarization	circular
Flight Spacecraft Antennas	
Type	Turnstile (body-fixed)
Position on flight spacecraft	Clock, 234° Cone, 153°
Gain	Above -1 db in 130-degree beamwidth
Polarization	Circular

TABLE LXXXI (Cont'd)

Receivers	
Type	Polarization diversity
Noise figure	
Preamplifier	3 db
Referred to antenna	9 db
Frequency Stability	±0.0001%
Predetection Bandwidth	85 kHz
Matched Filter Bandwidth	18 kHz
Threshold Sensitivity	-138.4 dbw
DATA HANDLING SUBSYSTEM	
Data Sequence Period	
Time Diversity	5 sec
Data frames per period	2.5 sec
TV	68
Penetrometer	2
Surface roughness	6
Other experiment	3
Diagnostic	2
Radio blackout	5
Frame Format	
Length	1064 bits
Synchronization	31 bit pseudo-random noise (PN) code word
Frame identification	4 bits

TABLE LXXXI (Cont'd)

Data Accuracy	7-bit, 10-bit, digital count as required
Channel Capacity (equivalent 7-bit)	
Experiment analog	186
Diagnostic analog	200
Experiment digital	8
Diagnostic digital	21
Flight Capsule Data Storage	
Blackout (100 second delay)	Serial, destructive read-out
Type	Ferrite core
Capacity	Approximately 100, 000 bits
Television	
Type	Word, destructive readout monolithic ferrite
Capacity	Approximately 850, 000 bits
Flight Spacecraft Data Storage	
Operating modes	2
Types of storage	Solid state, tape recorder
Solid state storage	
Quantity	2 (redundant)
Type	Ferrite core
Mission phase	Separation to entry
Operation	Continuous (readin 10 sec, readout 5 min)

TABLE LXXXI (Concl'd)

Readin rate	18, 000 bps
Readout rate	600 bps
Capacity	180, 000 bps
Tape Recorder	
Quantity	1
Type	Reel/Reel, dual track
Mission phase	Entry to impact
Operation	Continuous
Readin rate	18, 000 bps
Readout rate	As required by FS
Capacity	36 million bits

TABLE LXXXII

TELECOMMUNICATION SUBSYSTEM WEIGHT CHARACTERISTICS

Item	Quantity	Weight	Volume	Power
Flight Capsule Subsystem				
Transmitter	2	6 lbs.	100 in^3	170 watts
Antenna	2	14	5600	---
Directional Coupler	2	1	60	---
3 Port Circulator	2	5	70	---
RF load	2	1	140	1
Diagnostic Data Handling	2	8	200	4
Experiment Data Handling	2	10	300	6
Blackout Data Storage	2	4	140	2
Television Data Storage	2	22	800	7
Total		71 lbs	7410 in^3	190 watts
Flight Spacecraft Subsystem				
Receiver	4	14	400	16
Diplexer	2	3.5	180	---
Bit Synchronizer	2	2	180	2
Diversity Combiner	2	2	180	2
Antenna	2	2.5	---	---
Ferrite Core Buffer Storage	2	10	240	2
Tape Recorder	1	30	800	12
Total		64 lbs.	1980 in^3	34 watts

These sequences are initiated in one of two ways: either by a time-based signal (for example, a signal from the master timer) or by occurrence of a non-timed event (for example, indication by a radar altimeter that a predetermined altitude has been reached). Most sequences are initiated by a timed event. Regardless of the mode of initiating any given sequence, all succeeding events within the sequence are timer initiated. In addition to these events, certain other events are initiated by discrete commands from the Deep-Space Network (DSN) via the flight spacecraft.

5.5.8.2 Mechanization

Figure 120 shows a functional block diagram of the CC&S. This figure shows the sources of initiation signals and the sequences initiated for each phase of the mission.

Each of tne sequences is defined and described below.

1. Checkout Sequence -- The checkout sequence controls events which determine the operating status and condition of all other flight capsule subsystems. The checkout sequence is initiated by a discrete command from the flight spacecraft. The 13 events comprising this sequence then occur at fixed intervals in response to appropriate timings signals. The status and condition of the following listed items are checked during this sequence: thermal control, attitude control, power control, gas chromatograph, stable platform, television systems, and the attitude control and accelerometer calibrators. This sequence requires 90 minutes and is used as required. The required resolution is one minute.

2. Electrical Stimulation Sequence -- The electrical stimulation sequence is actually a subsequence of the checkout sequence. It is initiated by the master sequence or checkout sequence and provides a timed series of calibration signals to each of the accelerometers and gyros. The TV camera objective lenses are illuminated,and a set of pictures is taken. Calibration of gas chromatograph, acoustical densitometer, and mass spectrometer is based upon instrument response when a sample of known gas is released to each instrument being calibrated. The high- and low-altitude radar altimeters are calibrated by a self-contained calibration network. This sequence of 17 events takes 2 minutes. The required resolution is 1 second.

3. Separation Sequence -- The separation sequence consists of three timed events initiated by the master sequence. Separation is inhibited unless a discrete enabling command has been received. This sequence lasts 66 seconds. One-second resolution is required.

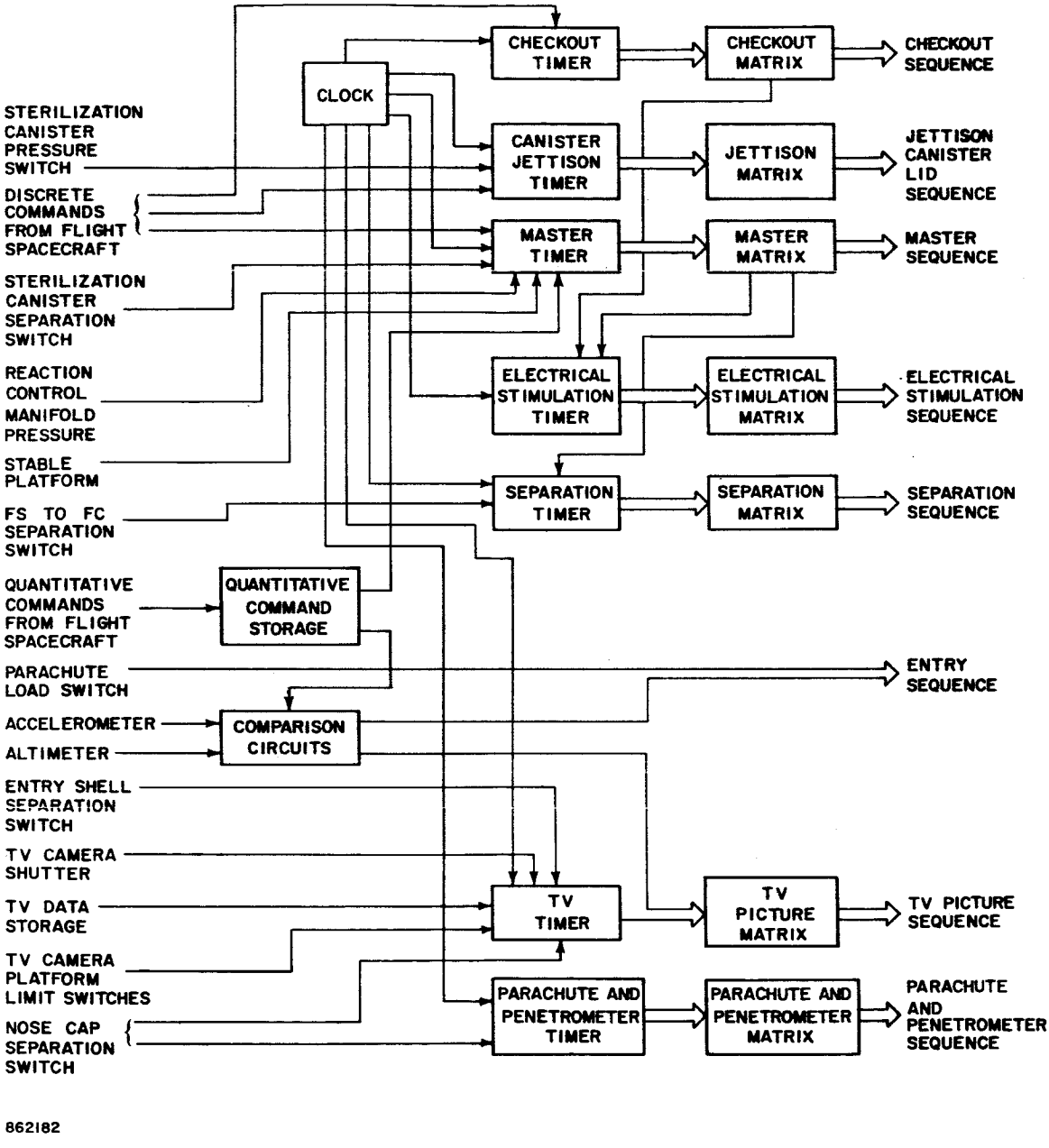

Figure 120 CENTRAL COMPUTER AND SEQUENCER FUNCTIONAL BLOCK DIAGRAM

4. Master Sequence -- The master sequence controls all events from final checkout and calibration through entry. It is initiated by a discrete command from the DSN via the flight spacecraft. It includes 22 timed events. The master sequence initiates checkout, battery recharge, initiation of separation sequence, transfer of the stored attitude-control quantitative commands to the ACS, ΔV rocket ignition, and arming of the entry pyrotechnics. A two-event timed sequence serves as a backup means of initiating ΔV rocket ignition. This backup sequence is initiated by a separation switch. The master sequence has 1-minute resolution.

5. Entry Sequence -- The entry sequence consists of 12 events, each controlled by non-timed computer outputs. Accelerometer and radar altimeter outputs are compared with levels preset by quantitative commands. When the outputs and levels correspond, appropriate signals are given to initiate pilot parachute deployment, to deploy the entry shell, and to start the penetrometer ejection sequence. Initiation of these events is, therefore, a function of Mach number and altitude.

6. Parachute and Penetrometer Deployment Sequence -- This sequence consists of five timed events initiated by the entry sequence, as noted in 5, above. During this sequence, the main parachute is deployed and four penetrometers are ejected.

7. TV Picture Sequence -- This sequence is initiated by a signal from any one of several timers. The timers start when a separation switch closes or when an appropriate signal provided by the entry sequence is received. The TV picture sequence controls the TV camera shutters as well as transfer of data into and out of the TV memories.

Signal inputs include discrete command words which provide a momentary switch closure signal to certain flight capsule subsystems. The discrete commands from the DSN via the flight spacecraft are:

Start Master Sequence

Inhibit Override - Drift of Stable Platform

Enable Separation

Jettison Sterile Canister Lid

Inhibit Override - Sterile Canister Pressure

Start Checkout Sequence

Release Calibration Gas Sample

Arm Separation System

Start Separation System

Start Electrical Stimulation Sequence

Open Cold-Gas Supply Valve

Separate flight capsule from flight spacecraft

Inhibit Override - Sterile Canister Lid Separation Switch

Inhibit Override - Reaction Control Pressure

In addition to these commands, the following listed quantitative commands are received by the flight capsule via the flight spacecraft. These quantitative commands, which represent magnitude information are stored in the CC&S quantitative command storage.

Thrust Vector Roll Command

Thrust Vector Pitch Command

Times of Cruise Maneuvers (in Master Sequence)

Maneuver Roll Angle

Maneuver Pitch Angle

Predicted Time of Entry

Altitude and Constant for Parachute Deployment

Altitude and Constant for Backup Parachute Deployment

Altitude and Constant for Penetrometer Deployment

Finally, the CC&S receives signals from other flight capsule subsystems, to enable various events to initiate still other events. These signals are:

Reaction Control Manifold Pressure

Flight Capsule - Flight Spacecraft Separation Confirmation

Sterilization Canister Lid Separation Confirmation

Acceleration

Parachute Riser Line Load

Pressure - Sterile Canister

Nose Cap Separation Confirmation

Altitude - Above 27, 500 feet

Altitude - below 27, 500 feet

Camera Platform, Limit Switch

Altitude Confirmation

6.0 ELECTRICAL POWER PROBE/LANDER ENTRY FROM THE APPROACH TRAJECTORY

6.1 GENERAL

The proposed EFAT mission is of 13-days duration. For over 12 days following separation the flight capsules' telecommunication subsystem will be virtually dormant. During the last day, the complete entry, descent, and post-landing mission will be conducted. The power profile finally adopted for the flight capsule electric power subsystem is shown in Figure 121. In the early phase of the study (Reference 1) two alternative power profile options were considered for each of two mission phases (cruise, post impact). The optional profiles resulted from consideration of (1) whether or not the command receiver was to be energized during cruise, and (2) whether or not relay link transmission would be used after impact. The calculations on which battery weights were based in the early phase of the study are given in Appendix IV. 4-15 of Reference 1. When it became apparent that the battery weight was excessive, various instruments, etc., were deleted from the flight capsule as necessary to bring the battery weight within acceptable limits. The resultant power profile is shown in Figure 121. The power requirements referred to in the following discussion correspond to that profile.

6.2 FUNCTIONAL REQUIREMENTS

Power subsystem functional requirements are as follows:

1. The subsystem must supply all power to the flight capsule from the time the preseparation checkout is initiated until the end of the mission.

2. The subsystem must provide power in accordance with the selected power profiles after heat sterilization and prior to launch.

3. The system must be kept fully charged by the flight spacecraft power supply.

4. All or any part of the power subsystem must operate in a thermally isolated container.

5. The power source must remain in a charged state under essentially open circuit conditions for at least 12 days (during the cruise period, see Figure 121 without losing more than 10 percent of its nominal capacity.

6. The subsystem that will be housed in the landed capsule has an additional constraint. It must survive planetary impact.

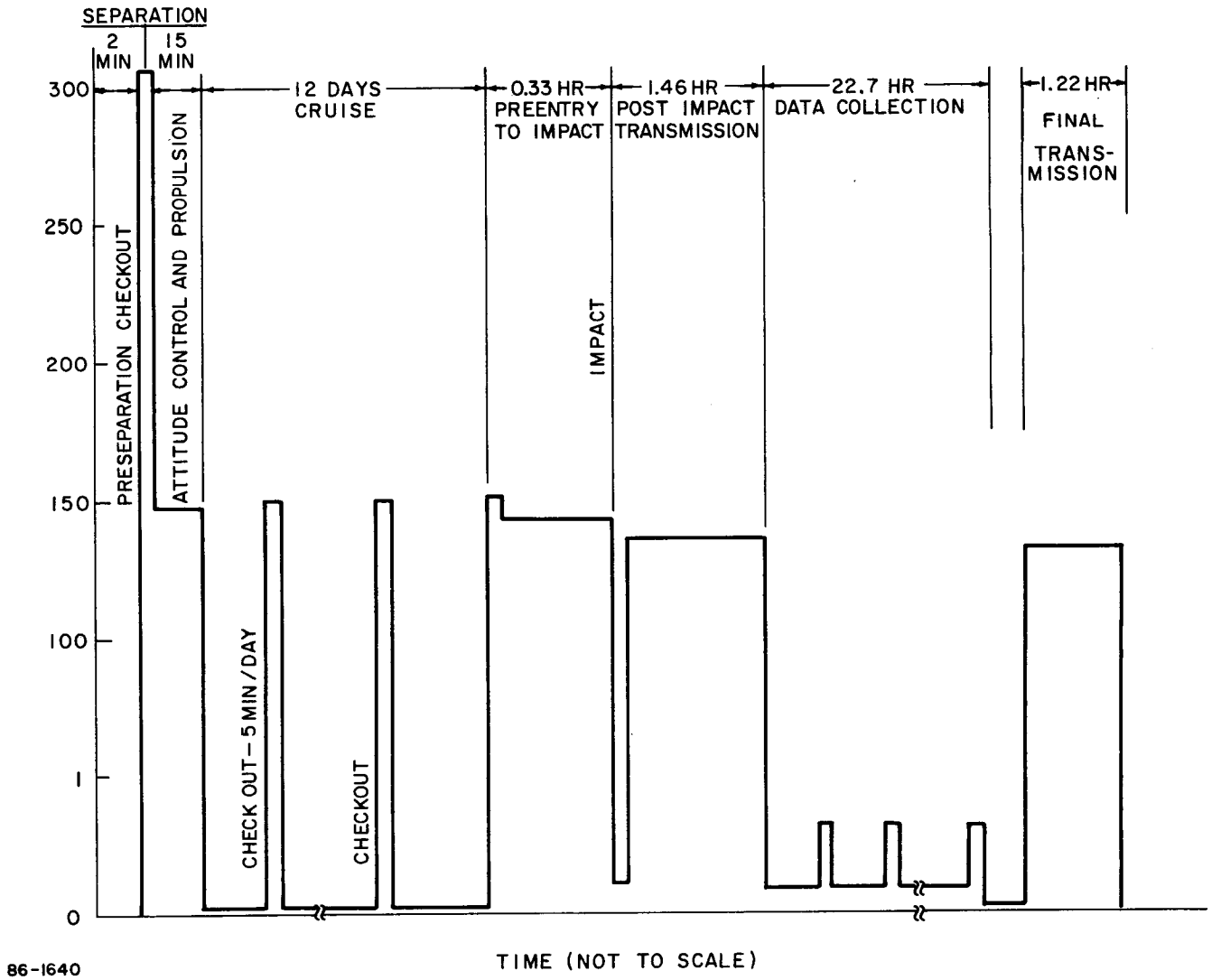

Figure 121 POWER PROFILE

In general, only total power levels rather than requirements for separate components are shown in the power profile in Figure 121. For example, the status check block represents power and energy used by the transmitters and instruments that operate only intermittently during the 12-day cruise period. The only continuous power user during that period is the central computer and sequencer (CC&S) which requires 0.1 watt.

The transmitters use raw DC power. All the other power users, however, require regulated power and condition it as required to satisfy their particular needs. A complete list of power requirements of each component permission phase is presented in Table LXXXIII. Transmitters are the major power user. It should be noted that where applicable the power levels shown on Table LXXXIII include power dissipated in the regulator.

The following paragraphs discuss various power sources and power conditioning techniques from the viewpoint of their ability to satisfy the requirements noted above.

6.3 POWER SOURCE DESCRIPTION

6.3.1 Selected Approach

Only one type of power source, a nickel-cadmium battery, can meet the applicable power requirements and environmental conditions. The battery will consist of a number of series-connected hermetically sealed nickel-cadmium cells packaged in a suitable container. These cells are the only type of cell that has been tested (References 16, 17, 18) and found able to meet the heat sterilization requirements. Figure 122 lists various alternative power sources and summarizes the reasons for their elimination from further consideration. Possible alternative power sources are silver-zinc batteries and the lithium chlorine fuel cell. These are discussed in further detail in subsequent paragraphs covering alternative approaches.

Two batteries will be used, as shown in the system schematic diagram, Figure 123. One battery (battery 2) will be located inside the landed capsule. The other (battery 1) will be attached to the flight capsule structure. Weight restrictions do not allow use of a fully redundant system. However, some measure of redundancy is achieved by using two separate battery regulator circuits. Furthermore, battery 2 can act as a backup for battery 1. The maximum energy drain on battery 2 even if it is used to supply backup power during entry and descent, will not prevent it from performing its full functions except under the most extreme temperature environment. Under extremely adverse conditions, it will be capable of providing 75 percent of the power required during the post-impact period. Characteristics of the two batteries are shown in Table LXXXIV. Appendix C describes the calculations used in determining the battery weights and sizes.

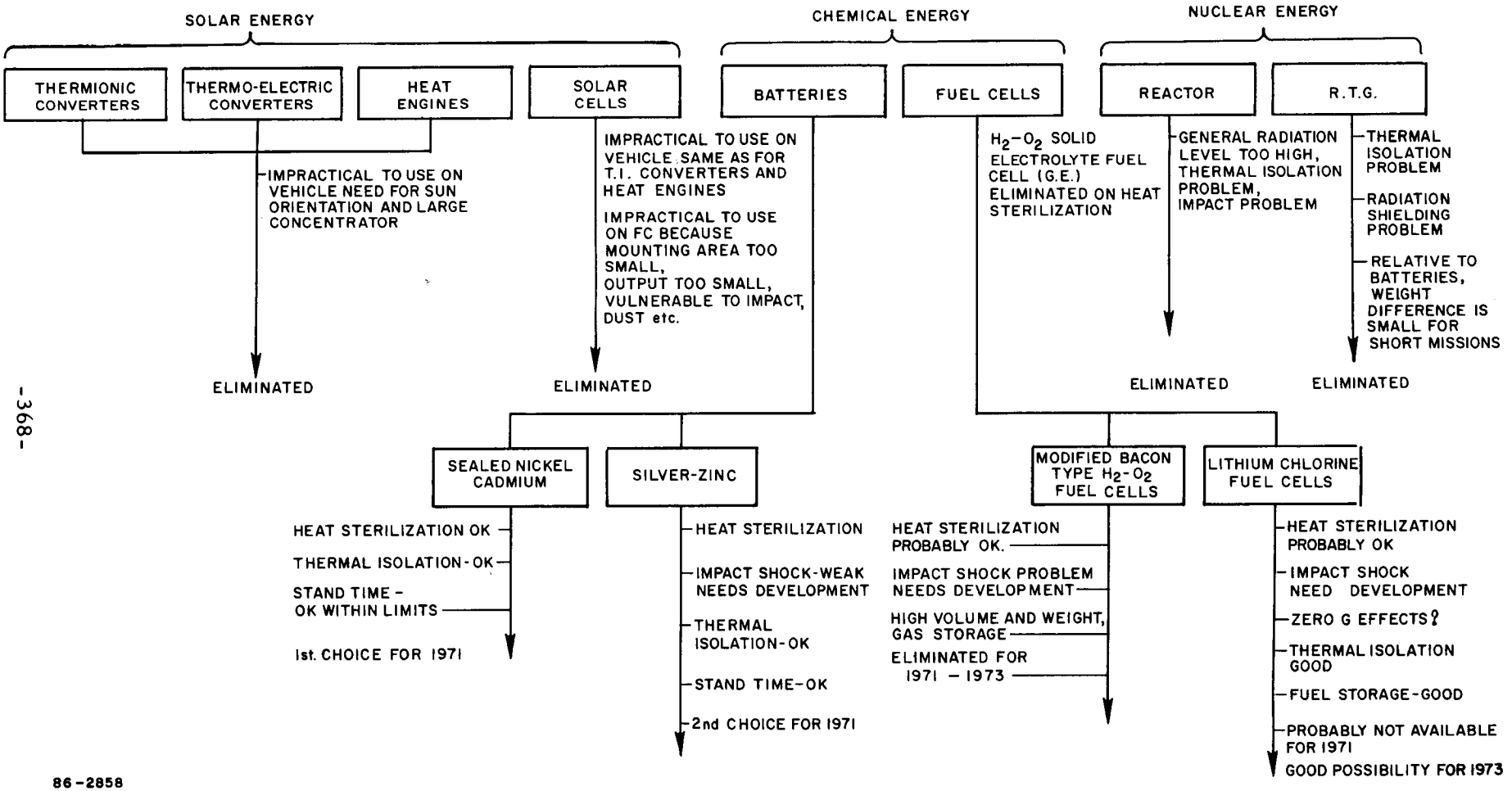

Figure 122 POWER SOURCES AND APPLICATION OF CONSTRAINTS

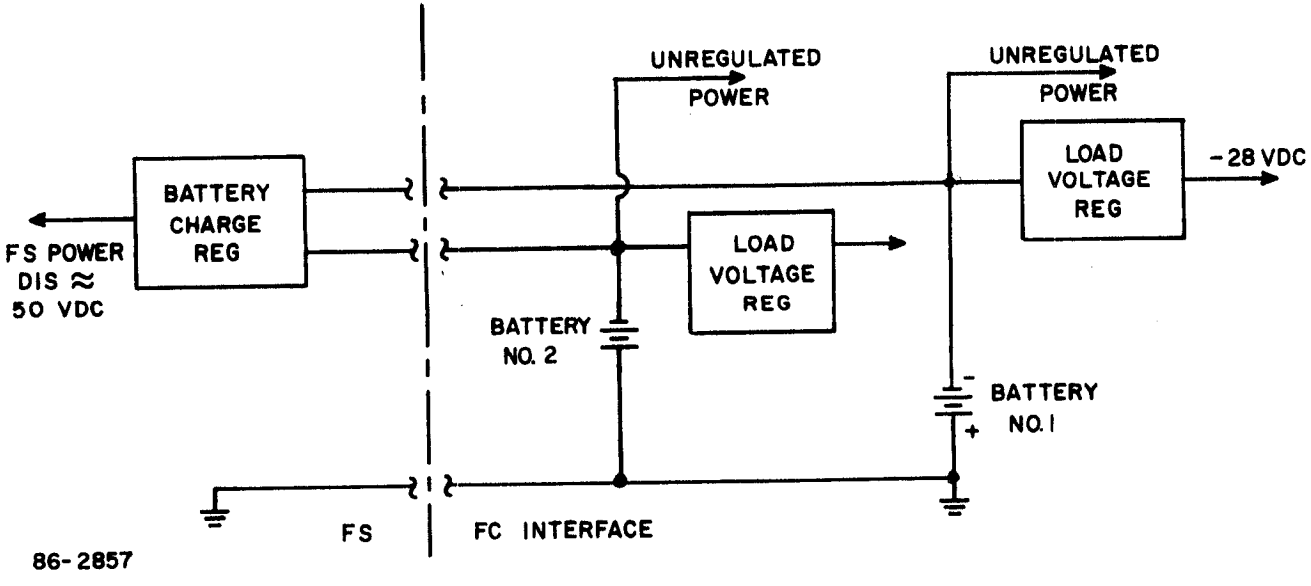

Figure 123 POWER SYSTEM CONFIGURATION BEFORE SEPARATION

TABLE LXXXIII
FLIGHT CAPSULE INSTRUMENTATION POWER REQUIREMENTS

	Command Receiver	Central Computer & Sequencer		Data Automation Equipment	Telemetry System	Relay Transmitter	Direct Transmitter & Amp.	Attitude Control	Radiometer	Accellerometer	Pressure Transducer	Temp. & Mass Spectrometer	Gas Chromatograph	Radar Altimeter	Beta Scatter	Atmospheric Density	Anemometers	Dust Particle Detector	Temp. & Pressure	Cosmic & Surface Radiation	Alpha Scatter and Water Detect.		Total Power Watts	Time of Phase Hours	Energy Watt Hours
Preseparation	3	3		10	5	75.5	111	50	2.1	2.9	0.4	14.6	5.7	14.3	0.4	5.7	1.4	0.6	1	1.1	3.0		311	0.03	10.4
Attitude Control & Propulsion	3	3		10	5	75.5	-	50	-	-	-	-	-	-	-	-	-	-	-	-	-		146.5	0.25	36.6
Cruise	-	0.1		-	-	-	-	-	-	-	-	-	-	-	-	-	-	-	-	-	-		0.1	288	28.8
Status Check	3	3		10	5	75.5	-	-	2.1	2.9	0.4	14.6	5.7	14.3	0.4	5.7	1.4	0.6	1	1.1	3.0		150	0.4	60
Preentry to Impact	3	3		10	5	75.5	-	-	2.1	2.9	0.4	14.6	5.7	14.3	0.4	5.7	-	-	-	-	-		142.6	0.33	48.2
Post Impact Transmission	3	3		10	5	-	111	-	-	-	-	-	-	-	-	-	1.4	0.6	1	-	-		135	1.46	197
Landed Data Collection Continuous	3	0.1		1	-	-	-	-	-	-	-	-	-	-	-	-	1.4	0.6	1	-	-		7.1	20.8	147
Landed Data Col. 5 Min/Hr	3	3		10	5	-	-	-	-	-	-	-	-	-	-	5.7	-	-	-	1.1	3.0		31.2	1.9	60
Post Mission Transmission	3	3		10	5	-	111	-	-	-	-	-	-	-	-	-	-	-	-	-	-		132	1.22	161

TABLE LXXXIV

CHARACTERISTICS OF NICKEL-CADMIUM BATTERIES

Item	Battery No. 1 Separation to Impact	Battery No. 2 Post Impact
Nominal Capacity One-hour Rate (ampere hours)	12	32
Output Voltage Under Load (volts)	25 to 33	25 to 33
Rated Energy at + 40°F (watt-hours)	327	914
Maximum Open Circuit Voltage at 40°F, (volts)	35	35
Minimum Charge Efficiency (%)	70	70
Continuous Trickle Charge Rate (ma)	50 to 125	100 to 300
Maximum Weight (pounds)	33	70.1
Maximum Volume (ft^3)	0.3	0.66

6.3.2 Alternative Approaches

Other power source approaches examined included those based on using solar energy, nuclear energy, and chemical energy. These are discussed in paragraphs 6.3.2.1 through 6.3.2.3, respectively.

6.3.2.1 Solar Energy

Solar energy sources investigated included silicon solar cells, thermionics plus concentrator, and heat engines plus concentrator. Because of the large (typically 9- to 10-foot diameter) concentrators (Reference 19, 20) needed by the thermionics and heat engines to convert the low solar-intensity at Mars (on the order of 500 watts per square meter), both thermionics and heat engines were eliminated from further consideration for flight capsule use.

Use of silicon solar cells poses many problems. For example, installation of solar cells on the vehicle outer skin is not compatible with heat shield requirements. Furthermore, the need for employing appropriate attitude control to facilitate communication with the flight spacecraft and Earth will very likely conflict with the sun-seeking needs of the solar cells. Erection of large (42 ft^2 for 200 watts) solar panels on the landed capsule is impractical. Quite apart from such considerations as breakage, dust storms, and the need for tracking the sun at all times during the day, a battery would still be necessary because only 14.3 hours of the Martian day would be in sunlight. By covering the flight capsule with solar cells, from 15 to 17 watts of power could be produced at aphelion for a weight of 15.5 pounds. However, the figure does not include any allowance for cells cracked from impact, cells covered by dust, dust storms in the atmosphere, or the possibility that the vehicle may land in a shaded site. Detailed calculations related to use of such power sources are included in Appendix IV.4-18 of Reference 1.

6.3.2.2 Nuclear Energy

Results of a preliminary study eliminated nuclear reactors from consideration because of nuclear radiation and thermal isolation problems. Radioisotope thermal generators (RTG's), on the other hand, are worthy of consideration. For long missions, such as a 30-day mission in 1973, an RTG/battery combination may be the only feasible low-weight power supply.

All aspects of use of thermoelectric RTG's are discussed in detail in Appendix IV. 4-60, Reference 1. Figure 124 shows the results of a parametric study of weight versus cold-junction temperature for a 30-watt RTG designed to use plutonium 238 (Pu 238) in the form of plutonium dioxide (PuO_2), as a fuel. A summary of the important results of the study of RTG's follows:

1. Neutron shielding -- The fuel should be Pu 238 (see Appendix IV. 4-16, Reference 1). The choice was based primarily on that material's relatively low level of gamma radiation. The half-life of the isotope is 86 years. The price is high, more than $600 per thermal watt, but availability is not considered to be a problem. Other radioisotopes (discussed in detail in Appendix IV. 4-16, Reference 1 are promethium (Pm) 45, thulium (Tm) 178, thallium (Tl) 204, and curium (Cm) 244.

2. Neutron Shielding -- The neutron count from Pu 238 may be reduced to between 8200 to 9500 neutrons per second per thermal watt ($n/sec/w_t$), see Appendix IV. 4-16, Reference 1.

3. Selection of Thermo-Elements -- The thermo-elements selected are lead-telluride (Pb-Te) or silicon-germanium (Si-Ge). The latter is preferred for reasons of reliability, ruggedness, etc., as discussed in Appendix IV. 4-16, Reference 1.

4. Thermal Isolation -- The results of a thermal analysis (see Appendix IV. 4-16, Reference 1) show that a 30-watt (electrical) RTG cannot be used inside a flight capsule surrounded with crushup type impact absorbent material unless means can be found for creating a good thermal path through the crushup material. This path may be in the form of a heat pipe or other appropriate means.

5. Safety Analysis -- One section of Appendix IV. 4-16, Reference 1, deals with the specific hazards and proposed safety measures related to use of Pu 238. Several of these hazards, when seen from the conceptual design point of view, present major problems. For example, a vehicle impacting on Mars at speeds in excess of 300 ft/sec presents a safety problem insofar as maintenance of the integrity of the fuel capsule is concerned.

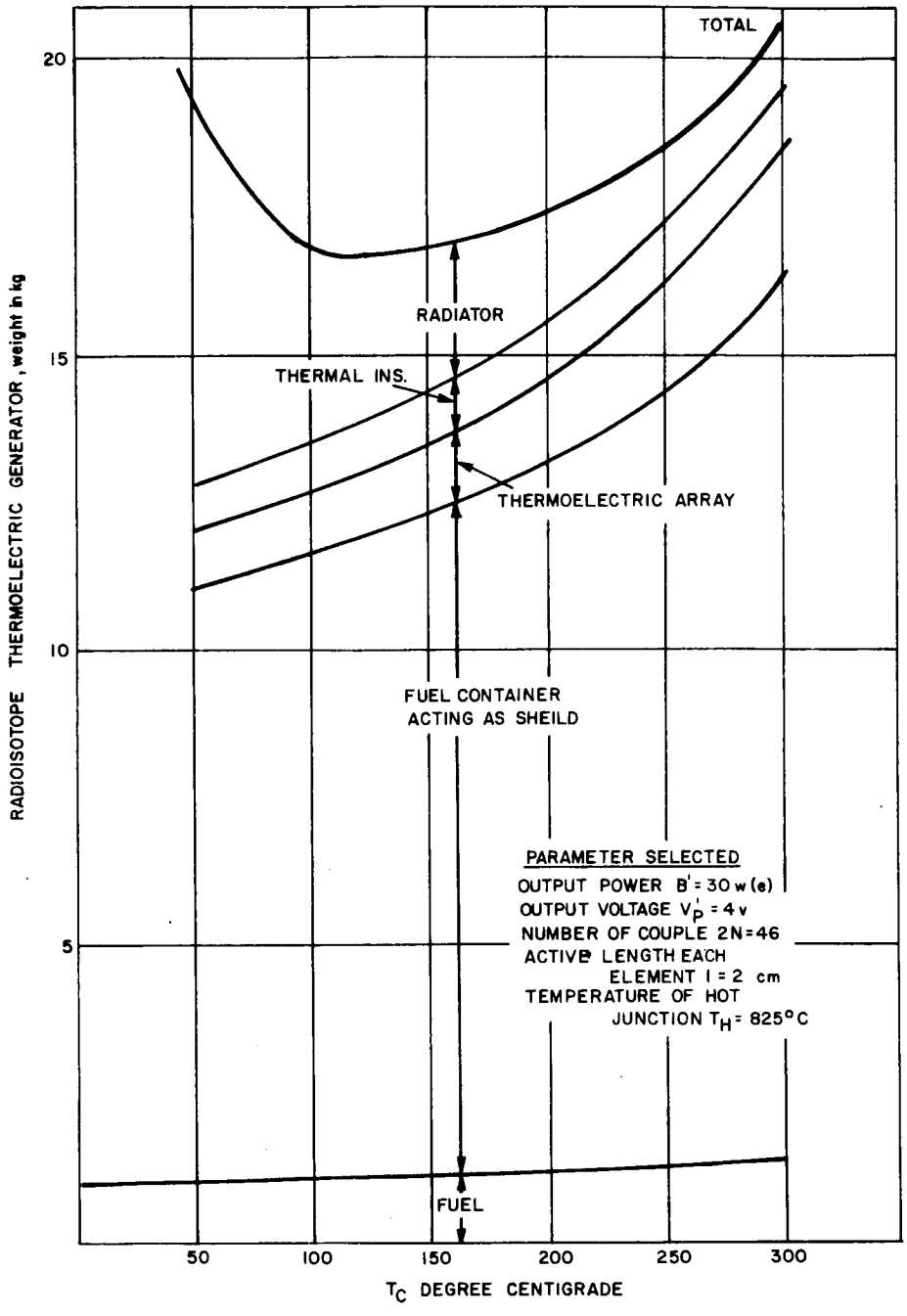

Figure 124 TYPICAL RTG WEIGHT VERSUS COLD JUNCTION TEMPERATURE

6. 3. 2. 3 Chemical Energy

Although the nickel-cadmium battery is currently the only available heat sterilizable battery, it is possible that by 1971, a silver-zinc secondary battery may replace it as the preferred (and only) choice. Silver-zinc batteries are much lighter than nickel-cadmium batteries and are, consequently, very attractive. However, potential charging control difficulties and construction weaknesses may mitigate against such a choice. Silver-zinc batteries with organic separators as well as those with inorganic separators (References 21 and 22) are currently being developed for use in a heat-sterilizable system. Silver-zinc cells are also discussed in detail in Reference 1.

Fuel-cell systems are also discussed in Appendix IV. 4-17 of Reference 1. The most promising power supply of this type is the lithium-chlorine fuel-cell system. This is a very new concept but has the advantages of least weight and size. Furthermore, it does not have to dissipate a great deal of heat, as does the RTG and other fuel cell systems. Of all the power sources, the lithium-chlorine fuel cell system is by far the lightest and for operating times of less than 500 hours, its performance surpasses that of the RTG. Figure 125 shows the comparative data on these two approaches. Use of a hydrogen-oxygen (H_2-O_2) fuel-cell system is hampered by the need for gaseous storage of the fuel - see Appendix IV. 4. 12 Reference 1. Although this system is potentially capable of being heat sterilized, this has not yet been accomplished.

The need for storing gaseous fuel effectivity negates the weight advantage of this system for a 24-hour mission. This situation would change drastically, however, if the heat sterilization requirement were removed. For an example of the impact of heat sterilization on the weight of the fuel tanks for H_2 O_2 systems of various power capabilities, see Table LXXXV.

6. 3. 3 Significant Tradeoffs

Several tradeoffs exist in the areas of weight, volume, heat dissipation, and system complexity. It should be noted that the latter term applied almost equally to both handling and component complexity.

The selected power source, the nickel cadmium battery is the heaviest and largest of the three major choices.

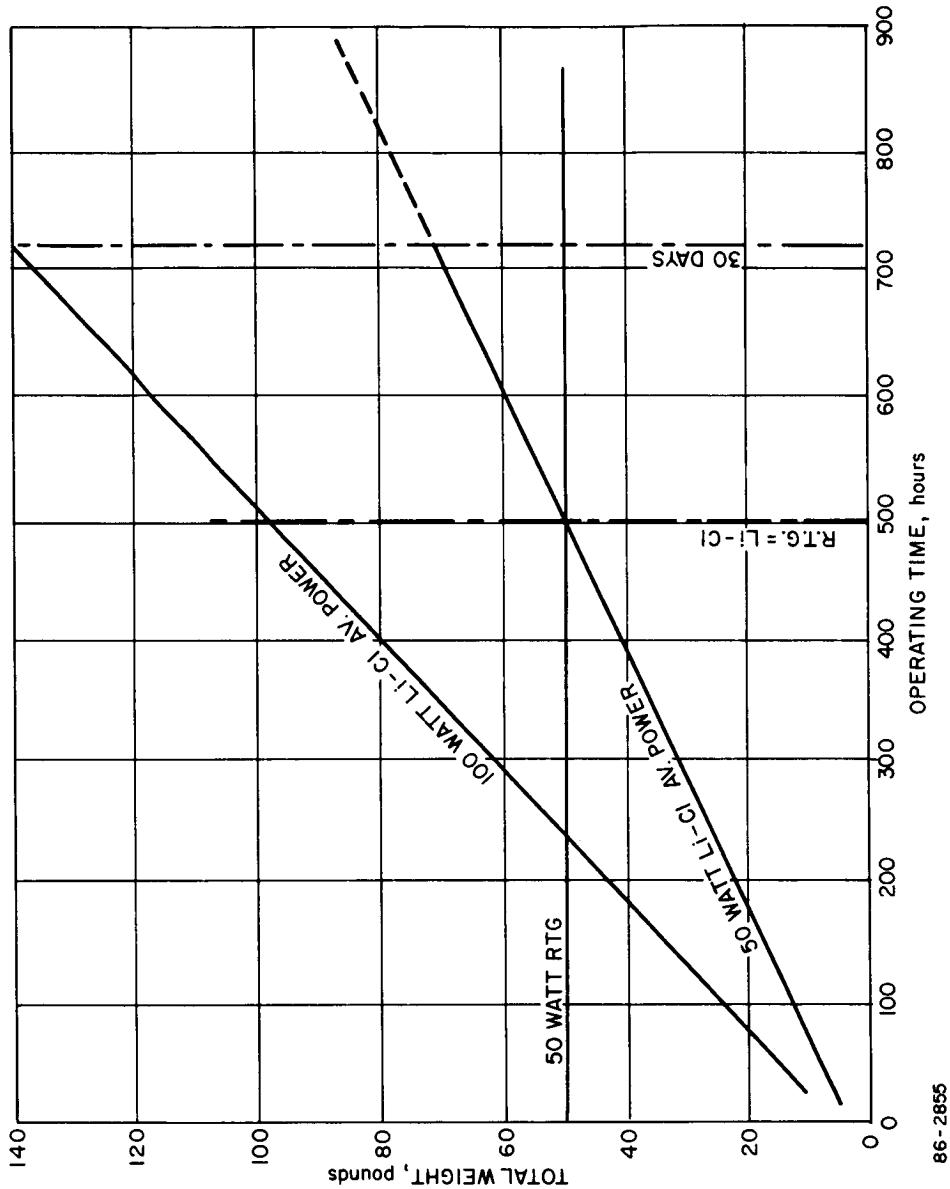

Figure 125 TOTAL SYSTEM WEIGHTS FOR Li-Cl AND RTG VERSUS TIME

TABLE LXXXV

WEIGHT OF FUEL OXIDIZER AND TANKS (REFERENCES 23 AND 24)

Power Required (kilowatt hrs)	Weight of H_2 Fuel (lbs)	Weight of O_2 Fuel (lbs)	Tank + Fuel Total Weight (Supercritical cryogenic storage) Note (1)	Tank + Fuel Total Weight (High-pressure Gas storage) Note (2)	Tank + Fuel Total Weight (Gas storage at +145°C) Note (3)
1	0.1	0.8	3	18	26
20	2.0	16.0	29	70	100
400	40.0	320.0	480	1560	2250

Notes: (1) Storage pressure at 300 psia for H_2 and 900 psia for O_2.

(2) Storage pressure at 1000 psia for H_2 and 7,500 psia for O_2.

(3) Assumes same pressures as in Note (2). No allowance for Material-strength change.

6.3.3.1 Heat Dissipation

At 20°C the estimated heat dissipation for the nickel-cadmium battery for a minimum 5-hour discharge period is approximately 10^{-2} thermal watt-hours per electrical watt-hour. This is about one-third that of a silver-zinc battery. At 0°C(32°F) the heat dissipation for a nickel-cadmium cell is doubled, but that of silver-zinc and silver-cadmium cells is tripled. The Li-Cl fuel dissipates about 10 percent of its power as heat. At low-power levels, at least, this can probably be absorbed by the cell's internal mass. At very low ambient operating temperatures (0°C and below) this type of heat absorption is an asset. At high temperatures, it may be a problem area. The question of heat dissipation for an RTG seems to be largely insoluble for power levels of 30 watts and higher when the unit is used in a thermally isolated flight capsule. The use of various methods of dissipating heat, such as heat pipes, have been investigated and several seem to promise success.

6.3.3.2 System Complexity

Again, as was the case in the area of heat dissipation, the nickel-cadmium battery is the recommended type of power source. As noted in the section on power conditioning, the equipment necessary for handling, charging, checkout, etc. of the nickel-cadmium battery is the simplest required for any of the candidate sources. The construction of the nickel-cadmium battery is also simple. No pressure relief valves, manifolds, or other equipment extraneous to the cells is required. Each cell is hermetically sealed. This allows use of a simple clamped-case holder. The silver-zinc battery, on the other hand, requires careful handling, fairly complex charging equipment, plus extraneous battery components. For example, gas control valves are needed to enable an argon (or other) gas to be supplied under pressure to the cells during heat sterilization. The peculiar charging characteristics of the silver-zinc cells and the possible dangerous consequences of over-charging them requires use of a charger circuit similar to that shown on Figure 126. The Li-Cl fuel cell is the most complex of the various power sources of interest. Its use requires startup squibbs, heaters, and control valves.

6.3.3.3 Conclusions on Tradeoffs

Except for its heavy weight and large volume, the nickel-cadmium battery appears to be the best choice. If weight is the major criterion, the choices probably would be the lithium-chlorine fuel cell system followed by the silver-zinc battery in that order.

6.3.4 Principal Problem Areas and Development Status

The principal problem area remaining in regard to nickel-cadmium cells is that of magnetic cleanliness. Nickel-cadmium cells are inherently magnetic and may have dipole values as high as 2 pole-centimeters per ampere-hour in the North-seeking direction (Reference 25). It may be possible to effect field cancellation to some extent by successively reversing the physical position of the battery cells or cell groups. If the resulting field is still too high to be acceptable, shielding will have to be used.

Large size (20 ampere-hour) cells have not yet been evaluated to determine their ability to withstand heat sterilization. The difference in the internal construction of large cells, as compared to that of the previously evaluated small-sized cells (References 16 and 17), may result in significantly different performance. A number of 20-ampere-hour (20 A-H) nickel-cadmium cells are currently being obtained for evaluation.

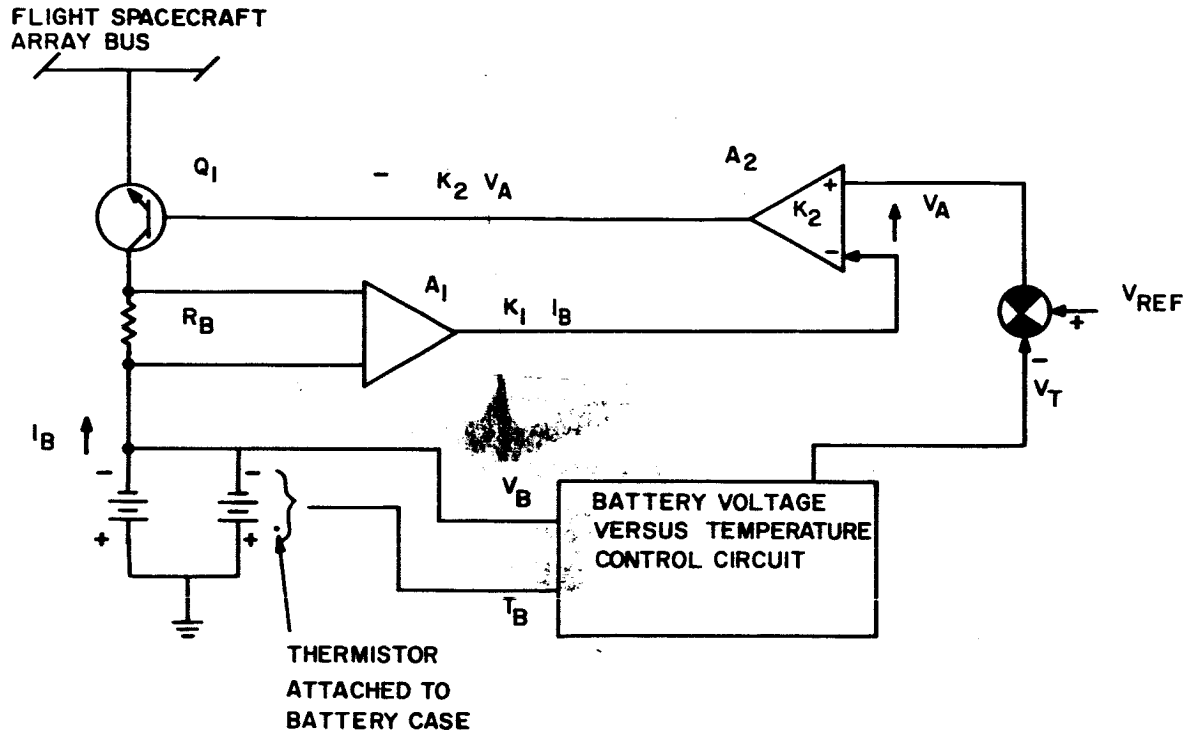

86-1246

Figure 126 PARTIAL SCHEMATIC-SILVER ZINC BATTERY CHARGE REGULATOR

The principal remaining problem area in regard to silver-zinc cells, remains that of successful heat sterilization. The ability of the cells to meet this requirement has not yet been demonstrated at Avco. Cells with organic separators failed under recently conducted tests at Avco and elsewhere (Reference 26), and modifications are currently being made by the manufacturer. Claims have been made (References 21 and 22) that cells using inorganic separators have been successfully heat sterilized, but such cells are not yet available for evaluation.

6.4 POWER CONDITIONING EQUIPMENT

6.4.1 Selected Approach

The selected power conditioning equipment consists of a continuous-trickle charge regulator and two separate-load voltage regulators, as shown in Figure 123. Any dc supply voltage from the flight spacecraft above 40 vdc is adequate. (The exact range depends on the flight spacecraft solar panel design.) The cutoff reference voltage will be provided by zener diodes, and the current will be supplied to the battery through a reistor and blocking diode at the nominal 100-hour rate. Provision is also made for switching to a higher rate charging with power being supplied from the flight spacecraft's power supply or, during the prelaunch period, by an external ground-based supply.

Load voltage regulation is provided by two buck-boost type voltage regulators (Reference 26). This type of regulator, as indicated in Figure 127 and 128, operates as follows: Initially, when the battery is fully charged, the terminal voltage is too high. The buck-boost regulator attenuates this voltage at an efficiency of from 85 to 95 percent, by means of a pulse-width regulator, to produce the 28-volt output. This is the "buck" mode of operation. As the battery discharges, the terminal voltage falls to 28 volts and the regulator turns itself off. Since the regulator is off, standby losses are reduced to a minimum (1 to 2 percent). This is the direct mode of operation. When the battery loading increases, or the battery is sufficiently discharged, the regulator detects the fact and turns itself on to raise the terminal voltage to the desired level. This is the boost mode of operation.

The approximate electrical characteristics of the buck-boost type voltage regulator are:

Rated Load	100 watts
Input	22 to 35 vdc
Output	28.0 vdc ± 1 percent
Ripple	Less than 0.10 volt peak-to-peak
Transients	Less than 0.75 volt for 7 amperes
Overload	100 percent (intermittent)

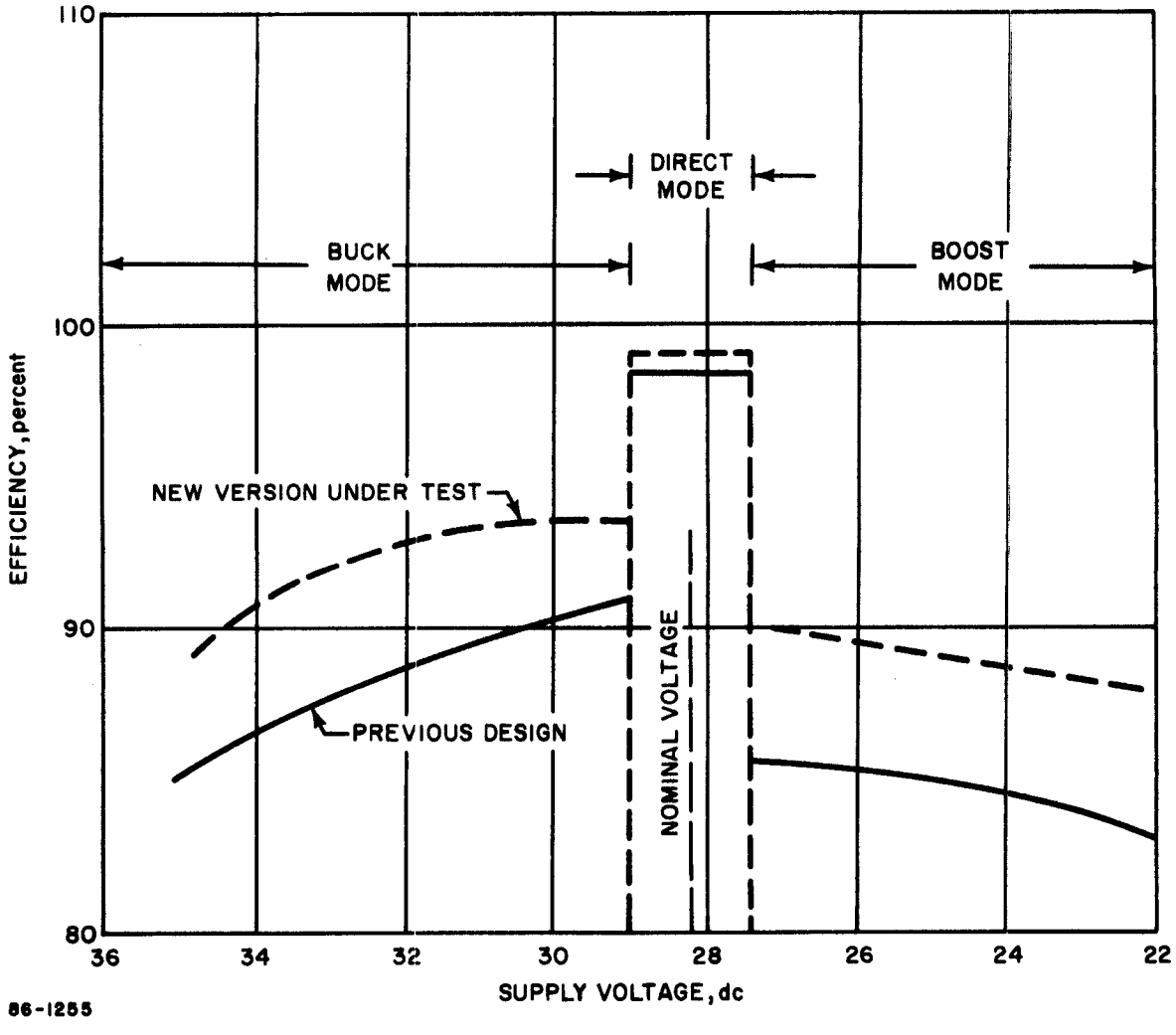

Figure 127 BUCK BOOST REGULATOR CHARACTERISTICS

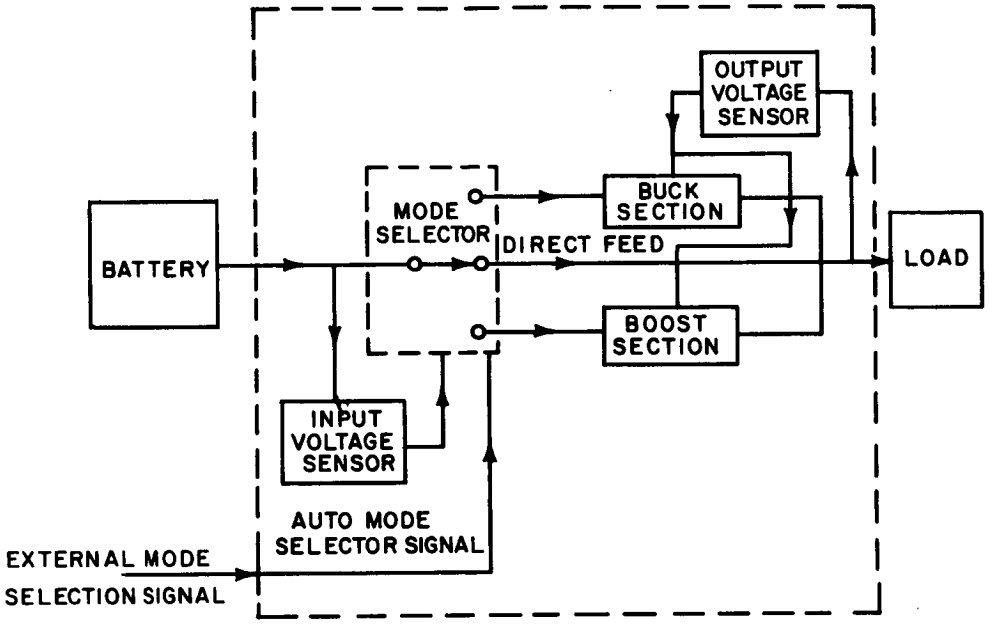

86-1256

Figure 128 BUCK BOOST REGULATOR SCHEMATIC

6.4.2 Alternative Approaches

6.4.2.1 Nickel-Cadmium Battery Charge Regulator

It has been Avco's experience (Reference 16 and 17) that heat-sterilized nickel-cadmium cells do not show sufficient voltage rise at the end of charge to enable end-of-charge conventional voltage cutoff techniques to be applied in charge regulation. There are at least three alternative approaches, however, as follows:

1. Use of a timed charging sequence, as shown on Figure 129.

2. Use of a coulometer connected in series with the battery and used to trigger the charge cutoff, as shown in Figure 130.

3. Continuous charging at a low rate, as shown on Figure 131.

A discussion of each of these options follows:

It is obvious that option 3 is the simplest. However, it carries the penalty of fixing the minimum time allowable between discharging the batteries and separation. Since the charge rate is known to affect the discharge efficiency of some alkali batteries (Reference 27) and would probably affect the nickel-cadmium batteries, a limit would be placed on battery discharge depth prior to separation. For example, assuming that 25 percent of the total battery capacity has been discharged, 25 percent of 100 hours (or 25 hours), plus a time allowance for charge efficiency losses, would have to be allowed at the 100-hour rate (c/100). If this time is acceptable, then option 3 (continuous-trickle charge) is preferred.

The need for a faster charge can be satisfied by switching from the trickle mode to a coulometer controlled charge made in which the battery is charged at the 10-hour rate (or less). Use of a coulometer (option 2) is a relatively new development (Reference 28). It consists essentially of a battery cell placed in series with the battery to be charged. During the time the coulometer is being charged up to 80 percent of its capacity, the coulometer cell voltage remains constant at approximately 0.1 volt. Immediately after the coulometer reaches 80 percent of full charge capacity, its cell voltage rises steeply to a full charge level of 1.00 volt. This abrupt change can be used as a trigger to cut off the charging at any point between 80 and 100 percent of battery-charge capacity. The major objection to its use is that it is a new and relatively untried method. The major advantage of its use is that the charge rate may be fast (as high as the 1-hour rate without causing potentially dangerous gassing).

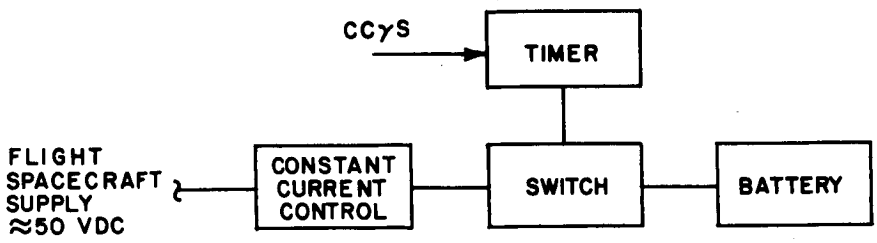

Figure 129 NI-CAD CHARGE REGULATOR 1971--OPTION 1

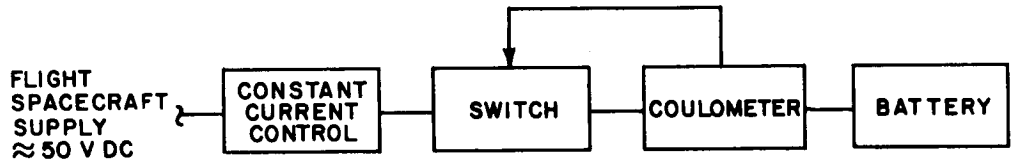

Figure 130 NI-CAD CHARGE REGULATOR 1971--OPTION 2

86-1253

Figure 131 NI-CAD CHARGE REGULATOR 1971--OPTION 3

Option 1. (use of a timer to control the charging sequence) is straightforward in concept but the most complex in implementation. It is, therefore, considered to be the least reliable approach. Accordingly, this method is not recommended.

Major or characteristics of a nickel-camium battery charge regulator are summarized on Table LXXXVI.

TABLE LXXXVI

NICKEL-CADMIUM BATTERY CHARGE REGULATOR

Charge Rates	50 to 400 ma.
Outputs	2
Temperature Cutoffs	Max: +160° F Min: 30° F
Reference Set	By zener diode
Full Charge Rates (optional mode)	1 to 3 amps, 2 outputs
Location	Flight spacecraft
Weight	1. 3 pounds
Volume	0. 03 ft. ^{3}

6. 4. 2. 2 Silver-Zinc Battery Charge Regulator

If a silver-zinc battery were selected instead of the nickel-cadmium battery, a special charge regulator would have to be used.

In contrast to the nickel-cadmium cell, the silver-zinc cell requires the charge current to be reduced rapidly to zero at full capacity. This necessitates an arrangement such as that shown in the partial schematic in Figure 126. The charger consists of amplifiers, temperature and voltage control circuits, a summing network, and a power transistor. Operation of the regulator, discussed in detail in Reference 1, is not repeated here.

6.4.2.3 Pulse-Width Modulated (PWM) Load Voltage Regulator

An alternative to the buck-boost regulator is the PWM series transistor regulator. A typical PWM regulator circuit is shown in Figure 132. Figure 133 shows the current, voltage, and power relationships for a typical circuit. In the circuit shown in Figure 132, a series transistor regulator utilizing pulse width modulation is used to regulate the output voltage. Pulse-width modulation is the term used here to denote the technique of controlling the average dc value of the output by varying the on to off time ratio of a series-connected transistor switch that is operating at essentially a constant frequency. As the series switching transistor operates in either a full-on or full-off mode, it can be used to control considerably more power than when it is used in a class A mode of operation with variable impedance. A filter is needed to obtain a low-ripple dc output voltage because of the variable width pulses in the voltage output. A schematic diagram showing addition of such filters is presented in Figure 134. The magnitude of the ripple increases as the ratio of on to off time decreases.

In general, this circuit is best adapted to conditions where the input voltage, E_{in}, is not much greater than the output voltage, E_o. A dc to dc converter would be necessary if E_{in} were less than E_o. Not only does the efficiency improve as the voltage differential between E_o and E_{in} decreases, but also the output ripple decreases.

6.4.3 Significant Tradeoffs

The weight and volume tradeoffs for the load voltage regulators are relatively insignificant on a component level. There is very little difference between the weight and size of a PWM converter and a buck-boost type. Comparative weight and volume data, together with other characteristics, for various power conditioning components, are shown in Table LXXXVII.

The most important tradeoff occurs in the area of the electrical output characteristics of the load voltage regulators. For the PWM regulator the condition $E_{in} > E_o$ must apply; otherwise a dc to dc converter must be added. The buck-boost regulator, on the other hand, needs no extra equipment and automatically switches to the boost mode whenever the input voltage drops below the required output level as shown in Figure 127. Since this type of regulator can operate at high efficiency at voltages as low as 22 vdc (less than 1 volt per cell, equivalent), virtually all of the battery capacity may be used. This represents a considerable weight saving as compared with the usual 70- to 80-percent maximum discharge. The regulation needs of the nickel-cadmium batteries differ considerably from those of the silver-zinc batteries, in that the battery regulator of

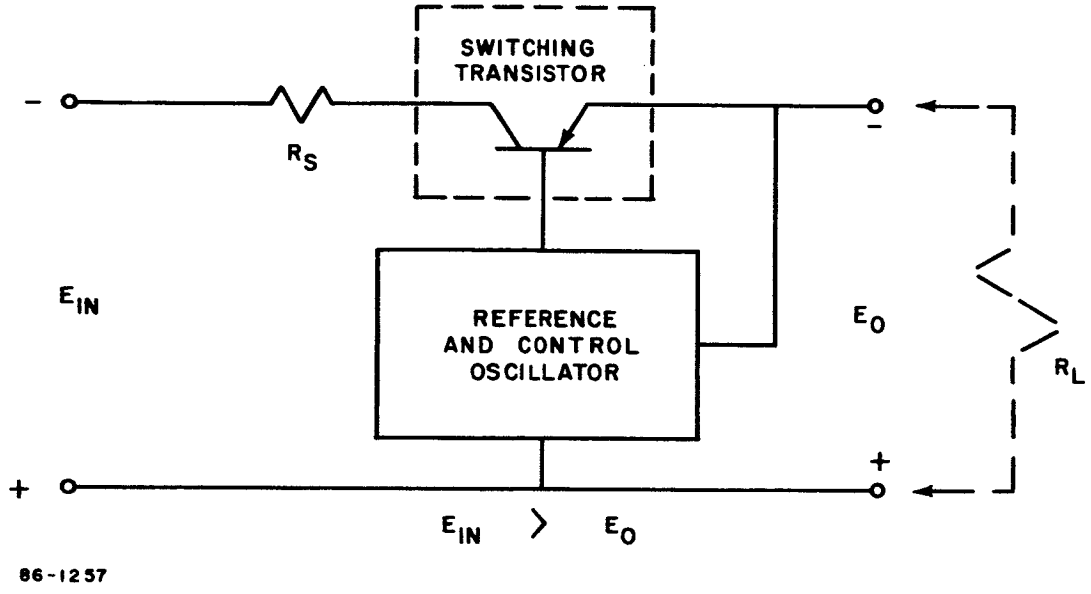

Figure 132 PULSE WIDTH MODULATED SERIES TRANSISTOR REGULATOR

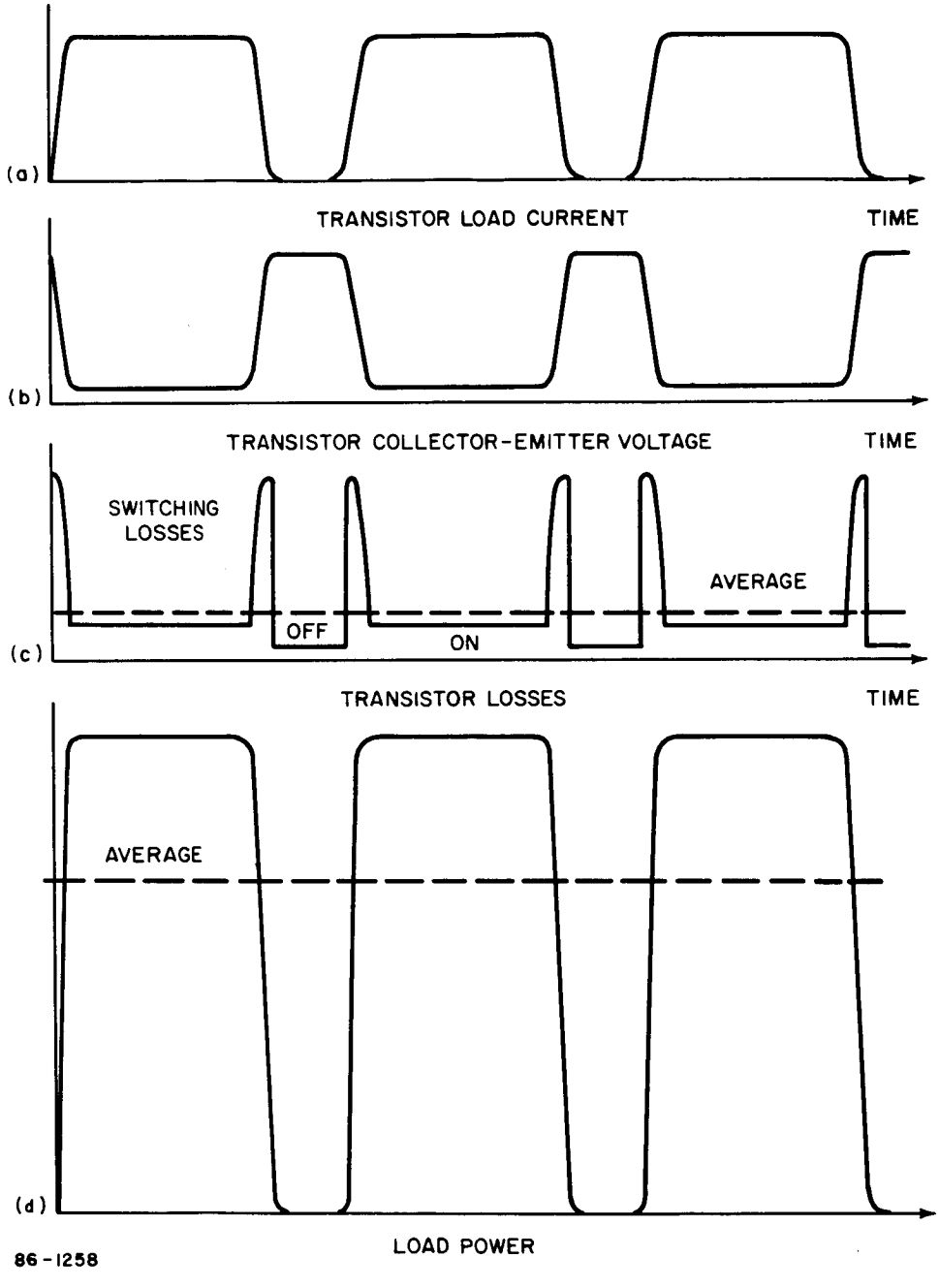

Figure 133 CURRENT, VOLTAGE, AND POWER RELATIONSHIPS FOR A PWM SERIES TRANSISTOR REGULATOR

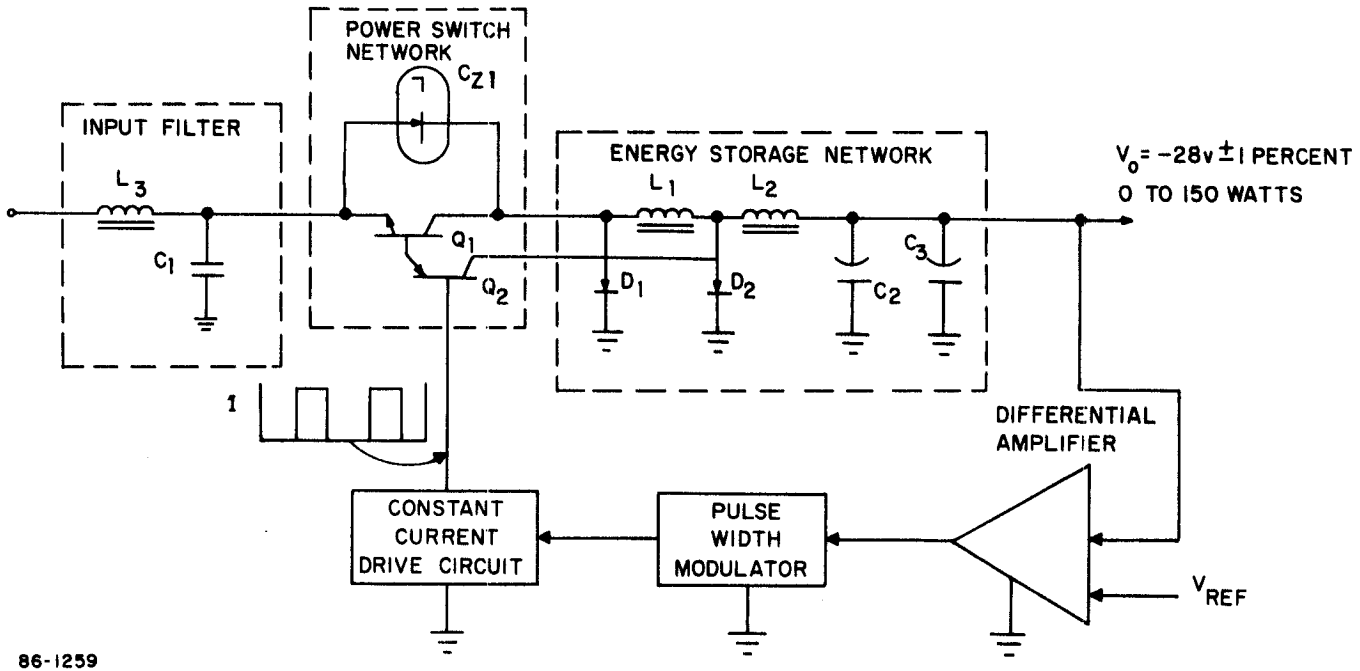

Figure 134 PARTIAL SCHEMATIC OF PWM REGULATOR

TABLE LXXXVII

CHARACTERISTICS OF POWER CONDITIONING ALTERNATIVES

Item	For Use With	Consists of	Estimated Wt. lbs.	Estimated Volume in^3	Comments
Timed Charge Regulator	Nickel Cadmium Battery	Timer, Switch, Const. Current Control	2	50	Depends on CC&S. complex
Coulometer Charge Regulator	Nickel Cadmium Battery	Coulometer cell, Switch, Cons. Current Control	2	50	Relatively New method Good Control
Full Control Capacity Charge Reg.	Silver Zinc Battery	Temp & Voltage Control Circuit, Amplifiers, Transistors, Switches, Reference Loads	1.3	40	A must for Silver Zinc Battery
Load Regulator Buck Boost Type	Nickel Cad or Silver-Zinc	Input & Output Voltage Sensors, Mode Selector, Buck and Boost Sections	2.5 (for 100 watt)	60	Best Utilization of Battery Capacity Not as efficient as P. W. M. at all power levels
Load Reg. P. W. M. Type	Nickel Cad or Silver-Zinc	Ref. and Control Oscillator, Switching Transistor, Amplifier, Switching and Filtering Network	2.0 (for (100 watt)	50	D. C. -D. C. converter Req'd if Ein < Eo High Ripple High Efficiency,

the former is inherently considerably better. For example, for equivalent 28-volt batteries being discharged at the 5-hour rate, the ΔV between the open voltage circuit and the plateau voltage for a nickel-cadmium battery is approximately 2.5 volts. For the silver-zinc battery it is at least 7 volts. The voltage swings of those nickel-cadmium battery subsystems that require output regulation will be limited by appropriate regulator design, to from 31 volts to open circuit (no load) to 23 volts under maximum load; this gives a maximum ΔV of 8 volts. Since it is expected that the output voltage will be 28 volts or less most of the time, use of a dissipative type series regulator or a PWM switching regulator would not be appropriate. The losses with either would be excessive.

Figures 135 and 136 show typical characteristics of a PWM series transistor regulator. It should be noted that higher voltage inputs result in less efficiency and higher weight. In general, the simplest regulators are also the most inefficient. However, other considerations may make the level of loss acceptable. For example, the loss in the current control circuit for the charger is estimated at an average of 8 to 10 watts.

There is not a great deal of difference in the weights and sizes of each of the types of regulators described above. For the silver-zinc battery there is no real alternative to use of a fully controlled capacity charge regulator of the type described. A trickle or float charge regulator would probably be preferable for reasons of simplicity if it could be used. There is, however, no evidence to date that such a regulator can be used in conjunction with a heat-sterilizable silver-zinc battery.

An important tradeoff area is that of reliability. Table LXXXVIII is provided to assist analysis of the failure rate of various types of regulators. This table gives the estimated types and quantities of parts required for several of the circuits described above. Those circuits for which no listing is given have not yet been sufficiently defined to permit compilation of such data.

TABLE LXXXVIII

CIRCUIT COMPONENT BREAKDOWN FOR RELIABILITY ESTIMATE

Component / Item	Transistors		Diodes		Resist	Capac.	Ind.
	Power	Low Level	Power	Low Level			
Charge Reg. (AG-Zn)	1	9	1	7	35	5	1
PWM Reg.	2	9	3	6	33	8	4
Charge Reg. Ni-Cd, Trickle Type	0	0	0	1	1	0	0

NOT INCLUDING CRUSHABLE STRUCTURE

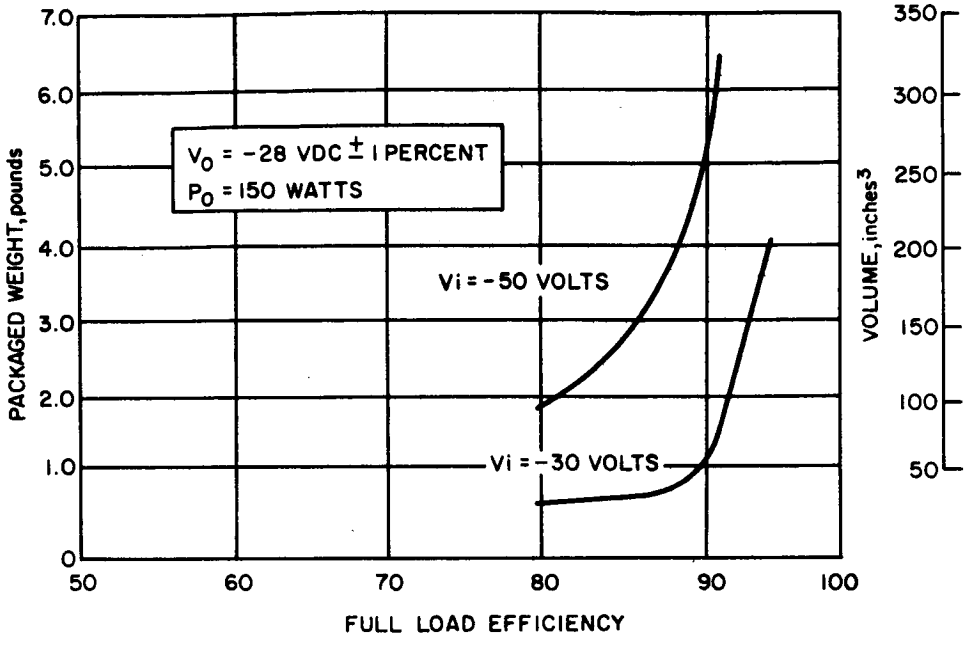

Figure 135 PWM SWITCHING REGULATOR CHARACTERISTICS

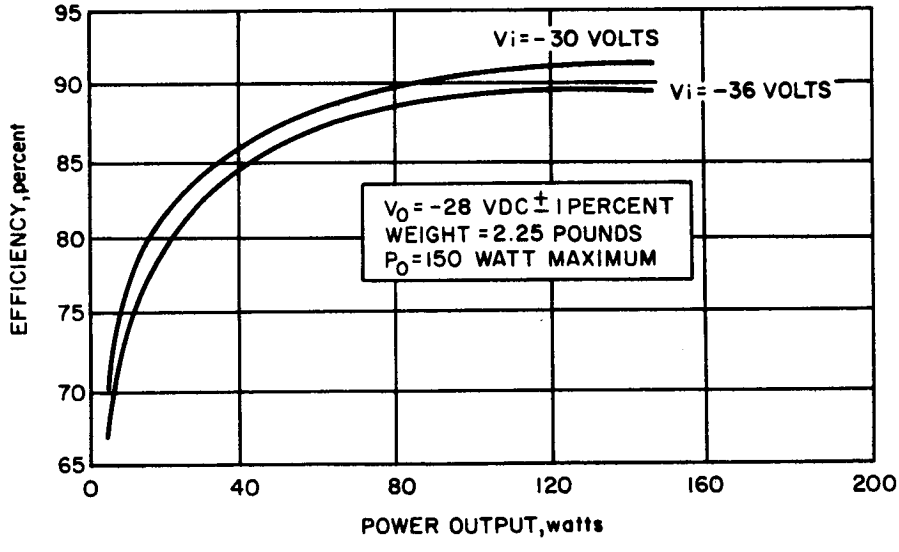

86-1261

Figure 136 PWM SWITCHING REGULATOR EFFICIENCY-LOAD POWER RELATIONSHIP

6.4.4 Principal Problem Areas and Development Status

6.4.4.1 Problem Areas

As with most of the other electrical components, the ability to meet the heat sterilization and high-impact shock requirements remains to be demonstrated.

6.4.4.2 Development Status

Buck-boost and PWM regulators have been constructed for the 100-watt levels.

6.5 SUMMARY OF SYSTEM CHARACTERISTICS

Table LXXXIX describes the physical characteristics of the selected electrical power subsystem. Table XC is also included to provide comparative data on alternative subsystems. Projected weights for alternative silver-zinc battery and lithium-chlorine fuel-cell power sources are shown, and the relative advantages of each of the alternatives are clearly indicated.

TABLE LXXXIX

PHYSICAL CHARACTERISTICS OF POWER SUBSYSTEM

Components	Weight (pounds)	Volume (ft^3)	Peak Heat Dissipation (watts)	Notes
Nickel Cadmium Battery				
Separation to Impact	33	0.3	50	Each cell is hermetically sealed by a glass to metal seal
Impact to End of Mission	70.1	0.66	10 to 15	
Load Voltage Regulator	3.5(2)	0.05	10 to 20	Hermetically sealed
Battery Charge Regulator				
Trickle plus full Charge	1.3	0.03	8 to 10	Located in flight spacecraft

TABLE XC

SALIENT CHARACTERISTICS OF THE ELECTRICAL POWER SUBSYSTEM - 1971

Source	Prime Nickel-Cadmium Battery	Back-up Silver-Zinc Battery	Back-up Lithium Chlorine Fuel Cell System
Delivered energy Separation to impact	184 watt hours	184 watt hours	184 watt hours
Weight-separation to impact	33 lbs.	14 lbs.	see post impact weight
Delivered energy post impact	565 watt hours	565 watt hours	565 watt hours
Weight-post impact	70.1 lbs.	28 lbs.	30 lbs. (supplied energy from separation to end of mission)
Output Voltage Limits Before Regulation	25 to 33 vdc	25 to 37 vdc	3.0 to 3.5 vdc*
Charge Regulator	Resistor and diode in series for unlimited trickle charge plus temperature compensated full rate charging.	Current controller with full capacity cut-off and temperature compensation	None required, extra fuel for extra discharge

*DC to DC converter required to raise voltage.

7.0 ELECTRICAL POWER PROBE/LANDER ENTRY FROM ORBIT

7.1 GENERAL

The power profile for the entry from orbit (EFO) mission is characterized by an essentially constant and continuous power discharge. The discharge time is slightly under one and one-half hours, as compared with approximate 13-day duration of the mission in the case of the entry from the approach trajectory (EFAT) mission. This difference significantly affects a number of design considerations. Some of the effects are favorable, particularly where the battery is concerned. For the EFO mission, a power control unit is combined with the batteries and regulators to form the complete electrical power subsystem. Figure 137 shows a block diagram of the proposed subsystem. The subsystem includes two batteries, two power converters, a dual power control unit and two battery chargers. The parts of the subsystem are so interconnected that the effects of failure of any component are minimized. In addition to the main electrical power subsystem, each penetrometer contains a rechargeable battery which must also be maintained in a charged condition.

7.2 FUNCTIONAL REQUIREMENTS

Power subsystem requirements are as follows:

7.2.1 Modes of Operation

The system operates in three alternative modes: (1) Cruise to encounter with planet, (2) Preseparation checkout, and (3) Separation to impact. During the cruise to encounter period (Mode 1) all power for battery trickle charging, temperature control, and subsystem checkouts is supplied to the flight capsule's power subsystem by the flight spacecrafts power supply. During the preseparation checkout all power is supplied by the flight capsule's batteries. However, when the checkout is completed the flight spacecraft's power supply is used to recharge the flight capsule's batteries.

From separation to impact all flight capsule power is supplied by the flight capsule's own batteries according to the power profile shown in Figure 138. Table XCI lists the various power users and indicates their anticipated power requirements.

7.2.2 Heat Sterilization

All components of the subsystem (except the battery chargers) must be capable of providing power in accordance with the power profile after heat sterilization and prior to launch.

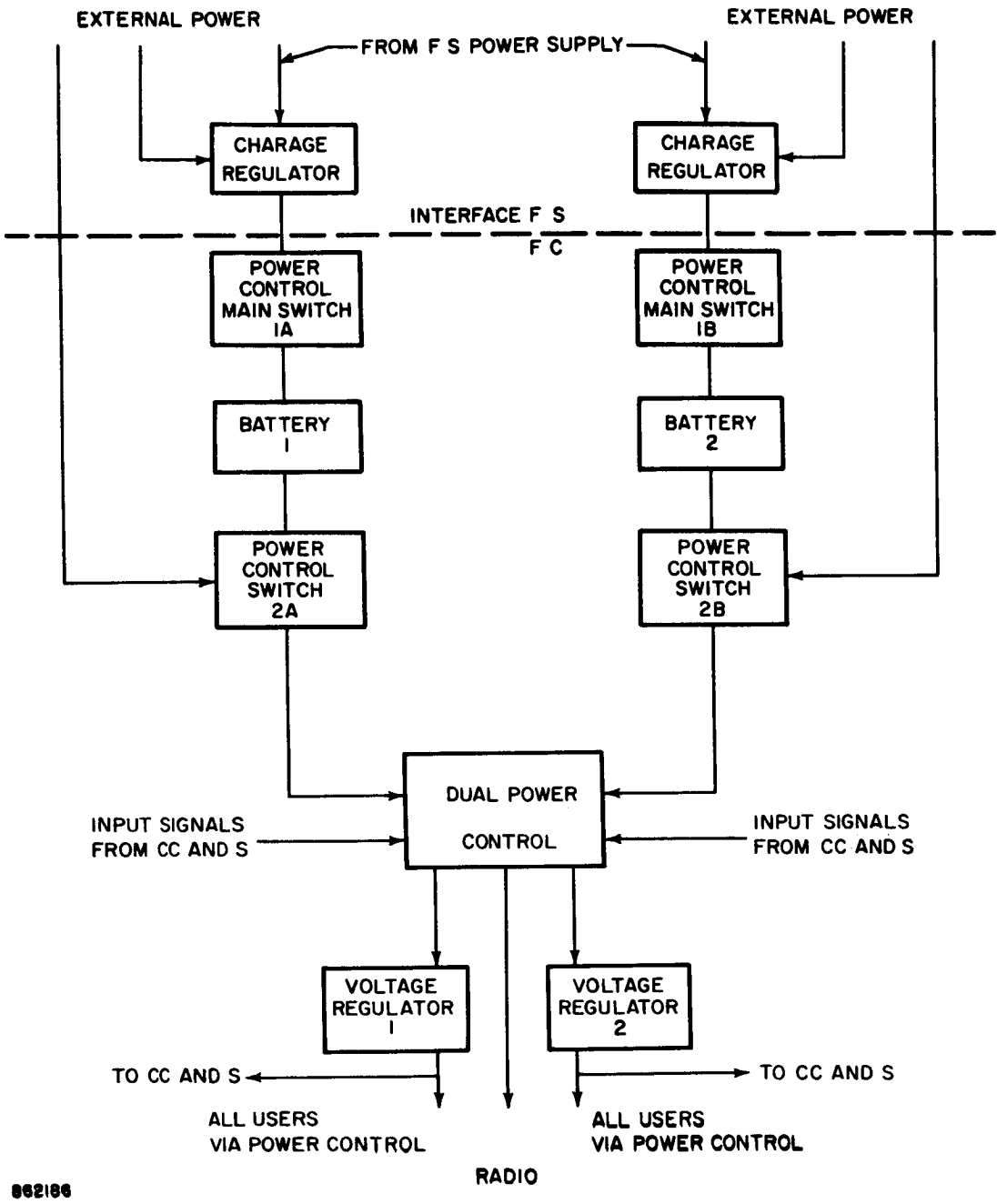

Figure 137 SCHEMATIC DIAGRAM OF POWER AND CONTROL SUBSYSTEM

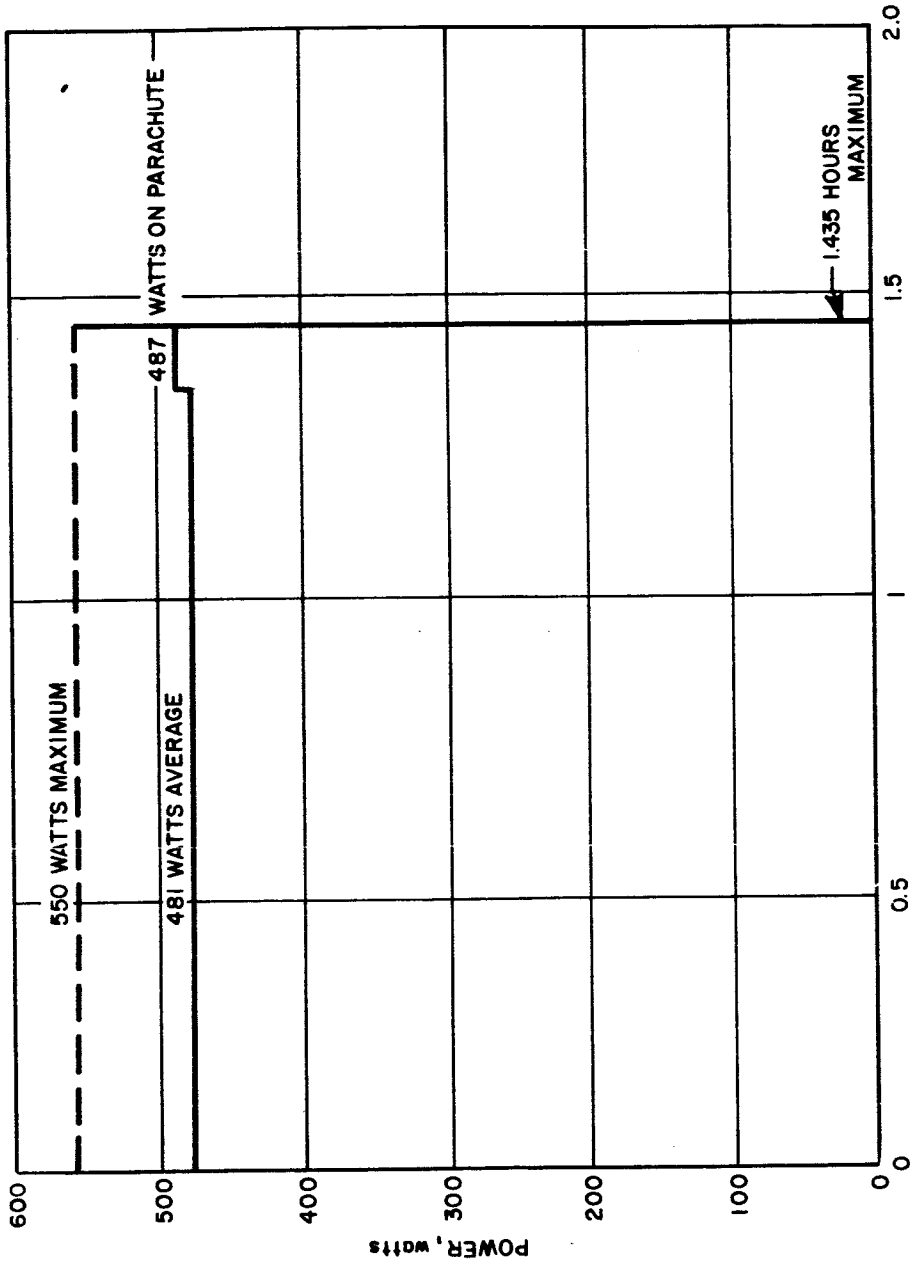

Figure 138 POWER PROFILE FOR FLIGHT CAPSULE

TABLE XCI

LIST OF POWER USERS

Part	Average Power in Watts
Transmitters	170 (not regulated)
Engineering Data Handling	6
Diagnostic Data Handling	4
Data Storage	1
Delay Data Storage	2
Doppler Radar	10/50
Mass Spectrometer	10
Radiation Detection	0.8
Accelerometer	10.5
Acoustic Densometer	4
Gas Chromatograph	4
Pressure Sensor	21.1
Beta Scatterer	0.3
Temperature Sensors	7.7
Radar Altimeter	60/4
Vibration	0.5
Ablation	0.8
Penetrometer Receiver	5.0
Water Detector	0.5
Television	5/27
ACS Electronics	10
Inertial Reference System	45.5
Gyro	10
Voltage Regulator	86
Total Power Requirements	486.5
For Different Operating Modes	474.7/480.7

7.2.3 Charging

The system must be compatible with the flight spacecraft's power supply and capable of being maintained fully charged by the battery chargers located on the flight spacecraft.

7.2.4 Power Control

The power control unit must perform appropriate power switching functions in response to proper signals not only from the flight spacecraft but also from the flight capsule's central computer and sequencer (CC&S) subsystem.

7.3 POWER SOURCE DESCRIPTION

7.3.1 Selected Approach

An hermetically sealed nickel-cadmium battery consisting of not more than 24 series-connected cells has been selected. The reasons for this selection are the same as those given in Section 6.0. Two batteries, each independently capable of meeting the requirements of the entire power profile will be used. The nominal discharge level per battery will not be less than 50 percent. Table XCII summarizes the battery characteristics.

TABLE XCII

NICKEL-CADMIUM BATTERY CHARACTERISTICS

Nominal Capacity (1-Hour Rate)	27 ampere-hours
Output Voltage Under Load	22 to 32 VDC
Rate Energy at +40°F	740 watt-hours
Maximum Open Circuit Voltage at 40°F	35 VDC
Minimum Charge Efficiency	70 percent
Continuous Trickle Charge Rate	150 ma to 250 ma
Maximum Weight	53 pounds
Maximum Volume	790 in^3 (0.46 ft^3)

7.3.2 Alternative Approaches

Because of the mission requirements for a short time of operation and a high rate of power output, nuclear energy and solar energy power sources are not applicable and their use offers no advantage either in weight or in other respects. They have not, therefore, received any further consideration.

A heat-sterilizable silver-zinc battery - if such exists - is a feasible alternative to the nickel-cadmium battery. The projected characteristics of such a battery appear in Table XCIII. These characteristics are based on probable use of a battery with an inorganic separator (References 21 and 22), as discussed in Appendix IV. A-15 of Reference 1.

The high (greater than 50 pounds) static weignt and the large volume of a hydrogen-oxygen fuel cell system even without the fuel and tanks, etc., eliminate this system from further consideration.

TABLE XCIII

SILVER-ZINC BATTERY CHARACTERISTICS*

Nominal Capacity (1-hour Rate)	27 ampere-hours
Output Voltage Under Load	25 to 37 vdc
Rated Energy at +40° F	800 watt-hours
Maximum Open Circuit Voltage	39 volts
Minimum Charge Efficiency	75 percent
Continuous Trickle Charge Rate	100 ma
Maximum Weight	27 pounds
Maximum Volume	330 in^3

* Characteristics listed are those of a projected heat sterilizable battery.

Another possible alternative is the lithium-chlorine (Li-Ci) fuel cell system. Such a system has been conceptually designed at Avco (Reference 29) Its projected characteristics are listed in Table XCIV. This is a very new system and although it is very promising, development work would have to begin immediately to make its use feasible on the 1971 mission.

TABLE XCIV

LITHIUM-CHLORINE FUEL CELL CHARACTERISTICS

Nominal Capacity (Single Cell Arrangement	270 ampere-hours
Nominal Voltage Under Load (Single Cell)	3.0 volts
Series Cell Arrangement Capacity	30 ampere-hours
Series Cell Nominal Load Voltage	27 vdc
Design Capacity (Series Cell)	50 ampere-hours
Estimated Maximum Weight (Series Cells)	10 pounds
Estimated Maximum Volume (Series Cells)	200 $in.^3$

7.3.3 Significant Tradeoffs

7.3.3.1 Weight and Volume

Certain tradeoffs can be made with regard to the nickel-cadmium and silver-zinc batteries in areas of weight and volume. A decrease in the number of cells in a battery generally results in a corresponding reduction in the weight and volume for a given number of watt-hours. The weight and volume savings continue until the number of cells is in the range from 10 to 14. The trend then reverses. However, the advantages gained by weight and volume savings are offset by the fact that the output voltage also goes down. This adversely affects the efficiency of the load voltage regulator particularly in the case of the buck-boost type regulator. It is thought that whatever gain is achieved by reducing the number of cells is at least counter-balanced by an accompanying loss in regulator efficiency.

This is particularly true with respect to large (greater than 20 ampere hours, A-H) capacity cells. In the preliminary design of the batteries this aspect would have to be investigated further to discover any possible advantages. Since there is no requirement for the battery to stand in a charged condition for a long time, the advantages that the silver-zinc battery can offer in this area do not apply and no allowance need be made for stand-time capacity losses. Even the effects of temporary high temperatures (200° F) are not likely to cause serious capacity loss. Results of recent tests (Reference 17) at Avco on heat-sterilized cells at a thermal soak temperature of +200° F showed that

they lost only a small percentage of their capacity. Figure 139 illustrates the results of such tests. The low loss is attributed to the fact that at the 1 to 2 hour rate (C/1.5) there is little time to build up to a debilitating power loss. Five-hour or six-hour rate discharges may produce different results. These findings remove another apparent advantage of the silver-zinc cells that generally operated better than the nickel-cadmium cell at high temperature but only at low current rates. The capacity losses or gains noted above affect the final design weight and volume of the battery and should be considered further.

7.3.3.2 System Complexity

The comments in Section 6.0 regarding the charge regulator required for the silver-zinc battery also apply here. Silver-zinc batteries are notoriously susceptible to damage when subjected to an overcharge or fast charge rates. Such conditions may very well exist following preseparation checkout. At that time approximately 130 watt-hours per battery have to be replaced in 2 to 3 hours. The effects of charging a liquid electrolyte cell rapidly in a zero-g field are apt to be both interesting and troublesome. For example, fast charging produces gas bubbles in silver zinc cells. In a 1-g field this does not cause any particular problem because the bubbles move away from the plates to the cell voids. In a zero-g field, however, the gas can just as easily stay near the plates, eventually covering the plate surface, and causing what is in effect, an open-cell condition.

The statements made in Section 6.0 regarding the complexity of Li-Cl fuel cells are not completely applicable in the case of the EFO mission. Because of the short operating time (less than 1.5 hours) a simplified concept, one without control valves and heaters, etc, can be used. The design approaches that of a battery. However, it is, essentially, a primary battery and it is difficult to see how its performance could be checked out effectively prior to use. It has the advantages of (1) requiring neither chargers nor power from the flight spacecraft and (2) the lowest nominal weight. The Li-Cl fuel cell should be considered further.

7.3.4 Principal Problem Areas and Development Status

The comments made in paragraph 6.3.4 in regard to the EFAT mission are equally applicable to the EFO mission.

7.4 POWER CONDITIONING EQUIPMENT

7.4.1 Selected Approach

The power control unit, as well as the charge regulators and load voltage regulators, are considered here under the general term "power conditioning equipment."

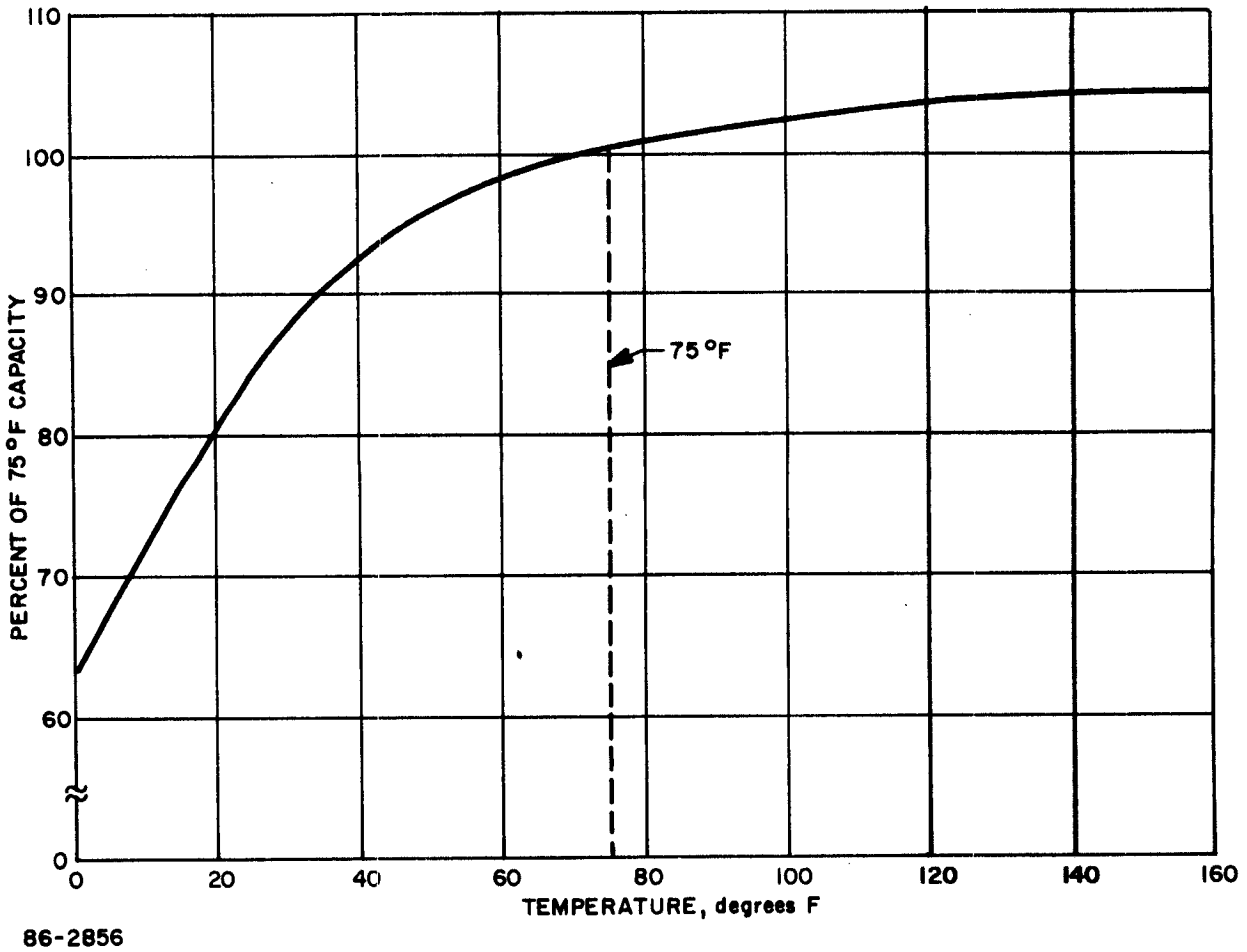

Figure 139 CAPACITY VERSUS TEMPERATURE FOR 3.5 AMP-HOUR NI-CAD CELLS

The selected equipment consists of two continuous-trickle charge regulators (with provisions for switching to a fast charge rate), a dual power control unit, and two load voltage regulators. Brief descriptions of these items follow.

7.4.1.1 Load Voltage Regulators

The load voltage regulators are, in general, of the buck-boost type described in paragraph 6.4. The principal differences are that the ones for the EFO mission are physically larger and can carry a greater load. The approximate electrical characteristics are summarized on Table XCV.

TABLE XCV

ELECTRICAL CHARACTERISTICS OF LOAD VOLTAGE REGULATOR

Rated Load	550 watts
Input	22 to 35 vdc
Output	28.0 vdc ±1 percent
Ripple	Less than 0.10 volts, peak-to-peak
Transients	Less than 0.7 volts for 7 amperes load change
Overload	100 percent (intermittent)

7.4.1.2 Charge Regulators

The charge regulator has two modes of operation: (1) a trickle, or float, charge mode, and (2) a fast charge mode. As described previously (paragraph 6.4), the reference voltage is provided by zener diodes. In the trickle charge mode the charging current is supplied to the battery through a resistor and blocking diode at a nominal 100-hour rate. A coulometer (Reference 28) such as that described in paragraph 6.4.2 may be used for the fast charge rate (Mode 2). It is not yet clear whether such a mode is required for the nickel-cadmium cell. Evaluation of large-sized nickel-cadmium cells at Avco should answer the question of whether or not fast charging is needed for such cells.

7.4.1.3 Power Control Unit

The power control unit consists of solid state switches, blocking diodes, fuses, and two mechanical switches. Its function is to switch all power to the appropriate users in response to signals from the CC&S. This arrangement relieves the CC&S of the need to switch high current levels. The two mechanical switches are used to connect the batteries or remaining subsystem to the flight spacecraft power supply or to the launch complex.

The solid-state switches are expected to be in the form of silicon controlled rectifiers (SCR's). Many alternative arrangements are possible. Some of these are discussed in Appendix D. The switches are turned on and off by a relatively low power pulse from the CC&S.

The possibility of spurious triggering of a given switch as a result of radio frequency interference (RFI) is also dealt with in Appendix D. It is found that adequate methods exist both to prevent the gate (trigger circuit) from being fired by applied RFI and also to suppress and shield any generated RFI. A block diagram of the power control subsystem is shown in Figure 140.

7.4.2 Alternative Approaches

7.4.2.1 Nickel-Cadmium Battery Charge Regulator

The alternatives to use of a trickle charge regulator are those described in paragraph 6.4.2.1. Except for the coulometer cells that has been incorporated in the selected charge regulator, only the possibility of using the timed charging sequence remains to be considered. After a brief study the latter approach has been rejected as being too complex in its implementation.

7.4.2.2. Silver-Zinc Battery Charge Regulator

The statements and description in paragraph 6.4.2.2. also apply in the case of the EFO mission.

7.4.2.3 Pulse Width Modulated (PWM) Load Voltage Regulator

In addition to the comments and description provided in paragraph 6.4.2.3 relative to the EFAT mission, the following considerations are applicable to the EFO mission. Extra emphasis is placed on the fact that a DC to DC converter would probably be required if the PWM load Voltage Regulator were used. If such a converter is not used, battery design flexibility would be lost because it would then be necessary to keep the battery

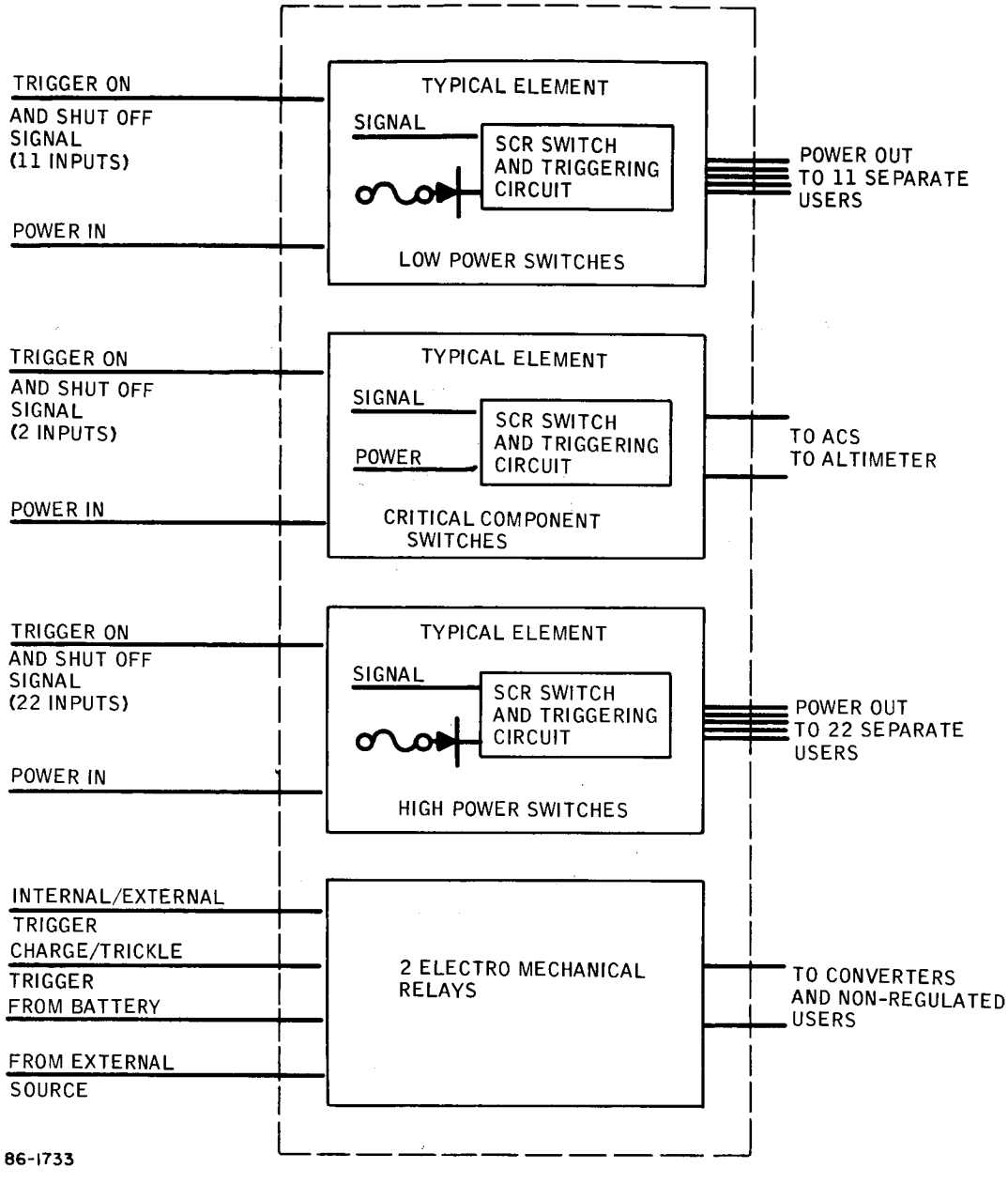

Figure 140 POWER CONTROL SUBSYSTEM

voltage above 28 vdc at all times. Addition of a DC to DC converter would, of course, decrease efficiency and increase battery weight. Although this aspect of the situation has not been studied in detail, it appears evident that use of a PWM load voltage regulator is not the approach to be followed.

7.4.3 Significant Tradeoffs

The most important tradeoff is that in which it was decided to use a buck-boost voltage regulator that allows virtually all of the battery capacity to be used. This more than offsets any weight disadvantage resulting from use of additional components.

Other tradeoffs similar to those noted in paragraph 6.4.3 can be made. By using solid state switches for the power control unit, both reliability and weight advantages are gained, although at the expense of creating a possible RFI problem.

In the area of fast battery charging, the tradeoff is that of the uncertainties of the coulometer method versus the possibility of too much gas generation at zero-g. The decision in this mater should be delayed until additional studies and, possibly, zero-g experiments, are conducted.

7.4.4 Principal Problem Areas and Development Status

The principal problem area is that of heat sterilization. It has not yet been demonstrated that the components are heat sterilizable. Development work is needed in the area of the method to be used for fast charging the battery. High impact resistance is not a problem here.

7.5 SUMMARY OF PHYSICAL CHARACTERISTICS

Table XCVI summarizes the physical characteristics of the flight capsule's electrical power subsystem.

TABLE XCVI

FLIGHT CAPSULE ELECTRIC SUBSYSTEM PHYSICAL CHARACTERISTICS

Item	Weight (pounds)	Volume (ft^3)	*Maximum Heat Dissipation (watts)
Battery	53 (2)	0.46 (2)	50
Load Voltage Regulator	12 (2)	0.17 (2)	50
Power Control	8.6	0.12	50
Totals	139	1.38	150

*Estimated as 3 to 5 times average dissipation for battery and power control.

8.0 RADAR SYSTEMS

8.1 GENERAL

Knowledge of the flight-capsule altitude is required for proper conduct of the experimental mission during entry and descent to the Martian surface. For instance, definition of the vertical structure of the atmosphere involves the generation of density-altitude profiles. In addition, a number of critical events such as parachute deployment and penetrometer jettison are best performed when capsule altitude is known. Determination of the size of the surface features observed in television pictures is aided through knowledge of the altitude at which they were taken. These factors and others discussed later, make it highly desirable to incorporate a radar-altitude measuring system (generally referred to simply as a radar system) into the flight-capsule payload.

The discussion of radar systems that follow is organized differently from the parallel format (entry from approach trajectory, EFAT, and entry from orbit, EFO) used in describing the telecommunication system. The discussion here is centered primarily on the radar system designed for use during the entry from orbit mission. The description of this radar system is generally applicable to the system used for entry from the approach trajectory. The EFO system includes all of the subsystems used in the EFAT system, and also incorporates several features not required in the EFAT mission. Significant design differences between the two systems are identified to assist understanding of the two systems.

The approach taken in this study was based on designing a radar system capable of satisfying the altitude measurement requirements of the present flight-capsule concept, which also has the growth potential necessary for satisfying the requirements of future landers. Accordingly, an integrated radar system consisting of three basic subsystem elements was defined. The three subsystems include a high-altitude altimeter, a low-altitude altimeter, and a three-beam velocity/attitude (V/A) radar system. The three-beam system measures range and range-rate along each of the three beams. The primary purposes of the integrated radar system are to provide flight capsule altitude information during the entry and descent phase of the mission and to measure the planetary wind velocity. The altitude information is used to initiate penetrometer deployment, to initiate changes in the data storage mode, to correlate science data with altitude, and to furnish backup means of initiating several events, such as heat-shield separation and parachute deployment. The secondary purpose of the radar system is to provide a back-up means for determining the flight-capsule attitude, and to measure the roughness of the surface of the planet. Surface-roughness data and wind-velocity data are desirable for the design of later lander vehicles.

8.2 FUNCTIONAL REQUIREMENTS AND CONSTRAINTS

8.2.1 Entry Trajectory and Vehicle Attitude Considerations

Before proceeding with the detailed discussion of the several measurements to be made by the radar system and the alternative schemes by which they may be implemented, it is appropriate to review the mission sequence appropriate for entry from orbit (EFO). The reference radar-system design is based on this mission concept.

The sequence of significant events prior to and during entry is as follows:

8.2.1.1 The flight capsule and flight spacecraft will be injected into an elliptical orbit from the transfer trajectory, and will remain in that orbit for sufficient time to permit accurate determination of orbit parameters and possibly to survey the flight capsule impact site. When these measurements are complete (which may take several days,) the flight capsule will be separated from the flight spacecraft and oriented for the proper entry angle under control of an active ACS. The de-orbit retro-thrust maneuver will then be performed.

8.2.1.2 A typical trajectory for the flight capsule as it is entering the Martian atmosphere is shown in Figure 141. The NASA model VM-3 atmosphere was used as an example in this figure in determining the time and altitude of occurrence of significant events. By definition, mission time, $t = 0$ starts when the descending flight capsule reaches an altitude of 800,000 feet. At this altitude, no significant aerodynamic forces are yet acting on the vehicle. The angle of attack will be adjusted to zero before this time so that the effects of entry heating will be minimized.

8.2.1.3 At an altitude of approximately 170,000 feet, a deceleration of 0.1 g is experienced. At this altitude plasma-induced blackout of radio-frequency communication is also likely to occur.

8.2.1.4 Deceleration increases during the next 42 seconds. The peak deceleration value is slightly over 13 g, as indicated on a typical g-time history curve shown in Figure 142. The radio frequency blackout ends when the velocity of the flight capsule had decreased to approximately 10,000 ft/sec. For the assumed trajectory, this corresponds to an altitude of 75,000 feet.

8.2.1.5 At the end of the communication blackout, sensed either from VSWR or deceleration measurements, the high-altitude altimeter subsystem will provide both altitude reference data for scientific measurements, and initiating signals for several specific events.

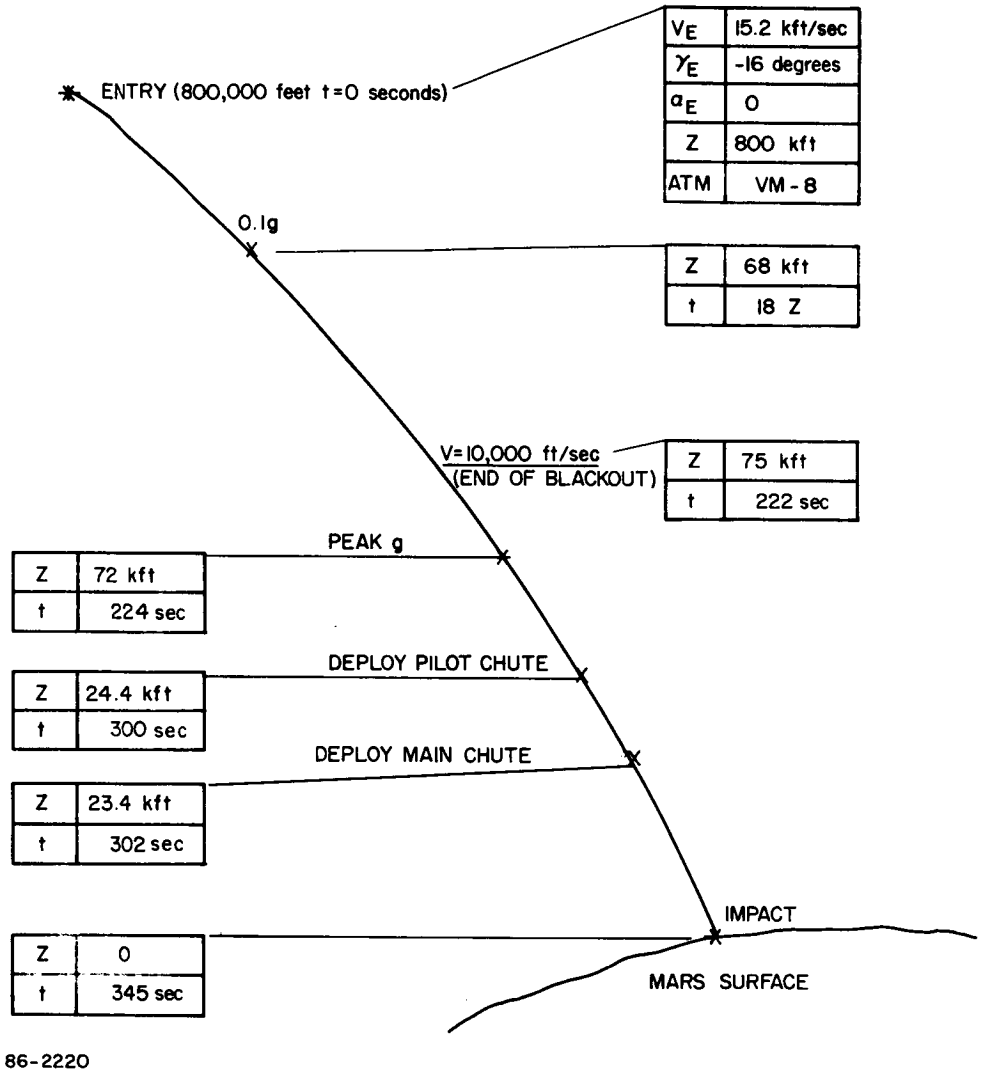

Figure 141 TRAJECTORY DATA SUMMARY

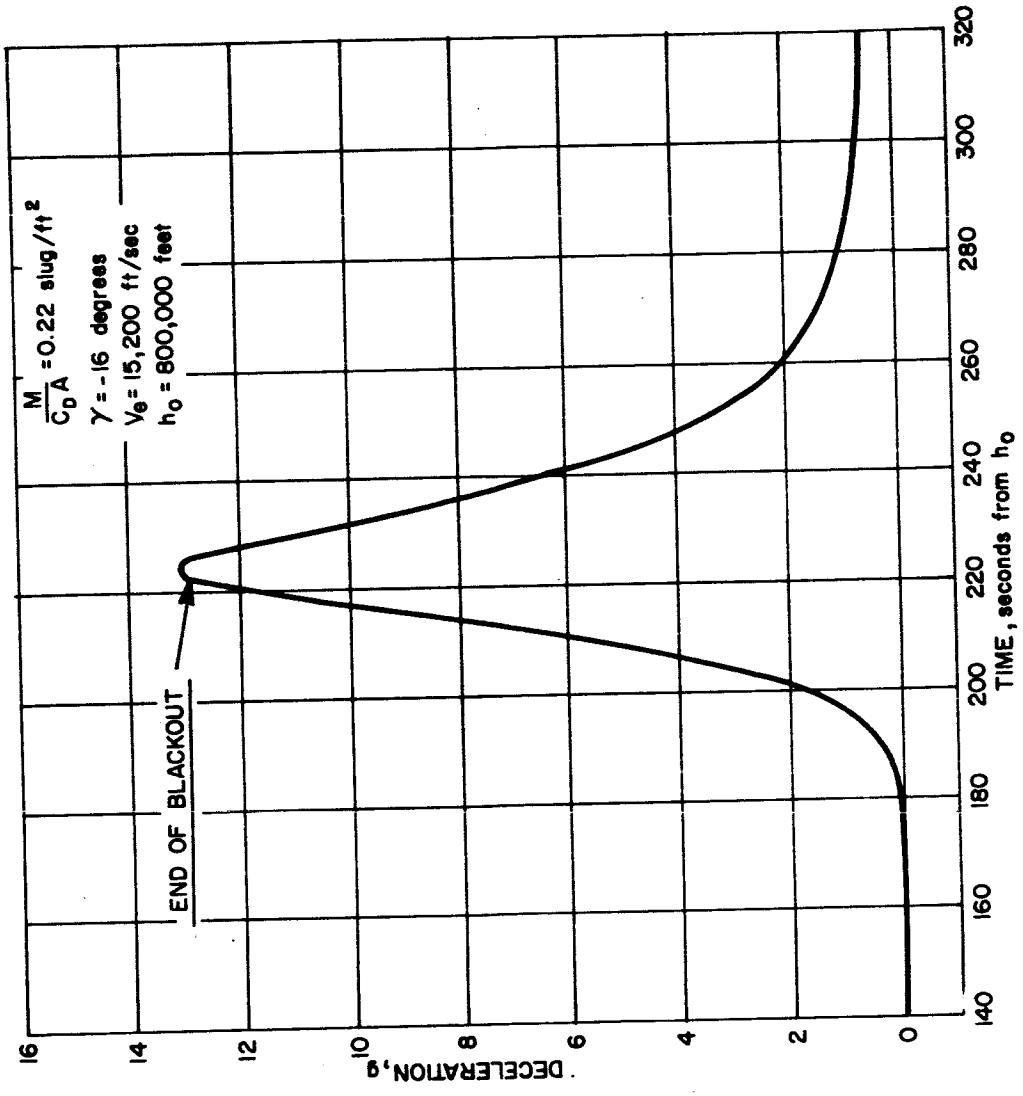

Figure 142 DECELERATION VERSUS TIME FOR VM-8 ATMOSPHERE

8.2.1.6 Since as long a descent time as possible is desirable from the viewpoint of the scientific mission, a pilot-parachute main-parachute scheme will be utilized. The pilot parachute will be deployed at a Mach number of approximately 1.2. The high altitude altimeter offers a possible means for determining when this velocity is reached. At some lower velocity, near Mach 0.85, the main parachute is fully deployed. The radar system could also provide backup means for initiating this event. It would supplement the primary mechanism -- a 2-second timed delay after pilot-parachute deployment. Because descent may take place above very high altitude local terrain, it is probable that some minimum altitude, for example 20,000 feet, would be used as an altitude criterion for main-parachute deployment.

8.2.1.7 Terrain roughness measurements will be made at several altitudes during descent, such as: at very high altitudes after radio-frequency blackout, at the approximate altitude of parachute deployment, and at the approximate altitude of penetrometer deployment. Since these measurements can best be made by spectral analysis of the scattered signal, use of a coherent system is desirable.

8.2.1.8 The penetrometer sequence will be initiated at an altitude of 3500 feet in response to a signal from the low altitude altimeter. The flight capsule's parachute-aided descent is not likely to follow a vertical path, since relatively high winds have been postulated for Mars. Wind gusts will cause parachute and suspended capsule motions that must be accurately determined so that television camera operation may be inhibited whenever the angle between the camera optic axis and the planet local vertical exceeds a predetermined value. The ability to compute the descent attitude will also be applicable to the next generation landers, which will require vertical descent as a preliminary to a soft touchdown. The motions caused by the wind will make it difficult to obtain accurate altitude information and to measure surface roughness and wind.

8.2.2 Altitude Measurement

The prime requirement of the radar altitude measuring subsystem is to continuously measure altitude from the end of radar blackout (approximately 250,000 feet)* to approximately 1000 feet. The altitude information will be used on board the flight capsule to initiate certain events and will also be relayed to Earth via the flight spacecraft to aid post-mission analyses. A 5 percent accuracy is required for altitude measurement.

* 250,000 feet corresponds to the highest altitude that 10,000 ft/sec is reached for any combination of entry angle, entry velocity, and atmosphere considered.

8.2.3 Wind-Velocity Measurement

8.2.3.1 Entry from Approach Trajectory

Study results indicate (see paragraph 8.5.1) that an accurate and reliable means of measuring wind velocity is with a three-beam radar. Such a radar, designed for this mission, would weigh approximately 30 pounds. The weight limitations in the EFAT approach are so critical that inclusion of such a radar would severely penalize the design. A low-weight, high-accuracy anemometer will be used to determine wind velocities after impact. Its operation, however, is contingent upon survival of impact of the flight capsule. In the event the flight capsule does not survive impact, a gross estimate (± 50 percent) of wind velocity is required prior to impact. As explained in paragraph 8.5.2, this measurement can be obtained from the low altitude altimeter.

8.2.3.2 Entry from Orbit

One mission requirement is that the wind-velocity profile be determined for the period starting with parachute opening and ending when the flight capsule reaches as low an altitude as is consistent with the time necessary to relay data to the flight spacecraft before impact. This period corresponds to an approximate altitude range from 25,000 to 100 feet. The winds postulated for Mars are a maximum of 350 ft/sec with a maximum gust component of 200 ft/sec. It is desirable that the wind measurement be accurate within from 10 to 20 percent.

8.2.4 Surface Roughness

Surface roughness must be determined quantitatively, not only because of its general scientific value but also because of its engineering significance in the design of soft landers. Surface roughness, as the term is used here, refers to the average bump height and the average distance between bumps. These dimensions should either be much smaller or much larger than the characteristic dimension of the lander to prevent it from tipping when it lands. Roughness data can be obtained from the television pictures. Additional, and possibly more precise information regarding roughness can be provided by radar by analysis of the spectrum of the return signal at different frequencies. This technique is described in paragraph 8.6.

8.3 HIGH-ALTITUDE RADIO FREQUENCY LINK ANALYSIS

8.3.1 Range, Beamwidth, and Accuracy Requirements

It is desirable to measure altitude from the highest altitude at which blackout ends to the lowest altitude at which the heat shield is jettisoned. Analysis of blackout conditions indicates that the highest altitude at which emergence from blackout occurs is 250,000 feet. The lowest operating altitude for the high-altitude altimeter is the minimum altitude for heat-shield jettisoning, approximately 20,000 feet.

The beamwidth requirement is established by the variation in look angle between the flight capsule roll axis and the local (Martian) vertical for the altitudes of interest. At entry, this angle is 90 degrees minus the entry angle. The latter may be as small as 12 degrees. After exposure to the aerodynamic forces of entry, the flight capsule roll axis can be assumed to be oriented close to the local vertical. As Figure 143 shows, the variation over the altitude range of interest can be as much as 78 degrees. However, because of the circular symmetry of the flight capsule, any side could be facing the planet. Therefore, a total beamwidth of 156 degrees is required.

The accuracy requirement for altitude measurement during the preparachute phase of entry is 5 percent. This figure is based on providing altitude measurements whose accuracy is consistent with that provided by the other scientific instrumentation.

8.3.2 Frequency Selection

The choice of the operating frequency for the high-altitude altimeter can be established by reference to the transmitter power versus frequency characteristics shown in Figure 144. The relationship shown there is derived from computations based on both the estimated performance characteristics of a practical receiver-antenna system and the actual dynamics of the environment in which the altimeter must operate. The general shape of the curve, however, can be established by heuristic reasoning as follows. There are five principle frequency-dependent factors in the radar range equation. These are: space loss, Doppler bandwidth, galactic noise temperature, antenna efficiency, and power generating efficiency. Noise figure frequency dependence is neglected here because the receiver is always looking at the ground. It is reasonable to assume that the ground contribution to system noise temperature will exceed that of the imperfect receiver. At very low frequencies, the power-frequency relationship is influenced by the space loss (f^2)*, Doppler shift (f), galactic noise (f^{-2}), and antenna efficiency (f^{-2}). The net power dependence is, therefore,

* The exponent in parenthesis represents the degree to which the transmitter power requirement varies with frequency.

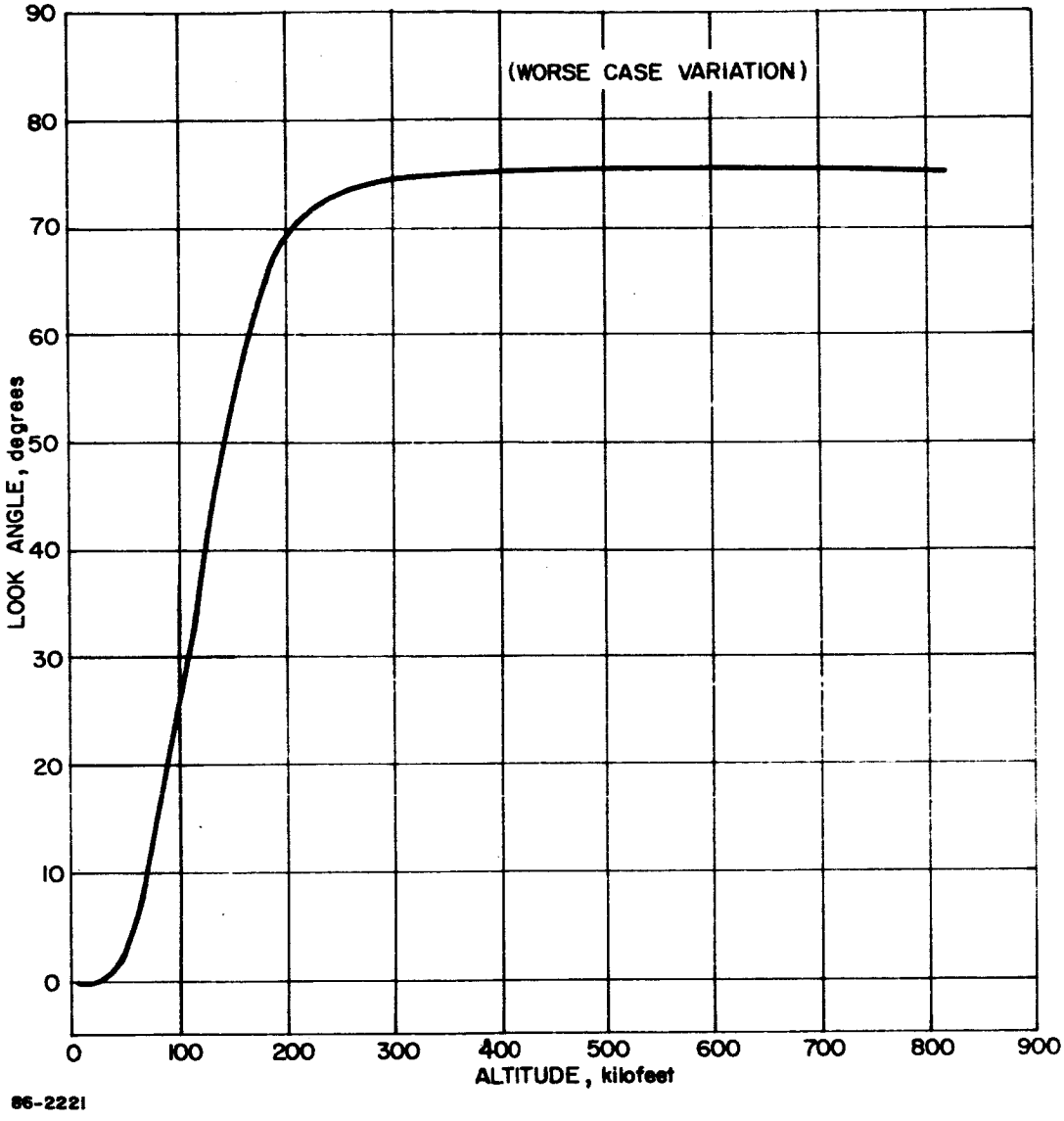

Figure 143 ALTIMETER LOOK ANGLE VERSUS ALTITUDE

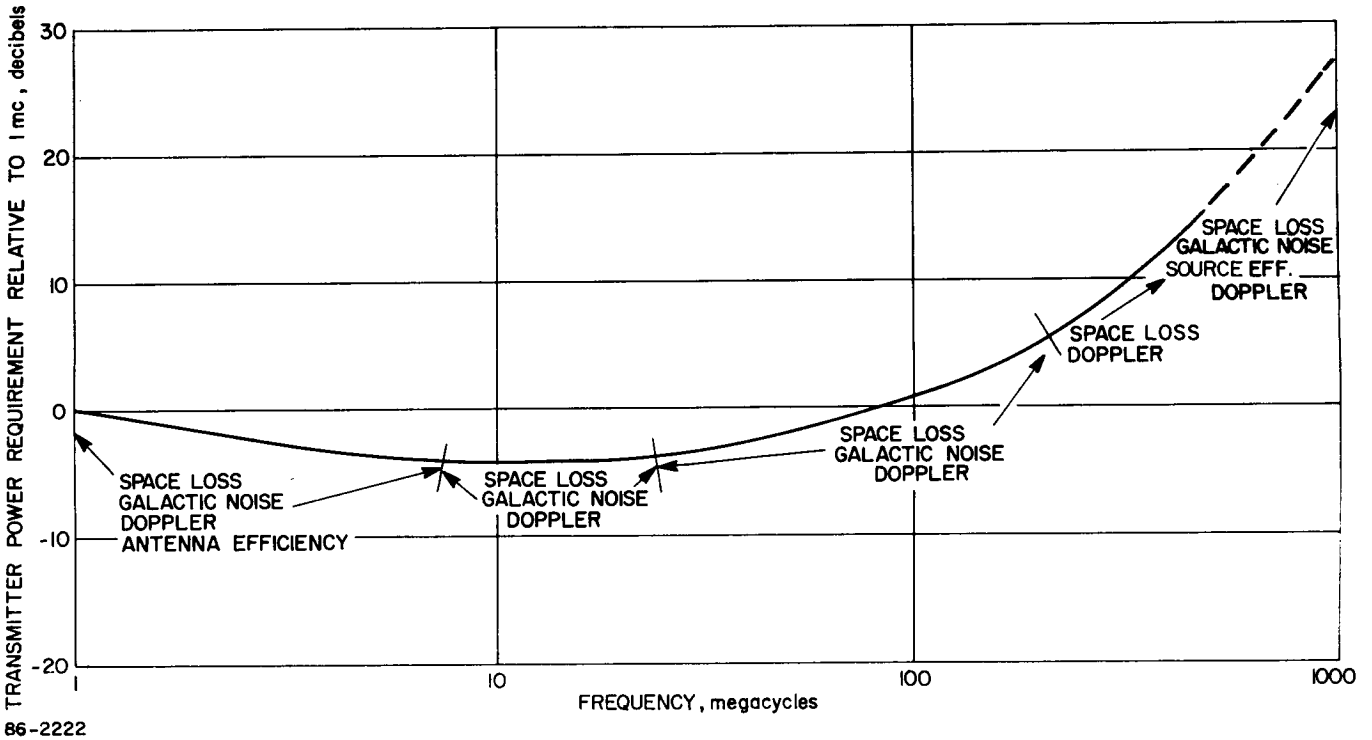

Figure 144 TRANSMITTER POWER REQUIREMENT VERSUS FREQUENCY

inversely proportional to frequency. At frequencies between 18 MHz and 200 MHz, approximately, the dependence changes because the antenna efficiency may be considered constant, * hence the net power-frequency ratio will be essentially linear. For frequencies slightly higher than 200 MHz, the galactic noise temperature is less than 300°K and makes a negligible contribution; hence, the power-frequency relationship is cubic. At frequencies above about 300 MHz, the efficiency of the power generating device begins to have a marked influence on the power requirements. Its efficiency decreases with increasing frequency. As a result, the net power-frequency relationship for frequencies above 300 MHz is such that power is proportional to more than the cube of frequency.

From the curve shown in Figure 144, it can be seen that the transmitter power requirement is at a minimum in the vicinity of 18 MHz.

Justifications for the findings regarding the manner in which these several frequency-dependent terms vary and affect transmitter power are given in the following paragraphs.

8.3.2.1 Space Loss

The antenna beamwidth is determined by the entry geometry described in paragraph 8.3.1. Therefore, its gain is frequency invariant and the effective capture area is inversely proportional to the square of the frequency. Since transmitter power is inversely related to the antenna capture area, power varies with the square of the frequency.

8.3.2.2 Galactic Noise

As seen in Figure 145, the sky brightness temperature varies as the inverse square of the frequency; hence, transmitter power due to this factor is inversely related to the square of the frequency.

8.3.2.3 Doppler Bandwidth

The receiver and the signal processing circuits must be designed to accommodate the maximum possible Doppler shift. This requirement defines the minimum predetection noise bandwidth, which is proportional to the first power of the carrier frequency. The predetection noise bandwidth is a critical parameter because the signal-to-noise ratio within it must be larger than unity. If the signal-to-noise ratio (SNR) is smaller than unity, the output signal-to-noise ratio will be the square of the input signal-to-noise ratio. It is not practical to design a system that will operate under that condition.

* In the range from 18 MHz to approximately 200 MHz, the physical antenna size, therefore, represents about one-half a wavelength. The gain will, therefore, be nearly constant.

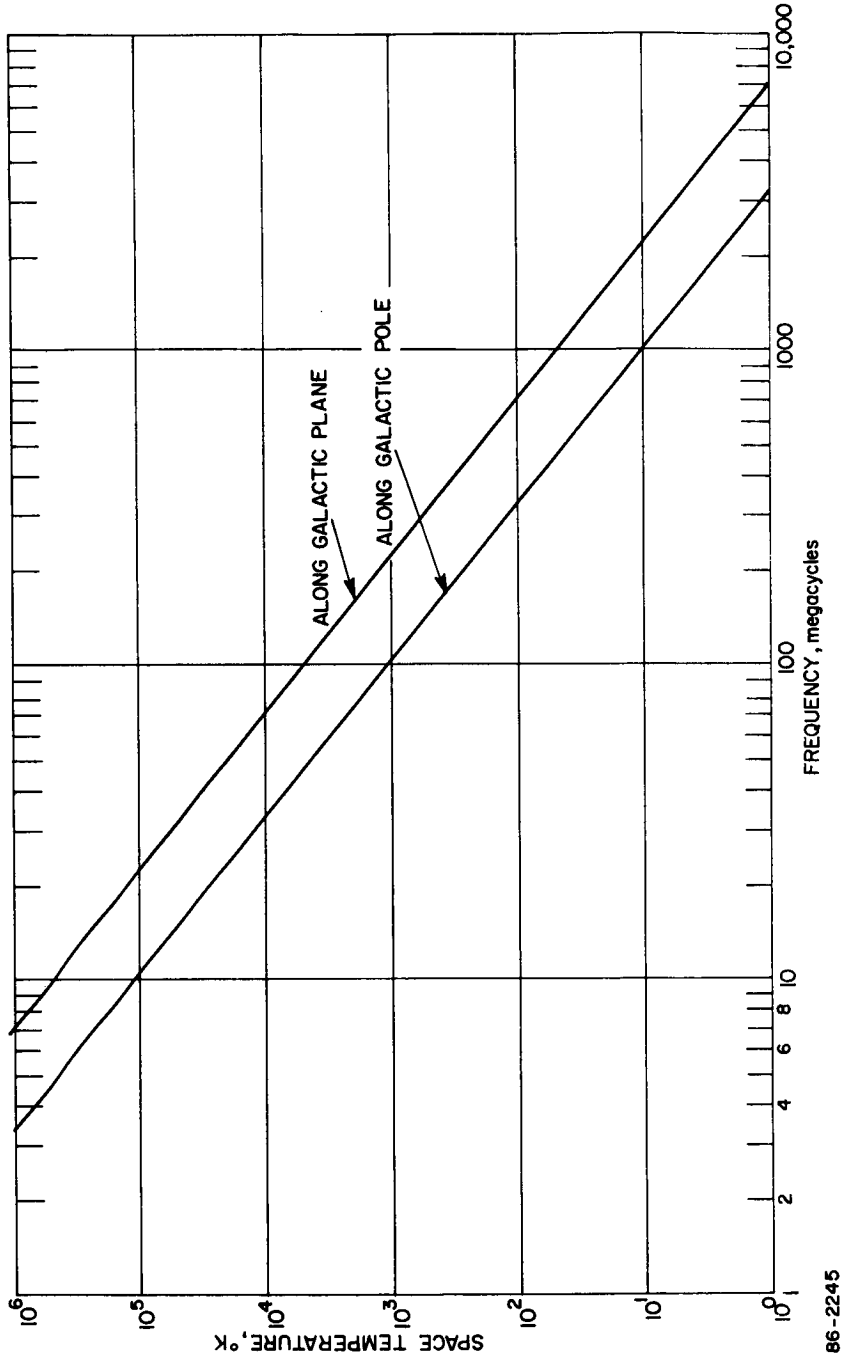

Figure 145 SKY TEMPERATURE VERSUS FREQUENCY

8.3.2.4 Antenna Efficiency

Items 1, 2, and 3, above indicate that the dependence of the transmitted output power on frequency is linear. If the selection of the frequency were based on those considerations alone, the lowest frequency available would be selected. However, the longest usable wavelength (and lowest usable frequency) is limited by the vehicle dimensions. The efficiency of a small radiating element is approximately proportional to the carrier frequency. Since an undersized antenna (one whose physical size is less than one-half a wavelength) must be complemented by a tuning element, the overall antenna efficiency drops sharply when the physical antenna size is much smaller than half of a wavelength. At frequencies less than the vehicle resonant frequency, * therefore, the transmitter power requirements depend on frequency approximately according to an inverse square law.

8.3.2.5 Power Generator Efficiency

In practice, the generating efficiency of radio power sources decreases with increasing frequency. As a consequence, the power demand of the altimeter rises somewhat at high frequencies.

8.3.2.6 Surface Roughness Measurement

Surface roughness information obtained from spectral analysis of the radar echo is determined in terms of the exciting wavelength. The most practical wavelength for this measurement is that which corresponds to the characteristic dimension of a landing vehicle. Therefore, an operating wavelength of the same order as the size of the vehicle is indicated.

8.3.2.7 Flight Capsule Shell as an Antenna

The frequency-power relationships discussed above suggest that the operating frequency be reduced until antenna efficiency becomes a significant limiting factor. It appears prudent, therefore, to consider using the entry shell itself as an antenna, thus minimizing transmitter power requirements. Fortunately, the support ring assembly of the entry shell can be excited to provide the desired radiation pattern. As shown on Figure 144, the minimum transmitter power requirement occurs at approximately 18 MHz. This corresponds to a wavelength of 70 feet, and coincidently, to the circumference of the entry-shell support ring.

* The vehicle resonant frequency refers to the conditions where the vehicle structure is excited as an antenna. The lowest vehicle resonant frequency is associated with the largest dimension and the method of excitation.

The flight-capsule shell can be considered as an antenna as follows. If the two continuous elements of the triple folded dipole shown in b. on Figure 146 are bent out, the circular configuration shown at c. on that figure results. Furthermore, the radiation from the middle element can be suppressed by screening. This evolution process indicates both the mode of excitation and the resonant wavelength, which is apparently equal to the circumference. Thus, for a 15-foot diameter flight-capsule entry shell, the resonant frequency required to provide the desired coverage is 18 MHz.

8.3.3 Modulation Selection

A high duty-cycle waveform should be used so that peak transmitter power is minimized and antenna breakdown problems are avoided. Such considerations as efficiency, power conservation, and reliability, led to adoption of an all solid state design. Two basic types of modulation suggest themselves for this design: frequency-modulated continuous wave (FM-CW) and long pulse amplitude modulation (AM); the latter is generally referred to as interrupted continuous wave (ICW).

The two principle factors to be considered in choosing between FM-CW and long pulse AM are: (1) isolation of the transmitted pulse from the receiver. and (2) the relative ease with which the desired information can be extracted from the demodulated signal. A discussion of each of these factors follows.

8.3.3.1 Isolation

The ability to measure altitude at 250, 000 feet under worst case assumptions of circuit losses, surface reflection coefficient, ionospheric shielding, and Doppler bandwidth, requires a system that uses a substantial amount of transmitter power. Any degradation in receiver performance would jeopardize altitude measurements. Unfortunately, receiver degradation will occur, due to the inevitable direct leakage of transmitter power into the receiver channel in an FM/CW system. In fact, at the transmitter power level necessary, the leakage will be of sufficient strength as to tend to overdrive the receiver with a resultant reduction in gain and an increase in the noise level.

The problem of providing adequate receiver-transmitter isolation is completely avoided in the long pulse AM system through time gating, i.e., the receiver is off when the transmitter is on.

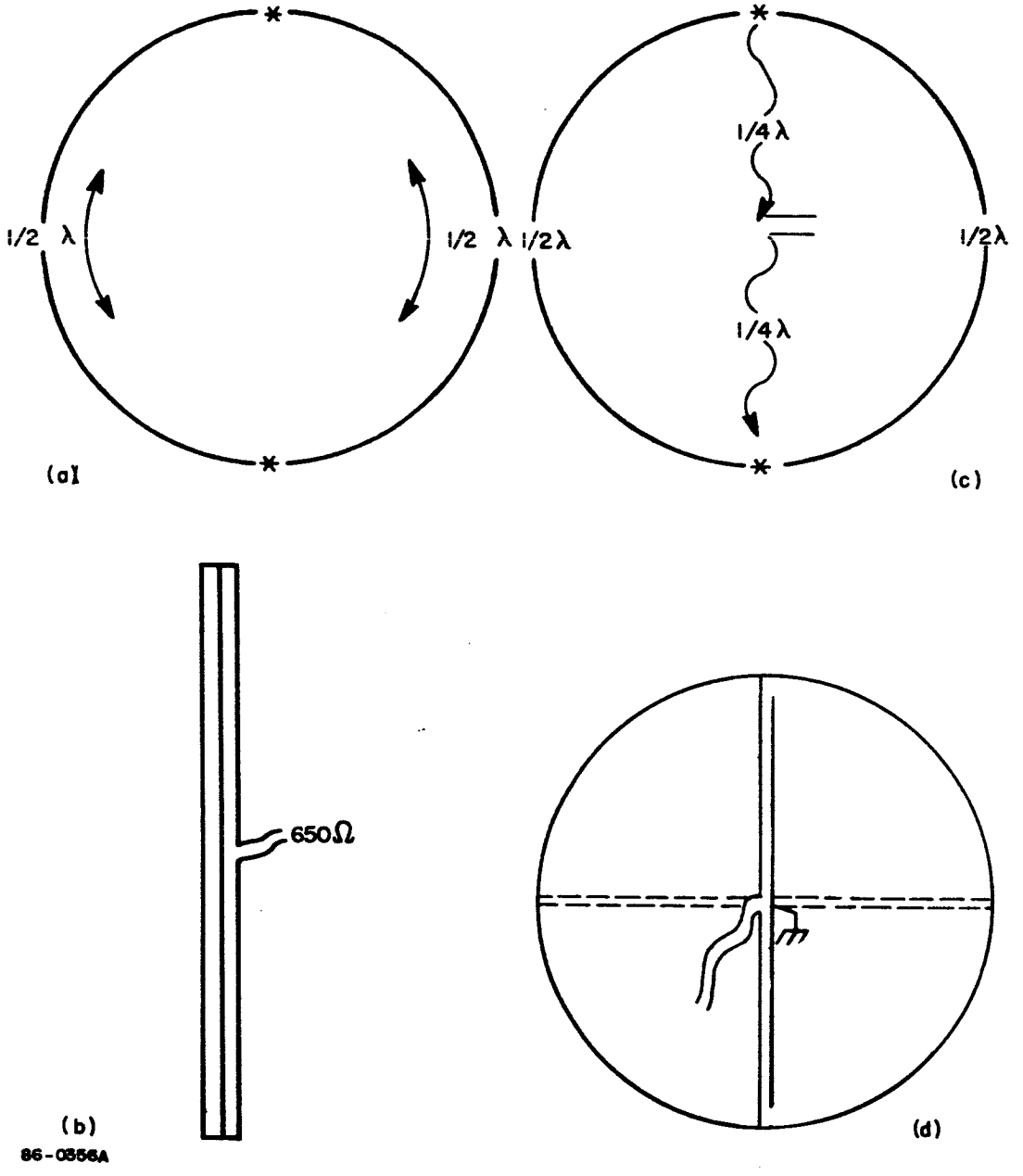

Figure 146 EVOLUTION OF RING ANTENNA

8.3.3.2 Information Recovery

The flight capsule horizontal velocity and descent velocity as well as the roughness of the Martian terrain are determined by spectral analysis of the altimeter echo. The Doppler spectrum is very easily recovered from long pulse amplitude modulation, since range-gating effects occur only at the echo transients. In the FM-CW system, however, the returns from surface areas at different ranges fall into different frequency bands, thereby making it difficult to separate range from range-rate effects. The high resolution properties of the FM-CW waveform are achieved by using large frequency deviations. These properties are necessary to avoid a large quantization error in the altitude reading. The performance features of the several modulation schemes considered for use in the high altitude altimeter are summarized in Table XCVII.

8.3.4 Transmitter Power Selection

Having determined the frequency of operation, the modulation technique, the antenna beamwidth, and the maximum altitude of operation, the transmitter power requirement may be computed. Before performing this computation, several factors influencing receiver sensitivity and signal-to-noise ratio will be discussed.

8.3.4.1 Noise

Consider the generic range tracker shown in Figure 147. The tracker shown is an optimum device, as discussed in Appendix V.3.E. If the feedback loop is opened so that the delay, τ, can be controlled by an experimenter, the cross correlation function

$$g(\tau) = \int y(t)\, x'(t-\tau)\, dt \qquad (1)$$

may be found empirically.

In this formula, $x(t)$ is the modulating waveform, $y(t)$ is the detected echo envelope perturbed by noise such that:

$$g(t) = x(t-\hat{\tau}) + n(t) \quad .$$

The integration period is one modulation cycle. Assume that $g(t)$ is represented by the solid curve in Figure 148. The width of the sensitive portion is termed the discriminator width. The limit levels $+s$

TABLE XCVII

COMPARISON OF MODULATION FOR HIGH ALTITUDE ALTIMETER

MODULATION	Antenna Breakdown	Isolation	Accuracy At Maximum Altitude	Accuracy At Minimum Altitude	Ancillary Functions (Wind and Descent Velocity; Surface Roughness)	Components Aspects	Growth Potential	Major Problems
Short Pulse	Likely	Good	Good	Good	Suitable	Requires Tube	Limited	Antenna Breakdown Optimum performance would require variable PRF and variable pulsewidth
FM-CW	No Problem	Intermediate	Will Require Relative High Power	Good	Poorly Suited	All Solid State	Excellent For Extremely Low Altitude	Quantization error; Difficult to derive Roughness and Wind Information
Long Pulse	No Problem	Good	Good	Good	Suitable	All Solid State All data processing by Switching Circuitry: can be microminiaturized	Promising for higher altitude. Low Altitude limit down to 150 feet seems feasible	Operation at extremely low altitude.

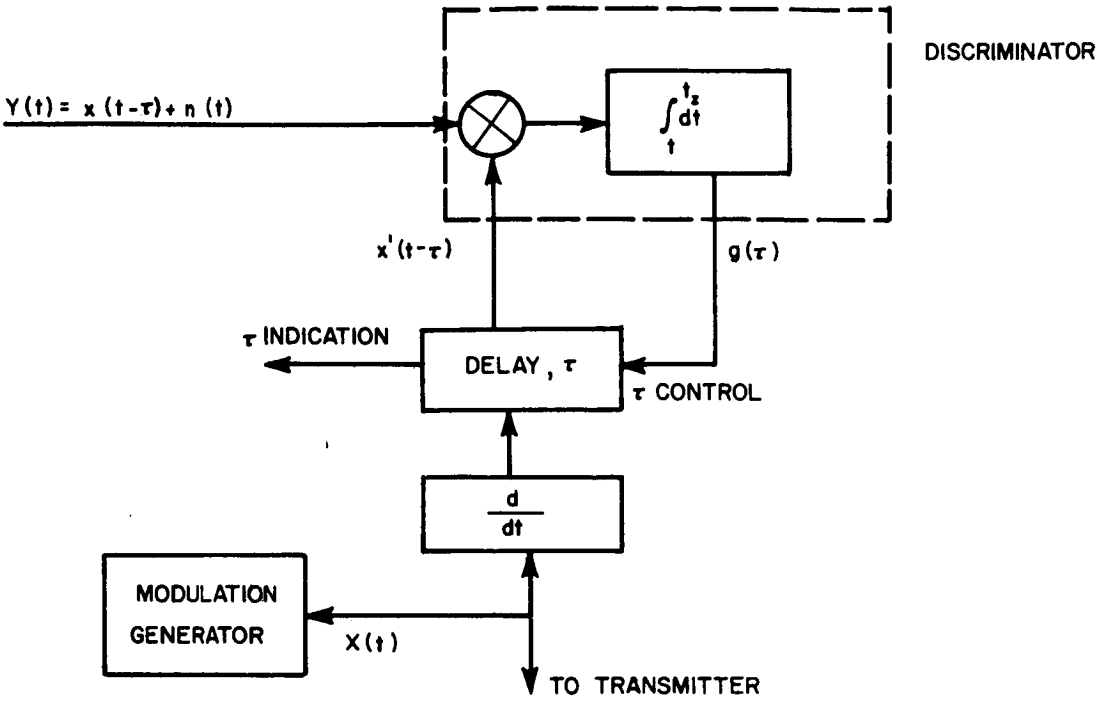

Figure 147 GENERIC RANGE TRACKER

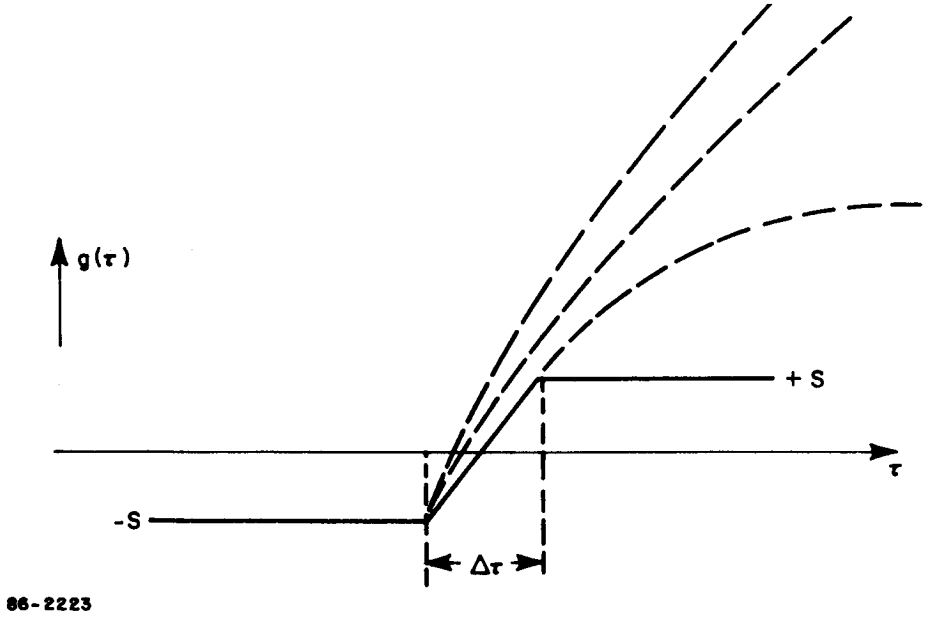

Figure 148 DISCRIMINATOR CHARACTERISTIC

and $-s$ are dependent on the signal level. When r is adjusted so that $g(r) = 0$, the discriminator output will still exhibit fluctuations in the root mean square value, due to noise, n. Conversely, if the tracker loop is closed, the tracker's interpretation of r will fluctuate by an amount:

$$\epsilon \approx \Delta T \frac{n}{s} = \frac{\Delta T}{(\text{signal to noise power ratio})^{1/2}}$$

provided $n < s$. If the latter condition is not fulfilled, the error for the curve shown will become indeterminate. Practical discriminator curves often taper off outside the sensitive region. As a result, the tracker will lose lock whenever the loop signal to noise ratio (SNR)is below unity (SNR < 1). If the signal to noise ratio is greater than unity (SNR > 1), the tracker's fluctuations will be confined to an interval corresponding to the discriminator width. For reasons described below, the discriminator width is chosen to be 2 percent of the altitude, and the worst case required signal to noise ratio is 10 db. The worst-case fluctuations in the altitude reading will be ± 0.3 percent. This error is much smaller than the uncertainty in the definition of what the radar target is.

Over rough terrain, the first return resolving capability of the altimeter (see paragraph 8.3.4.2 below) becomes the limiting factor on accuracy. In the proposed design, the discriminator curve is somewhat different from the solid curve shown in Figure 148 for the generic tracker. The sensitive region is estrapolated to the right, as one of the broken lines in the figure. This does not change the above considerations. However, the portion to the left of the sensitive region is a fixed bias level, externally inserted. This necessitates a modification of the noise consideration to include a false alarm rate criterion. This is discussed quantitatively in paragraph 8.7 where details of the proposed design are covered.

8.3.4.2 First Return Resolution

As shown in Appendix F, the optimum procedure for locating a rectangular pulse in time is to cross-correlate the receiver output with both a positive and a negative sampling rate. The maximum likelihood criterion is satisfied by so timing the sampling rates that the sum of the samples equals zero; in other words, perform combined leading and trailing edge tracking. In the case of a diffuse echo, the echo envelope will be smudged as illustrated in Figure 149. If the leading edge sample is weighted more heavily than the trailing edge, as illustrated in that figure, the sum of the samples will be zero earlier in time than if both pulses were equally weighted. By weighting the

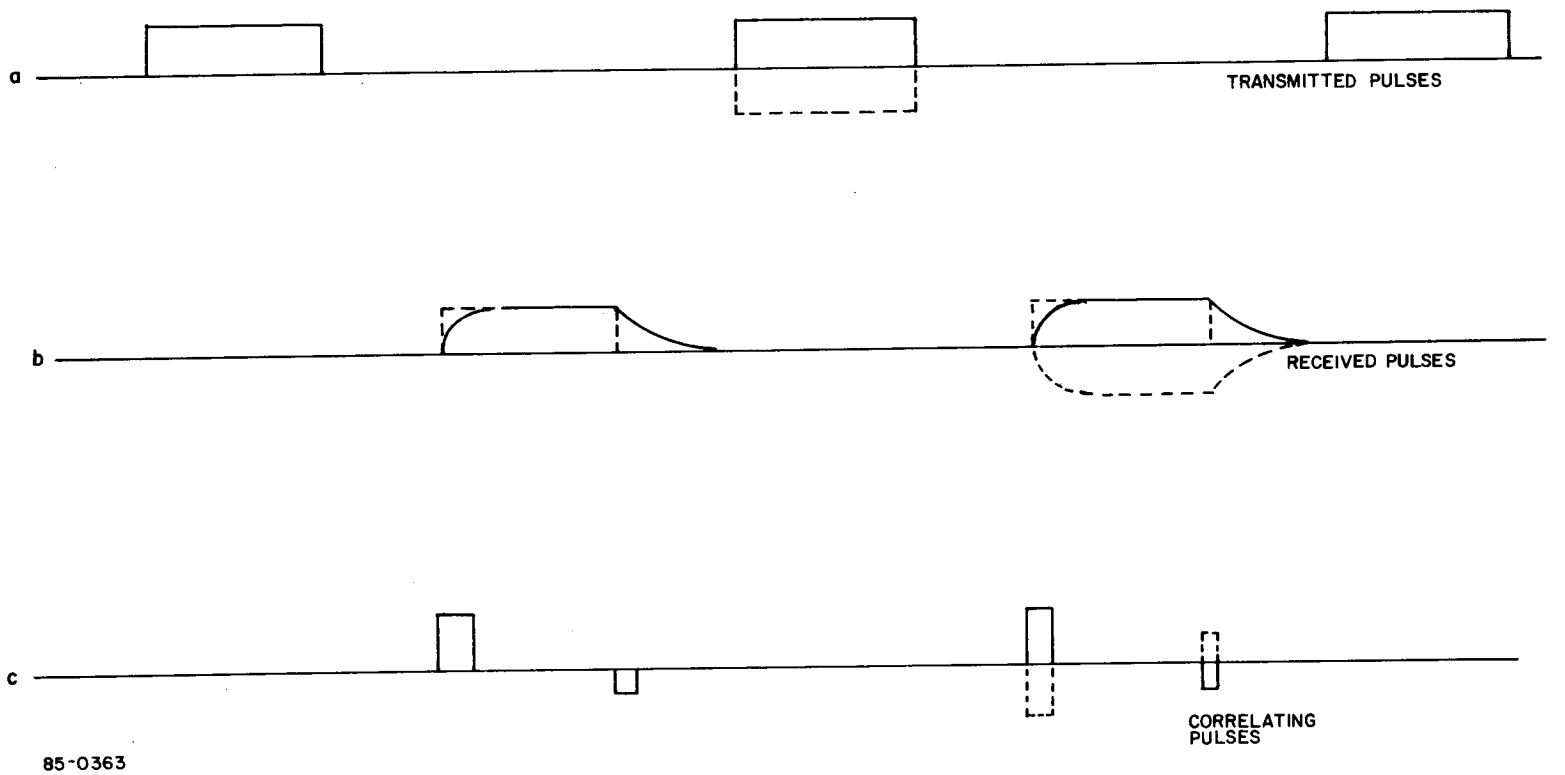

Figure 149 LONG PULSE ICW RADAR ALTIMETER WAVEFORM

leading edge, the averaging error is reduced since this approach discriminates in favor of the first return. Resolution can be limited to the first return by tracking the leading edge only. In that case, a fixed bias signal must be substituted for the output of the trailing edge sampling.

The first return originates at that portion of the terrain which is first illuminated; nominally, the ground directly below the flight capsule. This is, however, only a small portion of the area that will eventually be illuminated. The power loss resulting from considering only a small portion of the terrain can be determined by reference to Figure 150. If, for example, the slant distance to the edge of the area considered is 2 percent greater than the true altitude, then the reading can be assigned a 0.99 calibration factor since no object in the area considered has a range that differs by more than ± 1 percent from the true altitude. The radius of the area considered is:

$$r = [(1 + 0.02)^2 - 1]^{1/2} = 0.2$$

and the solid angle subtended is $(0.2)^2 \pi$. Therefore, if the illuminating source is isotropic, the power fraction striking the area considered is

$$\frac{(0.2)^2 \pi}{4\pi} = 0.01$$

$$= -20 \text{ db}$$

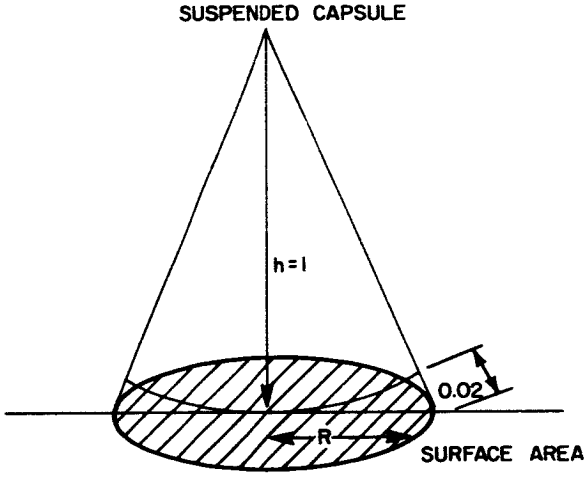

Figure 150 SURFACE ILLUMINATION GEOMETRY

8.3.4.3 Galactic Noise

The altimeter's sensitivity is limited by noise. At an operating frequency of 18 MHz, galactic noise is the only factor that must be considered. For an omnidirectional antenna in free space, the radiation

temperature at 18 MHz is 9×10^4 °K. In the absence of empirical data on the Martian ionosphere, no assumption will be made on it's ability to shield against this noise. Since the altimeter antenna will be exposed to 9×10^4 degrees Kelvin noise from only the overhead hemisphere, a factor of -3 db is considered adequate allowance for galactic noise. The altimeter radiated power will be based on a worst-case surface scattering coefficient of -30 db. It is assumed that the scattering will be strictly diffuse. In other words, the terrain is assumed to be highly absorptive and that as such it may be considered to be a black body at the physical temperature estimated for the Mars surface (300°K). Consequently, thermal radiation from the surface can be neglected and the backscattering of cosmic noise can be assumed to be attenuated by 30 db.

8.3.4.4 Noise Bandwidth

The technique of pseudo-coherent detection (discussed in paragraph 8.7) is used. The noise bandwidth is the width of the pass band of the filter used to select the Doppler shifted-carrier component of the echo spectrum. This filter must accommodate a maximum positive Doppler shift of

$$f_d = \frac{2v_r}{\lambda}$$

where v_r is the relative radial velocity component of the echoing object with respect to the vehicle. The maximum value of this component is 10,000 ft/sec. At an operating frequency of 18 MHz, f_d is approximately 500 Hz. We are now in a position to calculate the transmitter power requirement of the high-altitude altimeter. This computation, based on the factors shown in Table XCVIII, results in an estimated transmitter power of 25 watts.

8.4 LOW ALTITUDE RADIO FREQUENCY LINK ANALYSIS

8.4.1 Range, Beamwidth, and Accuracy Requirements

The range of altitude measurements extends from 27,500 feet to 1000 feet. The upper limit represents the highest altitude at which the entry shell is jettisoned and the low-altitude antenna is exposed. The lower limit represents the lowest altitude at which events are altitude controlled or the scientific data are altitude correlated.

The antenna beamwidth requirement is established by the maximum angle between the flight-capsule roll axis and the local Martian vertical for the altitudes of interest. In the absence of wind, this angle would be zero.

Wind introduces variations by causing the flight capsule to swing as shown in Figure 151. This figure shows the worst-case swing angle conditions. These occur in the model VM-4 atmosphere at the maximum postulated gust magnitude of 200 ft/sec. As can be seen at the right of the curve, the worst case beamwidth requirement is ± 90 degrees. The accuracy requirement for altitude measurement during the parachute descent phase is 5 percent. This accuracy is based on the requirement to deploy the first penetrometer at 3500 ± 175 feet. To perform this measurement accurately, the altimeter must discriminate against surface returns except the first. This is done by providing a high received signal-to-noise ratio. Because of the short ranges being considered, an altitude measurement accuracy of at least 5 percent can be obtained with reasonably low transmitter power levels.

TABLE XCVIII

TRANSMITTER POWER CONSUMPTION FOR HIGH ALTITUDE ALTIMETER

	(db)
Thermal noise T $\pm$ 90.000°K, B = 500 cps	-151 dbw
Hemisphere exposure to calactic noise	-3
Antenna gain (Two Way)	-2
Antenna pointing loss (Two Way)	+13
Free space loss F = 18 Mc, R = 250 x 10^3 feet	+96
Terrain scattering coefficient (see paragraph 8.3.4-3)	+30
Power fraction intercepted by surface (paragraph 8.3.4-2)	+20
Required Signal to noise ratio in 500 cps	+10
Circuit Losses	+1
Transmitter Power = Noise Power - Losses = -156 dbw + 170 db = 14 dbw = 25 watts	

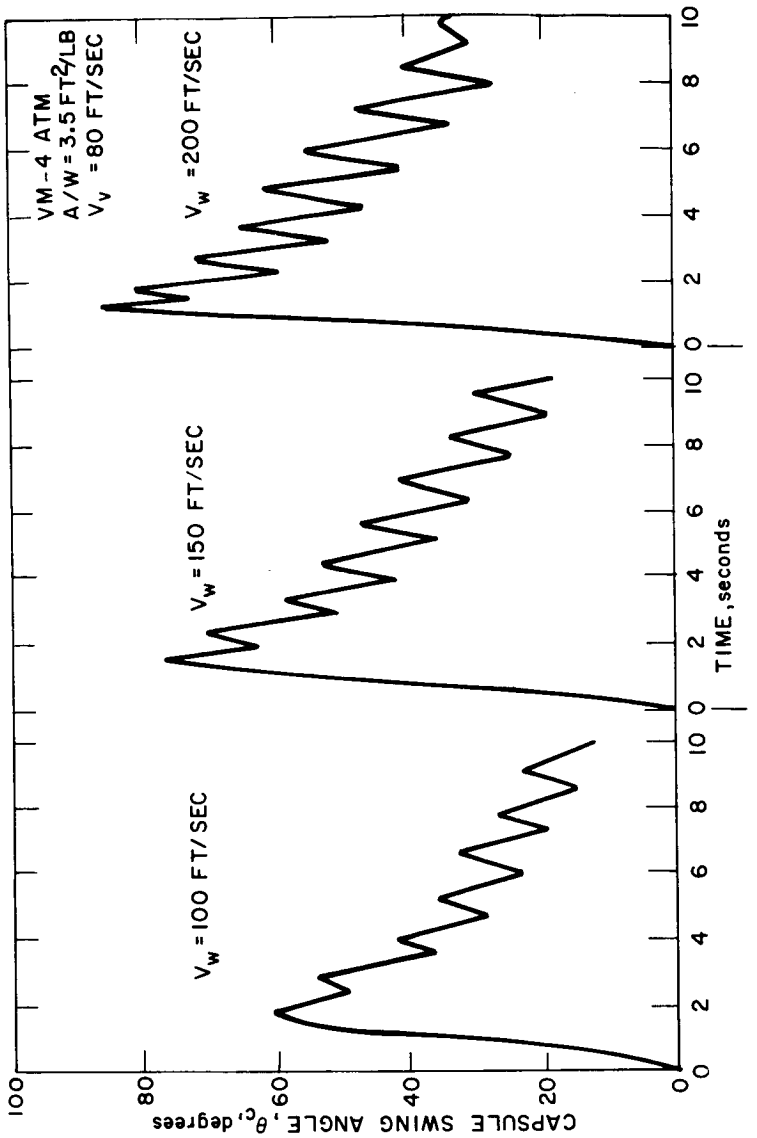

25-1161

Figure 151 PARACHUTE DYNAMICS -- CAPSULE SWING ANGLE

8.4.2 Frequency Selection

For the parachute descent phase, it is desirable to utilize a frequency higher than the 18 MHz chosen for radar operation during the preparachute phase. This choice is based on the following factors:

1. The flight capsule can no longer accommodate an antenna as large as the entry shell.

2. Reduction of transmitter power is of lesser concern because of the lower altitude involved.

3. Lower descent velocity at this time allows higher operating frequencies without correspondingly increased Doppler shifts and widened tracking loop noise bandwidths.

4. Surface roughness measurements at a second frequency considerably higher than 18 MHz are desirable.

5. Diffuse scattering is more likely as the frequency is increased; therefore, wind velocity can be estimated by spectral analysis.

After consideration of these factors, a frequency of 324 MHz was selected. This choice provides a further advantage in that it allows use of a single antenna for both the altimeter and the penetrometer receiving system.

8.4.3 Modulation Selection

The arguments presented in paragraph 8.3.3 in support of use of ICW modulation for the high altitude altimeter are equally valid for the low-altitude altimeter. The data handling circuits will be common to both. In fact, the only change necessary in the altitude tracker will be a simple multiplication of the clock frequency.

8.4.4 Transmitter Power Selection

Computation of the transmitter output-power requirements differs in two respects from that for the high altitude altimeter. A discussion of these changes follows.

8.4.4.1 Receiver Noise

Galactic noise becomes an unimportant factor at the 324 MHz operating frequency of interest. It is assumed that the system noise temperature is 1000°K. This corresponds to a conservative noise figure of 5 db.

8.4.4.2 Doppler Bandwidth

The maximum descent velocity after parachute deployment is 150 ft/sec, and the maximum wind velocity is postulated at 500 ft/sec. Consequently, the maximum velocity with respect to the surface is,

$$(\overline{500}^2 + \overline{150}^2)^{1/2} = 521 \text{ ft/sec}$$

The corresponding maximum Doppler shift is

$$f_d = \frac{2 v_r}{\lambda} = 347 \text{ Hz} .$$

Finally, the required transmitter power output is computed on the basis of the parameter values listed in Table XCIX. Although the computation shows a transmitter power requirement of 0.45 watt, one watt will be utilized. This increase is very small relative to overall electric power and control subsystem requirements, but it provides a substantial increase (3 db) in the signal-to-noise margin. This additional margin will permit operation of the altimeter at a higher altitude should such become necessary.

TABLE XCIX

TRANSMITTER POWER COMPUTATION FOR LOW ALTITUDE ALTIMETER

	(db)
Noise power ($KTBN_s$)	-173.4 dbw
Antenna gain (two way)	-12
Antenna pointing loss (two way)	+18
Free space loss (f=324 Mc, R=30x10^3 feet)	+103
Signal to Noise Ratio	+10
Fraction of Sphere contributing to echo	+20
Terrain scattering coefficient	+30
Circuit losses	+1
Transmitter Power = -185.4 dbw + 182 db	
= -3.4 dbw	
= 0.45 watt	

8.5 WIND VELOCITY MEASUREMENT RADIO FREQUENCY LINK ANALYSIS

Knowledge of wind velocities near the surface of the Earth is critical in designing hard (parachute-aided terminal descent) landers. The possibility that the wind-induced horizontal velocity may exceed the vertical velocity strongly influences the design of the impact reduction system. In soft (retroengine assisted terminal descent) landers, the total thrust requirement will be sufficiently large so that the incremental amount needed to offset wind effects will certainly not dominate the design, although it may be significant. In either case, however, the possibility of flight-capsule damage or burial by wind-blown particles represents a hazard which could be reduced if adequate knowledge of wind velocities were available. The major problem with any wind-velocity measurement associated with a nonsurvivable flight-capsule mission is that it is based on what is at best only a few minutes of sampling a highly variable phenomenon.

A limited number of wind-velocity measurement techniques are applicable to missions which do not survive landing. One or more fixed reference points (penetrometers) can be placed on the surface prior to flight-capsule impact. The wind-induced motion of the descending capsule relative to those reference points can then be measured. Alternatively, various radar techniques which make use of the effect of relative velocity on the radar return may be used. Motion of the descending capsule relative to a previously established inertial frame of reference may also be detected, or the effects of wind gusts can be determined from cruder measurements of capsule dynamics. All of these methods utilize the effect of the wind on the capsule. A different approach is based on placing a smoke generator on the surface of the planet and then deducing winds velocities and directions from the motion of the smoke plume as seen on the capsule television.

The following discussion deals with the radar methods. Discussion of the other measurement techniques mentioned above appears in Volume 5, Book 4, of this report.

8.5.1 Comparison of Radar-Type Wind Measurement Techniques

Two basic techniques will be considered here: 1) a wide-beam radar altimeter from which the horizontal velocity of the vehicle will be deduced by spectral analysis of the diffusely reflected return, and 2) a three-beam narrow-beam radar (velocity-altitude sensor). In the second technique, the horizontal velocity is measured by appropriate processing of range and range-rate measurements made along the three beams.

The velocity-altitude sensor technique is described in considerable detail in Appendixes G and H. The accuracy with which the vehicle horizontal velocity can be determined with this technique is discussed in these two appendixes and in paragraph 8.5.4 of this book.

The philosophy of using the radar altimeter for horizontal velocity measurement is discussed in Appendix F. As noted there, the spectrum of the radar return depends heavily upon the terrain features. If the surface is fairly smooth, the diffuse return will be very small and the edge of the spectrum may not be well defined. Even for a terrain reflecting a highly diffused return, it is seen that the edges of the spectrum have a small amplitude, with resultant poor definition of the spectrum edge. Another masking feature in regard to the spectrum edge is the effect of the vertical velocity on the spectrum. As shown in Appendix F, if the vertical velocity is greater than the horizontal, the higher frequency edge of the spectrum will be determined by this vertical component. Because of these disadvantages, it is concluded that spectral analysis of the wide-beam radar return will not provide an accurate measurement of the flight-capsule horizontal velocity. For this reason, a system based on direct measurement of motion along three beams has been adopted as the reference design. With this technique, worst-case in accuracies of approximately 20 percent for an actual horizontal velocity of 220 ft/sec are attainable -- the mean and rms errors are 13 and 9 percent respectively.

8.5.2 Entry from the Approach Trajectory Design

In the case of entry from the approach trajectory, the information capacity of the flight capsule to flight-spacecraft relay link is insufficient for transmitting the raw radar-echo waveform. Accordingly, data processing is performed on board the flight capsule. Processing consists of spectral analysis to yield the combined wind-velocity measurement and surface-roughness data. Wind velocity can be crudely determined from the echo Doppler spectral width. The computation, however, involves the antenna beamwidth, the effective value of which is a function of the surface roughness. These two measurements cannot be separated. The theory of obtaining wind velocity and surface-roughness information is treated in detail in Appendix F. The mechanization of the data-processing equipment required for this case is described in paragraph 8.9.1.

8.5.3 Entry From Orbit Design

It has been established that the velocity-altitude sensor will be used as the primary method for measuring vehicle horizontal velocity. The following paragraphs cover system requirements and the selected operating characteristics.

8.5.3.1 Range, Beamwidth, and Accuracy Requirements

The velocity-altitude sensor will operate over the altitude range from 30,000 down to 10 feet. (The compromises which must be made to attain a reasonable measurement accuracy at 10 feet are discussed in

paragraph 8.9.2.) Flight-capsule dynamics will determine the maximum range requirements. Since the three beams are at a 20-degree angle relative to the flight capsule roll axis, the maximum allowed angle that the flight capsule roll axis can make with the local vertical (due to vehicle dynamics) is 70 degrees. Beyond that angle, the velocity-altitude sensor cannot determine vehicle velocity. Obviously, the range increases rapidly as this limiting angle is approached. To limit power requirements to a reasonable value, a maximum angle of 60 degrees is considered. As shown elsewhere in this report, this angle (60 degrees) is exceeded for only a very small percentage of the mission parachute-aided descent phase. Thus, at maximum altitude, the maximum range is 172,000 feet. The shortest range, as mentioned above, corresponds to the minimum altitude (10 feet).

The beamwidth requirement is established primarily by the physical size of the antenna. To minimize spectral spreading and thereby minimize transmitter power, an infinitesimally narrow beam is desired, but an infinite aperture is required. Flight-capsule structural design limitations have, in fact, limited the aperture size to a diamter of approximately 17 inches. Results of iterative tradeoff studies involving frequency, accuracy, and transmitter power indicate that a 5 x 5-degree beam is both practical and consistent with other requirements.

The required accuracy of range and range-rate measurements is a function of the desired accuracy in determining the horizontal velocity of the flight capsule. It is shown in paragraph 8.5.4 that a worst-case accuracy of ± 25 percent of the actual horizontal velocity is attainable with a range rate accuracy of ± 4 percent on all three beams. For the range of horizontal velocities of interest (0 to 300 ft/sec) errors can be limited to a maximum of approximately 50 ft/sec.

8.5.3.2 Frequency Selection

The major determining factor in the choice of transmitting frequency is the size of the antenna aperture. Vehicle design considerations will allow a maximum antenna diameter of 17 inches. Thus, a frequency of approximately 13 GHz is required to obtain a 5 x 5-degree beamwidth with an antenna of that size.

8.5.3.3 Modulation Selection

Use of frequency-modulated carrier-wave modulation in conjunction with a homodyne receiver results in an extremely simple system. Compared with the long pulse (ICW) and narrow pulse systems, FM/CW yields the maximum transmitter efficiency. The greatest disadvantage associated with FM/CW modulation is that of isolation. This problem

arises from the fact that the antenna size restriction requires that the same reflecting surface be used for both the transmitting and the receiving antennas. The problem is discussed in considerable detail in paragraph 8.9. For the ranges of interest, isolation of 60 db is both sufficient and attainable.

8.5.3.4 Transmitter Power Selection

Several tradeoffs must be made among the propagation parameters before a design control chart can be defined. The first to be considered here are the maximum range and the received signal bandwidth. The associated geometry is shown in Figure 152. Angle θ_c is the angle between the flight-capsule roll axis and the local Martian vertical. Since the three antenna beams are at an angle of 20 degrees relative to the flight capsule roll axis, $\gamma_{max} = \theta_c + 20$ degrees. Thus, the maximum range will be determined by this angle and the fixed maximum altitude of 30,000 feet. Angle θ_c will exceed zero degree because of parachute dynamics in the presence of winds; this problem is discussed in greater detail elsewhere in this report.

It is shown in Appendix G, Equation (2), that the range-beat frequency, f_r , is given by

$$f_r = \frac{8 f_m \Delta f}{v_c R}$$

where

f_m = modulation frequency

Δf = peak-frequency deviation from the carrier

v_c = velocity of propagation

R = range

Due to the appreciable (5 degrees) antenna beamwidth, the signal spectrum will spread as a result of variations in range. Table C indicates the maximum ranges and signal bandwidths encountered in the mission. Thus, for large values of θ_c, power requirements for the resulting bandwidths will be prohibitive. Of course, if $\theta_c > 70$ degrees, one or more of the three beams could radiate horizontally or away from the planet, rendering the system useless. In Appendix F, it is seen that at the lowest altitudes, a deviation rate of 1.1 kHz was required to determine the range and range rate unambiguously. This deviation rate results in range-rate counting errors of 40 ft/sec. The counting error can be reduced, for

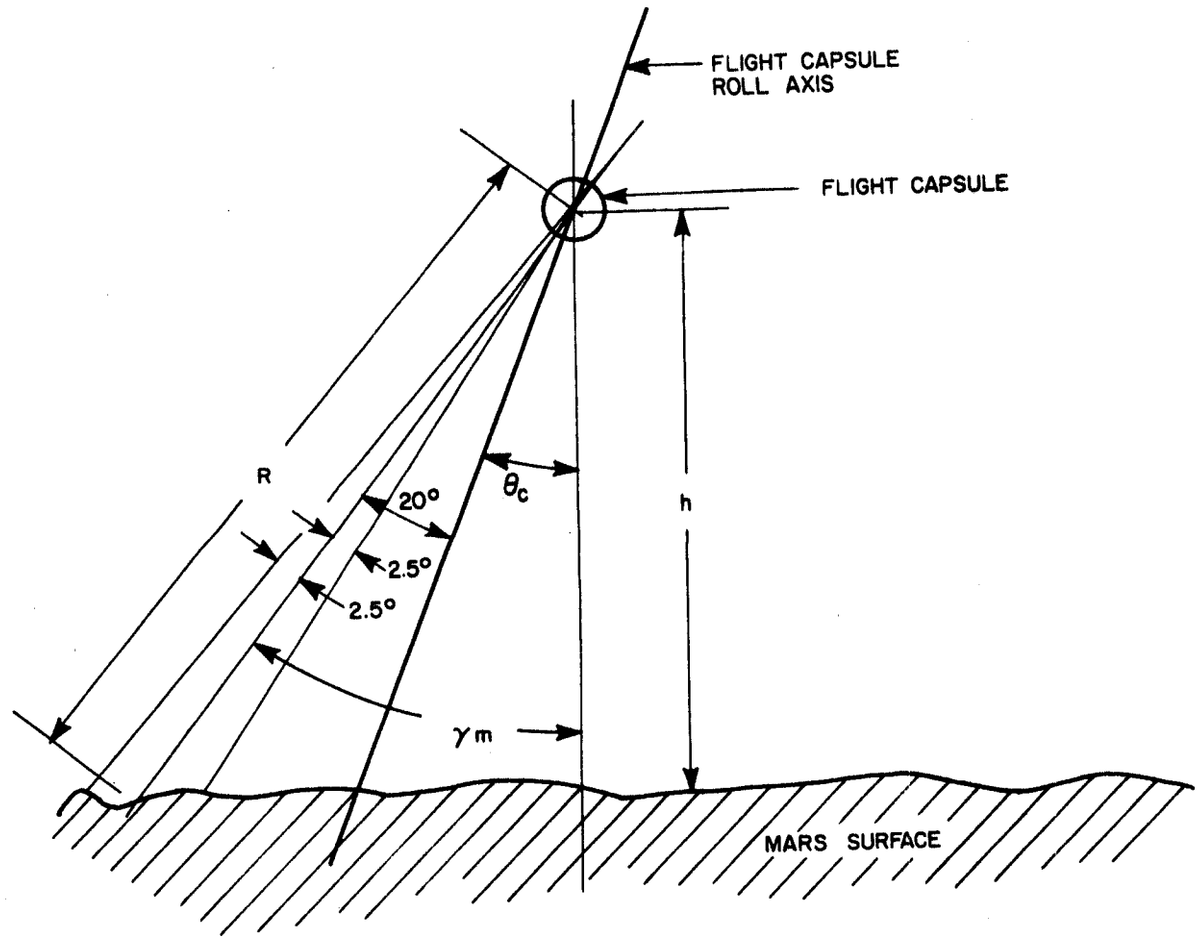

Figure 152 GEOMETRY FOR RANGE AND BANDWIDTH COMPUTATION

TABLE C

SIGNAL SPECTRAL SPREADING BECAUSE OF PAYLOAD DYNAMICS

θ_c	Signal BW/f_r	R_{max} (feet)	$f_{r\,max}$ (kc)	Signal spectrum spreading
0°	0.031	32,000	130	4 kHz
10	0.051	35,000	140	7
20	0.074	39,000	160	12
30	0.105	47,000	190	20
40	0.151	60,000	240	36
50	0.243	88,000	360	84
60	0.530	172,000	700	370

example, to 8 ft/sec by reducing the deviation rate to 220 Hz. This could result in range and range-rate ambiguities at altitudes less than 50 feet. However, these ambiguities will be resolved by the continuous tracking receiver. Loss of lock is not likely to occur at this altitude because of the large signal to noise ratio and the fact that only 0.5 second remains before impact.

The required transmitter power can now be computed with the aid of the following equation:

$$P_T = (S/N)_{AVG} + L_S + N_o + BW - 2G - \Phi - \psi - L_R$$

where the parameter symbols and their values are given in Table CI. It is seen that the required power is a strong function of γ_m. Therefore, due to the uncertainty in γ_m (θ_c + 20 degrees), P_T versus θ_c is plotted in Figure 153 for the maximum altitude, 30,000 feet. Elsewhere in this report, it is shown that the time during which θ_c exceeds 45 degrees represents only a very small percentage of the total parachute-aided descent time. Accordingly, only insignificant errors will be incurred if the measurement of the beat frequency is neglected when θ_c = 45 degrees. Care must be taken, however, to ensure that the tracking loop will reacquire quickly following any loss of lock. It should be noted, however, that although this value of θ_c results in the worst performance for range and range-rate measurements along one of the beams, the performance of the other two beams will be significantly improved.

Thus, as can be seen from Figure 153, the transmitter power required for adequate performance when θ_c = 45 degrees is 1 watt per beam.

TABLE CI

V-A SENSOR PARAMETERS

Symbol	Parameter	Value
P_T	Transmitter power	to be determined
h_{max}	Maximum altitude	30, 000 feet
R_{max}	Maximum beam range	$= \frac{h_{max}}{\cos \gamma_m}$
θ_c	Angle between flight-capsule axis and local vertical	0 to 90 degrees
γ_m	Maximum angle between any beam and local vertical	$= \theta_c + 20$ degrees
f_r	Range beat frequency	$= \frac{8 f_m \Delta f}{v_c} R$ (see Appendix G)
BW	Signal bandwidth	$= f_{r_{max}} \cos \gamma_m \left[\frac{1}{\cos (\gamma_m - 2.5°)} - \frac{1}{\cos (\gamma_m + 2.5°)} \right]$
G	Antenna Gain (15" dish)	30 db
Φ	Horizontal Plane beamwidth	5 degrees
ψ	Vertical Plane beamwidth	5 degrees
f_o	Carrier Frequency	13 GC
N_o	Noise spectral density (300°K, 12 db N. F.)	-102 dbm/mc
C	Circuit losses	3 db
σ degrees	$\frac{\text{Average echo area}}{\text{unit area}}$	-30 db
S/N (5 percent)	SNR required for 5 percent accuracy	10 db
L_R	Cross section loss	$= 10 \log \frac{\sigma \text{ degrees}}{4\pi \cos \gamma_m}$

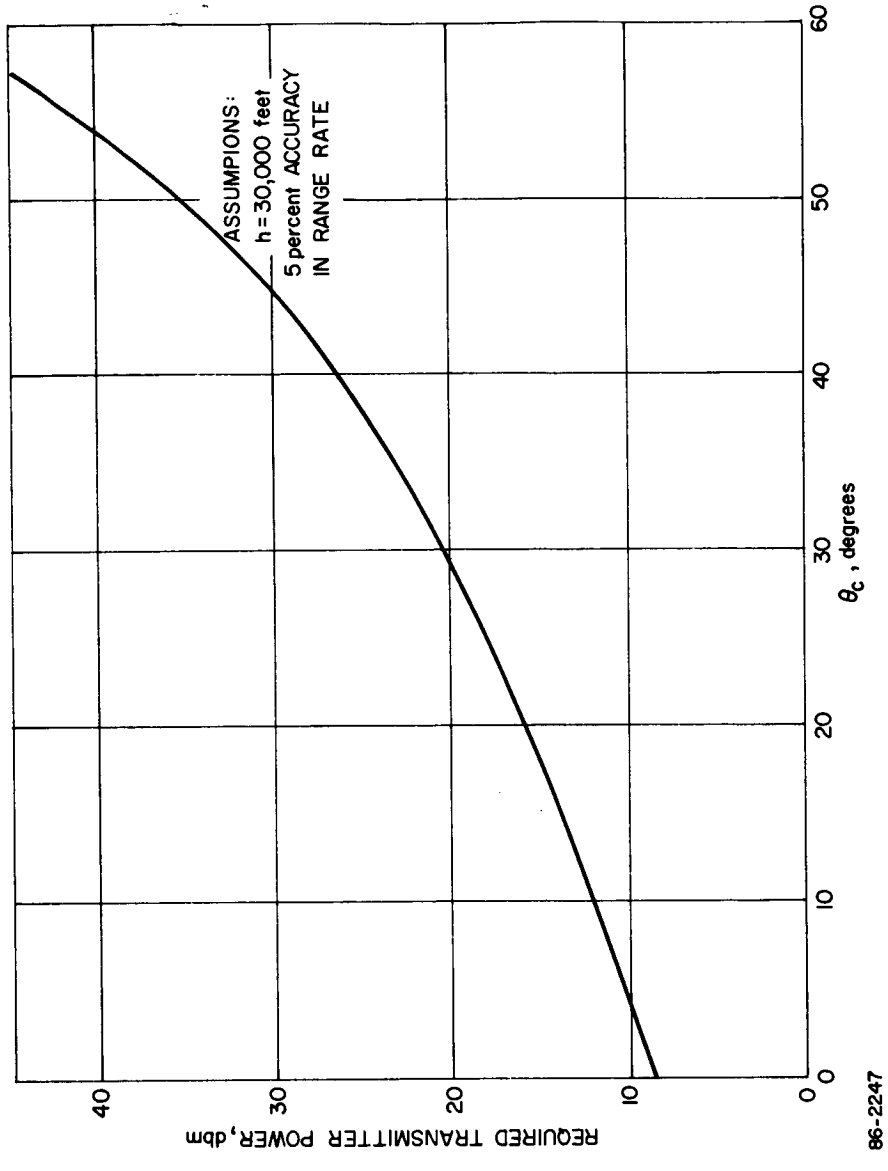

Figure 153 V.A. SENSOR POWER REQUIREMENT

8.5.4 Wind Velocity Error Analysis

An expression for the measurement error in the determination of the flight-capsule horizontal velocity is derived in Appendix F (Equations (61) and (67)). A computer program has been written to evaluate this expression for the following appropriate parameter ranges:

- Swing angle $-60° \leq \theta_c \leq 60°$
- Euler angle $-180° \leq \theta_c \leq 180°$
- Horizontal velocity (for all directions) $V_H = 220$ ft/sec
- Vertical descent velocity $V_Z = -100$ ft/sec
- Error in θ_c, $\Delta\theta_c = \pm$ 5 degrees
- Doppler velocity along each beam $\Delta D_n = \pm\ 0.05\ D_n$

These parameters are discussed in detail in Appendix F.

The number of discrete program inputs required to cover these parameter ranges yielded 6400 sample points. A statistical analysis was then performed on sample points. A total cumulative probability distribution can be computed if the probability density function (pdf) of each of the variables is known. The pdf's of all the parameters except θ are seen to obey uniform distributions over their respective intervals, i.e.; the wind velocity vector is equally likely to assume any orientation (0 to 360 degrees) ϕ, also, is equally likely to assume any orientation; and for the assumptions in $\Delta\theta$ and ΔD_n's (namely $\pm$ 5 degrees and $\pm\ 0.05\ D_n$) the probability that they will be plus is equal to the probability that they will be minus. The pdf for θ is unknown because it depends upon the Mars environment which is, at present, mostly conjectural. However, it may be positive or negative with equal probability. Therefore, cumulative distributions can be arrived at with the magnitude of θ as a parameter. Figures 154, 155, and 156 show the cumulative distributions as a function of the magnitude of the percent error for $|\theta|$ equal to 0, 30 and 60 degrees, respectively. The distribution of positive errors will be the same as for negative errors. Close examination of these figures indicates that the distributions are very similar for all values of $|\theta|$. Thus, regardless of the pdf for θ, no serious error will be incurred if a total cumulative distribution is computed merely by averaging the distributions for the three values of $|\theta|$. Results of this computation are shown in Figure 157.

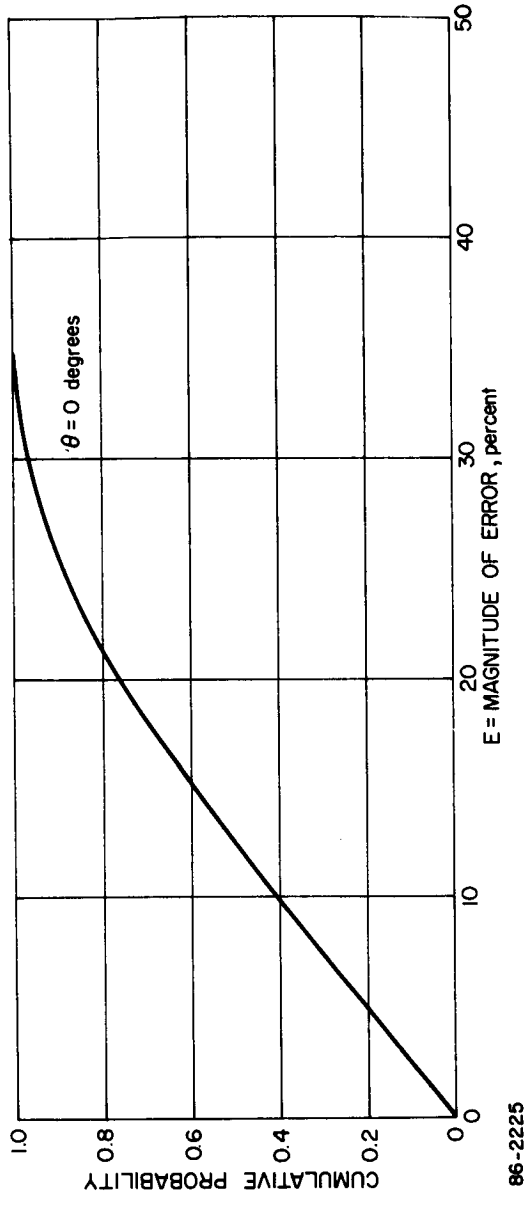

Figure 154 CUMULATIVE PROBABILITY OF ERROR IN MEASUREMENT OF WIND VELOCITY
θ = 0 DEGREE

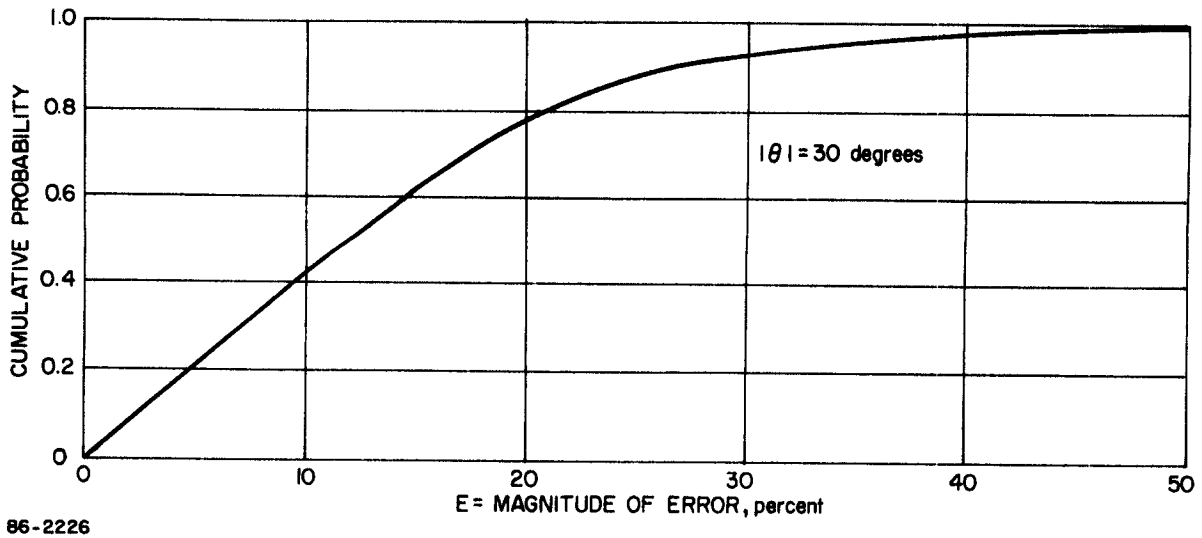

Figure 155 CUMULATIVE PROBABILITY OF ERROR IN MEASUREMENT OF WIND VELOCITY
$|\theta|$ = 30 DEGREES

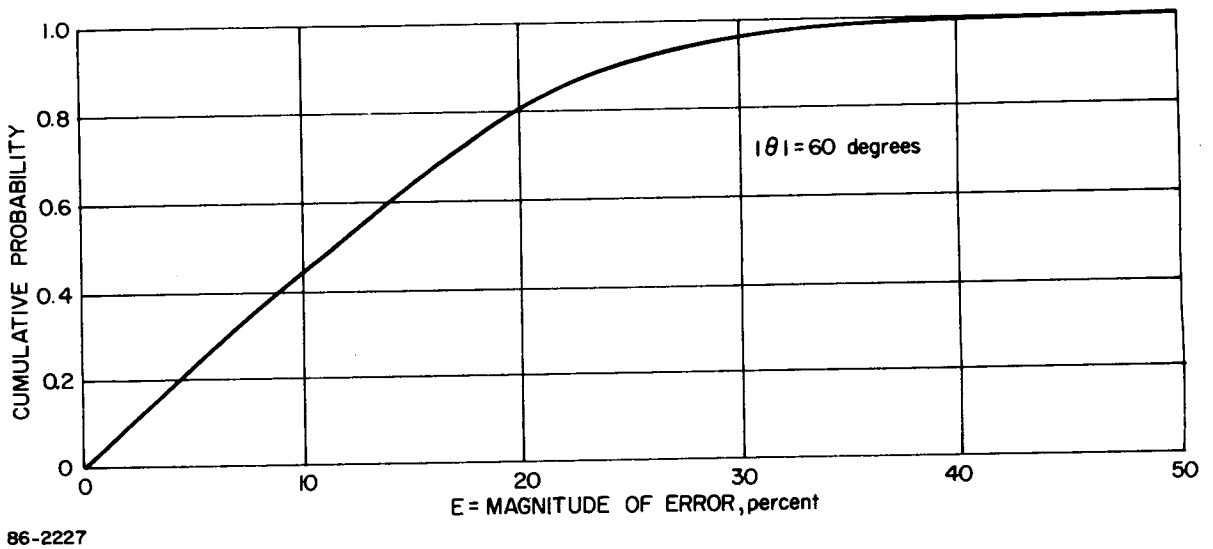

Figure 156 CUMULATIVE PROBABILITY OF ERROR IN MEASUREMENT OF WIND VELOCITY
$|\theta|$ = 60 DEGREES

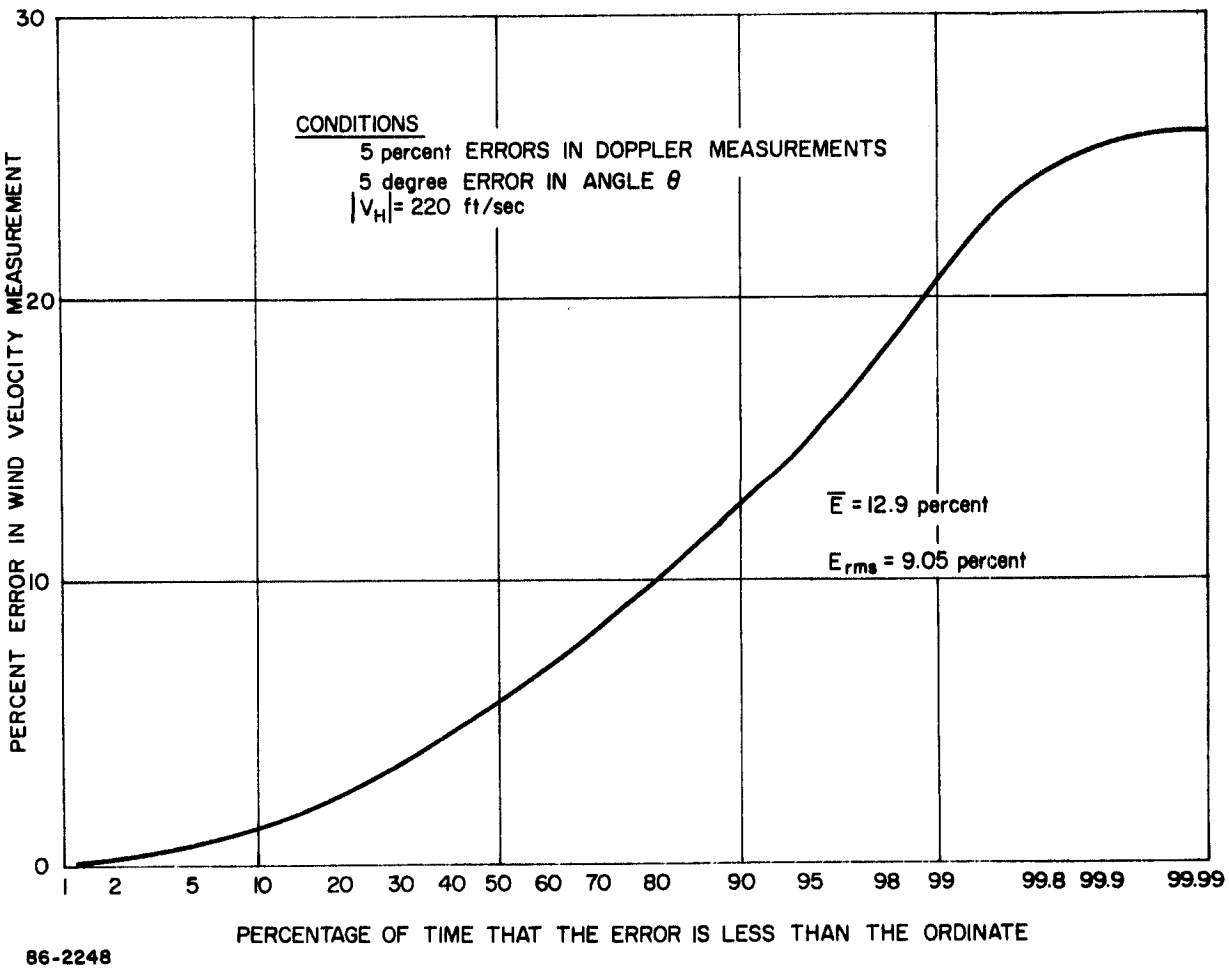

Figure 157 ERROR IN WIND VELOCITY MEASUREMENT

From the resulting distribution, the mean and rms errors have been computed.

They are

$\bar{E}$ = 12.9 percent

E_{rms} = 9.1 percent

Figures 158, 159 and 160 show typical behavior of the wind velocity measurement error as a function of θ, ϕ, and vehicle motion direction respectively, with all other parameters held fixed. Figures 161 and 162 show the envelope (or maximum) of errors as a function of θ for all possible velocity directions and with all other parameters held fixed. From these two curves, it is seen that the maximum (worst-case) errors will be approximately 25 percent (= 50 ft/sec).

8.6 SURFACE ROUGHNESS MEASUREMENT ANALYSIS

8.6.1 Spectrum Analysis

The Fourier transform of the echo-time waveform is its complex power spectrum. After removal of the modulation sidebands by narrow band filtering, the Doppler waveform constitutes a one-dimensional signature of the surface terrain characteristics. Figure 163 depicts the power spectra of the return signal associated with several terrain models. After sufficient study of these spectra, an experienced observer could construct a reasonable model of the terrain. The spectrum, in fact, may bear a resemblance to the terrain profile as is shown at b of the figure where the size and the location of hills can be deduced.

In the absence of a conventional definition for measurement of the surface roughness, the ratio between the powers in the diffuse and the specular components of the radar echo will serve as the criterion for roughness, thus

$$R = \frac{P_{diffuse}}{P_{specular}}$$

This definition is directly useful since the terms in the ratio can be readily obtained.

The roughness ratio, it should be understood, is not uniquely associated with a given terrain model. For example, a homogeneous surface comprised of bumps less than a wavelength high and dispersed throughout the area of interest will yield approximately the same roughness ratio as a smooth surface of similar size but interspersed with bumps more than a wavelength

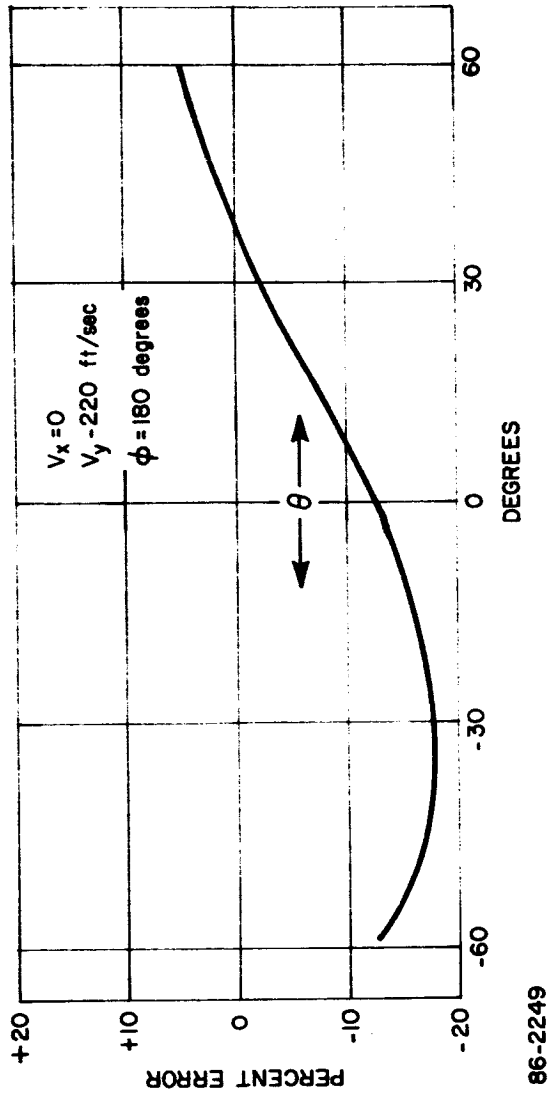

Figure 158 WIND VELOCITY MEASUREMENT ERROR VERSUS θ

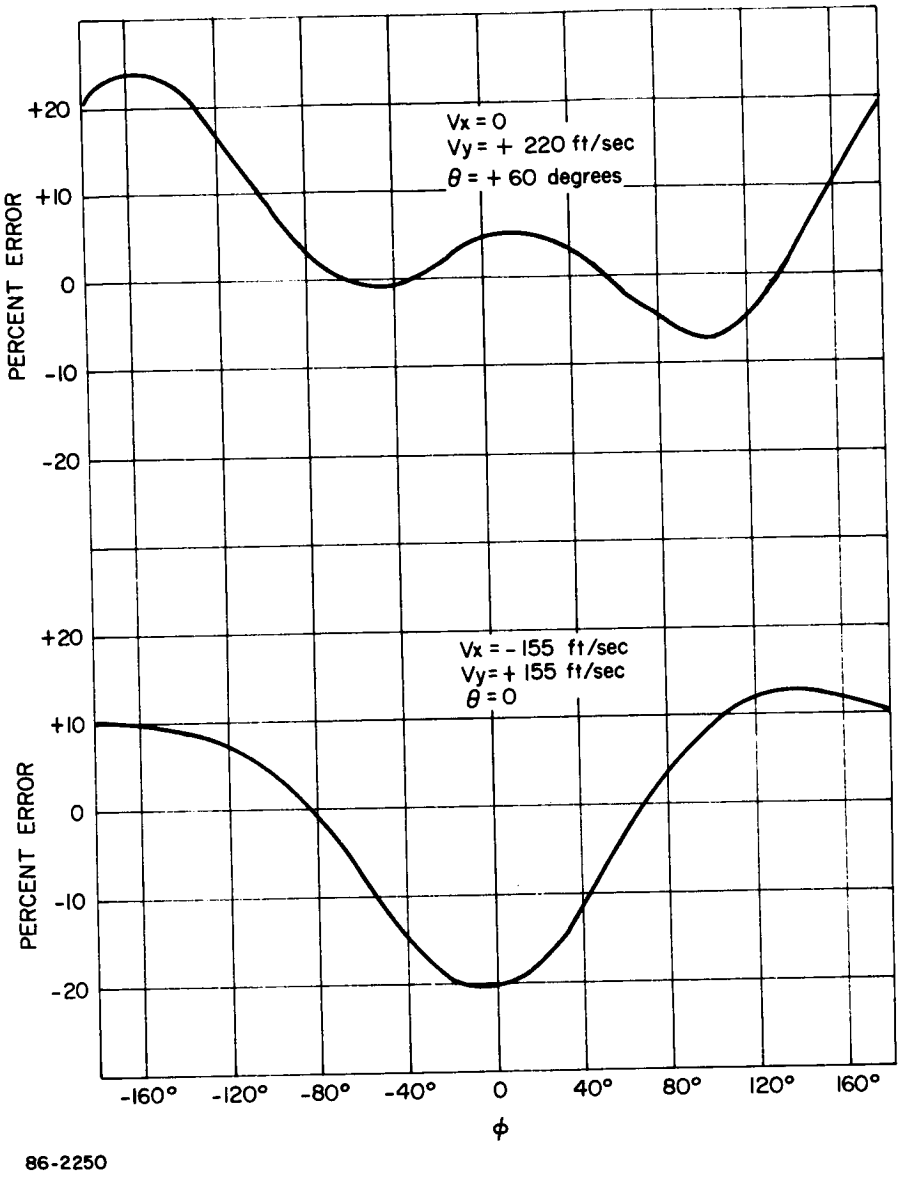

Figure 159 WIND VELOCITY MEASUREMENT ERROR VERSUS ϕ

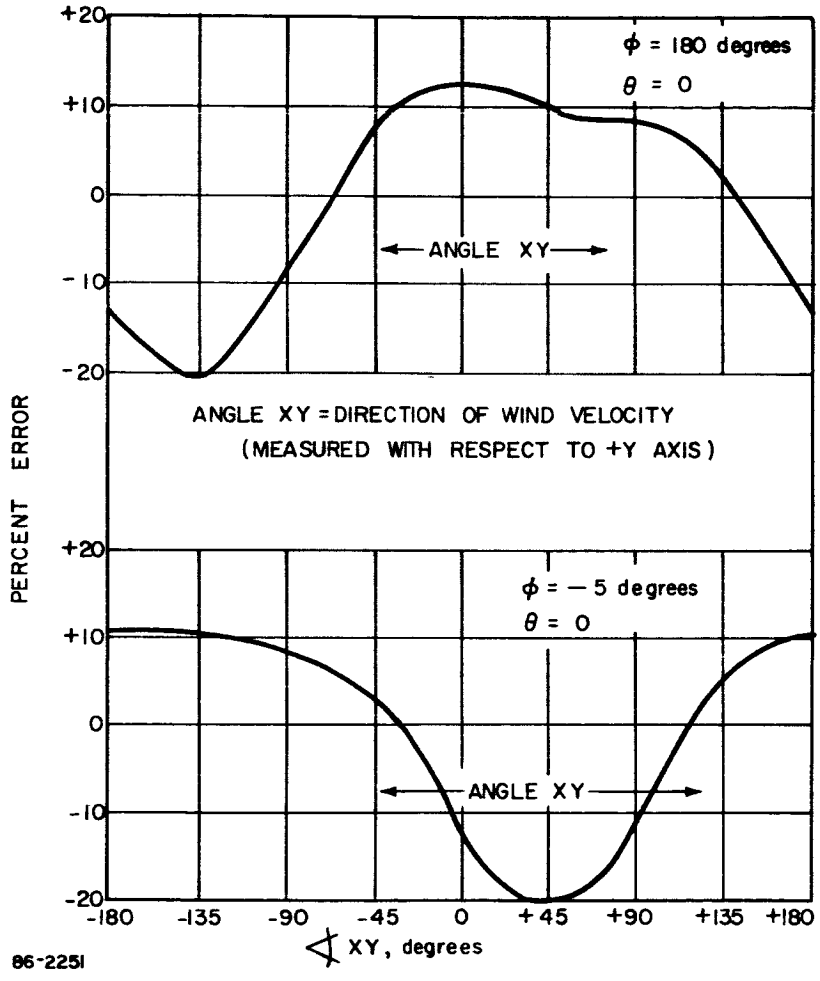

Figure 160 WIND VELOCITY MEASUREMENT ERROR VERSUS WIND DIRECTION

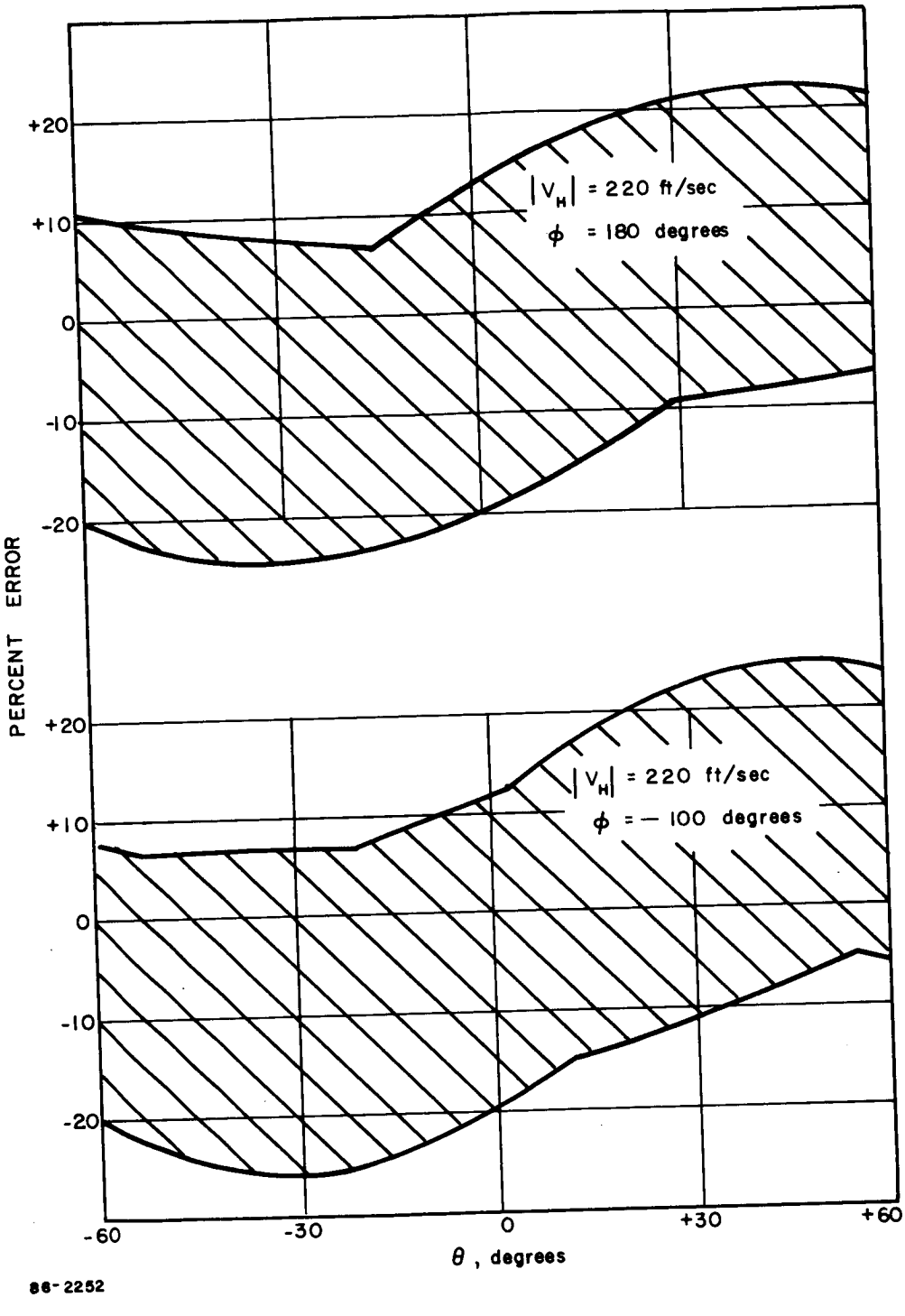

Figure 161 MAXIMUM WIND VELOCITY MEASUREMENT ERROR VERSUS ϕ = + 180 DEGREES, – 100 DEGREES

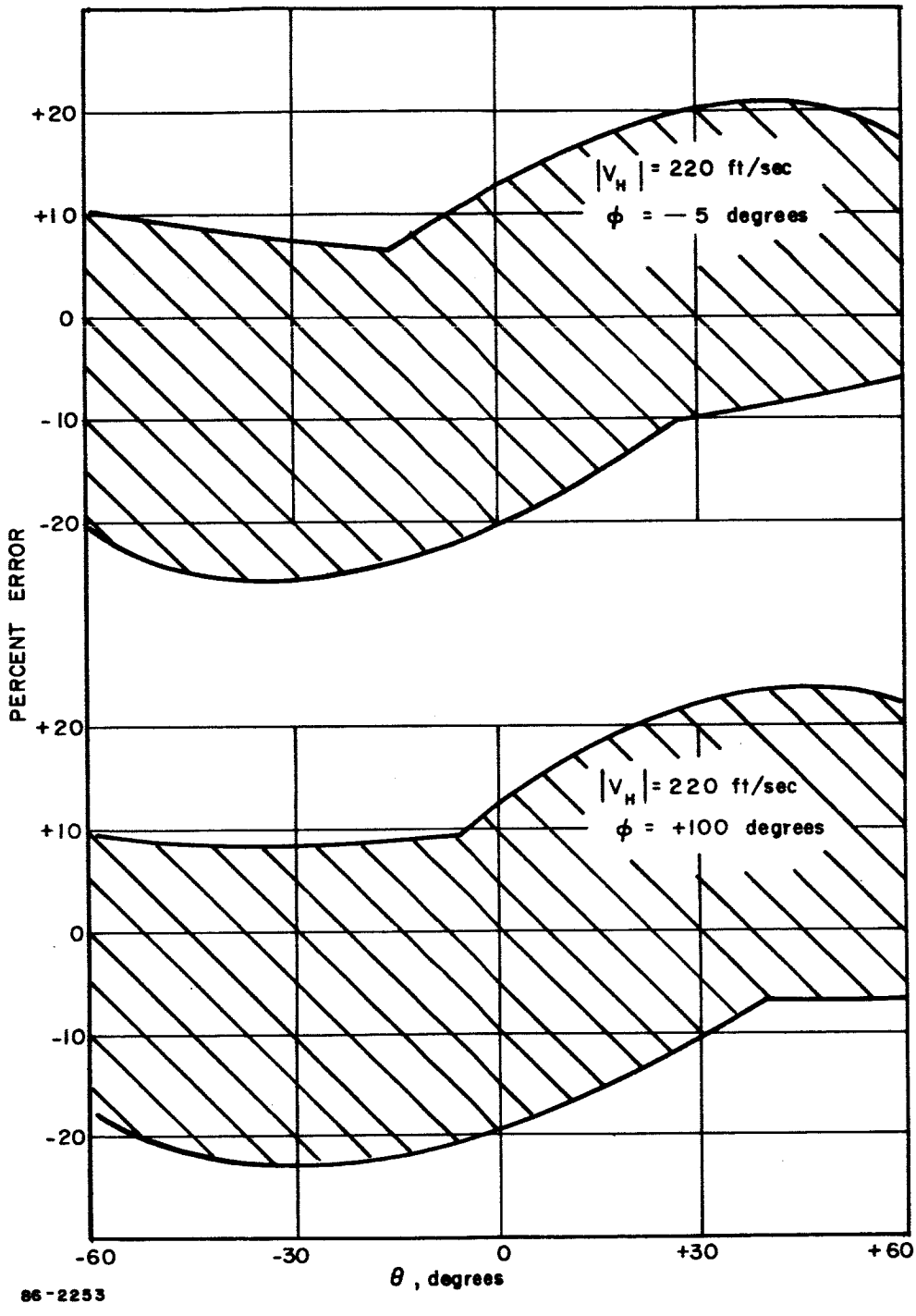

Figure 162 MAXIMUM WIND VELOCITY MEASUREMENT ERROR VERSUS ϕ = – 5 DEGREES, + 100 DEGREES

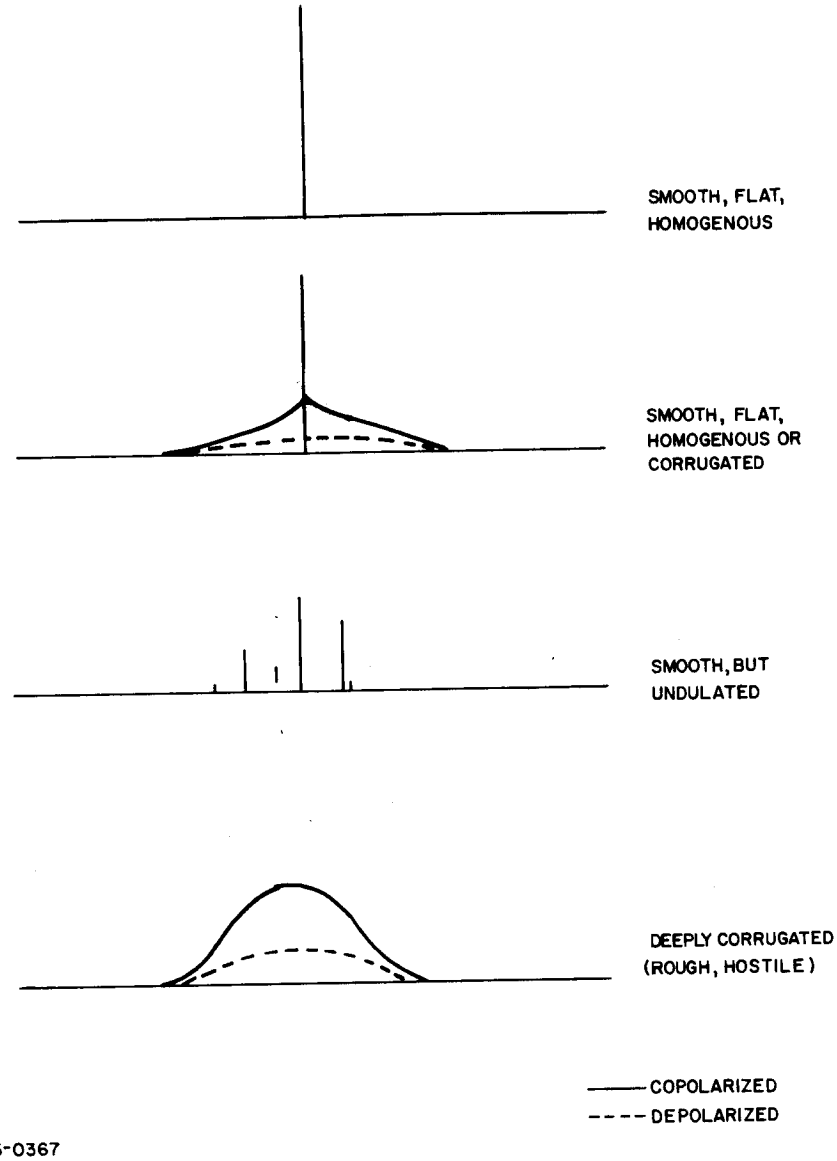

Figure 163 ECHO SPECTRA FROM VARIOUS TERRAINS

high. The roughness information is used primarily, however, to determine the probability of landing without tipping over, not necessarily to provide a picture of the terrain. Consequently, the roughness ratio, as defined above is valid for the purpose for which it is used.

Paragraph 8.9.1 describes the on-board data processing subsystem used in the case of entry from the approach trajectory. In the case of entry from orbit, the echo waveform is sampled on-board the flight capsule and relayed to the flight spacecraft for subsequent retransmission to Earth.

8.6.2 Side-Looking Radar Technique

This section describes a candidate Earth-data processing technique to derive the Mars surface profile from the relayed altimeter-echo waveform. When the radar wavelength is λ, the Doppler shift of an echo from a scatterer, which is seen under an angle ϕ with respect to velocity vector $\vec{v}$, is

$$f = -\frac{2v}{\lambda} \cos \phi \quad .$$

By differentiation

$$\dot{f} = -\frac{2v}{\lambda} \dot{\phi} \sin \phi \quad .$$

Some scatterers may be seen at a direction approximately normal to the velocity. In that case

$$f \approx 0$$

$$\dot{f} \approx -\frac{2v\dot{\phi}}{\lambda} = -\frac{2v^2}{\lambda\rho}$$

where:

ρ is the distance to the scatterer.

The echo waveform from a target which moves with respect to the radar is some function of time and it is always possible to devise a matched filter for it. In particular, scatterers broadside to the velocity vector give rise to a linear chirp whose rate is variable. An optimum filter may be matched to the chirp rate. Thus, if a received waveform $y(t)$ consists of noise $n(t)$ plus a waveform whose time scale is an unknown variable, then

$$y(t) = x(at - \tau) + n(t) \quad .$$

A matched filter, as the term is used here, is one which maximizes the correlation

$$g(\tau, \alpha) = \int y(t) \times (\alpha t - \tau)\, dt$$

with respect to the variable α, so that

$$\frac{dg}{d\alpha} = \int y(t) \cdot t \cdot \dot{x}(\alpha t - \tau)\, dt$$

$$= 0$$

where $\dot{x}$ is the first derivative with respect to the argument $(\alpha t - \tau)$

The above equation has been mechanized for linear chirp forms of $x(t)$.

The result is $\dot{f}$-tracker. This is distinguished from an f-tracker, which is the usual Doppler frequency tracker. The combination of measurement, of f, $\dot{f}$ and ρ plays a role in advanced navigation concepts. Figure 164 shows the elementary from of an f-tracker, designed to provide the correlation factor, $g(\tau)$. The latter function is a noisy waveform, each spike representative of a scatterer having traversed sequence. When appropriately rectified, g_t becomes $|g(\tau)|$. The latter may be considered to be a one-dimensional radar picture of the surface.

8.7 HIGH-ALTITUDE RADAR ALTIMETER SUBSYSTEM DESCRIPTION

8.7.1 Description of Selected Approach

A long-pulse, coherent, narrow-band radar system, modulated with interrupted continuous wave (ICW) has been selected as the reference-design altimeter. This system is compatible with present solid-state technology, it is appropriate for both the high and the low altitude regimes, and it minimizes duplication of equipment and switching complexities when transferring from the high-altitude mode of operation to the low-altitude mode of operation. In fact, the only physical switching that takes place at the transition altitude is to change the antenna and intermediate-frequency (IF) bandwidth. All other equipment is common to both altitude ranges of interest.

The following paragraphs describe the operation of the radar altimeter.

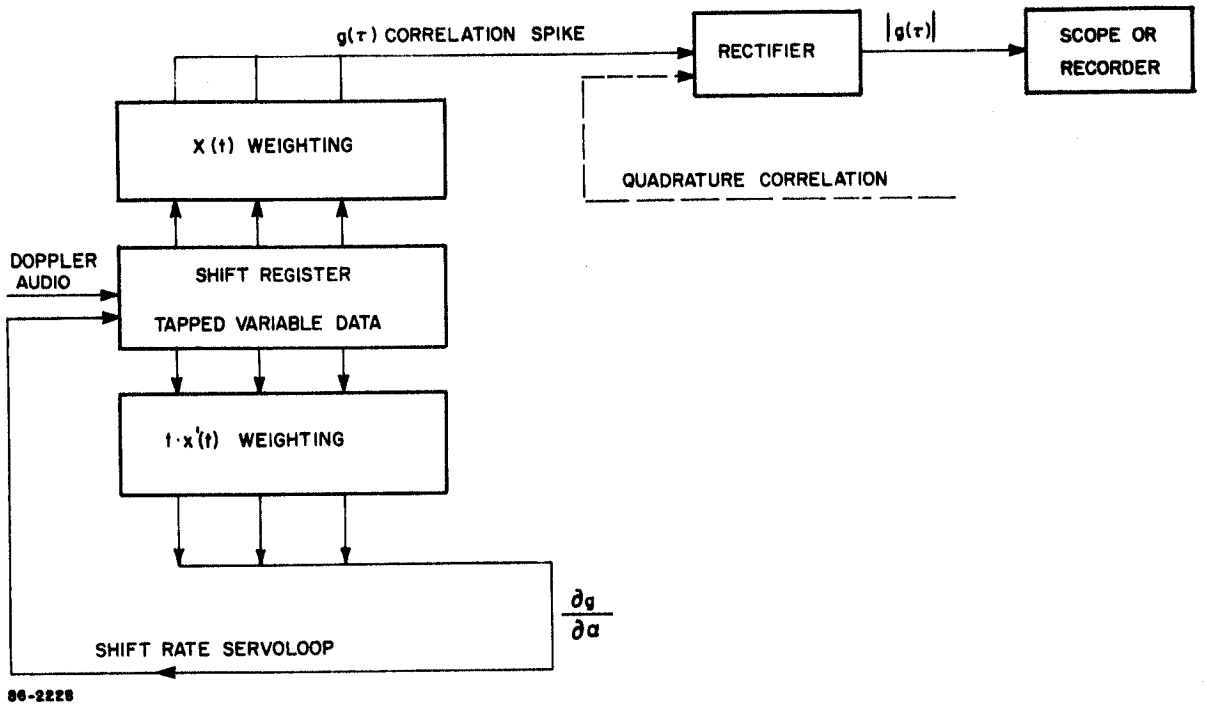

Figure 164 FREQUENCY RATE TRACKER AND CORRELATOR

8.7.1.1 Pseudo-Coherent Detection

Before proceeding with a description of operation, a brief review of the principle of coherent detection is appropriate since this principle is fundamental to operation of the selected approach. A simple illustration of coherent detection is shown in Figure 165. The associated waveforms are shown in Figure 166. Whenever a carrier is transmitted and the return signal is heterodyned with the original signal, a difference frequency is generated by the relative motion between the transmitting antenna and echoing surface. If the transmitted signal is ICW modulated, the received Doppler difference will also be ICW modulated, as represented in waveform a of Figure 166. When this signal (Doppler difference) is smoothed by passage through a low pass filter, waveform b results. This is merely the delayed envelope of the pulses in a. If waveform a is also delayed by this amount, as shown in c, the polarity of the narrow band signal b will correctly represent the polarity of the pulses in the wideband signal c. Multiplication of b by c results in the unipolar pulse train d, that contains unambiguous timing information on the transients. This information can now be cross-correlated and coherently integrated in a bandwidth consistent with the signal shown at b. This process can be described in frequency domain terms by stating that the central component of the Doppler modulation spectrum is used as a relatively noise-free reference for translating the spectrum to its original location around zero frequency.

8.7.1.2 Servoed Pulse Repetition Frequency Long-Pulse Ranging

The following description indicates in qualitative terms the way in which the pulse repetition frequency (prf) is controlled by the altitude measurement through a closed servo loop. Reference is made to the waveforms of Figure 167, and the block diagram shown in Figure 168. The diagram represents a model of the optimum range tracker described in Appendix E.

The transmitter is modulated with long pulses at a duty factor slightly less than 50 percent as represented in waveform a of Figure 167. The echo waveform, b, will show the same modulation; although, in the case of rough terrain, the waveform edges may be rounded and extended by echoes received from objects that are not directly (vertically) below. The waveform shown at c is a weighted sampling pulse. It is a cross-correlating signal used in conjunction with waveform b. The modulation pulses and the correlating function are interleaved with a variable time base. The time base is controlled by the pulse-repetition frequency. If the time scale of the figure is so adjusted that waveforms a and c always occupy the same fraction of a cycle, then a change in the prf will change the position of the echo pulses, b. Multiplication of

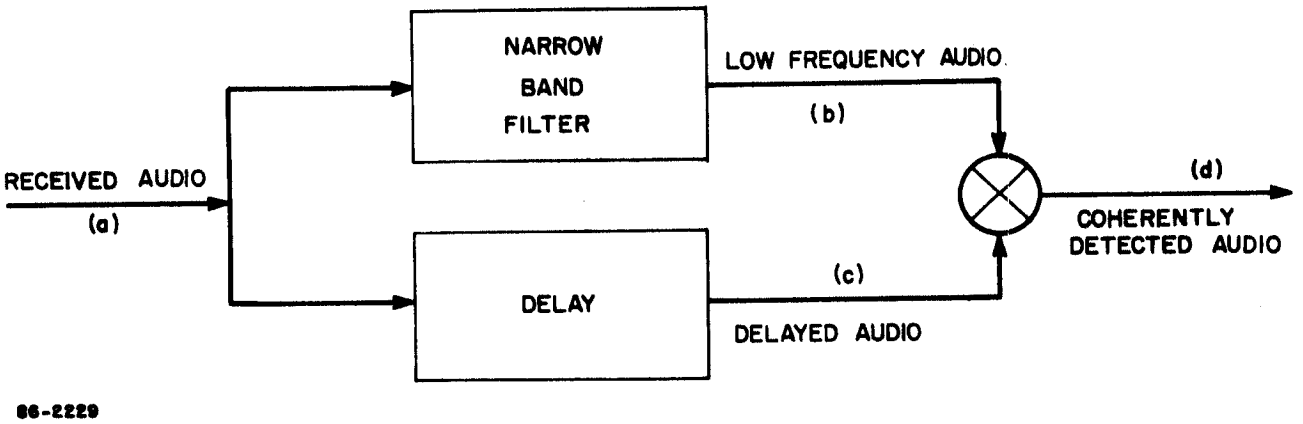

Figure 165 PRINCIPLE OF PSEUDO-COHERENT DETECTION

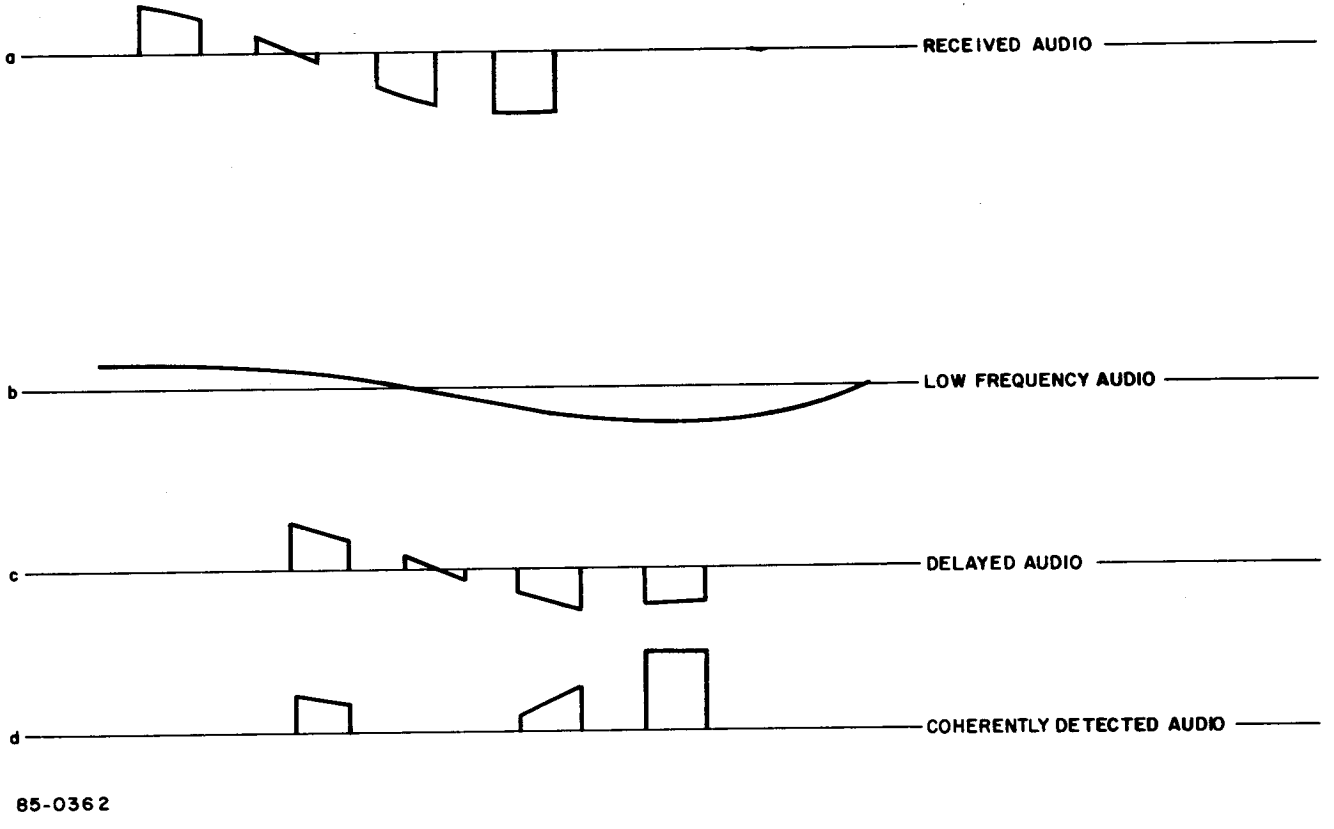

Figure 166 WAVEFORMS FOR LONG PULSE COHERENT DETECTION

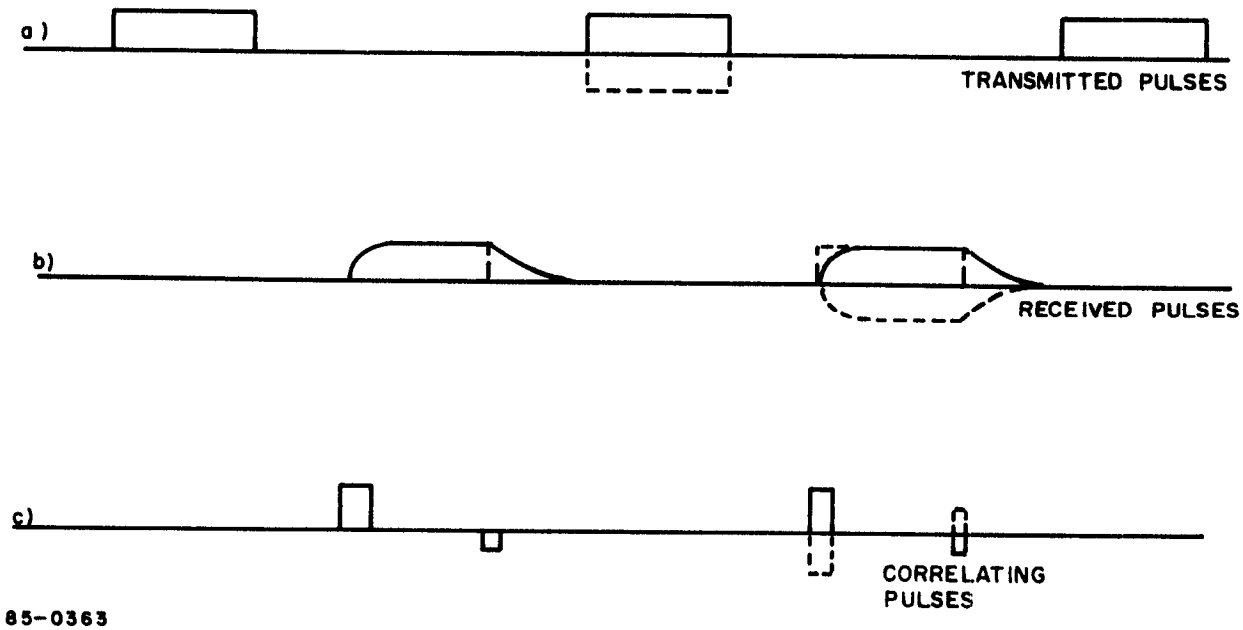

Figure 167 LONG-PULSE ICW RADAR ALTIMETER WAVEFORMS

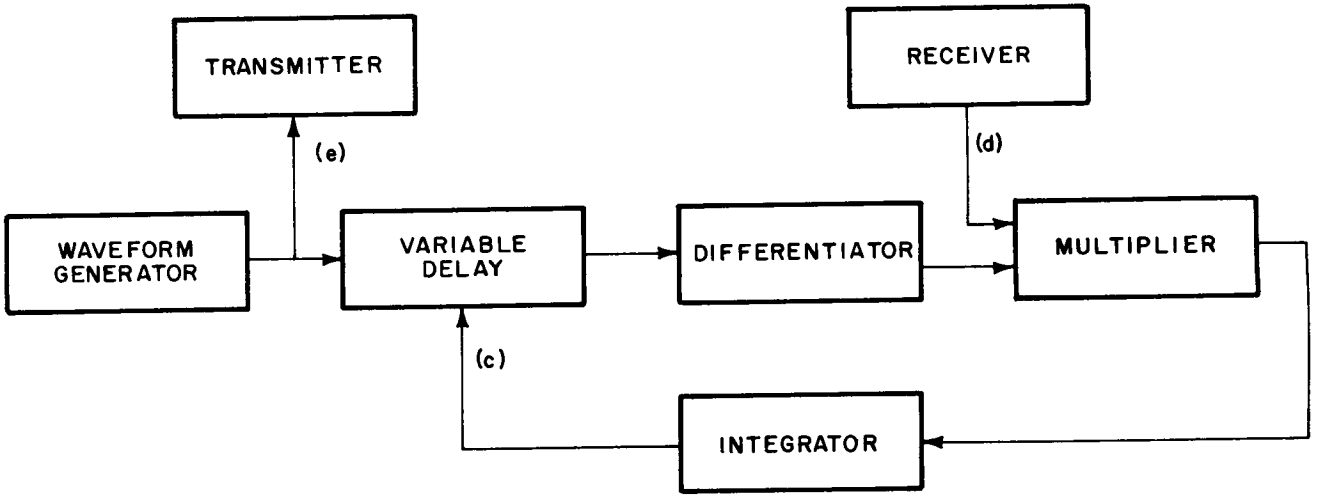

85-0349

Figure 168 OPTIMUM RANGE TRACKING RADAR

waveform b by waveform c, provides a voltage which is a measure of the relative timing between the sampling pulses c and the echo envelope b. A servo loop uses this voltage to control the prf so that the echo pulses will occur between the transmitter pulses and cause the pulse period to become the proportional analog of the altitude. The prf is now resonant in the altitude between the radar and the surface. However, ambiguous resonance will occur at all odd harmonic frequencies for a 50 percent duty-cycle system. Provision must be made to disregard the ambiguous altitude. The method of accomplishing this, together with other hardware details of the long pulse coherent altimeter system, is described in the following paragraphs.

8.7.1.3 Description of Operation

In the description of operation, which follows, reference is made to the altimeter block diagram shown on Figure 169. The numbers in parentheses refer to the corresponding blocks on the figure.

A crystal oscillator (1) provides a signal of stable frequency which is multiplied to the HF master frequency by the frequency multiplier (2). The master frequency is translated and amplified to the transmitted power level in the sidestep mixer and switch (3). The amount of sidestepping is the intermediate frequency as generated in the IF oscillator (8). During the receive period, the master frequency is fed to the mixer (5) as the local oscillator signal. After mixing, the signal is amplified in the IF amplifier (6) and heterodyned with the (local) IF signal in the single side-band mixer (7) for translation to the baseband frequency as represented wave-form a of Figure 166. The audio signal is then converted to binary form in the hard limiting amplifier (11). This allows the data processing described below to be performed exclusively with switching circuitry. The CW component of the echo is selected in the digital low-pass filter (12). The resultant signal is equivalent to waveform b of Figure 166. The wide-band signal is sampled in the sampling gate (13) and the resulting pulse is delayed in the bipolar delay flip-flop (14). The sampling pulse is generated in the modulation pulse generator (20). This pulse occurs immediately after the beginning of the receive cycle. Hence, this pulse is, in fact, the positive sampling pulse waveform c. The delay provided by the bi-polar delay flip-flop (14) is identical to that provided by the low-pass filter (12). The narrow-band signal from the low-pass filter (12) is again converted to a binary train in the limiting amplifier (15). The signals from the low-pass filter (14) and the limiting amplifier (15) are multiplied in the and gate (16) The operations of sampling, delay, and pseudo-coherent detection are performed in the opposite sequence to that described in the previous paragraphs. This reversal is permissible, since the sequence of multiplications done in the sampling gate (13)

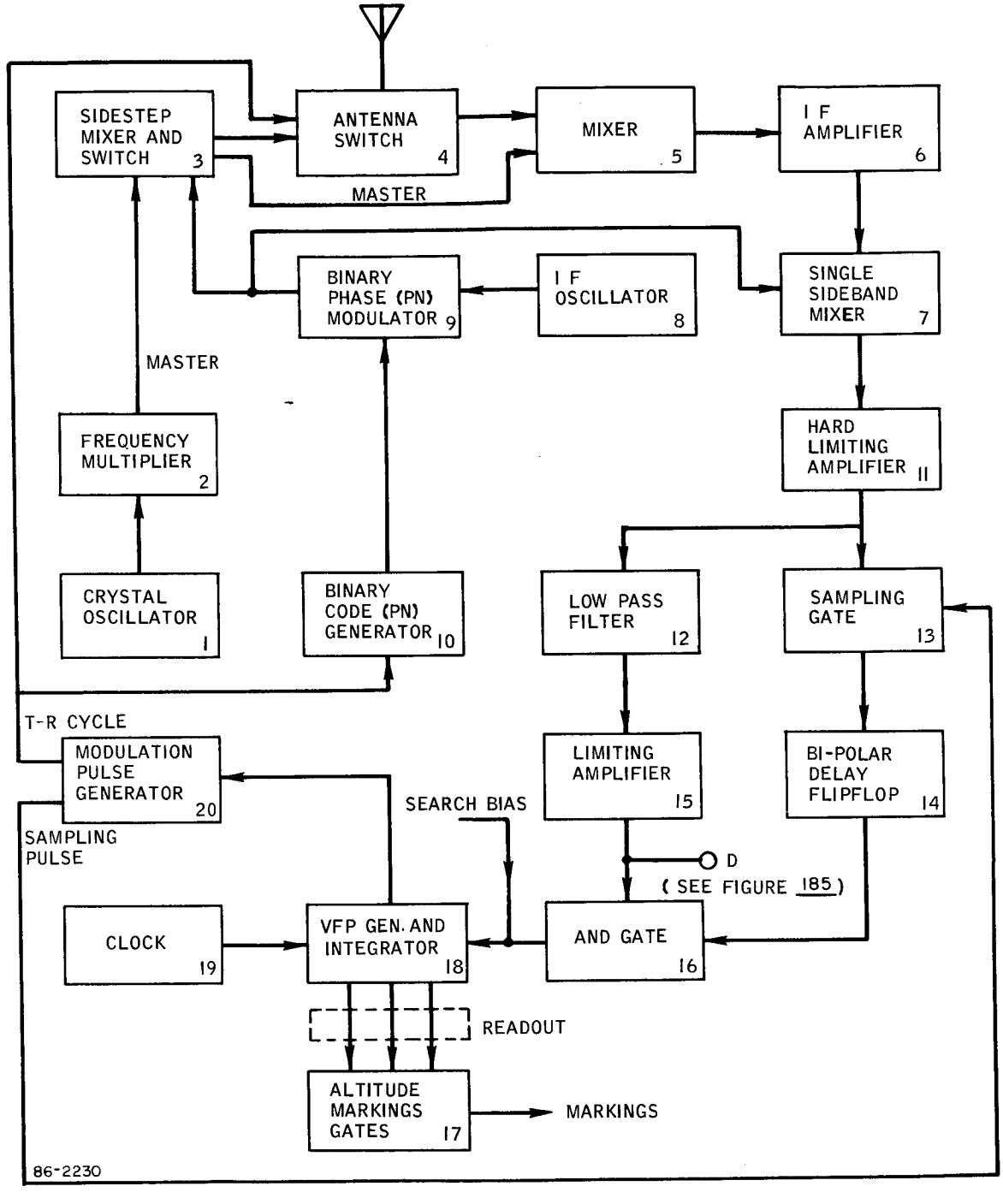

Figure 169 ALTIMETER BLOCK DIAGRAM

and the and gate (16) is immaterial, as is the timing of sampling, provided the rate is high enough. Sampling prior to delay offers an advantage, since the mechanization used to delay a single sample is much simpler than that needed for an unsampled waveform. The correlation product emerges from the and gate (16) and is subsequently integrated in the integrator (18). The latter is part of a variable frequency pulse generator, the VFPG (18). The VFPG provides the pulse train that triggers the modulation pulse generator (20). The modulation pulse governs the transmit-receive cycle and the sampling gating pulse is coupled with it. The servo loop which adjusts the prf is closed so that the echo pulse arrives just between the transmission cycles, as indicated in paragraph 8.7.1.2. For practical reasons, only the leading edge of the echo signal is tracked. The following example will indicate operation of the loop. It is assumed for the purposes of the example that the echo arrives during or before the sampling pulse. In that case, a pulse emerges from the AND gate (16). The VFPG and integrator (18) cause the sampling pulse to advance in time with respect to the echo leading edge. However, if the prf is too high, the echo arrives too late to be sampled and noise will cause ones and zeroes to emerge at random from the AND gate (16). This results in a random drift of the prf. To offset the omission of the negative trailing edge sampling, a search bias signal is inserted. This is in the form of extra zeroes. The search bias signal causes the prf to decrease in the absence of an echo signal coinciding with the sampling pulse. Since an echo always follows the transmitter pulse, this is a fool-proof search mode, and the servo loop will come to equilibrium with the sampling pulse occurring coincident with the first return leading edge (provided the received signal to noise ratio is sufficient). The binary phase modulator (9) and the binary PN code generator (10) prevent the ambiguous harmonic lock-on, referred to at the end of paragraph (3). The binary PN code generator (10) produces a pseudo-random sequence of bits for each pulse repetition cycle. This sign, or phase, label is imposed on the IF signal in the binary PN phase modulator (9) and on the transmitted signal in the sidestep mixer and switch. After reception, and only if the echo and the signal just transmitted belong to the same cycle, the PN code label is removed in the single sideband mixer (7). For instance, if the prf is exactly three times too high, the sampling pulse will coincide with the leading edge of the echo of an earlier transmitted pulse. However, the PN label of the earlier pulse is not correlated with the present pulse. As a result, the sampled signal has, effectively, zero strength, and the search bias will reduce the prf to the correct value.

8.7.1.4 Range Tracker Design Features

The theoretical operation of the automatic and continuous altitude tracker and the operation of the actual proposed tracker were presented in paragraphs 8.7.1.2 and 8.7.1.3. These paragraphs describe some

of the important performance features of the actual design. The features include: search speed, acquisition time, and false alarm error/rate.

1. Search Speed - The IF bandwidth is established by the width of the range gate. Based on the reasoning presented in paragraph 8.3.4, the width of the range gate is 2 percent of the echo delay time. Since a variable bandwidth system is undesirable, the IF bandwidth is so fixed so that it will accommodate the narrowest range gate. This corresponds to the minimum altitude. The designed lower-altitude limit of the altimeter is 18,000 feet which corresponds to a range gate of 0.7 microsecond. Hence, the IF bandwidth in the high altitude mode is 1.5 mc. A signal-to-noise ratio of +10 db is required in a 500 Hz bandwidth, as shown in Table XCVIII.

Therefore, at 250,000 feet altitude, integration of 3000 pulses $\left(\frac{1.5\ \text{MHz}}{500\ \text{Hz}}\right)$ is required to develop the minimum echo power to the +10 db SNR threshold. The search bias is set at a level appropriate for this integration requirement. Therefore, the search speed, which is the rate of progression of the altitude reading under influence of the search bias (in the absence of echo power in the range gate) is + 2 percent of the altitude per 3 seconds for the 1 kHz prf.

2. Acquisition Time -- The search speed, described in paragraph 1. above, does not apply when computing the normal acquisition time. The altimeter is designed to begin functioning at an altitude of 250,000 feet and the prf is set at 1 kHz. Unless the actual altitude is higher than 250,000 feet, the range gate will coincide with some echo signal. If the altitude is substantially less than 250,000 feet, the sampled signal is stronger than the threshold level, as can be seen from Figure 170. This is due not only to the lower altitude, but also to the fact that an increased surface area contributes to the power in the 2 percent range gate width. The increase in echo power reaches a maximum of 11 db above the threshold level*; this means that a voltage 12.6 times the search bias voltage acts in the tracker loop. Under these circumstances, the altitude reading changes at a rate of 2 percent each 0.24 second.

The acquisition time in the worst case may be determined as follows. It is assumed that the altitude at emergence from blackout is 75,000

* The 11 db improvement in acquisition time results from the fact that 1) the return from the entire surface area is utilized, causing a 17 db increase in signal power near the middle of the signal compared to that of the leading edge, and 2) the return from the entire surface can be considered as the return from an area of equivalent radar cross-section located at a slant range of twice the true altitude, thereby causing a 6 db decrease over that expected from 1., above. The net improvement is, therefore, 11 db.

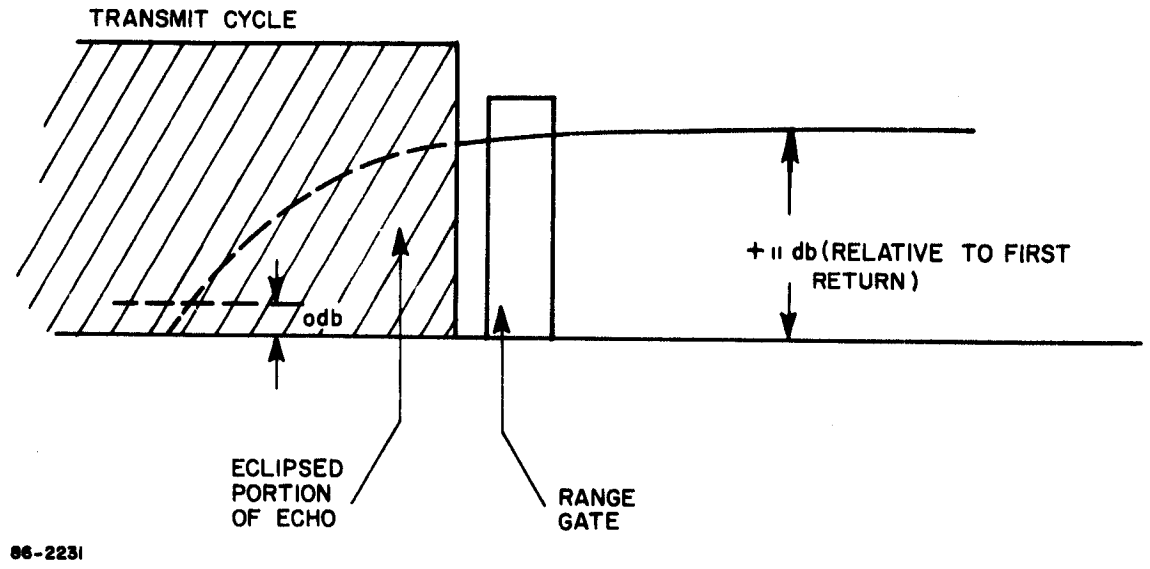

Figure 170 SIGNAL LEVEL DURING ACQUISITION

feet. Because of the reduced range, the echo power level is 10.5 times greater than the level at 250,000 feet. Hence, the rate of change of the altitude reading is 10.5 x (12.6) x 2 percent or 44 steps of +2 percent per second. The altitude misreading will be corrected in n logarithmic altitude steps of 2 percent each where n is found by $(1.02)^n = 250,000/75,000$. In the case under consideration n is 61. The acquisition time for the lowest possible altitude of emergence from blackout, therefore, is

$$\frac{61}{44} = 1.4 \text{ seconds}$$

3. False Alarm Error -- Acquisition time, as computed in 2., above, applies to a normal high altitude acquisition process and the search speed, as derived in paragraph 1, above, applies in the case of a tracker that has lost lock due to a strong noise burst. When the search bias is set at 10 db above the average noise level, the false alarm rate, Q_o, equals erf $3.2 = 5 \times 10^{-5}$. In the absence of a signal, one out of every 20,000 samples exceeds the search bias and will cause the tracker to move an erroneous step of 2 percent in altitude. Since, as shown in 1., above, the tracker requires 3000 pulses to recover from this mistake, the resulting average error is

$$\frac{3000}{20000} \times 2 \text{ percent} = 0.3 \text{ percent}$$

8.7.1.5 Readout Format

In the case of entry from approach trajectory, the relay-link data rate is low. Therefore, data derived from the altimeter must be presented to the telemetry system in the manner designed to conserve the number of bits to be handled. The altitude will be quantized in intervals consistent with the required accuracy. Thus, for an altitude accuracy of ± 1 percent, the range is quantitized in exponential steps of 2 percent. There are 280 such steps in the interval between 1000 to 250,000 feet, therefore, a 9-bit binary code would suffice to handle the data.

8.7.1.6 Ancillary Capabilities

In addition to satisfying the primary function of measuring altitude, the long pulse, coherent radar altimeter system is also capable of providing a coarse, or gross, measurement of surface wind velocity and of surface roughness. Since the wind-velocity measurement is of major importance, a 3-beam doppler velocity-attitude sensor is included in the design of the entry from orbit flight capsule to provide the required measurement accuracy. Surface roughness information and wind velocity information are both derived from spectral analysis of the return signal. The analysis may be performed either on board the flight capsule or at Earth. In the case of entry from orbit, the relay data rate is high enough to permit the sampled time waveform to be transmitted to the flight spacecraft. In the case of entry from

The approach trajectory, the relay-link data rate is so low that considerable on-board data processing will be necessary on board the flight capsule before the data is transmitted via the relay link. The data handling equipment is described in paragraph 8.9.1 and in Appendix H.

8.7.2 High-Altitude Altimeter Antenna System

In the proposed high-altitude altimeter antenna system, the entry shell of the flight capsule is used as the radiator. It is an extension of a triple-folded dipole concept in which the outer structural ring of the entry shell is excited as an antenna. The operating frequency was so chosen that its wavelength is approximately that of the circumference of the entry shell. In this concept, the radiation pattern will be similar to that of a dipole orthogonal to the plane of the vehicle and its one-half power beamwidth will be approximately 80 degrees. The on-peak gain of such a system will be approximately 3.0 db above an isotropic level.

Feasibility studies have been conducted over the past several months on a unique concept for a reentry vehicle antenna. In this approach, the vehicle itself is used as the radiator. The concept was developed early in the program in order to circumvent the possible need for cutting large holes in the vehicle skin. Since altimeter data is required prior to jettisoning the heat shield, the only reasonable alternative to large cutouts in the vehicle appeared to be use of a ring radiator. The entry shell is excited by the simple technique of connecting two balanced leads to the outer periphery of the structure at points half of a wavelength apart. For the ring to radiate, an RF choke must be used in the input network center to prevent the arm from radiating. This is equivalent to exciting only the outer arm of a triple-folded dipole.

The basic operating principle of this antenna concept may be understood more clearly if the input feeding the network of the vehicle radiator is considered to be equivalent to the center arm of a triple-folded dipole, and the external circumference of the vehicle is considered to be equivalent to the outer arm of such a dipole. Figure 171 illustrates the analogy schematically.

To demonstrate the feasibility of the above concept, it is only necessary to show that such an antenna has an on-peak gain which is very close to the on-peak gain of a free-space folded dipole; that is, 2.15 db above that of an isotropic radiator.

A test program was undertaken to evaluate the ring antenna concept which eliminates all structural and thermodynamic problems naturally associated with a resonant antenna structure. The test program included:

1. Impedance and pattern measurements on a triple-folded dipole. This was done to establish a frame of reference for measurements made on the ring antenna.

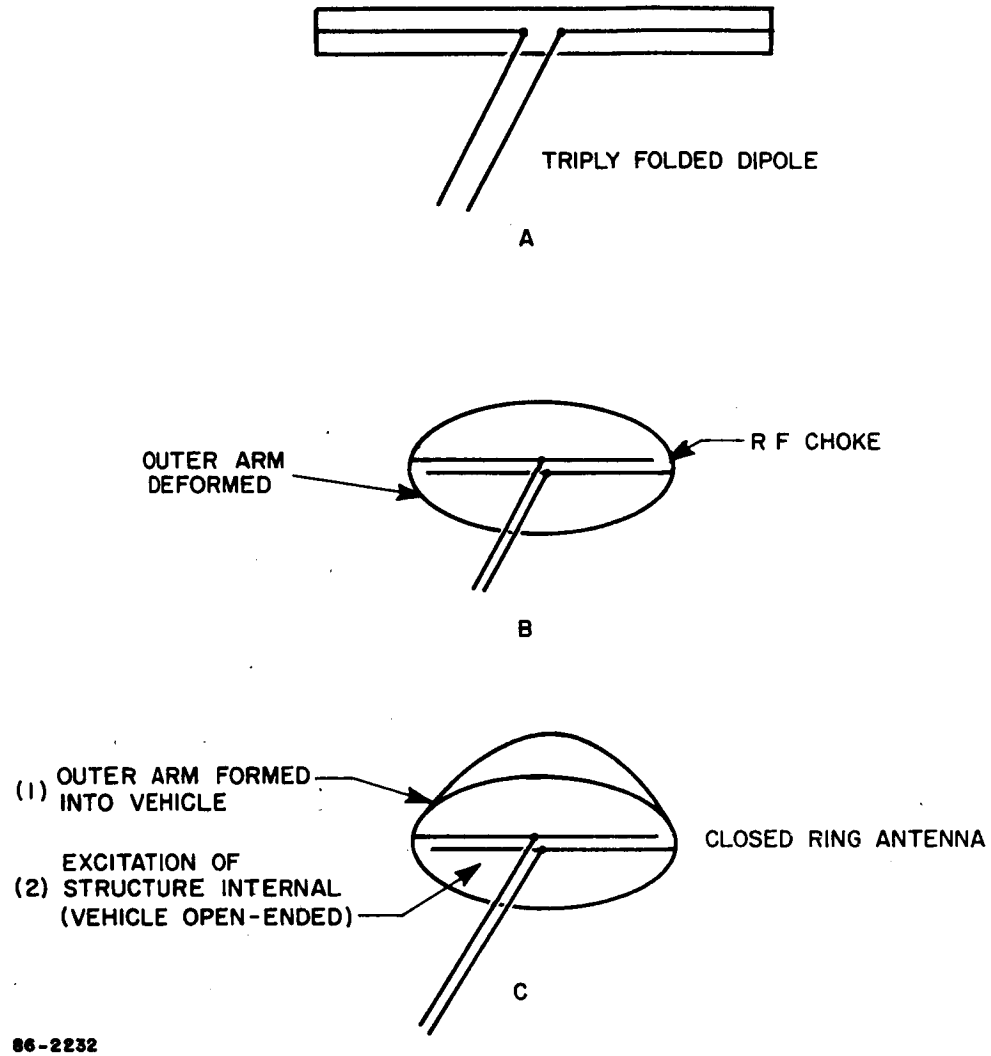

Figure 171 RING ANTENNA CONCEPT

2. Impedance and pattern measurements on a circular ring antenna backed by a conical section.

These measurements were continued until the peaks of the front and the back lobe patterns were approximately equal. This condition indicated that the center arm of the ring was not radiating. In designing a feeding network to be used in making these measurements, particular care was taken to shield the cables used to excite the external structure of the test mockup. Figures 172 and 173 show a sketch of the balun used in the test measurements and the associated impedance data for the ring antenna, respectively. It is assumed that this type of feed network design will not be necessary for the flight capsule itself since the transmitting module will possess balanced-output terminals. Figure 174 shows a schematic outline of the proposed 18 MHz ring antenna as it would be installed on the flight capsule and entry shell.

From the balanced output terminals of the transmitter, a length of the shielded two conductor line is brought to a power-splitting network, in the manner indicated on Figure 174. The two output lines are brought to the vehicle periphery from the power divider. There one side of each line is attached to the vehicle ring. The second side of each arm may be treated both as a shunt stub capable of being adjusted to tune out the reactance seen at the power dividing junction, and as a ground plane that serves to prevent the center arm of the vehicle from radiating. This feed arrangement permits efficient transition of power from the transmitter to the outer periphery of the vehicle and from there to free space.

Figure 175 is the radiation pattern of the ring antenna system. Both principal plane patters, E and H, are shown.

The similarity between these patterns and those of a free space dipole is quite striking. Half power beamwidths in the order of 80 degrees in the E-plane may be observed as well as the fact that both the dipole and ring antennas provide broad quasi-omni-directional coverage. Based on the results of the test program, it was concluded that:

1. The operating bandwidth will be limited by its input matching network. It is estimated the bandwidth will be in the order of that of a resonant loop.

2. Impedance matching can be accomplished by adjusting the on-center spacing of the two-conductor feed line. The reactive component of the input impedance of the antenna may be tuned out by properly adjusting the length of the shunt stub.

3. The ring antenna concept eliminates any structural and thermodynamic problems naturally associated with resonant structures at this frequency up to resonant antennas in the VHF band.

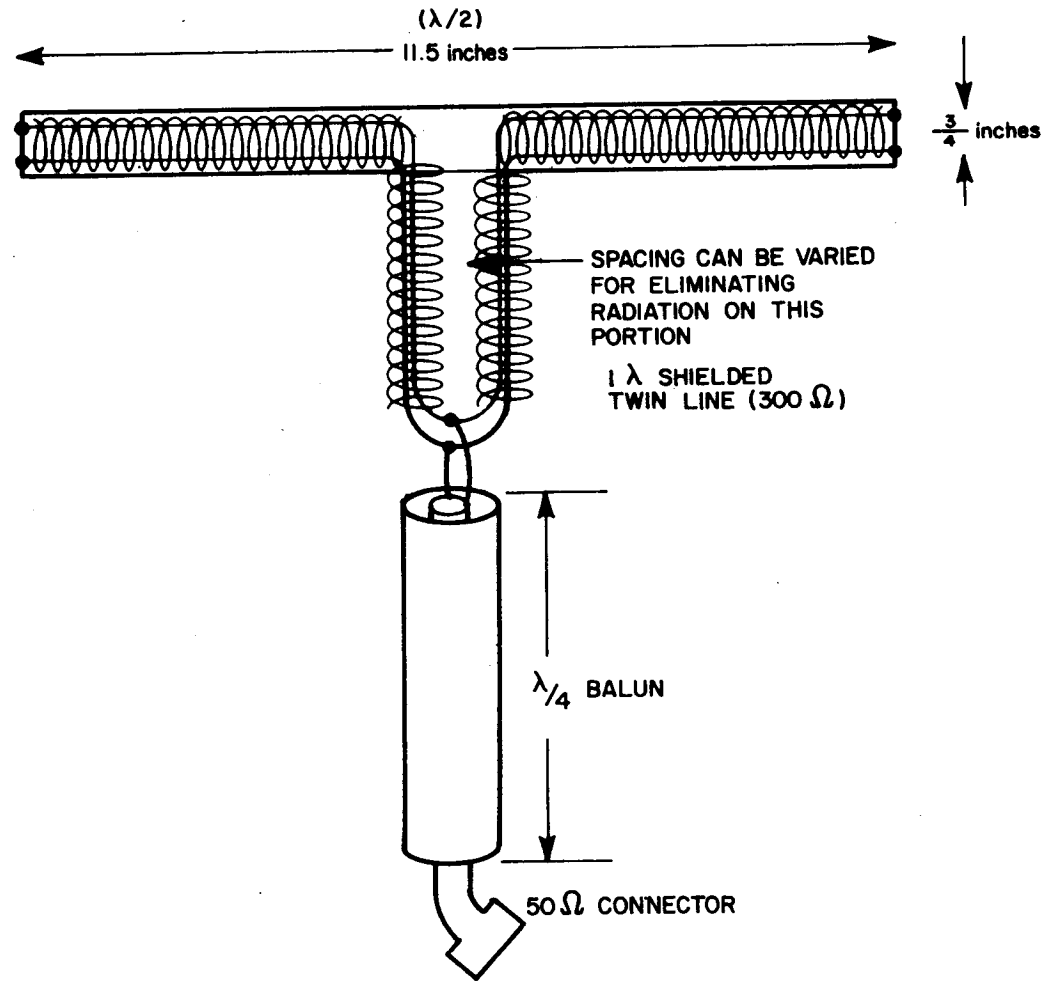

Figure 172 BALUN FOR TRIPLY FOLDED DIPOLE

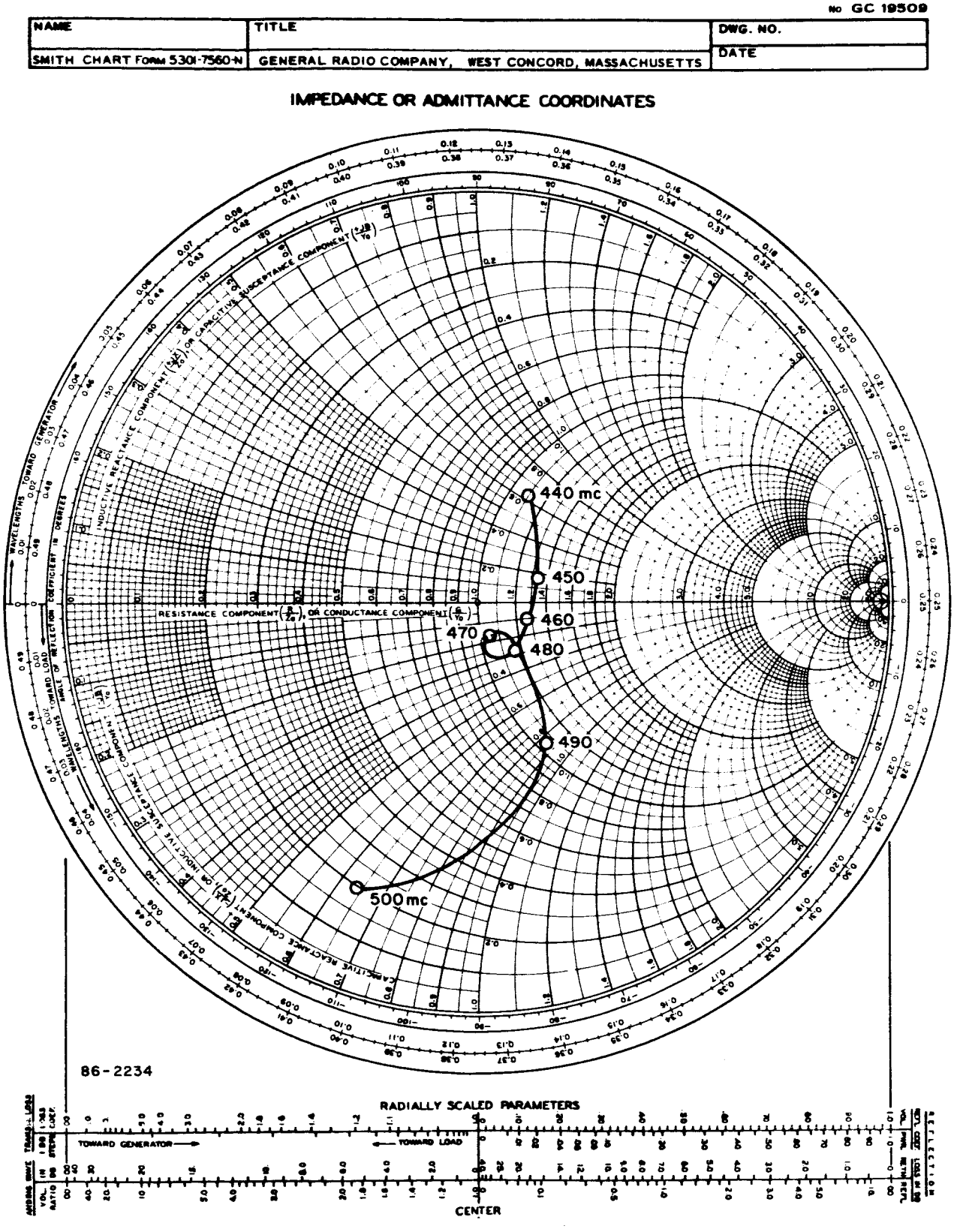

Figure 173 SMITH PLOT OF IMPEDANCE FOR TRIPLY FOLDED DIPOLE

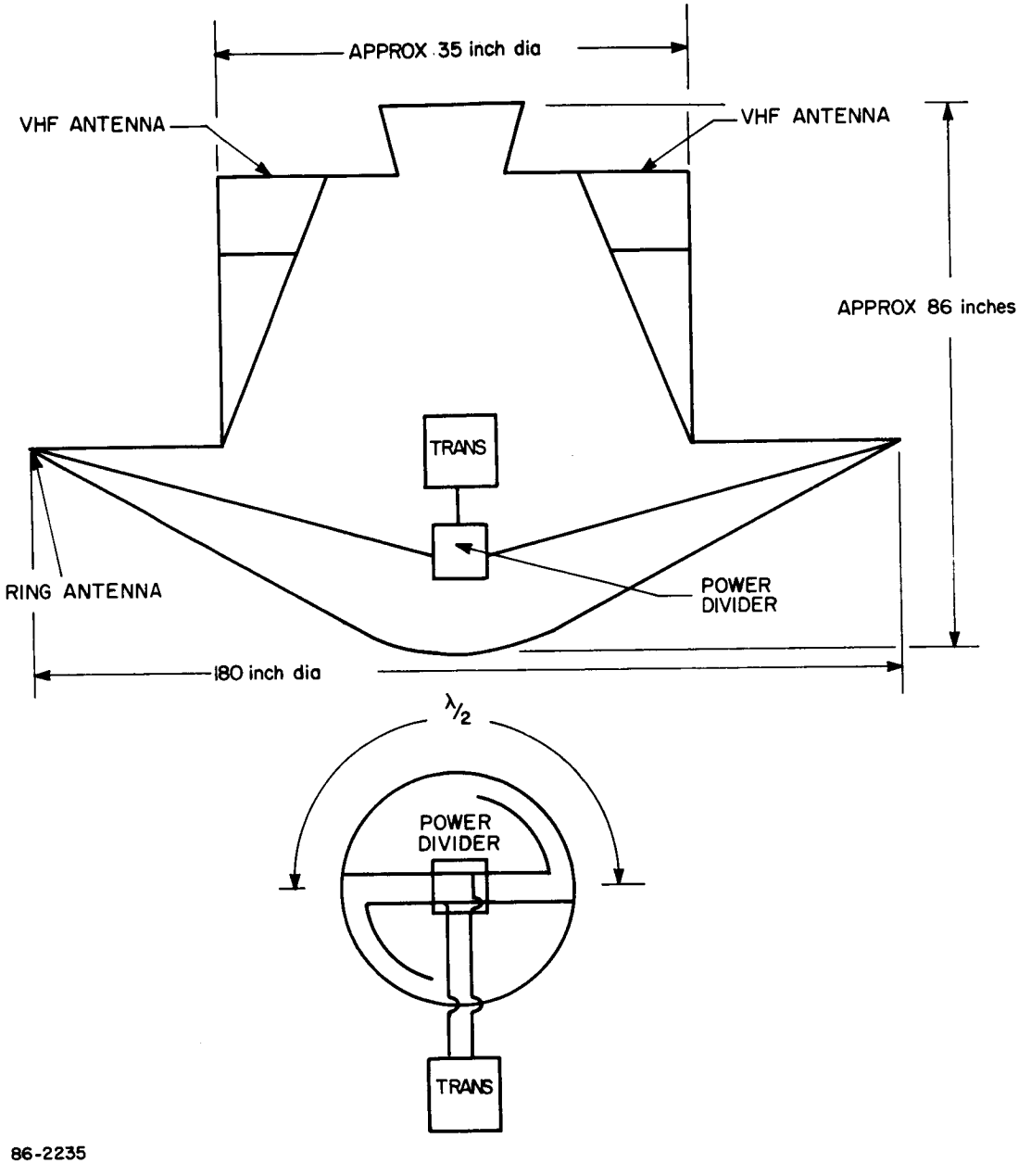

Figure 174 HIGH ALTITUDE ALTIMETER ANTENNA

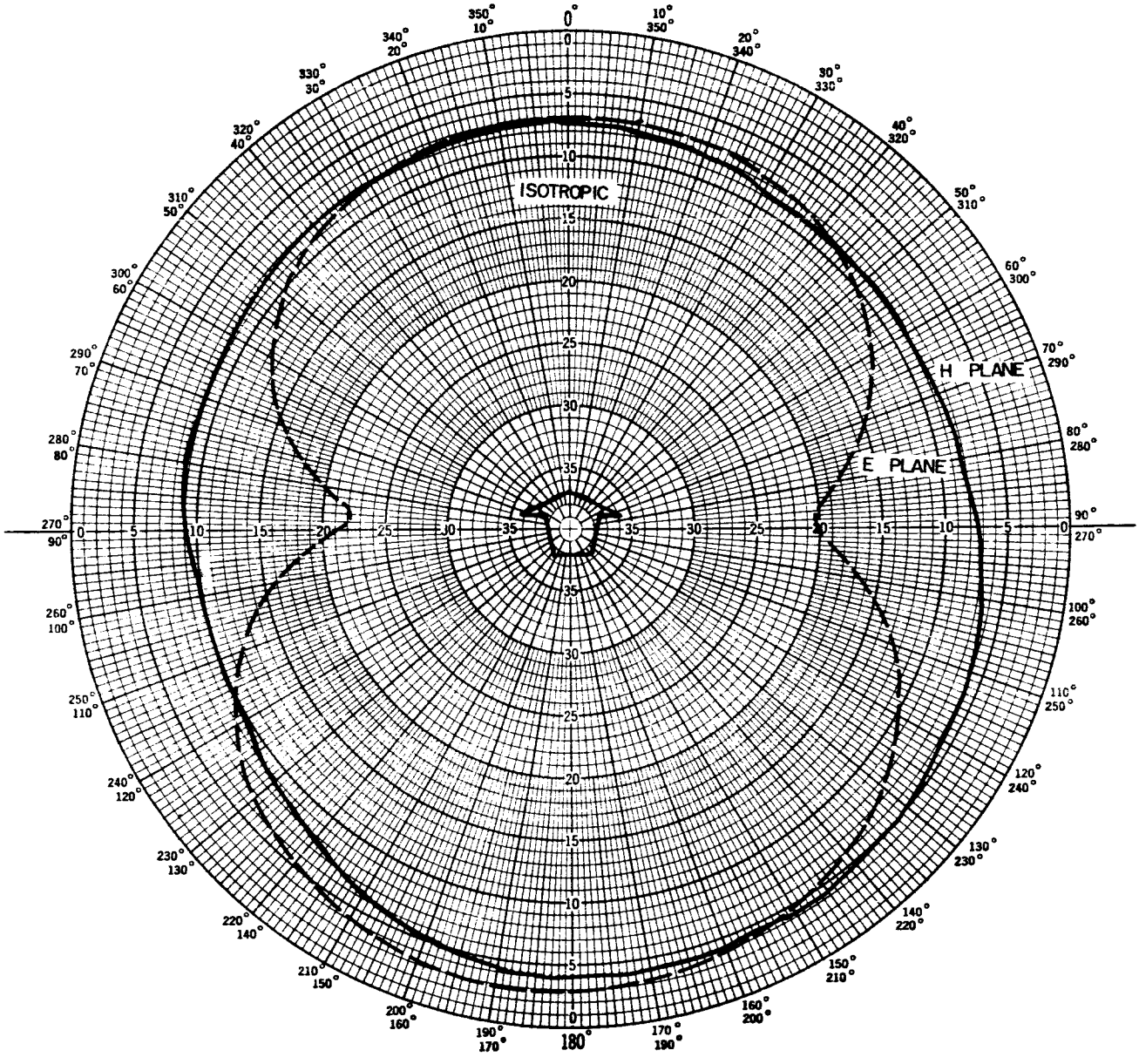

Figure 175 PATTERN MEASUREMENTS ON SCALED MODEL ANTENNA

4. The weight of the ring antenna and its input feed network is negligible.

Radiation patterns were also taken at 250 MHz on a slot antenna, flush mounted on the surface of a flat metallic ground plane. Tests were run in which the ground plane was covered with charred as well as one covered with uncharred silicone 2048. In each case the ground plane was 2-feet square and completely covered by a 0.250-inch thick layer of silicone 2048. The loss due to the charred dielectric (0.050-inch char layer) was negligible. Figures 176 and 177 show the patterns with and without the char layer, respectively. Projecting these results to the flight capsule with its purple blend heat shield, which is fabricated from a 66 percent silicone base, it was concluded that performance of a high altitude radar altimeter system operating at a frequency of approximately 18 MHz would not be seriously degraded during entry into the Martian atmosphere.

8.8 LOW-ALTITUDE RADAR ALTIMETER SUBSYSTEM DESCRIPTION

8.8.1 General

As noted previously, the low-altitude radar altimeter and the high-altitude radar altimeter both share the same electronic equipment. The principle differences between the two systems are the frequency of operation, the transmitted power, and the antennas. Frequency selection and transmitter power determination considerations were presented in paragraph 8.4. The low-altitude radar altimeter is described in paragraph 8.8.2.

8.8.2 Low-Altitude Antenna System

Several alternative designs were considered for the low-altitude altimeter. The two principal candidates were a pair of crossed slots fed in phase quadrature, and a planar logarithmic spiral antenna. The response of the logarithmic spiral antenna to a circularly polarized antenna is higher in the ± 90 degrees angular sectors than is the response of the crossed slot. This is attributed to the lower axial ratio of the spiral antenna. In other respects, however, the patterns for the spiral and the crossed slot antennas are quite similar. The low altitude antenna performing the dual function of receiving data from the penetrometer, and of transmitting and receiving RF power for the altimeter system. Since the penetrometer itself will be transmitting RF energy which is predominantly linearly polarized, a receiving antenna that is nearly circularly polarized for frequencies in the vicinity of 400 MHz will yield the most uniform coupling response. The axial ratio of the antenna will be allowed to approach 6.0 db. The axial ratio will increase as the operating frequency is lowered and finally will degenerate into linear polarization at the 324 MHz frequency required for successful operation of the altimeter system. Because of

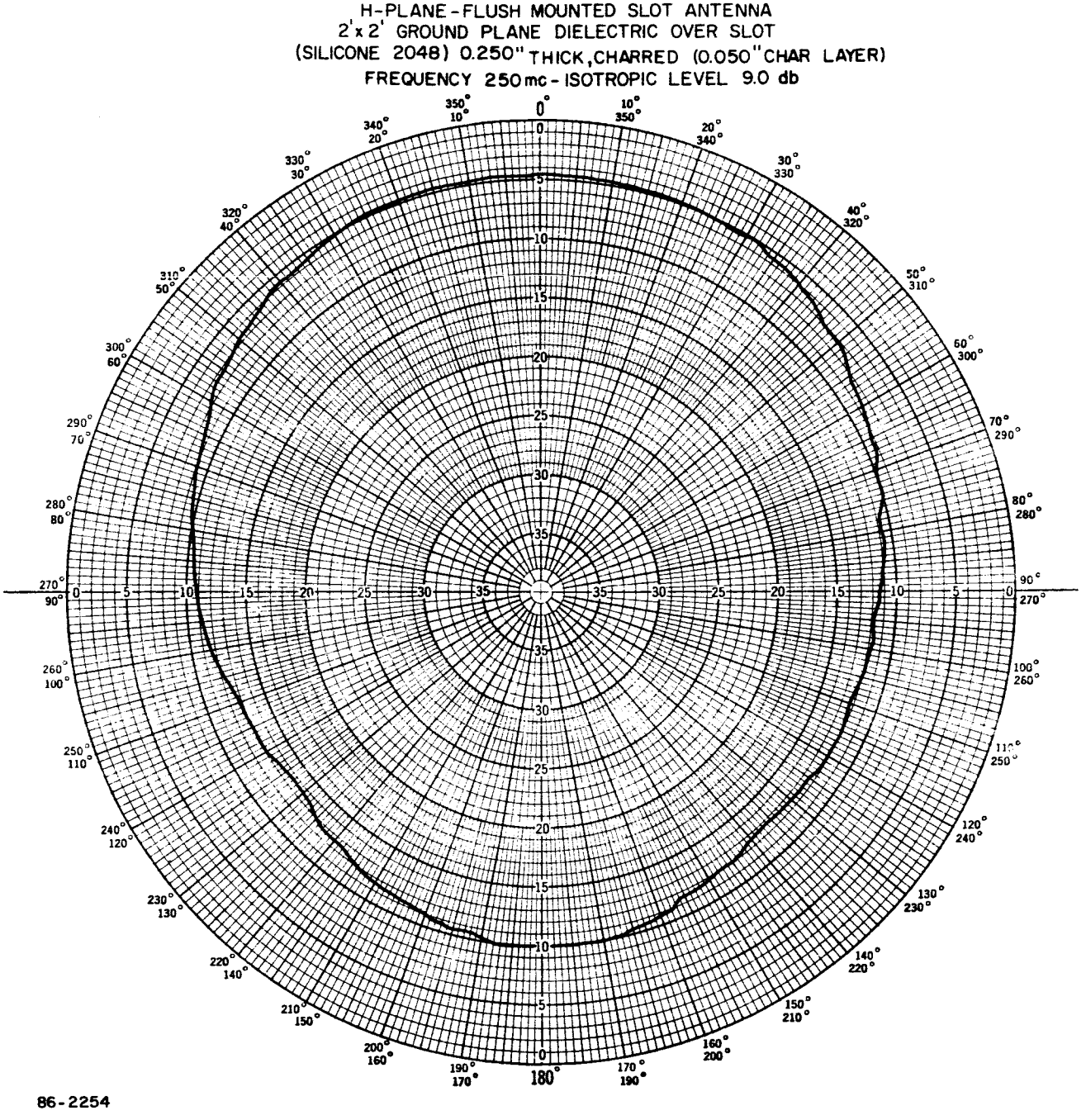

Figure 176 PATTERN MEASUREMENTS FOR SLOT ANTENNA WITH CHARRED DIELECTRIC

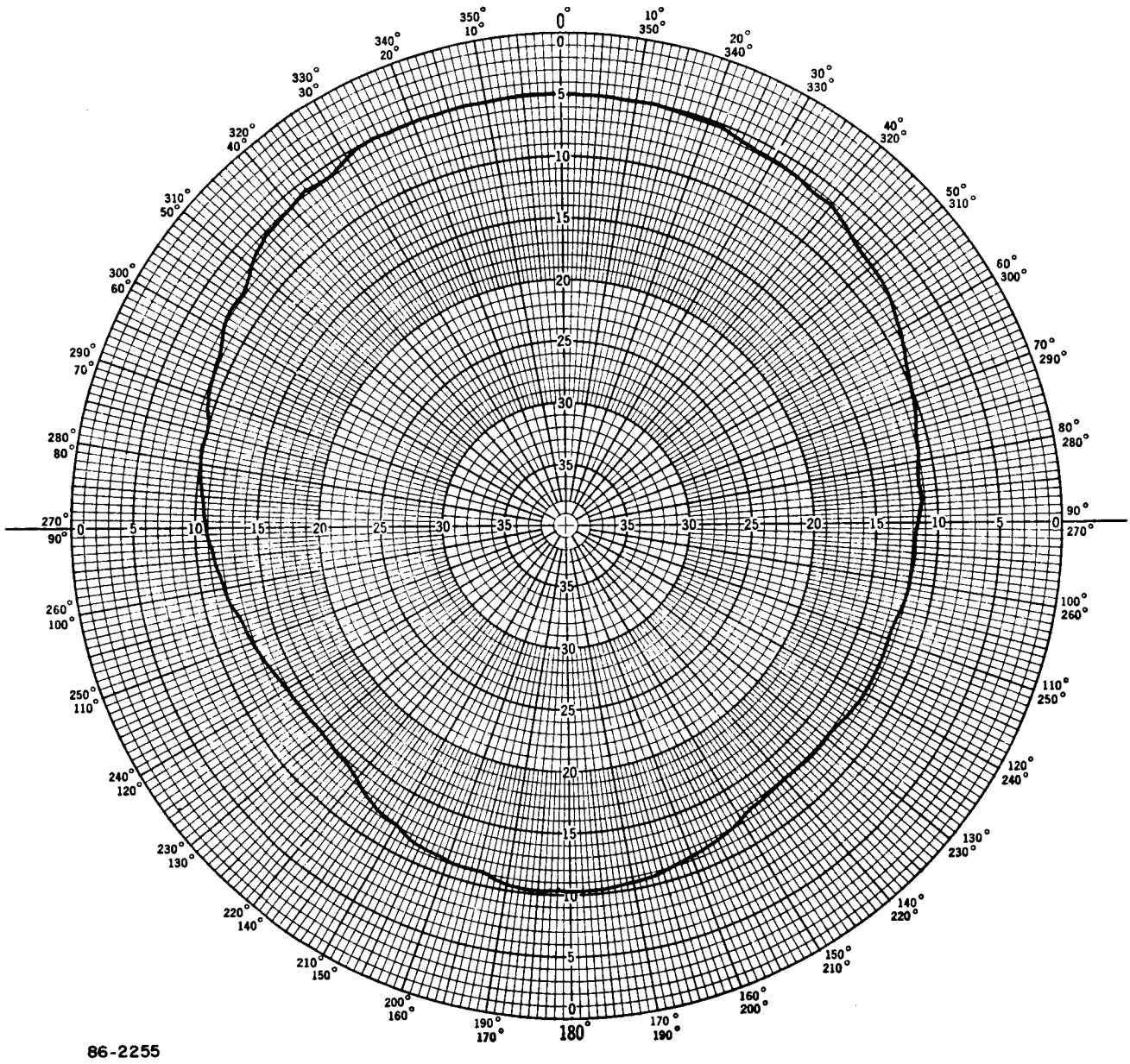

Figure 177 PATTERN MEASUREMENTS FOR SLOT ANTENNA WITHOUT CHARRED DIELECTRIC

the broadband coverage requirement 324 to 400 MHz, the planar logarithmic spiral antenna was selected for the low altitude system. Proper adjustment of the spiral arm length will permit this controlled axial-ratio response. Figure 178 shows the axial-ratio response versus the arm length of a logarithmic spiral antenna. A drawing of the logarithmic spiral antenna, complete with basic dimensions, is shown on Figure 179. Characteristics of this type of antenna are listed on Table CII.

The planar logarithmic spiral is described by the following equations:

$$P_1 = Ke^{a\phi}$$

$$P_2 = Ke^{a(\phi-\delta)}$$

TABLE CII

324 MHz SPIRAL ANTENNA

Mechanical Characteristics		
	Diameter	15 inches
	Height	8.2 inches
	Volume	4200 in.^{3}
	Weight	8 pounds
	Mounting	Recessed, flush
		Mounting Holes on flange
	Aperture radome	Teflon
Electrical Characteristics		
	Frequency	324 MHz
	Input impedance	50 OHMS
	Input VSWR	2:1
	Polarization	Linear
	Gain	6 db
	Beamwidth	3 db - 90 - 100 degrees
		10 db - 170 - 180 degrees

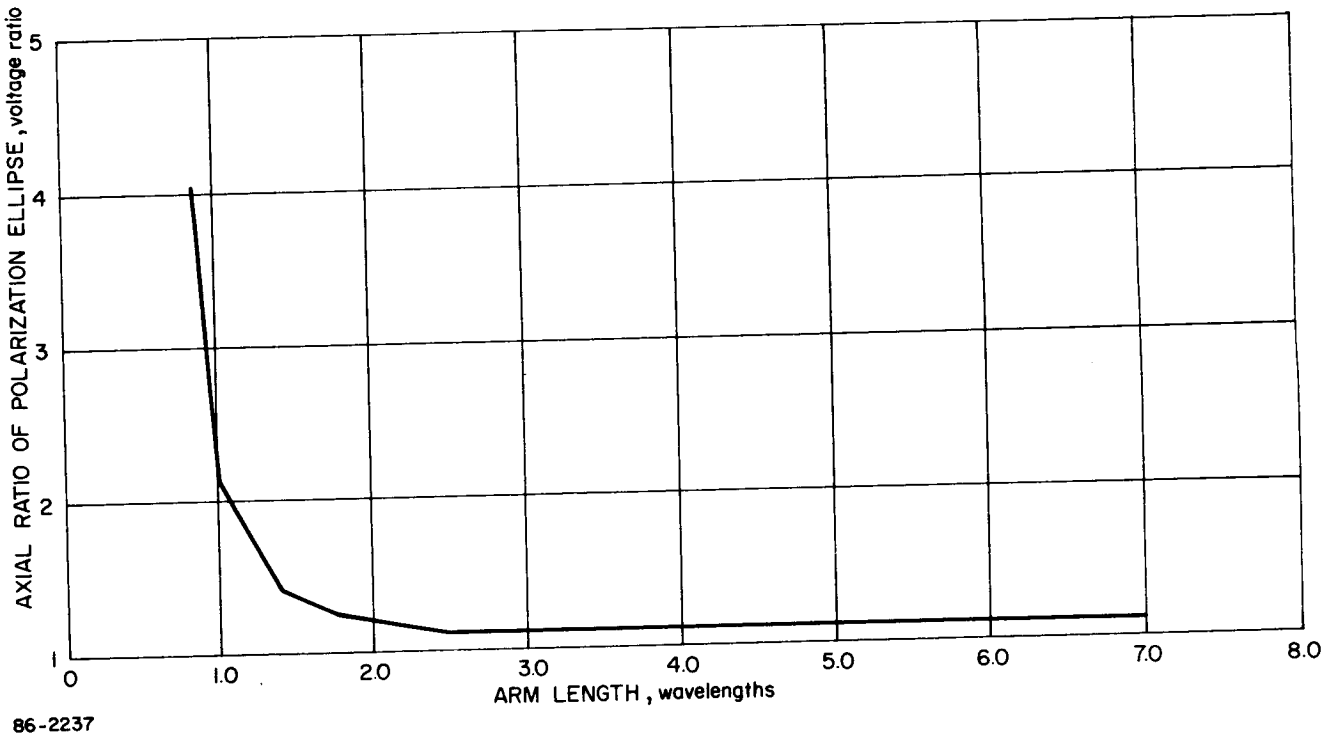

Figure 178 POLARIZATION OF RADIATION FIELD VERSUS ARM LENGTH FOR LOG SPIRAL ANTENNA

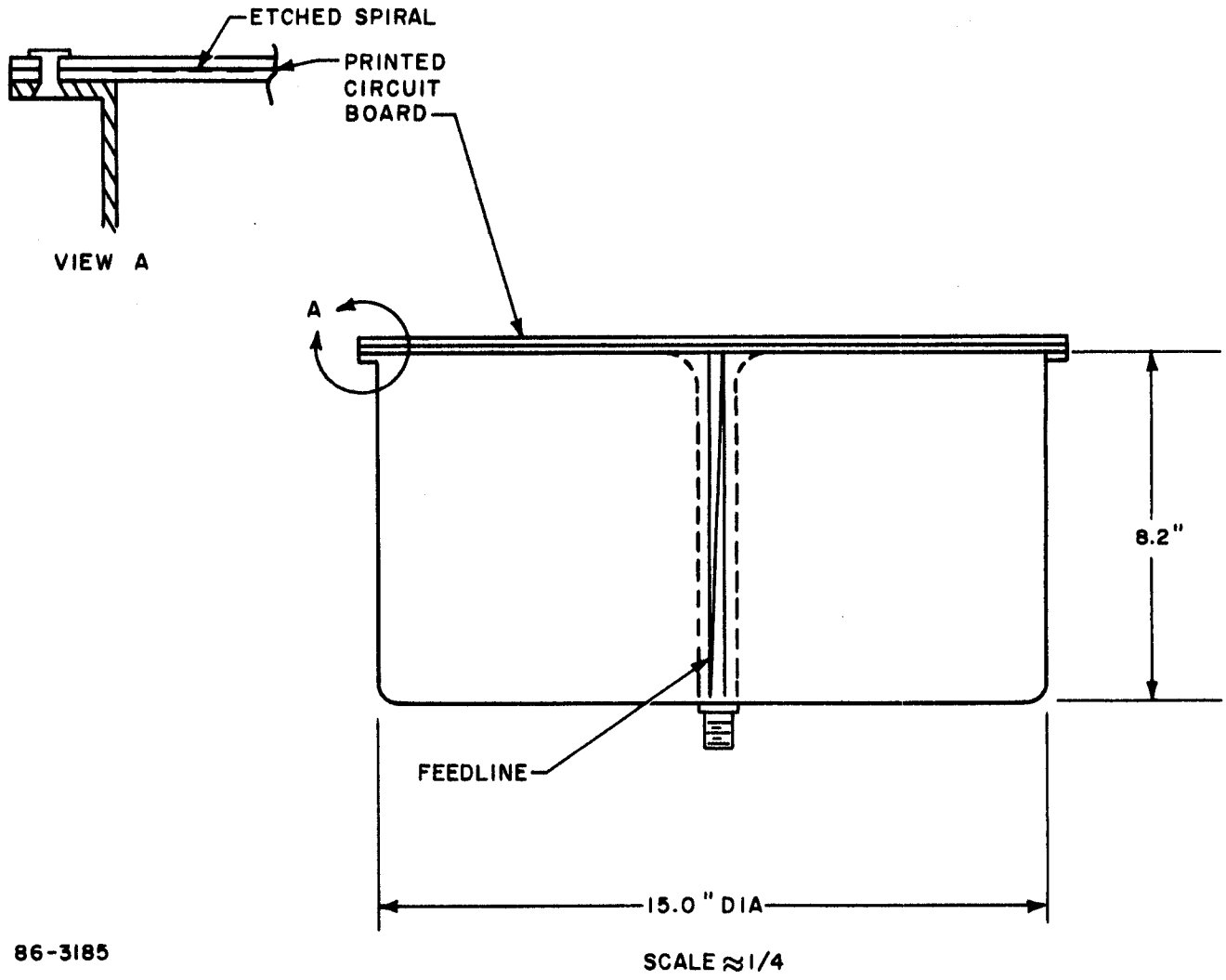

Figure 179 DIMENSIONS OF LOG SPIRAL ANTENNA

P_1, P_2 = edges of one arm.

ϕ = angle of revolution (which determines arm width)

K = determines the size of the terminal region.

a = controls the rate of the spiral.

Model spiral antennas were fabricated and tested. The following-listed parameters were used during the test program:

Scale frequency = 1510 MHz

Diameter (scaled) = 3.21 inches

α = 82.78 degrees

$a = \cot \alpha = 0.1268$

Number of turns = 4.42

δ = 90 degrees

K = 0.0473

Patterns were taken through four principal planes. The measured on-peak gain was approximately 7.0 db above an isotropic level. An on-beam peak axial ratio value of 3.75 db was obtained. Figure 180 shows the principal plane patterns of the antenna.

It is well known that the bandwidth of a planar logarithmic spiral may be extended to 20:1 or greater if measured in free space as a bi-directional radiator. In practical applications, bandwidth is limited primarily by the matching balun and the cavity used to convert the antenna into a uni-directional radiator. Some effort was expended in an attempt to increase the bandwidth of the cavity. The following paragraphs summarize the results of this effort.

Figure 181 illustrates the effect of cavity depth, s , on the gain on a spiral antenna. The data presented there demonstrates one of the major limitations on the operating bandwidth of a cavity-backed spiral antenna. If the designer is willing to tolerate a 3-or 1-db reduction in gain at the band edges, the resultant useable antenna bandwidths are 3:1 and 1.8:1, respectively. These conditions suffice for narrow band operation but are incompatible with the broad-band characteristics of the spiral antenna circuit. Several methods of achieving a broad-band cavity have been reviewed and are described below.

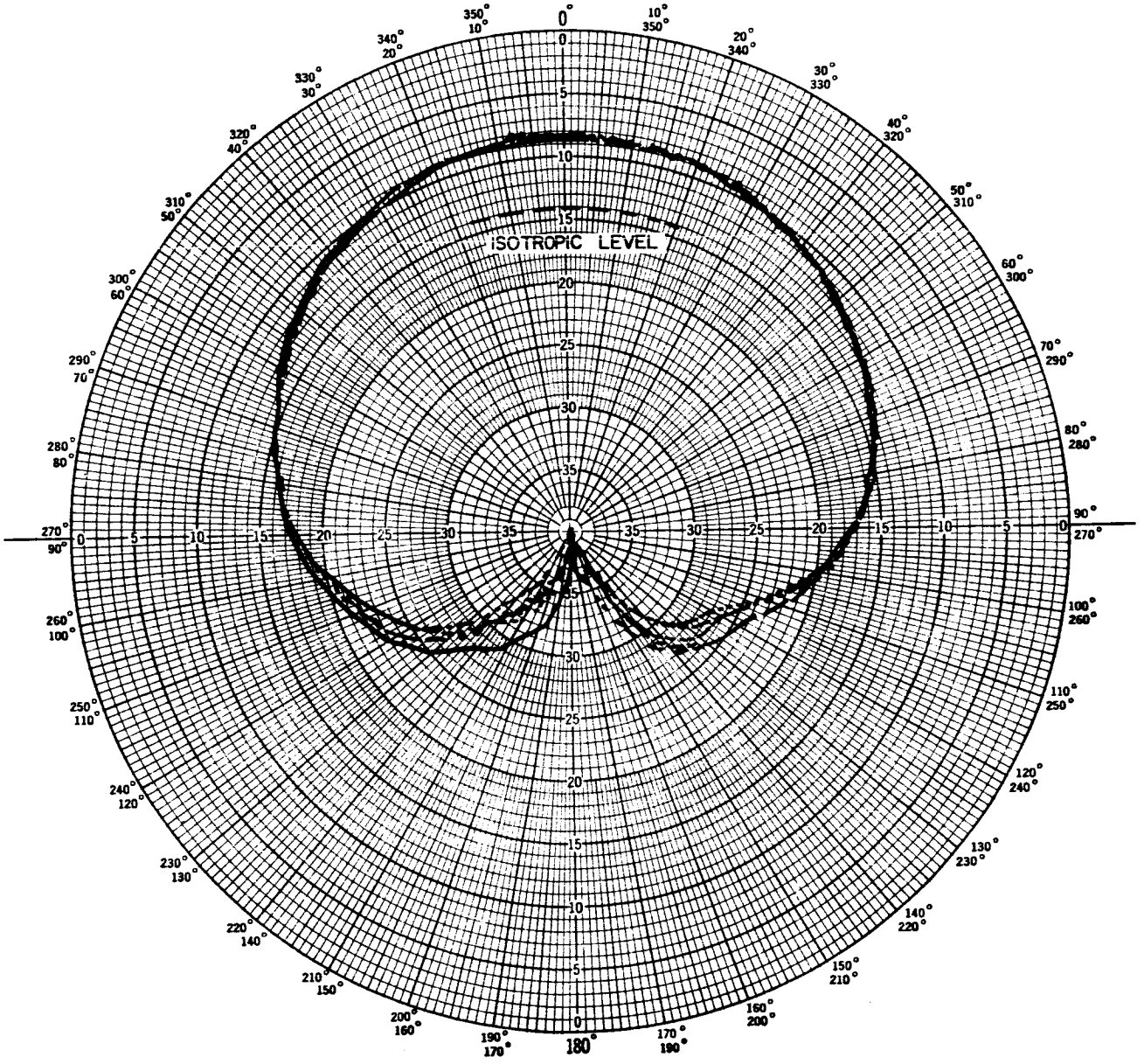

86-2239

Figure 180 PATTERNS FOR PRINCIPAL PLANES OF LOG SPIRAL ANTENNA

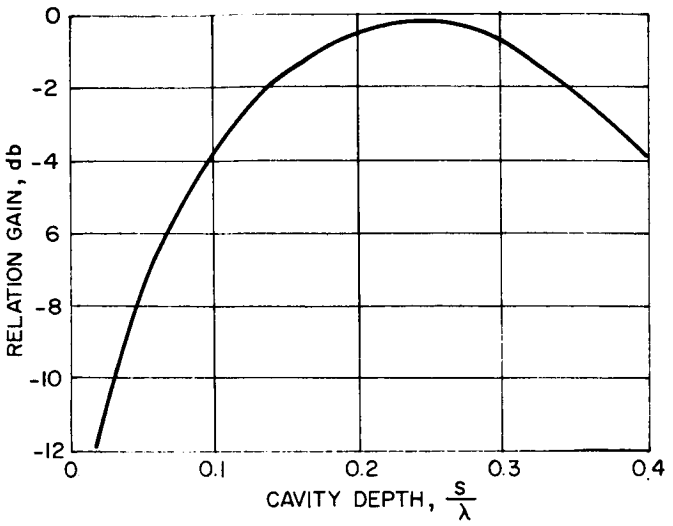

Figure 181 CAVITY DEPTH VERSUS GAIN

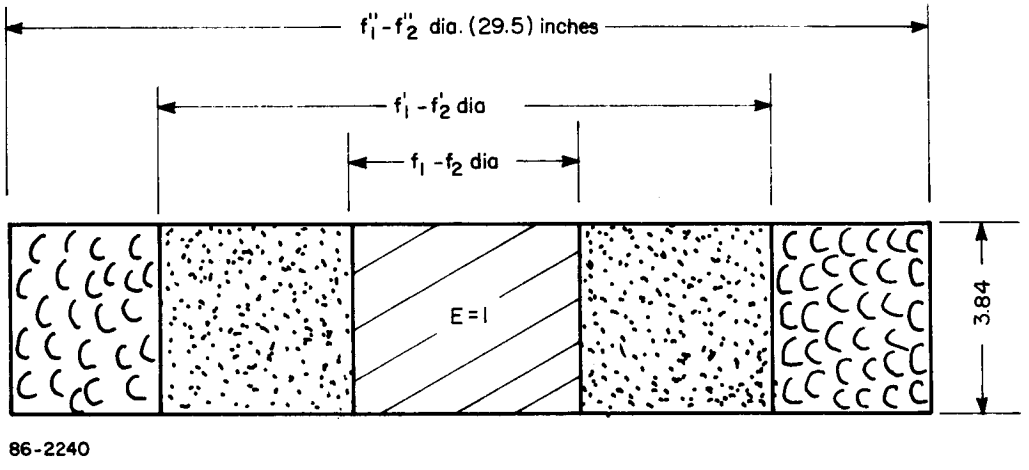

Figure 182 DIELECTRIC LOADED CAVITY

One method consists of loading the cavity with annular segments of low-loss dielectrics whose outside and inside diameters (OD and ID) correspond to a band of frequencies having a -1 db taper from some given frequency, f_o . This technique is illustrated in Figure 182. The frequency range over which each segment operates is shown in Figure 183 which presents data for the antenna bandwidths from 200 to 1000 MHz. For the particular antenna under consideration, a compromise was made between bandwidth and physical size. If the lower limit were reduced to 100 MHz, the antenna diameter would have to be doubled. If this design approach were applied to an antenna with a 10 to 1 bandwidth in the 100 to 10,000 MHz frequency range, the antenna package would have a diameter of 4.5 inches and a height of the order of 1 inch.

A second method of achieving broad-band operation is based on use of a sophisticated annular segment arrangement. This approach involves use of non-homogeneous dielectrics. Dielectric manufacturers now make available dielectric materials whose dielectric characteristics vary as a function of linear measure. These materials are obtained by blending certain materials of different specific gravities. When these compounds attain the desired state of equilibrium, the mixture is allowed to harden into blocks, rods, sheets, etc. as desired. Radial variations in cylindrical shapes can also be achieved by placing the dielectric fluid mixture into a special hardening centrifuge. This allows the dielectric mixture to arrange itself in a circular manner. The obvious advantage of using such a dielectric is a reduction in machining time.

A third technique of achieving broad-band characteristics is based on use of frequency-dependent dielectrics. The dielectric constant, ϵ of barium titanate, for example, will vary from $\epsilon = 100$ at 100 MHz to $\epsilon = 400$ at 1000 MHz. This compound, however, exhibits a high loss tangent.

An alternative to the use of frequency-dependent dielectrics is to load the cavities with dielectric materials in the manner shown in Figure 184. By suitable arrangement of angles α and β, and dielectrics ϵ' and ϵ'', distance h can be made equal to $\lambda/4$ over the designed operating frequency range of the antenna. This type of loading could possibly eliminate the -1 db taper in gain.

One problem associated with use of the logarithmic spiral antenna configuration may be the temperature extremes that will be experienced during the sterilization cycling and during descent onto the Martian surface. Descent temperatures may range from +300 to -100°F. This problem may be circumvented, however, by properly designing the structure of the antenna.

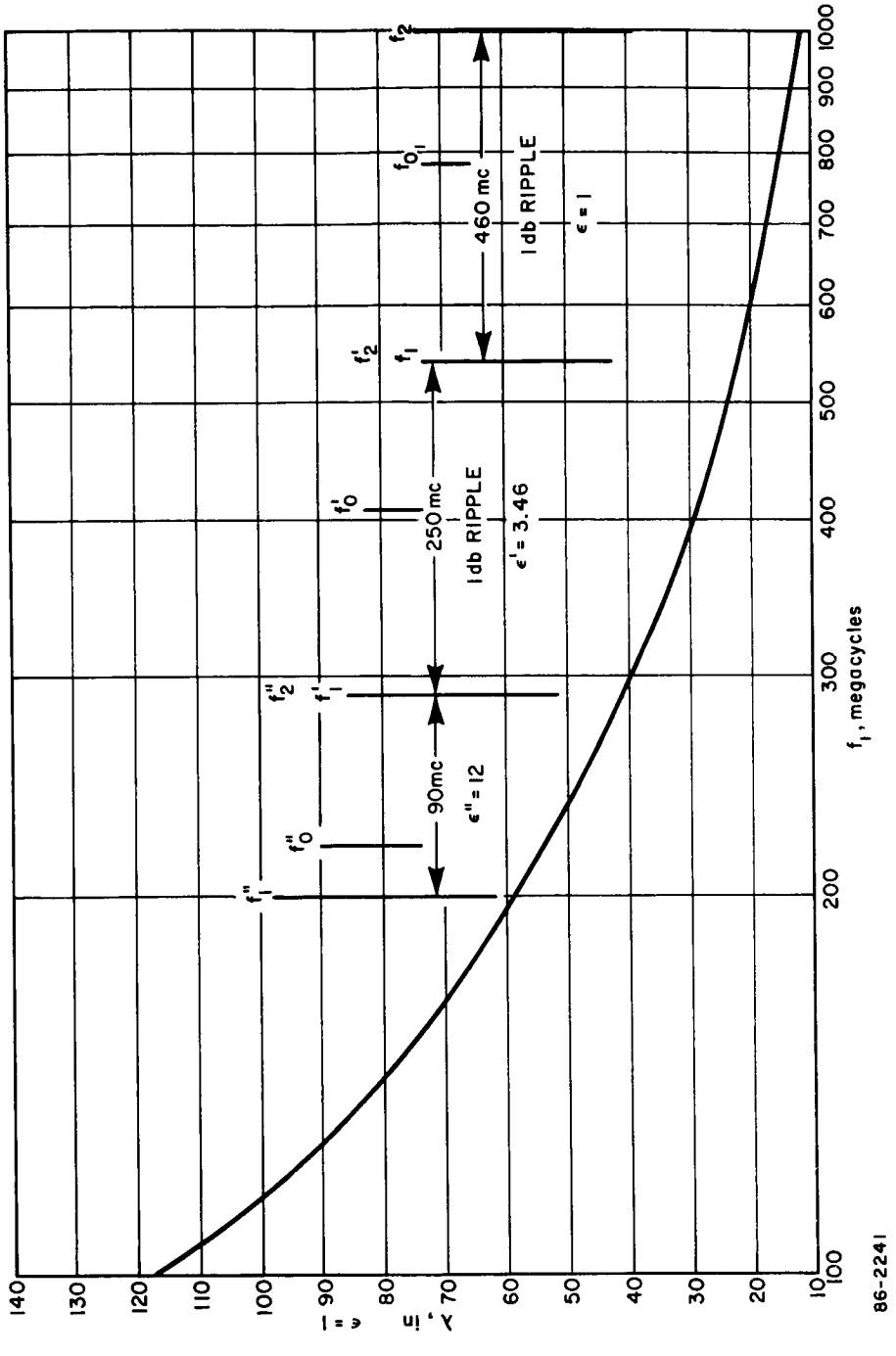

Figure 183 BANDWIDTH TAPER FOR 3 DIELECTRICS

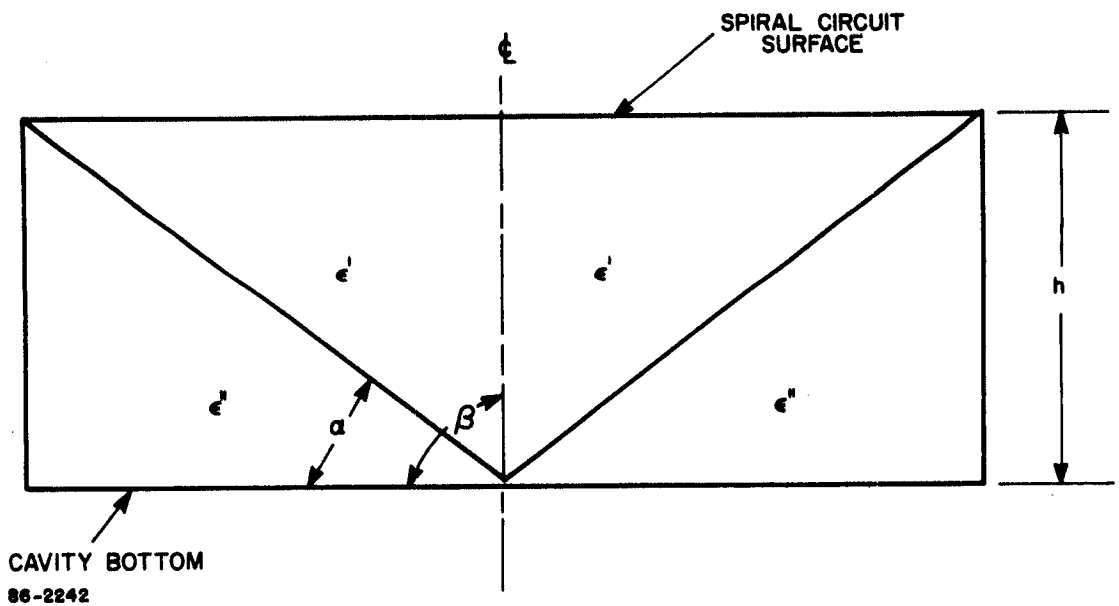

Figure 184 TAPERED COMPOSITE DIELECTRIC LOADING OF CAVITY

8.9 WIND MEASUREMENT SYSTEM DESCRIPTION

Selection of the radar technique used to measure wind velocity is based on the mode of entry of the flight capsule into the Martian atmosphere. The differences are in the areas of measurement accuracy, complexity, antenna design equipment, weight, and power consumption. The wind measurement radar subsystems used for entry from orbit and for entry from the approach trajectory are described in paragraphs 8.9.1 and 8.9.2.

8.9.1 Entry From Approach Trajectory Design

8.9.1.1 General

In entry from approach trajectory mode the flight capsule survives impact. A light-weight thermoelectric anemometer is then used to provide the primary measurement of wind velocity after impact. Since payload weight is already limited by the need for an impact attenuator, a scheme to obtain wind-velocity information during descent without need for additional equipment led to a consideration of using the radar altimeter of the flight capsule for this and for other reasons. Wind velocity is obtained from the altimeter-radar return by measuring the bandwidth of the diffuse spectrum. The mechanization necessary to obtain this data is described in paragraph 8.9.1.2 It is worth noting that by forming the ratio of the power in the diffuse echo to the power in the specular echo, the same equipment may also be utilized to obtain an estimate of surface roughness.

8.9.1.2 Reference Design

The processor shown in functional block diagram on Figure 185 operates as follows. The input signal is the hard-limited narrow band signal taken from point D as shown on Figure 169. The transients in this signal contain the information on the Doppler period. This information is processed to yield averaged parameters. From these, the surface roughness and wind velocity can be estimated. In the following description, the block numbers used refer to correspondingly numbered blocks on the data-processor diagram Figure 185. The transients in the Doppler audio set the counter (1) and load the buffer register (2). The counter (1) measures the Doppler period τ_k in terms of the number of clock pulses received from the clock (19) between two consecutive positive transients. Thus, each positive transient terminates a count, τ_k , in the counter (1) and initiates a new count. Meanwhile, τ_k is transferred into the buffer (2). The previous count, τ_{k-1}, stored in the buffer (2) is sent into the comparator (3), which determines which of two consecutive periods is larger and identifies the result as positive or negative. A train of pulses of the

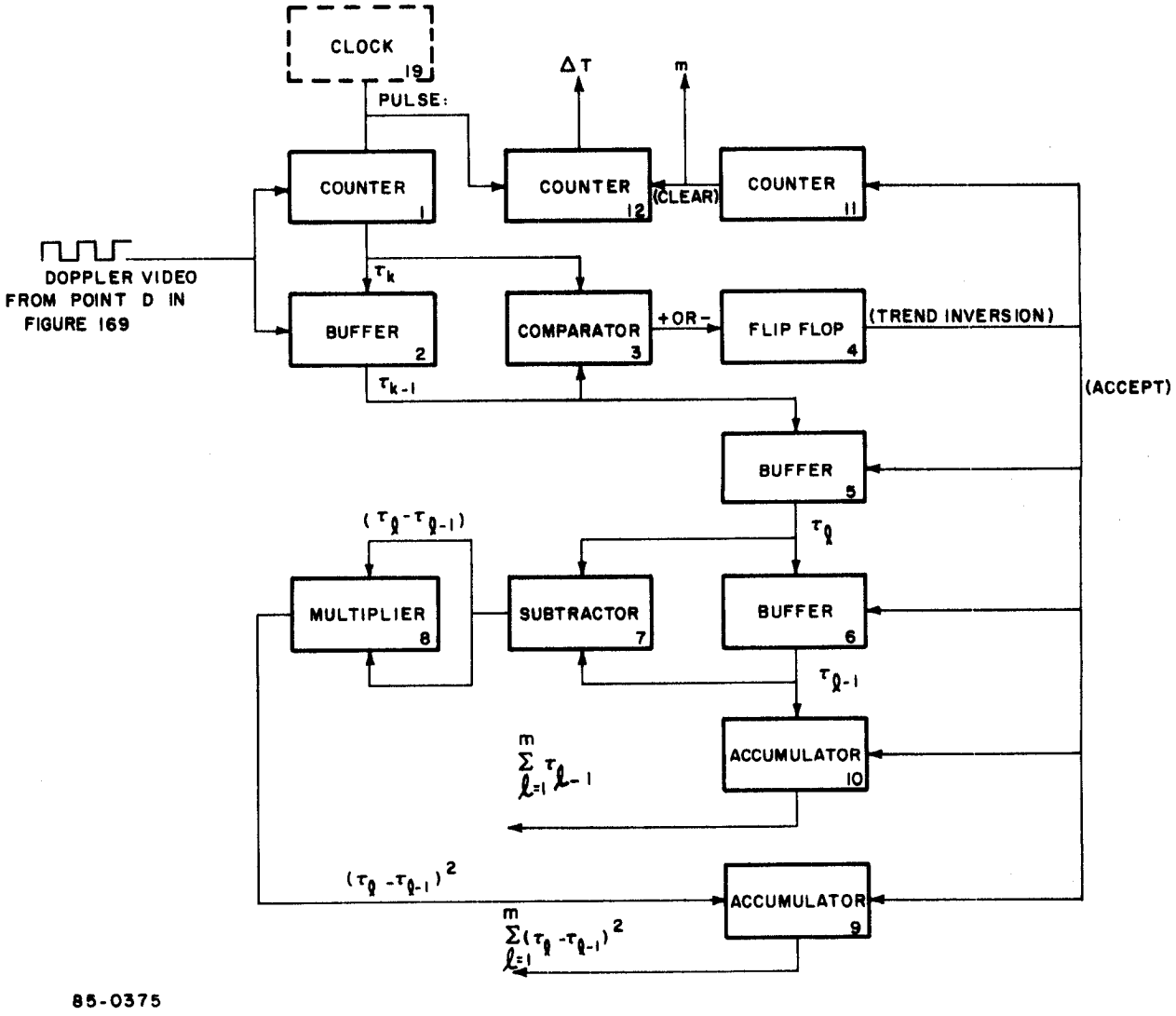

Figure 185 AUXILIARY DATA PROCESSOR

same sign from comparator (3) indicates that the Doppler frequency has a continuous upward or downward trend. The flip-flop (4) issues a pulse for each trend inversion. This signals the buffer (5) to accept the count of the corresponding Doppler period. As shown in Appendix H,the rate of occurrence of trend inversions equals the Nyquist rate in the Doppler information. Hence, the data accepted by the buffer (5) is non-redundant. Furthermore, two consecutive values τ_{l-1} and τ_l (τ_l is that value of τ_k which corresponds to a trend inversion) in this nonredundant set, are opposite maxima in the redundant set of counts, τ_k, when one value τ_l of the extremes is held in one buffer (5), the previous accepted value τ_{l-1} is held in the buffer (6). The subtractor (7) determines the variation ($\tau_l - \tau_{l-1}$) of the Doppler period. A preset number m of trend inversions is counted off in the counter (11). The observation time, ΔT, required to complete a count of m, is measured in another counter (12). The sum total of m consecutive independent values of the Doppler periods is determined in the accumulator (10).

The variations ($\tau_l - \tau_{l-1}$) in the Doppler period are squared in the multiplier (8) and the sum total of m of these squares is determined in accumulator (9). As shown in Appendix H, the parameters

ΔT

$$\sum_{l=1}^{m} \tau_{l-1} = m\,\bar{\tau}_{l-1}$$

$$\sum_{l=1}^{m} (\tau_l - \tau_{l-1})^2 = m\,\overline{(\tau_l - \tau_{l-1})^2}$$

together with a priori knowledge of m, contain all of the information necessary to describe surface roughness, wind velocity, and descent rate.

It is also shown in Appendix H the surface roughness (defined as the ratio between the powers in the diffuse and the specular echo) is:

$$R = \frac{P_{diff}}{P_{spec.}} = \frac{8\pi^2 \overline{(\tau_l - \tau_{l-1})^2}}{\bar{\tau}_l^2}$$

$$= 8\pi^2 m \frac{\sum_{l=1}^{m} (\tau_l - \tau_{l-1})^2}{\left(\sum_{l=1}^{m} \tau_l - 1\right)^2}$$

The wind velocity, v_{hor} is proportional to the bandwidth, Δf, of the diffuse echo, as follows:

$$\Delta f = \frac{2\, v_{hor}}{\lambda} \alpha \Delta\phi$$

where:

$\Delta\phi$ = the effective beamwidth

α = a correction factor (also depended upon $\Delta\phi$)

λ = wavelength.

The factor $\alpha\Delta\phi$ should be determined experimentally. It is also shown in Appendix H that the bandwidth of the diffuse echo equals the rate of occurrence of trend inversions, that is:

$$\Delta f = \frac{m}{\Delta T}$$

Accordingly, the wind velocity (horizontal velocity) is

$$V_{hor} = \frac{\lambda \Delta f}{2(\alpha\Delta\phi)}$$

$$= \frac{\lambda}{2(\alpha\Delta\phi)} \frac{m}{\Delta t} .$$

Finally, the descent rate is proportional to the average Doppler frequency

$$\bar{f}_{doppler} = -\frac{2 V_{vert}}{\lambda}$$

$$= \frac{1}{\tau_l - 1}$$

$$V_{vert} = \frac{\lambda \cdot m}{2 \sum_{l-1}^{m} \tau_l - 1} \quad .$$

8.9.2 Entry from Orbit Design

8.9.2.1 Reference Design

A block diagram of the basic three-beam V-A sensor is shown in Figure 186. The klystron transmitting tubes are frequency modulated by a triangular waveform at a rate, f_m , with a peak-to-peak deviation of $2\Delta f$. Two tubes at two different frequencies are used because of a size restriction on the antenna configuration. Since two of the antennas must share the same reflecting surface, two different frequencies are used to avoid any beamwidth spreading due to the combination of the two 5 x 5-degree beams. A small portion of the transmitter power is sampled and used as a coherent reference in the homodyne receiver. The preamplifier and filter must have a bandwidth wide enough to encompass the resulting beat frequency; this bandwidth is in the neighborhood of 500 kHz (see paragraph 8.5.3.4) thus necessitating a tracking loop. It is shown in paragraph 8.5.3.4 that in order to keep the power requirement reasonable, a tracking bandwidth of 50 kHz is required. The output of the pretracking filter is processed in the square-law detector and logarithmic amplifier to give amplitude information and is then entered in storage. The range and range-rate information is processed in the frequency tracker (discussed below) before being stored. All of this stored data is transmitted to Earth via the relay system. It can be processed there to yield vehicle velocity and vehicle attitude data as shown in Appendix E. If the V-A sensor is to be used as an on-board attitude determining device, a special purpose computer can be programmed to perform the required calculations (see Equations (55) and (56) of Appendix E).

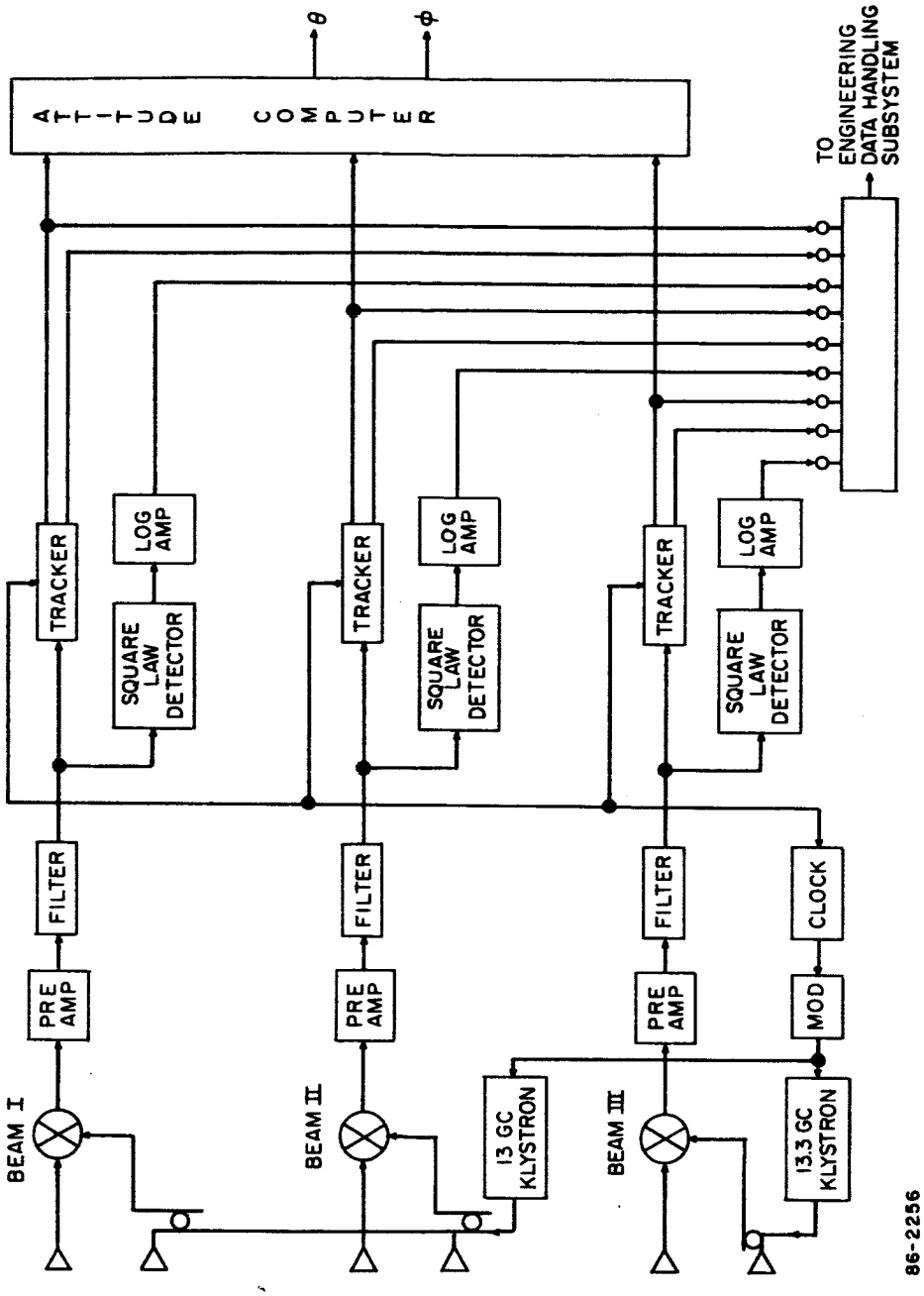

Figure 186 BLOCK DIAGRAM OF VA SENSOR

A discussion of one frequency tracker concept follows. As mentioned in Appendix G, the beat frequency in each receiver is found by taking the difference between the number of zero crossings in the signal on the upsweep of the transmitter frequency modulated (FM) signal and the number of zero crossings is a function of range and varies widely. If the echo spectrum is not tracked in frequency, the bandwidth of the filter through which the echo is passed into a frequency counter must be very wide in comparison to the extent of the echo. However, if the echo spectrum is tracked in frequency as the range changes, a much narrower filter can be used. This technique offers an added advantage in that it excludes most of the noise.

Figure 187 shows a block diagram of the tracker. The modulating frequency, f_m, is so controlled that the beat frequency with a normally projected beam, will be kHz at maximum range and 9 kHz at minimum range. Before minimum range is reached, however, the modulation frequency is changed. The new deviation rate is increased by a factor of 14 so that the beat frequency returns to approximately 140 kHz. The beat-frequency spectrum between 140 kHz and 500 kHz is passed by the tracker in order to accommodate effects of the greater values of angle γ_m (see Figure 152) created during wind gusts. The region in the vicinity of 550 kHz is passed by the tracker to enable noise-level measurements to be made in a spectral region free of the transmitted signal.

The pretracker amplifier-filter has a wide bandpass upper and lower with cut-off values of 9 and 600 kHz. The gain of this amplifier is small, hence, it can be considered linear. The output of the filter is translated upward 1 MHz by heterodyning its output with a 1 MHz crystal oscillator. The translated waveform is passed through a limiting amplifier and band-pass filter, then a narrow (1.009 to 1.600 MHz) and finally into a second mixer. The reference signal for the second mixer is the frequency of the tracking (voltage controlled oscillator). When tracking, the voltage controlled oscillator frequency is 1.9 mc above the echo signal at the limiter output. The second mixer output will therefore contain the echo signal centered roughly at 1.9 MHz by translation. A 50 kHz bandpass filter at the mixer output excludes most of the noise. The output of this filter is fed to the counter and logic circuits which form the range and range rate, as follows:

$$R = \frac{v_c}{8 \Delta f f_m} \cdot \frac{1}{2} [f_+ + f_-]$$

$$\dot{R} = \frac{v_c}{8 \Delta f f_m} \cdot \frac{1}{2} [f_- - f_+]$$

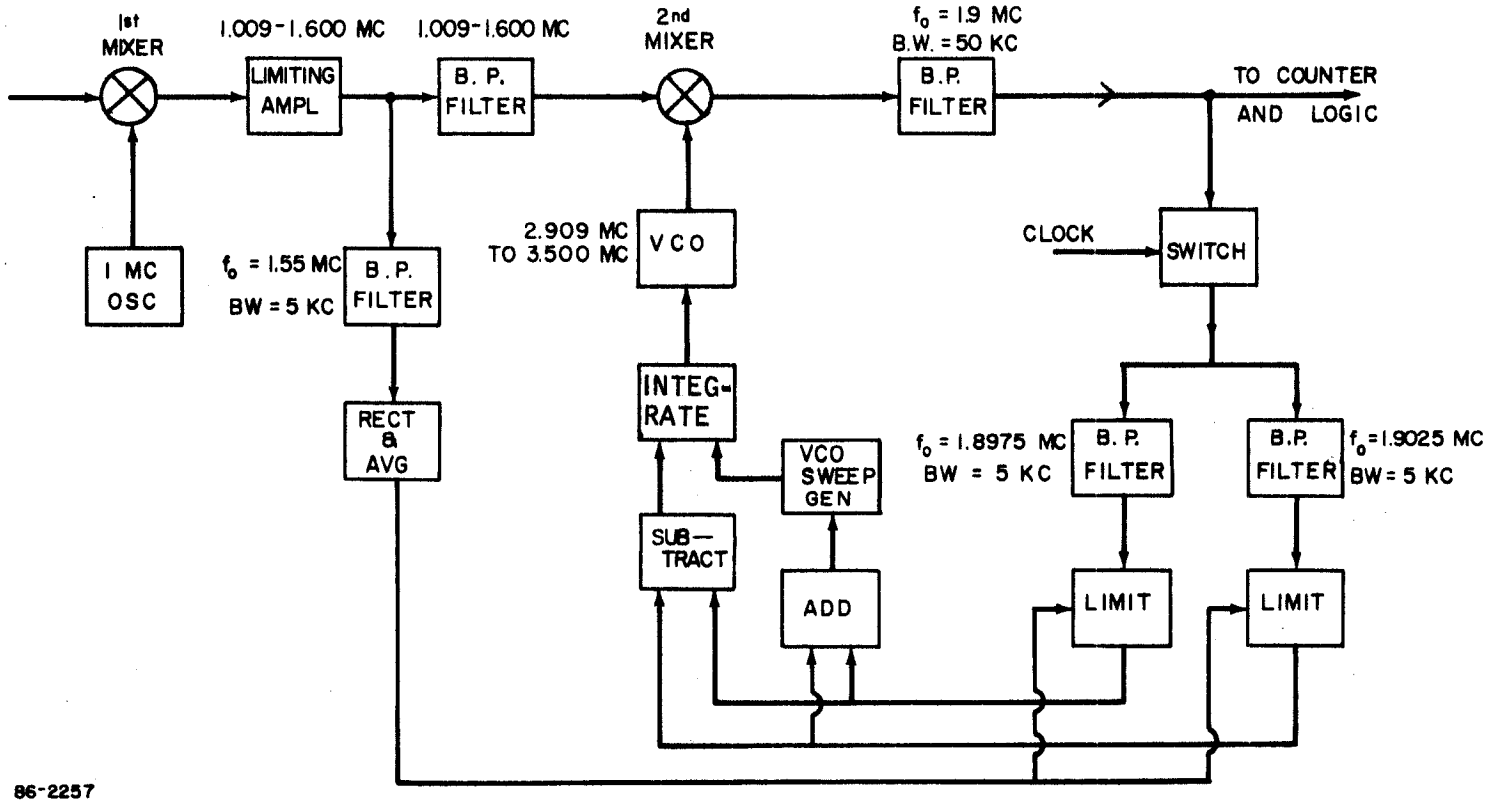

Figure 187 BLOCK DIAGRAM OF FREQUENCY TRACKER

The derivation of these equations is shown in Appendix G. The 50 kHz filter also passes the signal through a switch which is closed during the upswept half of the modulating signal f_m, and open during the downswept half of the modulating signal. Thus, the range tracking loop tracks the beat frequency during the upsweep only.

The switch output passes into two bandpass filters. Hence, the spectrum is split. The lower half passes through a 5 kHz bandpass filter, clipper, and rectifier. The upper half passes through a different 5 kHz bandpass filter and rectifier. The clipper circuits are biased diodes whose threshold levels are fixed according to the mean noise level outside the echo band. When the echo power in a 5 kHz band exceeds the noise power in a 5 kHz band by 10 db, the excess if passed through the clippers into the voltage-controlled oscillator-loop control circuits.

The two rectifier outputs are subtracted and the difference is fed to an integrator. The integrator output controls the voltage controlled oscillator frequency. The sum of the rectifier outputs is fed to the voltage-controlled oscillator sweep generator. When the sum of the rectifier outputs is above a pre-established threshold, the voltage controlled oscillator sweep generator is activated. As a result, the voltage controlled oscillator sweeps slowly over its 600 kHz operating range.

8.9.2.2 Major Tradeoffs

Measurement of wind velocities to an accuracy of 50 feet per second is adequate for the mission under consideration. However, if increased accuracy is required, there are certain tradeoffs that can be made. An obvious one is one of an active ac system capable of limiting the angle θ_c (the angle between the flight capsule roll axis and the local vertical) to fairly small values. This will result in smaller slant ranges, greater received signal powers, and better range rate accuracies, thus reducing the errors in velocity measurements. Figure 188 shows curves of wind velocity error as a function of θ_c for a fixed power (1 watt per beam), a fixed altitude (30, 000 feet), and accuracies of 1, 2, and 3 degrees in the measurement of angle θ_c. Angle θ_c is obtained from a reference inertial-platform measurement, thus, its accuracy is not a function of the received power. With this same philosophy, increased operating altitudes can be attained or a combination of both increased accuracy and increased altitudes can be attained. The increases are less, of course, when operating altitudes and accuracies are both increased.

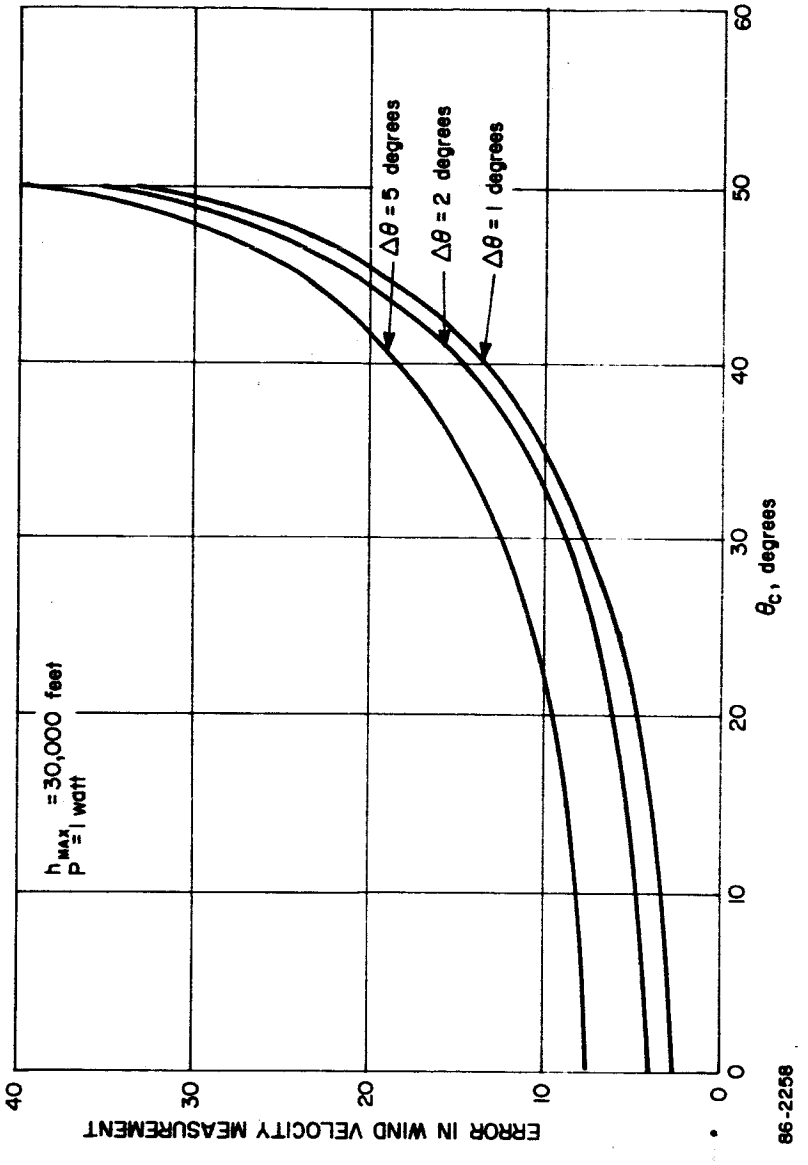

Figure 188 WIND MEASUREMENT ERROR VERSUS θ_c

8.9.2.3 Principal Problem Areas and Development Status

1. As shown in Appendix G, permissible frequency counting errors in the range rate measurement require fairly high frequency deviations in the transmitter tube. Peak-to-peak deviations of 200MHz at 13 g Hz will probably require some tube-development work.

2. The vehicle-size restriction requires that the same reflecting surface be used for both the transmitting and the receiving antennas. This presents a problem of isolation between the transmitting and receiving horns. If the noise sideband level of the microwave transmitting tube is 90 db below the center frequency amplitude, 60 db of isolation between the transmitting and receiving horns will keep the leakage signal approximately 15 db below the received signals at maximum altitude for the stand ranges under consideration. At lower altitudes, of course, the problem is less serious.

3. At the lowest altitudes, processing of the range and range rate data requires more complex programming because the physical spacing between antennas becomes appreciable. However, with knowledge of the angles θ and ϕ (see Appendix H) the data can be processed to yield the same accuracy in the horizontal velocity.

8.9.2.4 Doppler Antenna System

The velocity-sensing antenna system includes two parabolic antennas: one contains two transmitting and two receiving primary radiators, the second contains a single pair of transmitting and receiving primary feeds. Three beams will be produced, each 5 by 5 degrees at their one-half power points. Each of these beams will be tilted at an angle of 20 degrees with respect to the vehicle axis. Figure 189 illustrates the proposed design for the two-beam antenna. The proposed design takes advantage of the properties of a parabolic torus* to permit scanning at large angle off the central axis of the antenna. The torus is parabolic in one plane and circular in the other plane. This permits scanning along a circle concentric with the toric surface at a distance from the dish equal to the focal distance of the parabola. As can be seen from Figure 189, the diameter of the dish is 20 inches and the focal circle is located 5.8 inches from the dish. One pair of primary feed horns is directed at an angle of +20 degrees relative to the antenna axis: the other pair is directed at an angle of -20 degrees relative to the antenna axis. Each feed horn is designed to produce a 10 db illumination taper on the dish of 120 x 130 degrees for the H and E-plane respectively. The horns are designed to illuminate an aperture of approximately 13.5 wavelengths in both planes. This corresponds to the aperture required to produce a 5 x 5 degrees beam from the torus.

* Dolan, L., Recent Studies on Toric Reflectors, Rome Air Force Base Radiation Engineering Laboratory, Contract No. AF306(602)-1917.

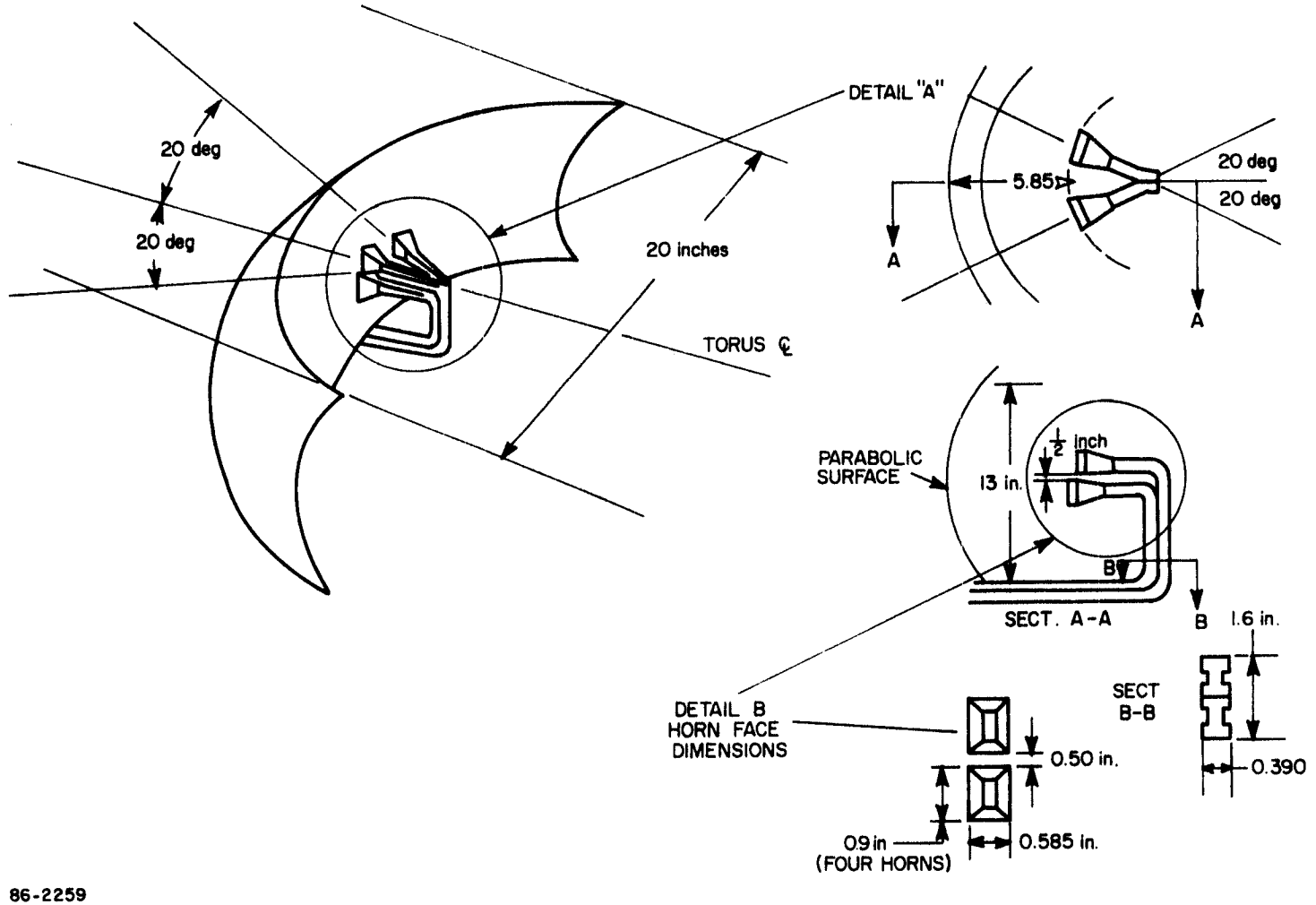

Figure 189 V TWO-BEAM ANTENNA FOR VA SENSOR

Aperture blocking by the feed horns will be very small since the ratio of the area of the primary feed-horn aperture to the area of the dish aperture is well in excess of one hundred to one. Isolation between feed horns whose H-plane are aligned has been measured. For an edge-to-edge separation of $\lambda/8$ values will in excess of 70.0 db were noted. The second (angle beam) antenna will produce a 5 x 5 degree beam orthogonal to the plane containing the two 5 x 5 beams.

The two-beam antenna, including the primary feed horns, and radome is estimated to weigh approximately 7 pounds.

8.9.3 Comparison with Surveyor RADVS

It was suggested previously that the radar altitude and Doppler velocity sensor (RADVS) presently intended for the Surveyor spacecraft would be an acceptable instrument for use on the flight capsule provided that it becomes flight qualified. The Surveyor spacecraft utilizes a radar altimeter and Doppler velocity sensor to provide spacecraft altitude and velocity information to the spacecraft flight-control system during the final portion of the lunar landing phase of the mission. The Doppler velocity sensor utilizes three continuous-wave radar beams to obtain three orthogonal velocity components which are referenced to the spacecraft roll axis. The radar altimeter uses a single-frequency modulated beam directed along the spacecraft roll axis to obtain data regarding the slant range to the lunar surface.

The following discussion indicates pertinent similarities and differences between the Surveyor RADVS and the flight capsule velocity altitude sensor, as well as the significant tradeoffs between them.

8.9.3.1 Similarities -- The flight capsule velocity altitude sensor

The flight capsule velocity altitude sensor and the Surveyor RADVS each use a 3-beam doppler radar, and measure the velocity vector along the beams. They both employ split antennas and operate at very nearly the same radar frequency. Each is capable of measuring altitude and vector velocities down to about 10 feet above the surface.

8.9.3.2 Differences

The principle differences between the altimeters arise from the different requirements related to the presence of an atmosphere on Mars. Measurement from very high altitudes implies that the flight capsule altimeter must interface with the heat shield so it can operate both before and after heat shield removal. To accomplish this

effectively, two functionally distinct altimeters, each operating at a different frequency and with separate antenna configurations, are utilized with velocity altitude sensor. The receiving and data-reduction circuits are common to both the high and low altitude measuring systems, however. The high-altitude altimeter employs the heat shield itself as its antenna and, accordingly, operates at a low frequency. No counterpart for this altimeter exists in the Surveyor since it is not required to measure altitude continuously. Instead, an altitude marking radar (AMR) system is used to provide a signal when an altitude of 56 miles is reached during descent. This signal is used to initiate operation of the retro-thrust control equipment.

The low altitude altimeter in the flight capsule operates at a wavelength which is a compromise between that needed to provide a strongly diffuse return for the surface-roughness measurement and that needed to provide a strongly specular return for the altitude measurement. The Surveyor altimeter operates at a much higher frequency, has a narrow beamwidth, and shares an antenna structure (split parabola) with one beam of the Doppler section. The differences between the Doppler velocity sections of the two radars also arises because of the presence of the Mars atmosphere. Measurement of wind requires determination of the swing angle of the flight capsule during parachute-aided descent.

Although a stable platform is included in the flight-capsule design as the primary means of determining this angle, the wind measurement is considered sufficiently important to the design of future landers to justify inclusion of back-up means for determining this angle. Consequently, each of the three beams of the flight capsule velocity altitude sensor measures both range and range rate. The Surveyor RADVS measures only range rate.

8.9.3.3 Significant Tradeoffs

It is emphasized that the Surveyor RADVS is a candidate only for the velocity-altitude section of the flight capsule radar system. It will not replace the high altitude altimeter essential to the Mars mission. Until the VHF surface-roughness measurement can be eliminated, the Surveyor RADVS will not replace the low altitude altimeter of the flight capsule.

The advantage of using a flight-qualified RADVS lies in the fact that it has substantially the same performance characteristics as those required by the velocity-altitude sensor of the flight capsule and that

it is a developed, flight-qualified device. Hence it exists, is operative, and the special checkout test equipment associated with it also exists and is operative. The use of the RADVS would result in substantial savings in system study, design, development, test, and qualification, and a large savings in cost. The disadvantage of utilizing RADVS is the sacrifice of a redundant means to determine flight-capsule attitude in the event the stable platform fails. The advantages far outweigh the disadvantage and it seems obvious that if the Surveyor RADVS becomes qualified, the reasonable course is to use it for the flight capsule.

8.10 SUMMARY OF PHYSICAL CHARACTERISTICS

The radar system consists of a three-beam velocity-altitude sensor and both a high-altitude altimeter and a low-altitude altimeter.

The velocity altitude sensor measures range and range rate from an altitude of 30,000 feet to approximately 10 feet. This information is used to determine both wind velocity and the attitude of the suspended capsule. The measurement accuracy depends upon the swing angle of the suspended capsule, but for swing angles up to 45 degrees, the accuracy exceeds ±25 percent. One watt is radiated in each of three 5 degree beams located 90 degrees apart in the x-y plane and inclined 20 degrees with respect to the flight capsule roll axis. The electronics package weighs 9 pounds, occupies a volume of approximately 1400 $in.^3$, and consumes 15 watts. Two linear polarized antennas are associated with the velocity altitude sensor. Both structures are toroids, the larger measures about 20 inches in width and is 13 inches in height. This structure contains a feed for both 13 and 13.3 gHz and weighs 7 pounds. The smaller structure measures 13 inches in width and is 16 inches in height; this contains a single feed for 13 MHz and weighs 5 pounds. The velocity-altitude sensor is modulated by FM-CW with a prf that varies 5 to 1 k Hz.

The altimeter system (high and low altitude altimeters) measure altitude from 250,000 feet down to approximately 1000 feet. It also measures surface roughness and provides an estimate of wind velocity; the latter measurements are obtained by spectrum analysis of the return echo. The altimeter is functionally divided into two sybsystems, i.e., the high-altitude altimeter and the low-altitude altimeter. The high altitude altimeter uses the support ring of the entry shell as the antenna. It functions from the high altitude limit to the altitude at which the entry shell is jettisoned, that is, about 30,000 feet. It operates at a frequency of 18 MHz and radiates 25 watts of ICW modulation. The pulse repetition frequency is altitude controlled and varies from 1 to 83 kHz.

The low-altitude altimeter operates from the altitude at which the entry shell is jettisoned down to an altitude of 1000 feet. It shares common electronic processing equipment with the high altitude altimeter, and the principle differences are in the frequency of operation, the transmitter power, and the antenna. The low altitude altimeter operates at a frequency of 324 MHz and radiates 1 watt of ICW modulation. The pulse repetition frequency is altitude controlled and varies from 83 to 250 kHz. A linear polarized logarithmic spiral antenna is used for the low-altitude altimeter. This antenna is 15 inches in diameter and 8 inches deep; its weight is 5 pounds.

The altimeter electronic package weighs 9 pounds, occupies 300 $in.^3$, and consumes 61 watts.

REFERENCES

1. "Comparative Studies of Conceptual Design and Qualification Procedures for a Mars/Probe/Lander," Prepared for Langley Research Center by Avco/RAD, Contract No. NAS 1-5224, RAD-TR-65-29, Volume IV, Book 3.

2. Lawson, J. L. and G. E. Uhlenbeck, Threshold Signals, McGraw-Hill Book Co., Inc., N. Y. pp 100-102 (1950).

3. Steinberg, J. L., and J. Lequeux, Radio Astronomy, McGraw-Hill Book Co., Inc., New York, pp. 27-30 (1960)

4. Rafuse, R. P., "Characterization of Noise in Receiving Systems," Chapter 15 in Lectures on Communication System Theory, E. J. Baghdady (ed.), N. Y., McGraw Hill Book Co., Inc. (1961)

5. Kerr, Donald E., Propagation of Short Radio Waves, McGraw Hill Book Co., Inc., New York, p. 663 (1951)

6. Kotel'nikov, V. A., et al., "Radar Studies of the Planet Mars in the Soviet Union" Soviet Physics-Doklady, Vol. 8, No. 8, pp. 760-763. (February 1964)

7. Goldstein, R. M., W. F. Gillmore, "Radar Observations of Mars," Science, Vol. 141, pp. 1171-1172 (September 1963)

8. Skolnik, M. I., Introduction to Radar Systems; N. Y. McGraw Hill Book Co., Inc., 1962.

9. Smith, Alex G., "Extraterrestrial Noise as a Factor in Space Communications", Proc. IRE, pp. 593-599 (April 1960)

10. Kundu, M. R., Solar Radio Astronomy, New York, Interscience Publishers, Inc., p. 3 (1965)

11. Lecture Notes: Radio Astronomy-Course 241, Harvard University, Prepared by Dr. G. R. Huguenin (1965)

12. Smith, J. H. and E. V. P. Smith, Solar Flares, The Macmillan Co., New York, pp. 209-211 (1963)

13. Springett, J. C. "Telemetry And Command Techniques for Planetary Spacecraft" in Advances in Communications, A. V. Balakrishman (ed.) N. Y. Academic Press (1964).

14. "Inter-Range Instrumentation group (IRIG) Telemetry Standards", IRIG Document Number 106-65, Revised July 1965.

15. Brennan, D. G., "Linear Diversity Combining Techniques," Proc. IRE, Vol. 47, pp. 1075-1102 (June 1950)

16. Koslover, M., Performance of Sealed Nickel Cadmium Cells After Exposure to the NASA Heat Sterilization Environment, Avco/RAD Technical Release AEDM-F510-340 (9 April 1965)

17. Koslover, M., Evaluation of Heat Sterilized Nickel Cadmium Cells Subjected to Variable Environments, Avco/RAD Technical Release AEDM-F510-477. (10 November 1965)

18. M. Koslover, Performance of Silver Zinc Cells After Exposure to the NASA Heat Sterilization Environment, Avco/RAD technical Release, AEDM-F510-481 (23 November 1965)

19. Brosens, Pierre, J. Solar Thermionic Generators for Space Power, ASME Paper No. 64-WA/Sol-1. Presented at ASME Annual meeting New York, N. Y. (29 November 1964).

20. Smith, Arvin H., "Thermionics: Auxiliary Power Application for Space" ASME Paper No. 63-MD-54 presented to ASME Design and Engineering Conference, New York, N. Y. (20-23 May 1963)

21. Berger, C., and F. C. Arrance, Silver-Zinc Battery Capable of Thermal Sterilization According to J. P. L. Specification X50-30275-TSTA. Douglas Aircraft Co. Report SM-48455 (March 1965)

22. Communication from A. D. Taylor of Douglas Aircraft to W. J. Schafer Avco/RAD. Subject; Battery Developments (December 13 1965)

23. Telecon: M. Koslover and W. A. Chandler, NASA Manned Spacecraft Center, Houston (9 September 1965) Subject: Article in "Astronautics and Aerospace Engineering" on Cryogenic Storage For Space Electrical Power (by W. A. Chandler) (May 1963)

24. Pratt & Whitney Aircraft Communication SE 133; Adaptation of Apollo for Space Station Application to J. F. Natale Avco/RAD(8 September 1963)

25. Radio Corporation of America, Astro-Electronics Division, Report; Mars Probe/Lander Study Program, Appendix XI-B; Magnetic Cleanliness, 2 (10 September 1965)

26. Westinghouse Electric Corporation; Report WAED 64.13E, Appendix B, Switching, Control and Protective Devices (March 1964)

27. Seiger, H. N., P. B. Pinches, H. I. Cohen, and R. C. Shair, Sealed Nickel Cadmium Batteries. Paper presented at 16th Annual Power Sources Conference, Atlantic City, New Jersey, (22-24 May 1962)

28. Henderson, I. H. S., and S. G. Ladan, Coulometric Charging Control of Sealed Nickel Cadmium Cells, Canadian Defense Research Chemical Lab; Technical Note No. 63-11 Presented to meeting of Electrochemical Society, New York, N. Y. (30 September 1963)

29. Koslover, M. "Development of a High Power Fuel Cell Battery" Avco/RAD Internal Paper, No number assigned (10 December 1965)

APPENDIXES

A. FLIGHT CAPSULE ANTENNA ANALYSIS

B. FLIGHT SPACECRAFT BIT SYNCHRONIZER ANALYSIS

C. BATTERY CALCULATIONS FOR REFERENCE POWER PROFILE

D. POWER CONTROL

E. DERIVATION OF A THEORETICALLY OPTIMUM RANGE TRACKER

F. DETERMINATION OF HORIZONTAL MOTIONS AND ATTITUDE WITH THE USE OF THE VELOCITY - ATTITUDE SENSOR

G. DESIGN CONSIDERATIONS FOR THE VELOCITY-ATTITUDE SENSOR

H. DOPPLER ECHO SPECTRUM AND ALTIMETER ANCILLARY FUNCTIONS

APPENDIX A

FLIGHT CAPSULE ANTENNA ANALYSIS

1.0 INTRODUCTION

This appendix presents the results of work conducted to determine the performance of the planar logarithmic spiral antenna selected as the reference design for the flight capsule telecommunication subsystem.

2.0 OBJECTIVES

The objectives of this appendix are the following:

1. To briefly summarize the basic properties of a planar logarithmic spiral antenna.

2. To establish the rationale for selecting the 18-inch diameter antenna as the reference design.

3. To explain in some detail the effect of the afterbody configuration of the flight capsule on a free-space pattern of a planar logarithmic spiral antenna, noting in particular, the patterns obtained from the separated vehicle, the entry vehicle, and the suspended vehicle.

4. To define the operating modes of the antenna system in relation to single and double contingency failure modes.

5. To justify the unique mounting configuration of the antennas.

6. To establish the efficiency of the antennas used during the measurement phase of the study and to predict a reasonable efficiency figure for actual flight antennas.

7. To define the weight and volume of the reference design.

8. To summarize the characteristics of the Relay Antenna Subsystem.

3.0 DISCUSSION

Data will be presented at each stage of the discussion in support of all conclusions. As a summary of the overall relay antenna system description, we shall display the far field patterns for the entire sphere of radiation surrounding the space capsule for the following conditions:

PRECEDING PAGE BLANK NOT FILMED.

1. With and without dielectric nozzle for the co-polarized and cross-polarized case.

2. With the metalic nozzle for co-polarized and cross-polarized case.

3. With the entry shell for the co-polarized transmitting case. Refer to Figure A-1 for a sketch of the proposed antenna and to Figure A-2 for its mounting configuration on the space capsule.

3.1 Basic Properties of the Planar Logarithmic Spiral Antenna

The planar spiral antenna has been extensively discussed in the literature. (see Bibliography at the end of this section). It is of value, however, to briefly indicate the basic properties of this antenna, which may be described by the following equations:

a) $P_1 = k e^{a\phi}$

b) $P_2 = k e^{a(\phi - \delta)}$

where P_1 and P_2 are the edges of one arm, ϕ is the angle of revolution, δ defines the arm width, k determines the size of the terminal region, and "a" controls the rate of spiral growth. The arm length must be one wavelength long for the antenna to produce circular polarization, and its diameter must exceed one-third wavelength for reasonable gain levels. Diameters on the order of 0.4λ to 0.5λ are optimum. The antenna produces circular polarization in broad angular distances from antenna boresight, much more so than a turnstile radiator. On peak gain of +5.0 db to +6.0 db above an isotropic level can be easily attained.

Since the spiral antenna is a balanced network, i.e., symmetrically constructed with respect to the feed point, the transmission line feeding this network must also be balanced. It is necessary to maintain the symmetry of the feed points with respect to ground to avoid difficulties with unbalanced currents on the line. If these currents are allowed to exist, undesirable radiation from the transmission line itself will occur, with resulting radiation pattern deterioration.

In most cases RF energy is transferred from the transmitter to the antenna system via a coaxial cable. Because coaxial transmission line is inherently unbalanced, some device must be used to connect the line to the antenna without destroying the electrical symmetry of the antenna.

A device which will isolate the balanced load (antenna) from the unbalanced line (coaxial cable) while providing efficient power transfer is a balun. The device illustrated in Figure A-3 is called a Type I or "bazooka" balun. Figure A-4 shows the equivalent circuit for this balun.

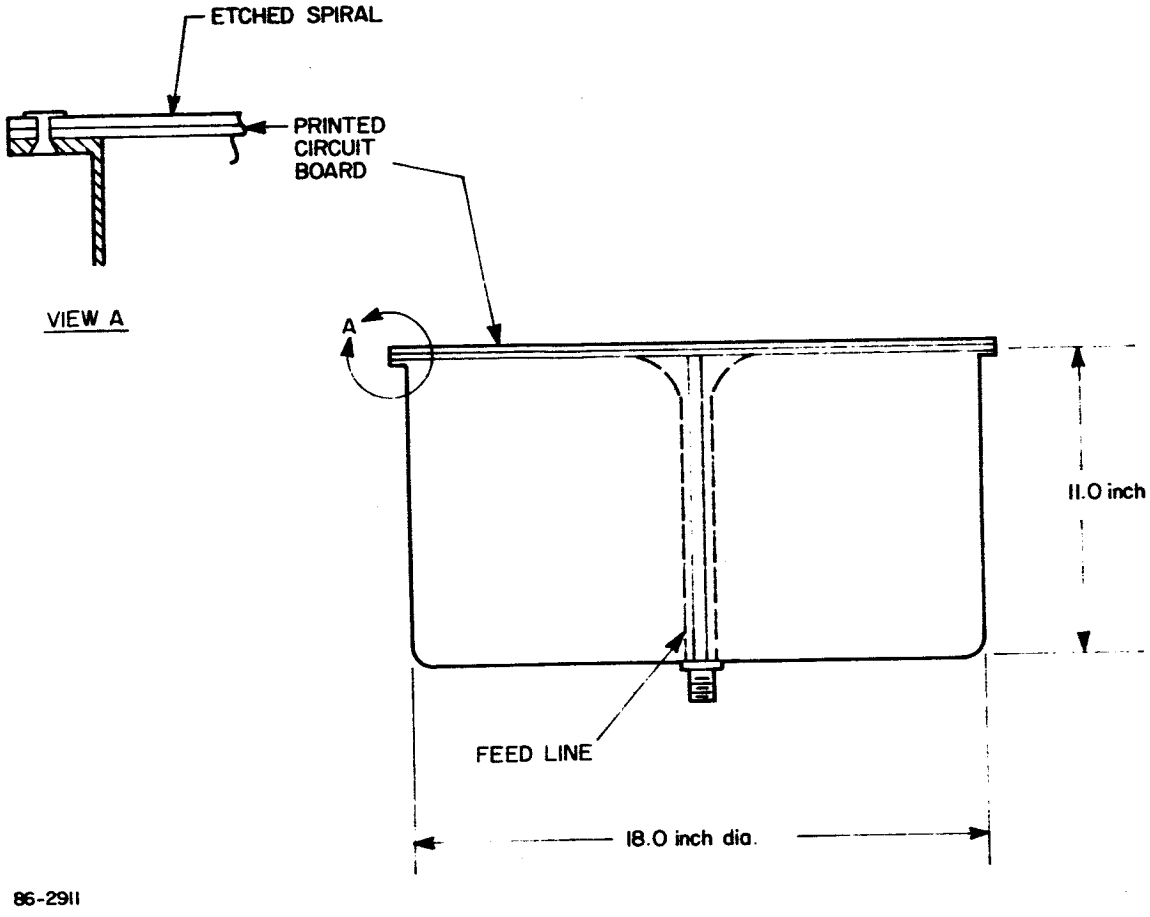

Figure A-1 FLIGHT CAPSULE RELAY LINK ANTENNA

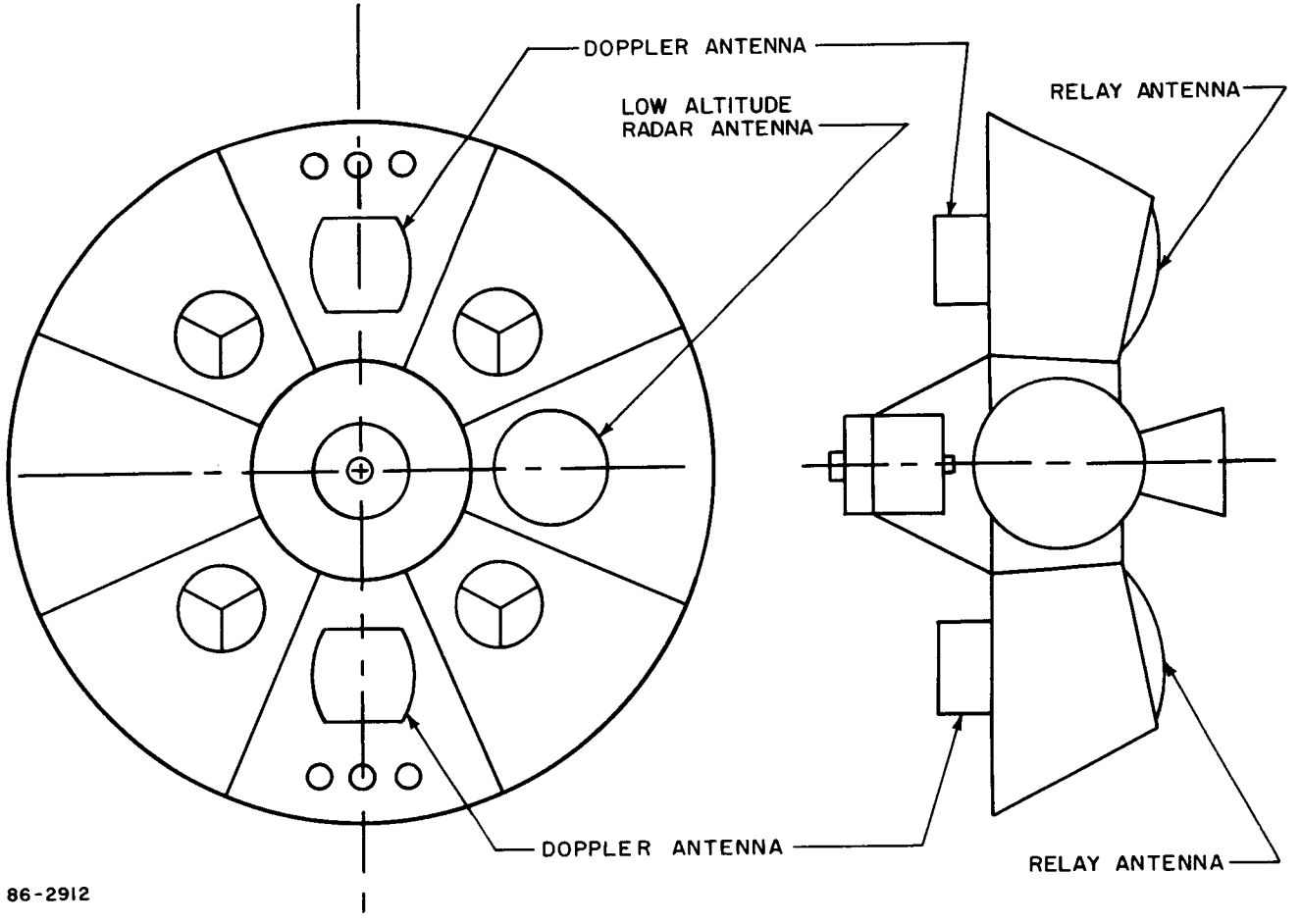

Figure A-2 FLIGHT CAPSULE ANTENNA SYSTEMS

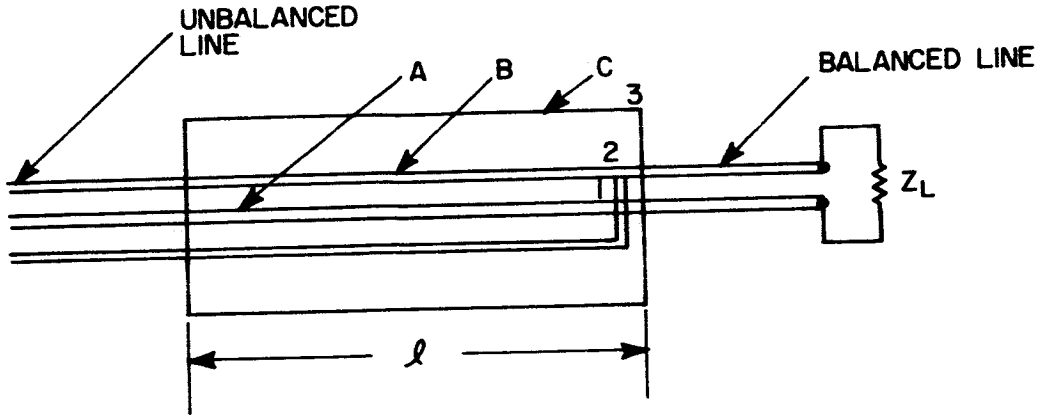

Figure A-3 TYPE I BALUN

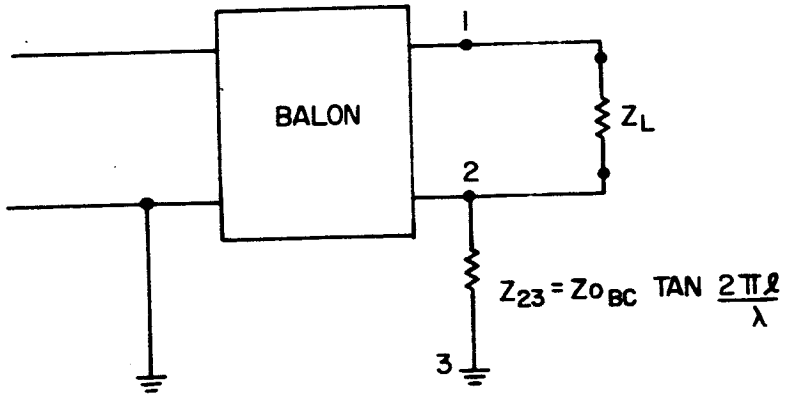

Figure A-4 EQUIVALENT CIRCUIT FOR TYPE I BALUN

In this balun the balanced pair of conductors is tied directly to the inner and outer conductors of the coaxial line at points 1 and 2. In addition a sleeve C, placed around the coaxial line, extends one-quarter wavelength from its junction with the balanced line. Thus, the outer conductor B of the coaxial line and the skirt C, the antenna cavity walls, form a second coaxial line the impedance of which, as measured between 2 and 3, is

$$Z_{23} = Z_{OBC} \tan \frac{2\pi l}{\lambda}$$

where Z_{23} is the impedance seen between 2 and 3, Z_{OBC} is the characteristic impedance of the coaxial line consisting of outer connector B and skirt C, l is the length of the skirt C, and λ is the wavelength at the operating frequency.

When $l = \lambda/4$, the impedance Z_{23} is very high (limited by the Q of the section) and there is no shunt path to ground from 2 to 3, and consequently no division of current at junction 2. Thus, both conductors of the dual line carry equal currents. There are however, paths to ground from each of the dual conductors because of the distributed capacitance and conductance. Since these paths are presumably equal, and since the currents in each of the dual conductors are equal and 180 degrees out of phase, the voltages to ground will be equal and 180 degrees out of phase, the dual line will be balanced.

If l does not equal $\lambda/4$, Z_{23} will not be a high impedance, and it is apparant from the equivalent circuit shown in Figure A-4 that an unbalanced path will exist between 2 and ground. Therefore, the impedance to ground from 1 will be significantly different from the impedance to ground from 2 and there will be a division of current at junction 2. The voltage as measured from 1 to ground and from 2 to ground will no longer be equal or 180 degrees out of phase, and the dual line will be unbalanced. The bandwidth of this type of balun is limited, but since the spiral antenna is narrow band also, the simplicity of this balun lends itself well to the design.

If it is desired to improve the match of the line to the antenna impedance, center conductor A shown in Figure A-3 can be constructed so that a one-quarter wavelength matching transformer will exist between the balanced and unbalanced line. If the characteristic impedance Z_{AB} is selected to satisfy the expression,

$$Z_{AB}^2 = Z_{in} Z_L,$$

an impedance match will result. Again the narrow band aspect of this feed element is not a critical factor for this particular antenna.

3.2 Selection of Antenna Diameter

In order to evaluate the spiral antenna radiation pattern, three antenna models were built, as well as a mockup of the spacecraft afterbody. Pattern measurements were taken in a large (60' x 20' x 20') Avco anechoic chamber at a scaled frequency of 1430 MHz. Table A-1 lists the parameters of the model antennas which were built. These were designed for an arm length of 1.5 λ.

Table A-2 summarizes the test measurement program.

Free-space patterns were taken of each of the models described in Table A-1 in order to insure system compatibility with this type of antenna, Figures A-5 through A-7 are principal plane patterns of each antenna model. Figure A-8 shows the reference coordinate system. Each pattern displays characteristics which are consistent with radiation coverage requirements. Particular attention should be called to their respective gains above an isotropic level, noting that the gain for the 13-inch (0.3 λ) antenna is considerably below that of the 18-inch (0.4 λ) and 22-inch (0.5 λ) models. Since the electrical performance of the 18-inch diameter and the 22-inch diameter antenna were so similar, the 18-inch diameter was selected as the optimum dimension for the reference design. This diameter antenna offered the best compromise between acceptable antenna performance and physical size.

3.3 Effect of Afterbody Configuration on Antenna Pattern

The next step in the study was to ascertain the pattern of the 18-inch spiral as modified by the flight capsule structure; i.e., to determine the effect of the separation vehicle, the entry vehicle, and the suspended vehicle on the pattern. For the first two stages, the entire 15-foot space capsule must be considered. For the last stage, the suspended vehicle, only the afterbody need be considered. The effect on the spiral pattern of the spacecraft was also considered in the context of look angle to the spacecraft. This point may be explained by considering the look angles for the separation vehicle, the entry vehicle and the suspended vehicle. The look angles for the first two conditions of the space capsule lie in the major lobe of the pattern which will undergo some slight rippling from the entry shell and the back lobe of the antenna as shown in Figure A-9. The figure shows the principal plane patterns of the antenna with and without the entry shell. During descent on the parachute the suspended vehicle is anticipated to sway up to ± 90 degrees. At look angles greater than 90 degrees the effect of the afterbody configuration on the pattern will be considerable since relatively large power level variations occur in the backlobe region of the antenna. These levels are 10 to 15 db below beam peak and are most susceptible to reflections from the afterbody.

TABLE A-1

PARAMETERS OF THE MODEL SPIRAL ANTENNAS

$$\text{Scale Factor} = \frac{270 \text{ MHz}}{1430 \text{ MHz}} = 0.189$$

Full-scale diameter	13"	18"	22"
Scaled diameter	2.46"	3.21"	4.15"
k	0.0473"	0.0473"	0.0473"
a	84.53°	82.78°	80.56°
Cot a = a	0.0955	0.1268	0.166
Number of turns	5.45	4.42	3.63
δ	90°	90°	90°

TABLE A-2

TEST MATRIX-ANTENNA PATTERN STUDY*

General Condition for Test	Modification to General Test Condition	Antenna Type Being Tested
I free space		0.33λ dia. planar spiral 0.4λ dia. planar spiral 0.5λ dia. planar spiral
II mockup "A" of flight capsule afterbody	1. Without Rocket Motor and Nozzle 2. With Rocket Motor/Without Nozzle 3. With Rocket Motor and With 3 Type Nozzles.	0.4λ dia. planar spiral
III mockup "C" of flight capsule afterbody	1. With 3 Metallic Nozzles 2. With 1 Dielectric Nozzle. 3. Antenna Tilted Away from Vehicle Axis 4. Antenna Tilted Toward Vehicle Axis	0.4λ dia. planar spiral and 0.5λ turnstile with metallic nozzle.
IV mockup "C" of flight capsule with entry shell	1. With Dielectric Nozzle	0.4λ dia. planar spiral

*All patterns measured in response to a cross-polarized, co-polarized, and linear transmitting antenna

Frequency 270 MHz full scale
1430 MHz scale measurement frequency

Scale factor: $\frac{270\ MH_z}{1430\ MH_z} = .189$

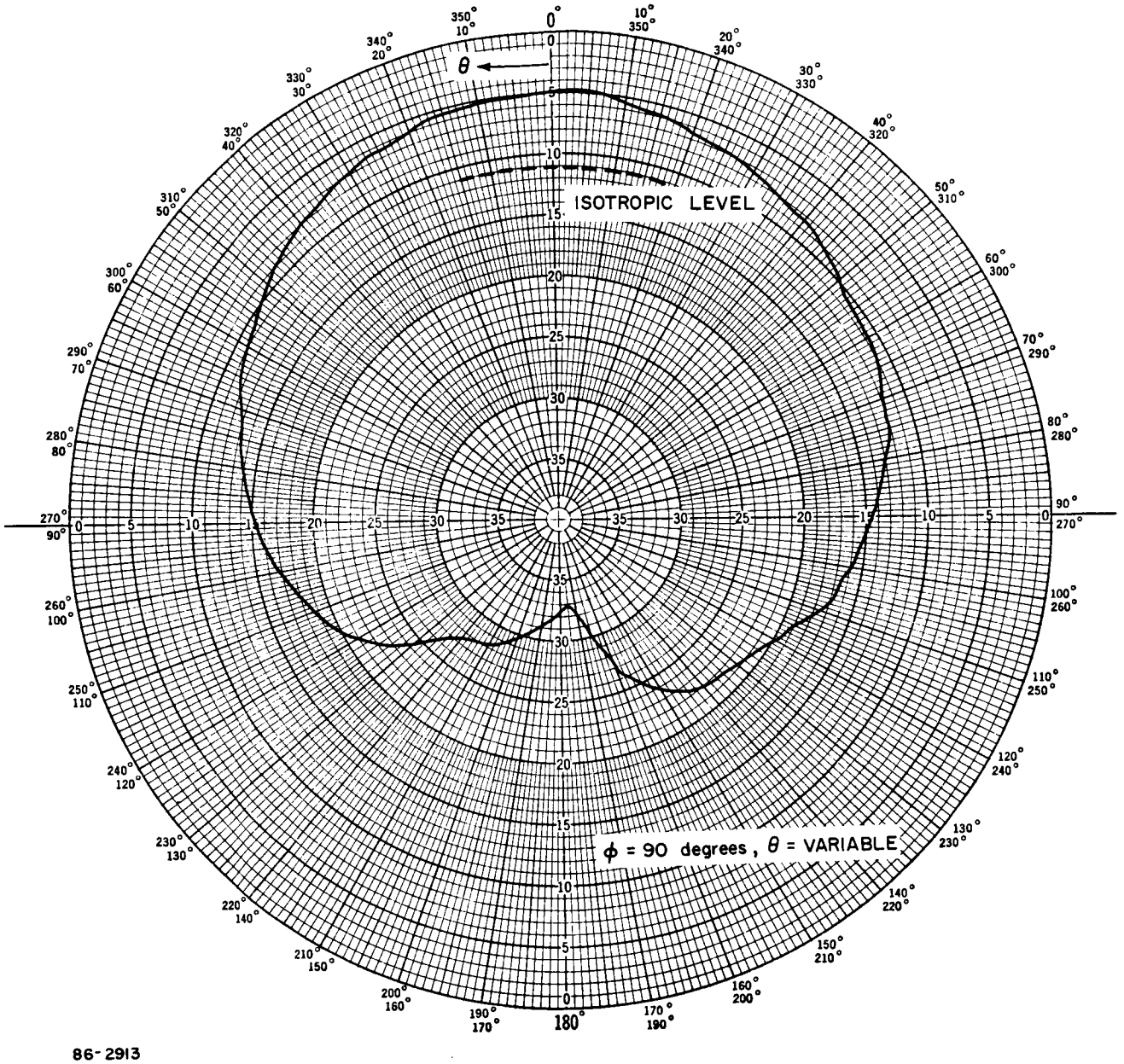

Figure A-5 PRINCIPAL PLANE PATTERN OF 0.5λ DIAMETER PLANAR LOG SPIRAL ANTENNA

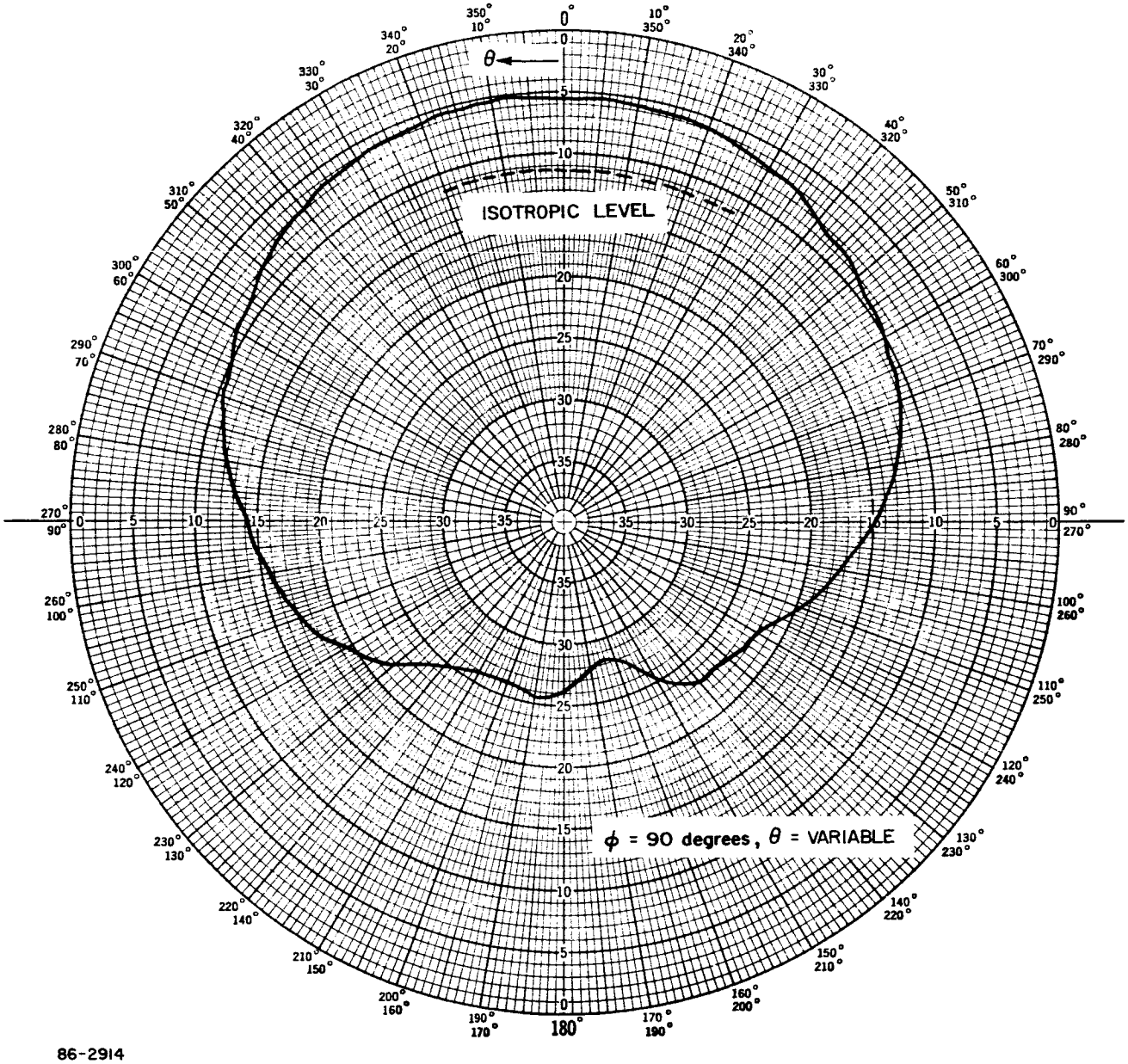

Figure A-6 PRINCIPAL PLANE PATTERN OF 0.4λ DIAMETER PLANAR LOG SPIRAL ANTENNA

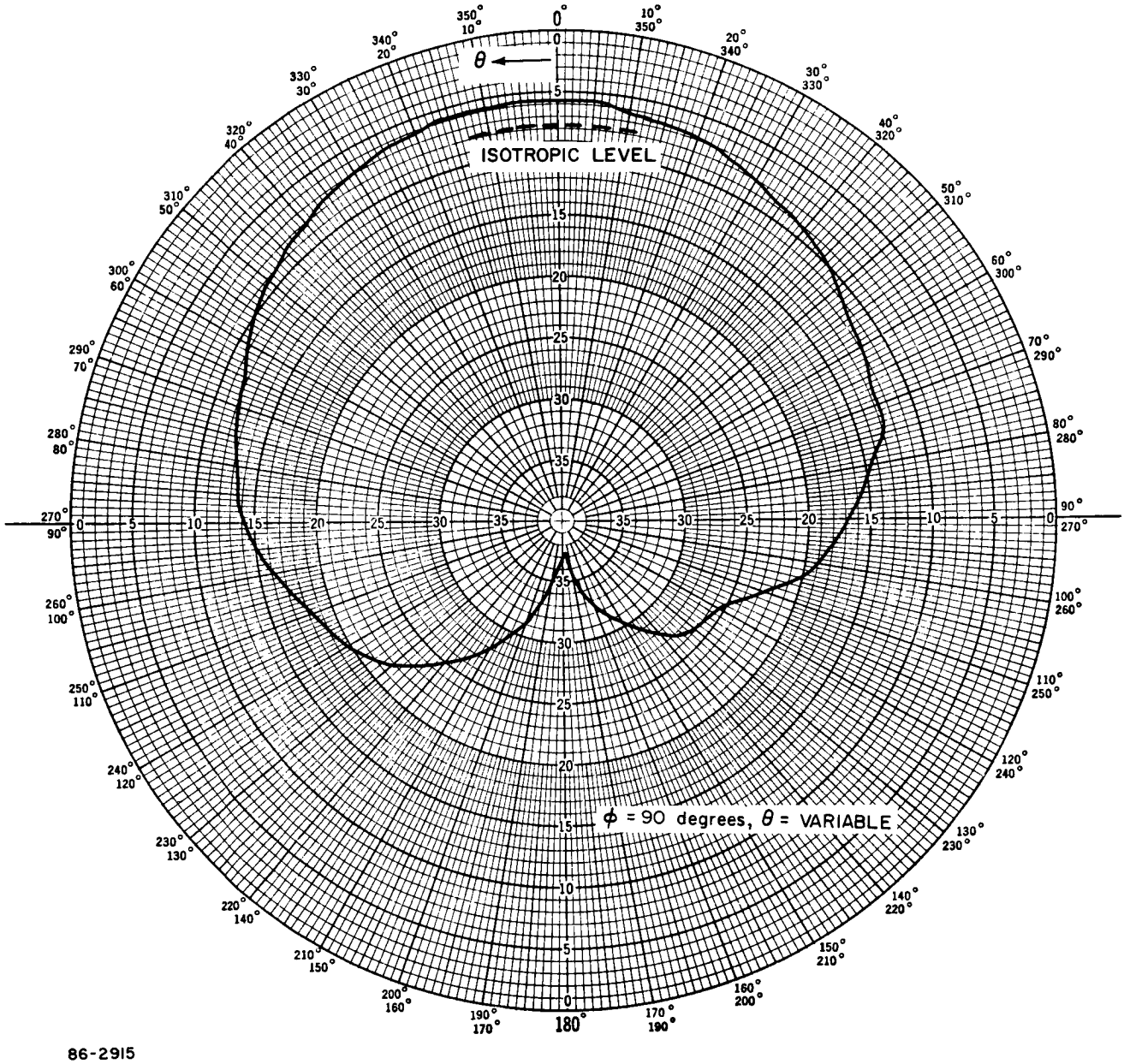

Figure A-7 PRINCIPAL PLANE PATTERN OF 0.3λ DIAMETER PLANAR LOG SPIRAL ANTENNA

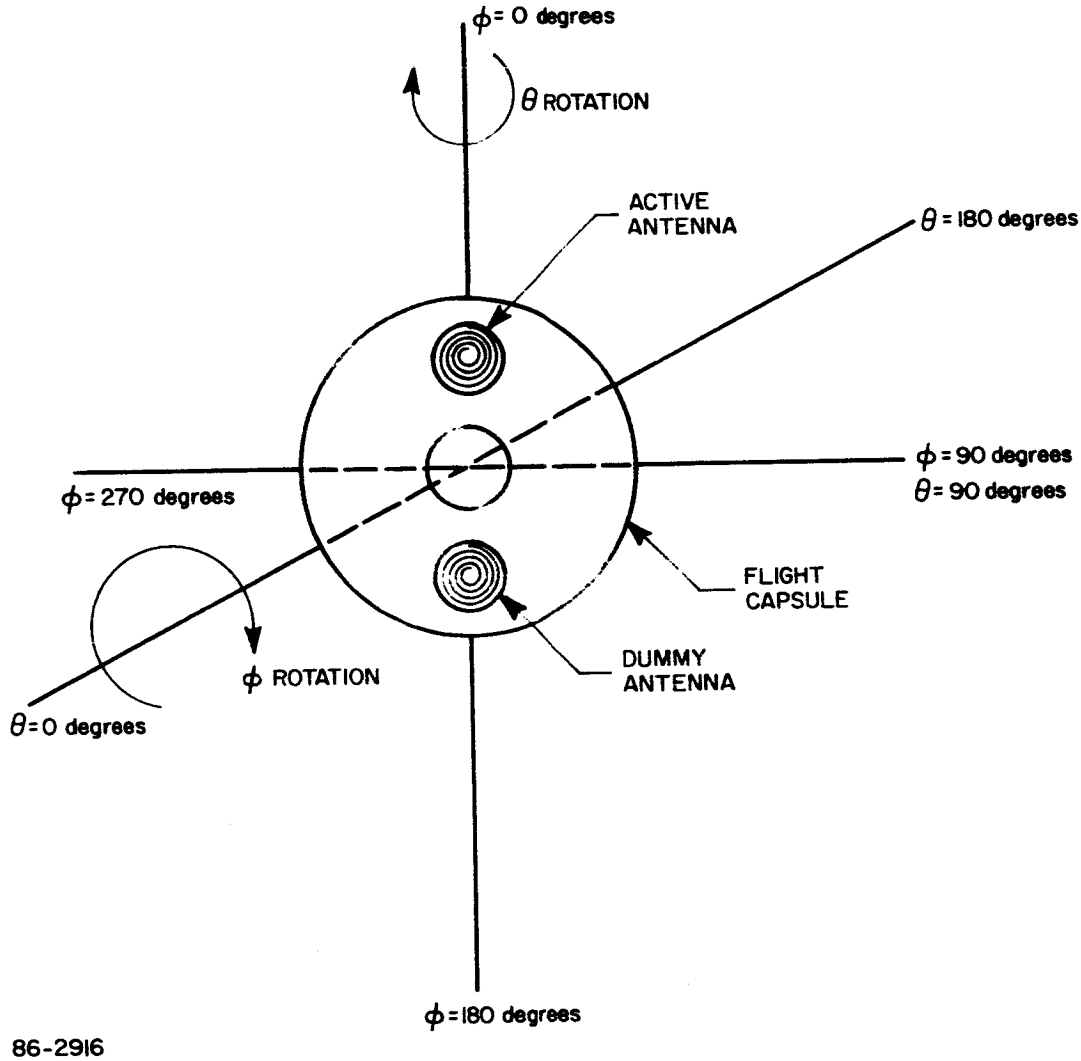

Figure A-8 ANTENNA MEASUREMENTS COORDINATE SYSTEM

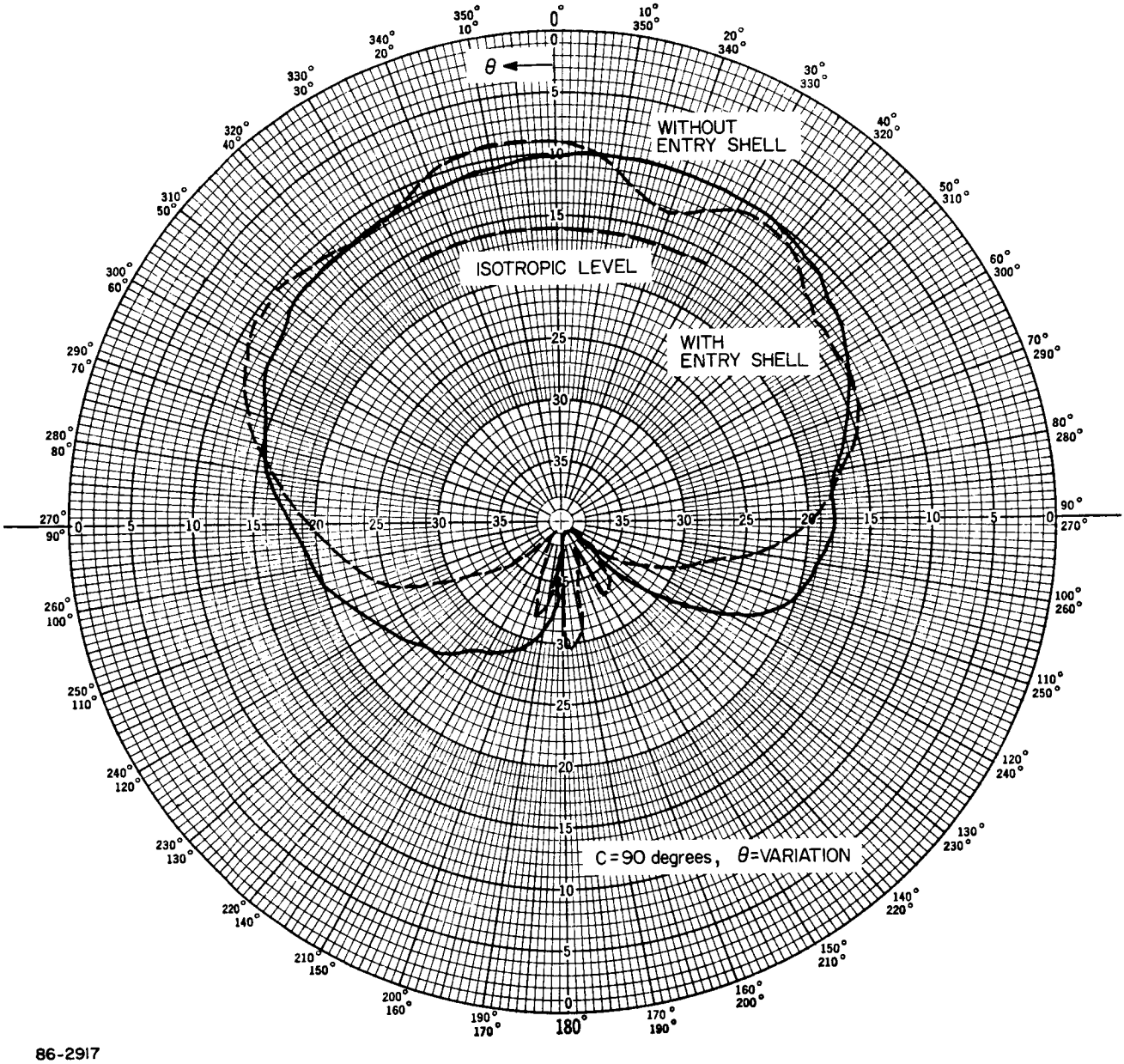

Figure A-9 FLIGHT CAPSULE ANTENNA PATTERN WITH AND WITHOUT ENTRY SHELL

Figure A-10 shows the effects of reflections on the antenna pattern at a look angle of 110 degrees. It can be seen from this figure, that if the antennas are aligned perpendicular to the longitudinal axis of the vehicle (no tilt) deep nulls occur in the antenna pattern. The depth of these nulls are reduced by tilting the antenna slightly (approximately 15 degrees) towards the longitudinal axis.

3.4 Antenna Efficiency

Several other points which pertain directly to the antenna itself are worthy of discussion, one is the efficiency of the antenna. It is well known that the efficiency of an antenna is simply the ratio of the measured gain to theoretical gain. The latter may be determined in either of two ways. The first is to take the value of the antenna half-power beamwidth and divide it into 4π steradians to obtain an approximation of the theoretical maximum value. The measured half-power beamwidth of this system is 95 degrees. Assuming that the free-space pattern is circularly symmetric we find:

$$\text{Gain} = \frac{41,253}{(95)^2} = 4.56 \ (6.62 \text{ db})$$

as the value for the directivity of the antenna. A second method is to integrate the antenna pattern numerically*. This method yields a value of 6.34 db. Comparing the measured gain of 6.0 db (see Figure A-6) to the average of the two theoretical values, results in an antenna efficiency factor of 90-percent. The measured gain is adjusted to compensate for an axial ratio of 3.75 db in the test model. A loss of 0.5 db can be attributed to the input VSWR of 2.1:1 for the model. The correlation of measured data with theory leads to the conclusion that a 90 percent efficient spiral antenna is realistic.

The efficiency factor must be modified to some extent in view of the possibility that the spacecraft may enter the Martian atmosphere at a very steep entry angle. Calculations have indicated that temperatures on the order of 900° F may occur on the surface of the antenna radome. This temperature can be reduced to 200° F on the surface of the antenna spiral by using a 0.3 to 0.4-inch thick randome. In addition to reentry heating, the ambient heat generated by the power being fed to the antenna as well as the use of a 0.3- to 0.4-inch radome will cause additional loss within the antenna system. The precise degree of loss can only be determined in laboratory measurements but a reduction of 1.5 db in antenna gain is a reasonable estimate. A 1.5-db loss would reduce the operating efficiency of the antenna to approximately 62 percent which is the design goal for the antenna system described above.

3.5 Antenna Axial Ratio

Another pertinent parameter of spiral antennas is the broad angular region where the axial ratio remains relatively low. Figure A-11 shows the

* Jasik Antenna Handbook, pg. 24-25.

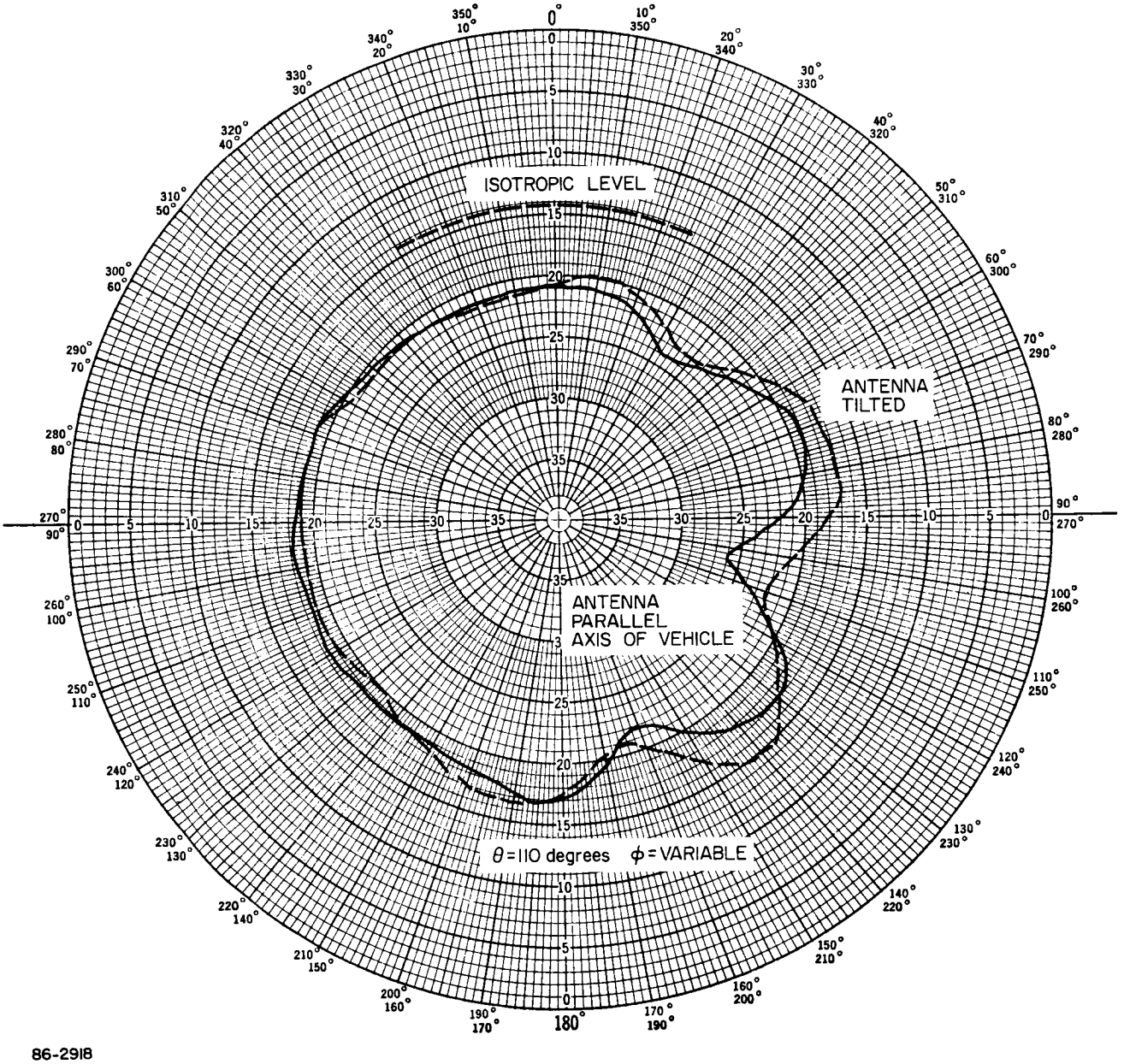

Figure A-10 FLIGHT CAPSULE ANTENNA PATTERN, WITH AND WITHOUT TILT

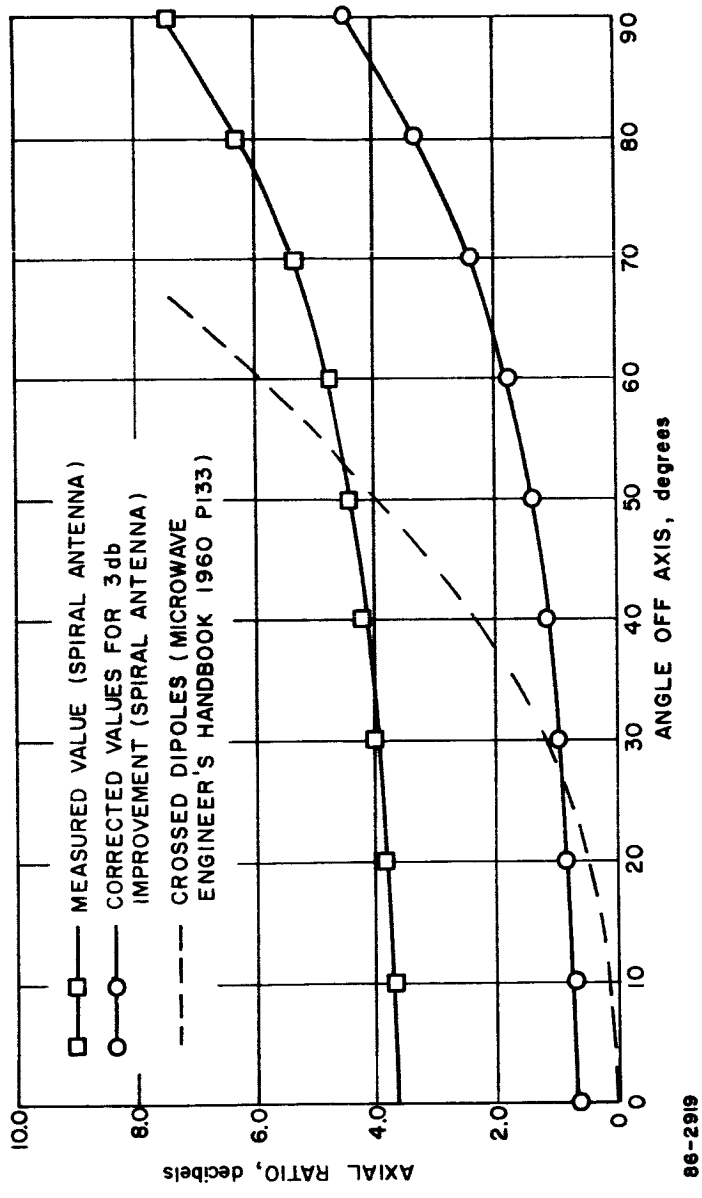

Figure A-11 AXIAL RATIO VERSUS LOOK ANGLE FROM ANTENNA AXIS

actual values obtained from the antenna model used for the pattern measurements in this study. The on-axis axial ratio of the test antenna is 3.75 db. With more careful design this can be reduced to less than 1.0 db. Superimposed on these curves are the off-axial ratios for a crossed dipole. In the θ = 70- to θ = 90-degree regions, the spiral displays notable improvement over the crossed dipole. This becomes significant when the look angles of interest lie in this region and the receiving antenna on the spacecraft is circularly polarized and also has a broad range of look angles. It should be pointed out that the degradation in axial ratio from θ = 0 degree, antenna boresight, to θ = 90 degrees, is on the order of 4.0 db.

3.6 Antenna Weight

A close study of the antenna weight required to produce a design that could be relied upon to maintain the physical integrity of the antenna is described below. Assume the following:

a) Antenna sealed and pressurized at one atmosphere

b) Antenna not sealed and loaded with foam

c) Antenna not sealed

Also assume the following environmental conditions:

1) Sterilization at 300°F for 36 hours - 1 cycle-antenna to be subjected to 3 cycles.

2) Pressure in space is a hard vacuum

3) Ambient temperature while antenna is radiating (-60°F to 200°F).

For the three antenna cases cited above, weight estimates was calculated.

3.6.1 Case I - Sealed and Pressurized

In order to withstand the 5000 pounds of force developed on the surface of the antenna a dielectric radome of approximately 0.4 inch thick would be required. For a typical fluorocarbon with a density of 0.0684 $lb/in.^3$ the window by itself would weigh approximately 7.0 pounds. In addition, a heavier structure with a large flange to accept an O-ring would be required. The total weight of such a structure would exceed 18.0 pounds.

3.6.2 Case II - Antenna Not Sealed and Loaded With a Dielectric

The cavity depth would be reduced from 11.0 to 7.1 inches if a dielectric constant of 2.0 is assumed for the foam. The dielectric radome as

well as the dielectric surface on which the spiral circuit is etched may be supported by the foam. The estimated weight for this structure is approximately 11.5 pounds.

3.6.3 Case III - Antenna Unsealed and Unloaded

By equalizing the pressure inside the antenna, the mechanical rigidity assumed in Case I may be curtailed. In particular, the antenna structure and mounting flange would be reduced, as well as the thickness of the randome. The estimated weight of this structure is approximately 8.0 pounds. The antenna structure is 7.0 pounds and the radome is 1 pound.

The thickness of the radome had to be increased to 0.4 inch thick in order to maintain a surface of the spiral antenna at or below 250°F. The weight of this radome is 7 pounds as we indicated above, and the weight of the antenna including the cavity and feed structure is 7 pounds. This results in an overall weight for the antenna of approximately 14 pounds.

3.7 Summary of Antenna Characteristics

At this point in the antenna description, it is reasonable to summarize the results of this study in a compilation of design objectives. These may be considered operating specifications which future hardware for this system must be required to meet. Refer to Table A-3.

The relay antenna system would consist of two planar logarithmic spiral antennas tilted at approximately 15 degrees to the space capsule axis. It has been demonstrated in the course of this discussion that the antenna system would function with an efficiency of greater than 62 percent. Experimental data has confirmed the fact that flight capsule geometry would modify the free-space pattern of the spiral antenna. A metallic rocket nozzle is unacceptable. Tilting the antenna towards the axis of the vehicle offers a significant radiation pattern improvement in the event of the single antenna system failure. A weight analysis of the antenna for various cases has been presented in detail. Finally, a list of operating requirements has been prepared. All of these factors comprise the total description of the VHF relay antenna system recommended for use on the flight capsule.

TABLE A-3

DESIGN REQUIREMENTS

Electrical	
Gain - 0.0 db at ± 90 degrees points from antenna boresight.	
Polarization	Circular
Axial patio	< 1.0 db
Efficiency	> 62 percent
Input VSWR	1.25:1.00 or less
Power handling capability	30 watts
Operating frequency	270 MHz
Mechanical	
Weight	8 pounds
Temperature	300°F for 36 hours (3 cycles)
Operating temperatures	-60 to +200°F
Shock and vibration	Undertermined

APPENDIX B

FLIGHT SPACECRAFT BIT SYNCHRONIZER ANALYSIS

1.0 INTRODUCTION

The relay data link between the flight capsule and flight spacecraft has been described in detail previously in this report. This data link operates at VHF and utilizes a non-coherent PCM/FSK modulation technique. The non-coherent PCM/FSK system performs synchronous detection at video frequencies. In order to achieve optimum system performance, accurate bit timing must be developed at the flight spacecraft. Both the frequency and phase of the received data clock must be accurately determined in order to provide the required sample and dump functions to the video dumped integrator. Thus, a bit synchronizer will be required on board the flight spacecraft to synchronize a local clock to the received NRZ data sequence and thereby provide the required timing functions for the receiving subsystem.

The relationship of the bit synchronizer to the flight spacecraft receiving subsystem is illustrated in Figure 113. The bit synchronizer must synchronize the local data clock to the combined output of the diversity combiner. The sample and dump pulses are derived from the reconstituted data clock and applied to the signal detector to allow individual bit detection.

It is the intent of the present appendix to consider some of the more detailed aspects of bit synchronizer performance suitable for a Mars entry mission. Rather than make an exhaustive study of the different bit synchronizer configurations suitable for this mission, it was decided to analyze the performance of a somewhat simplified configuration whose operation can be readily analyzed. Most bit synchronizer configurations are variations of this generic configuration and the resulting performance will be typical of a wide class of designs.

2.0 CONCLUSIONS AND RECOMMENDATIONS

From the analysis of the generic bit synchronizer presented in the following section, we conclude that the flight spacecraft bit-timing requirements can be met quite easily with simple circuitry. It is noted that the actual implementation of the bit synchronizer can take a number of forms, however, the performance will be quite similar to that obtainable with the basic system chosen for analysis.

Results indicate that even for a simple first-order tracking loop, the bit synchronizer for the PCM/FSK data link will allow rapid acquisition and will provide adequate bit-timing accuracy. The steady-state phase error present in the first-order loop as a result of initial frequency offset is shown to be

quite small and hence have a negligible effect on system performance. It is expected that the second-order loop, although much more difficult to analyze, will provide even improved performance.

Because of the limited communications time available in the Mars entry mission, the bit synchronizer must provide rapid acquisition of the data clock. Once the data clock has been acquired, the bit synchronizer must provide accurate tracking performance. These two requirements constitute the basic tradeoffs in most synchronizing systems. If the acquisition is to be extremely rapid, we must be willing to tolerate larger tracking inaccuracies. If the tracking accuracy can be relaxed somewhat, more rapid acquisition can be achieved. The design of any bit synchronizer must carefully weigh these tradeoffs in arriving at an optimum bit synchronizer configuration. It is recommended, therefore, that future effort be expended, both analytical and experimental, in an effort to arrive at a configuration which strikes a balance between the pertinent tradeoff parameters. The future effort should have the following objectives:

1. Determine the optimum bit synchronizer configuration consistent with the overall flight spacecraft receiving subsystem.

2. Assess the sensitivity of the bit-error rate on bit synchronizer performance in order to provide a more definitive tradeoff basis.

3. Promising bit synchronizer configurations should have their acquisition and tracking performance determined experimentally. Analytic treatment of other than the most simple system is extremely difficult.

4. Investigate the feasibility and desirability of utilizing coding schemes which will increase bit-transition density and thereby enhance the performance of the bit synchronizer.

3.0 ANALYSIS

The large majority of present PCM bit synchronizers utilize a phase-lock loop to develop the bit-rate timing. However, in order to provide phase lock, there must be present in the input to the phase-lock loop a discrete frequency component to which a VCO can be locked. The random NRZ PCM data train, on the otherhand, possesses a continuous $(\sin x/x)^2$ power spectrum, and hence contains no discrete frequency components. This being the case, it is not possible for a phase-lock loop to respond directly to the random pulse train. However, the frequency and phase of the timing waveform are contained in the random zero crossings of the PCM waveform since these zero crossing are spaced at integral multiples of the bit period. Intuition suggests that there should be some means of processing this random NRZ sequence to recover a discrete frequency component at the clock rate. Indeed, this is correct.

However, the processing schemes usually require some combination of filtering and nonlinear processing. This nonlinearity can take many forms, but most commonly is a rectifier or limiter differentiator. A block diagram of the generic bit synchronizer is illustrated in Figure B-1. The output of the nonlinear element forms one input of a phase detector, and the other input to the phase detector is a locally generated clock signal. The phase detector produces an output voltage proportional to the difference in phase between its two input signals. This phase error signal is applied to a servo loop so that the VCO frequency is continually adjusted to drive the phase error to zero.

In the generic bit synchronizer illustrated in Figure B-1 a great latitude exists in the implementation of the phase error measuring function. Our intent is to analyze the performance of this generic bit synchronizer independent of the method of implementation, and consequently an exhaustive treatment of different implementation approaches is not warranted. What we shall prefer at this time is to illustrate one implementation of the phase detector which is particularly well suited to the ensuing analysis, and at the same time is typical of most phase detectors suitable for this application. This phase detector along with the pertinent waveforms is illustrated in Figure B-2. The input NRZ sequence is first differentiated to produce a sequence of pulses occurring at transitions in the data. Note that the received NRZ sequence is illustrated as undergoing a transition between adjacent bits in Figure B-2. This will not be the case in actual practice, however, the present discussion is simplified by so illustrating and this will not be used in the analysis.

The differentiated pulses are subsequently rectified to produce a sequence of unipolar pulses occurring at data transitions. The unipolar pulses are then applied to a trigger circuit to provide control of a linear gate. The input to the linear gate is the ac coupled output of a function generator producing a triangular waveform. The triangular waveform is synchronized to the local clock. The output of the linear gate is then a sequence of amplitude modulated pulses located at the data transitions. The amplitude of the pulses convey both the sign and magnitude of the phase error over a ± 90-degree range. This arrangement will give a discriminator characteristic with stable nulls located at alternate half-cycles.

Using this phase detector implementation in the generic bit synchronizer illustrated in Figure B-1, the phase error will be presented in the form of discrete bi-polar pulses whose amplitude is proportional to phase error. This last fact allows the operation of the tracking loop to be linearized and analyzed as a sampled data servo system. A simplified block diagram of the bit synchronizer tracking loop subsequently appears as illustrated in Figure B-3. The input bit sync phase is $\theta_{in}(t)$ and the local clock phase is $\theta_o(t)$. The quantity $\theta_e(t)$ is the difference between input and output phase and is here assumed continuous. The continuous phase error $\theta_e(t)$ is sampled by switch s_1 for instants separated by integral multiples of the bit period τ . The sampling function controlling the switch s_1 is also illustrated in Figure B-3.

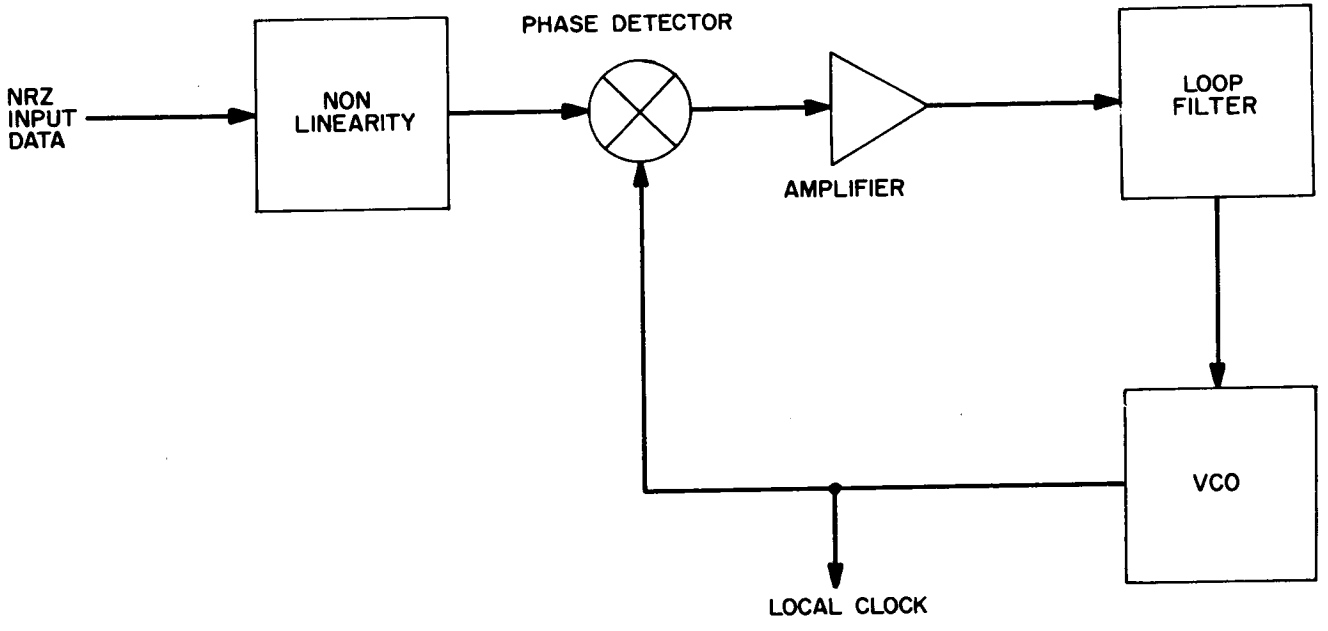

Figure B-1 GENERIC BIT-SYNCHRONIZER

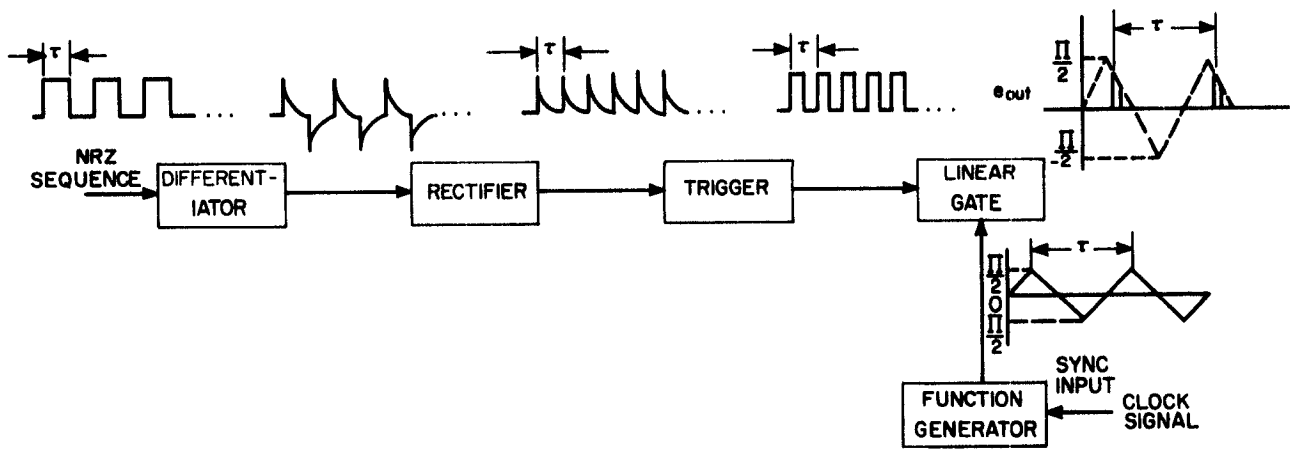

Figure B-2 TYPICAL PHASE DETECTOR IMPLEMENTATION

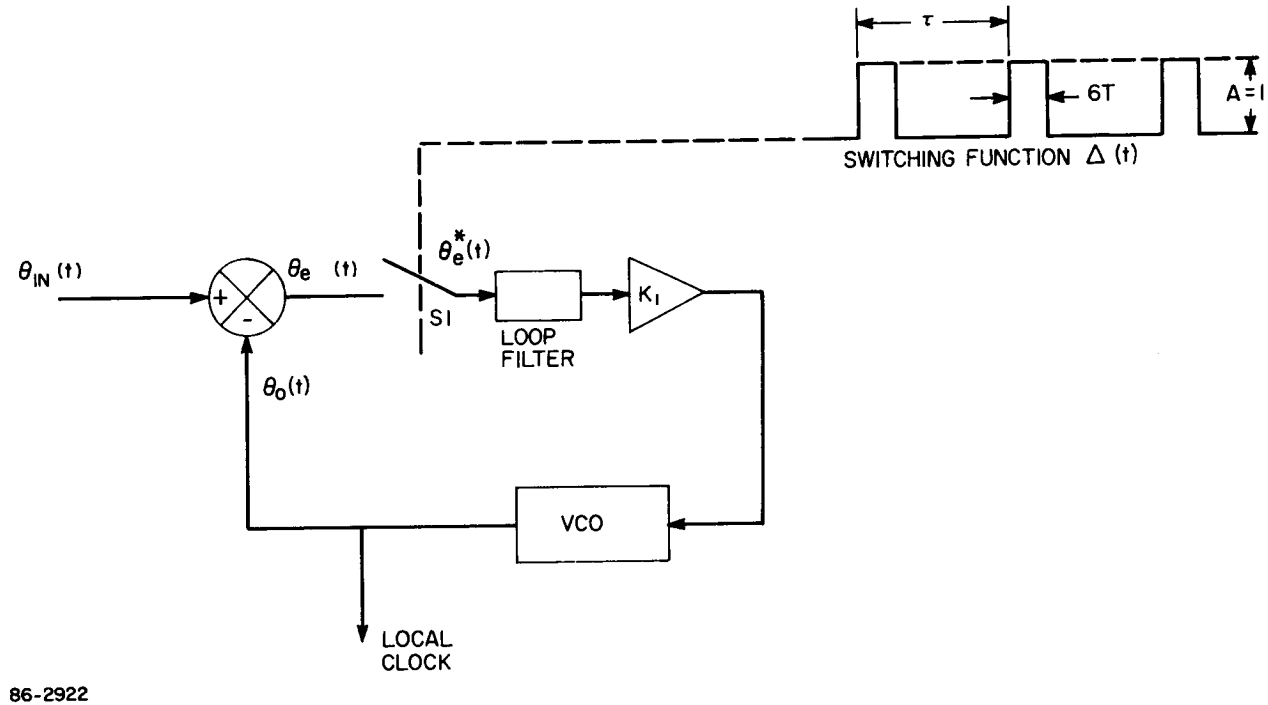

Figure B-3 LINEARIZED SAMPLED DATA TRACKING LOOP

The sampled error signal $\theta_e^*(t)$ is thus given by

$$\theta_e^*(t) = \theta_e(t) \sum_{n=-\infty}^{n=t/\tau} v(t' - n\tau) \tag{1}$$

where n is an integer, and v(t) is a single pulse of the sampling function shown in Figure B-3. The quantity $\theta_e^*(t)$ is subsequently applied to the loop filter with impulse response h(t) . The function of the loop filter is to limit the rate of change of the local clock frequency to values corresponding to those expected on the input signal. There are a considerable number of tradeoffs in the choice of the optimum loop filter. These considerations are more pertinent to a detailed design implementation and hence will not be considered at this time. Instead we will consider the simplified case of a type 1 loop, in which case no filtering is provided, and the sampled error signal $\theta_e^*(t)$ is applied directly to the VCO. The output of the VCO is a local clock frequency which is proportional to the amplitude of the input error signal. However, the variable upon which the linearized loop acts is phase, in which case the VCO can be represented by an integrator. Thus if $K_1 \theta_e^*(t)$ is applied as input to the VCO, the output phase $\theta_o(t)$ is given as

$$\theta_o(t) = K_1 \int_{-\infty}^{t} \theta_e^*(t')\, dt' \tag{2}$$

Note that the VCO sensitivity has been absorbed in the gain constant K_1 . Now substituting from Equation 1 into 2, we have

$$\theta_o(t) = K_1 \sum_{n=-\infty}^{t/\tau} \int_{-\infty}^{t} \theta_e(t')\, v(t' - n\tau)\, dt' \tag{3}$$

and if we assume that the sampling pulse duration $b\tau$ is small (i. e. , $b \ll 1$), then Equation (3) becomes approximately

$$\theta_o(t) \cong b K_1 \sum_{n=-\infty}^{t/\tau} \theta_e(n\tau) \tag{4}$$

From Equation 4 it is observed that if at any time a change $\Delta\theta_e$ occurs in θ_e this is felt immediately (except for a small sampling delay of maximum value τ) as a change $\Delta\theta_o$ in θ_o . The fraction

$$K = bK_1 \tag{5}$$

is the fractional part of the error $\Delta\theta_e$ which is applied as a correction immediately following a sync sample. If K is very small, there will be very little jitter in θ_o but the transient response of the loop will be very slow. If K is appreciable compared with unity, the transient response will be fast, but considerable jitter will result.

Sophisticated techniques are available for the computation of transient response and output variance of sampled-data loops, but this loop is simple enough to treat in a direct way.

If one makes a table of successive values of input phase, phase error and output phase, starting with zero error, Equation 4 leads to:

TABLE B-1

SEQUENCE OF EVENTS IN SAMPLED DATA SERVO LOOP

Sample Number	θ_{IN}	θ_e	θ_o
0	0	0	0
1	θ_1	θ_1	$K\theta_1$
2	θ_2	$\theta_2 - K\theta_1$	$K\theta_2 + K(1-K)\theta_1$
3	θ_3	$\theta_3 - K\theta_2 - K(1-K)\theta_1$	$K\theta_3 + K(1-K)\theta_2 + K(1-K)^2\theta_1$

The pattern is clear:

$$\theta_o]_n = K\theta_n + K(1-K)\theta_{n-1} + K(1-K)^2\theta_{n-2} + \ldots + K(1-K)^{n-1}\theta_1 \qquad (6)$$

where n is the sample number.

If a step in phase of magnitude θ_{in} is applied at the first sample and maintained, then after n samples:

$$\theta_o]_n = K\theta_{in}[1 + (1-K) + (1-K)^2 + \ldots (1-K)^{n-1}] \qquad (7)$$

$$= [1 - (1-K)^n]\theta_{in}$$

Equation (7) describes the transient response of the loop in terms of a single parameter, the gain K. Equation (6) can also be used to find the variance of θ_o when the loop is locked and the average value of the loop error is zero. In that case, θ_{in} can with no loss of generality be assumed to have zero mean, and a variance $<\theta_{in}^2>$. Since the predetection bandwidths of the wideband PCM/FSK system are very large compared with the reciprocal of the bit duration τ, successive samples of the sync phase-error signal are essentially independent. Now taking the square of equation 6 and averaging we have

$$<\theta_o^2> = K^2 <\theta_{in}^2>_n + K^2(1-K)^2 <\theta_{in}^2>_{n-1} + \ldots K^2(1-K)^{2n-2} <\theta_{in}^2>_1 \qquad (8)$$

All cross-product terms of the type $<(\theta_{in}^2)_n (\theta_{in})_{n-j}>$; $j \neq 0$, etc, vanish due to the assumed independence of the samples of θ_{in}. Also, since

$$<\theta_{in}^2>_n = <\theta_{in}^2>_{n-j} = <\theta_{in}^2> : \text{all } j \qquad (9)$$

Then

$$<\theta_o^2> = K^2[1 + (1-K)^2 + (1-K)^4 + \ldots (1-K)^{2n-2}] <\theta_{in}^2> \qquad (10)$$

$$= \frac{K^2}{1-(1-K)^2} \qquad <\theta_{in}^2> \; : \; 0 < K \leq 1$$

or

$$<\theta_o^2> = (K/2-K) <\theta_{in}^2> \qquad (11)$$

and for $K << 1$

$$<\theta_o^2> \approx \frac{K}{2} <\theta_{in}^2> \qquad (12)$$

Now if the input phase variance $<\theta_{in}^2>$ can be related to input SNR, it is possible to express the output phase variance $<\theta_o^2>$ in terms of input SNR. The block diagram of the pertinent part of the system under consideration is illustrated in Figure B-4. From previous[1] analysis of the wideband PCM/FSK system, the SNR at the input to the filter preceeding the bit synchronizer is given as

$$(S/N)_{b_o} = \frac{\left[Z\, b_o\, \tau N_o \left\{\frac{E}{b_o \tau N_o}\right\}\right]^2}{Z(Z\, b_o\, \tau N_o)^2 \{1 + E/b_o\, \tau\, N_o\}} \qquad (13)$$

[1] Part I Report, RAD / TR-65-29 Volume 4, Book 3, Appendix 4.8.

or

$$(S/N)_{b_o} = \frac{\left(\frac{E}{b_o \tau N_o}\right)^2}{2\left\{1 + \frac{E}{b_o \tau N_o}\right\}}$$

Now in passing through the filter of bandwidth n/τ (cps) the SNR improves by approximately the factor $\frac{b_o \tau}{n}$. This simplified approach does not take into account the spectral characteristics of signal plus noise appearing at the output of the envelope detectors, nor the effects of intersymbol interference. However, for the anticipated SNR's, the noise spectrum at the output of the envelope detectors is approximately flat, and if $n \geq 2$, the effects of intersymbol interference are essentially negligible. Thus, we have at the input to the bit synchronizer

$$\frac{S}{N} \cong \frac{b_o \tau}{n} \quad \frac{\left(\frac{E}{b_o \tau N_o}\right)^2}{2[1 + E/b_o \tau N_o]} \tag{14}$$

The above approximate approach is consistent with the system operating parameters and will lead to some easily interpreted results.

The jitter in the input sync phase θ_{in} will correspond to inaccuracies in the estimation of the data transition instants caused by the noise. The problem here is similar to the radar detection problem, where it is desired to estimate time delay from a received video pulse imbedded in noise. This problem has been considered by Skolnik[2] who shows that the mean square error in the measurement of the transition instant is given by

$$\langle T_R^2 \rangle = \frac{t_r^2}{2(S/N)} \tag{15}$$

where

t_r = video pulse rise time

S/N = SNR appearing at the input to Bit Synchronizer

Substituting from Equation 14 into 15 we have

$$\langle T_R^2 \rangle = \frac{n\, t_r^2}{b_o \tau} \quad \frac{[1 + E/b_o \tau N_o]}{(E/b_o \tau N_o)^2} \tag{16}$$

[2]Skolnik, M. I., Introduction to Radar Systems, McGraw-Hill Book Co. Inc., N. Y., pg. 464 (1962).

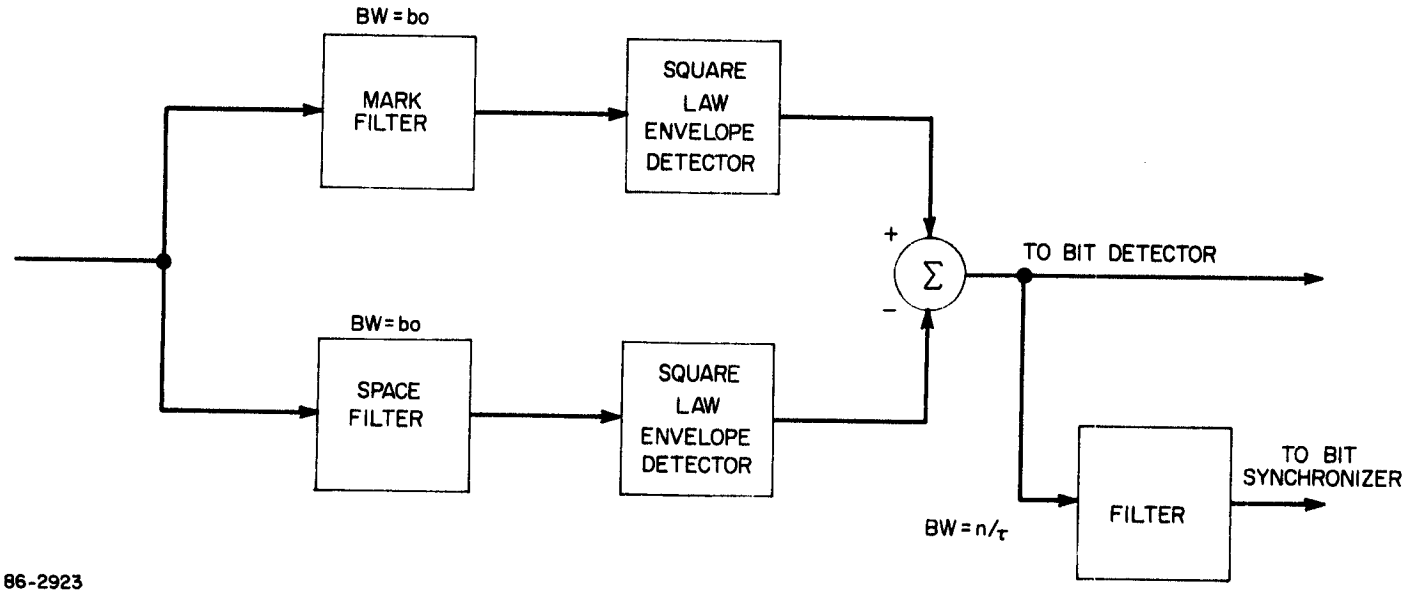

Figure B-4 PORTION OF WIDEBAND PCM/FSK SYSTEM PERTINENT TO DETERMINATION OF $(\theta_{IN})^2$

and if t_r is limited primarily by the rise time of the filter preceeding the bit synchronizer, then we have approximately

$$< T_R^2 > \cong \frac{\tau^2}{n\, b_o\, \tau} \quad \frac{[1 + E/b_o\, \tau\, N_o]}{(E/b_o\, \tau\, N_o)^2} \tag{17}$$

Now since the input sync phase $\theta_{in} = 2\pi f_m t$, the mean-square phase error becomes

$$< \theta_{in}^2 > \cong \frac{(2\pi\, fm)^2\, \tau^2}{n\, b_o\, \tau} \quad \frac{\left[1 + \dfrac{E}{b_o\, \tau\, N_o}\right]}{\left(\dfrac{E}{b_o\, \tau\, N_o}\right)^2} \tag{18}$$

and when we note that $fm = \dfrac{1}{\tau}$

$$< \theta_{in}^2 > \cong \frac{(2\pi)^2}{n b_o\, \tau} \quad \frac{\left[1 + \dfrac{E}{b_o\, \tau\, N_o}\right]}{\left(\dfrac{E}{b_o\, \tau\, N_o}\right)^2} \tag{19}$$

Thus substituting from Equation 19 into Equation 12 we have

$$< \theta_o^2 > \cong \frac{K}{2} \quad \frac{(2\pi)^2 \quad \left[1 + \dfrac{E}{b_o\, \tau\, N_o}\right]}{n\, b_o\, \tau \quad \left(\dfrac{E}{b_o\, \tau\, N_o}\right)^2} \tag{20}$$

This equation gives the variance of the output sync phase jitter in terms of the loop-gain factor K, the time-bandwidth product $b_o \tau$ and the IF SNR $\dfrac{E}{b_o\, \tau\, N_o}$. This is quite convenient and allows the analysis of the bit synchronizer performance in terms of the same parameters used to characterize the bit error probability performance of the wideband PCM/FSK data link.

For the present design, the IF filter bandwidths will be approximately 85 kHz and the operating bit rate will be 18,000 bps. This gives a $b_o \tau$ of approximately 4.7. From Figure 115 we see that the required IF SNR to achieve a bit error probability of 1×10^{-3} is 7 db. If the filter preceeding the bit synchronizer has a bandwidth equal to twice the bit rate (i.e., n = 2), then Equation 20 becomes

$$< \theta_o^2 > \cong \frac{K\, \pi^2}{20} \tag{21}$$

The rms sync phase error becomes

$$\theta_{o\,(RMS)} = \pi \sqrt{K/20} \tag{22}$$

This expression dictates a maximum value for the loop-gain constant K if the rms sync phase error is to be held below some fixed value. Table B-2 indicates the maximum value of K for a number of limits on $\theta_{o\,(rms)}$.

TABLE B-2

MAXIMUM VALUES OF LOOP GAIN FOR VARIOUS RELATIVE RMS ERRORS IN SYNC PHASE

$\frac{\theta_o\,(RMS)}{2\pi}$	Maximum Loop Gain K Maximum
1 (percent)	0.008
5 (percent)	0.20
10 (percent)	0.80

The table indicates quite clearly that if the sync phase error is to be held small, the loop gain must likewise be held quite small. Small values of loop gain imply longer acquisition times, however, and a tradeoff between allowable sync phase jitter and acquisition time must be made. As an example, suppose the allowable relative sync phase jitter is 10 percent and we are utilizing the maximum loop gain from Table B-2 (i.e. K = 0.8). Equation (7) gives an expression for the transient response of the loop to an initial phase error θ_{in} . The phase error after n samples have been processed is

$$\theta_e = (1-K)^n \theta_{in} \tag{23}$$

and solving for n

$$n = \frac{\log\left(\frac{\theta_e}{\theta_{in}}\right)}{\log\,(1-K)} \tag{24}$$

from which we can solve for the required number of samples (or data transitions) required in order to reduce the error θ_e to within some fraction of the input phase offset. Table B-3 has been constructed to illustrate this requirement.

TABLE B-3

NUMBER OF SAMPLES REQUIRED TO REDUCE THE PHASE ERROR TO WITHIN SOME SPECIFIED PERCENT OF INITIAL PHASE OFFSET

$\frac{\theta_e}{\theta_{IN}}$	Number Of Samples Required
1 (percent)	3
5 (percent)	2
10 (percent)	2

This table gives some indication of the acquisition capabilities of the bit synchronizer. For instance if a 10-percent sync phase jitter can be tolerated, the bit synchronizer will be required to process two samples before the phase error is reduced to within 10 percent of the initial phase offset. It should be noted that a sample is provided to the bit synchronizer only when the data undergoes a transition. Thus, for the particular case under consideration, only two data transitions must be received before the phase error is reduced to within 10 percent of the initial phase offset.

It should be obvious that in order to provide rapid acquisition, we must be willing to tolerate larger rms sync phase jitter. In the particular case considered above, we observed that if we were willing to tolerate an rms sync phase jitter of 10 percent, then the acquisition would require the processing of only a small number of samples. Since the bit rate is to be approximately 18,000 bps, we can be reasonably well assured that the required number of data transitions will be received and processed in only a fraction of a second. On the other hand, if we were to set more stringent requirements on the allowable rms sync phase jitter, the acquisition time would increase significantly. It is instructive at this time to illustrate the behavior of the acquisition characteristics as the allowable rms sync phase jitter is reduced. This behavior is indicated in Table B-4.

TABLE B-4

REQUIRED NUMBER OF SAMPLES TO REDUCE θ_e/θ_{IN} TO WITHIN SOME ACCEPTABLY SMALL PERCENT FOR DIFFERENT ALLOWABLE RMS SYNC PHASE JITTER

$\frac{\theta_o \text{ (RMS)}}{2\pi}$	$\frac{\theta_e}{\theta_{IN}}$	Number of Samples Required
1 (percent)	1%	560
	5%	370
	10%	280
5 (percent)	1%	20
	5%	13
	10%	10
10 (percent)	1%	3
	5%	2
	10%	2

Table B-4 indicates the increase in acquisition time as $\theta_{o\,(RMS)}$ is reduced. Even for relatively small rms sync phase jitter, however, the required number of samples to reduce the phase offset to within some acceptably small percent of its initial value is not prohibitive. With the data link bit rate at approximately 18,000 bps, the required number of data transitions for all of the cases depicted in Table B-4 will have occurred within a few seconds. Thus, it appears entirely feasible to design and construct a bit synchronizer for the wideband PCM/FSK data link which will allow rapid acquisition and will provide adequate bit timing accuracy.

In the foregoing analysis, it has been implied that the average frequency of the VCO in the bit synchronizer tracking loop is always exactly the same as the received data clock signal. If this condition is not met, there will be a continual drift in phase, requiring a constant phase error in the tracking loop in order to

correct the frequency. If, for instance, the frequency of the local clock is in error by Δf_B , the phase accumulated between sampling intervals or data transitions is

$$\Delta\theta = 2\pi (\Delta f_B)\, \bar{\tau}_s \tag{25}$$

where

Δf_B = frequency error in local clock

f_B = average clock frequency (channel bit rate)

$\bar{\tau}_s$ = average time between data transitions

Now suppose the local clock instability is one part in 10^3 (i.e., $\Delta f_B/f_B = 10^{-3}$) and if we assume $f_B = 18,000$ cps

$$\Delta\theta = 2\pi (10^{-3})(18 \times 10^3)\, \bar{\tau}_s \tag{26}$$

Table B-5 has been constructed similar to Table B-4 to illustrate the sequence of events within the tracking loop when the input phase changes by an amount $\Delta\theta$ between data transitions

TABLE B-5

SEQUENCE OF EVENTS IN BIT SYNCHRONIZER TRACKING LOOP FOR A FIXED FREQUENCY OFFSET

Sample	θ_{IN}	θ_e	θ_o
0	0	0	0
1	$\Delta\theta$	$\Delta\theta$	$K\Delta\theta$
2	$2\Delta\theta$	$2\Delta\theta - K\Delta\theta$	$2K\Delta\theta - K^2\Delta\theta + K\Delta\theta$
3	$3\Delta\theta$	$3\Delta\theta - 2K\Delta\theta - K(1-K)\Delta\theta$	$3K\Delta\theta + 2K(1-K)\Delta\theta + K(1-K)^2\Delta\theta$
4	$4\Delta\theta$		

The sequence should be quite clear. Thus, the output phase after $n-1$ samples, and upon the occurrence of the $n^{'th}$ sample is

$$\theta_o]_n = (n-1)\,K\,\Delta\theta + (n-2)\,K\,(1-K)\,\Delta\theta + (n-3)\,K\,(1-K)^2\,\Delta\theta \quad (27)$$

$$+ \ldots\ K(1-K)^{n-2}$$

The input phase at this point, however, has advanced to

$$\theta_{in}]_n = n\,\Delta\theta \quad (28)$$

The phase error at this point is then

$$\theta_e]_n = \theta_{in}]_n - \theta_o]_n \quad (29)$$

and hence

$$\theta_e]_n = n\,\Delta\theta - (n-1)\,K\,\Delta\theta - (n-2)\,K\,(1-K)\,\Delta\theta \quad (30)$$

$$- (n-3)\,K(1-K)^2\,\Delta\theta - \ldots K(1-K)^{n-2}\,\Delta\theta$$

At this point, we want to ensure that this series converges to some tolerable steady-state phase error. Letting $x = 1 - K$, Equation (30) becomes

$$\theta_e]_n = \Delta\theta\,\{n - (n-1)\,K - (n-2)\,Kx - (n-3)\,Kx^2 \quad (31)$$

$$- \ldots K\,x^{n-2}\,\}$$

which can be separated into two distinct series

$$\theta_e]_n = \Delta\theta\,\{n - Kn\,[1 + x + x^2 + \ldots x^{n-2}] \quad (32)$$

$$+ K\,[1 + 2x + 3x^2 + \ldots . (n-1)\,x^{n-2}]\}$$

or

$$\theta_e]_n = \Delta\theta \left\{ n - Kn \left[\frac{1 - x^{n-1}}{1 - x} \right] + K \frac{d}{dx} \sum_{m=1}^{n-1} x^m \right\} \tag{33}$$

$$= \Delta\theta \left\{ n - n(1 - x^{n-1}) + K \frac{d}{dx} x \left[\frac{x^{n-1} - 1}{x - 1} \right] \right\}$$

and finally we have

$$\theta_e]_n = \Delta\theta \left\{ n x^{n-1} + K \frac{d}{dx} x \left[\frac{x^{n-1} - 1}{x - 1} \right] \right\} \tag{34}$$

We desire now to determine the steady-state error given by

$$\theta_e]_{s.s.} = \lim_{n \to \infty} \theta_e]_n \tag{35}$$

Let us find the limit of each of the terms in Equation (34) separately. Considering the first term

$$\lim_{n \to \infty} n x^{n-1} = \frac{1}{x} \lim_{n \to \infty} \frac{n}{x^{-n}} \tag{36}$$

but the limit on the right is indeterminate since $x = 1-K<1$. By applying l'Hospital's rule

$$\frac{1}{x} \lim_{n \to \infty} \frac{n}{x^{-n}} = 1/x \lim_{n \to \infty} \frac{dn/dn}{\frac{d}{dn} x^{-n}} \tag{37}$$

$$= 1/x \lim_{n \to \infty} - 1/x^{-n} \ln x$$

$$= 0$$

since $x < 1$

Likewise for the second term in Equation 34 we have upon performing the indicated differentiation and passing to the limit

$$\lim_{n\to\infty} K \frac{d}{dx} \left[x \left(\frac{x^{n-1} - 1}{x - 1} \right) \right] = K \lim_{n\to\infty} \left\{ x \left[\frac{(x-1)(n-1)x^{n-2} - (x^{n-1} - 1)}{(x-1)^2} \right] + \frac{x^{n-1} - 1}{x - 1} \right\} \quad (38)$$

which becomes

$$\lim_{n\to\infty} K \frac{d}{dx} \left[x \left(\frac{x^{n-1} - 1}{x - 1} \right) \right] = \frac{K}{(x-1)^2} = 1/K \quad (39)$$

Thus we have from Equation (35)

$$\theta_e]_{ss} = \frac{\Delta\theta}{K} \quad (40)$$

and for an assumed frequency instability of one part in 10^3, we have from Equation (26)

$$\theta_e]_{ss} = 106/K\ \bar{\tau}_s \quad (41)$$

where, of course, τ_s is the average time between data transitions. Suppose for example that a data transition occurred on the average once every 10 data bits, then at a data rate of 18,000 bps, Equation (41) becomes

$$\theta_e]_{ss} = 106/K\ (10/18{,}000) \quad (42)$$

It was shown previously that a value K = 0.2 allows rapid acquisition with an rms sync phase jitter of 5 percent. For this case, the steady-state phase error due to a frequency offset Δf_B becomes

$$\theta_e]_{ss} = 0.295 \text{ rad} . \quad (43)$$

or about 17 degrees. Note that this steady-state offset can be reduced considerably by increasing the frequency accuracy and/or reducing the time between data transitions. An illustration of the nature of these tradeoffs is illustrated in Table B-6. The quantity N in Table B-6 is the average number of bits between data transitions.

TABLE B-6

STEADY STATE PHASE ERROR DUE TO FREQUENCY OFFSET FOR VARIOUS COMBINATIONS OF OSCILLATOR STABILITY AND DATA TRANSITION DENSITY

Oscillator Stability	N	$\theta_e]_{ss}$ (degrees)
1×10^{-3}	5	8.5
	10	17
	20	34
1×10^{-4}	5	.85
	10	1.7
	20	3.4
1×10^{-5}	5	.085
	10	.17
	20	.34

From the table, it can be concluded that for practical oscillator stabilities and reasonable data transition densities, the steady-state phase error due to frequency offset can be made negligibly small. However, the requirements on the VCO appear now to be that it possess good long-term stability and large phase deviation capabilities. These requirements are somewhat inconsistent in a physical oscillator. The requirements can be met, however, if we utilize a VCO in the form of a relaxation oscillator whose average frequency is locked to a crystal oscillator. This allows the VCO to have a wide deviation range while assuming the long term stability of the transmittal oscillator.

BIBLIOGRAPHY

1. Isbell, D. E. and R. Duhamel, Broadband Logarithmically Periodic Structure IRE N. C. R. (1957).

2. Bawer and Wolfe, The Spiral Antenna PT. 1 IRE Conv. Record (1960).

3. Burdine, The Spiral Antenna MIT Research Lab. Tech. (April 1955).

4. Dyson, The Equiangular Spiral Antenna PGAP (April 1959).

5. Kaiser, The Archimedian Two Wire Spiral Antenna PGAP (May 1960).

6. Curtiss, W. L., The Spiral Antennas PGAP (May 1960).

7. Riblett, H. B., A Broadband Spherical Satellite Antenna Proc. of IRE (April 1960).

8. Jasik, H., Antenna Handbook for Engineers.

9. Buranich, Godfrey, High Temperature Investigation and Development Cornell Aeronautical Laboratory Interim Eng. Report No. 6 Contract No. AF33(657) - 11100 Cal Report No. UB-1807-E-6 Period Ending (30 September 1964).

APPENDIX C

BATTERY CALCULATIONS FOR REFERENCE POWER PROFILE

1.0 INTRODUCTION

A listing of the user (instrumentation) power requirements is shown in Table C-1. This is shown in profile form in Figure C-1.

As before, the profile is divided between two batteries:

a) Preseparation to impact, and b) Post impact to end of mission.

Only calculations for the nickel cadmium battery will be included here. Sizes for the silver-zinc and lithium chlorine batteries will be estimated based on previous calculations. Design criteria are as called out in Appendix IV.4-15 of the mid-term report (Reference 1).

2.0 PRESEPARATION TO IMPACT

The following Table C-1 shows the power profile.

2.1 Power Profile

TABLE C-1

POWER PROFILE PRESEPARATION TO IMPACT

Period	Power Level (watts)	Time (hours)	Watt Hours
1. Preseparation check	311	0.03	10.4
2. ACS	146.5	0.25	36.6
3. Cruise	0.1	288.0	28.8
4. Status check	150	0.4	60.
5. Preentry to impact	142.6	0.33	48.2

In terms of ampere hours this power profile becomes the following: (see Table C-2.)

TABLE C-2

ENERGY SUMMARY

Period	Watts	Watt-Hours	Assumed Volts	Assumed Ampere-Hours
1	311	10.4	25	0.42
2	146.5	36.6	28	1.30
3	0.1	28.8	30	0.96
4	150	60	28	2.15
5	142.6	48.2	28	1.72
	Total →	184.0	Total →	6.55

2.2 Assignment of Derating Factors

In order to assign derating factors the apparent discharge rates must be calculated. The ampere-hour capacity is then modified by these and other derating factors to produce a design capacity.

Table C-3 shows apparent discharge rates and cell plateau voltages.

TABLE C-3

DISCHARGE RATES AND PLATEAU VOLTS

Period	Watts	Amps	*Rate	Cell V_p at +40°F Volts	Assumed Battery Volts
1	311	12.5	1.96	1.1	25
2	146.5	5.2	C/1.3	1.22	28
3	0.1	0.003	C/2200	1.3→1.35	30
4	150	5.35	C/1.25	1.22	28
5	142.6	5.1	C/1.3	1.22	28

*As compared with 6.6 Amperes discharge in 1 hour (C)

2.2.1 Derating Factors ϕ, Due To Discharge Rates

By assumption "m" of the design criteria, the maximum discharge rate is C/5, therefore penalties will have to be imposed. Except for period 3, all other periods are in violation of the criteria. No positive allowance is made for period 3. Assigned penalties are as follows:

Period 1, $\phi = 0.75$

Period 2, $\phi = 0.95$

Period 3, $\phi = 1.00$

Period 4, $\phi = 0.95$

Period 5, $\phi = 0.96$

Since period 1 accounts for approximately 5 percent of the total output a derating factor of 0.90 would be conservative $\phi_1 = 0.90$

2.2.2 Other Derating Factors

ϕ_2 Temperature: For +40°F operating $\phi_2 = 0.93$

ϕ_3, Stand Loss: This is taken to be no more than 10 percent in the 12 days cruise $\phi_3 = 0.90$.

Keeping Warm allowance: This is provided to allow for the battery keeping itself warm and is arbitrarily taken as 25 percent for the (Major) period of operating (Cruise)

$\phi_4 = 0.75$.

There are no other allowances to be made for nickel cadmium cells.

2.3 Design Amp-Hours and Watt Hours

2.3.1 Ampere-Hours

$$\text{Design ampere hours} = \frac{\text{ampere-hours initial}}{\phi_1 \times \phi_2 \times \phi_3 \times \phi_n}$$

$$\text{and Design ampere-hours} = \frac{6.6}{0.90 \times 0.93 \times 0.90 \times 0.75}$$

Design Capacity = 11.7 amp-hours

Percent allowance over minimum required capacity included in 11.7 ampere-hours

= (11.7/6.6 - 1) x 100

= 77.5 percent allowance

2.3.2 Watt-Hours

In order to assure 25 volts minimum for period 1 (the highest rate), 23 cells will be required. This will provide at least 25 volts for period 1, and match assumed voltage requirements for the remaining periods. The average voltage is $\frac{184 \text{ watt-hours}}{6.6 \text{ amp-hours}} = 28$ volts.

The approximate design watt-hours = 28 x 11.7

= 327 watts-hours

This checks with:

No. of cells x Plateau Volts (Av) x Design Capacity

or 23 x 1.22 x 11.7 = 329 watt-hours

The allowance is as before 77.5 percent

2.4 Total Battery Weight and Volume

A sealed nickel cadmium cell having a design capacity after sterilization of 11.7 ampere-hours at 75°F and the 5-hour rate would weigh approximately 1.2 pounds and have a volume of 17 in^3.

Total weight of cells = 1.2 x 23 = 27.5 pounds

Add 1 pound for connector and leads 1.0 pounds

Add weight of battery case (holder) 4.5 pounds

Total Weight = 33.0 lbs

Total Volume = $\frac{(23 \times 17)(1.3)}{1728} = 0.3$ ft^3
Including Case

2.5 Specific Energy

The resulting specific energy is as follows:

Overall Useful watt-hours/lb = $\frac{184}{33}$ = 5.6 W-Hk/lb.

Design watt-hours/lb = $\frac{327}{33}$ = 10.0 W-Hk/lb

Comments: Both the useful specific energy and design values are low for the following reasons:

a) Average discharge rate is high,

b) An external (extra) battery case weight has been added, and

c) A large allowance (25 percent) has been made for keeping itself warm.

3.0 CALCULATIONS FOR BATTERY NO. 2 POST IMPACT TO END OF MISSION

3.1 Power Profile and Energy Summary

The following Table C-4 shows the power profile for battery No. 2 and is taken from Table C-1 and Figure C-1.

TABLE C-4

POWER PROFILE -- POST IMPACT

Period	Power level Watts	Time Hours	Watt-Hours
1. Post impact transmission	135	1.46	197
2. Landed data collection continuous	7.1	20.8	147
3. Landed data collector intermittent	31.2	5 min/hour 1.9 hrs total	60
4. Post-mission transmission	132	1.22	161

In terms of Ampere-Hours the power profile becomes as shown next in Table C-5

TABLE C-5

ENERGY SUMMARY

Period	Watts	Watt-Hours	Assumed Volts	Amp-Hours
1	135	197	28	7.1
2	7.1	147	29	5.1
3	31.2	60	29	2.1
4	132	161	28	5.8
	TOTAL =	565 W-Hrs	TOTAL =	20.1 A-Hrs

3.2 Assignment Of Derating Factors

The first derating factors to be considered are for discharge rates, others are as follows: stand time temperature and keeping warm.

Table C-6 shows apparent discharge rates and cell plateau volts at +40° F.

TABLE C-6

DISCHARGE RATE AND PLATEAU VOLTS

Period	Watts	Amps	Rate*	V_P at +40° F, volts	Assumed Battery volts
1	135	4.8	C/4.2	1.23	28
2	7.1	0.25	C/80	1.3	29
3	31.2	1.1	C/18	1.25	29
4	132	4.7	C/4.3	1.23	28

*As compared with 20.1 amperes discharge in 1 hour (C)

3.2.1 Derating Factors Due to Discharge Rate ϕ_1

Periods 1 and 4 accounting for a little over half the energy used are at a rate slightly too high C/4.2 and C/4.3, as compared with the criteria of C/5. ∴ overall allowance is $\phi_1 = 0.98$

3.2.2 Other Derating Factors Are:

Temperature: for +40°F allows, $\phi_2 = 0.93$

Stand loss: Taken as 10 percent, $\phi_3 = 0.90$

Keep warm allowance: This is taken as 25 percent, $\phi_4 = 0.75$

No other allowances given.

3.3 Design Ampere-Hours and Watt-Hours

3.3.1 Ampere-Hours Capacity

$$\text{Design ampere-hours} = \frac{20.1}{\phi_1 \times \phi_2 \times \phi_3 \times \phi_4}$$

$$= \frac{20.1}{0.98 \times 0.93 \times 0.90 \times 0.75}$$

and Design Capacity = 32.6 amp-hours

Percent Allowance over minimum required capacity included in 32.6 amp-hours.

$$\frac{(32.6 - 1)}{20.1} \times 100 = 62 \text{ percent allowance}$$

3.3.2 Watt-Hours

23 cells are required to assure that the assumed battery voltages are met.

The average voltage is $\frac{565 \text{ watt hours}}{20.1 \text{ amp hours}}$ 28 volts

The approximate design watt hours = 28 x 32.6 A-H = 914 watt-hours
This checks approximately with 23 x 1.23 x 32.6 = 922 watt-hours and is in close enough agreement.

3.4 Total Battery Weight And Volume

For a design capacity (after sterilization) of 32.6 amp-hours, approximate cell weight is 2 pounds 9 ounces of 2.57 lb/cell. Cell volume is 38 in^3.

Total weight of cells = 2.57 x 23 = 59.1 pounds

Allow 1 pound for connector 1.0

Allow case weight for mounting 10.

Total 70.1 pounds

Total volume including case = $\frac{23 \times 38 \times 1.3}{1728}$ = 0.66 ft^3

3.5 Calculated Specific Energy

Useful watt-hours/pound = $\frac{565}{70.1}$ = 8.05 W-Hrs/lb

Design watt-hours/pound = $\frac{914}{70.1}$ = 13 W-Hrs/lb

These values are relatively high because the discharge rates are comparitively low. The useful (and design) specific energy would be higher by 10 to 14 percent if an external mounting case were not added.

4.0 SUMMARY OF BATTERY CHARACTERISTICS - REFERENCE DESIGN

Table C-7 summarizes the reference design battery characteristics.

TABLE C-7

SUMMARY OF BATTERY CHARACTERISTICS -- REFERENCE DESIGN

Battery	Weight (pounds)	Volume (cubic feet)	Peak Heat Dissipation (watts)	Load Voltage Range	Design Capacity (watt-hours)	Required Capacity (watt-hours)
No. 1 Preseparation to impact	33	0.30	≈ 53 *	25 to 30	327	184
No. 2 Post impact	70.1	0.66	≈ 10	28 to 30	914	565
* Occurs at Preseparation Time					1241	749

5.0 ESTIMATE OF WEIGHTS AND VOLUMES FOR SILVER-ZINC BATTERY AND LITHIUM-CHLORINE CELL ALTERNATIVES

5.1 Silver-Zinc Battery

5.1.1 Pre-separation to Impact

For a required capacity of 184 watt-hours, it was stated earlier that a design capacity of 327 watt-hours would be required for a nickel cadmium battery. Under the same rationale used for calculation of option II batteries in Section B of Appendix IV.4-15 (See mid-term report), the following modifications apply:

a. Temperature: The temperature allowance is changed from 7 percent ($\phi_2 = 0.93$) to 15 percent and $\phi_2 = 0.85$.

b. Zero "g" Loss: A zero "g" effect loss is added and estimated at 15 percent, $\phi_5 = 0.85$. No other changes are made. Thus the design watt-hour becomes:

$$\frac{184 \text{ watt-Hours}}{\phi_1 \times \phi_2 \times \phi_3 \times \cdots \phi_n}$$

or

$$\frac{184 \text{ watt-Hours}}{0.90 \times 0.85 \times 0.90 \times 0.75 \times 0.85} = 419 \text{ w-hr.}$$

Since the design watt-hours per pound was 32.5 it is assumed an analysis would result in a similar specific energy. The reference power profile is similar enough to the example to make this permissible.

The estimated battery weight is $\frac{419 \text{ w-hr}}{32.5 \text{ w-hr/lb}} = 12.9$ pounds

Since the case weight was originally estimated at 1.5 pounds and should be strengthened to allow for extra mountings, etc, an additional pound is added making the total 13.9 or 14 pounds.

The estimated volume (including the case) is scaled as being 0.076 ft^3

5.1.2 Post Impact

The required capacity here 565 watt-hours, and similar modifications have to be made for the derating allowances and self-heating needs etc.,. From Section C of Appendix IV.4-15 of the mid-term report (option III calculation), it can be seen that the only important change is in the temperature factor which is increased as before from 7 percent to 15 percent.

Operating on the design capacity of 914 watt-hours obtained earlier for the nickel-cadmium battery, we obtain the design watt-hours for the silver-zinc battery as (914) (1.08) w-hr. = 990 watt-hours. In this case the similar design specific energy is 35 w-hr/lb. Therefore the estimated weight is $\frac{990 \text{ w-hrs}}{35 \text{ w-hr/lb}} = \underline{28.3 \text{ pounds}}$

The estimated volume is scaled as being:

Volume: 0.22 ft^3

5.2 Lithium-Chlorine Cell Estimates

Assuming safety factor of at least 200 percent (allowing for test before launch), required watt-hours (assuming only one battery for both battery function) is 1498.

As before, the minimal design power is 150 watts which allows for 200-percent peaks for a few minutes.

Required fuel and tankage = 1.8 lb/Kwh x 1.5 Kwh = 2.7 pounds

Additional fuel for keeping warm during 12 day cruise = 6.25 pounds

	Weight
Total fuel and tanks = 6.25 lb + 2.7 lb =	8.95 pounds
Weight of four cells at 0.6 lb/sell	2.4
Weight of Auxiliary controls	4.0
Insulation	4.0
TOTAL	19.35 pounds

If two fuel battery assemblies are used, the weight of additional cells and controls etc. is approximately 10 pounds.

Therfore the total system weight = 29.35 pounds
use 30 pounds

In each fuel battery assembly three out of four cells are redundant.

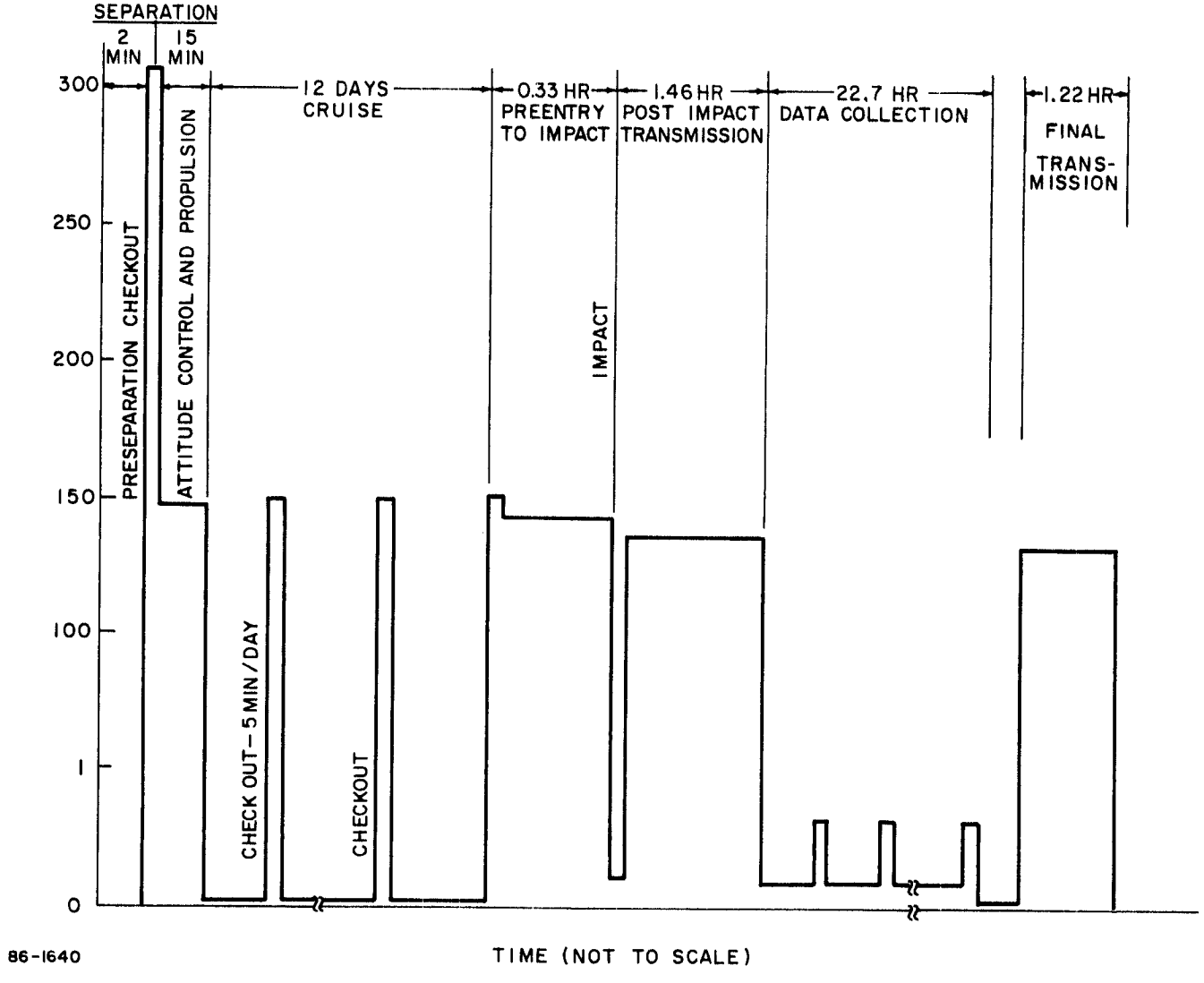

Figure C-1 FLIGHT CAPSULE POWER PROFILE

APPENDIX D

POWER CONTROL

1.0 SCR CIRCUITS

1.1 Introduction

An SCR (Silicon Controlled Rectifier) as used in the Power Control Unit serves as a switch. The SCR has a large impedance in the forward direction for large applied voltage when it has not been "fired." To "fire" an SCR requires that a small amount of current be fed into the gate when the anode is positive. When the gate current reaches the required level, the SCR "breaks over" and becomes a regular diode conducting heavily in the forward direction with very low impedance. This state will continue as long as a minimum threshold or "holding" current continues. When the current falls below the minimum the SCR switches off and has to be "fired" again. Figure D-1 illustrates the SCR voltage current characteristic.

All of the methods that follow describe means of turning off the SCR, using solid-state switches to interrupt the load. The advantages and disadvantages of each are also discussed and compared in a table at the end of the descriptions.

1.2 Methods of Turning Off SCR's

The methods described are:

a) GTO's (Gate Turnoff SCR's)

b) Flip-Flop Circuit

c) Cathode Pulse Turnoff

d) Load Sensitive Cathode Pulse Turnoff

e) Morgan Circuit

1.2.1 Gate - Turnoff SCR's

This type of SCR can be turned off (as well as on) at the gate. Larger units can turn off up to 5 amperes anode to cathode current. The problem associated with this type is the amount of gate current required to turn off the device. This can be as large as 1/30 to 1/5 of the anode current depending on the device, circuit, and environmental parameters. The GTO is turned off by applying a negative pulse to the gate.

If the maximum current available from the CC and S is:

Gate Current	Load	
10 ma	50 ma to 300 ma	current that can be turned off in this manner.
50	250 ma to 1.5 amp	
100	0.5 amp to 3 amp	

Clearly, this is the simplest and best method for switching low power users on and off.

1.2.2 SCR Flip-Flop Circuit

When SCR_1 is turned on from the CC and S, the capacitor C will charge through R_1 to approximately E with the polarity shown. If a second pulse from the CC and S now turns on SCR_2, the left (positive) side of the capacitor is grounded, making the right (negative) side approximately E volts below ground. If the time constant $R_L C$ is long enough, SCR_1 will be turned off.

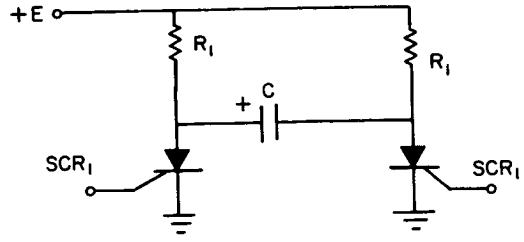

Figure D-1 SCR FLIP-FLOP CIRCUIT

This method is simple, light, and suitable for higher power application. Its disadvantages are, it requires 2 SCR's for each separate circuit, for high-power application a large capacitor is required. The voltage is constantly on the load, and switching is done by raising the load off ground. After SCR_1 is turned off-current is free to drain through R_1 and SCR_2 (R_1, however, can be very large).

This method would probably be practical for medium power users.

1.2.3 Cathode-pulse Turnoff

A typical Circuit is shown in Figure D-2. SCR_2 should be pulsed first to assure that the lower plate of C is near ground before SCR_1 is turned on. When SCR_1 is triggered, the voltage is applied to the load R_L.

The lower plate of the capacitor C is charged to approximately 2E through the resonant charging circuit L, C, and D. When SCR_2 is triggered on, the cathode of SCR_1 is raised to approximately 2E. This turns off SCR_1 due to a reverse voltage of approximately E.

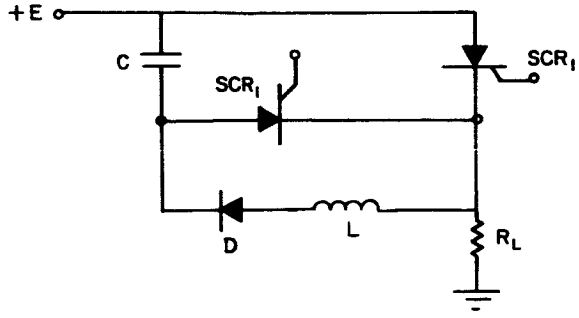

Figure D-2 SCR CATHODE PULSE TURN-OFF

The advantages to this type are light weight, suitable for higher power application, voltage is not constantly on the load, there is no standby current drain before or after switching. The disadvantages are, it requires 2 SCR's for separate circuit, for high-power applications a large capacitor is required, SCR_1 cannot conduct for long periods because the charge on C will leak off through D and SCR_2.

This method is practical for medium power users that operate for short periods.

1.2.4 Load-Sensitive Cathode Pulse Turnoff

This circuit shown in Figure D-3 functions in a similar manner to the previous circuit. Before SCR_1 is turned on, the lower plate of C should be grounded by pulsing SCR_2. When SCR_1 is triggered, the voltage is applied to the load R_L. However, due to the autotransformer action of the coil L, the lower plate of C is charged to a voltage higher than 2 E when the current is heavy in SCR_1. This provides additional energy stored in the capacitor to turn off SCR_1 when the current is heavy.

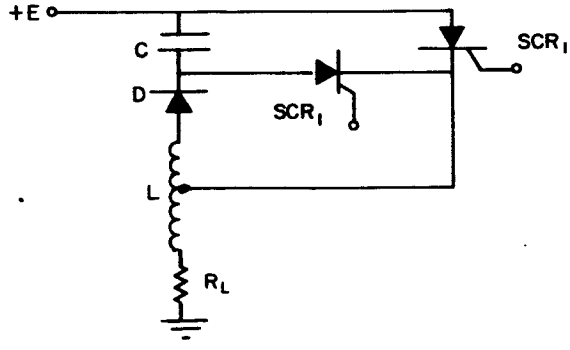

Figure D-3 LOAD SENSITIVE PULSE TURN-OFF

The advantages of this circuit are the same as the previous case with the added advantage that more energy is provided to turn off SCR_1. The disadvantages are the same.

1.2.5 Morgan Circuit

This is shown in Figure D-4. When SCR_1 is triggered, current flows to the load through the lower end of the autotransformer, and the current through the autotransformer is stepped up to charge the capacitor with the bottom plate positive with respect to E. The autotransformer saturates after a certain amount of load current buildup. When this happens, the impedance of the autotransformer decreases, allowing the voltage on the capacitor C to turn off SCR_1.

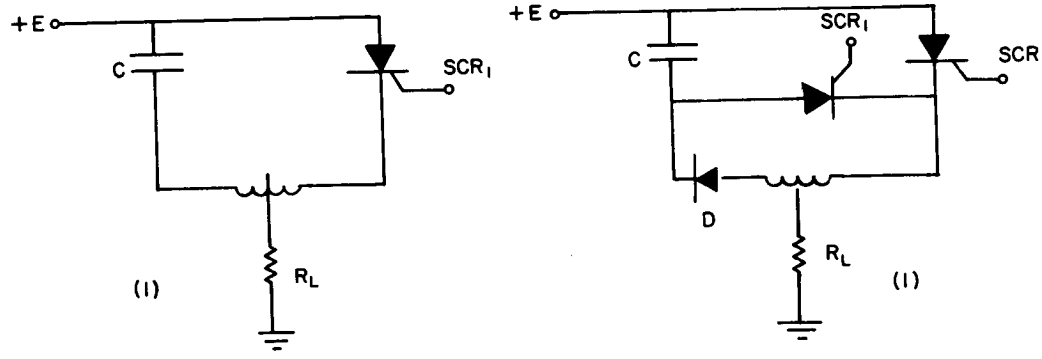

Figure D-4 MORGAN CIRCUIT

In the case of the revised Morgan circuit (2) (this is the same as (d) - load-sensitive cathode pulse turnoff), the charged capacitor does not turn off SCR_1 until SCR_2 is fixed.

Circuit (1) cannot be used unless a circuit that turns itself off after a period of time is desired. Circuit (2) has the same advantages and disadvantages as (d).

2.0 RADIO FREQUENCY INTERFERENCE IN SCR CIRCUITS[1]

2.1 Introduction

Since an SCR switches very rapidly, due to its inherently regenerative turning-on action, it tends to shock-excite the supply line. These fast rates of rise of current cause voltages to be induced in the distributed inductance of the supply line which will be oscillatory in nature. The fundamental frequency is determined by the parameters of the supply line and will generally be between 250 kHz and 2 MHz. Thus, an SCR is a generator of high-frequency voltages which can cause RFI or act upon other SCR circuits.

[1]Silicon Controlled Rectifier Manual – 2nd Edition 1961, G. E. Co.

Line disturbances can act upon the anode of an SCR directly or find their way into the trigger circuit and cause the SCR to fire spuriously. In either case, the SCR may be acted upon by the operation of neighboring SCR circuits.

2.2 Nature of RFI

Two types of interference can be identified. First, conducted RFI in which energy is transmitted along the power line and finds its way into other equipment and, radiated RFI in which the device causing the interference acts as a transmitter and "broadcasts" the interference to other devices capable of "receiving" this energy.

Since RFI is an overall systems problem, it does not lend itself to simple quantitative rules and must be approached from a point of view in which location of components, the manner in which they are mounted, location of wiring runs, etc. must be taken into account. However, the basic approach is to localize the initial high rate of rise of current to as small a section of the circuit as possible. This can be done by placing small inductances in the circuit where the rate of rise of the current is to be localized and by furnishing a return path for the high frequency component of this current.

2.3 Suppression of RFI

2.3.1 Suppression of Conducted RFI

Circuits for suppression of conducted RFI when RF ground is inaccessible and accessible are shown in Figures D-5 and D-6.

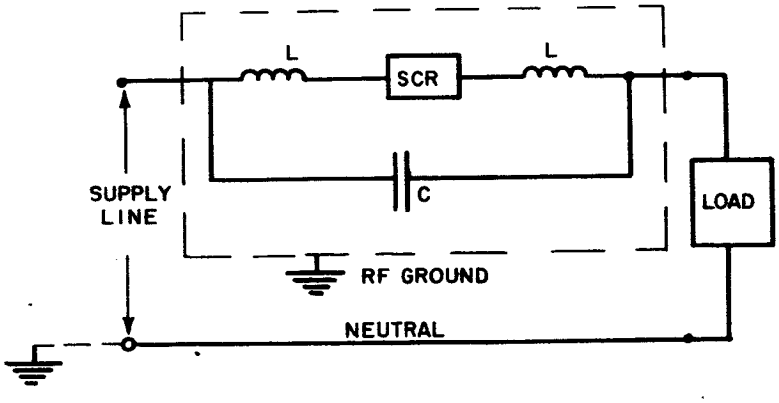

Figure D-5 CONDUCTED RFI SUPPRESSION WITH RF GROUND INACCESSIBLE

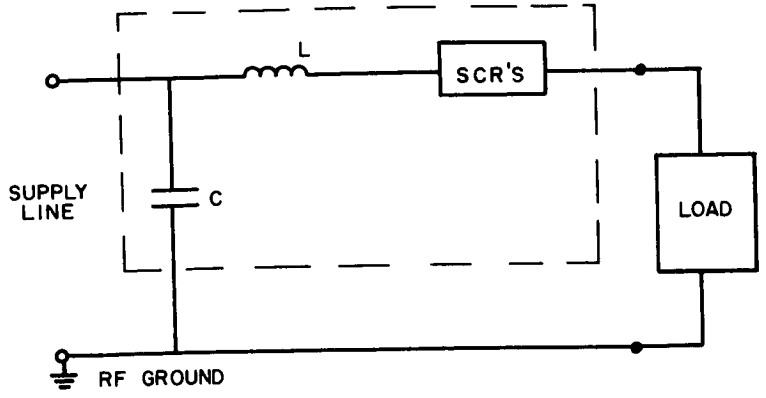

Figure D-6 CONDUCTED RFI SUPPRESSION WITH RF GROUND ACCESSIBLE

The values of L and C will depend on the amount of suppression desired, the layout of the circuit, the nature of the supply line, the nature of the load, and generally, the power level of the load.

Since the inductance must be in the circuit for only a few microseconds of the turn-on switching interval, and since it may be allowed to saturate after the turn-on interval, the size of the inductance can be very small.

2.3.2 Suppression of Radiated RFI

The best approach to radiated RFI has been electrostatic shielding. The dashed line in Figures D-5 and D-6 indicate the components that should be enclosed within the shielding. The shielding is then brought to a solid RF ground.

2.4 Interaction of SCR Circuits

Transients generated elsewhere in the circuit can act on the SCR trigger circuit and/or directly on the anode of the SCR causing it to follow or track another SCR system.

2.4.1 Interaction Acting on the Anode Circuit

This type of interaction is in the form of a forward voltage rise (dv/dt). When energizing the circuit, by a contactor, circuit breaker, etc., applicable dv/dt specifications must be met for the device.

The best means of suppressing this type of interaction is by negative gate bias, a capacitor (not over 0.1 μf) connected directly across the SCR, and RC network elsewhere in the circuit, or a combination of these steps.

2.4.2 Interaction Acting on the Trigger Circuit

These interactions also may cause the SCR to fire prematurely. There are no general rules for every firing circuit but methods of decoupling the trigger circuit against supply transients and gate transients are given below:

2.5 Methods of Decoupling

2.5.1 Decoupling Unijunction Transistor Firing Circuits Against Supply Transients

Depending on the particular circuit conditions, one or a combination of the following will be effective:

1. Use of isolation transformer with RF filter across the secondary.

2. Use of "boot-strap" capacitor between base two and the emitter of the UJT (see Figure D-7).

3. Use of a Thyrector diode connected across the supply to the unijunction circuit.

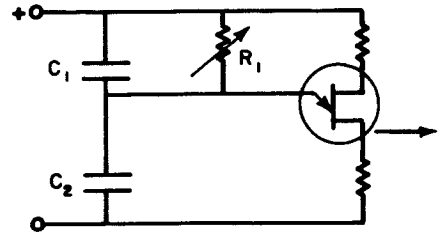

Figure D-7 CIRCUIT FOR DECOUPLING UJT FROM SUPPLY TRANSIENTS

If the condition, $\eta = \frac{C_1}{C_1 + C_2}$, where η = intransic standoff ratio is met, then positive or negative transients on the unijunction supply voltage will not fire the UJT.

2.5.2 Decoupling UJT Circuits Against SCR Gate Transients

Erratic firing can be caused by negative voltage transients appearing between the gate and cathode of the SCR's when transmitted to the UJT. When transformer coupling is used, these transients can be eliminated by using a diode bridge in the gate circuit of the SCR as shown in Figure D-8.

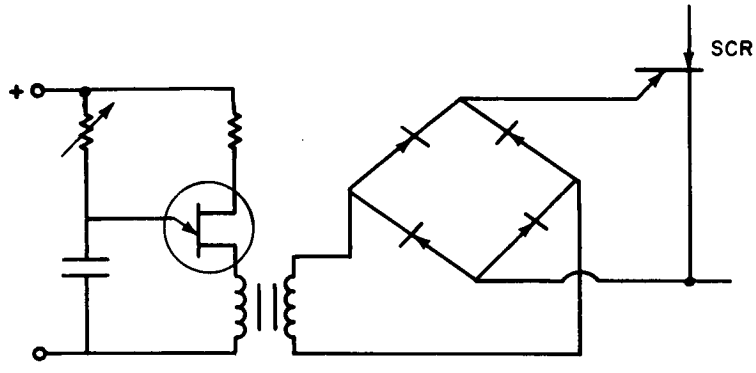

Figure D-8 CIRCUIT FOR ELIMINATING FIRING FROM SCR GATE TRANSIENTS

2.6 Design Practices to Minimize Sources of SCR Interaction

When the following considerations are met, it is often unnecessary to take additional steps to filter either trigger or anode circuits:

1. Operate parallel and potentially interacting SCR circuits from a low-reactance supply line.

2. If supply line has high reactance, consider using separate transformers to feed parallel SCR branch circuits; each transformer rated no more than required rating of branch circuit load.

3. Avoid purely resistive loads operating from low-reactance lines - they give highest rates of current rise on switching.

4. Keep load slightly inductive.

5. Keep both leads of a power circuit wiring run together.

6. Arrange magnetic components so as to avoid stray fields.

Table D-1 compares the various SCR turn-off circuits.

TABLE D-1

COMPARISON OF SCR TURN-OFF CIRCUITS

Circuit	Advantages	Disadvantages
G. T. O. - S. C. R.	Simplicity, light-weight	high gate current required
SCR flip-flop	Simplicity, light-weight high power applications	2 SCR's required, large capacitor required, high side of voltage constantly on load, slight current drain after switch off.
Cathode-pulse	Light weight, higher power application, high side of voltage not on constantly, no standby current drain	2 SCR's required, large capacitor required, SCR_1 can be on for short duration.
Load sensitive cathode pulse	Light weight, higher power application, high side of voltage not on constantly no standby current drain and more energy provided for turn off.	2 SCR's required, large capacitor required, SCR_1 can be on for short duration, and added weight of autotransformer.
Morgan	2) Light weight, higher power application, high side of voltage not on constantly no standby current drain and more energy provided for turn off.	2 SCR's required, large capacitor required, SCR_1 can be on for short duration, and added weight of autotransformer.
	1) Light weight, high power application, high side of voltage not on constantly no standby current drain and more energy provided for turn off. Shuts off when transformer saturates.	2 SCR's required, large capacitor required, SCR_1 can be on for short duration, and added weight of autotransformer. Shuts off when transformer saturates.

APPENDIX E

DERIVATION OF A THEORETICALLY OPTIMUM RANGE TRACKER

A theoretically optimum range tracker requires measurement of the dealy, τ, experiment by the echo, $x(t-\tau)$, of a transmitted waveform, $x(t)$. The received waveform, $y(t)$, consists of both the echo on a perturbing noise, $n(t)$. This may be expressed as

$$y(t) = x(t-\tau) + n(t)$$

The most likely value for the delay (τ) corresponds to that value of the delayed image, $x(t-\tau)$, of the transmitted waveform which most resembles the received waveform, $y(t)$.

Expressed mathematically, the correlation function

$$g(\tau) = \int y(t)\ x(t-\tau)\, dt$$

must be so maximized with respect to the delay, τ that

$$g'(\tau) = -\int y(t)\ x'(t-\tau)\, dt$$

$$= 0$$

This expression describes the general principle upon which operation of the optimum-design range tracking radar shown in block diagram form in Figure E-1 is based. Note that if $x(t)$ is a rectangular pulse, the first derivative of the image consists of two unit impulses with equal strength and opposite sense, and separated by an interval equal to the pulse duration (see also paragraph 8.3.3).

When the equation for $g'(\tau)$ is satisfied, the impulses, or sampling pulses as they are often called, coincide with the edges of the echo pulse (see paragraph 8.7.1).

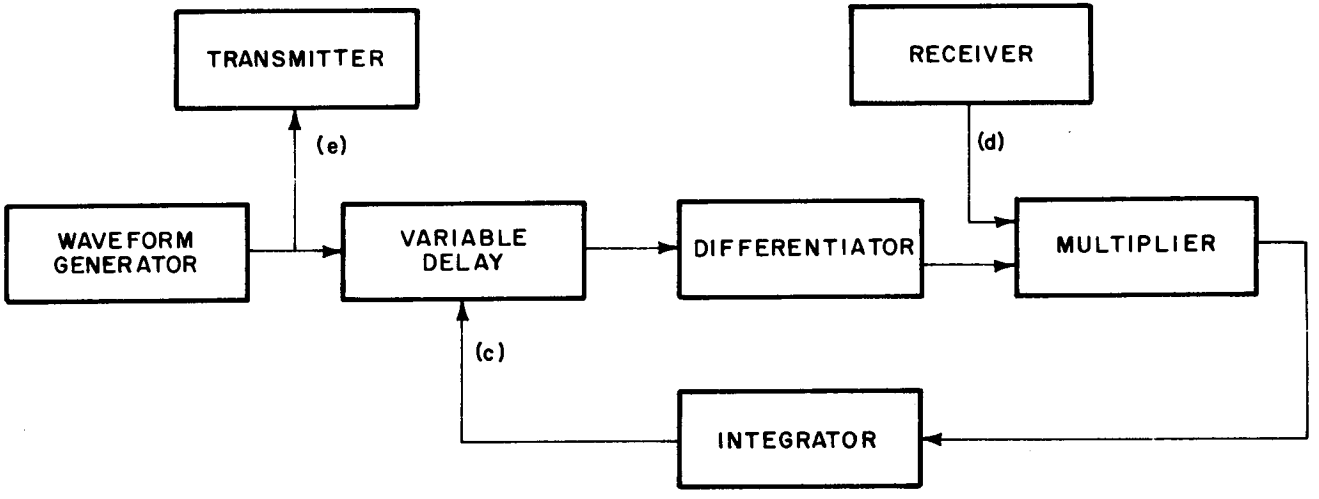

Figure E-1 THE OPTIMUM RANGE TRACKING RADAR

APPENDIX F

DETERMINATION OF HORIZONTAL MOTIONS AND ATTITUDE WITH THE USE OF THE VELOCITY - ATTITUDE SENSOR

1.0 INTRODUCTION

During the parachute-assisted descend phase of the flight capsule's approach to the planet, the capsule's horizontal motion and attitude with respect to a Mars orientated reference frame must be determined. It is the purpose of this appendix to demonstrate how a three-(narrow) beam Doppler radar velocity-attitude (V-A) sensor can be used to satisfy these requirements. The appendix also includes an error analysis of the flight capsule's horizontal velocity measurements capabilities.

2.0 DETERMINATION OF FLIGHT CAPSULE HORIZONTAL VELOCITY

The velocity-attitude sensor directs three narrow beams at the planetary surface, as illustrated in Figure F-1. The beams are directed at fixed angles with respect to the flight capsule's body-fixed rectangular coordinate system labeled (x,y,z). From the figure, it can be seen that beams 1 and 3 and the flight capsule's spin axis (z axis) lie in the same plane. It can also be seen that beams 1 and 2 are positioned symmetrically about the capsule's yaw (x) axis, and beams 2 and 3 are similarly positioned symmetrically about the capsule's pitch (y) axis. Included in Figure F-1 is a line representing the local planetary vertical. As the figure shows, the capsules spin axis is not initially aligned with the local vertical.

The first system requirements is that it be able to measure vehicle horizontal motions. The procedure for making each measurement is as follows: Let the vehicle velocity vector be expressed with respect to the flight capsules fixed coordinates as:

$$\vec{v} = v_x \vec{i} + v_y \vec{j} + v_z \vec{k} \tag{1}$$

where $\vec{i}, \vec{j}, \vec{k}$, are unit vectors along the flight capsule's x, y, z axes respectively, and v_x, v_y, v_z are likewise the scalar components along the corresponding body-fixed axes. Now let R_j be the radial velocity component along the j'th beam. If $\vec{r}_j$ is a unit vector along this j'th beam, then

$$\vec{r}_j = \frac{x_j}{R_j} \vec{i} + \frac{y_j}{R_j} \vec{j} + \frac{z_j}{R_j} \vec{k} \tag{2}$$

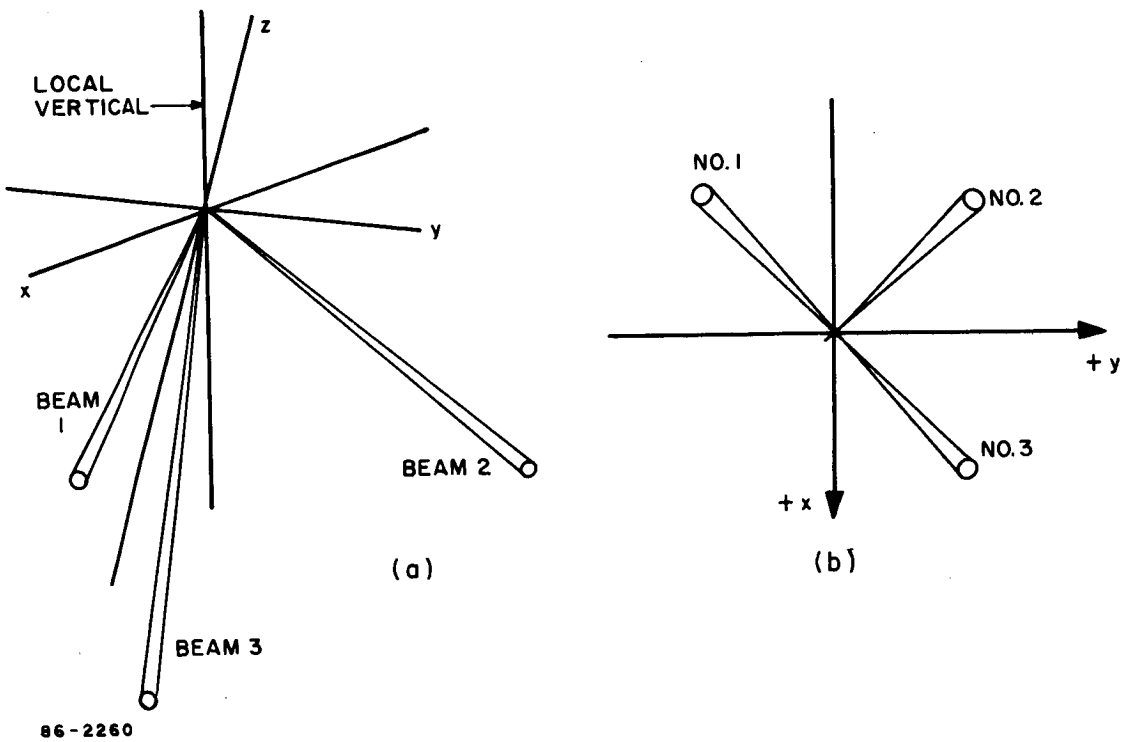

Figure F-1* a V-A SENSOR BEAM ARRANGEMENT

b VIEW ALONG FLIGHT CAPSULE SPIN AXIS

The scalar components in Equation 2 are, in fact, the direction cosines of the individual beams with respect to the body-fixed axes and are known quantitites. In particular,

$$\frac{x_1}{R_1} = \frac{x_2}{R_2} = -\frac{x_3}{R_3} = \alpha \tag{3}$$

$$\frac{y_1}{R_1} = -\frac{y_2}{R_2} = -\frac{y_3}{R_3} = \beta \tag{4}$$

$$\frac{z_1}{R_1} = \frac{z_2}{R_2} = \frac{z_3}{R_3} = \gamma \tag{5}$$

The radial velocity $\dot{R}_j$ is then given as

$$\dot{R}_j = v \cdot \gamma_j = v_x \frac{x_j}{R_j} + v_y \frac{y_j}{R_j} + v_z \frac{z_j}{R_j} \tag{6}$$

The range rate measured along each beam, in matrix notation, is

$$\begin{bmatrix} \dot{R}_1 \\ \dot{R}_2 \\ \dot{R}_3 \end{bmatrix} = \begin{bmatrix} \alpha & \beta & \gamma \\ \alpha & -\beta & \gamma \\ -\alpha & -\beta & \gamma \end{bmatrix} \begin{bmatrix} v_x \\ v_y \\ v_z \end{bmatrix} \tag{7}$$

The range rate measured along any beam is related to the doppler shift along that same beam by the relationship

$$f_j = 2 f o_j \frac{\dot{R}_j}{v_c} \tag{8}$$

where:

f_j = doppler shift measured along j'th beam

fo_j = operating frequency of j'th beam

v_c = velocity of light in same units as $\dot{R}_j$.

The quantity $2fo_j/v_c$ is a characteristic of the system design, and can be equated to a constant. Thus

$$K_j = \frac{v_c}{2\, fo_j} \tag{9}$$

Substituting the value of $\frac{v_c}{2\, fo_j}$ from Equation 9 into Equation 8, gives

$$\dot{R}_j = K_j f_j \tag{10}$$

Thus Equation (7) becomes

$$\begin{matrix} K_1 f_1 \\ K_2 f_2 \\ K_3 f_3 \end{matrix} = \begin{bmatrix} \alpha & \beta & \gamma \\ \alpha & -\beta & \gamma \\ -\alpha & -\beta & \gamma \end{bmatrix} \begin{bmatrix} v_f \\ v_y \\ v_z \end{bmatrix} \tag{11}$$

By using the following simplifying notation

$$[D] = \begin{bmatrix} K_1 f_1 \\ K_2 f_2 \\ K_3 f_3 \end{bmatrix} \tag{12}$$

$$[\Lambda] = \begin{bmatrix} \alpha & \beta & \gamma \\ \alpha & -\beta & \gamma \\ -\alpha & -\beta & \gamma \end{bmatrix} \tag{13}$$

$$[v] = \begin{bmatrix} v_x \\ v_y \\ v_z \end{bmatrix} \tag{14}$$

Equation 11 may be written in a more compact form, as follows

$$[D] = [\Lambda]\,[v] \tag{15}$$

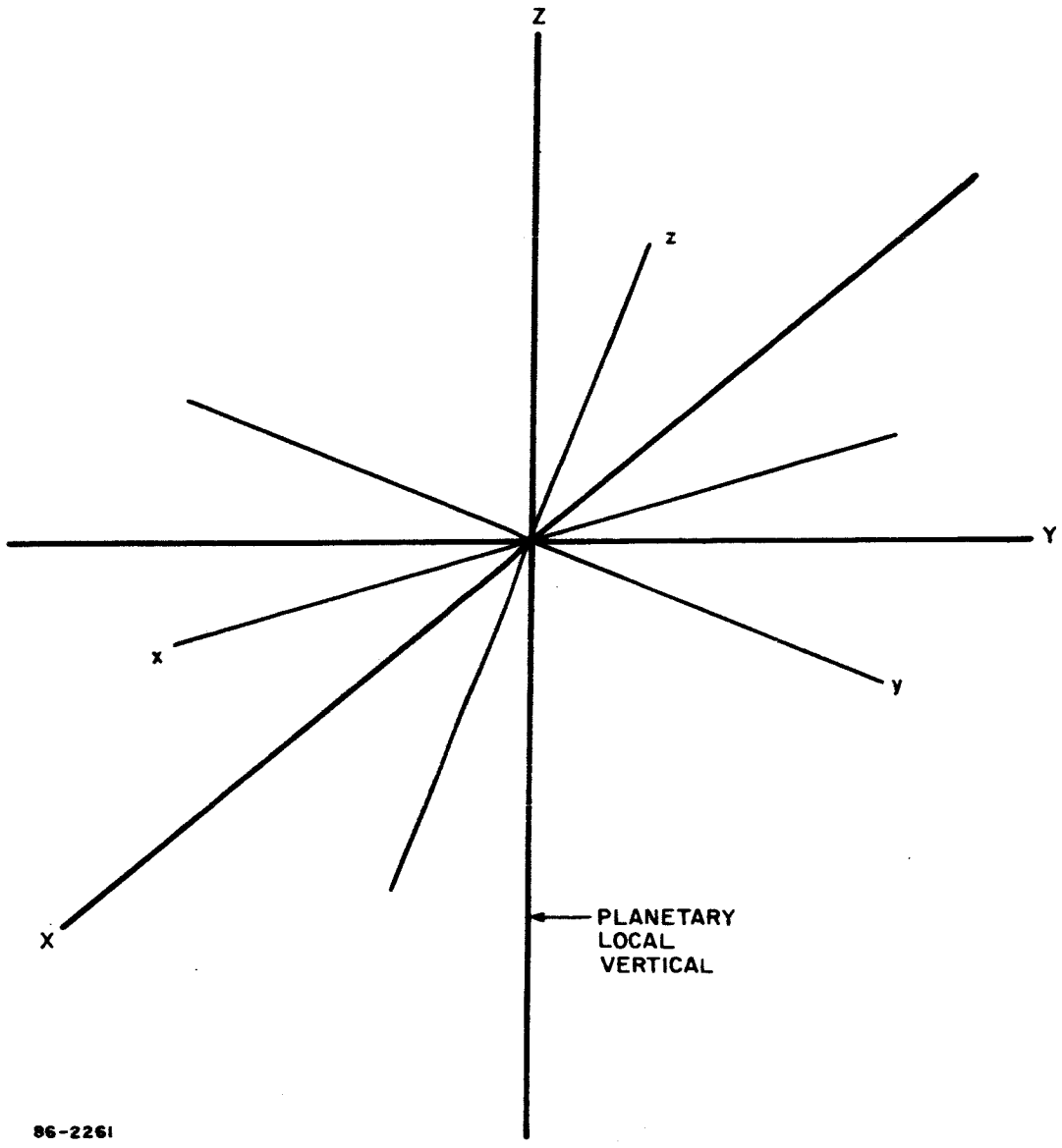

Figure F-2 COORDINATE SYSTEM GEOMETRY

Since matrix D consists of observables, matrix Λ is nonsingular, matrix v may be solved explicitly as follows:

$$[v] = [\Lambda]^{-1} [D] \tag{16}$$

It should be realized at this point that the velocity components determined by Equation (16) are measured along the body-fixed flight capsule vehicle axes and are not directly related to the planet-oriented coordinate system whose Z axis coincides with the local vertical passing through the flight capsule. To determine the horizontal vehicle motions, it is necessary to refer motion to the planet oriented coordinate system. This can be done by means of the direction cosines that define the coordinate transformation from body-fixed axes to the planet-oriented reference frame. The geometry of the transformation is illustrated in Figure F-2. The axis of the body-fixed coordinate system of the flight capsule are labeled x, y, and z. The planet oriented coordinate axes are labeled X, Y, and Z. The velocity components in the x, y, z system can be expressed in terms of the corresponding component velocities in the X, Y, Z system as

$$\begin{bmatrix} \sqrt{x} \\ \sqrt{y} \\ \sqrt{z} \end{bmatrix} = \begin{bmatrix} \Gamma_{xx} & \Gamma_{xy} & \Gamma_{xz} \\ \Gamma_{yx} & \Gamma_{yy} & \Gamma_{yz} \\ \Gamma_{zx} & \Gamma_{zy} & \Gamma_{zz} \end{bmatrix} \begin{bmatrix} V_x \\ V_y \\ V_z \end{bmatrix} \tag{17}$$

or

$$[v] = [\Gamma] [V] \tag{18}$$

where the elements of the Γ matrix are direction cosines between the axes identified in Equation 17 by appropriate subscripts, and elements of the V matrix are the velocity components along the planet-oriented axes. Now substituting Equation 18 into Equation 15 yields

$$[D] = [\Lambda] [\Gamma] [V] \tag{19}$$

The required vehicle velocities can now be determined if the Γ matrix is known. The Γ matrix can be determined as follows. The orientation of the flight capsule can be defined by Euler's angles ψ, ϕ, and θ. These are three independent quantities capable of defining the position of the x, y, and z body-fixed axes relative to the planet-oriented X, Y, Z. The Euler angles are defined as shown in Figure F-3.

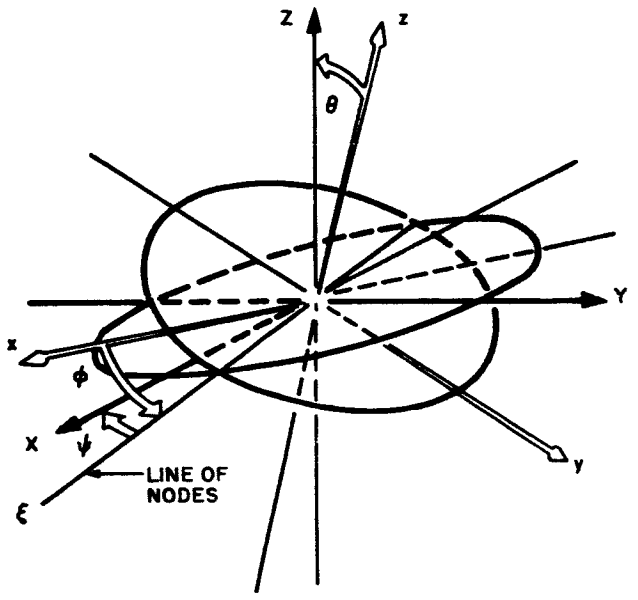

66-2262

Figure F-3 BODY FIXED AXES x, y, z RELATIVE TO XYZ AXES

In the process of aligning the x, y, and z axes with the X, Y, and Z axes, the flight capsule is first rolled through an angle ϕ about its spin (z) axis. This rotation aligns the x axis along the line ξ, called the line of nodes. This line is defined by the intersection of the xy and XY planes. The flight capsule is next rotated about the line of nodes (which now coincides with the x axis) through an angle θ until the z and Z axes are aligned. The final rotation is through an angle, ψ, about the z axis (which now coincides with X) so that the line of nodes and the X axis coincide. The Γ matrix can now be written in terms of the Euler angles as

$$[\Gamma] = \begin{bmatrix} (\cos\phi\cos\psi - \sin\phi\cos\theta\sin\psi) & (-\sin\phi\cos\psi - \sin\psi\cos\theta\cos\phi) & (\sin\theta\sin\psi) \\ (\cos\phi\sin\psi + \sin\phi\cos\theta\cos\psi) & (-\sin\phi\sin\psi + \cos\phi\cos\theta\cos\psi) & (-\sin\theta\cos\psi) \\ (\sin\theta\sin\phi) & (\sin\theta\cos\phi) & (\cos\theta) \end{bmatrix} \quad (20)$$

Now since no orientation of the X, Y axes in the horizontal plane is to be preferred, we can arbitrarily set $\psi = 0$, in which case Equation (20) becomes

$$[\Gamma] = \begin{bmatrix} \cos\phi & -\sin\phi & 0 \\ \sin\phi\cos\theta & \cos\phi\cos\theta & -\sin\theta \\ \sin\theta\sin\phi & \sin\theta\cos\phi & \cos\theta \end{bmatrix} \quad (21)$$

[1] Thompson, W. T., Introduction to Space Dynamics, John Wiley and Sons, Inc., New York, Chap. 3 (1961).

Now the flight capsule velocity vector can be explicitly solved for with respect to the planetary reference frame,

$$[V] = [T]^{-1} [\Lambda]^{-1} [D] \tag{22}$$

and in particular,

$$V_H^2 = V_X^2 + V_Y^2 \tag{23}$$

where

$$V_X = \left[\frac{\sin\phi \cos\theta}{2\beta} + \frac{\sin\phi \sin\theta}{2\gamma} \right] D_1 + \left[\frac{\cos\phi}{2\alpha} - \frac{\sin\phi \cos\theta}{2\beta} \right] D_2 + \left[-\frac{\cos\phi}{2\alpha} + \frac{\sin\phi \sin\theta}{2\gamma} \right] D_3 \tag{24}$$

and

$$V_Y = \left[\frac{\cos\phi \cos\theta}{2\beta} + \frac{\cos\phi \sin\theta}{2\gamma} \right] D_1 + \left[\frac{-\sin\phi}{2\alpha} \quad \frac{-\cos\phi \cos\theta}{2\beta} \right] D_2 + \left[\frac{\sin\phi}{2\alpha} + \frac{\cos\phi \sin\theta}{2\gamma} \right] D_3 \tag{25}$$

3.0 DETERMINATION OF FLIGHT CAPSULE ATTITUDE

The vector drawn from the flight capsule and perpendicular to the planetary surface capsule represented by

$$\vec{h} = h\vec{n} \tag{26}$$

where

h = vertical altitude

$\vec{n}$ = unit vector normal to the planetary surface

The range vector measured along the j'th beam with respect to body fixed axes is given by

$$\vec{R}_j = R_j \left(\frac{x_j}{R_j} \vec{i} + \frac{y_j}{R_j} \vec{j} + \frac{z_j}{R_j} \vec{K} \right) \tag{27}$$

Since vectors $(\vec{R}_1-\vec{R}_2)$, $(\vec{R}_2-\vec{R}_3)$ and $(\vec{R}_1-\vec{R}_3)$ all lie in the plane representing the planetary surface, and since $\vec{n}$ is perpendicular to all vectors lying on the planetary surface, then

$$(\vec{R}_1 - \vec{R}_2) \cdot \vec{n} = 0$$

$$(\vec{R}_2 - \vec{R}_3) \cdot \vec{n} = 0$$

$$(\vec{R}_1 - \vec{R}_3) \cdot \vec{n} = 0 \tag{28}$$

Writing $\vec{n}$ as

$$\vec{n} = n_x \vec{i} + n_y \vec{j} + n_z \vec{K} \tag{29}$$

and making appropriate substitution into Equation 26 gives

$$\alpha(R_1 - R_2)\, n_x + \beta(R_1 + R_2)\, n_y + \gamma(R_1 - R_2)\, n_z = 0$$

$$\alpha(R_2 + R_3)\, n_x + \beta(R_3 - R_2)\, n_y + \gamma(R_2 - R_3)\, n_z = 0$$

$$\alpha(R_1 + R_3)\, n_x + \beta(R_1 + R_3)\, n_y + \gamma(R_1 - R_3)\, n_z = 0 \tag{30}$$

This may be expressed in matrix notation as

$$\begin{bmatrix} (R_1 - R_2) & (R_1 + R_2) & (R_1 - R_2) \\ (R_2 + R_3) & (R_3 - R_2) & (R_2 - R_3) \\ (R_1 + R_3) & (R_1 + R_3) & (R_1 - R_3) \end{bmatrix} \begin{bmatrix} \alpha & 0 & 0 \\ 0 & \beta & 0 \\ 0 & 0 & \gamma \end{bmatrix} \begin{bmatrix} n_x \\ n_y \\ n_z \end{bmatrix} = 0 \tag{31}$$

or, in simplified form, as

$$[R]\,[\Lambda']\,[n] = 0 \tag{32}$$

where

$$[\Lambda'] = \begin{bmatrix} \alpha & 0 & 0 \\ 0 & \beta & 0 \\ 0 & 0 & \gamma \end{bmatrix} \tag{33}$$

It can be shown[2] that Equation (32) possesses non-trivial solutions for values of n_x, n_y, and n_z only if the determinant of the R matrix is zero. By forming the determinant of R, it can be shown that

$$|| R || = 0 \tag{34}$$

Thus, Equation 32 can be solved for the unique non-trivial values of n_x, n_y, and n_z. Angle θ can then be determined by observing the angle that vector $\vec{n}$ makes with the flight capsule's spin (z) axis. Thus

$$\vec{n} \cdot \vec{K} = \cos \theta \tag{35}$$

or

$$\cos \theta = n_z \tag{36}$$

Therefore,

$$\theta = \cos^{-1} n_z \tag{37}$$

The component $\sin \theta$ can likewise be determined, as follows:

$$|\vec{n} \times \vec{K}| = \sin \theta; \quad 0 \leq 90^\circ \tag{38}$$

or

$$\sin \theta = |n_y \vec{i} - n_x \vec{j}| \tag{39}$$

Therefore,

$$\sin \theta = (n_y^2 + n_x^2)^{1/2} \tag{40}$$

Angle ϕ may now be determined. As shown in Figure F-3, angle ϕ is the angle about the z axis through which the x axis is rotated to bring it into alignment with the line of nodes. The line of nodes lies both in xy plane and XY plane. The normal to the XY plane has already been defined as the unit vector n. Since the line of nodes is in the xy plane, it can be assumed to lie along the unit vector, that is

$$\vec{\xi} = \xi_x \vec{i} + \xi_y \vec{j} \tag{41}$$

and, since it is also in XY plane,

$$\vec{\xi} \cdot \vec{n} = 0 \tag{42}$$

---

[2]Guillemin, E. A., The Mathematics of Circuit Analysis, John Wiley and Sons, New York, Chap. 1, Sec. 9 (1959).

or

$$\xi_x n_x + \xi_y n_y = 0 \tag{43}$$

and

$$\frac{\xi_y}{\xi_x} = - \frac{n_x}{n_y} \tag{44}$$

Since

$$\frac{\xi_y}{\xi_x} = \tan \phi \tag{45}$$

then

$$\phi = \tan^{-1} \frac{\xi_y}{\xi_x} \tag{46}$$

and

$$\sin \phi = - \frac{n_x}{(n_y^2 + n_x^2)^{1/2}} \tag{47}$$

$$\cos \phi = - \frac{n_y}{(n_y^2 + n_x^2)^{1/2}} \tag{48}$$

The terms n_x and n_y in Equation (31) can be solved in terms of n_z . This is done by eliminating the last row from the matrix equation and rewriting it as

$$\begin{bmatrix} (R_1 - R_2) & (R_1 + R_2) \\ (R_2 + R_3) & (R_3 - R_2) \end{bmatrix} \begin{bmatrix} \alpha & 0 \\ 0 & \beta \end{bmatrix} = \begin{bmatrix} -\gamma & 0 \\ 0 & -\gamma \end{bmatrix} \begin{bmatrix} (R_1 - R_2) & 0 \\ 0 & (R_2 - R_3) \end{bmatrix} \begin{bmatrix} n_z \\ n_z \end{bmatrix} \tag{49}$$

Equation 49 can now be solved for n_x and n_y in terms of n_z . Thus, by Cramer's rule

$$n_x = - \frac{\gamma \beta \cdot n_z}{\alpha \beta} \frac{\begin{Vmatrix} (R_1 - R_2) & (R_1 + R_2) \\ (R_2 - R_3) & (R_3 - R_2) \end{Vmatrix}}{\begin{Vmatrix} (R_1 - R_2) & (R_1 + R_2 \\ (R_2 + R_3) & (R_3 - R_2) \end{Vmatrix}} \tag{50}$$

Solving Equation 50, by performing the indicated operations gives

$$n_x = \frac{\gamma}{a} \frac{R_1 (R_3 - R_2)}{R_2 (R_1 + R_3)} \tag{51}$$

By the same approach, the following value of n_y can be obtained

$$n_y = - \frac{\gamma a n_z}{a\beta} \frac{\begin{Vmatrix} (R_1 - R_2) & (R_1 - R_2) \\ (R_2 + R_3) & (R_2 - R_3) \end{Vmatrix}}{\begin{Vmatrix} (R_1 - R_2) & (R_1 + R_2) \\ (R_2 + R_3) & (R_3 - R_2) \end{Vmatrix}} \tag{52}$$

Again, by performing the indicated operations Equation 52 becomes

$$n_y = \frac{\gamma}{\beta} \frac{R_3}{R_2} \frac{(R_2 - R_1)}{(R_1 + R_3)} \tag{53}$$

As shown previously, in Equation 36,

$$\cos \theta = n_z$$

Substituting the values of n_x and n_z obtained in Equations (51) and (53) into Equation (40) yields

$$\tan \theta = \frac{\sin \theta}{\cos \theta} = \frac{\gamma}{R_2(R_1 + R_3)} \sqrt{\frac{R_1^2 (R_3 - R_2)^2}{a^2} + \frac{R_3^2 (R_2 - R_1)^2}{\beta^2}} \tag{54}$$

In the particular case where the beams are directed along planes making 45° angles with the flight capsule's body-fixed axis, $a = \beta$. Hence, Equation (54) becomes

$$\tan \theta = \frac{\gamma}{a} \frac{1}{R_2(R_1 + R_3)} \sqrt{R_1^2 (R_3 - R_2)^2 + R_3^2 (R_2 - R_1)^2} \tag{55}$$

If $R_1 = R_2 = R_3$ then $\tan \theta$ in Equation 55 will equal zero, hence, $\theta = 0$, and as was to be expected.

From Equation (46) then, there results

$$\tan \phi = \frac{\sin \phi}{\cos \phi} = - \frac{\beta}{a} \frac{R_1 (R_3 - R_2)}{R_3 (R_2 - R_1)}$$

$$= \frac{R_1}{R_3} \frac{(R_3 - R_2)}{(R_2 - R_1)} \tag{56}$$

4.0 FLIGHT CAPSULE HORIZONTAL VELOCITY ERROR ANALYSIS

From Equations (22) and (23) and under the condition that $\alpha = \beta$, the horizontal velocity is

$$V_H^2 = \left(\frac{\cos^2\theta}{4\alpha^2} + \frac{\sin 2\theta}{4\alpha\theta} + \frac{\sin^2\theta}{4\gamma^2}\right) D_1^2 + \left(\frac{1}{4\alpha^2} + \frac{\cos^2\theta}{4\alpha^2}\right) D_2^2$$
$$+ \left(\frac{1}{4\alpha^2} + \frac{\sin^2\theta}{4\gamma^2}\right) D_3^2 + \left(-\frac{2\cos^2\theta}{4\alpha^2} - \frac{\sin 2\theta}{4\alpha\gamma}\right) D_1 D_2$$
$$+ \left(\frac{\sin 2\theta}{4\alpha\gamma} + \frac{2\sin^2\theta}{4\gamma^2}\right) D_1 D_3 + \left(-\frac{2}{4\alpha^2} - \frac{\sin 2\theta}{4\alpha\gamma}\right) D_2 D_3 \qquad (57)$$

The horizontal velocity is given here in the form rather than V_H since this approach somewhat simplifies the subsequent error analysis. It should be noted that although V_H is not directly affected by the angle ϕ, the magnitude of the range rates (of the three beams) is directly affected by angle ϕ. Thus, if a fixed percentage error is assumed in the measurement of the range rates, the magnitudes of the error in range rate (and consequently in horizontal velocity error) will be a strong function of ϕ. The relative error in V_H^2 may be defined as

$$E(V_H^2) = \frac{V_H^2(\theta + \Delta\theta, D_1 + \Delta D_1, D_2 + \Delta D_1, D_3 + \Delta D_3) - V_H^2(\theta, D_1, D_2, D_3)}{V_H^2(\theta, D_1, D_2, D_3)} \qquad (58)$$

where $\Delta\theta$, ΔD_1, ΔD_2, ΔD_3 are the errors in the parameters θ, D_1, D_2 and D_3 respectively.

There are no errors in α and γ since these parameters are fixed exactly by the beam geometry. Writing a Taylor series expansion for the perturbation of V_H^2,

$$V_H^2(\Delta) = V_H^2(\theta + \Delta\theta \quad D + \Delta D_1, D_2 + \Delta D_2, D_3 + \Delta D_3)$$
$$= V_H^2 + \Delta\theta \frac{\gamma}{\gamma\theta} V_H^2 + \Delta D_1 \frac{\gamma}{\gamma D_1} V_H^2 + \Delta D_2 \frac{\gamma V_H^2}{\gamma D_2} + \Delta D_3 \frac{\gamma V_H^2}{\gamma D_3}$$
$$+ \text{higher order derivatives} \qquad (59)$$

where

$$V_H^2 = V_H^2(\theta, D_1, D_2, D_3) \qquad (60)$$

and $\Delta\theta$, ΔD_1, ΔD_2, ΔD_3 are small perturbations in the parameters. By performing the operations indicated in Equation (59) and substituting the values thus obtained into Equation (58) gives

$$
\begin{aligned}
E(V_H^2) = \frac{1}{4 V_H^2} \Bigg\langle & \Delta\theta \Bigg\{ \left[-\frac{\sin 2\theta}{a^2} + \frac{2\cos 2\theta}{a\gamma} + \frac{\sin 2\theta}{\gamma^2} \right] D_1^2 \\
& - \frac{\sin 2\theta}{a^2} D_2^2 + \frac{\sin 2\theta}{\gamma^2} D_3^2 \\
& + \left[\frac{2\sin 2\theta}{a^2} - \frac{2\cos 2\theta}{a\gamma} \right] D_1 D_2 + \left[\frac{2\cos 2\theta}{a\gamma} + \frac{2\sin 2\theta}{\gamma^2} \right] D_1 D_3 \\
& - \frac{2\cos 2\theta}{a\gamma} D_2 D_3 \Bigg\} \\
& + \Delta D_1 \Bigg\{ 2D_1 \left[\frac{\cos^2\theta}{a^2} + \frac{\sin 2\theta}{a\gamma} + \frac{\sin^2\theta}{\gamma^2} \right] \\
& + D_2 \left[-\frac{2\cos^2\theta}{a^2} - \frac{\sin 2\theta}{a\gamma} \right] + D_3 \left[\frac{\sin 2\theta}{a\gamma} + \frac{2\sin^2\theta}{\gamma^2} \right] \Bigg\} \\
& + \Delta D_2 \Bigg\{ 2D_2 \left[\frac{1+\cos^2\theta}{a^2} \right] + D_1 \left[-\frac{2\cos^2\theta}{a^2} - \frac{\sin 2\theta}{a\gamma} \right] \\
& + D_3 \left[\frac{-2}{a^2} - \frac{\sin 2\theta}{a\gamma} \right] \Bigg\} \\
& + \Delta D_3 \Bigg\{ 2D_3 \left[\frac{1}{a^2} + \frac{\sin^2\theta}{\gamma^2} \right] + D_1 \left[\frac{\sin 2\theta}{a\gamma} + \frac{2\sin^2\theta}{\gamma^2} \right] \\
& + D_2 \left[-\frac{2}{a^2} - \frac{\sin 2\theta}{a\gamma} \right] \Bigg\} \Bigg\rangle
\end{aligned}
\tag{61}
$$

The error in V_H may now be determined from the error in V_H^2 as follows. Let the perturbation in V_H be,

$$P(V_H) = V_H + \Delta V_H \tag{62}$$

The perturbation in V_H^2 is then

$$P(V_H^2) = V_H^2 + 2V_H(\Delta V_H) + (\Delta V_H)^2 \tag{63}$$

Thus, the error in V_H is,

$$E(V_H) = \frac{P(V_H) - V_H}{V_H} = \frac{\Delta V_H}{V_H} \tag{64}$$

and the error in V_H^2 is

$$E(V_H^2) = \frac{P(V_H^2) - V_H^2}{V_H^2} = \frac{2V_H(\Delta V_H) + (\Delta V_H)^2}{V_H^2} \tag{65}$$

when $\Delta V_H << V_H$, then

$$E(V_H^2) \cong \frac{2(\Delta V_H)}{V_H} = 2E(V_H) \tag{66}$$

or

$$E(V_H) \cong \frac{E(V_H^2)}{2} \tag{67}$$

A computer program has been written for to solve Equation (61) for various parameter values. The results are discussed in paragraph 8.5.4 of this report.

APPENDIX G

DESIGN CONSIDERATIONS FOR THE VELOCITY ATTITUDE SENSOR

1.0 INTRODUCTION

Appendix F showed that a three-(narrow) beam radar system can be used to measure the altitude, velocity, and attitude of a planetary probe relative to a planet-oriented reference frame. It was shown there that the minimum requirements could be met by a velocity-attitude sensor system designed to measure range and range rate along three pencil beams suitably oriented with respect to a flight capsule body-fixed coordinate system. This appendix discusses the instrumentation required for the basic velocity-attitude (V-A) sensor system.

2.0 RADAR SYSTEM DESIGN

The type of radar system chosen for the integrated altitude, velocity and attitude sensor is frequency modulated continuous wave (FM/CW). The FM/CW system appears attractive from the standpoint of minimizing system complexity, weight, and volume while concurrently maximizing transmitter efficiency. A block diagram of the basic three-beam system appears in Figure G-1.

In the FM/CW system illustrated in that figure, the klystron transmitting tube is frequency modulated by a triangular waveform at a rate f_m (in Hz). The peak frequency deviation is Δf (in Hz). A small fraction of the transmitter power is sampled and used as a coherent reference in the balanced mixers. The frequency-time relationships in the FM/CW system, in the absence of relative motion between the radar system and its target, are illustrated in Figure G-2. The time delay between the transmitted and received signals is $\tau = \frac{2R}{V_c}$. The range (R) is extracted by measuring the range beat frequency, f_r, given by

$$f_r = \dot{f}_o \, \tau \qquad (1)$$

where:

$\dot{f}_o$ = rate of change of transmitted signal frequency

τ = time delay corresponding to range to be measured

Since

$$\dot{f}_o = 4 f_m \Delta f, \quad \text{then} \quad f_r = (4 f_m \Delta f) \left(\frac{2R}{v_c}\right)$$

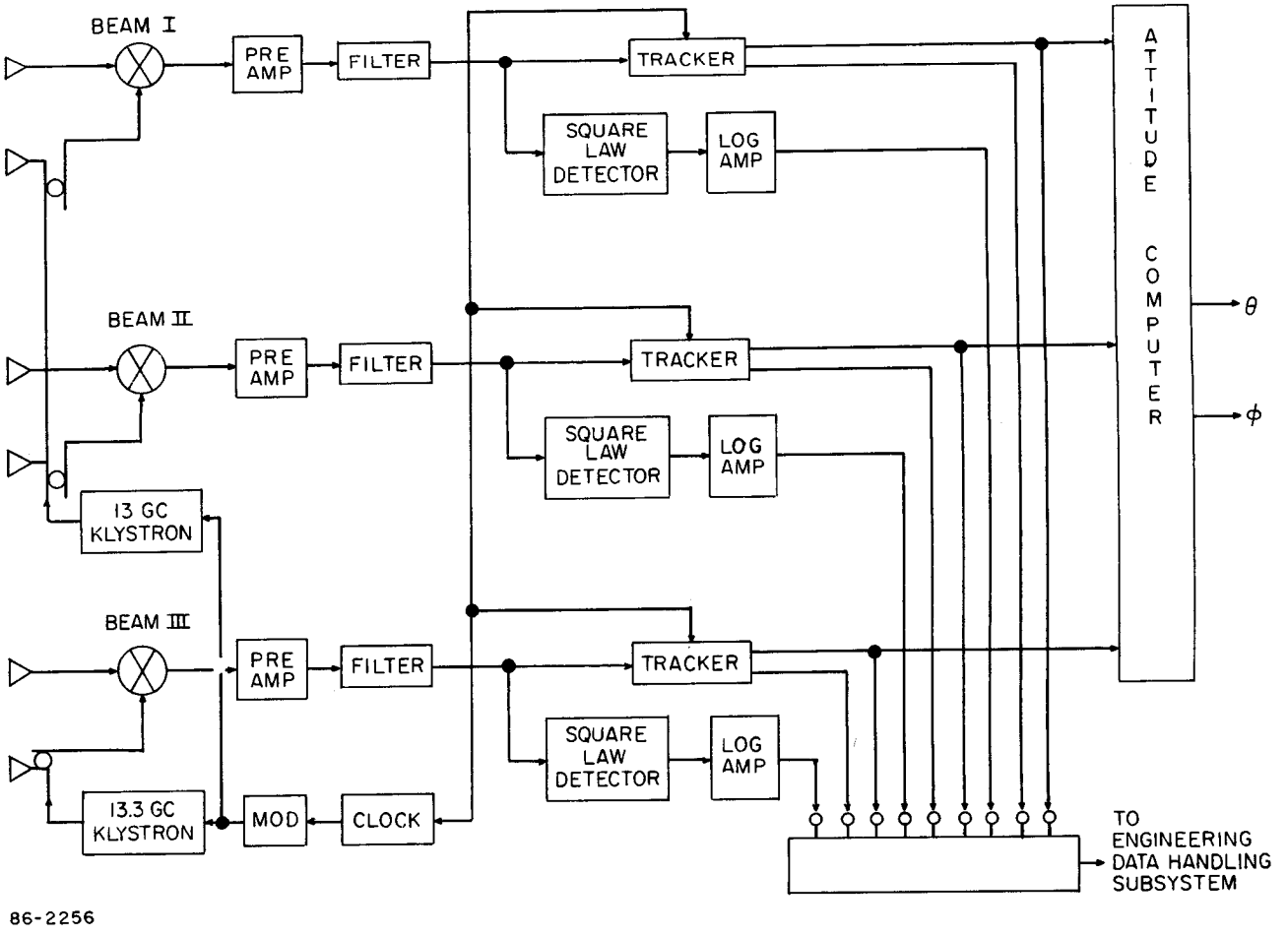

Figure G-1 BLOCK DIAGRAM OF VA SENSOR

or

$$f_r = \frac{8 f_m \Delta f}{v_c} R \qquad (2)$$

In the presence of doppler shifts resulting from relative motion between the radar and its target, the plot of instantaneous received frequency illustrated in Figure G-2 is shifted up or down by the appropriate doppler shift f_d (in Hz).

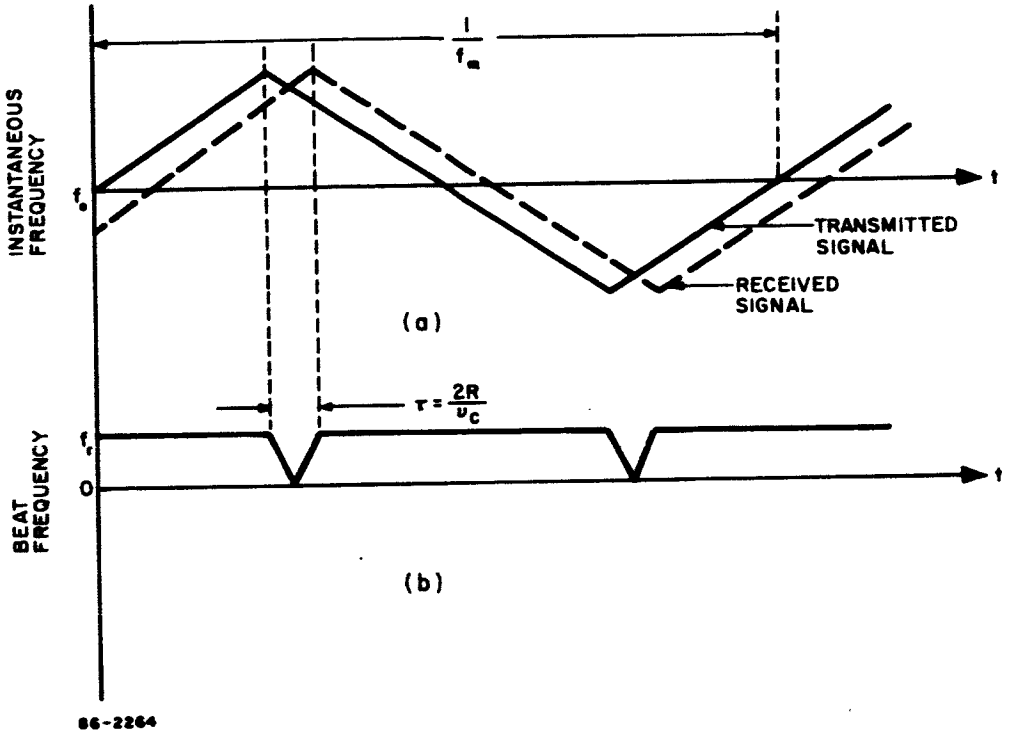

Figure G-2 FREQUENCY TIME RELATIONSHIPS IN FM/CW RADAR

The usual narrow-band approximation for f_d is

$$f_d = \frac{2\dot{R}}{v_c} f_o \qquad (3)$$

where:

f_o = transmitter center frequency

$\dot{R}$ = radial range rate

v_c = velocity of light in same units as $\dot{R}$

The frequency-time relationships for both a closing and an opening geometry are illustrated in Figure G-3. In the discussion that follows f_+ represents the beat frequency measured during the time the transmitted signal is increasing in frequency and f– represents the beat frequency measured during the time the transmitted signal is decreasing in frequency. From the same figure it can be seen that

For $f_d > 0$ (i.e., closing target)

$$f_+ = f_r - |f_d|$$

$$f_- = f_r + |f_d| \tag{4}$$

Therefore,

$$f_r = \frac{1}{2}(f_+ f_-) \tag{5}$$

and

$$f_d = \frac{1}{2}(f_- - f_+) \tag{6}$$

For $f_d < 0$ (i.e., opening target)

$$f_+ = f_r + |f_d|$$

$$f_- = f_r - |f_d| \tag{7}$$

Therefore,

$$f_r = \frac{1}{2}(f_+ - f_-) \tag{8}$$

and

$$f_d = \frac{1}{2}(f_- - f_+) \tag{9}$$

It can be seen from the above expressions that the FM/CW system enables the range frequency, f_r, and both the magnitude and sign of the doppler shift, f_d, to be determined uniquely by forming respectively the quantities

$$f_r = \frac{1}{2}(f_+ + f_-) \tag{10}$$

and

$$f_d = \frac{1}{2}(f_- - f_+) \tag{11}$$

In the system illustrated in Figure G-1 these quantities are formed by counting the beat frequency over the respective times defining f_+ and f_-. Appropriate

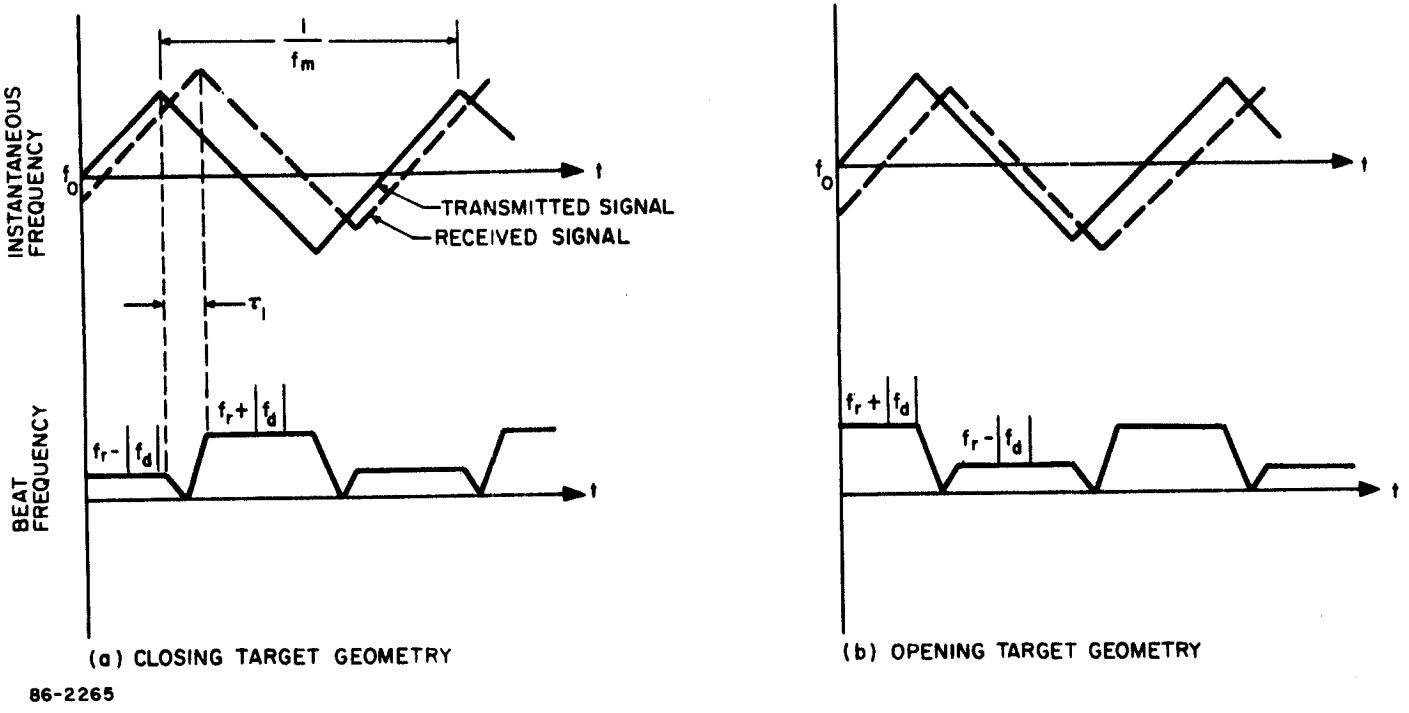

Figure G-3 FREQUENCY TIME RELATIONSHIPS IN FM/CW RADAR IN THE PRESENCE OF DOPPLER SHIFTS

synchronization pulses are used to signal the counter to initiate and terminate the intervals defining f_+ and f–. The computer forms the appropriate sum and differences given by Equations (10) and (11). The preceding discussion is based on the assumption that $f_r > f_d$. If this is not the case, the role of the sum and difference of f_+ and f– in determining f_r and f_d are interchanged. Thus, to avoid ambiguities, the system must be so designed that

$$f_{r\,(min)} \geq f_{d\,(max)} \tag{12}$$

This requirement significantly affects the overall radar system design. There is an additional inequality that must also be satisfied early in the design of an FM/CW radar system. If the time delay

$$\tau_1 = \frac{2R}{v_c} \tag{13}$$

amounts to an appreciable fraction of the total modulation cycle, shown on Figure G-3, significant errors can be introduced in the determination of f_+ and f–. It is necessary, therefore, that

$$\tau_1 = \frac{2R}{v_c} << \frac{1}{fm} \tag{14}$$

In particular, if τ_1 is to occupy only 1 percent of the total modulation cycle, then

$$f_m \leq \frac{V_c}{200\ R_{max}} \tag{15}$$

Let us now consider the maximum ranges involved for different maximum operating altitudes must be considered in designing the system. This requires analysis of the effects of possible flight capsule dynamics during parachute-aided descent. The three pencil beams will be directed at depression angles of 70-degrees relative to the body-fixed horizontal plane. If the vehicle can sway ±60 degrees about an equilibrium position, the depression angle (θ) could be as small as 10 degrees. The geometry is illustrated in Figure G-4.

As that indicates, the maximum range is given by

$$R_{max} = \frac{h_{max}}{\sin \theta_{min}} \tag{16}$$

where:

h_{max} = maximum operating altitude

θ_{min} = minimum depression angle

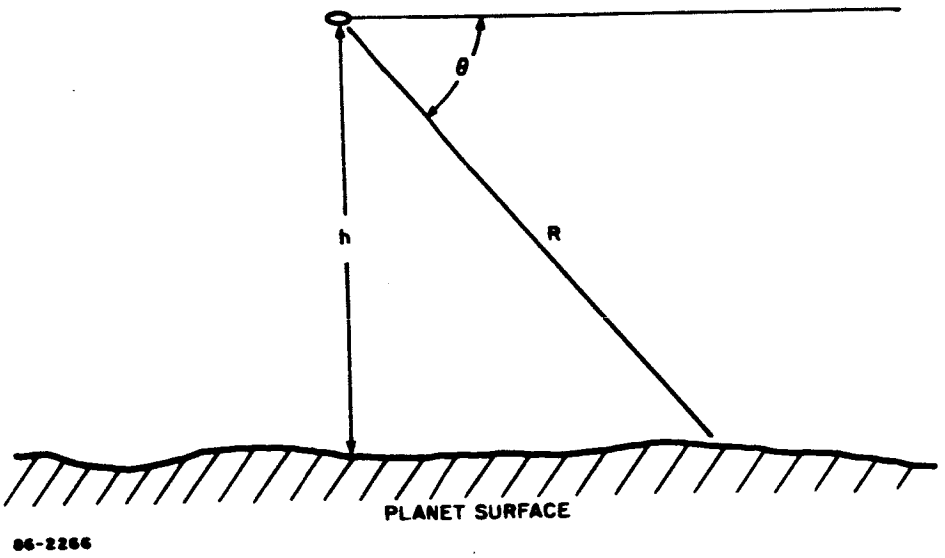

Figure G-4 GEOMETRY USED TO DETERMINE RANGE

As noted in Equation (16), in the absence of attitude stabilization the attitude displacement could be as great as ±60 degrees, resulting in θ_{min} = 10 degrees. Table G-1 indicates the maximum ranges involved for various maximum operating altitudes both for an attitude stabilized and a non-attitude stabilized flight capsule.

TABLE G-1

MAXIMUM RANGES FOR VARIOUS OPERATING ALTITUDES FOR BOTH STABILIZED AND NON-STABILIZED PAYLOAD

h_{max} (feet)	R_{max} (stabilized) (feet)	R_{max} (Non-Stabilized) (feet)
30,000	31,900	172,000
2,080	2,220	12,000
144	153	830
10	11	57

It is now possible to ensure that inequalities (12) and (15) are satisfied. Considering inequality (12) first, Equation (2) must yield

$$\frac{8 f_m \Delta f R_{min}}{V_c} \geq f_{d\,max} \tag{17}$$

Rearranging these terms gives

$$f_m \Delta f \geq \frac{v_c f_{d\ max}}{8 R_{min}} \tag{18}$$

Substituting into Equation (18) the value of f_m given in inequality (15) gives the peak frequency deviation

$$\Delta f \geq 25 \frac{R_{max}}{R_{min}} f_{d\,max} \tag{19}$$

The maximum doppler frequency, $f_{d_{max}}$, can be determined on the basis of certain assumptions regarding the flight horizontal capsule's and descent velocities. Equation (3) yields

$$f_{d_{max}} = 2 f_o \frac{\dot{R}_{max}}{v_c} \tag{20}$$

In the following calculations it is assumed that f_o = 13 gHz and that the maximum range rate $\dot{R}_{max}$ will be the maximum velocity attained by flight capsule.

Thus

$$\dot{R}_{max} = \sqrt{v_H^2 + v_Z^2} \tag{21}$$

where

v_H = payload maximum horizontal velocity

v_Z = payload maximum descent velocity

The maximum anticipated velocities are 300 fps for the horizontal component and 150 ft/sec for the vertical component. These values result in a maximum doppler shift of 8.9 kHz.

The values of Δf and f_m required to satisfy inequalities (12) and (15) can now be tabulated. These are listed in Table G-2.

TABLE G-2

REQUIRED MODULATION CHARACTERISTICS FOR FM/CW RADAR

v_H (ft/sec)	v_z (Hz)	$F_{d\,max.}$ (kHz)	h_{max} (feet)	h_{min} (feet)	$(\Delta F)min$ (MHz)	F_m(stabil.max) (Hz)	F_m(unstab. max) (Hz)
300	150	8.9	30,000	2080	3.2	155	29
			2080	144	3.2	2230	411
			144	10	3.2	32200	5900

As inequality (19) indicates, the required peak frequency derivation, Δf, is a function of the ratio R_{max}/R_{min}. This is evident in the Table. Furthermore, although Δf is not a function of whether or not the flight capsule is attitude-stabilized, the modulation rate f_m is a function of the capsule's stability.

The next step in the design of the integrated radar altitude, velocity, and attitude sensor is to consider the accuracy with which the required measurements can be obtained. The first source of error is the step error inherent in the use of the counter to measure the quantities f+ and f–. The average number of cycles N+ of the beat frequency f+ in one-half period of the modulation cycle is

$$N_+ = \frac{\bar{f}_+}{2f_m} \tag{22}$$

Similarly, for beat frequency f–,

$$N_- = \frac{\bar{f}_-}{2f_m} \tag{23}$$

Now for Equation (10)

$$\bar{f}_r = \frac{1}{2}\,[f_+ + f_-] \tag{24}$$

Substituting into Equation (24) values of f+ and f– obtained from Equations (22) and (23) gives

$$\bar{f}_r = f_m\,[N_+ + N_-] \tag{25}$$

The average range can now be obtained from Equation (2) by substituting into that equation the value of $\bar{f}_r$ obtained on Equation (25).

$$\bar{R} = \frac{v_c}{8\Delta f} [N_+ + N_-] \tag{26}$$

By letting $N_+ + N_- = N$, an integer, Equation (26) becomes

$$\bar{R} = \frac{v_c}{8\Delta f} N \tag{27}$$

Thus, the average range will be an integral multiple of $\frac{v_c}{8\Delta f}$ and the quantization error will be equal to

$$\delta R = \frac{v_c}{8\Delta f} \tag{28}$$

It should be noted that the fixed error is independent of the range and carrier frequency and is a function of the frequency deviation, Δf, only. Large frequency deviations are necessary if the fixed error is to be small. If the same frequency deviation is used at all altitudes, then the quantization error will also be the same at all altitudes. Therefore, the value of Δf is dictated by the low altitude. For example, an accuracy of ±2 feet at an altitude of 10 feet. The deviation is then

$$\Delta f \geq \frac{v_c}{(8)(2)} \tag{29}$$

or

$$\Delta f \geq 62 \text{ MH}_z$$

The step error in the counter also determines the accuracy with which the doppler shift can be measured, and, therefore, the accuracy with which range rate can be determined.

From Equation (3),

$$f_d = \frac{2\dot{R}}{v_c} f_o$$

Substituting into Equation (11) the values of f+ and f– obtained in Equations (22) and (23) give

$$f_d = f_m (N_- - N_+) \tag{30}$$

By substituting into Equation (30) the value of f_d obtained in Equation (3), and letting $N_- - N_+ = N$, an integer, Equation (30) becomes

$$\frac{2\dot{R}f_o}{v_c} = f_m N \tag{31}$$

Solving for $\dot{R}$ gives

$$\dot{R} = \frac{N f_m v_c}{2f_o} \tag{32}$$

The quantization error, then, is

$$\delta\dot{R} = \frac{f_m v_c}{2f_o} \tag{33}$$

f_m, therefore, is constrained as follows,

$$f_m \leq \frac{2\delta\dot{R}f_o}{v_c} \tag{34}$$

For a carrier frequency of 13 kHz and a 5-ft/sec quantization error, f_m must be equal to or less than 132 Hz. This contradicts the entries in Table G-2 which were based on inequality (18). However, the required range quantization error necessitated a larger Δf (Equation (29)), than that appearing the Table G-2 with the result that f_m must be 1.76 kHz to satisfy inequality (18). This is still too high to satisfy the quantization error constraint. A compromise must be made, therefore, between the desired range rate accuracy and the frequency deviation that can be attained in a microwave tube. Table G-3 shows the applicable tradeoff's.

TABLE G-3

QUANTIZATION ERROR AND FREQUENCY DEVIATION TRADEOFFS IN THE LOWEST ALTITUDE RANGE

Δf (MHz)	$f_{m(min)}$ (kHz)	Range Rate Quantization Error (ft/sec)	Range Quantization Error (feet)
25	4.36	164	0.5
50	2.18	82	2.5
100	1.09	41	1.2
200	0.55	22	0.6

It should be noted that this difficulty arises only in the lowest altitude range (144 to 10 feet). In the other two ranges considered in Table G-2 $f_m \Delta f$ (inequality (18)) does not have to be as large. Thus, the requirement for Δf can be relaxed and/or f_m can be made smaller to reduce the range rate quantization error. This, of course, would increase the quantization error on the range measurement. However, at higher altitudes, errors on the order of 10 feet can be tolerated.

Attainment of the above accuracies, however, is based on the assumption that the SNR is arbitrarily large, and that all inaccuracies can be attributed to the step error in the counter. In reality, there is a more fundamental restriction on accuracy and consistent with the operating SNR. Skolnik[1] gives the relative rms error in measuring frequency as a function of SNR as follows

$$\frac{\delta f}{f} = \frac{1}{2\pi \left(\frac{S}{N}\right)^{1/2}} \tag{35}$$

Thus, the error in measuring range or range rate is either that predicted by Equation (36) or the inherent quantization error, whichever is larger. Table G-4 indicates the SNR required from Equation (35) to achieve some typical measurement accuracies.

With these calculations complete, transmitted power requirements can be defined, as discussed in the following paragraphs.

TABLE G-4

SNR REQUIRED TO ACHIEVE VARIOUS RELATIVE RMS ACCURACIES IN MEASURING RANGE AND RANGE RATE

Relative rms Error (percent)	SNR Required (decibels)
1	24
5	10
10	4

3.0 TRANSMITTED POWER REQUIREMENTS

The transmitted power (P_T) requirements are determined from the familiar radar range Equation

[1]Skolnik, M. I., Introduction to Radar Systems, McGraw-Hill Book Co., N.Y., p. 462 (1962).

$$P_R = \frac{P_T G^2 \lambda^2 \sigma}{(4\pi)^3 R^4} \tag{37}$$

where:

P_R = received signal power

G = antenna gain

R = one-way range

σ = radar cross section

λ = wavelength of the frequency of interest

The radar cross section used in Equation (37) is defined as four times the ratio between the reflected power per unit solid angle in the direction of the source and the power per unit area in the incident wave. Thus, if the target were to scatter power uniformly over all angles, its radar cross section would be equal to the effective area from which power was extracted from the incident wave. The above definition of radar cross section is useful for targets which intercept only a small portion of the illuminating antenna beam. However, it loses its significance for targets of practically infinite extent, such as a planetary surface. In this latter case the radar cross section becomes a function of range, antenna pattern, and depression angle. It has been shown[2] that for the case of extended targets Equation (37) becomes

$$P_R = \frac{P_T \lambda^2}{(4\pi)^3} \int_A \frac{G^2(\theta, \phi)\, \sigma_o(\theta, \phi)}{R^4}\, dA \tag{38}$$

where the integration is carried out over the physical area illuminated on the surface of the planet. The angles θ and ϕ are, respectively, the depression angle and the azimuth angle (or look angle) measured from the beam axis. The geometry for a single-resolution element, dA, is shown in Figure G-5.

This element (dA) is equal to $(R^2\, d\theta\, d\phi)/\sin\theta$. Substituting this value into Equation (38) gives

$$P_R = \frac{P_T \lambda^2}{(4\pi)^3} \iint \frac{G^2(\theta, \phi)\, \sigma_o(\theta, \phi)\, d\theta\, d\phi}{R^2 \sin\theta} \tag{39}$$

[2]Moore, R. K., and C. S. Williams, Jr., Radar Terrain Return at Near Vertical Incidence, Proc. IRE, pp. 228-238 (February 1957).

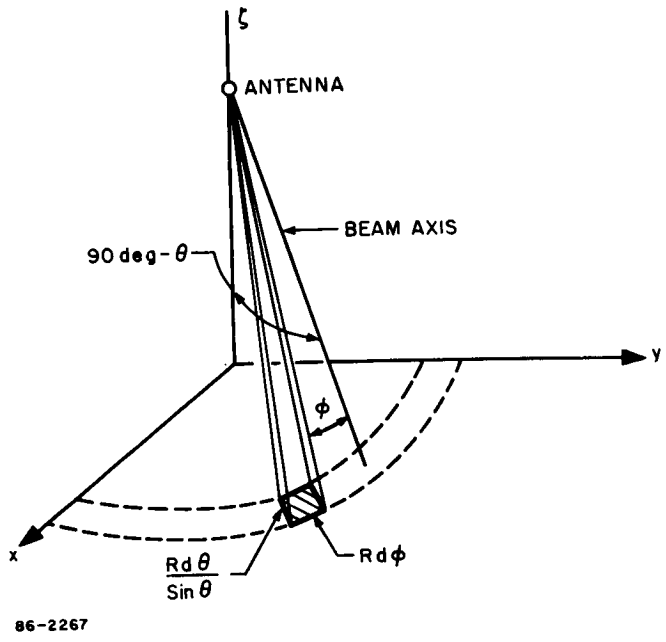

Figure G-5 GEOMETRY OF SINGLE RESOLUTION ELEMENT ON PLANETARY SURFACE

Actually, exact computation of the integral in Equation (39) requires a thorough statistical analysis due to the random nature of the planetary terrain. Rather than attempt this at the present time, the following customary simplications can be made.

The first such simplification is to consider the average received power. This can be defined as

$$< P_R > = \frac{P_T \lambda^2}{(4\pi)^3} \iint \frac{G^2(\theta, \phi) < \sigma_o(\theta, \phi) > d\theta d\phi}{R^2 \sin\theta} \tag{40}$$

where $<\sigma_o(\theta, \phi)>$ = average echoing area per unit area of the planetary surface. If it is assumed that the return results from scatterers uniformly distributed over the effective illuminated area on the surface of the planet, there is independent of θ, ϕ, and

$$\sigma^\circ = < \sigma_o(\theta, \phi) > \quad . \tag{41}$$

Substituting this value for $<\sigma_o(\theta, \theta)>$ into Equation (40) gives

$$< P_R > = \frac{P_T \lambda^2 \sigma^\circ}{(4\pi)^3} \iint \frac{G^2(\theta, \phi) d\theta d\phi}{R^2 \sin\theta} \tag{42}$$

In the case of the narrow (pencil) beam of interest, it can be assumed that the primary contribution to the integral in Equation (42) occurs only within the primary lobe of the antenna pattern. The quantity $G(\theta, \phi)$ is then given approximately as

$$G(\theta, \phi) = G \, \mathrm{Rect}_{\Phi}(\phi) \, \mathrm{Rect}_{\psi}(\theta - \theta_o) \tag{43}$$

where

ϕ = horizontal plane half-power beamwidth

ψ = vertical plane half-power beamwidth

θ_o = depression angle of beam axis

and

$$\mathrm{Rect}_{\Lambda}(\xi) = 1$$

where

$$(-\Lambda/2) \leq \xi \leq (+\Lambda/2)$$

and

$\mathrm{Rect}_{\Lambda}(\xi)$ = 0 for all other cases.

Thus, the integral in Equation (42) becomes approximately

$$< P_R > \cong \frac{P_T \lambda^2 \sigma^o}{(4\pi)^3} G^2 \iint \frac{\mathrm{Rect}_{\Phi}(\phi) \, \mathrm{Rect}_{\psi}(\theta - \theta_o) \, d\theta \, d\psi}{R^2 \sin\theta} \tag{44}$$

Assuming that $R^2 \sin\theta$ does not change appreciably over the illuminated area (a reasonable assumption for near-vertical incidence) then

$$\iint \frac{G^2(\theta, \phi) \, d\theta \, d\phi}{R^2 \sin\theta} \cong \frac{G^2 \Phi \psi}{R^2 \sin\theta_o} \tag{45}$$

Substituting this result in Equation (42) gives

$$< P_R > \cong \frac{P_T \lambda^2 G^2 \Phi \psi \sigma^o}{(4\pi)^3 R^2 \sin\theta_o} \tag{46}$$

The average received SNR can be expressed, therefore, as

$$\left(\frac{S}{N}\right)_{avg} = \frac{< P_R >}{N_o\ BW} \simeq \frac{P_T\ \lambda^2\ G^2\ \Phi\ \psi\ \sigma^o}{(4\pi)^3\ R^2\ N_o\ BW \sin\theta_o} \tag{47}$$

where:

N_o = noise spectral density

BW = receiver noise bandwidth

The transmitted power requirements can now be determined from Equation (47). In logarithmic notation, the equation may be written as

$$P_T = \left(\frac{S}{N}\right)_{avg} + L_s + N_o + BW - 2G - \Phi - \psi - L_R \tag{48}$$

where:

L_s = $20 \log_{10} \frac{4\pi R}{\lambda}$ (space loss)

L_R = $10 \log_{10} \frac{\sigma^o}{4\pi \sin\theta_o}$ (receiver loss)

The transmitted power requirements for the FM/CW system can now be calculated for the specific design parameters listed in Table G-5. These parameters correspond to an unstabilized system with a maximum operating altitude of 30, 000 feet. The following comments are pertinent regarding certain of the parameters on that table. The value of σ^o was chosen as -30 db. This choice is based on results obtained by Povejsil[3] et al. In particular, this reference shows plots of σ^o for typical Earth terrain versus the angle of depression θ degrees for a number of different frequencies. At 13 gHz the results indicate σ^o is approximately in the range from -20 to -30 db. The value assigned to σ^o is, essentially, a worst-case value. It will become apparent that the choice of σ^o can significantly effect transmitted power requirements.

The value assigned for the receiver noise bandwidth, BW, in Appendix E was determined as follows. The receiver must have a bandwidth at least wide enough to handle the sum of the frequency of the largest doppler shift and the largest range frequency, thus

$$BW \geq f_{d_{max}} + f_{r_{max}} \tag{49}$$

For the velocities considered, $f_{d_{max}}$ is 9 kHz. The value of $f_{r_{max}}$ is given by

$$f_{r_{max}} = \frac{8 f_m \Delta f}{v_c} R_{max} \tag{50}$$

[3] Povejsil, D. J., R. S. Raven, and P. Waterman, Airborne Radar, Boston Tech. Publishers, Inc., Cambridge, Mass., 1965, pp. 219-222. (1966).

TABLE G-5

FM/CW RADAR SYSTEM PARAMETERS

Symbol	Parameter	Value
P_T	Transmitted power	To be determined
h_{max}	Maximum operating altitude	30,000 ft
R_{max}	Maximum Range (see Table G-1)	172,000 ft
G	Antenna Gain (15-inch dish)	30 db
Φ	Horizontal plane beamwidth	5 degrees
ψ	Vertical plane beamwidth	5 degrees
f_o	Operating frequency	13 kMHz
N_o	Noise spectral density (12 db NF)	-102 dbm/MHz
θ_o	Depression angle	10 deg/minute
σ°	Average echoing area/unit area	-30 db
BW	Noise bandwidth	0.75 MHz

On the basis of previous considerations, as tabulated in Table G-3, 100 mHz has been selected for Δf. Therefore, the minimum f_m and quantization errors for all three ranges are the same as those shown in Table G-6.

TABLE G-6

Δf AND f_m FOR VARIOUS ALTITUDE RANGES

Altitude (feet)	Δf (MHz)	f_m	$\dot{R}$ Quantization Error (ft/sec)	R Quantization Error (feet)
30,000 to 2080	100	5 Hz	0.2	1.2
2080 to 144		77 Hz	3	1.2
144 to 10		1.1 kHz	41	1.2

By substituting the appropriate parameter values into Equation (50), and with the value for R_{max} given in Table G-1.

$$f_{r_{max}} \cong 0.74 \text{ MH}_z \tag{51}$$

The receiver noise bandwidth, BW, is, therefore

$$\begin{aligned} BW &\cong 0.74 \text{ m H}_z + 9\text{k H}_z \\ &\cong 0.75 \text{ m H}_z \end{aligned} \tag{52}$$

The transmitted power requirements are based on the values given in Table G-7. The value for the SNR required to achieve a specified relative rms error in measuring either range or range rate is taken from Table G-4. The resulting transmitted power requirements are summarized in Table G-8. This table indicates the average transmitted power requirements per beam for an unstabilized payload operating at altitudes from 30, 000 to 10 feet. It is obvious that even for allowable errors as high as 10 percent, the transmitter power requirements are prohibitive. The high power requirements are a direct result of the large bandwidth required to insure sufficient range resolution. If the range measuring requirement could be eliminated, as would be the case, for instance, if the flight capsule were stabilized and there were consequently no need to measure attitude, the transmitted power requirements could be significantly reduced. Likewise, if a suitable range tracking scheme could be developed which would enable f_r and f_d to be determined unambiguously, the bandwidth, and hence, the transmitter power requirements could be significantly reduced.

TABLE G-7

POWER BUDGET FOR FM/CW RADAR

L_s (R_{max} = 172, 000 ft)	149.1 db
BW_{mc} (0.75 MH_z)	-1.2 db
$-\Phi$ (5 degree Beamwidth)	10.6 db
$-\psi$ (5 degree Beamwidth)	10.6 db
$-L_R$ (σ° = -30 db, θ_o % 10 degrees)	33.4 db
Σ_1 =	202.5ddb
$-N_o$ (12 db NF)	102 db
2G (30 db gain)	60 db
	162 db
$P_T = \left(\frac{S}{N}\right)_{avg} + \Sigma_1 - \Sigma_2$	
$P_T = \left(\frac{S}{N}\right)_{avg+40;\,5\,db}$	

TABLE G-8

TRANSMITTED POWER REQUIREMENTS FOR VARIOUS RELATIVE RMS ACCURACIES

Relative rms Accuracy (percent)	P_T (h_{max} = 30, 000 ft)
1	2.8 kwatts
5	120 watts
10	28 watts

4.0 CONCLUSIONS

A number of problems must be resolved to enable the V-A sensor to be used as a suitable range and range rate measuring device. The tradeoffs that can be made to render the system suitable for such an application are discussed in paragraph 3.8.5 of this report.

APPENDIX H

DOPPLER ECHO SPECTRUM AND ALTIMETER ANCILLARY FUNCTIONS

1.0 INTRODUCTION

This appendix covers two aspects of radar altimeter operation. It shows that the radar echo contains all information needed to enable the altimeter to be used to obtain valid estimates of horizontal wind velocities and of the roughness of the planetary surface. It also indicates the basic requirements for a data processor capable of extracting wind velocity and surface roughness data from the radar echo signal.

2.0 DOPPLER SHIFT AND DOPPLER BANDWIDTH

For the geometrical conditions shown on Figure H-1, the doppler shift, f. of the radar echo is given by the following equation

$$f = \frac{2\vec{v} \cdot \vec{\rho}}{\lambda \cdot \rho} \qquad (1)$$

$$= 2 \frac{v}{\lambda} \cos \phi$$

where

$\vec{v}$ = vehicle velocity relative to the target

$\frac{\vec{\rho}}{\rho}$ = direction of radar target

λ = wavelength

and the angle ϕ is as defined on Figure H-1.

Differentiating Equation 1 with respect to ϕ yields the doppler spectrum width, Δf , in terms of the beamwidth, $\Delta\phi$, and the angle ϕ between the velocity vector and the antenna boresight. The doppler spectrum width can, therefore, be expressed as

$$\Delta f = - \frac{2v}{\lambda} \sin \phi \, \Delta\phi. \qquad (2)$$

If v is the horizontal velocity and the altimeter is looking vertically down at the planetary surface, then

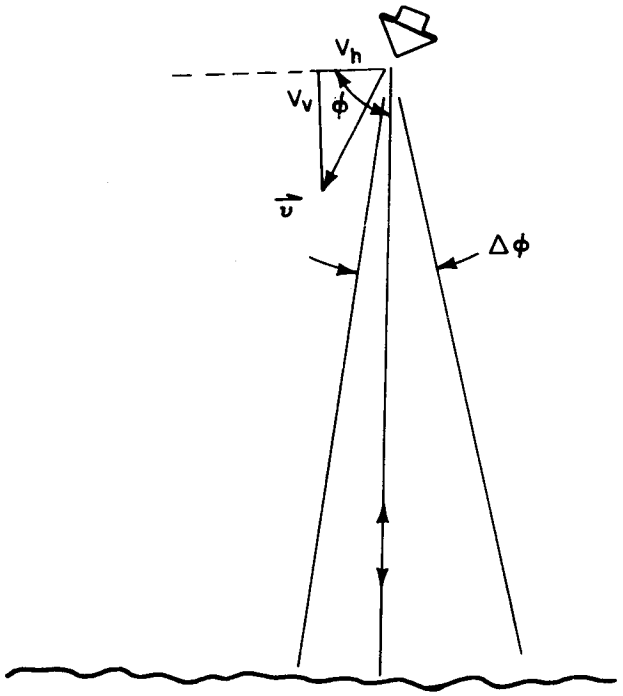

$$\bar{f} = \frac{2\vec{v}\cdot\vec{\rho}}{\lambda\,\rho}$$

$$\Delta f = -\frac{2v_h}{\lambda}\,\Delta\phi$$

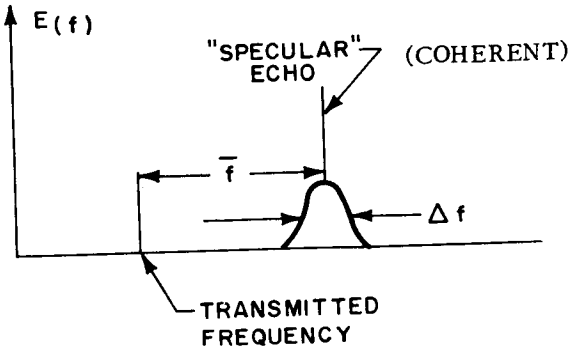

85-0350

Figure H-1 SPREAD OF DOPPLER FREQUENCIES

$$\Delta f = \frac{2v}{\lambda} \alpha \Delta\phi \qquad (3)$$

The factor α in Equation (3) represents some average value of sin ϕ. For many practical cases, it will not depart much from unity and, in any event, its value can be entered in the system by appropriate calibration.

3.0 TIME DOMAIN DATA REDUCTION

It is important to note that the proposed method of extracting wind-velocity and surface-roughness information from the radar return, involves measurement of the spectral bandwidth, the diffuse power in the return signal and the spectral power in the return signal. It is convenient to think of these parameters as being derived from the power spectrum. However, the complete power spectrum need not be constructed. Instead, only certain spectral characteristics are necessary in making the wind-velocity and surface-roughness measurements. These can be obtained by suitably processing the time waveform. This procedure is described in the following paragraphs.

Hard limiting of the echo waveform is applied in the time domain. Middleton and Van Vleck have determined that infinite clipping of a signal whose spectrum consists of a band centered around a dominating line will only negligible distort the power spectrum. In Figure H-2 the echo's coherent component due to

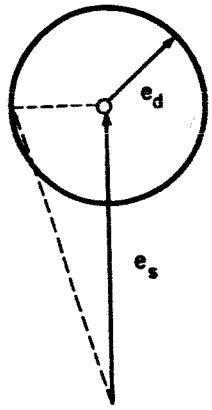

Figure H-2 REPRESENTATION OF DIFFUSE AND SPECULAR RETURNS

specular reflection is represented by the vector e_s. The diffuse echo can be represented by an additive random vector e_d. This echo randomly modulates the coherent component both in amplitude and phase. Hard limiting removes the amplitude modulation, but the phase modulation remains unaffected (provided $|e_s| > |e_d|$). It is clear from Figure H-2 that the depth of the phase modulation is a measure for the relative power in the diffuse echo. It is also clear that the rate of the phase modulation equals the difference between the frequency of the coherent component and the modulating frequency. The rate, therefore,

serves as a measure for the bandwidth of the diffuse spectrum. Hence, the parameters that must be extracted from the echo are the rate and the index of phase modulation.

In the ancillary functions data processor, described in paragraph 8. 9. 1. 1, the doppler cycle length, τ , is measured and extreme values τ_l are registered at the time of trand inversions. These are defined as

$$\tau_{k-1} \qquad (4)$$

$$\tau_{k+1}$$

where either both are less than τ_k or both are greater than τ_k . The train of intervals, τ_k , represent an essentially instantaneous doppler frequency, that is,

$$f_k = \frac{1}{\tau_k} \qquad (5)$$

This frequency may be interpolated to form a continuous function of time. Such a function is shown in Figure H-3. Since frequency is the rate of change of phase, then

$$f = \frac{1}{2\pi} \frac{d\phi}{dt} \qquad (6)$$

and trend inversions are those points for which

$$\frac{df}{dt} = \frac{d^2\phi}{dt^2} \qquad (7)$$

$$= 0$$

If the central frequency specular signal component is denoted by a vector $\vec{e}_c$ and the "skirt" frequency component is represented by the fluctuating vector $\vec{e}_d$, then

$$\vec{e}_s > \vec{e}_d \qquad (8)$$

when the specular echo dominates and, to a close approximation

$$\phi = \frac{e_d}{e_c} \qquad (9)$$

where ϕ equals the deviation of the noise-like phase modulation of the doppler-shifted specular echo.

In this concept the trend inversions are the inflection points, or axis crossings of the phase modulation. They occur twice in each cycle of the modulating waveform and they occur at exactly the Nyquist rate. It follows, therefore, that the rate of occurrence of trend inversions equals the bandwidth of the diffuse echo spectrum.

4.0 AVERAGE AND VARIANCE OF THE DOPPLER PERIOD

Let the deviation of the doppler period from its average value,

$$\bar{\tau}_l = \frac{1}{\bar{f}_o} \tag{10}$$

be denoted by $\Delta\tau$.

The variation in the period τ can be interpreted as a phase modulation onto a signal of center frequency f_o . The phase deviation is then

$$\Delta\phi = 2\pi f_o \Delta\tau \tag{11}$$

For small phase deviations, the power in the modulation, E_m , is

$$E_m = E_o (\Delta\phi)^2 \tag{12}$$

$$= 4\pi^2 E_o f_o^2 (\Delta\tau)^2$$

where E_o = carrier power.

The parameter $\Delta\tau$ is not measured directly. Instead, the total derivation

($\Delta\tau_l - \Delta\tau_{l-1}$) is measured. The variance of the probability distribution of the sum of two independent doppler periods is twice that of the probability distribution for a single observation, hence

$$\text{RMS}(\Delta\tau) = \frac{1}{\sqrt{2}} \text{RMS}(\Delta\tau_p + \Delta\tau_q) \tag{13}$$

On the other hand, the measured parameters ($\tau_l - \tau_{l-1}$) are equivalent to the peak values of the sum of two values for the deviation $\Delta\tau$. Therefore,

$$(\tau_l - \tau_{l-1}) = \sqrt{2}\ (\Delta\tau_p + \Delta\tau_q) \tag{14}$$

$$= \text{RMS}(\Delta\tau)$$

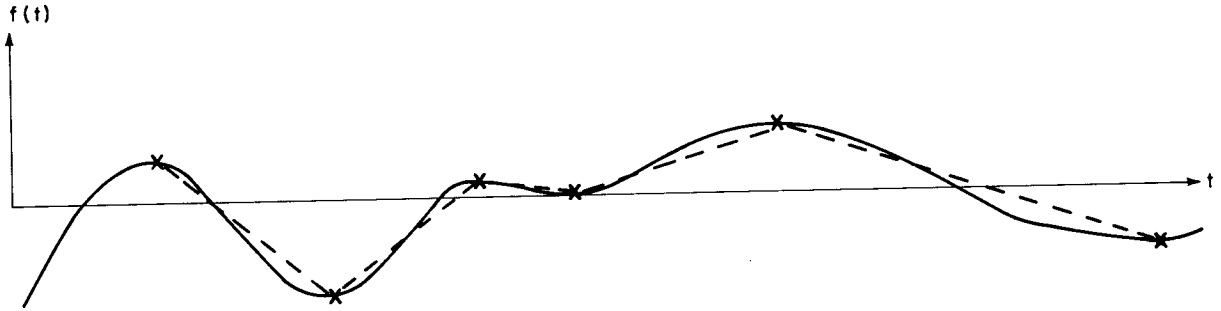

85-0351

Figure H-3 TRENDS INVERSIONS

Squaring and averaging Equation (14) gives

$$\overline{(\tau_l - \tau_{l-1})^2} = \overline{(\Delta r)^2} \tag{15}$$

The average power of the phase modulation can then be expressed as

$$\bar{E}_m = 4\pi^2 \bar{E}_o f_o^2 \overline{(\Delta r)^2} \tag{16}$$

$$= 4\pi^2 \bar{E}_o f_o^2 \overline{(\tau_l - \tau_{l-1})^2}$$

The phase modulation actually represents only one-half of the noncoherent (diffuse) portion of the echo power, that is

$$E_m = \frac{1}{2} E_{diff} \tag{17}$$

The coherent component of the echo is the specular component, that is

$$E_{spec} = E_o \tag{18}$$

The surface roughness, R , can be defined as the ratio between the diffuse and the specular echo. It can be expressed, therefore, in terms of these components of the echo as follows:

$$R = \frac{E_{diff}}{E_{spec}} = 8\pi^2 f_o^2 \overline{(\tau_l - \tau_{l-1})^2} \tag{19}$$

$$= 8\pi^2 \frac{\overline{(\tau_l - \tau_{l-1})^2}}{\bar{\tau}_l^2}$$